Faculty of Technology
School of Engineering, Media and Sustainable Development

Modelling and Simulation of Membrane Bioreactors for Wastewater Treatment

PhD THESIS

Tomasz Janus

Submitted in partial fulfilment of the requirements
for the degree of Doctor of Philosophy

September, 2013

I dedicate this thesis to Marta for her constant support, helping me in getting through difficult times and, most importantly, for her unconditional love.
I love you very much.

Abstract

The work presented in this thesis leads to the formulation of a dynamic mathematical model of an immersed membrane bioreactor (iMBR) for wastewater treatment. This thesis is organised into three parts, each one describing a different set of tasks associated with model development and simulation.

In the first part, the Author qualitatively and quantitatively compares various published activated sludge models, i.e. models of biochemical processes associated with bacterial growth, decay, lysis and substrate utilisation in activated sludge systems. As the thesis is focused on modelling membrane bioreactors (MBRs) which are known to experience membrane fouling as a result of adsorption of biopolymers present in the bulk liquid onto and within the membrane, all activated sludge models considered in this thesis are able to predict, with various levels of accuracy, the concentrations of biopolymeric substances, namely soluble microbial products (SMP) and extracellular polymeric substances (EPS). Some of the published activated sludge models dedicated to modelling SMP and EPS kinetics in MBR systems were unable to predict the SMP and EPS concentrations with adequate levels of accuracy, without compromising the predictions of other sludge and wastewater constituents. In other cases, the model equations and the assumptions made by their authors were questionable. Hence, two new activated sludge models with SMP and EPS as additional components have been formulated, described, and simulated. The first model is based on the Activated Sludge Model No. 1 (ASM1) whereas the second model is based on the Activated Sludge Model No. 3 (ASM3). Both models are calibrated on two sets of data obtained from a laboratory-scale system and a full-scale system and prove to be in very good agreement with the measurements.

The second part of this thesis explains the development of two membrane fouling models. These models are set to describe the loss of membrane permeability during filtration of various solutions and suspensions. The main emphasis is placed on filtration of activated sludge mixtures, however the models are designed to be as general as feasibly possible. As fouling is found to be caused by a large number of often very complex processes which occur at different spatial as well as temporal scales, the two fouling models developed here have to consider a number of significant simplifications and assumptions. These simplifications are required to balance the model's accuracy, generality and completeness with its usability in terms of execution times, identifiability of parameters and ease of implementation in general purpose simulators. These requirements are necessary to ascertain that long term simulations as well as optimisation and sensitivity studies performed in this thesis either individually on fouling models or on the complete model of a MBR can be carried out within realistic time-scales. The first fouling model is based on an idea that fouling can be subdivided into just two processes: short-term reversible fouling and long-term irreversible fouling. These two processes are described with two first order ordinary differential equations (ODEs). Whilst the first model characterises the membrane filtration process from an observer's input-output

point of view without any rigorous deterministic description of the underlying mechanisms of membrane fouling, the second model provides a more theoretical and in-depth description of membrane fouling by incorporating and combining three classical macroscopic mechanistic fouling equations within a single simulation framework. Both models are calibrated on a number of experimental data and show good levels of accuracy for their designated applications and within the intended ranges of operating conditions.

In the third part, the first developed biological model (CES-ASM1) is combined with the behavioural fouling model and the links between these two models are formulated to allow complete simulation of a hollow fibre (HF) immersed membrane bioreactor (iMBR). It is assumed that biological processes affect the membrane through production of mixed liquor suspended solids (MLSS), SMP and EPS which cause pore blockage, cake formation, pore diameter constriction, and affect the specific cake resistance (SCR). The membrane, on the other hand, has a direct effect on the bulk liquid SMP concentration due to its SMP rejection properties. SMP is assumed to be solely responsible for irreversible fouling, MLSS is directly linked to the amount of cake depositing on the membrane surface, whereas EPS content in activated sludge affects the cake's SCR. Other links provided in the integrated MBR model include the effects of air scouring on the rate of particle back-transport from the membrane surface and the effects of MLSS concentration on oxygen mass transfer. Although backwashing is not described in great detail, its effects are represented in the model by resetting the initial condition in the cake deposition equation after each backwash period.

The MBR model was implemented in Simulink® using the plant layout adopted in the MBR benchmark model of Maere et al. [160]. The model was then simulated with the inputs and operational parameters defined in [36, 160]. The results were compared against the MBR benchmark model of Maere et al. [160] which, contrary to this work, does not take into account the production of biopolymers, the membrane fouling, nor any interactions between the biological and the membrane parts of an MBR system.

Publications

During the course of this project, a number of publications and public presentations have been made based on the work presented in this thesis. They are listed here for reference.

- **C. Hartung, T. Janus, and B. Ulanicki** *Concept of a dynamic model of SMP and EPS formation based on the Activated Sludge Model No. 1*, Water Management Challenges in Global Change, Taylor & Francis, London, UK, ISBN: 978-0-415-45415-5, Proceedings of 9th International Computers and Control in the Water Industry Conference, De Montfort University: Leicester, (2007) p. 461-468.
- **T. Janus, P. Paul, and B. Ulanicki** *Development and validation of a multi-configurable MBR fouling model*, Proceedings of the 2nd European Water and Waste Water Management Conference, ThinkTank, Birmingham, (2008).
- **P. Paul, and T. Janus** *Validation and calibration of a multi-configurable membrane bioreactor fouling model*, Proceedings of the 2nd Oxford Membranes and Water Research Event, Oxford University; St Hilda's College, (2008).
- **T. Janus, P. Paul, and B. Ulanicki** *Modelling and simulation of short and long term membrane filtration experiments*, Desalination and Water Treatment, Vol. 8 (2009) p. 37-47.
- **T. Janus** *Membrane technologies for wastewater treatment*, Editorial, Water and Sewerage Journal, Ten Alps Publishing, Issue 2, (2009).
- **T. Janus and B. Ulanicki** *Modelling SMP and EPS formation and degradation kinetics with an extended ASM3 model*, Desalination, Vol. 261, Issue 1-2 (2010) p. 117-125.
- **T. Janus** *Short and long term simulations of membrane fouling with a behavioural and mechanistic model*, 3rd Oxford Membranes and Water Research Event, Oxford University; Lady Margaret Hall, (2010).
- **T. Janus** *Integrated mathematical model of a MBR reactor including biopolymer kinetics and membrane fouling*, 12th International Conference on Computing and Control for the Water Industry, CCWI2013, Perugia, Italy, (2013).

Acknowledgements

First of all I would like to thank my doctoral supervisor and my line manager Professor Bogumil Ulanicki for giving me the opportunity to perform this research, for his invaluable comments and the final check of the contents of my thesis, as well as for turning a blind eye when I was neglecting my other duties at work during the final months of my PhD study.

Secondly, I would like to express my sincere gratitude to Professor Maciej Nowicki, thanks to whom and his scholarship fund I was given an opportunity to spend 12 months in two leading German universities. I used this time to broaden my research interests in the area of mathematical modelling what helped me a great deal in conducting research disseminated in this thesis.

I wish to express my most sincere gratitude and appreciation to Prof. Robert Field from Oxford University, Prof. Ingmar Nopens from Ghent University and my fellow colleague, Dr. Shashi Paul from De Montfort University for kindly agreeing to review my thesis and for their thoughtful and detailed comments.

Special thanks go to my beloved Marta for her encouragements, patience and fine cuisine.

Most importantly, none of this would have been possible without the love and patience of my immediate family - my mum, dad, grandmother and my deceased grandfather, to whom I would like to express my heart-felt gratitude.

I would also like to thank my fellow colleagues and friends, both past and present, from Water Software Systems - Parneet Paul, Anna "Mała" Strzelecka, Żygomir Rzęzikupa Fakalach and Nayaranoloteph Übergott, thanks to whom each and every day spent in the office was full of fun and banter. I have had a great time during my work here with all the silly jokes, pranks, inappropriateness and shenanigans of all sorts.

I would like to acknowledge two following industrial collaborators whom I had the distinct pleasure of working with during the first year of my PhD study: Mr Steve Goodwin, the Managing Director of Aquabio Ltd. and Dr Alan Merry, the Technical Director of ITT Sanitaire. Without Steve's financial as well as technical involvement this project would not have been able to progress. Alan provided access to the ITT's invaluable experimental data and was kind to share his vast expert knowledge with me and my colleagues during numerous project meetings. Without the flux stepping experiment performed by Alan himself, calibration of the behavioural fouling model would not have been possible.

My words of deepest gratitude go to two modern day IT visionaries: Dr Richard Stallman, the founder of Free Software Foundation and Mr. Linus Torvalds, the initiator of GNU/Linux kernel. Although I know, the two of you have been in a long-lasting argument over the ethical and philosophical issues of software licenses and GNU/Linux coding standards, I hope you will not mind if I acknowledge both of you in the same

place. If it wasn't for you guys I would not have been able to enjoy the freedom of free software, whichever license/copyright notice it is published under.

Very special thanks also go to Donald Knuth and Leslie Lamport for giving us TEX typesetting system and LATEX markup language. Without your developments, writing of this thesis would have taken much more time and, most probably, would have involved lots more frustration.

A big thank you goes to the creators of numerous film documents which I often watched to relax after long hours spent on this thesis. I would specifically like to acknowledge the following people: Peter Joseph, the creator of *Zeitgest* movie series, John Pilger for his numerous insightful and extremely thought provoking documentaries, Adam Curtis the maker of *The Century of the Self*, Charles Ferguson the director of *The Inside Job*, Michael Moore for *Capitalism the love story*, Sam Bozzo and Maude Barlow for making *Blue Gold: World Water Wars* and numerous BBC reporters, writers and researchers behind so many educational and incredibly well made documents.

I would also like to acknowledge all those anonymous software developers who participated in the developments of the following free and open source software packages: **GNU/Linux OS**, TEX/LATEX editor **Kyle**, SVG graphics editor **Inkscape**, diagram creation program **Dia**, and the office suite **Libre Office**. Without all of you development of this thesis would surely have been significantly more difficult.

I would like to sincerely thank all the authors of the publications which inspired the work described in this thesis, particularly (in alphabetical order): Tao Jiang, Chrysi Laspidou, Shuang Liang, Thomas Maere, Chase Duclos-Orsello, and Xiaodong Zhao. All new developments presented in this thesis are merely a continuation of your work and adaptation of your findings into a different field of science.

I would also like to thank all of my climbing buddies, friends from the Tower Climbing Centre in Leicester and the Climbing Station in Loughborough. I would like to thank Olivier Leger for hard but fun workouts and assistance in crushing numerous interesting boulder problems.

Last but not least, special thanks go to my buddy Tomek Chomiuk for all the fun at indoor climbing walls and various crags across the UK and abroad, for open-source, for hundreds of hours spent on chatting and thousands of lines of text exchanged via email.

In conclusion, I recognise that this research would not have been possible without the financial assistance of De Montfort University who paid my tuition fees and enabled me to work on my PhD during work hours.

Contents

List of Tables

List of Figures

Chapter 1

General introduction

Contents

1.1 Introduction

Work documented in this thesis represents the first step towards the development of a thoroughly calibrated and validated dynamic mathematical model of an immersed membrane bioreactor (iMBR) for wastewater treatment. Although the membrane bioreactor (MBR) model created in this thesis and described in Chapter 7 represents an immersed outside-in hollow fibre (HF) system with air-sparging, backwashing and relaxation as cake control mechanisms, the fouling models developed and explained in Chapter 6 are able to describe both immersed and side-stream configurations. It is thus possible to reconfigure the MBR model presented here using different models developed in this thesis in order to represent other MBR systems such as an immersed flat sheet (FS) system or various side-stream configurations with crossflow as a cake control mechanism.

Until now only a handful of MBR models have been developed and described in the scientific literature. These models are additionally found to provide a rather simplistic description of, either, activated sludge kinetics, membrane fouling, or both. They are also unable to represent the main synergic interactions that occur between various parts of a MBR system, such as the links between soluble microbial products (SMP) and extracellular polymeric substances (EPS) kinetics and fouling, the links between

the bioreactor's operating conditions and SMP rejection, etc. Whilst a multitude of modelling studies on selected subsystems of MBR reactors have been performed and described in literature, it seems that adaptation and modification of these models and linking them together in order to create an integrated MBR model capable of describing the major synergic effects between the activated sludge biocenosis and the membrane has either been a very challenging task or has not yet been a focus of the research teams working in this area.

The MBR models created up to date are either grey-box, i.e. part mechanistic part empirical and hence restricted to specific reactor configurations and field conditions, or predominantly mechanistic but lacking the description of all components of the system and/or of functional interconnections between these components. Fully comprehensive, generic, mechanistic MBR models ready for application in industrial projects are not yet available due to a highly complex nature of MBR systems where some of the processes are not yet fully understood and thus very difficult to model. Therefore, modellers usually choose simpler data-driven models which can be synthesised from the available pieces of information without the necessity of understanding all mechanistic principles governing the system.

The first major component of a MBR model is the model of the activated sludge bioreactor. Although several scientist proved that it was possible to predict some behaviour of a MBR system using one of the standard IAWQ activated sludge models (ASMs) combined with a membrane filtration model [41], such models are unable to calculate two important quantities characteristic of a MBR, namely soluble microbial products (SMP) and extracellular polymeric substances (EPS). These two groups of organic substances are produced as by-products of microbial activity and are found to lead to membrane fouling, i.e. reduction of its permeability with time. They are also partially retained in the system by the membrane. Many researchers, e.g. [247, 266, 167, 253, 262] found that SMP is adsorbed inside membrane pores leading to reduction of pore diameters and thus an increase of the membrane's total resistance. Although EPS cannot penetrate into membrane pores alike SMP, they bridge the gaps between flocs within the cake structure leading to an increase in the cake's specific cake resistance (SCR) and hence, cause higher trans-membrane pressures (TMPs).

In order to describe membrane fouling as a function of bulk liquid SMP and EPS concentrations, the implemented activated sludge model needs to be able to predict the formation and degradation kinetics of these two main biofoulants. This task can be accomplished through a development of a brand-new biological model or through an extension of the existing one, the latter being a preferred option. The new outputs of this extended biological model, i.e. mixed liquor SMP and EPS concentrations are then to be used as arguments in the equations of membrane fouling thus linking the biological model to the membrane fouling model. Development of the new ASMs with SMP and EPS as new state variables, creation of new fouling models and formulation of bi-lateral links between these two subsystems are the three main tasks that are carried out in this thesis. These three tasks are described in more detail later in this chapter

and in the subsequent chapters dedicated specifically to each individual task.

Dynamic simulation has proved itself over the years to be an efficient and handy tool for analysis, optimisation, decision support, controller design and process design of many individual wastewater treatment processes as well as complete wastewater treatment plants (WWTPs). Dynamic simulation has many advantages over traditional 'static' design and analysis methods due to addition of time dimension which allows the user to assess the system's behaviour under explicitly defined time-dependent inputs, parameters and disturbances. Although simulation methods with dynamic mathematical models are significantly more computationally demanding than solving static, algebraic model equations, the computational power of modern personal computer is high enough to carry out complex and detailed simulation studies. An ever increasing performance of personal computers allowed the development of several commercial WWTP simulation packages which are now widely used by engineering consultants, plant operators, regulatory bodies and contracting firms. The software packages such as, in alphabetical order: **Asim** (Holinger AG), **Biowin** (EnviroSim Associates Ltd), **GPS-X** (Hydromantis Inc.), **SassPro V2** (HTI Systems), **Simba** (Ifak System GmbH), **Stoat** (WRc plc) and **West** (Hemmis) are not used solely for 'advanced' tasks specifically requiring the dynamic mathematical models, i.e. controller design, on-line and off-line decision support, model based control, etc. but recently also begin to gradually replace the traditional static design methods for WWTP design.

Wastewater treatment plants are inherently very complex physical systems accommodating many interdependent and time-varying biological, chemical, and physical processes with large number of time-varying inputs and parameters. Additionally, the inputs (i.e. wastewater quantity and composition), model parameters (e.g. bacterial growth rates, biomass yields, settling velocities, etc.), and disturbances (e.g. run-off intensities, toxicity in the influent, etc.) are often highly uncertain. Nevertheless plant design calculations are usually carried out with simple static equations obtained from time-dependent equations, often in the form of ordinary differential equations (ODEs) and sometimes partial differential equations (PDEs) through removal of time dimension and further subsequent simplifications. This process of simplification however necessitates that the effects of variability and uncertainty of all inputs, parameters, and disturbances are accounted for by introduction of single peaking and safety factors. This means that in static design methods final results are multiplied by factors larger than one, leading to an addition of extra reactor volumes and an increase of pipe diameters, pump sizes, etc. the temporal variability and uncertainty is therefore not directly modelled and thus, their effects on the plant's performance and its outputs, e.g. effluent quality, cannot be accurately predicted and accounted for in the final design. The choice of these safety and peaking factors is additionally often based on the engineers' experience and intuition and is seldom backed up with prior measurements, thus it rarely reflects the local environmental conditions. A bespoke, accurate design of a WWTP with traditional static design methods is therefore rather difficult.

Despite of all of the above described shortcomings, simple static design methods

have been successfully applied for the design of new and refurbishment of the existing WWTPs over many years. Gradually though, these static methods have been replaced by simulation methods. This change of approach to WWTP design is mainly driven by legislation which puts more stringent constraints on effluent quality, what in turn demands from the investors to use more technologically complex processes equipped with more accurate and robust control systems. As the modern treatment plants become more advanced and the discharge consent limits are being gradually lowered, the required robustness and efficiency of final designs can only be ascertained by employing accurate dynamic models. Dynamic simulation allows the process engineers to test the plant's behaviour under many different operational scenarios with bespoke, user-defined time-varying inputs, disturbances and parameters, which may additionally be based on on-site measurements.

Apart from the above mentioned clear advantages of simulation methods over static design procedures, dynamic models also have several other useful practical applications. Once a dynamic model of a WWTP is calibrated and used for process design, it can later be reused for further process optimisation, assistance in plant start-up and commissioning, training of plant operators, development and testing of automatic control strategies, synthesis and tuning of controllers, diagnosis, risk analysis, fault detection and decision support. A few out of hundreds of such application on large-scale objects are mentioned below. Ladiges and Günner [132] used a dynamic model of wastewater and sludge process trains to choose the most economical plant extension option after further 250,000 PE had been connected to a 1,860,000 PE municipal WWTP. The simulation results suggested that only a sludge process train needed to be upgraded with additional storage volume and no changes to the wastewater processing units needed to be made, contrary to what the initial non-simulation based feasibility studies had suggested. The proposed solution was then implemented and proved satisfactory after 3 years of operation [131]. The author of this thesis during his professional experience as a process engineer used a calibrated dynamic model of an activated sludge process to integrate process design and control strategy design within a single step and then test the robustness of this approach through analysis of the simulated effluent concentrations over an extended time period [112]. The process design was also supplemented with Computational Fluid Dynamics (CFD) analysis of final settlement tanks (FSTs). Dynamic process simulation allowed to obtain a bespoke near-optimum design based on the available information of local conditions, operators' preferences and acceptable levels of risk. CFD in turn allowed to optimise the geometry of the existing assets and to maximise their reuse. Both design and simulation exercises led to reduced operational expenditures (OPEX) and capital expenditures (CAPEX) in comparison to the initial solution obtained in the earlier feasibility studies. More recently, Cierkens et al. [33] successfully used an ASM2d-based model of Eindhoven WWTP together with its catchment and river models in order to synthesise better control strategies for the integrated catchment system based on the available on-line sensor data and historical influent data (e.g. storm events). This model was intended to serve as an important future decision support tool for WWTP and sewer system operators. Rodriguez-Roda

et al. [211] applied a deterministic WWTP model created in a commercial software package GPS-X as a tool for diagnosis, supervisory control and prediction within a multi-layer hybrid knowledge-based/deterministic decision support system (DSS). This DSS was then installed at a full-scale WWTP in Granollers, Spain. The work showed that mechanistic process models can be successfully integrated into supervisory control and data acquisition (SCADA) systems and used as on-line tools for prediction, high level (supervisory) control and decision support.

Although mathematical models of the, so called, 'conventional' process units such as activated sludge and biofilm bioreactors, final settlement tanks, sludge thickeners, trickling and sand filters, anaerobic digestion units etc., are available off-the-shelf in all commercial simulation packages, mathematical models of MBR units, whether immersed or sidestream, are not readily available or the ones that are on offer are very simplistic. Currently, predefined MBR models are included in process unit libraries of most recent releases of the three popular process simulation packages: Biowin, GPS-X and West. However, none of the above models is able to predict the concentrations of the most dominant biofoulants, i.e. SMP and EPS inside the bioreactor and, what is required for the integration of the biological and filtration models, link these concentrations to the rates of different membrane fouling mechanisms, such as pore constriction, pore blockage, cake filtration, etc. Additionally, these models do not provide any detailed mechanistic description of the membrane fouling and the fouling control mechanisms. Hence, simulation-based process design, process and energy optimisation, troubleshooting, etc. which can be easily performed with commercial simulation packages on conventional treatment processes such as activated sludge process or anaerobic digestion cannot be carried out to a similar degree on MBR systems.

The gap between the availability of general-purpose mathematical models for the, so-called, 'conventional' processes and MBRs is apparent and needs to be bridged to allow MBR systems to be integrated into larger mixed-process WWTP simulation studies. Development of a mechanistic MBR model will allow to carry out similar simulation-based studies on MBR systems to what is already possible on other wastewater treatment processes. Process unit manufacturers, system integrators and various engineering companies will have a tool which may allow them to improve their designs, derive better process control strategies and, at a later stage, use the mathematical models on-line to assist with the decision making or to act as a tool for training the operators. A mechanistic MBR model may therefore help to improve the designs of existing MBR systems, improve their energy-efficiency, robustness and control algorithms. As a result of these improvements the MBR systems may be given a more competitive edge over 'conventional' treatment processes.

The MBR model developed in this thesis is based on the system of ordinary differential equations (ODEs) and algebraic equations (AEs) which allow it to be implemented and simulated in general purpose commercial simulation environments such as Simulink® or their free-software alternatives such as Scicos, OpenModelica or JModelica. The main intention of the author was to create a model that, first and foremost, can

be used by the scientific and the engineering community to address various day-to-day problems facing process engineers and scientists working on MBR systems. The model presents itself as a more complete mechanistic alternative to less extensive mathematical models of MBR units that have been created up to date, such as the models of Lee et al. [140], Busch et al. [19], Saroj et al. [217], Mannina et al. [163] and Maere et al. [160].

At the same time the new model aims to answer some of many still unanswered questions about various mechanisms and processes occurring in MBR reactors or where the findings are conflicting. These questions together with the proposed answers and suggestions supported by the knowledge gained during the course of this research project will be described in the latter chapters of this thesis. It is still unknown what exactly causes fouling and how fouling is linked to the concentrations of various types of biopolymers. The mechanisms of fouling are still not completely understood and what is even less understood are the mechanisms of membrane clogging. With regards to activated sludge kinetics, it is still unknown how the biopolymers are produced under highly time-varying conditions and in a response to, e.g. toxicity, salinity, low and high dissolved oxygen (DO) concentrations, temperatures or shear. The movement of air-bubbles in the vicinity of the membrane surface during air-scouring and the shear rates on the membrane surface caused by the movement of air bubbles are also not yet well understood. A detailed description of all these processes is currently either impossible due to the lack of available knowledge or is infeasible as the produced models would have been very complex, slow, and contain large numbers of unidentifiable or difficult to identify parameters. They would therefore require very elaborate experimental procedures for parameter identification and high computing power for simulation. The main intention of the author is thus to strike a practical balance between the complexity and the accuracy of the MBR model and its ease of use, i.e. to provide a detailed enough description of the processes to allow the user to perform process optimisation studies but, at the same time, to produce a model which will not require vast amounts of effort to set-up, calibrate, validate and execute the model.

In addition to strictly scientific and practical value, the developments described in this thesis are also of economic significance as the global MBR market continues to grow with its total value forecasted by Global Industry Analysts [73] to reach $888 million by 2017. MBR market was valued by BCC market research analysts at an estimated $337 million in 2010. It is rising at a compound annual growth rate (CAGR) of 13.2% and is expected to reach $627 million by 2015, as shown in Figure 1.1. MBRs gradually become a preferred solution over the, so-called, 'conventional' processes, e.g. traditional bioreactor/final settlement tank configurations due to increasingly stringent effluent discharge norms, rising water scarcity and enhanced emphasis on water reuse and recycling for freshwater conservation. Additionally, small footprint of these systems makes this technology suitable for refurbishment of old plants [73]. A comprehensive mathematical model of a MBR may generate higher sales of this technology, help to integrate it with the existing WWTP processes in plant refurbishment designs, optimise final designs,

allow bespoke developments of control strategies, allow integrated catchment modelling studies to be carried out with MBR models connected to sewer and river water quality models and can be used to train future plant operators.

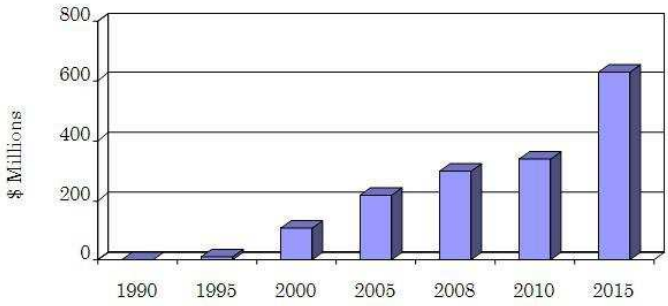

Figure 1.1: Membrane bioreactor market, 1990-2015 ($ millions), BCC Research 2012.

A more detailed introduction to the MBR technology in wastewater treatment where MBR systems are explained from the practical and research perspective is provided in Chapter 2. Meanwhile, Section 1.2 of this chapter lists and explains the aims and objectives of this thesis, while Section 1.4 provides a general overview of the developed MBR model and lists the addressed topics.

As some of the work reported in this thesis was carried out as part of a collaborative Department of Trade and Industry (DTI) project No. TP/3/DSM/6/I/15123 entitled *'Improving the design and efficiency of membrane bioreactor (MBR) plant by using modelling, simulation and laboratory methods'*, it has to be noted that some of the elements of research described here were influenced by collaboration with other researchers and research students participating in this project. The main contributions claimed in this thesis are however solely the work of the author. Portions of the work that were due to other individuals participating in the project and had to be included in this thesis for the sake of completeness, are clearly marked throughout this document including the names of the contributors.

1.2 Aims and Objectives

This thesis intends to:

1. Systematise the knowledge on modelling membrane bioreactors (MBRs) for wastewater treatment.
2. Analyse and compare the existing theories and models of biopolymer production in activated sludge systems.
3. Develop two new activated sludge models with SMP and EPS kinetics, based respectively on IAWQ Activated Sludge Model No. 1 (ASM1) and Activated Sludge Model No. 3 (ASM3).
4. Investigate different fouling mechanisms and mathematical fouling models for microfiltration (MF) and ultrafiltration (UF) membranes.

5. Develop two new fouling models in which the fouling mechanisms are dependent on the selected activated sludge properties such as mixed liquor suspended solids (MLSS), SMP and EPS, and thus can be linked to the outputs of the activated sludge models. Moreover, the fouling models shall be applicable to simulate full-scale MBR systems, what in turn requires the description of cake buildup control mechanisms such as backwashing, relaxation, air scouring and provision of cross-flow. The first model is intended for use in long-term simulation studies and in practical applications where the effort spent on model set-up, calibration and execution should be reduced to minimum. The second model shall provide a detailed mechanistic description of membrane fouling mechanisms and serve as a tool for increasing our understanding and for interpretation of membrane fouling.
6. Provide bi-lateral links between the developed activated sludge and fouling models, i.e. allow the modelled fouling processes to depend on the conditions present inside the bioreactor and, vice-versa, the mixed liquor composition to be influenced by the time-varying rejection properties of the membrane.
7. Create a dynamic mathematical model of an immersed MBR as a combination of one of the newly developed activated sludge models with one of the developed fouling models and investigate the properties and behaviour of this MBR model through numerous simulations under different inputs and operating conditions.

The developed MBR model is intended to serve the following purposes:

1. Capture the knowledge on modelling MBR systems in a single mathematical model ready to be used in purpose-built WWTP simulation software and in general purpose simulators.
2. Advance the knowledge on modelling biopolymer kinetics in activated sludge systems through the development and validation of two new biopolymer activated sludge models.
3. Advance the knowledge on modelling fouling of semi-permeable membranes through the development of two comprehensive fouling models.

The MBR model is developed for process engineers as a tool for process design, process optimisation, energy optimisation, controller design, training of operators and on-line and off-line decision support at MBR-based WWTPs. It can also assist researchers with practical experiments carried out on lab-scale MBR systems and on MBR pilot plants.

1.3 Problem statement, outline and analysis

Whilst the previous sections of this chapter provide a brief introduction to this thesis and, in particular Section 1.2 familiarises the reader with the main aims and objectives, the main purpose of the text so far has been to raise the reader's understanding of mathematical modelling of MBR systems solely from a practical perspective, i.e. to

describe the subjects covered in this work as would have been done by a practitioner. The purpose of this section is somewhat different as it states and outlines the problem from a strictly scientific, not a practitioner's point of view.

MBR reactors, as was described in the previous sections of this chapter, are very complex systems hosting a myriad of processes of different nature from biological, chemical to physical. Additionally, these processes occur over a large range of spatial and temporal scales. For instance, whereas time constant of the oxygen uptake process in the bioreactor is in the range of seconds to minutes, the process of hydrolysis may happen over the period of minutes to hours, biomass decay processes take, depending on the environmental conditions, between hours and days. Motion of a liquid phase in a 3 phase liquid-solid-gas multiphase flow problem inside a bioreactor and an immersed membrane tank (if separate from the bioreactor) can itself be characterised with a large range of spatial and temporal scales. Whereas large whirls have characteristic length scales comparable to the length scales of the domain (e.g. metres in full-scale applications) and characteristic frequencies of less than 1 Hz, the smallest eddies are of the size of Kolmogorov microscales, i.e. micrometres and have characteristic frequencies of kHz [242]. Membrane fouling, whose mathematical description forms the backbone of all membrane filtration models in MBR systems, shall in fact be considered as a combined effect of a number of processes which all attribute to the loss of membrane permeability at different temporal and spatial scales. Fouling processes leading to the so-called irreversible fouling occur on molecular and microparticle scales and are rather slow with time constants of hours to days. Cake buildup on the membrane surface on the other hand is a rather quick process which tends to occur within minutes and is caused by deposition of relatively large particles of the size of fractions of millimetres to millimetres depending on local conditions such as mean crossflow velocity (CFV) or mean air-bubble rise velocity and frequency.

A graphical representation of a generic MBR modelling task not limited to any specific process configuration is shown in Figure 1.2 which visualises the key components of a MBR model and the interconnections between these components in order to show the model's functional structure and complexity. As it usually happens with mathematical modelling of any complex system, the model developer is faced not just with the tasks strictly related to model formulation, implementation and validation but, first and foremost, with model selection, i.e. needs to determine at an early stage of the process which phenomena are dominant and shall be be included in the model and which ones are less significant and can thus be omitted. The modeller often needs to draw the line between model accuracy and complexity versus simplicity and the ease of use. As can be seen in Figure 1.2, the number of processes, factors, parameters, properties etc. describing a MBR system is already large and this list could easily be extended even further. By taking a pragmatic approach only the most dominant processes, properties and variables of a MBR model are shown in Figure 1.2. Otherwise the resulting graph would have been cluttered and very difficult to read. Although the choice of blocks used to produce Figure 1.2 is very subjective and definitely not exhaustive, the figure

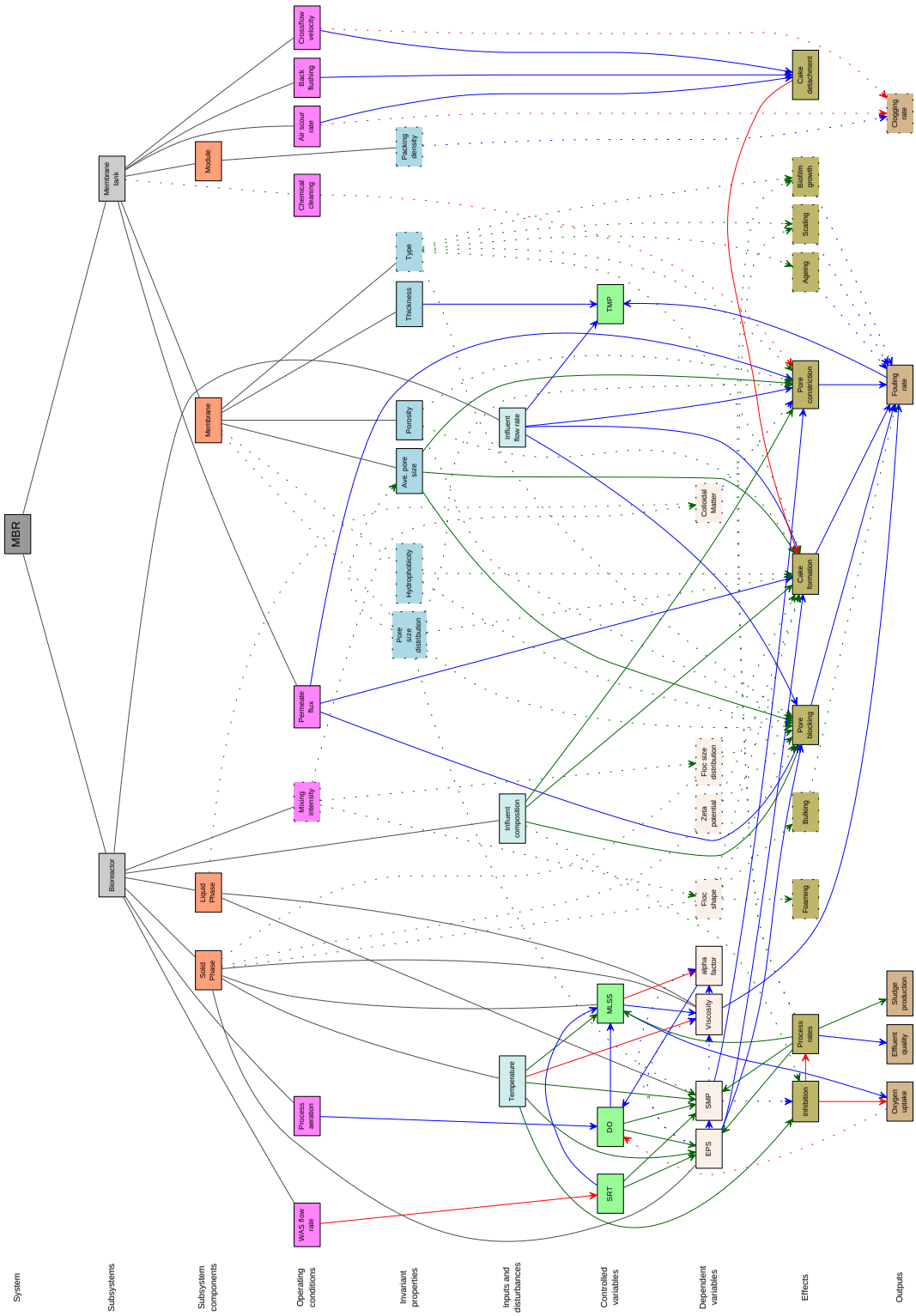

Figure 1.2: Graphical representation of a generic MBR modelling problem.

can hopefully allow to demonstrate the complexity of any MBR modelling task and the challenges facing the modeller who embarks upon the development of a complete mechanistic mathematical model of a MBR.

Figure 1.2 displays the causal and non-causal relationships between the blocks representing respectively: the main system (dark grey), subsystems (light grey), subsystem components (salmon), operating conditions (lilac), invariant properties (light blue), inputs and disturbances (cyan), controlled variables (light green), dependent variables (ivory), effects (khaki) and final outputs (light brown). The non-causal relationships are represented with dark grey straight lines whereas the causal relationships are shown with arrow lines in which the arrows point from the cause to the effect. The arrows of blue colour represent positive causal relationships, i.e. increase in the magnitude of the cause leads to an increase in the quantity of the product, the red arrows represent a negative causal relationship, whereas the dark green arrows represent causal relationships which are either unknown, or the findings so far are conflicting, or the relationship is non-linear exhibiting local maximum (maxima) or minimum (minima). The blocks and the connecting lines that are drawn with solid lines represent the parts which are chosen for the MBR model described later in this thesis, while the objects and relationships which are not included in the MBR model are drawn with dotted lines.

Components shown in Figure 1.2 describe the fundamental macroscopic quantities of a MBR system, such as: effluent composition, sludge production, oxygen demand, process aeration air-flow rates, membrane fouling rates, TMP, air scouring and/or CFVs and membrane permeation rates. Other quantities such as condition of the components, e.g. membrane ageing, air-diffuser fouling, etc. as well as capital expenditures (CAPEX) and operational expenditures (OPEX) are not included in the description of a MBR model shown here. CAPEX and OPEX can however be calculated at a later stage from the model outputs, such as daily sludge production, process aeration rates, permeate pumping rates, TMP, air-scouring rates, CFVs, chemical cleaning and backwash regimes, etc. provided that the required plant design information, i.e. process volumes, equipment, instrumentation, etc. had been provided.

Figure 1.2 shows that a MBR model requires a rather large number of building blocks which are often interlinked with one another forming complex mathematical relationships. These mathematical relationships as well as the mathematical models themselves are frequently unknown or their parameters are difficult to identify. The task of encapsulating all available knowledge and all important properties and characteristics of a MBR and its processes within a single mathematical model is thus very difficult. The reasons for this state of affairs are summarised below.

1. The number of subsystems, i.e. equations, state variables and parameters to be included in the MBR model is vast leading to a mathematically complicated and computationally demanding model.
2. The number of connections between the subsystems is very high, i.e. many biological and physico-chemical processes described in the model depend on a large

number of other processes. This leads to a situation where one parameter drives not only one but many processes and where one output depends on a combined effect of several simultaneously occurring processes.

3. Due to the above, identification of the model parameters and states is very difficult, if not impossible. Large number of processes being modelled (and thus mathematical equations) necessitates the introduction of many state variables, some of which cannot even be measured and identified.
4. Many of the processes cannot be represented in the model either because of the lack of available information required to properly describe these processes in mathematical terms, the lack of available experimental data for parameter identification or motivated by the need of keeping the model within practical levels of complexity.

For all of the above reasons, building a MBR model from all the blocks shown in Figure 1.2 would be rather impossible and if we imagined that all processes and links could be mathematically described in mechanistic terms, the resulting model would have become impractical due to its number of equations and parameters leading to long execution times during simulation. The author thus adopted a pragmatic approach where one has to compromise between the completeness of the mathematical description and the complexity of the model structure. The blocks and links shown in Figure 1.2 with dotted lines were eliminated and the model structure was consequently reduced to one presented in Figure 1.3. This model structure was adopted during the development of the MBR model presented in this thesis.

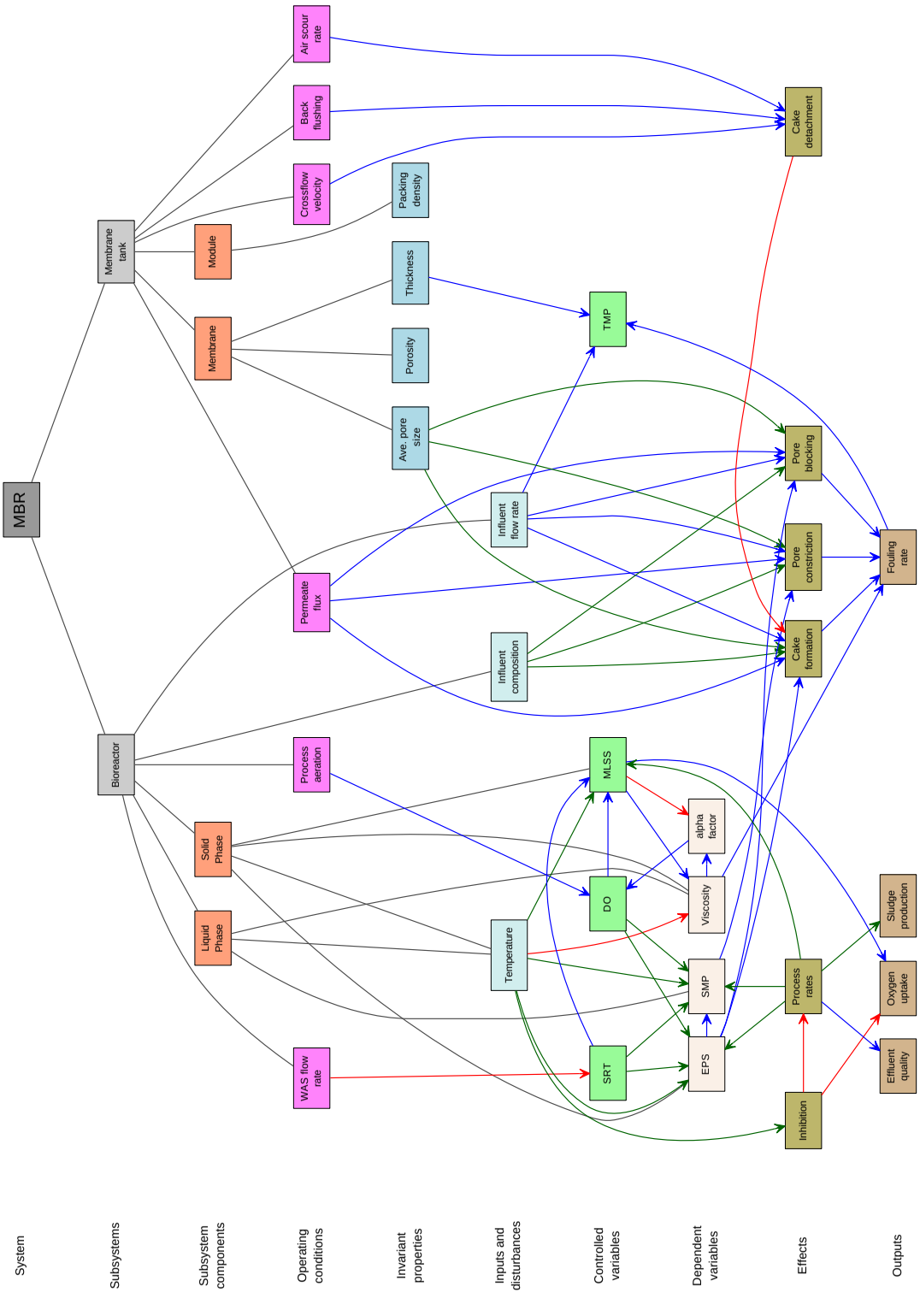

Figure 1.3: Graphical representation of a simplified MBR modelling problem.

1.4 Model overview

1.4.1 Topics addressed in the MBR model

The MBR model developed in this thesis addresses the following:

1. The biological part of the model describes all activated sludge state and composite variables characteristic of the International Association on Water Quality (IAWQ) family ASM models. The model predicts the concentrations of various wastewater constituents in the bioreactor and in the effluent on top of the fundamental process variables such as oxygen demand and excess sludge production. Additionally, the model is able to predict the bulk liquid SMP and EPS concentrations which shall be used as inputs to the fouling model equations.
2. The fouling part of the model describes various fouling mechanisms such as pore constriction, pore blockage and cake formation in case of the three-mechanism classical fouling model or, in case of the simpler behavioural model, irreversible and reversible fouling, which collectively attribute to the loss of membrane permeability over time.
3. The modelled fouling prevention and control mechanisms include cake detachment due to CFV and air scouring and cake removal by back-flushing and relaxation. Back-flushing is assumed to cause an instantaneous and complete removal of cake deposits from the membrane surface. The time-dependent back-flow of water and detachment of solid particles due to velocity field are not explicitly modelled, therefore the model is not able to predict the effects of back-flush flow rates and back-flush duration times on the efficiency of cake removal nor the pressure loss during back-washing.
4. The bulk liquid SMP and EPS concentrations are linked to the relevant fouling equations as later described in Chapter 6 and Chapter 7.

The bi-lateral links between the bioreactor and the membrane connecting the fouling rates to the biopolymer concentrations, cake deposition to coarse bubble aeration, and biopolymer concentrations in the bioreactor to the retentive properties of the membrane, are formulated as follows:

1. SMP is considered to be the main foulant causing pore constriction / irreversible fouling. SMP is assumed to deposit inside membrane pores causing the reduction of pore diameters and thus, the increase in membrane resistance.
2. EPS is assumed to promote cake formation / reversible membrane fouling by filling the voids between activated sludge flocs and thus lowering the cake's porosity, hence increasing its specific cake resistance (SCR).
3. SMP concentrations in the bulk liquid depend mostly on the SMP rejection properties of the membrane which are found to influence the bulk liquid SMP concentrations more than the biological processes inside the bioreactor themselves. EPS is assumed to adhere to activated sludge flocs and is therefore fully retained in

the bioreactor.

4. Cake deposition control by air scouring is modelled with a one-dimensional (1D) multiphase air-liquid flow model of Zaisha and Dukler [268] under an assumption that the air-liquid flow regime inside the membrane module resembles slug flow. The deposited cake particles are assumed to detach from the membrane surface once the shear stresses caused by an upward motion of air bubbles and liquid slugs exceed the inter-particle forces keeping the particles on the membrane surface. These forces are represented for simplicity with a single static friction coefficient [176].

1.4.2 Topics not addressed in the MBR model

The following topics are not be addressed in the MBR model due to, either, lack of sufficient amount of knowledge required for the development of the required models, difficulties with the identification of model parameters, or the need to keep the complexity and the size of the complete MBR model at feasible levels.

1. The membrane rejection properties are not explicitly modelled. Rejection of solid particles and EPS is assumed to be 100% whereas rejection of SMP maintains a constant value between 0% and 100%. Although it was found that SMP rejection may depend on sludge retention time (SRT) [226], the relationship between SMP rejection and SRT is likely to be characteristic of just one MBR process and thus not general. Additionally the membrane rejection properties are also likely to change with filtration time as the membrane gets progressively fouled. However, there is no data currently available to derive any form of mathematical model of this process as well as to support the findings and the model of [226]. It is assumed that rejection of SMP on the membrane is caused by sieving. The effects caused by formation of a dynamic layer on the membrane surface, which is believed to act as a prefilter for the incoming liquids creating an effect as if the membrane had smaller pore diameters, are also not included in the model.
2. The biological model considers the influent wastewater to be characterised by fractions of chemical oxygen demand (COD), nitrogen (N) and phosphorus (P). Information about the molecular nature and the chemical composition of the influent is not captured anywhere inside the biological model. Hence, any changes that chemical composition of the substrates might have on the substrate utilisation rates cannot be predicted. The model thus demands a recalibration once the nature and the composition of the influent changes. As a result of this simplification, toxicity effects caused by the presence of some specific components detrimental to the biocenosis cannot be explicitly modelled and would require an introduction of new state variables, parameters, and possibly complete new equations into the biological model.
3. Membrane properties such as the membrane type, hydrophobicity, pore structure and pore size distribution are not explicitly included in the fouling model equa-

tions. The effects that all these properties have on the membrane characteristics are all lumped into single individual fouling equation parameters which need to be adjusted in the model on the case by case basis.

4. Activated sludge properties such as the floc size distribution, fraction of colloidal matter, floc shape, zeta potential or filament amount are not modelled nor used as the inputs to the MBR model. Similarly to the membrane properties, these parameters are implicitly included in the fouling model within specific fouling rate constants which are adjusted during calibration in order to match the model outputs to the experimental data.
5. The MBR model cannot predict the recovery of irreversible fouling during in-line or off-line chemical cleaning. It is expected that the simulation horizons will not exceed the time in which it is necessary to perform a chemical clean on the membrane. Although the model for in-line chemical cleaning could have been helpful during testing of long-term fouling control strategies, the mechanisms of chemical cleaning are not yet fully understood and hence very hard to describe in mathematical terms.
6. Although membrane module clogging has equally detrimental effects on membrane performance as the membrane fouling, clogging mechanisms are not yet fully understood and are thus not included in the MBR model. Clogging models are of significant importance for the description of immersed membrane configurations, especially in HF systems where hair and other solid materials which manage to pass through the primary treatment stage deposit within the fibre bundles. However, as the description of clogging would necessitate the development of a complex CFD hydrodynamic model and a complex characterisation of the bulk liquid, this task is left for future investigations.
7. The model cannot describe fouling due to biofilm growth on the membrane surface. The biological processes taking place near the membrane ans inside the forming biofilms are therefore also not included in the model.
8. Scaling is not modelled here as it is found to occur in MBRs only under specific conditions and for influents with high levels of hardness. Scaling is more dominant in UF, nanofiltration (NF) and reverse osmosis (RO) membranes where concentration polarisation is more prominent due to higher retention of salt molecules on the membrane, causing local salt concentrations to exceed their maximum solubility and precipitate on the membrane surface.
9. The model also cannot predict how the membrane properties deteriorate due to ageing. The MBR model is however only intended for shorter term simulations where the membrane deterioration effects are insignificant and have no effect on the outputs.
10. The biological model, although capable of predicting the bulk liquid SMP and EPS concentrations, is unable to differentiate between different groups of these biopolymeric substances with regards to their chemical composition or molecular weight distribution (MWD). Whilst various researchers found that different chemical

compounds making up SMP have different fouling strengths, e.g. polysaccharides were found to be four times stronger foulants than proteins [267], the biochemical pathways of different components forming SMP and EPS in activated sludge systems are still unknown.

11. The model is unable to predict the removal of trace organics such as emerging contaminants which MBR systems are found to exhibit an improved capability of, over the conventional activated sludge processs (ASPs).
12. The impacts of shear caused by mixing, CFV and air sparging on break-up and agglomeration of flocs are not described. The model is thus unable to predict the activated sludge floc size distribution (FSD) or an increased release of SMP and EPS from flocs observed in practice under elevated shear rates.
13. The fouling model provides no description of the so-called *conditional fouling* where, due to various interactions between the membrane and the mixed liquor, various soluble components present in the wastewater get adsorbed on the membrane surface leading to irreversible fouling, even at zero fluxes. The effects of conditional fouling are partially accounted for by assigning appropriate initial conditions for membrane resistance at the beginning of each simulation.
14. The so-called TMP jump which has been found to occur in long-term constant flux membrane filtration at permeation fluxes even below the critical flux [266] cannot be predicted in the simpler one of the two developed fouling models whilst the more complex fouling model is able to predict such behaviour but has not been thoroughly validated.
15. Last but not least the MBR model cannot describe the effects on any additives such as flocculants, coagulants or adsorbent reagents such as powdered activated carbon (PAC) on the membrane fouling.

1.4.3 MBR model structure

Figure 1.4 describes the MBR model block diagram which represents a high level model structure whilst indicating its main subsystems and signals.

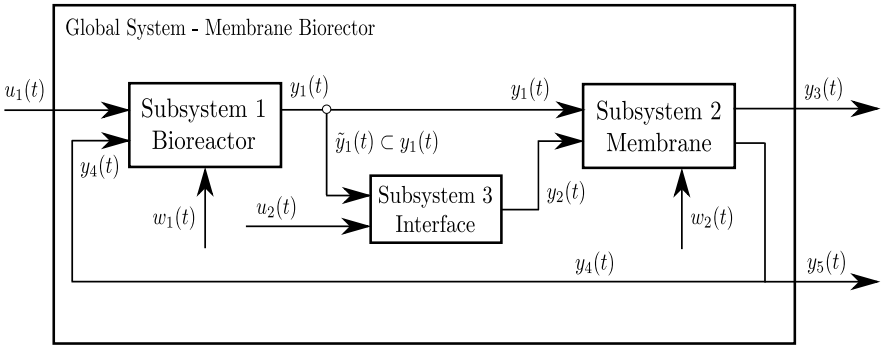

Figure 1.4: Generalised structure of the MBR model.

The model in Figure 1.4 is subdivided into three subsystems: the Bioreactor (Subsystem 1), the Membrane (Subsystem 2) and the Interface (Subsystem 3). Subsys-

tem 1 receives an input vector $u_1(t)$ associated with the influent flow and composition plus an output vector $y_4(t)$ associated with the retentate outflow from the membrane and produces an output vector $y_1(t)$. Some of the flow is diverted from the retentate recirculation loop $y_4(t)$ forming an output vector $y_5(t)$ associated with the surplus activated sludge (SAS) wastage stream. The subvector $\tilde{y}_1(t) \subset y_1(t)$ is composed of the selected state variables of Subsystem 1 which are found to cause membrane fouling: $\tilde{y}_1(t) = (S_{SMP}\ X_{EPS}\ X_{MLSS})^T$, where S_{SMP} denotes the concentration of soluble microbial products (SMP) (g m^{-3}), X_{EPS} denotes the concentration of extracellular polymeric substances (EPS) (g m^{-3}) and X_{MLSS} is the concentration of mixed liquor suspended solids (MLSS) (g m^{-3}). T denotes a matrix transpose operator and is not to be confused with the bulk liquid temperature which has been assigned the same symbol. Subsystem 3 receives a signal $\tilde{y}_1(t)$ and and input vector $u_2(t)$. For an immersed 'backwashable' membrane configuration $u_2 = (q_{air}\ t_{filt}\ t_{back})^T$, where q_{air} denotes the coarse bubble aeration rate (m^3 h^{-1}), t_{filt} denotes the filtration time (s), and t_{back} is the backwash time (s). Subsystem 3 converts the signals $\tilde{y}_1(t)$ and $u_2(t)$ into the fouling rates and the parameters which form an output signal $y_2(t)$. Outputs from the bioreactor $y_1(t)$ and the interface $y_2(t)$ become the inputs to Subsystem 2 which produces two output vectors: $y_3(t)$ associated with the permeate stream and $y_4(t)$ associated with the retentate stream. Subsystem 1 and Subsystem 2 receive two external disturbance vectors, $w_1(t)$ and $w_2(t)$ which, in this case, consist of just two signals - the liquid temperature, T and the air temperature, T_{air}. The membrane is affected by the processes occurring upstream in the bioreactor through two forward loops: the direct forward loop $y_1(t)$ and the indirect forward loop through Subsystem 3. The membrane, in turn, has an effect on the behaviour of the upstream-placed bioreactor through a feedback loop $y_3(t)$ representing the retentate stream.

All biological activated sludge models (ASMs) as well as the complete benchmark model of a MBR are implemented in a wastewater modelling package Simba® from iFak GmbH, Germany running under MATLAB®. The membrane fouling models are implemented in MATLAB® and Simulink®.

1.5 Organisation of this thesis

The thesis is structured into three parts as illustrated in Figure 1.5.

Part I is preceded with Chapter 1 and Chapter 2 which are intended to provide an introduction to MBR technology and to help put the developments brought about in this thesis into practical context. In addition to providing a brief and concise overview of the membrane technology in wastewater treatment applications, Chapter 2 also outlines the most challenging issues currently facing a further development of MBR systems and describes current research priorities within the field. The aims and tasks set out within this research programme are broken down into smaller portions of work which are then outlined followed by a brief description of the research problems they attempt to address.

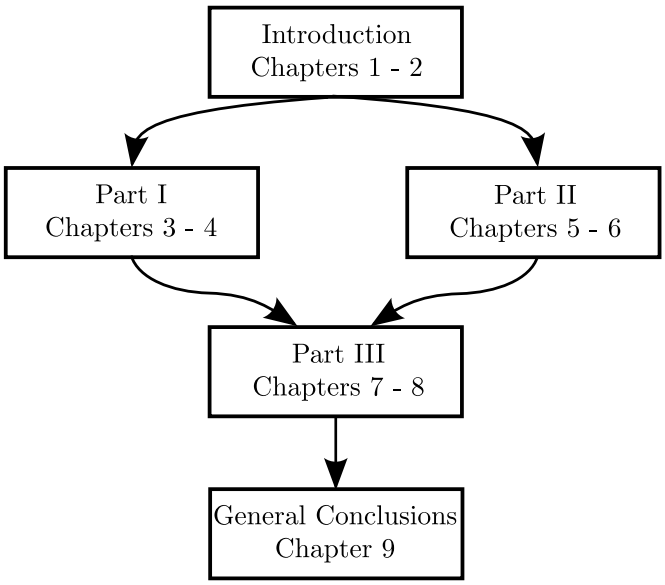

Figure 1.5: Schematic representation of the structure of the overall thesis.

Part I comprises Chapters 3 and 4 and is primarily devoted to the analysis of the existing activated sludge models extended with SMP and EPS kinetics and to the development of the new extended activated sludge models. The work documented in Part I is built on the findings of Leuderkind and Piret who identified SMP production kinetics in bacterial cultures and the work of Laspidou and Rittmann [135; 136] who linked the SMP and EPS kinetics in bacterial cultures within a single theory of biopolymer production and degradation. The SMP and EPS production and degradation kinetics of Laspidou and Rittmann [135; 136] were then adapted and incorporated within the activated sludge model (ASM) framework leading to the formulation of two new activated sludge models. The first model is based on the Activated Sludge Model No. 1 (ASM1) and the second is formed on the basis of the Activated Sludge Model No. 3 (ASM3).

Chapter 3 reviews the existing SMP and EPS ASM models through analysis of their strengths and weaknesses. Attention is placed on two areas: (a) the added SMP and EPS kinetic equations and (b) the links between the added SMP and EPS kinetic equations and the original kinetic equations of the underlying ASM models. The first area is investigated by analysing the structure and the parameters of the biopolymer kinetic equations and examining their behaviour in simulation studies under selected operating conditions. The links between SMP and EPS kinetic equations and the original process equations of the underlying ASM models exist in the model as a consequence of the addition of new stoichiometric parameters and modification of the original stoichiometric parameters in order to ascertain the closure of mass and charge balance equations. The newly added stoichiometric parameters associated with SMP and EPS kinetics appear in the stoichiometric relationships of the original ASM state variables, thus creating the links between the new kinetic equations and the original ASM model kinetics. These effects are analysed through investigation of the model structure, sensitivity analysis studies for the newly introduced kinetic parameters and comparison of the new and the original ASM model outputs from various simulation studies under different operating

conditions. The outputs being compared were: unit sludge production, unit oxygen demand, and effluent COD, total nitrogen (TN), ammoniacal nitrogen (NH_4^+-N), nitrate nitrogen (NO_3^--N), SMP and EPS concentrations.

Following unsatisfactory results of the analysis of the published ASM-based biopolymer models described in Chapter 3, Chapter 4 focusses on the development of two new, combined SMP and EPS activated sludge models. The new models are intended to eliminate the deficiencies of the current biopolymer ASMs, i.e. ensure the closure of carbon (C), N, charge and, where applicable, total suspended solids (TSS) mass balances, improve the accuracy of SMP and EPS predictions, and eliminate the negative effects that the added biopolymer kinetic and stoichiometric parameters have on the prediction accuracies of the original ASM state variables. The SMP kinetics of Leuderkind and Piret and the integrated SMP and EPS metabolic model of Laspidou and Rittmann [135; 136] are incorporated into two IAWQ models: ASM1 and ASM3. The kinetic and stoichiometric parameters identified in two different calibration studies are combined with literature values to create a set of default parameters for both models. The most sensitive kinetic and stoichiometric parameters are identified via local sensitivity analysis at different operating points. The complexity of both models is assessed through analysis of the number of parameters, equations and state variables followed by parameter sensitivity study. The new SMP and EPS ASM1-based model is used to formulate the integrated MBR benchmark model described in Chapter 7.

Part II comprises Chapters 5 and 6 and is primarily concerned with the second aspect of modelling MBR reactors, namely mathematical description of membrane fouling. The work described here is carried out in three steps. The first step is to review and analyse various theories of fouling found in literature and assess their applicability to describe fouling in MBRs for wastewater treatment. In the second step, theoretical principles of attachment and detachment of macromolecules and particles to/from membrane leading to irreversible and reversible fouling are analysed on a microscopic, particle scale. SMP transport across the membrane is also investigated through simulation of a 1D advection-diffusion equation for solute transport in a porous medium. In the third step, two fouling models are formulated. The first model builds on the work of Liang et al. [149] and expands this model with new equations describing flux dependent SMP deposition mechanisms, cake detachment due to presence of shear and back-flushing. The second model is formulated on the idea of Duclos-Orsello et al. [50] who expressed flux decline in a constant-TMP dead-end filtration process with an analytically derived equation obtained by integrating and combining three classical fouling equations: pore constriction, pore blockage, and cake formation. The model proposed here follows the same idea but presents the model in a differential form, where all three equations are solved simultaneously whilst cake formation occurs in sequence after pore blockage. The model is not restricted to constant-TMP filtration and can be used to simulate filtration where both TMP and flux vary in time.

Chapter 5 looks at various processes occurring during filtration of solutions and suspensions through UF and MF rejection membranes. Different theories and mathe-

matical models of membrane fouling and reversible and irreversible fouling control are analysed and their applicability for modelling membrane filtration of wastewater mixtures are assessed. This Chapter is therefore intended to be used as a road map and a reference guide for modelling fouling in MBR systems. The main emphasis is placed on selection of the most dominant fouling mechanisms. Dead-end as well as cross-flow filtration regimes are addressed and various processes associated with these two different modes of operation are described in mathematical terms on a macroscopic as well as microscopic scale. At the end of this chapter, several published fouling models are reviewed and assessed based on a number of criteria such as complexity, accuracy, identifiability of parameters, extensibility and applicability to modelling MBR systems. Whilst the list of publications describing fouling models is very long, the Author decided to choose only those models for further analysis which seemed to be most applicable for the purpose of this thesis, i.e. for integration with biological models. The study presented in this chapter served as a basis for the development of the two fouling models described in Chapter 6.

The second chapter of Part II, namely Chapter 6 describes the formulation of two new fouling models. Whilst the first model describes just the 'observable' behaviour of the membrane, i.e. the TMP and total membrane resistance as a function of time and permeate flux, the second model takes a more detailed, 'first principle' approach where the underlying fouling mechanisms are described with theoretically derived equations. The first, 'behavioural' model is based on the concept of Liang et al. [149] who subdivided fouling into two parts: the long-term irreversible fouling and the short-term reversible fouling. The model proposed in Chapter 6 adopts the same concept but extends the model of Liang et al. [149] through an introduction of flux dependent SMP deposition, addition of different cake control mechanisms, and addition of a back-flushing mechanism. Whilst the fouling equations adopted in the first fouling model differ from the widely accepted theoretical fouling equations, the model was proven to predict the behaviour of rejection membranes during filtration of wastewater mixtures at a technical scale with very good levels of accuracy. We shouldn't however forget that this model is a significant simplification of the fouling phenomena and is created for the purpose of quick deployment and easy parameter identification, and is only valid within a limited operational range, i.e. limited range of permeate fluxes and simulation time horizons. The model is unable to predict certain phenomena observed during filtration through semipermeable membranes such as e.g. two-stage TMP profiles [266]. The second proposed fouling model is able to represent these phenomena by adopting a more detailed mechanistic approach. Classical filtration laws are combined and solved simultaneously in a single three mechanism fouling model. The model assumes that all three fouling processes: pore constriction, pore blockage and cake formation take place on the membrane during filtration of polydisperse suspensions, however cake formation occurs in sequence after pore blockage. The model follows the idea originally proposed by Duclos-Orsello et al. [50]. The published model of Duclos-Orsello et al. [50] is modified as follows: an additional state variable which represents the resistance under the blocked area is introduced; pore constriction parameter is flux-dependent; particle back-

transport mechanisms are added. The model is found to exhibit very good agreement with the measurements as explained in detail in Chapter 6.

Part III comprises Chapters 7 and 8 and builds on the developments presented in Part I and Part II. Chapter 7 describes the formulation of an integrated MBR model where the ASM3-based SMP and EPS biological model developed in Chapter 4 is combined with the behavioural fouling model developed in Chapter 6. The MBR model layout is built using the plant layout featured in the paper of Maere et al. [160] who created a simple MBR benchmark model in a similar fashion to what had earlier been done for a conventional ASP/FST process [37, 36]. However, whilst the model of Maere et al. [160] does not consider membrane fouling or production of biopolymers in the bioreactor, the integrated MBR model described in Chapter 7 describes both of these aspects and additionally considers bi-lateral links that occur between the biological and the fouling parts of the model. Chapter 8 describes the results of the simulations performed on the newly developed integrated MBR model with inputs and operating parameters defined in COST624 [37], Copp [36] and Maere et al. [160]. Model outputs include effluent concentrations of the selected state variables as well as composite variables such as COD and TN as well as various quality indices and energy consumption indicators. Outputs from this integrated MBR model are then compared with the outputs of the MBR benchmark model of Maere et al. [160].

The combined EPS and SMP production ASM1-based model (CES-ASM1) biological model adopted in the MBR system described in Chapter 7 contains three new state variables compared to the Activated Sludge Model No. 1 (ASM1) originally used in Maere et al. [160]. This difference in the number of state variables necessitated that the model inputs and quality and energy performance indicators had to be reformulated in CES-ASM1. Care was taken to ascertain that the new biological model and the original model of Maere et al. [160] receive the same influent loads and composition and therefore, the outputs from these two models can be quantitatively compared. CES-ASM1 is combined with the behavioural fouling model described in Chapter 6 using the plant layout adopted from Maere et al. [160]. The biological and the fouling model are interfaced and linked together using the following relationships: (a) Irreversible fouling depends on the SMP concentrations which are predicted in the biological model, whilst the rate of SMP deposition depends on flux; (b) The specific cake resistance (SCR) used in the reversible fouling equation depends on the EPS content in the activated sludge which, again, is predicted in the biological model; (c) SMP retention on the membrane affects SMP concentration in the bioreactor, which in turn has an effect on the rates of other activated sludge process kinetics; (d) Cake detachment from the membrane is linked to coarse-bubble aeration rates. This functional link is obtained from the 1D quasi steady-state slug-flow simulation in a staggered grid representing a HF outside-in membrane module.

Chapter 8 describes the simulation results obtained from the integrated MBR model simulated with the inputs and simulation scenarios defined in COST624 [37], Copp [36] and later adopted in Maere et al. [160]. The outputs obtained from the new

MBR model are then compared with the results of the MBR benchmark of Maere et al. [160]. The quantities being compared include state variables, composite variables, and different environmental quality and energy consumption indicators described in Chapter 7. The simulation results show that the CES-ASM1 model predicts lower sludge yields and lower denitrification rates to ASM1. Such behaviour is a direct result of the alteration of the organic substrate pathways caused by introduction of the SMP and EPS kinetics. The results also indicate that the variations of the SMP and EPS content in MLSS in response to diurnal variations in the influent flow and loading rates are too small to have a significant impact on the membrane fouling whilst the fouling rates are highly dependent on fluctuations of solids concentration in the membrane tank and the flow rates. It has to be noted that the biological model used in the study does not describe how biopolymer production changes in response to environmental stress, such as low/high salinity, temperature, oxygen concentration, toxicity, shear, etc. The model has only been calibrated on the systems which either operated under steady-state conditions or in a batch mode. In order to ascertain that the model can correctly predict the biopolymer concentrations also under diurnal flow and load patterns, the model needs to be first validated under dynamic conditions.

Finally, Chapter 9 provides the overall conclusions of the original Author's work presented in Chapters 3-8 and outlines the areas for further research.

1.6 Contributions

During duration of this research project a number of contributions have been made to the field of modelling and simulation of MBR systems. Three major contributions have been identified - one for Part I and two for Part II of this thesis. A number of less significant contributions have also been identified and listed below.

Part I

Major contribution

- The major contribution of Part I is the development of two new activated sludge models which extend the 'standard' IAWQ ASM models with SMP and EPS kinetics. The new models are considered to represent a higher level of complexity and sophistication from the previous activated sludge models found in literature. The new models are able to reproduce the bulk liquid SMP and EPS concentrations in the activated sludge systems without compromising the prediction accuracy of other parameters characterising the state of the activated sludge. See Chapter 4.

Subsidiary contribution

- An extensive and systematic review of the existing activated sludge models with biopolymer production kinetics has been carried out. The models have been qual-

itatively and quantitatively evaluated and then compared, followed by an assessment of their practical application to simulation of MBR systems. See Chapter 3.

Part II

Major contributions

- The first major contribution of Part II has been the development of a behavioural fouling model. The model is based on the concept of Liang et al. [149] who subdivided fouling into two parts: the long-term irreversible fouling and the short-term reversible fouling. The new model proposed in this thesis adopts the same concept and extends the old model by introducing flux dependent SMP deposition, various cake detachment mechanisms and a back-flushing mechanism. The new model is able to predict TMP over a broad range of permeate fluxes and hydrodynamic conditions. This constitutes a significant improvement to the old model which was only valid over a rather narrow range of operating conditions. See Chapter 6.
- The second major contribution of Part II has been the generalisation and combination of the classical filtration laws to form a single three mechanism fouling model. Similarly to the earlier publications of Duclos-Orsello et al. [50] it is assumed that the three following fouling processes: pore constriction, pore blockage and cake formation, occur simultaneously. The proposed model expands the existing models through introduction of the following changes: additional state variable representing the resistance under the blocked area is introduced; pore constriction parameter is flux-dependent; particle back-transport mechanisms are added to the cake formation equation. See Chapter 6.

Subsidiary contributions

- A brief, structured description of various fouling mechanisms and theories, supplemented with mathematical equations, is provided in Chapter 5 to provide the reader with a broader understanding of membrane filtration and fouling in MBRs. The reader is provided with a review of different fouling mechanisms and fouling models accompanied with a critical review of their strengths and weaknesses.
- Particle back-transport is analysed on a particle level by breaking down the forces acting on a single particle and a subsequent investigation of the particle deposition criteria. See Chapter 5.

Part III

Subsidiary contributions

- The ASM1-based activated sludge model described in Chapter 4 has been integrated with the behavioural fouling model illustrated in Chapter 6 to form a comprehensive description of a hollow-fibre immersed MBR reactor. The result-

ing model of a MBR contains bidirectional links between the biological and the filtration part of the system. It is assumed that SMP in the bioreactor directly affect pore constriction/irreversible fouling whereas EPS have an influence on cake formation/reversible fouling as they affect the specific cake resistance (SCR). The retentive properties of the filtration membrane affect the bulk liquid SMP concentrations as the membrane retains the SMP particles inside the bioreactor. The back-transport of particles from the membrane surface to the bulk liquid, i.e. cake detachment, is linked to coarse-bubble aeration rate using a mathematical expression derived from the 1D slug-flow hydraulic model. See Chapter 7.

- The bioreactor and the membrane models are connected and arranged in such a manner as to represent the MBR benchmark simulation model (BSM-MBR) plant layout of Maere et al. [160]. As a result, a de-facto new benchmark model is created. This model offers a higher level of sophistication than BSM-MBR by describing the interactions between both parts of the system and thus producing more realistic results. See Chapter 7.
- An extensive simulation study using the new MBR benchmark model has been conducted to evaluate the model's performance and compare its results against the benchmark model of Maere et al. [160]. The MBR model has been simulated under various dynamic inputs to evaluate its behaviour over a range of operating points. See Chapter 8.

Chapter 2

MBR technology in wastewater treatment

Contents

2.1 Brief technology overview

Definition 1. A membrane bioreactor (MBR) is a type of an activated sludge process for wastewater treatment in which the biomass is retained in the bioreactor by microporous semipermeable pressure-driven rejection membranes, usually operating in the microfiltration (MF) and ultrafiltration (UF) range. The membranes are used for biomass separation and effluent clarification and therefore serve as a replacement for final settlement tanks (FSTs) traditionally used in a conventional activated sludge process (CASP).

Replacement of sedimentation with micro- or ultra- filtration allows in MBR systems to maintain significantly higher mixed liquor suspended solids (MLSS) concentrations compared to conventional activated sludge processs (ASPs) whilst obtaining almost complete clarification with ∼99.9% removal of solids. Whilst MLSS concentrations in MBR systems are only capped from the practical reasons at around ∼20,000 mg/L in a trade-off between capital expenditures (CAPEX) associated with reactor's volume

and operational expenditures (OPEX) associated with process aeration costs, mixing costs and fouling control, the maximum allowed MLSS in CASP is in practice around just 4,500 mg/L due to the existence of the, so called, maximum permissible solids flux as explained in the Kynch's theory of sedimentation [130]. Membranes used in MBR systems are driven by pressure difference called trans-membrane pressure (TMP) which creates energy potential allowing water with soluble components to pass through the membrane whilst all particulate matter on are retained on the membrane surface. Other types of membrane applications are extractive and diffusive systems which are used to either extract or introduce a specific component through a selective membrane. These two types of membranes however serve a different purpose and whilst such applications are still in a research stage they will not be discussed further in this thesis. Semipermeable membranes are used in MBRs not only to retain the particulate matter inside the bioreactor but also to provide a barrier for much smaller particles such as colloids and individual bacterial cells. Hirani et al. [94] recorded 5-7 log removals of coliform bacteria whereas Simmons et al. [223] observed 2-5 log removals of human enteric viruses for a range of different membranes and membrane bioreactors. Retention efficiencies for bacteria, viruses and various colloidal substances depend on the membrane material, membrane type, membrane pore size distribution (PSD) as well as the operating conditions which may promote or hinder such processes as e.g. formation of a gel layer which is found to act as a secondary barrier to impurities in the feed stream ultimately causing higher rejection efficiencies [251, 252].

Definition 2. Membrane is a thin film-like porous structure separating two fluids. It acts as a selective barrier between these two phases, allowing some specific particles, molecules, or substances through when exposed to the action of a driving force while blocking the passage of others. According to International Union of Pure and Applied Chemistry (IUPAC), porous membranes can be divided into three categories based on their pore diameters: microporous ($\bar{d}_p < 2\,\text{nm}$), mesoporous ($2\,\text{nm} < \bar{d}_p < 50\,\text{nm}$), and macroporous ($\bar{d}_p > 50\,\text{nm}$), where $\bar{d}_p$ denotes the mean pore diameter.

For a given membrane, the driving force applied on one side of the membrane controls the rate of passage of the permeating components. This driving force results either from the pressure (ΔP), concentration (Δc), temperature (ΔT) or electric potential (ΔE) difference across the membrane. Classification of major membrane separation techniques is provided in Table 2.1.

Selectivity of a membrane can be exploited to achieve one of the three goals:

1. Retain suspended and/or solute components whilst removing the solvent phase (rejection membranes).
2. Selectively extract constituents (extractive membranes).
3. Introduce some components in a molecular form (diffusive membranes).

As briefly noted in the beginning of this section, MBRs employ pressure-driven rejection membranes of the MF or UF type. Hence, only these two types of membranes will be considered throughout this thesis.

Table 2.1: Classification of major membrane separation techniques - Narębska [177].

Driving force	Process	Applied membrane	Separation mechanism
ΔP	Microfiltration (MF)	Porous	Pore flow
ΔP	Ultrafiltration (UF)	Porous asymmetric	Pore flow
ΔP	Nanofiltration (NF)	Porous, asymmetric with ions on surface	Pore flow + Donnan effect
ΔP	Reverse osmosis (RO)	Porous, asymmetric	Solution-diffusive (or sorption-capillary solvent flow)
Δc	Gas separation (Gs)	Asymmetric with non-porous dense skin	Sorption-diffusive
Δc	Pervaporation (Pv)	Asymmetric, nonporous	Sorption-diffusive
Δc	Vapour permeation (VP)	Asymmetric, nonporous	Sorption-diffusive
Δc	Dialysis (D)	Polymeric, strong hydrated	Capillary transport
Δc	Membrane extraction (ME)	Porous	Diffusion
Δc	Liquid membranes (LM)	Liquid	Solution-diffusive
ΔT	Membrane distillation (MD)	Porous, lyophobic	Diffusion
ΔE	Electrodialysis (ED)	Gel, ionic	Ion migration

ΔP = Pressure difference, Δc = Concentration difference, ΔT = Temperature difference, ΔE = Electric potential difference

2.1.1 Membranes in MBR systems for wastewater treatment

Pressure-driven rejection membranes are composed of inorganic compounds, e.g. ceramics, metals, glass and graphite, or organic compounds such as different types of polymers. With regards to membrane structure, the membrane with pores of significant sizes making up a large area compared to the total membrane area is termed *porous*, while one with no discernible pores in the macroscopic sense is termed a *nonporous* or *dense* membrane. Membrane with reasonably cylindrical pores where the aerial porosity on both sides of the membrane is identical is termed a *symmetrical* isotropic membrane, while one with conical pores where porosity in the surface layer is lowest and grows perpendicular to the surface, is called a porous *asymmetrical* anisotropic membrane. Asymmetric membranes can also be dense.

One of the biggest problems facing MBR operators is the loss of membrane's permeability due combined effects of **fouling** and **clogging**.

Definition 3. Membrane **fouling** is a combined effect of a number of physical, chemical and biological processes which all lead to the decrease of membrane's permeability and thus increase of its resistance. As a result, the membrane creates a higher pressure drop during filtration and requires higher TMPs in order to maintain the required flux values.

Fouling leads to an increase in capital expenditures (CAPEX) as well as operational expenditures (OPEX) in MBR plants. CAPEX are associated with periodic purchasing of new membrane modules once the detrimental effects of fouling can no longer be reversed. OPEX are due to permeate pumping, control of reversible fouling (such as air-

scouring, backwashing and provision of crossflow velocity (CFV)), and use of chemicals for removal of irreversible fouling.

Extent of membrane fouling depends on the membrane characteristics and interaction with the feed and biomass as well as on the operational procedures. In particular, membrane fouling is believed to be affected by several different factors, mostly soluble microbial products (SMP) and bound extracellular polymeric substances (EPS) concentrations in the bulk liquid, membrane type, floc size distribution and sludge morphology, and can be controlled by maintaining appropriate hydrodynamic and bioprocess conditions in the bioreactor and application of periodic cleaning procedures (backwashing, relaxation and chemical cleaning). Membrane fouling needs to be kept under control and at economical levels as it leads to reduced productivity, shortened membrane lifetime and increased operational costs.

Fouling can be classified into the following three categories, based on the following:

- **Permeability recovery**. *Reversible fouling* is the type of fouling that can be recovered by physical means such as backwashing or relaxation. *irreversible fouling* is the type of fouling that cannot be removed by physical means, but can be recovered with chemical reagents, such as caustics, oxidants, acids or various other chemical substances such biocide agents, chelating agents such as EDTA, and enzymatic detergents. Chemical clean can be performed either on-line or off-line. *Irrecoverable fouling* is the type of fouling which cannot be removed with any known methods and ultimately leads to the loss of productivity and finally necessitates the replacement of the membrane modules.
- **Inorganic/organic type of the foulants**. Inorganic fouling is caused by adsorption and precipitation (scaling) of dissolved inorganic solutes out of solution onto the membrane surface. Organic fouling is caused by formation of biofilms on the membrane surface due to biological activity in the feed and by attachment of various colloidal and particulate substances of biological origins, such as bacteria, SMP, EPS, etc.
- **Mechanistic fouling mechanism**. Fouling can be approximated with one of the five mechanistic models for membrane fouling such as: pore constriction, pore blocking, cake formation, biofilm growth and gel-layer formation.

Definition 4. Clogging results from obstruction of membrane module channel passages by various solid materials leading to restriction of flow in the vicinity of the membrane surface (sludging) and blocking of membrane channel inlets (matting). Clogging can be reduced through application of appropriate upstream screening and provision of adequate turbulent conditions within the membrane modules.

2.1.2 Process configurations

Membrane bioreactors can be configured either as a sidestream process in which the membranes are placed outside the bioreactor or as an immersed process where the

membranes are submerged in the bulk liquid. In the sidestream process mixed liquor is pumped at velocities of around $2 - 5$ m s^{-1} through an externally located membrane module. During its passage a fraction of the liquid's volume is filtered and leaves on the other side of the membrane as *permeate*. The remaining volume of slightly concentrated liquid called *retentate* is rejected by the membrane and flows out on the other end of the membrane module and back into the bioreactor. In immersed process, pumping and recirculation is avoided as the membrane is directly immersed in the bulk liquid. Whereas in sidestream systems the driving force is provided by recirculation pumps creating high flow and pressure conditions inside the membrane module, immersed membranes are operated with suction pumps creating vacuum on the permeate side of the membrane. Both configurations are represented in a schematic diagram in Figure 2.1.

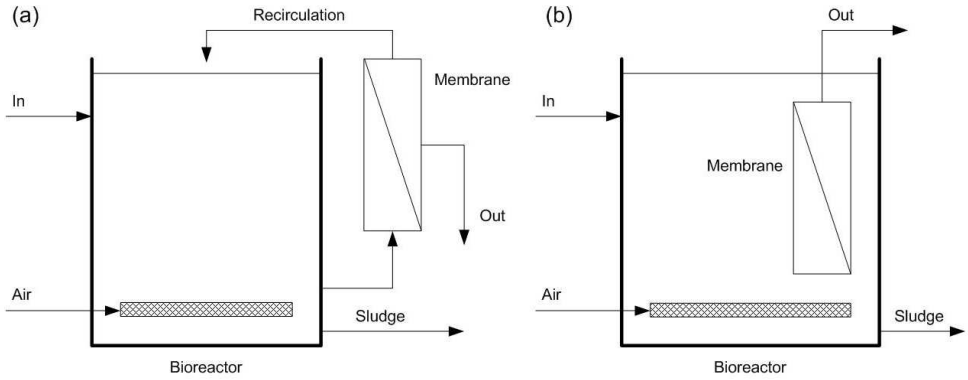

Figure 2.1: Membrane placement and flow routing in sidestream (a) and immersed (b) MBR configurations.

The underlying mechanisms of filtration, the operating conditions and the types of membranes used in both configurations are fundamentally different what necessitates adoption of different control and operating strategies, especially in the area of fouling control. Both systems differ significantly and have different associated capital expenditures (CAPEX) and operational expenditures (OPEX). The mode of filtration in sidestream systems is called *cross-flow* because the liquid runs parallel to the membrane surface and perpendicular to the permeate flow across the membrane. On the other hand, immersed systems operate in the, so called *dead-end* filtration, where the feed flow is in the same direction as the permeate flow. Whilst cross-flow mode of operation simultaneously combines filtration and prevention of cake buildup, dead-end filtration requires additional mechanisms to counter-affect particle deposition. In order to create shear conditions on membrane surface, air bubbles are injected at the bottom and parallel to the membrane, what is known as *air scouring*.

In sidestream MBRs the main method of reversible fouling control is by creating crossflow velocity (CFV) near the membrane surface. Originally, the permeate flow rate was solely dependent on the recirculation flow rate which was proportional to the pressure difference across the length of the module. Such process was very expensive to operate as the CFV had to be unnecessarily higher than required from the point of

view fouling control in order to generate the required TMP across the membrane. In order to detach the permeate and fouling control mechanisms and, at the same time, increase the operational flexibility of the sidestream systems, some designs now include a permeate suction pump which assists in permeate withdrawal and allows the operators to increase the pressure difference across the membrane without necessarily increasing the recirculation. Some of the newer sidestream MBRs also allow air to be injected into the module to generate more turbulent conditions on the feed side of the membrane and hence intensify cake detachment, thus further reducing the requirement for high CFVs. As a consequence of large shear rates produced by high CFVs, sidestream systems can operate under relatively high sustainable permeate fluxes of around $50-100$ L m^{-2} h^{-1} whilst immersed system are only able to achieve fluxes of about $15-50$ L m^{-2} h^{-1}. Operation under high flux rates in sidestream systems comes at the cost of higher required energy inputs which may vary between $3-15$ kWh m^{-3} - significantly larger than $0.3-0.6$ kWh m^{-3} characteristic of the immersed systems. The actual energy consumption in a MBR unit will however greatly depend on its configuration and the manner in which the unit is operated.

In the absence of the recirculation stream, TMP in immersed MBRs is generated solely by the suction pump installed on the permeate side of the membrane. In some systems equipped with flat sheet (FS) membranes and operating at low permeate fluxes, the required flux rate can sometimes be achieved solely under hydrostatic head. The suction pump is only used for assistance and to allow a greater operational flexibility. Cake deposition is usually prevented, as described in the previous paragraph, by provision of coarse air bubbles which induce shear on the membrane surface and cause the deposited particles to detach and return back to the bulk liquid or even prevent the particles of certain sizes to reach the membrane. The so-called *selective deposition* is described in greater detail Chapter 5 in Section 5.4. Although immersed MBRs operate under lower fluxes which implies lower energy demand for pumping and amelioration of reversible fouling compared to sidestream MBRs, this comes at the cost of higher required CAPEX for purchasing of additional membrane surface area.

Membranes in both MBR configurations have to be periodically subjected to chemical cleaning in order to remove the effects of the, so-called irreversible fouling and, at the same time, to get rid of other larger deposited materials which clog the channels in the membrane modules. Chemical cleaning of membrane modules can be carried out inside the membrane unit housing, which is called cleaning in place (CiP) or off-line after they have been removed from the whole unit.

Immersed MBRs are usually equipped with flat sheet (FS) or hollow fibre (HF) membranes whereas sidestream configurations most often use multi-tube (MT) membranes. Since immersed systems operate at lower fluxes and therefore require more membrane area per flow but are less energy intensive and operate at smaller TMPs they are usually used in municipal and large scale wastewater treatment applications. As the side-stream configurations are more energy intensive but operate at higher fluxes and are therefore more compact whilst also offering higher operational flexibility they

are usually used in industrial applications.

Comparison of various properties of the sidestream and immersed MBRs against a CASP are summarised in Table 2.2.

Table 2.2: Comparison of sidestream and immersed MBR configurations against conventional activated sludge processs (CASPs).

	CASP	Sidestream MBR	Immersed MBR
Typical configuration[1)]	ASP + FST	T, PF	HF, FS
Mode of operation		Crossflow	Moderate crossflow
Packing density		High	Low
CAPEX			
Footprint	Normal	>10 times smaller	
Clarifier	Yes	No	
Tertiary treatment	Sand filtration	No	
Process stability	Susceptible to bulking and toxicity	Susceptible to toxicity and high flows	
OPEX			
MLSS (mg L^{-3})	$< 4,500$	$8,000 - 20,000$	
HRT (h)	$6 - 24$	$2 - 6$	
SRT (d)	< 20	$15 - 100$	
Sludge yield (gSS $g^{-1}BOD_5$)	> 0.75	< 0.8	
Bioreactor volume (m^3)	Normal	4-5 times smaller	4 times smaller
TMP (bar)	N/A	$3 - 6$	$0.05 - 0.5$ (vacuum)
α factor	$0.6 - 0.8$	$0.3 - 0.7$	$0.3 - 0.7$
Permeate flux rates (L m^{-2} h^{-1})	N/A	$50 - 100$	$15 - 50$
Permeability (L m^{-2} h^{-1} kPa^{-1})	N/A	$0.07 - 0.3$	$0.5 - 5$
Recycle ratio (m^3 feed m^{-3} effluent)	$1.5 - 2.5$	$25 - 75$	N/A
Sup. velocity (m s^{-1})	N/A	$2 - 6$	$0.2 - 0.3$ [2)]
Sup. velocity (m^3 air m^{-3} permeate)	N/A	N/A	$7 - 30$
Energy consumption (kWh m^{-3})	$0.15 - 0.25$ [3)]	$4 - 12$ [4)]	$0.2 - 1$ [4)]
Fouling control methods	N/A	CFV, backwashing, chemical cleaning	aeration, backwashing, backpulse, relaxation, chemical cleaning

[1)] T - tubular, PF - plate and frame, HF - hollow fibre, FS - flat sheet

[2)] Calculated from gas superficial velocity - Yamanoi and Kageyama [263]

[3)] Based on Europe's larger plants - inversely proportional to scale

[4)] Depending on size

MBRs gradually become more popular on the industrial as well as municipal wastewater treatment markets. Their success can be mainly attributed to their superior effluent quality and a much smaller physical footprint compared to CASP. As the effluent quality requirements get more stringent and water unit prices become higher making water recycling options more viable, while membrane unit prices continue to fall, the MBR technology is becoming more cost-effective against conventional wastewater treatment solutions. Recent market indicate that the market value of the MBR technology was approximately $217 million in 2005 and rising at an average annual growth rate of 10.9% - significantly faster than other competitive processes such as aerated filters or sequencing batch reactors (SBRs) [116]. As shown in Figure 1 on page 7 BCC research shows that the global market for membrane bioreactor technology is expected to grow at a compound annual growth rate (CAGR) of 13.2% increasing in value from

an estimated $150 million in 2002 to a forecasted $627 million by 2015.

2.1.3 Types and classification of semipermeable membranes

The most common membrane processes in water and wastewater treatment are, respectively, reverse osmosis (RO), nanofiltration (NF), ultrafiltration (UF) and microfiltration (MF). Each filtration process is characterised with its filtration spectrum, i.e. range of particle/molecule diameters which are rejected by the filtration medium. In membrane filtration, filtration spectrum depends on the membrane PSD and on its surrogate parameter, molecular weight cut-offs (MWCOs) - see Figure 2.2.

Traditional particle filtration in the far right of the filtration spectrum is usually used for effluent polishing (tertiary treatment) to remove larger solid particles after final sedimentation. RO and NF are normally used in water treatment and are seldom installed on wastewater treatment plants (WWTPs). Nevertheless RO and NF can be installed after MF and UF as a so-called 'toilet to tap' solution where wastewater is completely treated and converted to drinking water. Whilst full-scale municipal WWTPs of this kind are still rare, NF and RO applications in industrial wastewater treatment are increasingly more common.

RO is the finest level of filtration available and forms a barrier to all dissolved salts and inorganic molecules and organic molecules with molecular weights (MWs) over 100 Da. Rejection of dissolved salts is typically from 95% to over 99% what allows production of fresh drinking water from saline and brackish waters. The effluent is completely devoid of bacterial cells and viruses. NF rejects particles of the size over 1 nm (10 Å) and has a MWCO of 100-20,000 Da. NF can remove virtually all cysts, bacteria, viruses and humic substances. Dissolved salts are rejected at the ratios of 20-98%. Salts with monovalent anions have rejections of 20-80% whereas salts with divalent anions have higher rejections of 90-98%.

MBR reactors are equipped either with UF or MF membranes. UF filtration provides a barrier for macro-molecular particles in the range between 20 to 1,000 Å, i.e. up to 0.1 μm. Most of the colloids, proteins, microbiological contaminants and large organic molecules are rejected whereas all dissolved salts and smaller molecules pass through the membrane and end up in the permeate. Most UF membranes have MWCO values between 10,000 and 200,000 Da. MF membranes remove particles in the size of approximately 0.1 to 1 μm. Suspended particles and large colloids are rejected while macromolecules and dissolved solids pass through the membrane.

Semipermeable rejection membranes, regardless of their type, whether MF, UF, NF or RO, are characterised with the following parameters which determine their permeability characteristics, susceptibility to fouling, mechanical resistance, resistance to environmental conditions and influence the membrane module design:

1. Material;
2. Porosity;

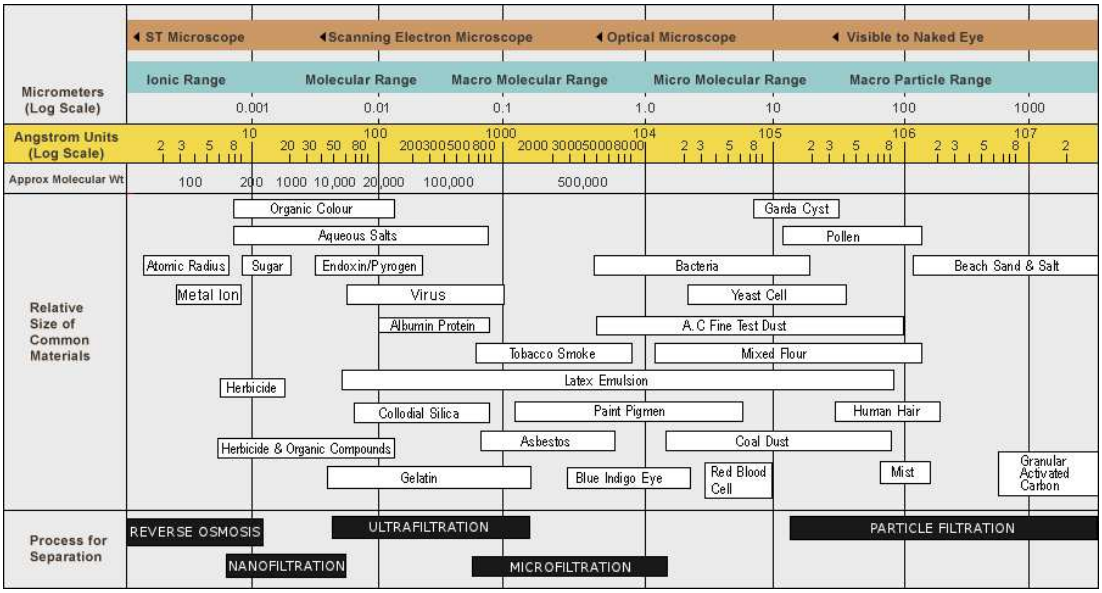

Figure 2.2: Membrane filtration spectrums, molecular weight cutoffs, and types of retained substances for different membrane filtration processes © Copyright 1990, 1984 Osmonics Inc. Minnetonka, Minnesota, USA .

[1)] Approximate molecular weight is measured in Daltons (Da)

3. Pore size distribution (PSD);
4. Hydrophobicity (measured as a contact angle);
5. Surface roughness (measured with atomic force microscopy);
6. Surface charge (measured as ζ potential);
7. Clean membrane permeability;
8. Packing density;

2.1.4 Advantages of MBR technology

Advantages of MBR systems versus conventional treatment processes are listed below:

1. High quality, completely clarified (i.e. near zero effluent suspended solids) and, to a large degree, disinfected effluent produced in a single treatment process. The level of disinfection depends on the membrane pore size distribution (PSD) as well as the operating conditions. Whilst MF membranes are capable of removing most of bacterial cells, the UF membrane modules can remove bacteria and some viruses - see Figure 2.2 for details.
2. Independent control of sludge retention time (SRT) and hydraulic retention time (HRT). In CASP, the maximum obtainable MLSS concentration and therefore SRT within a given reactor volume, depends on sludge separation and thickening in a FST. Clarification and thickening processes in turn depend on the hydraulic conditions inside the FST and decrease with the upflow velocity (UFV), recirculated activated sludge (RAS) and influent flow rates. They are also dependent on sludge floc size distribution (FSD) and morphology which vary with the bioreac-

tor's HRT. As a consequence, SRT cannot be controlled independently of HRT as the maximum attainable MLSS concentration is highly dependent on the influent flow rate to the plant. Conversely, in MBRs sludge separation efficiency is affected neither by MLSS nor influent flow rates. Hence, no risk of biomass washout other than through foaming exists. It is thus theoretically possible to maintain a wide range of MLSS concentrations and SRTs irrespectively of the flow rate through the plant.

3. Higher MLSS concentrations and higher SRTs compared to CASP process lead to an improved removal of trace organics through establishment of specialist microorganisms in sludge biocenosis [203]. MLSS concentrations in CASP reactors are limited to around 2,000-4,500 mg L^{-1} depending on sludge settleability, as higher sludge concentrations would lead to the violation of the critical permissible mass flux in the FSTs [130]. MBRs, on the other hand, can operate with poor settling, non-flocculent and filamentous sludges at MLSS concentrations of around 8,000-20,000 mg L^{-1}. This allows the bioreactor's volume to be reduced by 200% to 500% compared to CASP. Higher MLSS concentrations are also possible but at the cost of increased OPEX due to cake buildup on the membrane surface and reduction of oxygen transfer.
4. Smaller land footprint compared to CASP as a result of elimination of FSTs and tertiary processes such as e.g. biological aerated filters (BAFs) or sand filters and reduction of the bioreactor's volume as mentioned above. The reduction in footprint can be as high as 70% depending on initial CASP design, i.e. treatment process complexity, amount and type of tertiary treatment units, etc. Lower land requirements make MBRs an attractive option for construction in developed urban areas as part of a decentralised wastewater treatment system, grey-water recycling within buildings and when retrofitting older WWTPs on congested sites.
5. Reduced waste activated sludge (WAS) production as a result of longer SRTs promoting sludge lysis and stabilisation. Operation at longer SRTs also leads to higher and more stable removal of organic matter and ammoniacal nitrogen (NH_4^+-N), thus higher effluent quality.
6. Ease of operation due to elimination of complicated recycling streams and FSTs and combination of biological and sludge separation processes in a single tank. This point is however debatable due to additional required maintenance procedures for periodic membrane cleaning and ultimately replacement as well as occasional suppression of foaming in MBRs caused by accumulation of biopolymers, especially EPS, [116].

In summary, the above characteristics of MBR systems enable them to be cost-effective in applications where either land is scarce, high effluent quality is required or where treated effluent needs to be reused at source.

2.1.5 Disadvantages of MBR technology

MBR systems also possess a number of disadvantages over CASP systems. These disadvantages are outlined below:

1. Larger operational expenditures (OPEX) associated with purchasing membrane cleaning chemicals and energy consumption for process aeration and sustained operation of the membranes. The energy costs in membrane filtration result from permeate pumping, backwashing, and provision of CFV and/or aeration for reversible fouling control. The chemicals are used to partly recover the membrane's permeability lost due to irreversible fouling. Higher process aeration costs of a MBR compared to a conventional activated sludge process (CASP) result from lower O_2 transfer rates. O_2 transfer rates are found to be hindered by the presence of suspended solids and diminish exponentially with MLSS as described in Equation 7.21 on page 225. Due to lower O_2 transfer rates, higher volumetric air-flows in diffused air aeration systems are required to supply the same amounts of oxygen to aerobic microorganisms in activated sludge. A break-down of energy usage for different activities in an immersed HF MBR equipped with ZeeWeed membranes is shown in Figure 2.3. Figure 2.3 shows that membrane aeration is the second largest consumer of energy after process aeration.
2. Higher CAPEX incurred mainly by installation and replacements of relatively expensive membrane modules. MBR systems also require better upstream screening, typically with 1-3 mm spacings to prevent the clogging of the membrane channels, especially by fibrous materials such as hair. These capital costs can often be partly offset by lower costs of construction due to smaller process volumes and lower land requirements.
3. Higher risk of foaming promoted by larger air flows and accumulation of EPS.
4. Greater sensitivity to shock loads as a consequence of lower HRT, thus smaller volumes and hence lesser attenuation. Although MBR systems are less prone to biomass washouts at high flow rates than conventional systems equipped with FSTs which can only thicken and return a certain flux of solids depending on floc shape, surface area and sludge volume index (SVI), MBRs are still prone to high flow rates. Once the permeate flux exceeds the so-called critical-flux, severe fouling of the membrane begins. This implies higher operating costs for subsequent chemical cleaning and pumping under higher TMPs, which ultimately leads to lower productivity as a result of the decline in the permeate flow.
5. Lower dewaterability of the surplus activated sludge resulting from the presence of the so called pin-point flocs, i.e. flocs with diameters below 1 mm. The pin-point flocs are produced in MBR systems by shear forces caused by cross-flow (in side-stream systems) and mixing and aeration (in immersed systems). The shear forces acting on the flocs lead to collisions which in turn cause the flocs to rupture ultimately leading to a decrease in floc diameters. Sludge of poor dewaterability requires larger sludge processing facilities and higher doses of coagulants and

flocculants, therefore increasing both CAPEX and OPEX of WWTPs.

6. Although MBRs combine several otherwise separate processes such as bioreactor, FST and various tertiary treatment units within a single tank, hence they are less complex than CASPs, they often require more complex control and automation equipment as well as specialised staff to enable smooth and robust operation of the membranes.
7. Due to relatively high although gradually decreasing CAPEX and OPEX, MBRs are still less competitive than CASP systems on large municipal wastewater treatment plants (WWTPs) where only intermediate effluent quality is usually required and the land availability is usually not an issue.
8. Most of the above deficiencies are related to membrane fouling and membrane channel clogging which have been defined earlier - see Definition 3 on page 28 and Definition 4 on page 29.

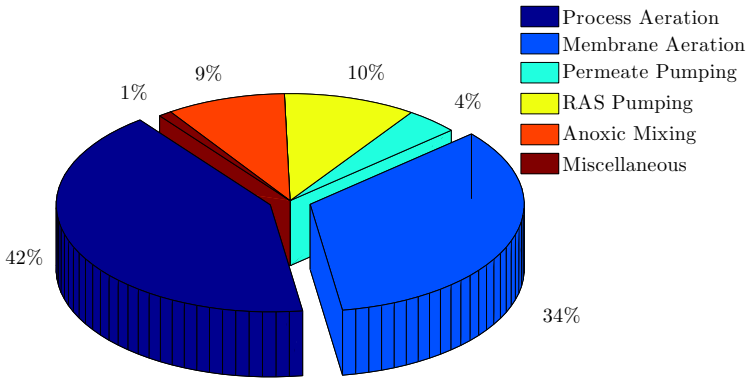

Figure 2.3: Energy consumption in a Zenon ZeeWeed immersed MBR Chris Jeffery, Zenon Environmental Inc., SAWEA Workshop 2005 .

In summary, large treatment efficiencies and high effluent quality achievable within small process volumes, i.e. process intensification comes at a cost of higher OPEX and often also CAPEX. MBR systems are thus viable under certain circumstances e.g. where land availability is an issue and high effluent quality, water reuse and/or robust and maintenance-free operation are required and play a crucial factor in the selection of an appropriate treatment process. Where land availability and water scarcity are not an issue and effluent consents can be met without extensive tertiary treatment (i.e. in cases of large scale municipal WWTPs discharging to large non-sensitive water bodies) MBRs lose their competitive edge over conventional processes due to higher OPEX. Although most of research and development in this area is currently focussing on reducing this gap and, as a result of this research, MBRs are gradually becoming more energy efficient, the difference in treatment economies of MBR and CASP systems (see Table 2.2 for reference) still has a limiting effect on the growth of the MBR market.

2.1.6 Applications of MBR technology

Thanks to their advantages, as listed above in Section 2.1.4, MBRs are applied in many different wastewater (WW) treatment schemes. The list presented below is by no means exhaustive, although shows a variety of uses for the MBR technology.

1. Municipal WW treatment where high effluent quality is required (i.e. effluent is discharged to a sensitive water body or is further treated on NF or RO membranes;
2. Municipal WWTP refurbishments where process capacity needs to be increased but the available land is limited;
3. Industrial WW treatment with process water recycling, e.g. in the water intensive food industry;
4. Industrial WW treatment where sludge bulking is likely or where removal of specific contaminants such as e.g. endocrine disruptors is required;
5. Packaged MBR plants which require small footprint, very low maintenance and modular design;
6. Black-water / grey-water / rainwater recycling plants;

2.2 Research trends in MBR reactors

As a substantial part of OPEX of a MBR reactor is required to counter the negative effects of membrane fouling, most of the research projects on MBRs are either directly or indirectly focused on minimisation of fouling. Most of the research is focussed on seeking optimal operating conditions, development of membranes less prone to fouling, more energy-efficient reactor designs, influent pretreatment and dosing of various additives. This thesis is focused on the first task, i.e. development of a mathematical model of an immersed membrane bioreactor (iMBR) which can be used for model-based process optimisation, minimisation of energy consumption and development of energy-conserving operational and control strategies.

Selection of optimal operating conditions is not straightforward because the same process outputs are affected by more than one control variable. For example, increasing air-scouring will raise the energy costs for aeration but at the same time, lower the reversible fouling rates and thus, decrease the energy costs for permeate pumping. It is however also possible that raising the air-scouring rate may increase rather than decrease fouling by promoting the formation of denser cakes of higher specific cake resistance (SCR). Process engineers usually need to find a compromise between CAPEX and OPEX. Higher capital investments for larger bioreactor volumes or total membrane area will lead to lower MLSS concentrations and lower operating fluxes and hence decrease the reversible and irreversible fouling rates. By increasing the MLSS concentration and therefore the SRT, on the other hand, cake accumulation will also increase but irreversible fouling and often also reversible fouling may become smaller due to lower SMP and EPS contents in the bulk liquid. Too much of an increase in MLSS will

however substantially decrease the oxygen transfer efficiency leading to higher required airflow rates for process aeration and will increase the rates of clogging and reversible fouling.

Such complex operational issues facing MBR plant operators led to heavy research and development in the area of process control and optimisation, development of cheaper and less prone to fouling membranes, influent pretreatment, development of anti-fouling additives and optimisation of membrane modules designs. Some of the research areas associated with MBR systems are listed below.

1. Better understanding of membrane fouling and clogging mechanisms;
2. Interactions between biological and membrane parts of the process;
3. New membrane processes and applications, e.g. forward osmosis in sewer-mining;
4. Cheaper and more resistant membranes;
5. Less fouling membranes (surface modification, new membrane materials);
6. Additives;
7. Influent pretreatment;
8. Mitigation/reduction of fouling through new control strategies and fouling control devices;
9. Membrane module design optimisation;
10. Bioreactor design;
11. Integrated systems, such as activated sludge (AS)-MBR, biofilm-MBR, anaerobic MBR, etc.

2.3 Research questions addressed in this thesis

Since, as described earlier, MBRs are often criticised for relatively high OPEX due to their high energy demands and consumption of chemicals, this research is focused on creating an immersed MBR model which can be used by plant designers and operators for energy and process optimisation. This model is validated on a number of experimental data and can be integrated with other process models for the purpose of plant-wide design, control-strategy design, optimisation, decision support and education. The research first explores the existing theories and empirical evidence on polymer production in activated sludge systems and fouling of MF and UF membranes. As most of the existing models were found to be either incapable or not thorough enough to be used in an integrated MBR model, new models were developed for both parts of the system, leading to new knowledge. Selected new models are linked together through specific interface models and share the same state variables - see Figure 1.4. These models relate the reversible and irreversible fouling rates to the SMP and EPS concentrations predicted by the activated sludge model (ASM), link cake detachment to coarse bubble aeration rates and permeate fluxes, define SMP deposition as a function of permeate flux, and describe SMP retention on the membrane as a function of SRT. The integrated

MBR model is built using the plant layout used in the MBR benchmark publication of Maere et al. [160] and simulated with the inputs and under the operating parameters defined in COST624 [37], Copp [36] and Maere et al. [160].

The aims of this research can be broken down into answering the following specific research questions:

1. Can a combined SMP and EPS kinetic model of Laspidou and Rittmann [135] be integrated into ASM1 and ASM3 activated sludge models and used to successfully predict the SMP and EPS production in a real wastewater treatment system.
2. Can a simple behavioural fouling model be used for the description of a full scale MF or UF filtration system.
3. Is it possible to predict a two-stage TMP profile with a three mechanism mechanistic fouling model.
4. What functional relationship exists between the superficial air velocity in coarse bubble aeration and shear stresses on the surface of immersed hollow-fibre membranes.
5. Can a developed MBR benchmark model allow more comprehensive and realistic simulation and optimisation studies of MBR systems.

2.4 Summary

To summarise, MBR is an intensified activated sludge process offering superior treatment efficiency in a much smaller reactor volume compared to a CASP process. The apparent benefits of MBRs come at a cost of higher operational and often capital expenses, thus limiting the use of membrane reactors to applications where either superior effluent quality or small footprint are required. The applications of MBRs are many in water-intensive industries where it becomes cost-effective to recycle wastewater into process water. As membrane modules get progressively cheaper, requirements for treated effluent quality become more stringent, and operation of MBRs gradually becomes more cost-effective, the market for MBRs, both in industrial as well as municipal WW treatment applications, grows in size.

Fouling and clogging of membranes are however still a major concern. Thus, significant research and development efforts are made to limit the extents of fouling and clogging either through a development of lesser fouling membranes, more energy efficient module designs, process modification, invention of fouling reduction additives, and process optimisation. The last task can be achieved either on a physical system, which is likely to be very time-consuming and costly, or with the help of dynamic mathematical models. Since at present no such models are available for MBR systems, work presented in this thesis describes the development of a dynamic mathematical MBR model for process optimisation and simulation.

Part I

Modelling of Activated Sludge

Chapter 3

Overview and comparison of activated sludge models

Contents

3.1 Principles of modelling activated sludge systems

Activated sludge bioreactors are very complex systems with regards to hydraulics, biochemical reactions and variability of influent wastewater composition. Activated sludge

bioreactors are thus very difficult to model and one has to make a significant number of simplifications before constructing a feasible activated sludge bioreactor model that can be simulated within realistic time-scales.

Activated sludge bioreactors come in different shapes, sizes and configurations, although in this thesis, only a small subset of them, namely aerated continuously fed immersed membrane bioreactors (MBRs) are considered. For more information about these as well as other types of activated sludge bioreactors the reader is referred to Tchobanoglous et al. [236]. A brief overview of MBR reactors and the MBR technology has been provided in Chapter 2.

3.1.1 Bioreactor hydraulics

Flow patterns through continuous flow bioreactors are very complex in nature due to often complicated tank geometries as well as positioning and construction of inlets, outlets, mixers, baffles and aeration devices. Depending on these features as well as various operating conditions, such as e.g. liquid and air flow rates and mixing intensities, reactors may exhibit a number of usually unwanted hydraulic conditions such as internal recirculation loops, density currents, short-circuits and dead-zones [123]. These hydraulic conditions affect the residence time distributions (RTDs) of the liquid, solid and gaseous phases in the mixed liquor.

To represent all of the above mentioned hydrodynamic effects in a mathematical model one has to discretise the bioreactor's geometry into usually very large number of 'elements' or 'volumes' and solve the discretised Navier-Stokes equations of mass, momentum, and energy conservation on the resulting grid of points called a mesh. The model takes shape of a, usually, large set of algebraic equations which tend to require significant processing power and memory resources for solving. The number of equations and thus, the required computational effort additionally become higher if reactive flows with biochemical reactions are to be considered. Although Computational Fluid Dynamics (CFD) has been applied to simulate a number of various processes for wastewater treatment, e.g. [42, 14, 112, 71], a fully dynamic three-dimensional (3D) flow simulation coupled with biochemical activated sludge model is not likely to be realistic on a desktop computer in the near future due to very long expected simulation times, possibility of poor convergence and the time it takes to formulate and set-up such a model for a physical unit. Although attempts are being made to simulate activated sludge bioreactors with CFD models coupled with activated sludge models [198], most of the times, hydrodynamics of the bioreactor are neglected and reactors are assumed to exhibit ideal plug flow or completely-mixed flow patterns.

However, as full scale bioreactors seldom exhibit a fully mixed or ideal plug-flow behaviour, the internal flow pattern will usually fall somewhere in between these two extremes. These intermediate, not fully-mixed nor plug-flow conditions are usually modelled with a cascade of reactors as shown in Figure 3.1. As the number of reactors (N) in the cascade increases, the residence time distribution (RTD) in the cascade

tends to resemble one of a plug-flow and ultimately reaches one of ideal plug-flow when $N \to \infty$. The structure of the cascade of bioreactors can be adjusted by varying the number, volumes and sequence of completely stirred tank reactors (CSTRs), recycle rates, addition of sidestream tanks to represent dead-zones, introduction of by-passes to represent short-circuits, etc.

Identification of the 'tank-in-series' model topology is usually carried out first by identifying recirculation zones, dead-zones and short-circuits in the physical system through tracer tests, i.e. the analysis of time response to pulse or step change in the concentration of an introduced substance to the influent, and then by fitting the response curve of the mathematical 'tanks-in-series' model to the measurements [193]. Practical experiences with identification of the structures of wastewater treatment plant models using the 'tanks-in-series' approach often show that the structure of connections between reactors changes with operating conditions (influent flow rate, aeration rate, mixing, etc.) [3]. As tracer tests are usually carried out at just a single operating point, the modelled RTD is very likely to differ from the RTD of the physical system upon the change of the operating conditions. Despite of its limitations, this approach is at present the only viable option for process engineers due to high computational demand posed by hydrodynamic models, as already mentioned above.

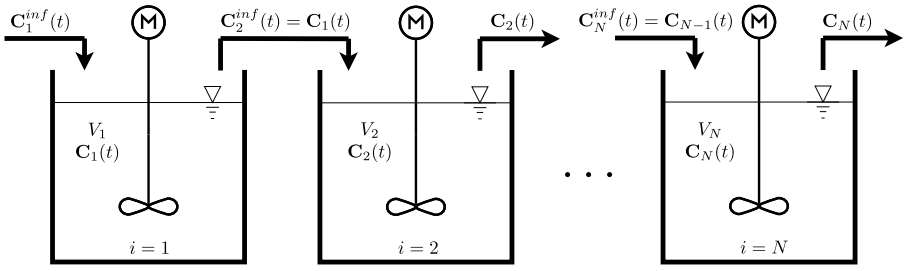

Figure 3.1: Graphical representation of a cascade of N CSTRs.

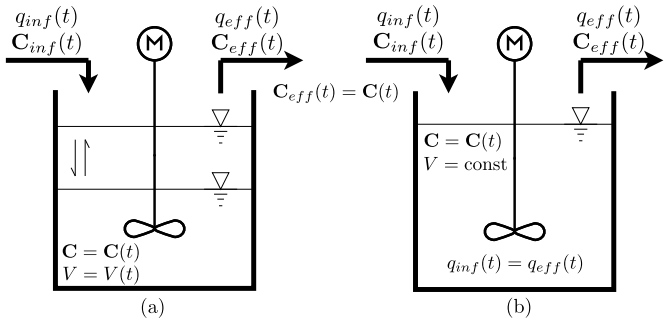

Figure 3.2: Graphical representation of a variable (a) and constant (b) volume CSTRs.

Each bioreactor in Figure 3.1 and Figure 3.2 is described with a general mass balance equation of the following form.

$$\frac{d}{dt}\left(\mathbf{C}\,V\right) = \sum \text{sources} - \sum \text{sinks} \tag{3.1}$$

where $\mathbf{C}$ denotes the vector of concentrations of various components in the bioreactor and V is the liquid phase volume.

Concentration $C \in \mathbf{C}$ of each component inside the bioreactor is diminished by sinks and increased by sources. In the bioreactors described in this thesis, these sinks and sources are attributed to the mass flow of liquid with main outflow and inflow, mass flow of air (e.g. aeration), secondary inflows and outflows (e.g. chemical dosing or waste activated sludge (WAS) withdrawal) and biochemical reactions in the bulk liquid. If aeration and chemical dosing are disregarded, mass balance equation for any CSTR can be written as follows:

$$\frac{d}{dt}(\mathbf{C}\,V) = q_{inf}\,\mathbf{C}_{inf} - q_{eff}\,\mathbf{C}_{eff} + \mathbf{r}\,V \tag{3.2}$$

where $\mathbf{C_{inf}}$, $\mathbf{C}$ and $\mathbf{C_{eff}}$ denote the vectors of concentrations of all considered wastewater constituents respectively in the influent, bulk liquid and effluent; $\mathbf{r}$ is the vector of reaction rates and $\dim(\mathbf{r}) = \dim(\mathbf{C})$; V is the reactor's active volume and q_{inf}; and q_{eff} are the influent and effluent flow rates.

After differentiating Equation 3.2 with respect to t and bearing in mind that in a completely stirred tank reactor (CSTR) $\mathbf{C}_{eff} = \mathbf{C}$, the mass balance of a variable volume CSTR can be expressed with a set of two following ordinary differential equations (ODEs).

$$\frac{d\mathbf{C}}{dt} = \frac{q_{inf}}{V}(\mathbf{C}_{inf} - \mathbf{C}) + \mathbf{r} \tag{3.3}$$

$$\frac{dV}{dt} = q_{inf} - q_{eff} \tag{3.4}$$

with I.C. $\mathbf{C}(0) = \mathbf{C}_0$ and $V(0) = V_0$

The ratio $\frac{q_{inf}}{V}$ in Equation 3.3 defines the dilution rate D, i.e. a reciprocal of the hydraulic retention time (HRT).

As the active volume of a constant volume CSTR is time invariant, the left hand side of Equation 3.4 becomes zero and the mass balance model of the CSTR reduces to just a single equation.

The reaction term $\mathbf{r}$ in Equation 3.3 can be calculated using different models and modelling approaches as described in Section 3.1.2 below.

3.1.2 Principles of modelling biochemical reactions

Biochemical process kinetics can be modelled on a macroscopic and on a microscopic level. The *macroscopic models*, which are used in this thesis, describe the biochemical processes with mass balance equations for elementary elements C, N, and P using gross formulae for the biomass, substrates and products. Substrates are assumed to be converted into products and biomass in a single step without any consideration of complex reactions occurring on a single cellular level. Macroscopic models do not consider any variations in composition and activity of individual cells and often lump various bacterial species into one biomass type characterised by its concentration: X (g m^{-3}), maximum growth rate: $\hat{\mu}$ (d^{-1}), decay rate k_D (d^{-1}), yield coefficient Y (–)

and other kinetic and stoichiometric parameters such as, e.g. Monod constants K for different substrates. On the contrary, *microscopic models* describe complex metabolic reactions taking place on a cellular level and take into account the cell composition, availability of enzymes, cell history, storage of metabolic intermediates, etc.

Kinetic models, whether macroscopic or microscopic can be *deterministic* or *stochastic*. *Deterministic* models assume that biochemical reaction pathways and their stoichiometric and kinetic parameters can be determined and, given the same initial conditions, the reactions will each time lead to the same evolution of model states (i.e. concentrations of substrates, by-products, products and biomass) over time. The stochastic approach assumes that all or some quantities in the model are random or stochastic. These quantities are modelled using probabilities and frequency distributions rather than 'crisp' values. Stochasticity and probability may be applied to microscopic as well as macroscopic models. In the microscopic approach, a stochastic model may, for example, consider the probability of a cell dividing under certain environmental conditions or the probability that the energy input to a reaction inside a cell exceeds the required activation energy.

Although most real-life biochemical reactions exhibit some stochastic behaviour, stochastic effects become more apparent in pure bacterial cultures rather than large mixed bacterial cultures. In mixed cultures, stochastic effects are averaged due to bacterial diversity where more than one species are responsible for the same processes whilst being in direct competition over e.g. substrates. If, randomly, one bacterial species dies off, other similar species take over their role thus making the effect of elimination of one bacterial species on the process outputs negligible. This behaviour of mixed bacterial cultures allows us to model the kinetics of the activated sludge systems using strictly deterministic models such as these described in Section 3.2 below.

For more information about different types of reactors and standard kinetics the reader is referred to *The encyclopedia of bioprocess technology* [64]. If the reader wishes to find out more about the state of the art in modelling and simulation of activated sludge WWTP using various mathematical approaches a very good review of this subject was published by Gernaey et al. [70].

3.2 Activated Sludge Models

Activated sludge systems can be described with various types of mathematical models from simple empirical ones, different forms of artificial intelligence (AI), to detailed mechanistic multi-species models of deterministic and stochastic nature. The approach generally accepted in the engineering and scientific community is to use a system of ordinary differential equations (ODEs) for macroscopic description of bacterial growth, decay and biochemical reactions in mixed cultures of activated sludge biocenosis, later referred to as activated sludge models (ASMs). Such models are described in Section 3.2.3, whilst the basic principles of activated sludge modelling are outlined in

Section 3.2.1 below.

3.2.1 Structure of activated sludge models

Vector of reaction rates, $\mathbf{r} \in \mathbb{R}^{\mathsf{n}}$ in Equation 3.2 and Equation 3.3 takes the form:

$$\mathbf{r} = \begin{pmatrix} r_1\left(\widehat{\mathbf{C}}_1 \subseteq \mathbf{C}, \mathbf{u}\right) \\ \vdots \\ r_n\left(\widehat{\mathbf{C}}_n \subseteq \mathbf{C}, \mathbf{u}\right) \end{pmatrix} \tag{3.5}$$

r_j where $j = 1 : n$ represents the rate of change of the concentration of the j-th component C_j due to biological and chemical reactions occurring inside the bioreactor. $\mathbf{C}$ is the vector of concentrations of soluble, colloidal and particulate components, including bacterial biomass. $\widehat{\mathbf{C}}_j$ is the vector of concentrations which are used as arguments in the rate equation r_j. $\mathbf{u}$ is the vector of external inputs such as e.g. temperature T. The number of reaction rates n is equal to the number of unknown concentrations in order to form a closed system of equations mandatory to ascertain the existence of a unique solution to a system of ODEs. Each component C_j is a substrate or a product of one or more biological or chemical processes, such as nitrification, hydrolysis, ammonification, etc. These processes $\mathbf{p} \in \mathbb{R}^{\mathsf{m}}$ can be represented in the following vector form:

$$\mathbf{p} = \begin{pmatrix} p_1\left(\breve{\mathbf{C}}_1 \subseteq \mathbf{C}, \mathbf{u}\right) \\ \vdots \\ p_m\left(\breve{\mathbf{C}}_m \subseteq \mathbf{C}, \mathbf{u}\right) \end{pmatrix} \tag{3.6}$$

where m denotes the number of processes. Each reaction rate r_j for component j can be expressed as a linear combination of several process rates p_i

$$\forall\ j \in \langle 1, n \rangle : \quad r_j = \sum_{i=1}^{m} a_{i,j}\ p_i \tag{3.7}$$

Equation 3.7 can also be written in the more popular matrix form as follows:

$$\mathbf{r} = \mathbf{A}^T\ \mathbf{p} \tag{3.8}$$

where $\mathbf{A} \in \mathbb{R}^{\mathsf{m} \times \mathsf{n}}$ is the matrix of stoichiometric parameters, also called the *Petersen Matrix*.

$$\mathbf{A} = \begin{pmatrix} a_{1,1} & \cdots & a_{1,n} \\ \vdots & \ddots & \vdots \\ a_{m,1} & \cdots & a_{m,n} \end{pmatrix}$$

Each stoichiometric parameter $a_{i,j}$ in matrix $\mathbf{A}$ represents the link between the rate of the i-th process p_i and the rate of change of the concentration of the j-th component C_j due to that process. If $a_{i,j} > 0$ then the component C_j is a product, if $a_{i,j} < 0$ then the component C_j is a substrate, and if $a_{i,j} = 0$ the component C_j does not take part in

that process. In simulations of continuous flow and constant volume CSTRs, the vector of state variables $\mathbf{x} \in \mathbb{R}^{\mathsf{n}}$ is equal to the vector of concentrations in the bulk liquid, $\mathbf{x} = \mathbf{C}$. Thus, if we replace $\mathbf{C}$ with $\mathbf{x}$, then $\dot{\mathbf{x}} = \mathbf{r}$ and Equation 3.8 can be written as:

$$\dot{\mathbf{x}} = \mathbf{A}^T \, \mathbf{p} \tag{3.9}$$

Each and every process $p \in \mathbf{p}$ must satisfy two main laws of chemistry: the *Law of Conservation of Mass* also known as the *Law of Conservation of Matter* and the *Law of Conservation of Energy*. The first law states that during an ordinary chemical reaction the mass of products equals the mass of reactants. Matter can be neither created nor destroyed, though it can be rearranged. The second law states that energy cannot be created or destroyed, but can change its form. In the context of activated sludge models (ASMs), conservation of these two fundamental laws necessitates that, in the most general form, each process p conserves the mass of carbon (C), nitrogen (N), phosphorus (P) and net electrical charge. The amounts of C, N, P and electrical charge in all components are written in a mass and charge conservation matrix:

$$\mathbf{I}_{4\times n} = \begin{pmatrix} I_{1,1} & \cdots & I_{1,n} \\ \vdots & \ddots & \vdots \\ I_{4,1} & \cdots & I_{4,n} \end{pmatrix} \tag{3.10}$$

where $I_{i,j}$ denotes the amount of C if $i = 1$, N if $i = 2$, P if $i = 3$ and electrical charge if $i = 4$ for the j-th component. Each reaction $r \in \mathbf{r}$ must satisfy all four balance equations, what imposes restrictions on the choice of stoichiometric parameters $a_{i,j} \in \mathbf{A}_{m\times n}$. In order to satisfy all balance equations the following matrix equation needs to be true.

$$\mathbf{A}_{m\times n} \, (\mathbf{I}_{4\times n})^T = \mathbf{0}_{m\times 4} \tag{3.11}$$

In order to satisfy the above equation, out of k non-zero stoichiometric parameters in the Petersen matrix $\mathbf{A}$, $k - 4\,m$ parameters are manually selected and the rest, i.e. $4\,m$ parameters need to be calculated by solving Equation 3.11 to ensure the conservation of mass and charge.

3.2.2 Reaction kinetics

The processes $p \in \mathbf{p}$ in Equation 3.6 represent various biochemical enzymatic reactions carried out by different types of bacteria in the activated sludge process. These reactions are associated with consumption of substrates, production of products, consumption or release of energy and growth or decay of biomass. In a general form, the rate of a process with one substrate and one bacterial biomass can be written as:

$$k(X, S) = \hat{k} \, \tau(X, S) \, \theta(T) \tag{3.12}$$

where $k(X, S)$ (kg m^{-3} d^{-1}) denotes the process rate under field conditions, $\hat{k}$ (d^{-1}) is the process rate under no substrate limitation and at usually 20°C, $\tau(X, S)$ is the

process rate dependency function on substrate (S) and biomass (X) concentrations and $\theta(T)$ is a non-dimensional temperature dependency coefficient.

In the ASM models the process rates $k(X, S)$ are usually proportional to the biomass concentration X (kg m^{-3}) and thus $\tau(X, S) = \tau(S)\, X$. Equation 3.12 then takes the following form:

$$k(X, S) = \hat{k}\, \tau(S)\, \theta(T)\, X \tag{3.13}$$

The value of $k(X, S)$ is lower than the maximum process rate rate $\hat{k}$ due to substrate limitation effects, diffusion effects, inhibition, competition for the same substrate by different types of bacteria, etc. These effects are accounted for in a non-dimensional function $\tau(S) < 1$, which may take one of the following forms as shown in Table 3.1.

Table 3.1: Reaction kinetics dependent on single substrate concentration.

	Model	Kinetics expression, $\tau(S)$
1	1$^{\text{st}}$ order kinetics	S
2	2$^{\text{nd}}$ order kinetics	$S^{\,2}$
3	n$^{\text{th}}$ order kinetics	$S^{\,n}$
4	Blackman	$\min(1, K_B\, S)$
5	Teissier	$1 - \exp(-K_T\, S)$
6	Monod	$\dfrac{S}{K_M + S}$
7	Moser	$\dfrac{S^R}{{K'_M}^R + S^R}$

K_B, K_T, K_M,and K'_M denote rate constants respectively for the Blackman, Teissier, Monod and Moser equations. Monod kinetics is a specific case of Moser kinetics where $R = 1$.

If the modelled process is additionally dependent on e.g. diffusion of substrate from bulk liquid to the bacterial cell or is inhibited by biomass or toxic effects, kinetic equations presented in Table 3.2 may be used for mathematical description of the process kinetics. In case of inhibition by single substrate S, product P or biomass X several kinetic equations developed by various researchers as these listed in Table 3.3 may be used. The population dynamics of bacterial species in ASM models consider two opposite mechanisms: growth and decay. The net growth of a bacterial species which considers biomass growth, maintenance, decay, and lysis is calculated as superposition of these two opposing mechanisms as shown in Equation 3.14.

$$\mu(X, S) = \hat{\mu}\, \tau(S)\, \theta(T)\, X - k_D\, \theta(T)\, X \tag{3.14}$$

where $\mu(X, S)$ (d^{-1}) denotes the net bacterial growth rate under field conditions, $\hat{\mu}$ (d^{-1}) denotes the maximum bacterial growth rate under no substrate limitation and k_D

Table 3.2: Reaction kinetics dependent on single substrate concentration with additional effects.

	Model	Kinetic expression, $\tau(S)$
1	Inhibition by biomass and diffusion effects limiting growth (Contois)	$\frac{S}{K_C\,X+S}$
2	Reduction of substrate concentration in the proximity of bacterial cells due to diffusion resistance (Powell)	$\frac{S-K_L\,\tau(S)}{K_M+S-K_L\,\tau(S)}$
3	Additional diffusive stream of substrate to bacterial cells (Mason and Milles)	$\frac{S}{K_M+S}+K_D\,S$
4	Influence of toxic substances included in substrates (Vavilin)	$\frac{S^R}{K_M^{R-P}\,S_0^P+S^R}$

K_C, K_M, K_L, K_D are the model parameters and S_0 (g m^3) denotes initial substrate concentration. Equation 3 is provided in an implicit form. R and P are adjustable constants.

(d^{-1}) is the bacterial decay coefficient and is most often assumed to be independent of milieu conditions other than the temperature T. Whilst bacterial growth processes are modelled with often complex kinetic expressions, biomass decay, lysis and maintenance processes are traditionally lumped in ASM models into a single expression with 1st order kinetics with respect to the biomass concentration X and the decay coefficient k_D (d^{-1}).

Whilst Equations 3.12-3.14 describe the dynamics of biochemical processes in a single culture - single substrate scenario, ASM models are multi-substrate and mixed-culture. Individual bacterial culture dynamics are dealt with by introducing new equations for every process and every bacterial species. As bacteria often require more than one substrate for their growth whilst being inhibited by the presence or absence of other substrates, their dynamics depend on a number of substances S. In a non-interactive model it is assumed that the overall process rate is dependent only on the most limiting substrate, which can be expressed with the following equation:

$$k\,(S_1,S_2,\ldots,S_N)=\hat{k}\cdot\min\{\tau_1(S_1),\tau_2(S_2),\cdots,\tau_N(S_N)\} \tag{3.15}$$

where $\tau_i(S_i)$ is the process rate limiting function for substance S_i. Activated sludge models introduced in the next Section 3.2.3 and used throughout the rest of this thesis follow an interactive model approach where the process rate is dependent on all rate limiting substances:

$$\mu\,(S_1,S_2,\ldots,S_N)=\hat{\mu}\cdot\tau_1(S_1)\cdot\tau_2(S_2)\cdot\ldots\cdot\tau_N(S_N)=\hat{\mu}\cdot\prod_{i=1}^{i=N}\tau_i(S_i) \tag{3.16}$$

For more information about modelling of bioprocesses, including process kinetics and material transport, the reader is referred to Flickinger and Drew [64].

Table 3.3: Inhibition kinetics for a single inhibitor.

	Model	Kinetic expression, $\tau(S)$
1	Competitive inhibition (Haldane)	$\frac{S}{K_M + S + \frac{S^2}{K_I}}$
2	Non-competitive inhibition (Yeruzalimsky)	$\frac{S}{K_M + S} \frac{1}{1 + \frac{C_I}{K_I}}$
3	Edwards	$\frac{S}{K_M + S} \exp\left(-\frac{C_I}{K_I}\right)$
4	Generalised equation of non-competitive inhibition (Yano and Koya)	$\frac{S}{K_M + S} \frac{1}{1 + \left(\frac{C_I}{K_I}\right)^N}$
5	Teissier type expression	$\exp\left(-\frac{C_I}{K_I}\right) - \exp\left(K_T\, S\right)$
6	Ghose and Tyagi	$\left(1 - \frac{C_I}{K_I}\right) \frac{S}{K_M + S}$
7	Levenspiel	$\left(1 - \frac{C_I}{K_I}\right)^N \frac{S}{K_M + S}$
8	Han and Levenspiel	$\left(1 - \frac{C_I}{K_I}\right)^M \frac{S}{K_M \left(1 - \frac{C_I}{K_I}\right)^M + S}$

K_I is an inhibition constant for either a substrate S, product P or biomass X. C_I is a concentration of a substrate, product or biomass (depending on what is inhibiting the reaction) and M and N are adjustable constants.

3.2.3 Overview of IAWQ activated sludge models

The most popular and widely accepted activated sludge models, e.g. Activated Sludge Model No. 1 (ASM1), Activated Sludge Model No. 2 (ASM2). Activated Sludge Model No. 2d (ASM2d), and Activated Sludge Model No. 3 (ASM3) were developed by the Task Group on Mathematical Modelling for Design and Operation of Biological Wastewater Treatment formed by International Association on Water Quality (IAWQ). These models are intended to be able to predict the performance of single-sludge activated sludge systems and to serve as a tool for engineers for process design and optimisation of activated sludge wastewater treatment plants (WWTPs). Although the above mentioned models are the most well known ASMs within the engineering and scientific communities, other activated sludge models were published and successfully used in a number of studies. The model of Barker and Dold [9, 10] proved itself capable of describing full-scale activated sludge reactors and is incorporated in a commercial WWTP simulator BIOWIN® [52]. Similarly, another commercial software GPS-X® by Hydromantis Inc. contains their own model called Mantis [108]. The list of activated sludge models that have been developed since the publication of ASM1 in 1987 is too extensive to cover in this brief overview. We will therefore concentrate only on the four major IAWQ models, which will later form the basis for the development of

MBR-specific models ASMs described in Chapter 4.

Activated Sludge Model No. 1 (ASM1)

The first of the IAWQ family models, ASM1 was published in 1987 by Henze et al. [85; 86]. The goal was to create a simple mathematical model able to predict the performance of single-sludge activated sludge systems carrying out aerobic carbon removal, nitrification and denitrification. The model does not describe any phosphorus (P) removal mechanisms. ASM1 uses 8 process equations: *Aerobic growth of heterotrophs*, *Anoxic growth of heterotrophs*, *Aerobic growth of autotrophs*, *Decay of heterotrophs*, *Decay of autotrophs*, *Ammonification of soluble organic nitrogen*, *Hydrolysis of entrapped organics* and *Hydrolysis of entrapped organic nitrogen*. These process equations use 13 state variables which denote the fractions of chemical oxygen demand (COD) - soluble readily biodegradable: S_S, soluble inert: S_I, particulate slowly biodegradable: X_S, particulate inert: X_I, particulate inert from biomass decay: X_P, heterotrophic biomass: X_H and autotrophic biomass: X_A; fractions of N - soluble organic: S_{ND}, ammoniacal: S_{NH}. particulate organic: X_{ND}, nitrates and nitrites: S_{NO}; and two other state variables - oxygen: S_O and alkalinity: S_{ALK}. The model contains 19 stoichiometric and kinetic constants used as parameters for the process rate equations. ASM1 was originally designed to predict sludge production and oxygen demand in activated sludge systems. Accuracy of effluent quality prediction was given less of a weight. Although ASM1 has proved itself to perform very well in a large range of applications with regards to oxygen demands, sludge yields, sludge retention times (SRTs) and effluent quality, the model has a number of restrictions:

1. In its original form the model assumed constant temperature, i.e. temperature dependency functions for kinetic parameters were not included. Since its publication the model was however expanded with Arrhenius equations to account for the variability of process rates with bulk liquid temperature.
2. The model does not describe the limiting effects of alkalinity as well as N, P and other inorganic nutrients on biomass growth.
3. The ammonification kinetics cannot be practically identified.
4. ASM1 differentiates between inert particulate organic material originating from the influent (X_I) and biomass decay (X_P). However, in reality, these two COD fractions cannot be distinguished from each other.
5. Hydrolysis which kinetic parameters are hard to identify has a significant effect on the predicted oxygen demand and denitrification rates.
6. The effects of death, predation, biomass lysis, endogenous respiration of storage products are not individually modelled but instead they are described as a combined effect of lysis, hydrolysis and growth mechanisms.
7. Hydrolysis of organic matter and hydrolysis of organic nitrogen are modelled as one process. Hence, it is assumed that these two processes occur simultaneously

and with equal rates.

8. The model does not describe the processes of intermediate cell storage of poly-hydroxyalkanoates (PHA) and glycogen by microbial cells at elevated substrate concentrations under aerobic and anoxic conditions.
9. It is assumed that the entrapment of particulate organic matter in the biomass is instantaneous.
10. The biomass yields and the decay rates are assumed to be independent of the type of electron acceptor, i.e. aerobic, anoxic and anaerobic decay rates and yields are assumed equal. As anoxic and anaerobic yields and decay rates are found to be lower than those under the aerobic conditions, ASM1 tends to give erroneous predictions of various state variables, especially Ammoniacal N, at high SRTs and large anoxic fractions.
11. ASM1 is unable to predict directly observable mixed liquor suspended solids (MLSS). This limitation is usually overcome through introduction of an additional state variable representing inert solids [108].
12. The model assumes that biomass dies-off accordingly to the *death-regeneration* concept instead of the *endogenous decay* model. The death-regeneration concept assumes that the products of biomass decay go back to the respiratory cycle and are used as substrates for biomass growth. At high SRTs this 'recycling loop' of organic substrates becomes more dominant leading to over-prediction of oxygen demands and denitrification rates. Hence, ASM1 may be difficult to calibrate on long SRT systems such as e.g. MBRs or biofilm reactors.

Although the model was introduced over 20 years ago and despite of its drawbacks and limitations, it is still considered 'state of the art' when the plant model does not require P removal. This popularity of ASM1 is owed to the simplicity of its structure, large number of available publications dealing with model calibration, identification, simplification, etc. [225, 114, 230, 56] and large number of available full scale WWTP case-studies. Due to the extensive amount of knowledge on the use of ASM1, it is not only a preferred choice for the of-the-shelf use but also as a base-model for various extensions as later described in Section 3.2.4.

Activated Sludge Model No. 2 (ASM2)

Activated Sludge Model No. 2 (ASM2) was developed and published 7 years after ASM1 in order to allow simulation of activated sludge systems with excess biological phosphorus removal (EBPR) [87]. In order to account for new biological processes, the model introduces phosphorus accumulating organisms (PAO) which are able to carry out EBPR. PAO are modelled with consideration of internal cell structure (structured biomass) in order to represent the amount of stored poly-phosphates and PHA. The model contains 17 state variables composed of fractions of COD - fermentation products: S_A, fermentable, readily biodegradable COD: S_F, inert soluble: S_I, inert particulate: X_I, slowly biodegradable: X_S, cell internal storage products: X_{PHA}, autotrophic or-

ganisms: X_A, heterotrophic organisms: X_H, and phosphorus accumulating organisms: X_{PAO}; fractions of N - dinitrogen: S_{N_2}, ammonium and ammoniacal nitrogen: S_{NH}, nitrates and nitrites: S_{NO}; fractions of P - inorganic soluble phosphorus: S_{PO_4} and polyphosphates: X_{PP}; as well as: alkalinity: S_{ALK}, dissolved oxygen: S_O, and total suspended solids: X_{TSS}. ASM2 uses 17 process rate equations: *Aerobic hydrolysis*, *Anoxic hydrolysis*, *Anaerobic hydrolysis*, *Aerobic growth on* S_F, *Aerobic growth on* S_A, *Anoxic growth on* S_F, *Anoxic growth on* S_A, *Fermentation*, *Lysis of* X_H, *Storage of* X_{PHA}, *Storage of* X_{PP}, *Aerobic growth of* X_{PAO} *on* X_{PHA}, *Lysis of* X_{PAO}, *Lysis of* X_{PP}, *Lysis of* X_{PHA}, *Growth of* X_A, and *Lysis of* X_A. The process rate equations contain a total number of 61 parameters (21 stoichiometric and 40 kinetic). The number of parameters for the amount of state variables is significant which impairs the model's identifiability [18]. The model's limitations are listed below:

1. Valid for municipal wastewater only.
2. Unable to model processes with ingress of S_A into the aeration tank.
3. Wastewater must contain sufficient amounts of Mg^{2+} and K^+.
4. Valid only for pH close to neutrality and temperatures in the range of 10-20°C.
5. Suffers from identifiability problems due to large amount of parameters, processes and unobservable state variables.
6. The model does not account for a denitrifying activity of PAO, i.e. that PAO can uptake ortho-phosphates not only under aerobic but also under anoxic conditions.

Activated Sludge Model No. 2d (ASM2d)

Activated Sludge Model No. 2d (ASM2d) extends the Activated Sludge Model No. 2 (ASM2) by providing the description of the anoxic uptake of ortho-phosphates, hence solving one of the ASM2's limitations. This extension was published by Henze et al. [88] 4 years after the original publication of ASM2 instigated by the findings of Kerrn-Jespersen and Henze [119], Mino et al. [170], Meinhold et al. [165] who demonstrated that PAO consist of two fractions, one of which is capable of carrying out denitrification. In order to describe the activity of denitrifying phosphorus accumulating organisms (DPAO) ASM2d introduces two new processes for PAO: *Anoxic storage of* X_{PP} and *Anoxic growth on* X_{PHA}. The model additionally adds two processes for precipitation of phosphorus with $Fe(OH)_3$, namely *Precipitation* and *Redissolution*, thus bringing the total number of processes to 21. Addition of these two last processes necessitates introduction of two additional state variables representing the concentrations of metal hydroxides, e.g. $Fe(OH)_3$: X_{MeOH} and metal phosphates: X_{MeP}, i.e. insoluble compounds of phosphates and metal ions. ASM2d contains 19 state variables, 22 stoichiometric parameters and 45 kinetic parameters, many of which are unidentifiable [18]. The model suffers from the same limitations as its predecessor ASM2 except the last limitation, which has been remediated by modelling PAO respiration under anoxic conditions.

Activated Sludge Model No. 3 (ASM3)

Activated Sludge Model No. 3 (ASM3) was published in 1999 by Gujer et al. [79] to correct some of the earlier mentioned defects of ASM1. The main alterations included: (a) an introduction of a storage mechanism for organic substrates prior to their utilisation, (b) substitution of death-regeneration model with cell lysis and decay with endogenous respiration process, (c) removal of soluble and particulate organic nitrogen from the list of state variables, (d) elimination of the ammonification process, (e) differentiation between aerobic and anoxic decay rates and biomass yields, and (d) explicit calculation of MLSS. Compared to ASM1, ASM3 provides a more detailed description of internal cell processes (storage) and a more accurate model of cell decay and lysis over a wide range of operating conditions. The impact of hydrolysis on other processes such as denitrification is reduced and degradation of soluble and particulate organic nitrogen is accounted for in hydrolysis, decay and growth processes [79].

Whereas in the original formulation of ASM1 [85] temperature dependency functions for the kinetic expressions were not included, the kinetic rates in ASM3 are temperature dependent. ASM3 introduces 14 state variables - 7 soluble and 7 particulate. The soluble state variables are: dissolved oxygen S_O, inert soluble organics S_I, readily biodegradable organic substrates S_S, ammonium plus ammonia nitrogen S_{NH}, dinitrogen S_{N_2}, nitrate plus nitrite nitrogen S_{NO}, and alkalinity S_{ALK}. The particulate state variables are: inert particulate organics X_I, slowly biodegradable organics substrates X_S, heterotrophic biomass X_H, cell internal storage products of heterotrophic biomass, X_{STO}, autotrophic biomass X_A, and total suspended solids (TSS) X_{TSS}. ASM3 considers 9 following processes: *Hydrolysis*, *Aerobic storage of* S_S, *Anoxic storage of* S_S, *Aerobic growth of heterotrophs*, *Anoxic growth of heterotrophs*, *Aerobic endogenous respiration*, *Anoxic endogenous respiration*, *Aerobic respiration of storage products*, and *Anoxic respiration of storage products*. These processes are parametrised with 21 kinetic and 15 stoichiometric parameters. ASM3 eliminates some of the limitations of ASM1 whilst maintaining similar levels of complexity. Identifiability of model parameters is improved by reducing the dependency of the heterotrophic activity on hydrolysis and by breaking up the substrate flow circle originally present in the death-regeneration process through substitution with endogenous respiration. This modification has a significant effect on modelling MBR systems which operate at high SRTs usually over 20d and up to 100d [116]. In such systems, the processes of bacterial decay, cell lysis and maintenance play a more important role in the overall process performance than in e.g. conventional activated sludge processs (ASPs). Due to a more realistic description of decay processes in ASM3 this model is more suited for modelling MBR plants. From personal experiences of the author, modelling high SRT systems with ASM1 using the default kinetic and stoichiometric parameters results in over-prediction of denitrification rates and oxygen consumption whereas predictions obtained from ASM3 are much closer to the observed values.

3.2.4 Modified activated sludge models

All of the above described IAWQ models have common limitations as a consequence of the adopted model structure and the assumptions made by the authors in order to balance realism with model complexity, usability and computational demand. In all the models mentioned above no consideration was given to how changes in the nature of the influent composition affect the bacterial growth rates, decay rates and yields. Instead, all organic components in the influent, effluent and mixed liquor are described with a surrogate parameter COD and its fractions. The pH factor is assumed to remain constant and near neutrality. The only indication of a likely change in pH can be deduced through observation of the changes in the bulk liquid alkalinity. The biomass is considered homogeneous and does not undergo any changes in species diversity. Soluble effluent COD is not calculated. Instead it is assumed that the amount of soluble chemical oxygen demand (SCOD) in the effluent is equal to the influent soluble inert COD (S_I) which is assumed to pass through the system untreated. In fully nitrifying systems where complete biodegradation of the 'biodegradable' forms of carbon takes place, the above assumption is not true, because soluble COD is also 'created' in the system as a consequence of biopolymer production during biomass growth and decay. ASM models also do not account for the uncertainty of model parameters and the influent composition.

Despite of these limitations different ASM models have been successfully applied to describe a multitude of wastewater treatment processes and became the standard in dynamic modelling of WWTPs. A comprehensive description of all IAWQ activated sludge models (ASMs) can be found in Henze et al. [89]. General information about the state of the art activated sludge WWTP modelling and simulation with various white-box and black-box modelling approaches can be found in Gernaey et al. [70]. A technical report by Melcer et al. [166] provides more thorough information about activated sludge models with respect to calibration, identification of parameters and influent characterisation.

In an attempt to reduce some of the models' limitations, original ASM models have been modified to suit the specific needs of their authors. Some of these models are now implemented in commercial WWTP modelling packages. A quick overview presented below is neither comprehensive nor complete. It only serves a purpose of demonstrating that various alterations to ASM models are possible and allow us to solve a vast range of problems encountered in practice.

Iacopozzi et al. [110] and Kaelin et al. [117] extended ASM3 with two-step nitrification and two-step denitrification. In a similar approach, nitrite and nitrate variations were simulated with two-stage nitrification, multi-stage denitrification, and phosphorus removal by Pai et al. [196] using a modified ASM2d model. Two-stage denitrification was also modelled by Ni and Yu [180] with a modification of ASM3. Lubello et al. [158] developed a modified version of ASM1 to improve the prediction accuracy of sludge production over a wide range of SRTs. Predictions of sludge production and some biomass

kinetics were also improved in ASM2d by Hao et al. [83] through the introduction of the processes of predation and viral infection. The main purpose of their publication was to evaluate the contributions of predation and viral infection to minimisation of sludge production in a sequencing batch reactor (SBR). Modification of a similar fashion was also made to ASM1 in order to enable the simulation of endogenous maintenance, cell death and predation processes [183]. ASM1 was also expanded by Wang et al. [249] to include the effects of oxygen diffusion into bacterial flocs in order to simulate simultaneous nitrification and denitrification (SND) at low dissolved oxygen (DO) concentrations. Due to identifiability issues and complexity of ASM2d [18], Rieger et al. [208] developed and validated a biological phosphorus removal (Bio-P) module for ASM3, thus allowing the ASM3 model to be used for the simulations of WWTPs with excess biological phosphorus removal (EBPR). Takacs [234] provided a theoretical description of pH kinetics and precipitation of various salts in activated systems, which can be implemented in different ASM models. At present, at least two commercial WWTP simulation packages incorporate pH calculation in their biological models allowing the users to investigate inhibition effects caused by low and high pH. The activated sludge and digestion model (ASDM) implemented in BioWin® [9, 10, 43] is based on an integrated activated sludge - anaerobic digestion model that has been extended with water chemistry, simulation of pH, and various chemical reactions. A comprehensive activated sludge model (MANTIS2) which includes a pH model was also developed on another commercial WWTP simulation platform GPS-X®. In MANTIS each biological, physical and chemical reaction is dependent on concentrations of inorganic state variables contributing to charge (pH) balance [74].

3.3 Special model considerations for MBRs

Although the original activated sludge models (ASMs) described in Section 3.2.3 have been successfully implemented in a multitude of WWTP modelling, design and simulation projects, the applicability of standard activated sludge models such as ASM1, ASM2, ASM2d, ASM3 or Barker and Dold [9, 10] to modelling membrane bioreactors (MBRs) is limited for three following reasons. Due to elevated MLSS concentrations and higher SRTs compared to conventional activated sludge (CAS) processes, activated sludge flocs in MBRs tend to be smaller [258], have smaller zone settling velocity, higher sludge volume index (SVI), lower filterability, and different water content [67]. Reduction of floc diameters compared to CASP systems leads to faster mass transfer rates between the bulk liquid and the flocs, hence different overall process kinetics. Higher SRTs mean that cell maintenance, decay and lysis play a more dominant role in the activated sludge kinetics. These processes are however not very well described in standard ASM models. Standard ASM models cannot predict the four main properties of activated sludge which affect membrane fouling, namely: floc size distribution (FSD), sludge morphology, bulk liquid soluble microbial products (SMP) and extracellular polymeric substances (EPS).

Despite the differences between MBR and CAS process kinetics, in majority of cases it is still possible to achieve a satisfactory level of calibration of a MBR process with a standard ASM model [57]. The downside of this approach however still lies in the inability of the original ASMs to predict the concentrations of main membrane foulants, as well as the sludge FSD and morphology. Modelling the FSD requires elaborate and mathematically complex descriptions of flocculation and deflocculation processes and accurate assessment or description of turbulence levels inside the bioreactor. In order to model the sludge morphology, one has to introduce new bacterial species, such as filamentous bacteria and define their growth and respiration kinetics. Whilst modelling and simulation of sludge morphology and FSD are too complex to consider in this thesis, the developments will focus on an easier task of modelling the SMP and EPS kinetics and introduction of these kinetic equations to ASM models.

Other characteristic properties of MBRs (excluding sludge FSD and morphology) are lower oxygen transfer rates and higher bulk liquid viscosities due to elevated concentrations of solids. The MBR-specific properties listed below need to be included in a mathematical model of a MBR to ensure a proper description of the process.

1. SMP.
2. EPS.
3. Hindered oxygen transfer.
4. Higher bulk liquid viscosity.
5. Long SRT thus significant share of cell maintenance, decay and lysis.

SMP and EPS contents in the mixed liquor are found to correlate with floc strength and resistance to shear and to influence various activated sludge properties such as floc size distribution (FSD), dewaterability, settleability and compressibility, non-settleable solids (NSS) fraction, stirred sludge volume index (SSVI), cake filtration properties such as capillary suction time (CST) and filtration resistance, hydrophobicity, viscosity, and surface charge.

In MBR systems, bound EPS co-deposit together with bacterial cells on filtration membranes filling the voids between the cells and forming potentially compressible cakes with high hydraulic resistance [266, 146], thus causing membrane fouling. SMP are found to lead to a decrease in the overall membrane filterability [175, 121, 214] and cause the so-called 'irreversible fouling', although not under all operating conditions [44]. SMP are also found to comprise the majority of soluble organic material in the effluents from biological WWTPs and their presence is, therefore, of particular interest in terms of achieving effluent biological oxygen demand (BOD) and COD standards [8].

As bound and free EPS and SMP have been reported in numerous publications to constitute the two major fouling components in MBRs they are given a particular level of attention in the next sections of this chapter and then later on throughout this thesis. Specifically, Chapter 4 introduces two new ASM models with SMP and EPS kinetics. One of these two models is later combined in Chapter 7 with a fouling model to allow

simulation of a complete MBR process.

3.4 Definition and overview of SMP and EPS

EPS and SMP are, in broad terms, by-products of the metabolic activity of bacterial cultures and are excreted by these microorganisms during their growth, decay, or in a response to changing environmental conditions [185, 256, 35].

Although a precise definition of SMP has not yet been agreed in the scientific community, here we will adopt the definition proposed by Noguera et al. [185]:

Definition 5. Soluble microbial products (SMP) are the pool of organic compounds that result from substrate metabolism (usually with biomass growth) and biomass decay during complete mineralisation of simple substrates, which are released by microorganisms and then diffuse through the cell membrane into the outer environment, are lost during synthesis or are extracted for some purpose.

This definition excludes intermediate products of bacterial metabolism such as volatile fatty acids (VFA) in anaerobic systems, because these products are formed through metabolism of substrates entering the system with the influent and therefore are not of a purely microbial origin in the strict sense of Definition 5. SMP are made of different organic compounds, such as humic and fulvic acids, polysaccharides, proteins, nucleic acids, organic acids, amino acids, antibiotics, steroids, exocellular enzymes, siderophores, structural components of cells and products of energy metabolism [8].

It is clear that the term SMP applies to quite a large pool of different chemical compounds and thus SMP are likely to exhibit quite different physico-chemical and biological properties including two most important ones in the context of this thesis, i.e. *fouling strength* and *biodegradability*, depending on the system configuration, influent composition, operating conditions, and others. SMP can be classified into many categories based on their: (a) biological origin, (b) molecular weight (MW), (c) chemical composition (d) inhibitory and metal chelating properties, (e) effects on membrane fouling, (d) biodegradability.

From the biological (metabolic) point of view, SMP can be classified into three categories, (Chudoba [32]).

1. Compounds produced as a result of substrate metabolism and bacterial growth. These compounds are denoted in many kinetic models as utilisation associated products (UAP).
2. Compounds released during the lysis and degradation of microorganisms. These compounds are in turn denoted as biomass associated products (BAP).
3. Compounds excreted by microorganisms during their interaction with the environment. These compounds are released by bacteria in response to changing environmental conditions such as toxicity, shock temperature changes, changes in the composition of the organic substrates in the influent, shear, etc. These

mechanisms of SMP production are not very well understood and are usually not modelled. Thus, most SMP kinetic models consider just the first two of the above SMP categories, UAP and BAP.

A detailed explanation of the origins of SMP is provided in Kuo [129] and later quoted in the most comprehensive, up to this date, review of SMP by Barker and Stuckey [8]. Kuo [129] cited the following factors as the main causes of SMP production in bacterial cultures: (1) maintenance of concentration equilibrium, (2) starvation, (3) presence of energy source, (4) substrate-accelerated death, (5) low availability of required nutrients, (6) relieving environmental stress (to e.g. extreme temperature changes or osmotic shocks), (7) normal bacterial growth and metabolism.

Chemical composition of SMP in the bulk liquid depends mainly on the type and the composition of the influent but also on the type of the activated sludge process and the operating conditions. Depending on its chemical composition, SMP will exhibit different biodegradability, molecular weight distribution (MWD), toxicity, and chelating properties. Most of the biological effluents are found to be biodegradable to a certain degree and ranging, in one particular study of Owen et al. [195] carried out on an effluent of an anaerobic baffled reactor (ABR), between 65% and 82%. Thus, only 18% to 35% of SMP entering the receiving body will not be biodegraded. Toxicity of SMP is however of a bigger concern. Many researchers have found that the effluents from biological treatment may exhibit higher toxicity than the influents and this toxicity is mostly attributed to SMP. In particular, Rappaport et al. [204] showed a greater mutagenic response in secondary effluents than in primary effluents. Additionally Chudoba [31] found that SMP can be inhibitory to nitrification.

These findings are of great significance for those working with MBR systems, because MBRs, due to the presence of microfiltration (MF) or ultrafiltration (UF) membranes retaining some of SMP inside the bioreactor, exhibit higher bulk liquid SMP concentrations than conventional activated sludge systems. This in turn means that activated sludge in MBRs is potentially subject to higher levels of toxicity which can negatively affect some processes such as, e.g. nitrification.

The molecular weight (MW) distribution of SMP is affected by substrate type and operating conditions, and generally exhibits a bimodal distribution with MWs of either $\lesssim 1\,\mathrm{kDa}$ or $\gtrsim 10\,\mathrm{kDa}$. Depending on the shape of the molecular weight distribution (MWD) and the type of the membrane, certain MBRs are found to exhibit greater or lesser fouling propensities. Other researchers attribute the differences in the fouling properties of various SMP to their their chemical composition instead of their MWDs. Yigit et al. [267] found that the carbohydrate fractions of both SMP and EPS contributed to fouling more than the protein fractions. Similarly, Grelier et al. [78] identified the concentration of the colloidal and soluble polysaccharides of the liquid phase as the predominant parameter causing membrane fouling. In a review paper on fouling in membrane bioreactors Le-Clech et al. [138] summarised that the carbohydrate fraction from the soluble microbial product is the main factor causing fouling in MBRs, although the role of the protein compounds in the development of fouling is still to be

clarified.

Whilst SMP are made of substances that are mostly dissolved in water, EPS are considered to be formed from a pool of compounds of similar composition and the same origin as SMP but which are bound to bacterial cells. The definition of EPS adopted and used throughout this thesis is as follows:

Definition 6. EPS are a complex mixture of high molecular-weight polymers produced by bacteria and other microorganisms through active secretion, shredding of cell surface material and cell lysis. EPS forms a three-dimensional highly hydrated gel matrix which immediately surrounds bacterial cells and protects them against environmental stress and toxicity, thus contributing to the cell adaptability, resiliency, and its functional roles in the environment [151, 240, 216, 138].

EPS are, similarly to SMP, composed of different classes of macromolecules such as polysaccharides, proteins, nucleic acids, phosphor-lipids, humic substances and other polymeric compounds [256]. However, proteins and carbohydrates are the most dominant fractions [154]. From a morphological point of view these different organic compounds are found in a number of physical states such as sheaths, capsular polymers, condensed gel and loosely bound polymers. EPS together with SMP form construction materials for microbial aggregates such as biofilms and flocs, and play an important role in their formation and maintenance of their cohesion [256, 151, 240, 216].

Understanding SMP and EPS production mechanisms in activated sludge systems is important for a number of reasons, some of which have already been mentioned or can be inferred from the definitions and short descriptions provided above. First of all, EPS and SMP form a majority of the secondary treatment effluent COD while SCOD of most of these effluents can be, in fact, attributed entirely to SMP. Therefore, information about SMP and EPS in an activated sludge system allows us to estimate the effluent soluble and total COD concentrations, especially in the systems such as MBRs which operate at long SRTs. EPS and SMP, as mentioned earlier, allow bacteria to aggregate and form flocs and biofilms. They affect the activated sludge FSD by increasing the flocs' resistance to breakage under shear and thus promoting larger flocs or, on contrary, creating large and loose flocs which break under shear.

SMP and EPS in the bulk liquid therefore have an effect on such macroscopic sludge properties as non-settleable fraction, SVI and SSVI, CST, and specific cake resistance (SCR). These macroscopic properties affect, respectively, clarification, settleability/thickening, dewatering and pressure drop across the membrane due to cake formation.

SMP are found to adsorb inside the pores and on the membrane surface leading to constriction of pores and formation of a gel layer. Additionally EPS and, to a lesser degree, SMP are found to fill the void spaces between flocs and bacterial cells leading to increased resistance to filtration and thus pressure drop across the cake.

As briefly described in this section, production of SMP and EPS in the bioreac-

tor depends on influent composition, various operating and environmental conditions, and changes of these environmental conditions posing additional stress on the microorganisms. Whilst SMP and EPS are traditionally assumed to originate from 'normal' bacterial growth and bacterial decay under stable environmental conditions, production of biopolymers in response to environmental stress, i.e. changing environmental conditions is not well understood and hence not modelled. Whilst various researchers pointed out accelerated production of biopolymers under extreme temperatures, osmotic shocks, presence of toxic substances, i.e. conditions associated mainly with influent characteristics, it is hypothesised that also operational conditions such as levels of turbulence and hence shear on the surface of bacterial flocs caused by mixing in immersed MBR systems and pumping in sidestream MBRs are likely to affect biopolymer production and/or release from bacterial cells. Different types of behaviour of microorganisms in response to high levels of shear may be hypothesised. Under higher levels of turbulence EPS attached to bacterial cells may detach and find themselves in the bulk liquid while the bacteria will try to produce more EPS to accommodate for the loss of cell-bound EPS. While the amount of turbulence is increased and higher shear stresses are applied to bacterial flocs, bacterial colonies may sense the need to protect themselves from the rupturing forces by releasing more EPS and forming denser, stronger flocs. It may also possible that under conditions where only a fraction of biomass is exposed to highly turbulent conditions these organisms may release some enzymes to the environment communicating to other bacteria of the same species through 'quorum sensing' to prepare for changing conditions. Hence, local changes in environmental conditions such as e.g. shear may have a more global impact in the system. Under more 'extreme' conditions bacterial cells exposed to high shear forces may rupture releasing the internally stored biopolymers to the liquid phase, hence leading to an increase in SMP concentration. It is also possible that in a response to a sufficiently large change in a particular environmental parameter or a number of parameters, bacteria will initially start to produce significantly larger amounts of biopolymers but this production may decrease over time as the bacteria gradually adapt to a new state of the system. These are only hypothetical scenarios for biopolymer production in response to high shear which need to be experimentally tested and shall be left for further research. Although biopolymer production in response to environmental stress may be significant under certain conditions, e.g. when high crossflow velocities CFVs are applied in tubular membranes to control cake formation which can result in increased irreversible fouling, modelling of such biopolymer production mechanisms is beyond the scope of this thesis. Hence we will limit our focus to biopolymer production under steady environmental conditions. Overview of such models is provided in Section 3.5.

More information, although possibly a bit outdated, about various factors affecting SMP production, properties of SMP and their origins, supported with experimental findings, can be found in an extensive review of SMP by Barker and Stuckey [8].

3.5 Overview of SMP and EPS kinetic models

3.5.1 SMP kinetic models

It is generally accepted that production of SMP in activated sludge systems obeys the Leudeking-Piret equation [144] shown below.

$$r_{SMP} = \frac{d\,S_{SMP}}{dt} = \underbrace{\alpha \frac{d\,X}{dt}}_{\frac{d\,S_{UAP}}{dt}} + \underbrace{\beta\,X}_{\frac{d\,S_{BAP}}{dt}} \tag{3.17}$$

where r_{SMP} denotes the SMP production/utilisation rate (g COD m^{-3} d^{-1}), S_{SMP}, S_{UAP}, S_{BAP} and X denote, respectively the concentrations of SMP, UAP, BAP and biomass in the bulk liquid (g COD m^{-3}), α is the UAP formation coefficient (–) and β is the BAP formation coefficient (d^{-1}).

Depending on the type of the system being modelled, the coefficients α and β may be assigned different values or form different functional relationships with e.g. various substrate concentrations as arguments. In mixed bacterial cultures, different bacteria may have different SMP kinetics as shall be shown in Section 3.6. These differences can be reflected in the values of parameters α and β.

Whilst Equation 3.17 assumes that SMP originate from active metabolism (UAP) and decay (BAP) of various microorganisms in the microbial biocenosis, SMP may also be produced, as was mentioned earlier, in response to changes in various environmental conditions and during hydrolysis/dissolution of undissolved polymers (EPS) and are consumed as substrates by heterotrophic microorganisms. All these processes are represented in Equation 3.18 below.

$$r_{SMP} = \frac{d\,S_{SMP}}{dt} = \underbrace{\alpha \frac{d\,X}{dt}}_{\frac{d\,S_{UAP}}{dt}} + \underbrace{\beta\,X}_{\frac{d\,S_{BAP}}{dt}} + \underbrace{k_{hyd}\,X_{EPS}}_{\frac{d\,S_{BAP}}{dt}} - \underbrace{\sum_i \varepsilon_i\,p_i}_{\text{sinks}} + \underbrace{\gamma\,f\left(c,\,\frac{dc}{dt}\right)}_{\frac{d\,S_{EAP}}{dt}} \tag{3.18}$$

where S_{SMP} denotes the bulk SMP concentration (g COD m^{-3}), k_{hyd} denotes the EPS hydrolysis rate (d^{-1}), and p_i denotes the i^{th} process rate (usually expressed in g m^{-3} d^{-1}) where SMP are used as a substrate.

The last term in Equation 3.18 represents the increase/decrease in SMP concentration in response to the changes in environmental conditions. The rate of change of the concentration of environment associated products (EAP) cannot be assigned any equation at the moment due to the lack of knowledge about these processes and the lack of supporting data. Hence, the term was assigned a hypothetical function f which is assumed to depend on the quantity of an environmental parameter c such as, e.g.

temperature, concentration of a toxic substance, pH value, etc., its rate of change $\frac{dc}{dt}$, and a stoichiometric coefficient γ. It's a hypothetical assumption and the function is likely to have a much more complex form, e.g. depend on enzyme levels inside the bacterial cells, etc.

3.5.2 EPS kinetic models

Whilst modelling of SMP kinetics received a lot of attention over the years, only a few researchers attempted to model EPS formation kinetics in microbial populations in general and even fewer studies are related specifically to activated sludge systems. EPS and SMP production in a single bacterial culture was measured by Hsieh et al. [102; 101] and used for the development of a simple biokinetic mathematical model. Their experimental data was later used by Laspidou and Rittmann [135; 136] in order to test the validity and applicability of their combined SMP and EPS mathematical model and their unified theory of SMP and EPS formation in microbial systems [135]. A good fit between their mathematical model and the data was later demonstrated on an activated sludge system in a laboratory-scale glucose fed MBR by Chae and Shin [21]. The model of Laspidou and Rittmann [136] is later incorporated into ASM1 and ASM3 models leading to the development of two new models - the combined EPS and SMP production ASM1-based model (CES-ASM1) and the combined EPS and SMP production ASM3-based model (CES-ASM3), as described in Chapter 4.

The kinetic model of Laspidou and Rittmann [136] assumes that EPS in microbial systems are produced as by-products of active microbial activity (i.e. growth) and lost through hydrolysis/dissolution leading to formation of BAP as shown in Equation 3.19.

$$r_{EPS} = \frac{d\,X_{EPS}}{dt} = \underbrace{\alpha' \frac{dX}{dt}}_{\text{growth-associated}} - \underbrace{k_{hyd}\,X_{EPS}}_{\text{hydrolysis to BAP}} \tag{3.19}$$

where r_{EPS} denotes the EPS production/utilisation rate (g COD m^{-3} d^{-1}), X_{EPS} denotes the bulk EPS concentration (g COD m^{-3}), α' is the growth associated EPS formation coefficient (–) and k_{hyd} (d^{-1}) is the EPS hydrolysis rate introduced in Equation 3.18.

3.6 ASM models with SMP and EPS kinetics

In order to describe the production of biopolymers in activated sludge rather than single culture systems, equations introduced in Section 3.5 were added to different ASM models. The approaches and assumptions used for the formulation of such models, such as the types of biopolymers used in the model and how the biopolymer kinetics are related to original ASM model processes, were often quite different. Hence, the published ASM models with biopolymer kinetics exhibit often very different properties

and behaviours. The differences between different published models together with the apparent strengths and weaknesses of each one of them are highlighted in the subsequent sections. Four of the described models are later selected for simulations on a fictitious WWTP layout. The results of these simulations are then analysed and compared, as explained in detail in Section 3.7.

3.6.1 Extended ASM1 model of Lu et al. [157]

Lu et al. [157] incorporated SMP production and utilisation kinetics within the Activated Sludge Model No. 1 (ASM1). SMP was assumed to originate as a by-product of biomass growth and biomass decay. The first type of SMP is called UAP whereas the latter type is termed BAP. Additionally, BAP instead of S_S, as initially specified in ASM1, was assumed to be the sole product of hydrolysis. Both types of SMP were assumed to biodegrade at equal rates. SMP kinetics adopted in the model of Lu et al. [157] are described with the following two equations.

$$\frac{dS_{UAP}}{dt} = \underbrace{\gamma_{UAP,H}\ (p_{2a} + p_{2b} + p_{3a} + p_{3b})}_{\text{heterotrophic growth}} + \underbrace{\gamma_{UAP,A}\ p_8}_{\text{autotrophic growth}} \tag{3.20}$$

$$\frac{dS_{BAP}}{dt} = \underbrace{(1 - f_B)\ (p_5 + p_{10})}_{\text{bacterial decay}} + \underbrace{p_6}_{X_S \text{ hydrolysis}} - \underbrace{\frac{1}{Y_{SMP}}\,(p_{2b} + p_{3b})}_{\text{utilisation}} \tag{3.21}$$

p_{2a}, p_{2b}, p_3, etc. denote the rates of processes contributing to production and utilisation of SMP and are defined in the original article of Lu et al. [157] together with all state variables, Petersen matrix, and kinetic and stoichiometric parameters.

The model of Lu et al. [157], although quoted in many thematically related publications, contains several fundamental errors which pose questions about its usability in real life applications. The model is not structurally correct as it violates the COD, N and charge balance equations defined in Equation 3.11 in Section 3.2.1. Additionally, the UAP formation constant for autotrophic biomass growth $\gamma_{UAP,A}$ is equal to 1.56, which means that 56% more SMP than biomass is produced during autotrophic growth. This value seems to be significantly overestimated as it is hard to believe that the amount of SMP produced under normal operating conditions could be higher than the yield of bacterial biomass. Finally, the model assumes that BAP, apart from being produced during biomass decay, is also the sole product of X_S hydrolysis. This assumption is dubious as, by definition, SMP are the products of strictly biological origin, not of enzymatic hydrolysis of the substrates coming into the system with the feed stream. Additionally, the model only describes SMP kinetics whilst EPS kinetics are not included.

Lack of closure in the balance equations was rectified by the Author by adjusting the selected stoichiometric parameters in the Petersen matrix in order to satisfy constraints given in Equation 3.11. The adjusted model with the modified stoichiometric parameters

is given the name 'Lu closed' as opposed to 'Lu original' which denotes the original model of Lu et al. [157]. The Petersen matrix of the modified model of Lu is given in the Appendix in Section **??**.

The model of Lu et al. [157] extends ASM1 by 2 state variables, 4 processes and 9 stoichiometric and kinetic equations bringing the numbers up to, respectively, 16 states (including molecular nitrogen N_2 and alkalinity), 12 processes and 29 parameters.

3.6.2 Extended ASM3 model of Oliveira-Esquerre et al. [192]

Oliveira-Esquerre et al. [192] extended the ASM3 model with the biopolymer model of a simpler structure to the one implemented by Lu et al. [157]. The model of Oliveira-Esquerre et al. [192] adds only one state variable S_{MP} which lumps the growth-related UAP and decay-related BAP into one term simply called microbial products (MP). The model extends ASM3 by two new processes (aerobic and anoxic storage of MP) thus increasing the total amount of processes to 12 and adds 5 new kinetic and stoichiometric parameters bringing the total number of parameters to 40.

The biopolymer kinetics of Oliveira-Esquerre et al. [192] are provided in Equation 3.22. Information about individual process equations p_i, where i is the process number, as well as the added kinetic and stoichiometric coefficients can be found in the original research paper of Oliveira-Esquerre et al. [192].

$$\frac{dS_{MP}}{dt} = \underbrace{\gamma_{MP,H}\ (p_4 + p_5)}_{\text{heterotrophic growth}} + \underbrace{\gamma_{MP,A}\ p_{10}}_{\text{autotrophic growth}} + \underbrace{f_B\ (p_6 + p_7 + p_{11} + p_{12})}_{\text{endogenous respiration}} - \underbrace{(p_{2b} + p_{3b})}_{\text{internal storage}} \tag{3.22}$$

In a similar fashion to other published biopolymer ASM models, SMP (or using this model's terminology, MP) originate from biomass growth and biomass decay (modelled in ASM3 as endogenous respiration) and are consumed as a substrate in aerobic and anoxic bacterial respiration. Contrary to the model of Lu et al. [157] SMP do not originate from hydrolysis of X_S.

The model of Oliveira-Esquerre et al. [192], as shall be later shown in Section 3.7, substantially under-predicts bulk liquid SMP concentrations, compared to other SMP models and the experimental data. This behaviour is a result of the assumption that SMP storage occurs at the same maximum rate as the storage of readily biodegradable substrates S_S. Bearing in mind that a default maximum storage rate $k_{sto,20}$ for X_S in ASM3 is equal to 12.5 d^{-1} whilst the maximum process rates of growth and endogenous respiration processes, e.g. maximum heterotrophic growth rate $\mu_{H,20}$ or heterotrophic lysis and decay rate $b_{H,20}$, are significantly lower, respectively 3.0 d^{-1} and 0.3 d^{-1}, SMP utilisation in Oliveira-Esquerre et al. [192] dominates over SMP production, causing low bulk liquid SMP concentrations.

In order to increase the output SMP concentrations in the Oliveira model, one could introduce a new kinetic constant $k_{sto,MP}$ for aerobic and anoxic MP storage processes and assign to it a lower numerical value to $k_{sto,20}$, thus reducing SMP storage and utilisation rates in the system. Another possibility could be to increase the values of either the heterotrophic growth-related MP formation constant $\gamma_{MP,H}$ or the fraction of MP generated in biomass lysis f_B.

However, as will be shown in Section 3.7, SMP kinetics in Oliveira-Esquerre et al. [192] are strongly inter-connected with other process kinetics through SMP-related stoichiometric parameters. In order to maintain the fundamental COD, N and charge balances in the model, these parameters need to appear not only in the SMP rate Equation 3.22 but also in the rate equations of other state variables in the model, respectively: dissolved oxygen S_O, ammoniacal nitrogen S_{NH}, dinitrogen S_{N_2}, nitrites and nitrates S_{NO}, alkalinity S_{HCO}, and total suspended solids X_{TSS}. Relatively minor changes in the SMP-related stoichiometric parameters are thus found to affect not just the output SMP concentrations but also the values of the above mentioned, non-SMP-related state variables, hence making identification of SMP-related model parameters difficult.

3.6.3 Extended ASM1 model of Ahn et al. [2]

Ahn et al. [2] developed an extension of ASM1 with 3 new components UAP, BAP and EPS, 5 new processes and 8 new stoichiometric and kinetic parameters. The metabolic pathways of SMP and EPS in Ahn et al. [2] follow the model structure of Laspidou and Rittmann [136], where, as shall be described later, UAP are released during bacterial growth and, at the same time, taken up by bacteria as substrates, BAP originate as by-products of bacterial decay and products of EPS hydrolysis and are used as substrates by heterotrophic bacteria together with UAP, whereas EPS originate as by-products of bacterial growth (together with UAP) and are lost during hydrolysis to BAP.

Although the SMP and EPS pathways adopted by Ahn et al. [2] seem conceptually valid in the light of available evidence [135], the model was not given sufficient description to allow the reader to judge its structural correctness or implement it on a computer to carry out further studies if required. Specifically, the publication lacks a complete description of the model structure, i.e. the Petersen matrix, the mathematical formulation of the five additional processes and the values of the kinetic and stoichiometric parameters in the SMP and EPS related processes. Finally, the model was calibrated on a very limited amount of data (three steady-state SMP and EPS concentrations for three different SRTs), and therefore, a) dynamic behaviour of the model could not be identified b) the accuracy of the estimated parameters is questionable.

3.6.4 SMP and EPS model of Ni et al. [182]

Ni et al. [182] developed a model for SMP and EPS kinetics in activated sludge systems

based on their previous work from a year earlier [181]. SMP and EPS kinetics adopted in the model are given in Equations 3.23-3.25.

$$\frac{dS_{UAP}}{dt} = \underbrace{\frac{k_{UAP}}{Y_{H,S}} p_1}_{\text{growth on } S_S} - \underbrace{\frac{1}{Y_{UAP}} p_3}_{\text{UAP utilisation}} \tag{3.23}$$

$$\frac{dS_{BAP}}{dt} = \underbrace{p_5}_{\text{EPS hydrolysis}} - \underbrace{\frac{1}{Y_{BAP}} p_4}_{\text{BAP utilisation}} \tag{3.24}$$

$$\frac{dX_{EPS}}{dt} = \underbrace{\frac{k_{EPS}}{Y_{H,S}} p_1}_{\text{growth on } S_S} - \underbrace{p_5}_{\text{EPS hydrolysis}} \tag{3.25}$$

where p_1, p_3 and p_4 denote, respectively, the growth rates on S_S, S_{UAP} and S_{BAP}, and p_5 denotes the X_{EPS} hydrolysis rate. The values of stoichiometric parameters in Equations 3.23-3.25 can be found in the original publication of Ni et al. [182]. These parameters as well other kinetic and stoichiometric constants in the model were calibrated with good results on the data obtained from a lab-scale SBR.

Although the model of Ni et al. [182] was proven to give good SMP and EPS predictions, the model contains just 8 state variables (oxygen S_O, (readily-biodegradable) substrate S, inert particulate COD X_I, heterotrophic biomass X_H, internally stored products X_{STO}, and S_{UAP}, S_{BAP} and X_{EPS}) and is therefore not a full ASM model. The model of Ni et al. [182] is not considered for further investigations but the findings presented in the original paper of the authors were taken into account during the development of the new ASM models described in Chapter 4.

3.6.5 Extended ASM2d model of Jiang et al. [115]

Jiang et al. [115] argued that the existing SMP models were too complex and over-parametrised and therefore very difficult to calibrate due to lack of available measurements and the difficulties with obtaining appropriate measurements for the calibration of, often complex, biopolymer production and utilisation kinetics. Their work was thus focused on minimisation of the additional model complexity caused by incorporation of biopolymer kinetics into the base ASM model and on minimisation or, if possible, reduction of correlations which often exist between various SMP-related parameters in other biopolymer kinetic models.

Jiang et al. [115] introduced 4 additional stoichiometric and kinetic SMP-related parameters and 2 stoichiometric parameters for N and P contents in SMP thus bringing the total number of parameters from 69 to 75. The first four SMP-related parameters were identified in three dynamic batch experiments carried out under different scenarios in order to isolate certain processes and identify the characteristic parameters of each individual process. Jiang et al. [115] also introduced 2 new state variables (S_{UAP} and S_{BAP}) thus increasing the total number of variables to 21 and 6 new processes leading

to 27 processes in total.

UAP and BAP process kinetics of Jiang et al. [115] are shown in Equations 3.26 and 3.27. Descriptions of process rate equations p_i and all the kinetic and stoichiometric parameters can be found in the original research article of Jiang et al. [115].

$$\frac{dS_{UAP}}{dt} = \underbrace{\frac{f_{UAP}}{Y_H}\sum_{i=4}^{i=7} p_i}_{\text{heterotrophic growth}} + \underbrace{\frac{f_{UAP}}{Y_H}\sum_{i=13}^{i=14} p_i}_{\text{PAO growth}} + \underbrace{\frac{f_{UAP}}{Y_A}\, p_{18}}_{\text{autotrophic growth}} - \underbrace{\sum_{i=25}^{i=27} p_i}_{\text{SMP hydrolysis}} \tag{3.26}$$

$$\frac{dS_{BAP}}{dt} = \underbrace{f_{BAP}\sum_{i=\{9,15,19\}} p_i}_{\text{lysis}} - \underbrace{\sum_{i=22}^{i=24} p_i}_{\text{SMP hydrolysis}} \tag{3.27}$$

Whilst in the previous models SMP was used directly as a substrate for storage and bacterial growth, BAP and UAP in the model of Jiang et al. [115] need to undergo hydrolysis to fermentable products S_F prior to their utilisation. The rationale for this approach is supported by observations that the majority of SMP have MWs>20 kDa. Such large molecules are unlikely to pass through cell membranes before prior hydrolysis. As UAP are found to have smaller MWs from BAP, they are assumed to be more readily biodegradable than BAP. The difference between the biodegradability of UAP and BAP is accounted for in the model by assigning a higher value to the UAP hydrolysis constant $k_{h,UAP}$ compared to $k_{h,BAP}$. Degradation of BAP and UAP is associated with the same biomass yield (Y_H) as degradation of readily biodegradable substrates - S_S and S_F but occurs at a lower rate.

The model of Jiang et al. [115] seems to be conceptually appropriate and is structurally correct (except small N and P imbalances in the added 6 processes due to a difference in the N and P contents in soluble inert organics S_I and fermentable products S_F) whilst striking a good balance between the complexity of biopolymer kinetics and simplicity of the adopted mathematical equations. The SMP-related kinetic and stoichiometric parameters were identified using experimental data from the batch test experiments whilst other non-SMP-related parameters were obtained from a lab-scale MBR reactor. The measurements obtained from the MBR system did not include SMP, thus the SMP-related kinetic parameters could not be validated. Although the adopted SMP model has a simple structure with identifiable parameters, ASM2d itself suffers from over-parametrisation and thus, poor parameter identifiability, as described in detail in Brun et al. [18]. The model of Jiang et al. [115] is not able to predict EPS concentrations which constitutes its main disadvantage in the context of this thesis.

3.6.6 Other ASM-based biopolymer models

A number of other ASM models with biopolymer kinetics can be found in the scientific literature. However as these models were either not sufficiently documented, the

biopolymer kinetic models were too simplistic or identification procedures employed for model calibration were not sufficient to assure confidence in the model parameters, they were not considered for further study. One of such models was published by Lee et al. [140] and used ASM1 as the base model. The model however was not fully described in the paper, SMP were assumed to originate only from biomass decay and additionally, all SMP-related parameters were taken from literature, i.e. were not identified empirically. Saroj et al. [217] published a short paper with simulation results from their modified ASM3 model incorporating simultaneous substrate utilisation and storage, and simple biomass-associated EPS production kinetics. Polymer kinetics were assumed to depend on hydrodynamic conditions, temperature and concentration/potential of toxic substances. The model was however not well described in the publication nor was it calibrated and EPS kinetics were not described in a mathematical form in the publication.

3.6.7 CES-ASM1 and CES-ASM3

Two new ASM models were developed by the author of this thesis to fill the gap in modelling activated sludge dynamics with SMP and EPS kinetics. These models are described, analysed, and simulated in Chapter 4. The first model is an extension of ASM1 and is called the combined EPS and SMP production ASM1-based model (CES-ASM1) whereas the second model extends the ASM3 model an is called the combined EPS and SMP production ASM3-based model (CES-ASM3). As described above, the existing models, except the model of Ahn et al. [2], which is not well documented and the model of Ni et al. [182], which does not constitute a full ASM model, only take SMP kinetics into account whilst EPS kinetics are not considered at all. Furthermore, many of the existing ASM models with SMP kinetics are found to be either structurally incorrect or to provide possibly erroneous results.

The models developed in Chapter 4 are based on the 'unified theory for extracellular polymeric substances, soluble microbial products, and active and inert biomass' of Laspidou and Rittmann [135], thus consider both SMP and EPS kinetics. The metabolic pathways of SMP and EPS in CES-ASM1 and CES-ASM3 are visualised in Chapter 4, respectively in Figure 4.1 on page 84 and Figure 4.2 on page 85. Both models are calibrated on experimental data obtained from a batch and a continuous-flow lab scale bioreactor and a full-scale continuous-flow bioreactor. CES-ASM1 adds 7 new processes to 15 original processes of ASM1 and 20 kinetic and stoichiometric parameters raising the total number of parameters to 39. The model has 17 states. CES-ASM3 adds 6 new processes to 12 original ASM3 processes and 22 parameters making the total number of parameters in the model equal to 58 and calculates 16 state variables. Both models assume that UAP and BAP are biodegradable, but the degradation kinetics of BAP are slower from the degradation kinetics of UAP and of readily biodegradable substrates S_S [28]. The models also include the process of slow hydrolysis of inert particulate organic compounds, however it has been switched off in the simulations presented in Section 3.7 of this chapter.

Both models proved to provide good predictions of biopolymer concentrations but appear to be over-parametrised. CES-ASM3 also assumes that all substrates have to be stored before utilisation and CES-ASM1 does not consider any intermediate storage, whilst it has been demonstrated that some part of the substrates is directly used by the cell while the remaining part is internally stored within the cell [224]. These seem to be two most significant weaknesses of CES-ASM1 and CES-ASM3.

3.6.8 Recent developments in modelling biopolymer kinetics

Since the development of CES-ASM1 and CES-ASM3, several other biopolymer models have been published in the literature. Mannina et al. [163] incorporated the SMP kinetic model structure of Jiang et al. [115] and linked it with a fouling model to describe a hollow fibre (HF) immersed membrane bioreactor (iMBR). Tian et al. [238] modified the ASM3 model through adoption of the concept of simultaneous growth and storage of organic substrates by heterotrophic bacteria and introduction of the SMP formation and degradation kinetics. The SMP kinetics were identified in batch experiments in a similar way to what was described in Jiang et al. [115]. The model was then validated on the results form a lab-scale MBR. Chen et al. [25] used the extended Fourier amplitude sensitivity test for evaluation of the sensitivity and uncertainty associated with the model of Tian et al. [238].

Although the new models offer a significant improvements over the earlier published models, they do not address the issue of simultaneous modelling of SMP and EPS within a ASM model framework.

3.7 Comparison of ASM-biopolymer models

The verbal comparison of biopolymer ASM-based models is followed by a numerical comparison through simulations of a fictitious plant shown in Figure 3.3. Six models are selected for the simulations: (1) the model of Lu et al. [157], (2) the model of Oliveira-Esquerre et al. [192], (3) the model of Jiang et al. [115], (4) CES-ASM1, (5) CES-ASM3. The sixth (6) model is the model of Lu et al. [157] which has been modified by the author of this thesis in order to fix (close) the mass and charge imbalances present in the original Lu model. This model is later referred to as *Lu closed*. The mass and charge imbalances in the original Lu model were corrected by changing the appropriate stoichiometric coefficients in the Petersen matrix in order to satisfy Equation 3.11. In addition to numerical analysis all of the considered biopolymer models were compared with regards to the number of biopolymer state variables, total number of state variables, number of biopolymer kinetic equations, total number of kinetic equations, number of biopolymer-related parameters, and total number of parameters. All this information has been collated in Table 3.4.

The fictitious plant shown in Figure 3.3 is based on three CSTRs - an anoxic tank V_{anox} and two aerobic tanks $V_{aer,1}$ and $V_{aer,2}$ equipped with diffused air bubble

Table 3.4: Comparison of ASM models with biopolymer components with regards to number of state variables, processes, and model parameters.

Model name	Base ASM model	Biopolymer states	No. of new processes	Number of new parameters	Tot. no. of states	Tot. no. of processes	Tot. no. of parameters	Comments
Lu et al. [157]	ASM1	S_{UAP},S_{BAP}	4	9	16*	12	29	* Including N_2 and S_{ALK}, Unbalanced
Lu closed	ASM1	S_{UAP},S_{BAP}	4	9	16*	12	29	* Including N_2 and S_{ALK}, Closed balances
Oliveira-Esquerre et al. [192]	ASM3	MP	2	5	14	12	40	Low effluent SMP concentrations
Ahn et al. [2]	ASM1	S_{UAP},S_{BAP},X_{EPS}	5	8	17*	13	28	* Including N_2 and S_{ALK}, Not well documented, hence not used for simulations
Jiang et al. [115]	ASM2d	S_{UAP},S_{BAP}	6	6	21	27	75	
CES-ASM1*	ASM1	S_{UAP},S_{BAP},X_{EPS}	7	20	17	15	39	* Including slow hydrolysis and N_2 and S_{ALK}
CES-ASM3*	ASM3	S_{UAP},S_{BAP},X_{EPS}	6	22	16	18	58	* Including slow hydrolysis

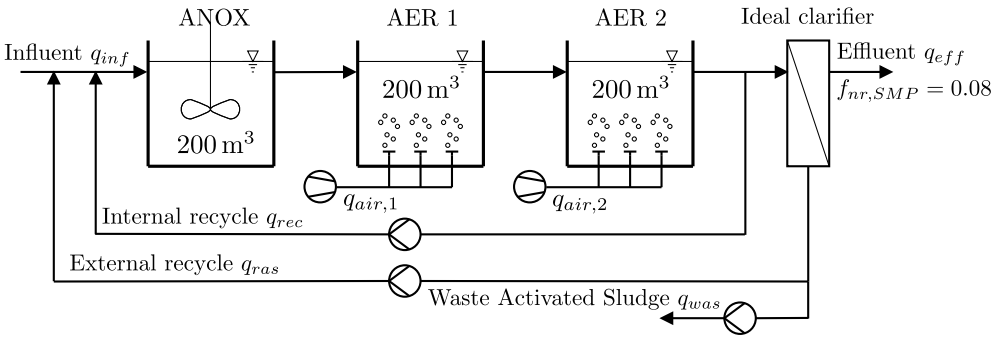

Figure 3.3: Flow diagram of a fictitious plant layout used for comparison of biological models.

aeration. Each tank has an active volume of 200 m^3. The airflow rates $q_{air.1}$ and $q_{air,2}$ are individually adjusted with two separate proportional integral (PI) controllers set to maintain a constant DO setpoint $S_{O,set}$ = 1.5 mgO$_2$/L. An ultrafiltration membrane with mean pore diameter of 0.03 μm and SMP rejection of 92% [115] is modelled as an ideal clarifier. The parameter $f_{nr,SMP} = 0.08$ defines the proportion of SMP which passes through the membrane and ends up in the permeate. The internal recirculation rate and external recirculation rate are in proportion to the influent flow rate q_{inf}, respectively: $q_{rec} = 3 \times q_{inf}$, $q_{ras} = 0.05 \times q_{inf}$. The sludge wastage rate q_{was} is adjusted by a PI MLSS controller in order to maintain the MLSS concentration in the second aeration tank at a required setpoint.

The simulations are performed for a number of operating conditions defined, respectively by different combinations of MLSS setpoints, DO setpoints, Temperatures, and HRTs. Ranges of the above parameters are defined below: $MLSS_{set} = \{3,000 : 3,000 : 30,000\}$ mg/L, $DO_{set} = \{0.5 : 1.0 : 4.5\}$ mgO$_2$/L, $T = \{9.0 : 3.0 : 21\}$ °C, $HRT = \{2, 6, 10, 15, 20\}$ hrs. In each of the four sensitivity studies, each parameter is varied within its specified range whilst the other parameters remain at their default values, i.e. $MLSS_{set}^{default}$ = 12,000 mg/L, $DO_{set}^{default}$ = 1.5 mgO$_2$/L, $T_{set}^{default}$ = 14 °C, $Q_{inf}^{default}$ = 2000 m^3/d which gives a default HRT, $HRT^{default}$ = 7.2 h. In each simulation run, the influent concentrations are kept at constant levels: TKN_{inf} = 30 mgN/L, TP_{inf} = 4 mgP/L, SMP_{inf}=0 mgO$_2$/L. Influent COD is kept at a constant value of $COD_{inf}^{default}$ = 300 mgO$_2$/L except in the sensitivity study to HRT, where HRT is adjusted in the system by manipulating the influent flow rate Q_{inf} whilst, for each Q_{inf}, COD_{inf} is adjusted using Equation 3.28 in order to maintain the same influent organic load to the plant.

$$COD_{inf} = \frac{Q_{inf}^{default}\, COD_{inf}^{default}}{Q_{inf}} \tag{3.28}$$

Each simulation in all four sensitivity studies is run for t_{simu} = 400 d in order to allow sufficient time for convergence to steady-state. Results of the steady-state sensitivity studies for $MLSS_{set}$, DO_{set}, T, and HRT are shown, respectively in Figure 3.4, Figure 3.5, Figure 3.6, and Figure 3.7. Each figure shows changes in the selected outputs: O_2 demand, Sludge yield, SRT, and bulk liquid concentrations in the second aerobic tank: S_{NH}, S_{NO}, TN, S_{ALS}, S_{SMP}, X_{EPS} in response to changes in the selected set-

points: $MLSS_{set}$, DO_{set}, as well as T and HRT. Outputs obtained from the original ASM models, i.e. ASM1, ASM2d, and ASM3 are included in the plots to provide the points of reference for comparative analysis of the biopolymer models .

The figures show that the models of Lu and Oliveira respectively overpredict and underpredict the oxygen demand in the system with an error margin up to $\pm 50\%$. Additionally the model of Oliveira is found to significantly overestimate sludge yield in the system and underpredict bulk liquid S_{NO} concentrations. The model of Lu and its modified version 'Lu closed' are found to produce very low concentrations of S_{NH} compared to their base model ASM1. Whilst SMP concentrations predicted from the original Lu model are relatively high compared to the outputs from other biopolymer models, SMP predictions in 'Lu closed' are very low. SMP concentrations produced by the Oliveira model are even lower than these in 'Lu closed' and reach the values as low as 0.1 mg/L. Although by adjusting the SMP production related kinetic and stoichiometric parameters in the Oliveira model it is possible to increase the output SMP concentrations, however still to very low levels of around $10 - 30$ mg/L, this procedure leads to deterioration of the prediction accuracy of other model state variables such as, e.g. S_{NH} and S_{NO}. The model of Jiang et al. [115], as well as CES-ASM1 and CES-ASM3 exhibit very similar behaviour to their base models, respectively ASM2d, ASM1, and ASM3. CES-ASM3 and the model of Jiang et al. [115] predict very similar SMP concentrations whilst SMP concentrations in CES-ASM1 are 60% higher. The only models including the EPS kinetics are CES-ASM1 and CES-ASM3. EPS concentrations produced by these two models are similar, although CES-ASM1 predicted higher bulk liquid EPS concentrations to CES-ASM3. Higher values of SMP and EPS in CES-ASM1 compared to CES-ASM3 are a direct result of giving the heterotrophic growth rate on BAP μ_{BAP} a zero value and assigning a low value to the EPS hydrolysis rate $k_{hyd,EPS}$ in the CES-ASM1 model - see Table 3.5. Table 3.5 lists all biopolymer-related kinetic and stoichiometric parameters for both models as well as some original ASM1 and ASM3 parameters if their values are not default. Under equivalent sets of biopolymer-related kinetic and stoichiometric parameters CES-ASM1 and CES-ASM3 predict very similar concentrations of SMP and EPS as shown in Section 4.5 of Chapter 4.

In order to assess the performance of the biopolymer models, the outputs from each biopolymer model have been compared to the outputs of its base ASM model. The closer the biopolymer model's behaviour is to its base ASM model, the lower are the effects of additional biopolymer kinetics on the overall model behaviour, hence easier model calibration. Since the models are required to offer good prediction accuracy of all state variables, not just biopolymer related ones, an introduction of biopolymer kinetics cannot jeopardise the model's accuracy in other areas. Since the original ASM models have been extensively validated and are found to offer good 'off-the-shelf' predictions with default parameters, the closer the new model is to its base model, the easier will be its application in the modelling studies of different sorts. It is also more plausible from a scientific point of view that biopolymer kinetics, which are felt to be of secondary importance, do not dominate over other, more significant processes, such

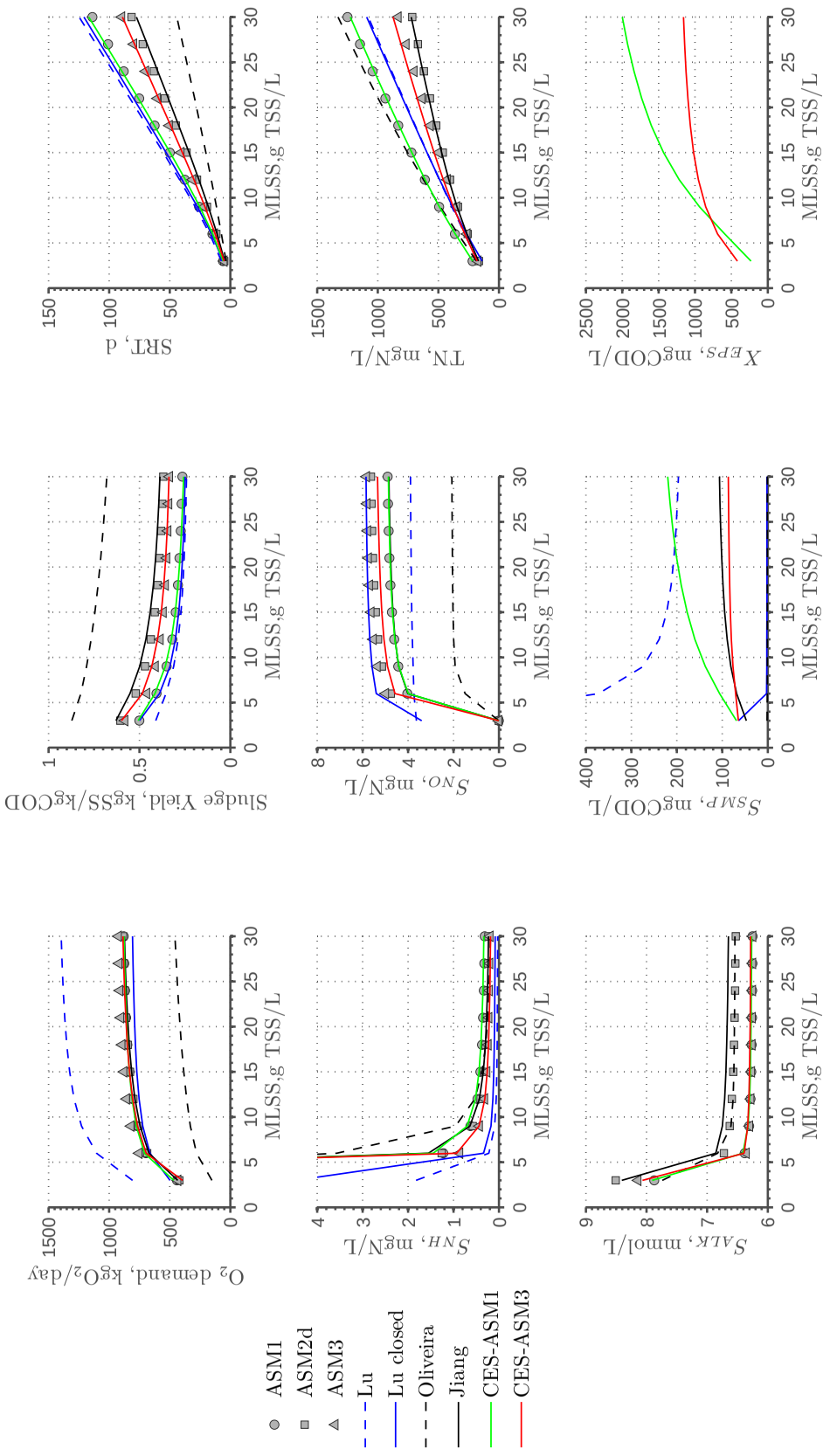

Figure 3.4: Selected outputs of the compared ASM models at different MLSS setpoints.

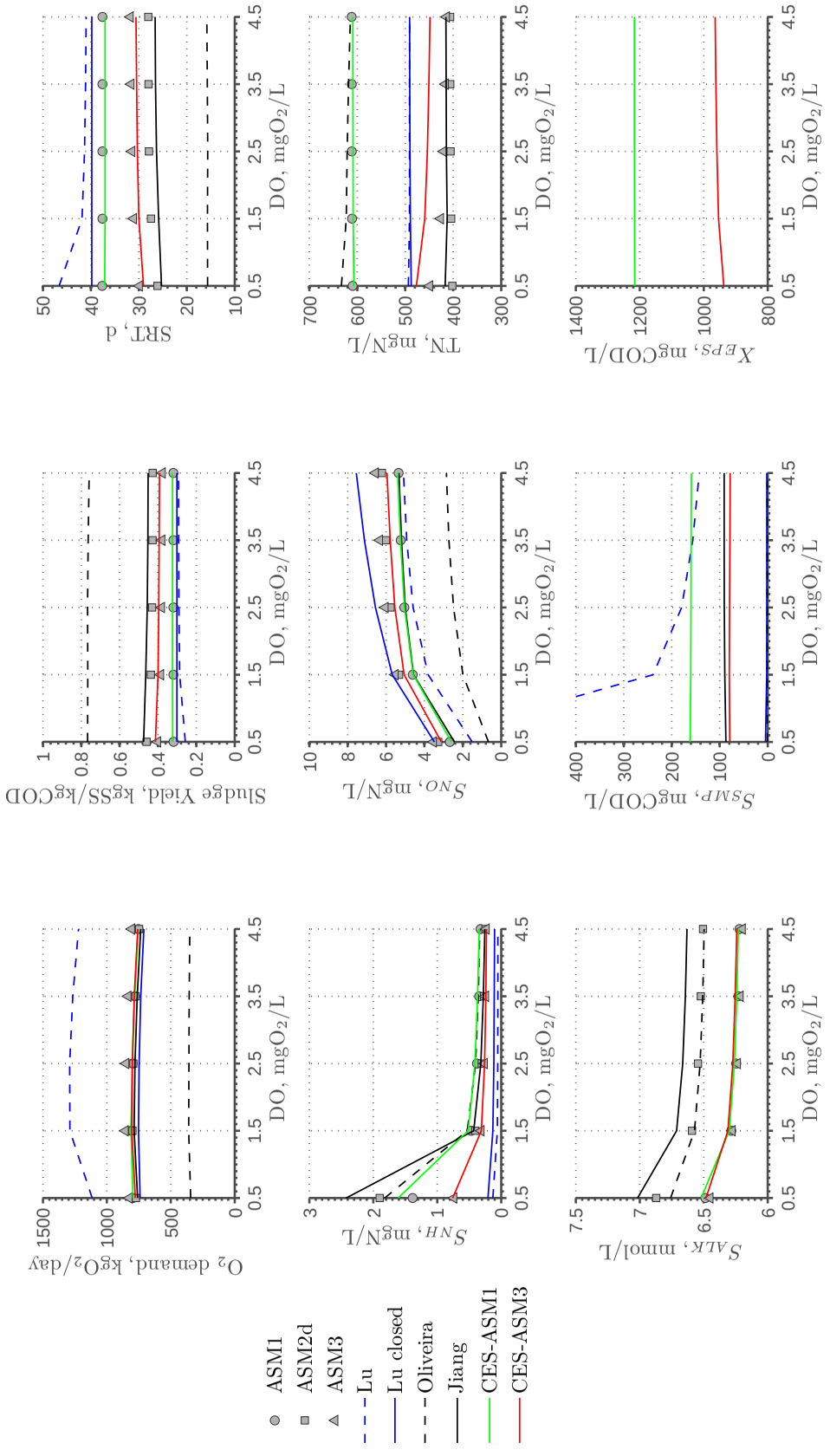

Figure 3.5: Selected outputs of the compared ASM models at different DO setpoints.

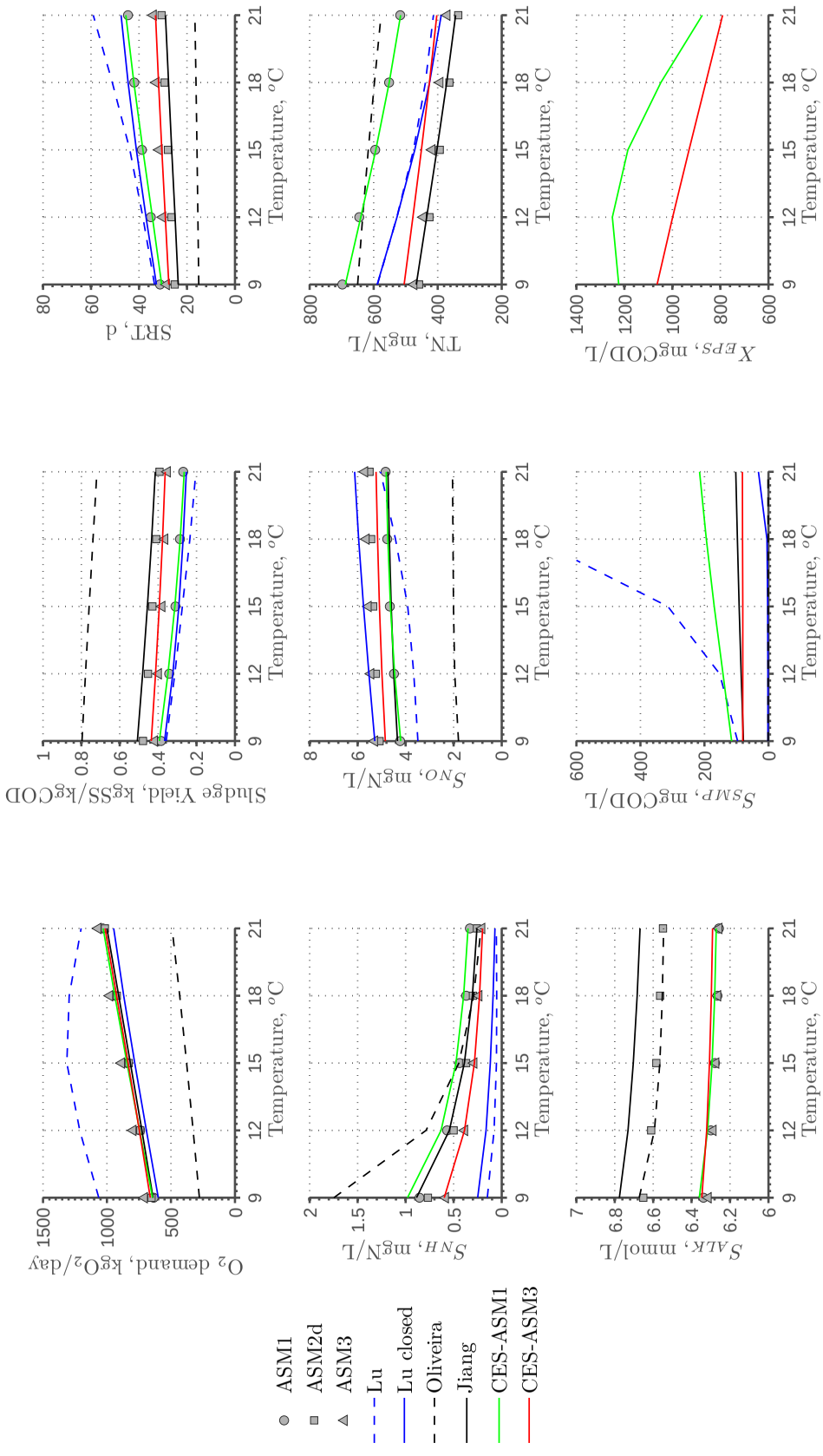

Figure 3.6: Selected outputs of the compared ASM models at different liquid temperatures.

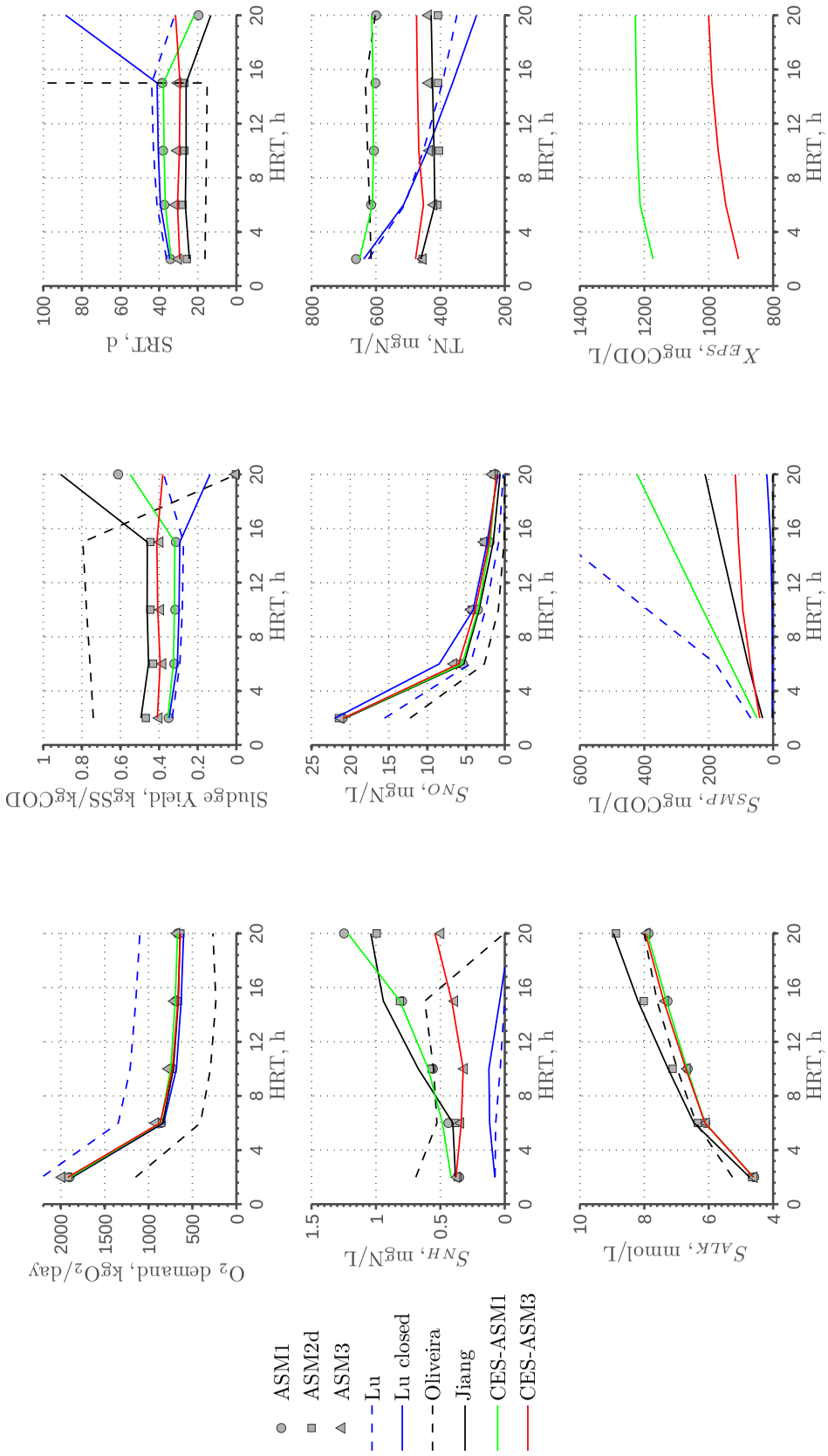

Figure 3.7: Selected outputs of the compared ASM models at different HRTs.

Table 3.5: Kinetic and stoichiometric parameters for SMP and EPS kinetics in CES-ASM1 and CES-ASM3 used in the model comparison study.

Parameter	Symbol	Unit	CES-ASM1	CES-ASM3
ASM1 and ASM3 parameters				
Yield of heterotrophic biomass	Y_H	$gX_H\ g^{-1}\ X_{STO}$	0.6	–
Half sat. coefficient for incorporation of NH_4^+/NO_3^- by heterotrophs K_{NHNO}	$gN\ m^{-3}$	0	–	
Aerobic yield of heterotrophic biomass	$Y_H^{O_2}$	$gX_H\ g^{-1}\ X_{STO}$	–	$0.8/\gamma_H$
Anoxic yield of heterotrophic biomass	Y_H^{NO}	$gX_H\ g^{-1}\ X_{STO}$	–	$0.65/\gamma_H$
Aerobic yield of stored product per S_S	$Y_{STO}^{O_2}$	$gX_{STO}\ g^{-1}\ S_S$	–	$0.8/\gamma_H$
Anoxic yield of stored product per S_S	Y_{STO}^{NO}	$gX_{STO}\ g^{-1}\ S_S$	–	$0.7/\gamma_H$
CES-ASM1 and CES-ASM3 kinetic parameters				
Max. spec. heterotrophic growth rate on S_{UAP}	$\mu_{UAP,20}$	d^{-1}	0.45	–
Max. spec. heterotrophic growth rate on S_{BAP}	$\mu_{BAP,20}$	d^{-1}	0.00	–
Max. X_I hydrolysis rate	$k_{h,X_I,20}$	d^{-1}	0.00	0.00
Max. X_P hydrolysis rate	$k_{h,X_P,20}$	d^{-1}	0.00	–
S_{BAP} storage rate constant	k_{STO}^{BAP}	$gS_{BAP}\ g^{-1}\ X_H\ d^{-1}$	–	0.1
S_{UAP} storage rate constant	k_{STO}^{UAP}	$gS_{UAP}\ g^{-1}\ X_H\ d^{-1}$	–	0.1
Max. X_{EPS} hydrolysis rate	$k_{h,EPS,20}$	d^{-1}	0.055	0.17
CES-ASM1 and CES-ASM3 stoichiometric parameters				
Fraction of S_{UAP} produced during heterotrophic growth	γ_H	$gS_{UAP}\ g^{-1}\ X_H$	0.0924	0.0193
Fraction of S_{UAP} produced during autotrophic growth	γ_A	$gS_{UAP}\ g^{-1}\ X_A$	0.00	0.00
Half saturation constant for S_{BAP}	K_{BAP}	$gS_{BAP}\ m^{-3}$	85	85
Half saturation constant for S_{UAP}	K_{UAP}	$gS_{UAP}\ m^{-3}$	100	100
Yield coefficient for heterotrophic growth on SMP	Y_{SMP}	$gX_H\ g^{-1}$SMP	0.45	–
Fraction of S_{BAP} produced from biomass decay	f_{BAP}	$gS_{BAP}\ g^{-1}(X_H$ or $X_A)$	0.017	0.0215
Fraction of X_{EPS} produced during X_H cell growth	$f_{EPS,h}$	$gX_{EPS}\ g^{-1}\ X_H$	0.045	0.12
Fraction of X_{EPS} produced during X_A cell growth	$f_{EPS,a}$	$gX_{EPS}\ g^{-1}\ X_A$	0.00	0.00
Fraction of X_{EPS} produced from X_H decay	$f_{EPS,dh}$	$gX_{EPS}\ g^{-1}\ X_H$	0.015	0.05
Fraction of X_{EPS} produced from X_A decay	$f_{EPS,da}$	$gX_{EPS}\ g^{-1}\ X_A$	0.00	0.00
Fraction of X_{EPS} produced during storage of internal substrates	$f_{EPS,STO}$	$gX_{EPS}\ g^{-1}\ X_H$	–	0.12
Fraction of S_S produced from X_{EPS} hydrolysis	f_S	$gS_S\ g^{-1}\ X_{EPS}$	0.4	0.4
N content of S_{BAP}	i_{XBAP}	$gN\ g^{-1}\ S_{BAP}$	0.06	0.07
N content of X_{EPS}	i_{XEPS}	$gN\ g^{-1}\ X_{EPS}$	0.06	0.07
Fraction of N released in X_I hydrolysis	f_{N,X_I}	$gN\ g^{-1}\ X_I$	0.02	0.02
Fraction of N released in X_P hydrolysis	f_{N,X_P}	$gN\ g^{-1}\ X_P$	0.086	–
Aerobic yield of stored product per S_{BAP} and S_{UAP} (SMP)	$Y_{STO,SMP}^{O_2}$	$gX_{STO}\ g^{-1}$SMP	–	0.80
Anoxic yield of stored product per S_{BAP} and S_{UAP} (SMP)	$Y_{STO,SMP}^{NO}$	$gX_{STO}\ g^{-1}$SMP	–	0.70

as e.g. nitrification or denitrification.

The models are assessed by calculating the average relative deviation (ARD) between the outputs of the biopolymer models $\left(x_{sim}^{bio}\right)$ and the outputs of the base ASM models $\left(x_{sim}^{ASM}\right)$ - see Equation 3.29.

$$ARD = \frac{1}{n}\sum_{i=1}^{n}\left(\frac{\left|x_{sim}^{ASM} - x_{sim}^{bio}\right|}{x_{sim}^{ASM}}\right)\cdot 100\% \tag{3.29}$$

The overall results are presented with a bar plot in Figure 3.8. The model of Oliveira-Esquerre et al. [192] deviates the most from its base ASM3 model with ARDs up to 15%. The 'Lu' and 'Lu closed' models also produce significantly different outputs to their base ASM1 model, especially with regards to nitrification, denitrification and oxygen demand. The model of Jiang et al. [115] is characterised with ARDs up to only 2%, while CES-ASM1 and CES-ASM3 have ARDs below 1%.

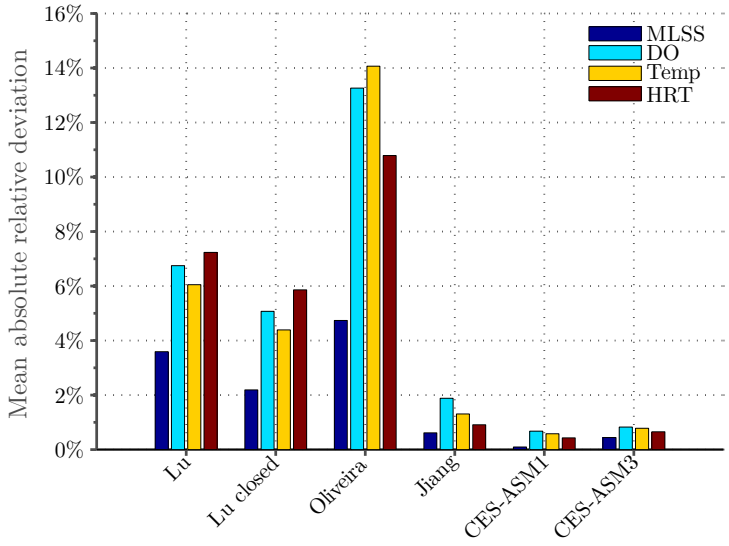

Figure 3.8: Average relative deviations between the biopolymer models and the original ASM models in all four sensitivity studies.

The results show that the models of Lu et al. [157] and Oliveira-Esquerre et al. [192] are inappropriate, because they deviate too much from their base ASM models as a result of the influence that the biopolymer-related stoichiometric parameters have on the original reaction terms such as the heterotrophic growth or autotrophic growth. The model of Jiang et al. [115] is conceptually correct but it does describe the EPS kinetics and additionally it is based on a very large and complex ASM2d model which has a large number of unidentifiable parameters [18]. These findings justify the development of CES-ASM1 and CES-ASM3, which shall be described in Chapter 4.

1

Chapter 4

Development of new activated sludge models

Contents

4.1 Introduction

This chapter presents two new dynamic activated sludge models which, apart from describing, so called, standard activated sludge processes, also predict the formation and degradation kinetics of bacterial biopolymers: soluble microbial products (SMP) and extracellular polymeric substances (EPS). The first model, later referred to as combined EPS and SMP production ASM1-based model (CES-ASM1) is based on Activated Sludge Model No. 1 (ASM1) by Henze et al. [86], while the second model, later referred to as combined EPS and SMP production ASM3-based model (CES-ASM3) is based on Activated Sludge Model No. 3 (ASM3) [79]. Both models have been briefly

outlined in Chapter 3 in Section 3.6.7. CES-ASM3 presented in this chapter is a slight modification of the model published in Janus and Ulanicki [111]. CES-ASM3 as well as CES-ASM1 described here feature an additional process of slow hydrolysis of unbiodegradable particulate substrates as suggested by Spérandio and Espinoza [227] and Lubello et al. [158]. Additionally, the kinetic and stoichiometric parameters for nitrification, namely maximum autotrophic growth rate μ_A, autotrophic decay rate b_A and Monod half-saturation constant for ammoniacal nitrogen K_{NH} have been adjusted accordingly to the published observations of Spérandio and Espinoza [227] - see Section 4.2 for further reference.

CES-ASM1 and CES-ASM3 add an extended unified theory of production and degradation of SMP and EPS developed by Laspidou and Rittmann [135; 136] into, respectively ASM1 and ASM3, although with one significant conceptual correction. Whilst Laspidou and Rittmann [135; 136] assume that all biomass associated products (BAP) in the system originate from hydrolysis of EPS, researchers such as Aquino and Stuckey [7] postulate that BAP is produced during EPS hydrolysis as well as bacterial cell lysis and decay. In fact, BAP had already been earlier defined as SMP fraction strictly originating from biomass decay by Lu et al. [157]. The lack of direct active cell decay-related SMP production in Laspidou and Rittmann [136] was found to be the main cause of discrepancies between model predictions and measurements of SMP [169]. Hence, CES-ASM1 and CES-ASM3 incorporate both pathways of BAP formation as shown in Figures 4.1 and 4.2.

Both models were calibrated on published experimental results from batch and continuous flow laboratory and pilot plant experiments [102, 101, 267] and proved to be in good agreement with the measurements. Standard sets of parameters were chosen for both models as a combination of calibrated parameter values and values obtained form literature. CES-ASM1 and CES-ASM3 were then used to predict SMP and EPS production in an activated sludge system under various operating conditions. The simulation results are shown in Section 4.5 and indicate increased production of SMP and EPS at higher mixed liquor suspended solids (MLSS), lower temperatures and lower sludge retention times (SRTs). The models also predict a slight increase in SMP and EPS concentrations with increasing dissolved oxygen (DO).

From the modelling perspective SMP can be subdivided into two groups, based either on their origin or chemical composition. In most models, as mentioned in Chapter 3, SMP are subdivided into utilisation associated products (UAP) which are produced during substrate metabolism and into biomass associated products (BAP) which originate directly from biomass as products of decay, lysis and cell maintenance. If we look into chemical composition of SMP which determines such properties of SMP as molecular weight (MW) size distribution or hydrophobicity, we can subdivide and quantify different types of chemical compounds constituting SMP and EPS such as, e.g. proteins (PP) and polysaccharides (PS). SMP and EPS have already been found to exhibit different fouling properties depending on their chemical composition [78, 207]. Most of the models developed to date have not looked into chemical composition of

SMP and CES-ASM1 and CES-ASM3 are no different in this respect. The reason for this state of matters is that the metabolic pathways leading to production of individual groups of chemicals in SMP are not yet understood. The Author however believes that development of a mathematical model which will be capable of predicting (some) chemical composition of SMP and EPS such as, e.g. the PS and PP fractions, might be helpful in furthering our understanding of SMP and EPS production in microbial systems and might allow us to develop better functional links between biological and fouling models.

ASM1 and ASM3 were chosen to form the basis for, respectively CES-ASM1 and CES-ASM3. ASM1 was selected for its simplicity and its widespread use in the engineering community. Additionally, ASM1 is used as a biological model in the COST simulation benchmark [36] as well as the recently developed membrane bioreactor (MBR) benchmark model of Maere et al. [160]. Thus, using a ASM1-based biopolymer model will allow easier comparison of benchmark results with the results of the integrated MBR model. ASM3 was chosen as the base for the second model because, from the Author's experience, ASM3 is easier to calibrate for long sludge age systems as a result of replacing the 'death-regeneration' concept with endogenous respiration and introduction of substrate storage mechanism [89]. ASM3 solves several well-known limitations of ASM1 as reported in Gujer et al. [79] and, with additional equations, can be used to simulate, for example, a two-stage nitrification process [110, 117] or excess biological phosphorus removal (EBPR) [208]. More information about ASM1 and ASM3 can be found in, respectively, Sections 3.2.3 and 3.2.3.

The new biopolymer-related state variables of CES-ASM1 and CES-ASM3 are listed below.

1. S_{UAP} (gCOD m^{-3}): Utilisation associated products UAP. This is a fraction of SMP which is produced as a by-product of substrate utilisation and cell growth.
2. S_{BAP} (gCOD m^{-3}): Biomass associated products BAP. This is a fraction of SMP which is independent of cell growth rate and is a by-product of cell lysis and decay as well as EPS hydrolysis/dissolution.
3. X_{EPS} (gCOD m^{-3}): Extracellular polymeric substrates EPS.

In most experimental studies, EPS and SMP are assumed to be composed of only two fractions: proteins (PP) and polysaccharides (PS). As activated sludge models represent biopolymer concentrations in the units of mg COD/L whilst the measurements of PP and PS are given in, respectively mg of bovine serum albumen (BSA) per litre and mg $C_6H_{12}O_6$ per litre in accordance to the methods of Lowry et al. [156] and Dubois et al. [49], PP and PS measurements need to be converted to chemical oxygen demand (COD) for model calibration purposes. In order to achieve such conversion Equation 4.1 first introduced in [115] can be used.

$$S_{COD} = (1.5\ S_{PT} + 1.07\ S_{PS})/0.65 \tag{4.1}$$

CES-ASM1 and CES-ASM3 assume that production of EPS in activated sludge systems obeys the Leudeking-Piret equation [144] with a reformulated non-growth associated term and an additional reaction term for EPS hydrolysis/dissolution:

$$r_{EPS} = f_{EPS}\,\mu\,X + f_{EPS,d}\,b\,X - k_{h,EPS}\,X_{EPS} \tag{4.2}$$

where μ (d^{-1}) denotes the microbial growth rate, X (gCOD m^{-3}) denotes the biomass concentration, X_{EPS} (gCOD m^{-3}) is the EPS concentration, f_{EPS} (–) is a nondimensional growth associated EPS formation coefficient, $f_{EPS,d}$ (–) is the non-growth associated EPS formation coefficient, b (d^{-1}) is the microbial decay rate, and $k_{h,EPS}$ (d^{-1}) is the rate of EPS hydrolysis/dissolution.

Production of utilisation associated products (UAP) is associated with biomass growth and substrate utilisation and can be expressed with a reformulated equation of Rittmann and McCarty [209]:

$$r_{UAP} = (\gamma_{UAP}/Y)\ \mu\,X \tag{4.3}$$

where γ_{UAP} (–) is the UAP formation coefficient, and Y (–) denotes the biomass yield.

BAP are assumed to originate from biomass decay and hydrolysis/dissolution of EPS and their production kinetics follow can be expressed with Equation 4.4:

$$r_{BAP} = f_{BAP}\,b\,X + (1 - f_S)\,k_{h,EPS}\,X_{EPS}\,Y_{BAP} \tag{4.4}$$

where f_{BAP} (–) is the BAP formation coefficient, f_S (–) is the fraction of S_S produced from EPS hydrolysis/dissolution and Y_{BAP} (–) is the unit conversion between EPS and SMP. Y_{BAP} is equal to 1 as all modelled carbonaceous substrate concentrations including EPS and SMP have the same unit of mg COD/L.

Accordingly to Equation 4.4 part of BAP is biomass associated SMP whereas the rest can be regarded as soluble EPS since they originate from hydrolysis/dissolution of extracellular polymeric substances (EPS). Kinetic pathways of SMP and EPS in CES-ASM1 and CES-ASM3 are presented, respectively, in Figure 4.1 and Figure 4.2.

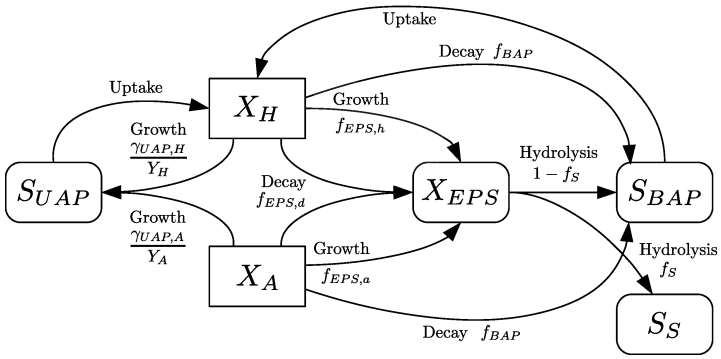

Figure 4.1: EPS and SMP formation and utilisation pathways in CES-ASM1.

UAP as well as BAP are taken up by heterotrophic biomass X_H for growth and res-

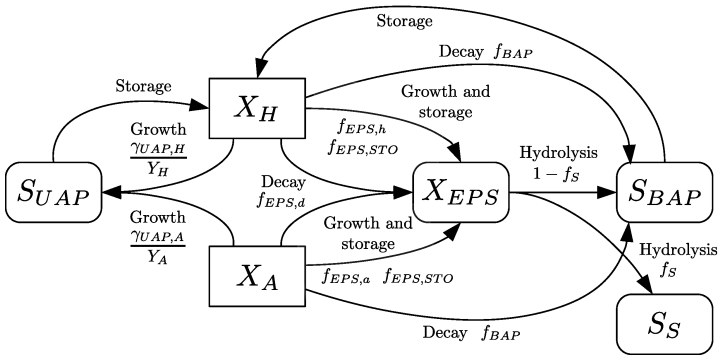

Figure 4.2: EPS and SMP formation and utilisation pathways in CES-ASM3.

piration (in CES-ASM1) and growth and respiration with prior storage (in CES-ASM3). UAP are produced during the growth of X_H and X_A, whilst BAP originate from X_H and X_A decay and X_{EPS} hydrolysis. X_{EPS} are produced during both, growth and decay of X_H and X_A in CES-ASM1 and during storage, growth, and decay of X_H and X_A in CES-ASM3.

4.2 Nitrification and slow hydrolysis kinetics

Spérandio and Espinoza [227] reported that ASM1 and ASM3 with default kinetic and stoichiometric parameters overestimate sludge production at high SRTs (over 50 days) whilst giving correct predictions (ASM1) or slightly underestimating the sludge production (ASM3) under lower SRTs up to 30 days. Differences in predicted sludge yields between ASM1 and ASM3 for lower SRTs result from different treatments of death and decay processes in these two models. As a result, ASM1 tends to predict higher amounts of unbiodegradable organic matter in the sludge, due to overestimation of decay processes in the *death-regeneration* model [227].

It was postulated that organic compounds which are inert at moderate SRTs become biodegradable under elevated SRTs such as these observed in MBR systems. Biodegradability of these 'unbiodegradable' particulate components can be introduced into activated sludge model (ASM) models through provision of a mechanism of slow hydrolysis of 'unbiodegradable' particulates. This process leads to reduction of the amounts of particulate inert products of biomass decay X_P and particulate inert organic matter X_I in the system and thus, reduction of mixed liquor volatile suspended solids (MLVSS).

Lubello et al. [158] extended the ASM1 model with slow hydrolysis of X_P and X_I, swapped death-regeneration with a simple decay process and validated their model on two separate sets of data from two different MBR pilot plants. The authors attributed poor predictions of MLVSS in ASM1 and ASM3 to a false assumption that inert products of biomass decay cannot be biodegraded. This assumption is only valid for limited values of SRTs. For higher SRTs this unbiodegradable material undergoes slow hydrolysis to soluble substances, thus leading to lower sludge yields. Moreover, sludge

production is hard to determine for high SRT systems due to the fact that respirometric techniques are short-term. Hence, otherwise hydrolysable fraction is identified in the tests as inert particulate [158]. Following the approach of Lubello et al. [158] CES-ASM1 and CES-ASM3 incorporate slow hydrolysis kinetics of X_P (CES-ASM1), and X_I (CES-ASM1 and CES-ASM3). Both hydrolysis rates are expressed with first order kinetics as shown in Equations 4.6 and 4.5.

$$\frac{dX_P}{dt} = -k_P\, X_P \tag{4.5}$$

$$\frac{dX_I}{dt} = -k_I\, X_I \tag{4.6}$$

where k_P and k_I denote X_P and X_I hydrolysis rates respectively, and both are assigned the value of 0.013 d^{-1}.

The nitrogen contents in X_I and X_P ($f_{N,I}$ and $f_{N,P}$) are given the values originally proposed by Lubello et al. [158], which are, respectively 0.020 gN $\mathrm{gCOD}_{X_I}^{-1}$ and 0.086 gN $\mathrm{gCOD}_{\mathrm{cell}}^{-1}$.

Both inert particulate fractions are hydrolysed into soluble inert organic matter (S_I) and readily biodegradable substrates (S_S). Fractions of S_I produced in X_I and X_P hydrolysis are denoted with stoichiometric parameters $f_{I,I}$ and $f_{I,P}$, respectively. The rest of the products of X_I and X_P hydrolysis form readily biodegradable soluble substrates (S_S). $f_{I,I}$ and $f_{I,P}$ have been assigned null values in accordance with the observations of Lubello et al. [158].

Spérandio and Espinoza [227] postulate that MBRs have different nitrification kinetics to conventional ASMs and therefore MBRs should be modelled using different autotrophic biomass growth and decay rates to the default rates used in ASM1 and ASM3. They proposed $\mu_A = 0.45$ d^{-1} and $b_A = 0.04$ d^{-1} as the values more characteristic of MBR systems. The half-saturation constant for nitrification is found to be higher in MBRs than in conventional activated sludge (CAS) systems [228] and additionally increases with SRT. The values of this half-saturation constant found by Spérandio and Espinoza [227] in batch test experiments for an unknown mathematical model (most likely ASM1 or ASM3) ranged from 0.25 mgN/L at MLSS of around 1.5 g/L to 0.65 mgN/L at MLSS of 7.5 g/L.

4.3 CES-ASM1 and CES-ASM3 model structure

Each ASM model is defined by the Petersen matrix, the vector of process rate equations, and the table of values of the kinetic and stoichiometric parameters. Additionally, each model is supplemented with a table of stoichiometric parameters for calculation of composite variables. Composite variables are the variables which are not explicitly calculated in the model, but can be derived as a linear combination of the state variables. Whilst only a few state variables can be directly measured in the system, composite variables are usually measurable with simple wet chemistry methods. The stoichiometric

parameters for calculation of composite variables in CES-ASM1 and CES-ASM3 are given in Table 4.4 and Table 4.6, respectively.

The vector of composite variables **c** in both models is given in Equation 4.7.

$$\mathbf{c}^T = [\text{SBOD}_\infty\ \text{XBOD}_\infty\ \text{BOD}_\infty\ \text{SBOD}_5\ \text{XBOD}_5\ \text{BOD}_5\ \text{SCOD}\ \text{XCOD}\ldots \\ \text{COD}\ \text{STKN}\ \text{XTKN}\ \text{TKN}\ \text{TN}\ \text{VSS}\ \text{TSS}] \tag{4.7}$$

The vectors of state variables for CES-ASM1 ($\mathbf{x}_1$) and CES-ASM3 ($\mathbf{x}_2$) are given below.

$$\mathbf{x}_1{}^T = \left[S_I\ S_S\ X_I\ X_S\ X_H\ X_{EPS}\ S_{UAP}\ S_{BAP}\ X_A\ X_P\ S_O\ S_{NO}\ S_{N_2}\ S_{NH}\ S_{ND}\ X_{ND}\ S_{ALK}\right]$$

$$\mathbf{x}_2{}^T = \left[S_O\ S_I\ S_S\ S_{NH}\ S_{N_2}\ S_{NO}\ S_{HCO}\ S_{BAP}\ S_{UAP}\ X_I\ X_S\ X_H\ X_{STO}\ X_A\ X_{EPS}\ X_{TSS}\right]$$

The values of composite variables in each model are calculated with Equation 4.8

$$\mathbf{c} = \mathbf{C}^T\ \mathbf{x} \tag{4.8}$$

where **C** denotes the matrix of stoichiometric parameters for composite variables given in Table 4.4 and Table 4.6. For CES-ASM1 $\mathbf{x} = \mathbf{x}_1$ whereas for CES-ASM3 $\mathbf{x} = \mathbf{x}_2$.

The following two sections list the composite variable calculation tables, Petersen matrices and SMP, EPS, and slow hydrolysis kinetics for both models, whilst entire descriptions of CES-ASM1 and CES-ASM3, i.e. Petersen matrices, all process rate equations, and all kinetic and stoichiometric parameter values are given in the Appendix.

4.3.1 Combined SMP and EPS Activated Sludge Model No.1

Model structure

UAP, BAP, and EPS kinetics in CES-ASM1 follow the pathways shown in Figure 4.1. Their kinetics equations together with the kinetic equations of slow hydrolysis of X_I and X_P are listed in Table **??**. Petersen matrix for CES-ASM1 is presented in Table 4.3. Values of the kinetic and stoichiometric parameters used in the kinetic equations and in the Petersen matrix can be found in the Appendix.

Aerobic growth rates on S_{BAP} and S_{UAP} are proportional to maximum specific growth rates on, respectively, S_{BAP} (μ_{BAP}) and S_{BAP} (μ_{BAP}) and heterotrophic biomass concentration X_H. They additionally depend on the substrate concentration (S_{BAP} and S_{UAP} respectively), oxygen concentration (S_O) and alkalinity (S_{ALK}). Anoxic growth occurs at a lower rate to aerobic growth. This rate reduction is modelled with an anoxic reduction factor η_g. Anoxic growth depends on substrate concentration (S_{BAP} and S_{UAP}), alkalinity (S_{ALK}) and nitrate concentration (S_{NO}), and is inhibited by oxygen. Hydrolysis of EPS is modelled with first order kinetics with respect to the EPS concentration (X_{EPS}).

Table 4.1: Process rate expressions for SMP and EPS kinetics and slow hydrolysis in CES-ASM1.

No.	Process	Process rate equation
$p_{1,b}$	Aerobic growth on S_{BAP}	$\mu_{BAP} \frac{S_{BAP}}{K_{BAP}+S_{BAP}} \frac{S_O}{K_{OH}+S_O} \frac{S_{ALK}}{K_{ALKH}+S_{ALK}} X_H$
$p_{1,c}$	Aerobic growth on S_{UAP}	$\mu_{UAP} \frac{S_{UAP}}{K_{UAP}+S_{UAP}} \frac{S_O}{K_{OH}+S_O} \frac{S_{ALK}}{K_{ALKH}+S_{ALK}} X_H$
$p_{2,b}$	Anoxic growth on S_{BAP}	$\mu_{BAP}\, \eta_g \frac{S_{BAP}}{K_{BAP}+S_{BAP}} \frac{K_{OH}}{K_{OH}+S_O} \frac{S_{NO}}{K_{NO}+S_{NO}} \frac{S_{ALK}}{K_{ALKH}+S_{ALK}} X_H$
$p_{2,c}$	Anoxic growth on S_{UAP}	$\mu_{UAP}\, \eta_g \frac{S_{UAP}}{K_{UAP}+S_{UAP}} \frac{K_{OH}}{K_{OH}+S_O} \frac{S_{NO}}{K_{NO}+S_{NO}} \frac{S_{ALK}}{K_{ALKH}+S_{ALK}} X_H$
p_7	Hydrolysis of X_{EPS}	$k_{h,EPS}\, X_{EPS}$
p_8	Hydrolysis of X_I	$k_{h,X_I}\, X_I$
p_9	Hydrolysis of X_P	$k_{h,X_P}\, X_P$

$\mu_{BAP} = e^{-0.069\,(20-T)}\ \mu_{BAP,20}$, $\mu_{UAP} = e^{-0.069\,(20-T)}\ \mu_{UAP,20}$, $k_{h,EPS} = e^{-0.11\,(20-T)}\ k_{h,EPS,20}$, $k_{h,X_I} = e^{-0.11\,(20-T)}\ k_{h,X_I,20}$, $k_{h,X_P} = e^{-0.11\,(20-T)}\ k_{h,X_P,20}$

Table 4.2: Process rate expressions for SMP and EPS kinetics and slow hydrolysis in CES-ASM3.

No.	Process	Process rate equation
$p_{2,b}$	Aerobic storage of S_{BAP}	$k_{sto}^{BAP} \frac{S_{BAP}}{K_{BAP}+S_{BAP}} \frac{S_O}{K_O+S_O} X_H$
$p_{2,c}$	Aerobic storage of S_{UAP}	$k_{sto}^{UAP} \frac{S_{UAP}}{K_{UAP}+S_{UAP}} \frac{S_O}{K_O+S_O} X_H$
$p_{3,b}$	Anoxic storage of S_{BAP}	$k_{sto}^{BAP}\, \eta_{NO} \frac{S_{BAP}}{K_{BAP}+S_{BAP}} \frac{K_O}{K_O+S_O} \frac{S_{NO}}{K_{NO}+S_{NO}} X_H$
$p_{3,c}$	Anoxic storage of S_{UAP}	$k_{sto}^{UAP}\, \eta_{NO} \frac{S_{UAP}}{K_{UAP}+S_{UAP}} \frac{K_O}{K_O+S_O} \frac{S_{NO}}{K_{NO}+S_{NO}} X_H$
p_{13}	Hydrolysis of X_{EPS}	$k_h^{EPS}\, X_{EPS}$
p_{14}	Hydrolysis of X_I	$k_{h,X_I}\, X_I$

$k_{sto}^{BAP} = e^{-0.07\,(20-T)}\ k_{sto,BAP,20}$, $k_{sto}^{UAP} = e^{-0.07\,(20-T)}\ k_{sto,UAP,20}$, $k_h^{EPS} = e^{-0.04\,(20-T)} \cdot k_{h.EPS,20}$, $k_{h,X_I} = e^{-0.04\,(20-T)} \cdot k_{h,X_I,20}$

Table 4.3: Stoichiometric (Petersen) and composition matrix for CES-ASM1, j: process, i: component.

	Model components i	1	2	3	4	5	6	7	8	9	10	11	12	13	14	15	16	17
j	Processes	S_I	S_S	X_I	X_S	X_H	X_{EPS}	S_{UAP}	S_{BAP}	X_A	X_P	S_O	S_{NO}	S_{N_2}	S_{NH}	S_{ND}	X_{ND}	S_{ALK}
	Heterotrophic organisms																	
p_1	Ammonification														1	−1		$\frac{1}{14}$
p_{2a}	Aer. growth on S_S		$-\frac{1}{Y_H}$			$1-\frac{1}{f_{EPS,h}}$	$f_{EPS,h}$	$\frac{\gamma_H}{Y_H}$				x_{2a}			y_{2a}			$-\frac{i_{XB}}{14}$
p_{2b}	Aer. growth on S_{BAP}					$1-\frac{1}{f_{EPS,h}}$	$f_{EPS,h}$		$-\frac{1}{Y_{SMP}}$			x_{2b}			y_{2b}			$-\frac{i_{XB}}{14}$
p_{2c}	Aer. growth on S_{UAP}					$1-\frac{1}{f_{EPS,h}}$	$f_{EPS,h}$	$-\frac{1}{Y_{SMP}}$				x_{2c}			y_{2c}			$-\frac{i_{XB}}{14}$
p_{3a}	Anox. growth on S_S		$-\frac{1}{Y_H}$			$1-\frac{1}{f_{EPS,h}}$	$f_{EPS,h}$	$\frac{\gamma_H}{Y_H}$					x_{3a}	$-x_{3a}$	y_{3a}			$\frac{1-Y_H}{40\,Y_H}-\frac{i_{XB}}{14}$
p_{3b}	Anox. growth on S_{BAP}					$1-\frac{1}{f_{EPS,h}}$	$f_{EPS,h}$		$-\frac{1}{Y_{SMP}}$				x_{3b}	$-x_{3b}$	y_{3b}			$\frac{1-Y_H}{40\,Y_H}-\frac{i_{XB}}{14}$
p_{3c}	Anox. growth on S_{UAP}					$1-\frac{1}{f_{EPS,h}}$	$f_{EPS,h}$	$-\frac{1}{Y_{SMP}}$					x_{3c}	$-x_{3c}$	y_{3c}			$\frac{1-Y_H}{40\,Y_H}-\frac{i_{XB}}{14}$
p_4	Decay of heterotrophs				$1-f_P-f_{EPS,dh}-f_{BAP}$	−1	$f_{EPS.dh}$		f_{BAP}		f_P						$i_{XP}-f_P\,i_{XP}$	
p_5	Hydrolysis of org. compounds		1		−1													
p_6	Hydrolysis of org. N															1	−1	
p_7	Hydrolysis of X_{EPS}		f_S				−1	$1-f_S$								$i_{XEPS}-i_{XBAP}\,(1-f_S)$		
p_8	Hydrolysis of X_I	$f_{I,I}$	$1-f_{I,I}$	−1											$f_{N,I}$			
p_9	Hydrolysis of X_P	$f_{I,P}$	$1-f_{I,P}$								−1				$f_{N,P}$			
	Autotrophic organisms																	
p_{10}	Aerobic growth of autotrophs						$f_{EPS,a}$	$\frac{\gamma_A}{Y_A}$		$1-f_{EPS,a}$		$-\frac{\frac{64}{14}-Y_A}{Y_A}$	$\frac{1}{Y_A}$		$-i_{XB}-\frac{1}{Y_A}$			$-\frac{i_{XB}}{14}-\frac{1}{7\,Y_A}$
p_{11}	Decay of autotrophs				$1-f_P-f_{EPS,da}-f_{BAP}$		$f_{EPS,da}$		f_{BAP}	−1	f_P						$i_{XP}-f_P\,i_{XP}$	
	Composition matrix																	
1	ThOD (g ThOD)	1	1	1	1	1	1	1	1	1	1	-1	$-\frac{64}{14}$	$-\frac{24}{14}$				
2	Nitrogen (g N)					i_{XB}	i_{XEPS}		i_{XBAP}	i_{XB}	i_{XP}		1	1	1	1	1	
3	Ionic charge (Mole$^+$)												$-\frac{1}{14}$		$\frac{1}{14}$			-1

This model assumes that ThOD is identical to the measured COD. 1 gS_O = -1 gThOD, 1 gS_{NH} = 0 gThOD, 1gS_{NO} = -64/14 gThOD, 1 gS_{N_2} = -24/14 gThOD.

Calculation of composite variables

The matrix of stoichiometric parameters used for calculation of composite variables in CES-ASM1 is shown in Table 4.4. It is assumed that S_{UAP} does not contain any nitrogen and that S_I, X_I, and X_P do not count towards biological oxygen demand (BOD). Particulate inert materials (X_{II}) are not considered in CES-ASM1, therefore the model does not explicitly calculate the inert suspended solids (ISS) and thus is unable to predict the total suspended solids (TSS). TSS concentrations can be inferred from the calculated volatile suspended solids (VSS) concentrations using the parameter $i_{vt} = \frac{VSS}{TSS}$. Parameter f_{BOD}, where $f_{BOD} = \frac{BOD_5}{BOD_\infty}$ is used to calculate BOD_5 from BOD_∞. VSS are obtained from particulate chemical oxygen demand (XCOD) by multiplying XCOD by a reciprocal of i_{cv} where $i_{cv} = \frac{XCOD}{VSS}$ and is either assumed, calculated from theoretical equations, or measured.

4.3.2 Combined SMP and EPS Activated Sludge Model No.3

Model structure

UAP, BAP, and EPS kinetic pathways in CES-ASM3 are presented in Figure 4.2. Their production and degradation pathways are the same as in CES-ASM1 with one major difference. Whilst UAP and BAP in CES-ASM1 are directly used as a substrate, the same components in CES-ASM3 need to be first stored inside the bacterial cells prior to being used as a substrate. These storage mechanisms are one of the main features of ASM3. Kinetics of UAP and BAP storage processes and slow hydrolysis of X_I are listed in Table **??**. Petersen matrix for CES-ASM3 is presented in Table 4.5. The values of kinetic and stoichiometric parameters used in the kinetic equations and in the Petersen matrix can be found in Appendix IV.

S_{BAP} and S_{UAP} are taken up for storage by heterotrophic microorganisms under aerobic and anoxic conditions together with readily biodegradable substrates (S_S). The rates of S_{BAP} and S_{UAP} storage are proportional to maximum storage rates k_{sto}^{UAP} and k_{sto}^{BAP} and heterotrophic biomass concentration (X_H). The rates of storage are also dependent on substrate concentration (S_{BAP} and S_{UAP} respectively) and oxygen concentration (S_O). Storage under anoxic conditions occurs at a lower rate to aerobic storage. This rate reduction is modelled by introducing an anoxic reduction factor η_{NO}. Anoxic storage depends on substrate concentration (S_{BAP} and S_{UAP}) and nitrate concentration (S_{NO}) whilst being inhibited by oxygen (S_O). EPS hydrolysis is modelled with first order kinetics with respect to X_{EPS}.

Calculation of composite variables

Matrix of stoichiometric parameters for calculation of composite variables in CES-ASM3 is shown in Table 4.6. Similarly to CES-ASM1, S_{UAP} is assumed not to contain any nitrogen and S_I, X_I do not count towards BOD. Contrary to CES-ASM1, CES-ASM3

Table 4.4: Composite variable calculation table for CES-ASM1.

	$SBOD_\infty$	$XBOD_\infty$	BOD_∞	$SBOD_5$	$XBOD_5$	BOD_5	SCOD	XCOD	COD	STKN	XTKN	TKN	TN	VSS	TSS
S_I							1		1						
S_S	1		1	f_{BOD}		f_{BOD}	1		1						
X_I								1	1					$i_{cv}{}^{-1}$	$i_{cv}{}^{-1}\, i_{vt}{}^{-1}$
X_S		1	1		f_{BOD}	f_{BOD}		1	1					$i_{cv}{}^{-1}$	$i_{cv}{}^{-1}\, i_{vt}{}^{-1}$
X_H		1	1		f_{BOD}	f_{BOD}		1	1		i_{XB}	i_{XB}	i_{XB}	$i_{cv}{}^{-1}$	$i_{cv}{}^{-1}\, i_{vt}{}^{-1}$
X_{EPS}		1			f_{BOD}	f_{BOD}		1	1		i_{XEPS}	i_{XEPS}	i_{XEPS}	$i_{cv}{}^{-1}$	$i_{cv}{}^{-1}\, i_{vt}{}^{-1}$
S_{UAP}	1		1	f_{BOD}		f_{BOD}	1		1						
S_{BAP}	1		1	f_{BOD}		f_{BOD}	1		1	i_{XBAP}		i_{XBAP}	i_{XBAP}		
X_A		1	1		f_{BOD}	f_{BOD}		1	1		i_{XB}	i_{XB}	i_{XB}	$i_{cv}{}^{-1}$	$i_{cv}{}^{-1}\, i_{vt}{}^{-1}$
X_P								1	1		i_{XP}	i_{XP}	i_{XP}	$i_{cv}{}^{-1}$	$i_{cv}{}^{-1}\, i_{vt}{}^{-1}$
S_O															
S_{NO}													1		
S_{N_2}															
S_{NH}										1		1	1		
S_{ND}										1		1	1		
X_{ND}											1	1	1		
S_{ALK}															

Table 4.5: Stoichiometric (Petersen) and composition matrix for CES-ASM3, j: process, i: component.

	Model components i	1	2	3	4	5	6	7	8	9	10	11	12	13	14	15	16
j	Processes	S_O	S_I	S_S	S_{NH}	S_{N2}	S_{NO}	S_{HCO}	S_{BAP}	S_{UAP}	X_I	X_S	X_H	X_{STO}	X_A	X_{EPS}	X_{TSS}
	Heterotrophic organisms																
p_1	Hydrolysis		f_{S_I}	$1-f_{S_I}$	y_1			z_1				-1					t_1
$p_{2,a}$	Aerobic storage of S_S	x_{2a}		-1	y_{2a}			z_{2a}						$Y_{STO,O_2}-f_{EPS,STO}$		$f_{EPS,STO}$	t_{2a}
$p_{2,b}$	Aerobic storage of S_{BAP}	x_{2b}			y_{2b}			z_{2b}	-1					$Y_{STO,SMP,O_2}-f_{EPS,STO}$		$f_{EPS,STO}$	t_{2b}
$p_{2,c}$	Aerobic storage of S_{UAP}	x_{2c}			y_{2c}			z_{2c}		-1			$Y_{STO,SMP,O_2}-f_{EPS,STO}$			$f_{EPS,STO}$	t_{2c}
$p_{3,a}$	Anoxic storage of S_S			-1	y_{3a}	$-x_{3a}$	x_{3a}	z_{3a}						$Y_{STO,NO}-f_{EPS,STO}$		$f_{EPS,STO}$	t_{3a}
$p_{3,b}$	Anoxic storage of S_{BAP}				y_{3b}	$-x_{3b}$	x_{3b}	z_{3b}	-1					$Y_{STO,SMP,NO}-f_{EPS,STO}$		$f_{EPS,STO}$	t_{3b}
$p_{3,b}$	Anoxic storage of S_{UAP}				y_{3c}	$-x_{3c}$	x_{3c}	z_{3c}		-1			$Y_{STO,SMP,NO}-f_{EPS,STO}$			$f_{EPS,STO}$	t_{3c}
p_4	Aerobic growth	x_4			y_4			z_4		$\gamma_H/Y_{H,O_2}$			$1-f_{EPS,h}$	$-1/Y_{H,O_2}$		$f_{EPS,h}$	t_4
p_5	Anoxic growth				y_5	$-x_5$	x_5	z_5		$\gamma_H/Y_{H,NO}$			$1-f_{EPS,h}$	$-1/Y_{H,NO}$		$f_{EPS,h}$	t_5
p_6	Aerobic endogenous respiration	x_6			y_6			z_6	f_{BAP}		f_{X_I}		-1			$f_{EPS,dh}$	t_6
p_7	Anoxic endogenous respiration				y_7	$-x_7$	x_7	z_7	f_{BAP}		f_{X_I}		-1			$f_{EPS,dh}$	t_7
p_8	Aerobic respiration of X_{STO}	x_8												-1			t_8
p_9	Anoxic respiration of X_{STO}					$-x_9$	x_9	z_9						-1			t_9
	Autotrophic organisms																
p_{10}	Nitrification	x_{10}			y_{10}		$1/Y_A$	z_{10}		γ_A/Y_A					$1-f_{EPS,a}$	$f_{EPS,a}$	t_{10}
p_{11}	Aerobic endogenous respiration	x_{11}			y_{11}			z_{11}	f_{BAP}		f_{X_I}				-1	$f_{EPS,da}$	t_{11}
p_{12}	Anoxic endogenous respiration				y_{12}	$-x_{12}$	x_{12}	z_{12}	f_{BAP}		f_{X_I}				-1	$f_{EPS,da}$	t_{12}
	EPS and X_I hydrolysis																
p_{13}	Hydrolysis of X_{EPS}			f_S					$1-f_S$							-1	t_{13}
p_{14}	Hydrolysis of X_I		$f_{I,I}$	$1-f_{I,I}$	$f_{N,I}$						-1						t_{14}
1	ThOD (g ThOD)	-1	1	1		$-24/14$	$-64/14$		1	1	1	1	1	1	1	1	
2	Nitrogen (g N)		i_{N,S_I}	i_{N,S_S}	1	1	1		$i_{N,S_{BAP}}$		i_{N,X_I}	i_{N,X_S}	$i_{N,BM}$		$i_{N,BM}$	$i_{N,X_{EPS}}$	
3	Ionic charge (Mole$^+$)				1/14		$-1/14$	-1									
4	TSS (g TSS)										i_{TSS,X_I}	i_{TSS,X_S}	$i_{TSS,BM}$	$i_{TSS,STO}$	$i_{TSS,BM}$	$i_{TSS,EPS}$	1

This model assumes that ThOD is identical to the measured COD. 1 gS_O = -1 gThOD, 1 gS_{NH} = 0 gThOD, 1gS_{NO} = -64/14 gThOD, 1 gS_{N_2} = -24/14 gThOD.

Stoichiometric parameters x_i y_i z_i and t_i were calculated from mass and electric charge conservation equations and are given in the Appendix in Table 9.9.

calculates TSS concentrations explicitly as a state variable.

Table 4.6: Composite variables calculation table for CES-ASM3.

	$SBOD_\infty$	$XBOD_\infty$	BOD_∞	$SBOD_5$	$XBOD_5$	BOD_5	SCOD	XCOD	COD	STKN	XTKN	TKN	TN	VSS	TSS
S_O															
S_I							1		1	i_{N,S_I}		i_{N,S_I}	i_{N,S_I}		
S_S	1		1	f_{BOD}		f_{BOD}	1		1	i_{N,S_S}		i_{N,S_S}	i_{N,S_S}		
S_{NH}										1		1	1		
S_{N_2}															
S_{NO}													1		
S_{ALK}															
S_{BAP}	1		1	f_{BOD}		f_{BOD}	1		1						
S_{UAP}	1		1	f_{BOD}		f_{BOD}	1		1	$i_{N,S_{BAP}}$		$i_{N,S_{BAP}}$	$i_{N,S_{BAP}}$		
X_I								1	1		i_{N,X_I}	i_{N,X_I}	i_{N,X_I}		
X_S		1	1		f_{BOD}	f_{BOD}		1	1		i_{N,X_S}	i_{N,X_S}	i_{N,X_S}		
X_H		1	1		f_{BOD}	f_{BOD}		1	1		$i_{N,BM}$	$i_{N,BM}$	$i_{N,BM}$		
X_{STO}								1	1						
X_A		1	1		f_{BOD}	f_{BOD}		1	1		$i_{N,BM}$	$i_{N,BM}$	$i_{N,BM}$		
X_{EPS}		1	1		f_{BOD}	f_{BOD}		1	1		$i_{N,EPS}$	$i_{N,EPS}$	$i_{N,EPS}$		
X_{TSS}														i_{vt}	1

4.4 CES-ASM1 and CES-ASM3 model calibration

Kinetic and stoichiometric parameters of both models were identified on two sets of measurements from two different experiments. The first set of data was obtained from the experiments of Hsieh et al. [101] who investigated the SMP and EPS production in a pure bacterial culture of *Pseudomonas atlantica* cultivated in a glucose medium in a batch as well as a continuous flow lab scale bioreactor. The second set of data was taken from Yigit et al. [267] who measured the SMP and EPS levels in a bulk liquid of a submerged MBR pilot plant fed with raw domestic sewage and operating at five different MLSS concentrations.

Whilst the first set of data allowed identification of model parameters governing the model dynamics, the obtained parameters are characteristic of a single bacterial culture which is likely to have quite different properties from the mixed bacterial population of activated sludge. The second experiment, although did not provide the necessary measurements required for identification of model dynamics, allowed for the identification of a subset of kinetic and stoichiometric parameters in an activated sludge system fed with real wastewater. The parameter values obtained from both experiments were then combined with the findings of various researchers and published in literature in order to derive a set of initial parameter values for use in simulations of MBR systems. Further description of the experimental data, manual procedures and automatic algorithms used in the calibration and the obtained parameter values are provided in Sections 4.4.1 and 4.4.2 below.

4.4.1 Calibration on the data set of Hsieh et al. [102; 101]

In order to identify the biopolymer-related model parameters in both models on the set of data obtained from the continuous flow and batch bioreactors (Hsieh et al. [101]), both experimental setups were modelled in the MATLAB® environment. Both mathematical models were then simulated with CES-ASM1 and CES-ASM3 under the operating and initial conditions conforming to the physical setup. The kinetic and stoichiometric parameters selected for calibration were manipulated by the optimisation procedure `fminsearchbnd` implemented under MATLAB®. `fminsearchbnd` computes a Nelder-Mead non-linear simplex algorithm [178] with constraints, such that the adopted measure of error between the measurements and the model outputs is minimal. The objective function used in this calibration procedure is described in detail later in this section. The parameters were calibrated on continuous flow and batch reactor data under one optimisation procedure resulting a single parameter set describing the behaviour of both reactors.

The experiments were carried out by Hsieh et al. [102] on a single strain of bacteria *Pseudomonas atlantica* NCMB 301. The batch as well as the continuously fed bioreactor were fed with artificial seawater medium with 2 g L^{-1} of glucose added as a carbon source and 0.5 g L^{-1} NH_4Cl, 0.1 g L^{-1} KH_2PO_4 and 1.22×10^{-4} g L^{-1} $FeCl_3 \cdot 6H_2O$.

The reactor used in the study had a total volume of 2.0 L and a working volume between 500 to 1500 mL. Aeration was provided by sparging with filter-sterilised air at a volumetric flow rate of 2 L min^{-1}. pH was maintained at 7.0 by automatic addition of 1M solution of NaOH. Temperature was maintained at $25 \pm 2\,^{\circ}C$. In the continuous-flow experiment, steady-state conditions were defined by consecutive observations of at least three stable measurements of selected parameters, i.e. concentration of biomass, glucose, EPS and SMP after operation for a minimum period of 3 times the hydraulic retention time (HRT) [101].

The working volume of the bioreactor in the continuous-flow mode was equal 1420 mL. Although the reactor was not equipped with a mechanical mixer, recirculation provided with the peristaltic pump at ratios over 1300:1 allowed to model the reactor as a completely stirred tank reactor (CSTR). The recycle flow rate was typically set at 8 L min^{-1} although was sometimes reaching values as high as 50 L min^{-1}. The medium feed rates were always below 6 mL min^{-1}. Batch experiments were carried out on the same bioreactor at the same volume and recirculation rates but with zero feed flow. Bacterial dry weight (i.e. the sum of active biomass and polymers) was measured by weighing a centrifuged and sedimented sludge after drying it at 105°C for 24 hours. Glucose concentration was determined with the Calbiochem glucose test kit (EMD Bioscience La Jolla, CA). Biopolymers were measured with the method explained in Platt et al. [199]. More information about the experimental setup, experimental procedures and obtained experimental results can be found in the original publications of Hsieh et al. [102; 101].

Bacterial culture in the experiment of Hsieh et al. [101] was cultivated in a 2.0 g L^{-1} glucose medium. As the theoretical chemical oxygen demand (ThCOD) of glucose is equal to 1.067 mg O_2 (mg $C_6H_{12}O_6)^{-1}$ and glucose is soluble and entirely biodegradable, the influent COD is assumed to be composed only of soluble readily biodegradable matter (S_S) at concentration of 2,133 mgO_2 L^{-1}. Influent S_{NH} concetration was set to 125 mg N L^{-1} which corresponds to 0.5 g L^{-1} NH_4Cl used by Hsieh et al. [101]. Based on other pieces of information provided in Hsieh et al. [101] the influent (continuous flow reactor) and initial (batch experiment) X_{EPS} concentrations were set to 10 mg COD L^{-1}. All other COD an nitrogen (N) fractions in the influent were set to zero. DO concentration in the mixed liquor was set to 1.5 mg O_2 L^{-1}. Reactor volumes and flow-rates were taken from the original article.

As the reactors were inoculated with a pure heterotrophic bacterial culture of *Pseudomonas atlantica*, autotrophic biomass activity in CES-ASM1 and CES-ASM3 had to be switched off by setting the autotrophic growth rate μ_A to zero. As the autotrophic activity was not considered here, parameters governing the SMP and EPS kinetics in the autotrophic biomass were not estimated. It was then assumed that the unidentified SMP and EPS kinetic and stoichiometric parameters for the autotrophic biomass are equal to these of the heterotrophic biomass. Although this is very likely to be a false assumption, the relative error it may cause on the calculated mixed liquor EPS an SMP concentrations is very small as the autotrophic mass fraction in activated

sludge systems is found to be between 2% and 5% depending on operating conditions and influent characteristics. This very low influence of autotrophic activity on mixed liquor SMP and EPS concentrations was later confirmed in the parameter sensitivity study described in Section 4.7. Outputs from the calibrated CES-ASM1 and CES-ASM3 models are presented alongside relevant measurements respectively in Figure 4.3 and Figure 4.4. SMP concentrations shown on the plots correspond to the sum of S_{UAP} an S_{BAP}, total biomass is the sum of X_H and X_{EPS} and S denotes the concentration of readily biodegradable substrates (S_S). The estimated parameter values for CES-ASM1 are shown in Table 4.7 whereas the estimated parameters for CES-ASM3 are given in Table 4.8.

The objective function used for parameter identification has been defined as follows:

$$\text{RMSPE} = 100\% \sqrt{\frac{\sum_{j=1}^{m}\sum_{i=1}^{n}\left(\frac{y_{i,j}-\hat{y_{i,j}}}{y_{i,j}}\right)^2}{\sum_{j=1}^{m} n_j}} \tag{4.9}$$

where $m = 4$ denotes the number of measurement series, n_j denotes the number of measurement points in the j-th series, $y_{i,j}$ denotes the i-th measurement in the in the j-th series, and $\hat{y}(i,j)$ denotes the i-th model prediction in the j-th series.

The root mean square percentage error (RMSPE) was chosen in order to assign the same weights to all four measurements (biomass (X); substrate (S); SMP (S_{SMP}); and EPS (X_{EPS})) despite the differences in their magnitudes. Thus, once the model is calibrated, it will provide predictions of all four quantities with similar relative accuracies. RMSPE was chosen as an objective function over mean absolute percentage error (MAPE) in order to penalise larger errors, whilst allowing small errors to continue over larger number of points.

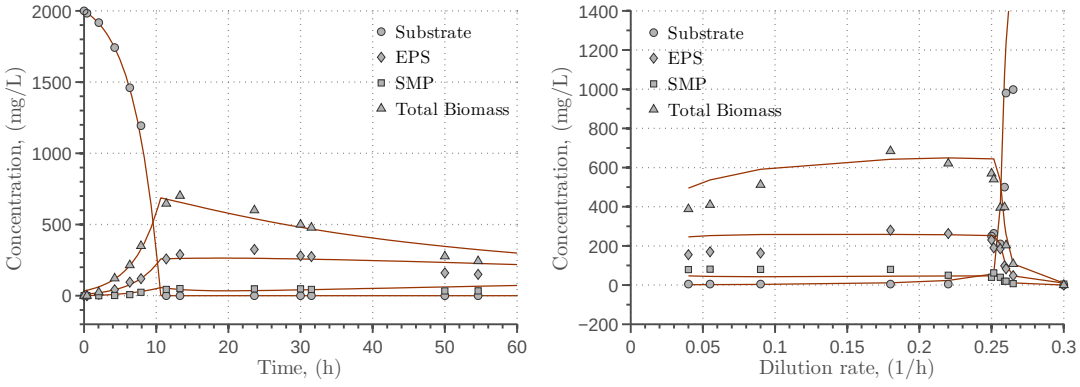

(a) (b)

Figure 4.3: Results of CES-ASM1 calibration on the batch reactor data (a) and continuous flow reactor data (b) from Hsieh et al. [102; 101].

Figures 4.3 and 4.4 show good qualities of fit for both mathematical models with small differences between CES-ASM1 and CES-ASM3 resulting from different growth

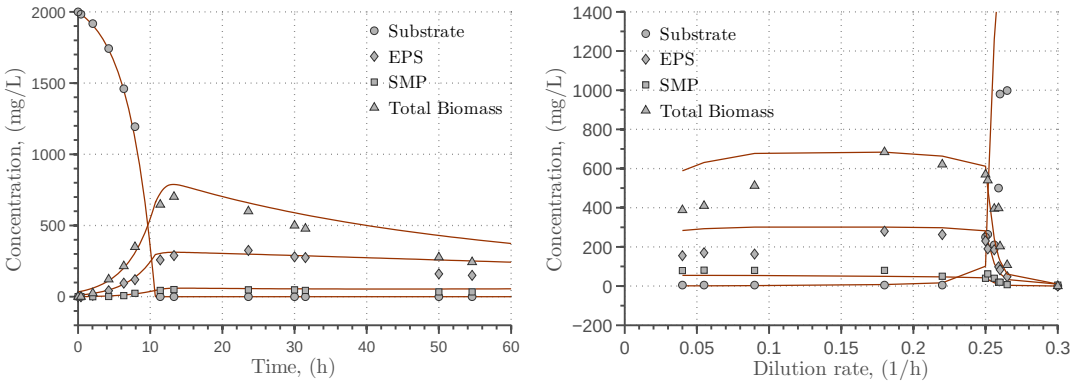

(a) (b)

Figure 4.4: Results of CES-ASM3 calibration on the batch reactor data (a) and continuous flow reactor data (b) from Hsieh et al. [102; 101].

and decay formulations in the underlying models. As already described in Section 3.2.3 the death regeneration concept in ASM1 has been replaced in ASM3 with endogenous respiration, resulting in a very different description of bacterial decay. This altered the flow of organic substrates, affected the substrate utilisation kinetics and necessitated slightly different mathematical formulations of SMP and EPS kinetic equations in both models.

Since CES-ASM1 and CES-ASM3 attempt to describe many different SMP and EPS metabolic pathways as identified by various researchers, the models add quite a bit of complexity to the already complicated and over-parametrised ASM1 and ASM3 models. A rather significant number of parameters and equations are introduced to describe different SMP and EPS production mechanisms. Whilst some of these parameters vary with the type of wastewater and operating conditions and also significantly influence the model outputs, thus need to be easily identifiable, the other might either be universal for a wide range of influents and processes or may not significantly affect the model outputs. In the latter case it is not required that these parameters are identified in every simulation project and, as it is a common practice in activated sludge modelling, are usually left at their default values. Nevertheless, for the purpose of defining default parameter sets for both activated sludge models, all new parameters need to be identified somehow. Numerous simulations with different sets of parameters showed that SMP, EPS, substrate and biomass concentrations data provided by Hsieh et al. [101] was not sufficient to identify all new parameters in CES-ASM1 and CES-ASM3. It was observed that it is possible to obtain different combinations of parameters which would lead to the same or very similar SMP and EPS concentration profiles, especially when parameters of the opposing processes such as, e.g. SMP or EPS production and utilisation are considered. Wherever possible, literature values of the stoichiometric and kinetic parameters governing SMP and EPS production were adopted, thus reducing the number of parameters to be identified from the experimental data. Identification of all model parameters would require a large number of separate and appropriately designed batch test experiments. Such experiments were not performed here. For the

time being, a combination of the parameters adopted from the literature and identified on the experimental data of Hsieh et al. [101] are proposed as a default parameter set which can serve as a starting point for various simulations. All these parameters for CES-ASM1 and CES-ASM3 are listed, respectively in Table 4.7 and Table 4.8.

It was difficult to obtain a good model fit for SMP concentrations in both bioreactors. Whilst increasing f_{BAP} (stoichiometric parameter governing BAP production in bacterial lysis) and lowering the heterotrophic growth rate on BAP ($\mu_{BAP,20}$ in CES-ASM1 and $k_{STO,BAP,20}$ in CES-ASM3) allows us to raise effluent SMP concentrations in the continuous flow process up to the required levels, such a combination of parameters causes increased BAP release under starvation conditions and leads to gradual increase of SMP at the end of the cycle in the batch process. Such behaviour is not supported by the experiments where SMP concentrations tend to decay and ultimately achieve a constant final value as the times goes by. Unsure of the accuracy of the measurements and the methodology used, the model was calibrated in such a way as to provide a compromise between the levels of fit between the SMP measurements and model outputs in the continuous flow reactor and the batch reactor. Results of the calibrations are presented in Figure 4.3 for CES-ASM1 and Figure 4.4 for CES-ASM3.

During the fitting process of substrate (S) and biomass (X) curves to the data, three original ASM3 parameters in CES-ASM3: μ_H, k_{STO}, and $b_{H,O2}$ had to be increased and $Y_{H,O2}$ had to be lowered with regards to default ASM3 values. Similarly in CES-ASM1 the maximum heterotrophic growth rate was increased from a default value of 6.0 d^{-1} to 9.35 d^{-1}. Also, the heterotrophic yield parameter Y_H was decreased from 0.67 to 0.34 gCOD g^{-1} COD and the Monod constant K_S was lowered from default 20 to 5 gCOD m^{-3}. These changes were necessary to describe the kinetics of *Pseudomonas atlantica* which differ significantly from the kinetics of a mixed population biocenosis of activated sludge. Additionally, it was assumed that the decay rate under anoxic conditions in CES-ASM3 is, similarly to ASM3, half of the decay rate under aerobic conditions and that the respiration rate of X_{STO} is equal to the respiration rate of X_H. $Y_{H,NO}$ was therefore adjusted along with $Y_{H,O2}$ to obtain the same anoxic to aerobic sludge yield ratio as in the original ASM3 model. Since ASM1 does not differentiate between biomass yields under aerobic and anoxic conditions, this procedure was unnecessary for CES-ASM1. This adjustment was only of a cosmetic relevance as the experiments were performed under completely aerobic conditions and therefore the value of the anoxic yield had absolutely no impact on final calibration results. Both models assume that N fractions in S_{BAP} and X_{EPS} are equal to those of the biomass (i.e. 0.07) and adopt the Monod constants for storage (in CES-ASM3) and utilisation (in CES-ASM1 of S_{BAP} and S_{UAP} from the growth kinetics on SMP as a substrate published by Noguera et al. [185]. CES-ASM3 additionally assumes that storage yields for SMP in CES-ASM3 are equal to the storage yields for S_S, and that production of X_{EPS} by heterotrophic biomass happens during growth and during storage of internal substrates. The same yield coefficient are used for both processes (growth and storage).

All other SMP and EPS kinetic and stoichiometric parameters have been obtained

through parameter estimation as indicated in Tables 4.7 and 4.8.

4.4.2 Calibration on the data set from Yigit et al. [267]

Both mathematical models were additionally calibrated on a second set of experimental data obtained by Yigit et al. [267] in an immersed MBR pilot plant fed with raw domestic sewage and operated at five different MLSS concentrations {4,600; 6,600; 8,600; 10,100 and 12,600 mg L^{-1}}. The purpose of this study was to identify the model parameters in a real wastewater treatment scenario, because the previous calibration was performed on a pure culture of a marine bacterium *Pseudomonas atlantica* which is very likely to exhibit very different kinetics to a mixed-culture biocenosis of activated sludge. *Pseudomonas atlantica* acts as a primary producer of biofilms and secretes relatively large quantities of extracellular products, therefore the kinetic and stoichiometric parameters governing SMP and EPS production characteristic of this bacterial species are probably higher than those of the activated sludge.

The experiment performed by Yigit et al. [267] was accurately replicated in the simulation. First, steady state was attained by executing the simulation for 200 days at the MLSS setpoint of 4,600 mg L^{-1}. The next four MLSS levels in the bioreactor were achieved by setting the biomass wastage rate to zero and allowing the biomass concentration reach another setpoint. The kinetic and stoichiometric parameters selected for calibration were calculated with constrained Nelder-Mead algorithm [178] implemented in a function `fminsearchbnd` running under MATLAB®. Similarly to previous calibration, root mean square percentage error (RMSPE) between the measurements and model predictions was chosen as an objective function for minimisation. The objective function considers both SMP and EPS, i.e. 10 data points. Calibration results for both models are shown in Figure 4.5. Values of the calibrated parameters for CES-ASM1 are listed in Table 4.7, whereas the calibrated parameter values for CES-ASM3 are shown in Table 4.8.

Figure 4.5 shows that measured SMP and EPS concentrations are in a linear relationship with MLSS, whereas the models exhibit a slightly non-linear character despite of eliminating several processes causing the non-linearity by setting the appropriate kinetic parameters to zero - see Tables 4.7 and 4.8. Notwithstanding this slight non-linear characteristics of the model outputs against the linear shape of the data, the models were able to reproduce the EPS concentrations precisely, whereas the SMP predictions were less accurate. Both models predict a smaller increase of the bulk liquid SMP concentration with MLSS than the measurements suggest. All parameters of the underlying ASM1 and ASM3 models were left at their default values except heterotrophic biomass yield (Y_H) in CES-ASM1 and aerobic and anoxic yields in CES-ASM3 which were altered accordingly to the formulae shown in Table 4.7 and Table 4.8. These yields were modified in order to account for extra biomass loss due to SMP and EPS production.

Both models tend to underestimate biomass-associated SMP production whilst possibly overestimating SMP uptake rates by the biomass. A linear relationship between

bulk liquid SMP and EPS concentrations and MLSS means that, in this particular experiment, production of biopolymers is proportional only to the amount of biomass, whereas in CES-ASM1 and CES-ASM3 biopolymer production is proportional to the biomass concentration as well as the biomass growth rate. In order to adjust both models to fit the data, especially with regards to SMP concentrations, the storage constants for S_{UAP} and S_{BAP} in CES-ASM3 (k_{STO}^{BAP} and k_{STO}^{UAP}) were set to zero. The same procedure was carried out in CES-ASM1 for the maximum specific growth rate on BAP ($\mu_{BAP,20}$) and the maximum specific growth rate on UAP ($\mu_{UAP,20}$). In other words it was assumed that BAP and UAP are non-biodegradable.

In a similar fashion to the SMP related parameters, the EPS production constants: f_{EPS}^{H}, f_{EPS}^{A}, and f_{EPS}^{STO} in CES-ASM3 were also set to zero, which means that EPS is no longer a product of substrate utilisation and originates only from biomass decay. In CES-ASM1 the same effect was accomplished by setting $f_{EPS,h}$ and $f_{EPS,a}$ to zero.

Other SMP and EPS kinetic and stoichiometric parameters identified in this calibration task are shown in Table 4.7 for CES-ASM1, whereas for CES-ASM3 these parameters are presented in Table 4.8.

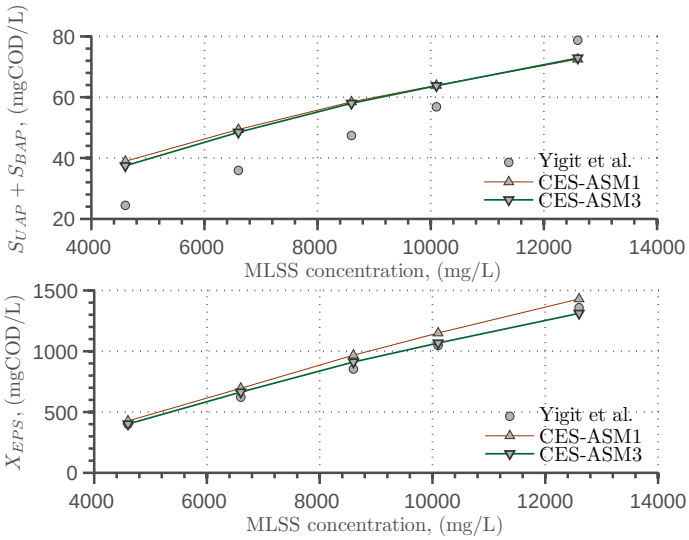

Figure 4.5: Results of CES-ASM1 and CES-ASM3 calibration on the experimental data published in Yigit et al. [267]

4.4.3 Default parameter set for CES-ASM1 and CES-ASM3

For the purpose of undertaking further simulation studies with a complete model of an immersed MBR as described in Chapter 7 and Chapter 8 default parameter sets for each of the two new biological models were established. Default parameters for CES-ASM1 are shown in Table 4.7 whereas the default parameter set for CES-ASM3 is presented in Table 4.8.

All original parameter values in ASM3 were adopted in CES-ASM3 except yield coefficients for heterotrophic biomass which were changed in order to reflect the effects of biopolymer production on biomass growth. S_{UAP} and S_{BAP} storage constants were

assumed to be equal to 0.1 d^{-1} while X_{EPS} hydrolysis constant $k_{h,EPS}$ was set to 0.17 d^{-1} in order to be in accordance with the findings of Laspidou and Rittmann [136]. Similarly to the second calibration study and based on the results of the sensitivity analysis described later in Section 4.7, stoichiometric parameters for SMP and EPS kinetics in the autotrophic biomass were set to zero. The stoichiometric parameters for EPS: $f_{EPS,h}$, $f_{EPS,STO}$, and $f_{EPS,d}$ were assigned values obtained in the first calibration exercise. The values of γ_H and f_{BAP} were carried forward from the second calibration study.

Similarly to CES-ASM3, yield coefficient in CES-ASM1 was adjusted in order to model the effects of biopolymer production in the system. All other ASM1 parameters were left at their default values. $\mu_{UAP,20}$ and $k_{h,EPS,20}$ were chosen after Laspidou and Rittmann [136] while $\mu_{BAP,20}$ was given an assumed value. All but two stoichiometric parameters have been adopted from the results of the second calibration exercise, except f_{BAP} which was adopted from Jiang et al. [115] and $f_{EPS,h}$ which was adopted form Laspidou and Rittmann [136].

Table 4.7: Kinetic and stoichiometric parameters for SMP and EPS kinetics of the CES-ASM1 model identified in two calibration studies and reported in literature.

Parameter	Symbol	Unit	Calibration 1 Value	Calibration 1 Method	Calibration 2 Value	Calibration 2 Method	Data set for simulations	Reported values/range	References
ASM1 parameters									
Max. spec. heterotrophic growth rate	$\mu_{H,20}$	d^{-1}	9.35	Fitted	6	Default	6	Default	[89]
Max. spec. autotrophic growth rate	$\mu_{A,20}$	d^{-1}	0	Assumed	0.8	Default	0.8	Default	[89]
Yield coefficient for heterotrophic biomass	Y_H	$gX_H\ g^{-1}\ S_S$	0.34	Literature *	$0.67/(1+\gamma_H)$	Literature	$0.67/(1+\gamma_H)$	Default	[89]
Half sat. coeff. for S_S in het. growth	K_S	gCOD m^{-3}	5	*****	20	Default	20	Default	[89]
CES-ASM1 kinetic parameters									
Max. spec. heterotrophic growth rate on S_{UAP}	$\mu_{UAP,20}$	d^{-1}	0.57	Fitted	0***	Assumed	0.45	0.45-0.50	[136, 157]
Max. spec. heterotrophic growth rate on S_{BAP}	$\mu_{BAP,20}$	d^{-1}	0.135	Fitted	0.0***	Assumed	0.05		
Maximum X_{EPS} hydrolysis rate	$k_{h,EPS,20}$	d^{-1}	0.14	Fitted	0.055	Fitted	0.17	0.03 (anaerobic) - 0.17	[6, 136]
CES-ASM1 stoichiometric parameters									
Fraction of S_{UAP} produced during heterotrophic growth	γ_H	$gS_{UAP}\ g^{-1}\ X_H$	$0.096\,Y_H$	Fitted	0.092	Fitted	0.092	0.017-0.096	[136, 115]
Fraction of S_{UAP} produced during autotrophic growth	γ_A	$gS_{UAP}\ g^{-1}\ X_A$	$0.096\,Y_A$	Assumed	0**	Assumed	0 **		
Half saturation constant for S_{BAP}	K_{BAP}	$gS_{BAP}\ m^{-3}$	85	Literature	85	Literature	85	30-85-500 (anaerobic)	[157, 185, 6]
Half saturation constant for S_{UAP}	K_{UAP}	$gS_{UAP}\ m^{-3}$	100	Literature	100	Literature	100	30-100-500 (anaerobic)	[157, 185, 6]
Yield coefficient for heterotrophic growth on SMP	Y_{SMP}	$gX_H\ g^{-1}$SMP	0.45	Literature	0.45	Literature	0.45		[136]
Fraction of S_{BAP} produced from biomass decay	f_{BAP}	$gS_{BAP}\ g^{-1}(X_H$ or $X_A)$	0.068	Fitted	0.017	Fitted	0.0215	0.0215	[115]
Fraction of X_{EPS} produced during X_H cell growth	$f_{EPS,h}$	$gX_{EPS}\ g^{-1}\ X_H$	0.35	Fitted	0	Assumed	0.18	0.03 (anaerobic) - 0.18	[6, 136]
Fraction of X_{EPS} produced during X_A cell growth	$f_{EPS,a}$	$gX_{EPS}\ g^{-1}\ X_A$	0.35	Assumed	0	Assumed	0**		
Fraction of X_{EPS} produced from X_H decay	$f_{EPS,dh}$	$gX_{EPS}\ g^{-1}\ X_H$	0.05	Fitted	0.045	Fitted	0.045		
Fraction of X_{EPS} produced from X_A decay	$f_{EPS,da}$	$gX_{EPS}\ g^{-1}\ X_A$	0.05	Assumed	0**	Assumed	0**		
Fraction of S_S produced from X_{EPS} hydrolysis	f_S	$gS_S\ g^{-1}\ X_{EPS}$	0.4	Fitted	0.4	Assumed	0.4		
N content of S_{BAP}	i_{XBAP}	$gN\ g^{-1}\ S_{BAP}$	0.07	Literature	0.07	Literature	0.07	0.07	[115]
N content of X_{EPS}	i_{XEPS}	$gN\ g^{-1}\ X_{EPS}$	0.07****	Literature	0.07	Literature	0.07		

* Laspidou and Rittmann [136].
** EPS and SMP formation kinetic parameters for autotrophic biomass are set to zero as they have been found not to affect SMP and EPS concentrations.
*** UAP and BAP are assumed to be unbiodegradable.
**** N content in EPS is assumed to be the same as in BAP.
***** Reduced from a default value of 20 to 5 in order to eliminate overshoot of substrate profile near a 10 hour mark in the batch stepping experiment (although the choice was subjective and hence the reduced value was not incorporated in the default parameter set)
Parameter fitting was performed manually (parameters adjusted by hand) during the two described calibration exercises. Some of the parameters have been calculated as a function of other parameters which had been fitted, assumed or taken from the literature.

Table 4.8: Kinetic and stoichiometric parameters for SMP and EPS kinetics of the CES-ASM3 model identified in two calibration studies and reported in literature.

Parameter	Symbol	Unit	Calibration 1 Value	Calibration 1 Method	Calibration 2 Value	Calibration 2 Method	Data set for simulations	Reported values/range	References
ASM3 parameters									
Heterotrophic maximum growth rate	μ_H	d^{-1}	12	Fitted	2.0	Literature	2.0	2.0	[79]
Autotrophic maximum growth rate	μ_A	d^{-1}	0	Assumed	1.0	Literature	1.0	1.0	[79]
Storage rate constant	k_{STO}	$gS_S\ g^{-1}\ X_H\ d^{-1}$	30	Fitted	5	Literature	5	5	[79]
Aerobic endogenous respiration rate of X_H	b_{H,O_2}	d^{-1}	0.60	Fitted	0.2	Literature	0.2	0.2-0.74	[79, 102]
Anoxic endogenous respiration rate of X_H	$b_{H,NO}$	d^{-1}	0.30	Assumed	0.1	Literature	0.1	0.1	[79]
Aerobic respiration rate of X_{STO}	b_{STO,O_2}	d^{-1}	0.60	Assumed	0.2	Literature	0.2	0.2	[79]
Anoxic respiration rate of X_{STO}	$b_{STO,NO}$	d^{-1}	0.30	Assumed	0.1	Literature	0.1	0.1	[79]
Aerobic yield of heterotrophic biomass	Y_{H,O_2}	$gX_H\ g^{-1}\ X_{STO}$	0.43	Fitted *	$0.80/(1+\gamma_H)$	Calculated	$0.80/(1+\gamma_H)$	0.63	[79]
Anoxic yield of heterotrophic biomass	$Y_{H,NO}$	$gX_H\ g^{-1}\ X_{STO}$	0.40	Assumed	$0.65/(1+\gamma_H)$	Calculated	$0.65/(1+\gamma_H)$	0.54	[79]
Aerobic yield of stored product per S_S	Y_{STO,O_2}	$gX_{STO}\ g^{-1}\ S_S$	0.80	Literature	$0.80/(1+\gamma_H)$	Calculated	$0.80/(1+\gamma_H)$	0.85	[79]
Anoxic yield of stored product per S_S	$Y_{STO,NO}$	$gX_{STO}\ g^{-1}\ S_S$	0.70	Literature	$0.70/(1+\gamma_H)$	Calculated	$0.70/(1+\gamma_H)$	0.80	[79]
CES-ASM3 kinetic parameters									
S_{BAP} storage rate constant	$k_{STO,BAP}$	$gS_{BAP}\ g^{-1}\ X_H\ d^{-1}$	1	Fitted	0	Fitted	0.1		
S_{UAP} storage rate constant	$k_{STO,UAP}$	$gS_{UAP}\ g^{-1}\ X_H\ d^{-1}$	0.1	Fitted	0	Fitted	0.1		
X_{EPS} hydrolysis rate constant	$k_{H,EPS}$	$gX_{EPS}\ g^{-1}\ X_H\ d^{-1}$	0.4	Fitted	0.055	Fitted	0.17	0.03 (anaerobic) - 0.17	[6, 136]
CES-ASM3 stoichiometric parameters									
Fraction of S_{UAP} produced during heterotrophic cell growth	γ_H	$gS_{UAP}\ g^{-1}\ X_H$	0.04	Fitted **	0.0193	Fitted	0.0193	0.017-0.096	[136, 115]
Fraction of S_{UAP} produced during autotrophic cell growth	γ_A	$gS_{UAP}\ g^{-1}\ X_A$	0.04	Assumed	0	Assumed	0 ***		
Saturation constant for S_{BAP}	K_{BAP}	$gS_{BAP}\ m^{-3}$	85	Literature	85	Literature	85	30-85-500 (anaerobic)	[157, 185, 6]
Saturation constant for S_{UAP}	K_{UAP}	$gS_{UAP}\ m^{-3}$	100	Literature	100	Literature	100	30-100-500 (anaerobic)	[157, 185, 6]
Aerobic yield of stored product per S_{BAP} and S_{UAP} (SMP)	$Y^{O_2}_{STO,SMP}$	$gX_{STO}\ g^{-1}$SMP	0.80	Assumed	0.80	Assumed	0.80		
Anoxic yield of stored product per S_{BAP} and S_{UAP} (SMP)	$Y^{NO}_{STO,SMP}$	$gX_{STO}\ g^{-1}$SMP	0.70	Assumed	0.70	Assumed	0.70		
Fraction of S_{BAP} produced during cell lysis	f_{BAP}	$gS_{BAP}\ g^{-1}(X_H$ or $X_A)$	0.05	Fitted	0.0215	Literature	0.0215	0.0215	[115]
Fraction of X_{EPS} produced during cell growth of X_H	$f_{EPS,H}$	$gX_{EPS}\ g^{-1}\ X_H$	0.12	Fitted	0	Fitted	0.12	0.03 (anaerobic) - 0.18	[6, 136]
Fraction of X_{EPS} produced during cell growth of X_A	$f_{EPS,A}$	$gX_{EPS}\ g^{-1}\ X_A$	0.12	Assumed	0	Assumed	0 ***		
Fraction of X_{EPS} produced during storage of internal substrates	$f_{EPS,STO}$	$gX_{EPS}\ g^{-1}\ X_H$	0.12	Assumed	0	Fitted	0.12		
Fraction of X_{EPS} produced during cell decay of X_H	$f_{EPS,dh}$	$gX_{EPS}\ g^{-1}\ X_H$	0.05	Fitted	0.175	Fitted	0.05		
Fraction of X_{EPS} produced during cell decay of X_A	$f_{EPS,da}$	$gX_{EPS}\ g^{-1}\ X_A$	0.05	Assumed	0.175	Assumed	0 ***		
Fraction of S_S produced during X_{EPS} hydrolysis	f_S	$gS_S\ g^{-1}\ X_{EPS}$	0.4	Fitted	0.4	Assumed	0.4		
N content of S_{BAP}	$i_{NS_{BAP}}$	$gN\ g^{-1}\ S_{BAP}$	0.07	Literature	0.07	Literature	0.07	0.07	[115]
N content of X_{EPS}	i_{NXEPS}	$gN\ g^{-1}\ X_{EPS}$	0.07	Literature	0.07	Literature	0.07		

* Biomass net yield: $Y_{H,O2} \cdot Y_{STO,O2} = 0.43 \cdot 0.85 = 0.37$. Laspidou and Rittmann [136] - 0.34.
** $\gamma_H/(Y_{H,O2} \cdot Y_{STO,O2} = 0.04/0.43 = 0.093$
*** EPS and SMP formation kinetic parameters for autotrophic biomass are set to zero as they have been found not to affect SMP and EPS concentrations. Parameter fitting was performed manually (parameters adjusted by hand) during the two described calibration exercises. Some of the parameters have been calculated as a function of other parameters which had been fitted, assumed or taken from the literature.

4.5 Final simulation results

CES-ASM1 and CES-ASM3 were simulated with default parameters on a treatment plant layout shown in Figure 4.6 in which separation membrane is substituted with an ideal clarifier. The model is simulated at different operating conditions in order to investigate SMP and EPS production under different DO setpoints, MLSS setpoints, SRTs, and temperatures. The results are recorded once the model has been simulated for a sufficiently long amount of time required to reach steady-state in the system. Ranges of variability of the operational parameters are as follows: DO: 0.5–6.0 mgO_2/L, SRT: 12–250 d, MLSS: 3,000–30,000 mg/L, and temperature: 8–26 ^oC. DO concentrations in the system are maintained by a proportional integral (PI) controller which manipulates the amount of airflow provided to the tank. MLSS setpoints are maintained by a second PI controller which adjusts the sludge wastage rate q_{was}. Different SRTs are obtained in the system for a given MLSS by changing the influent organic load and hence, the food to mass ratio (F:M).

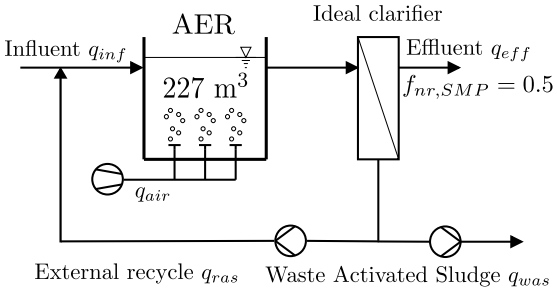

Figure 4.6: Plant layout used in final simulations with CES-ASM1 and CES-ASM3 models.

The simulation results with CES-ASM1 and CES-ASM3 biological models are compared against the model outputs of Jiang et al. [115] as shown in Figure 4.7 and Figure 4.8. SMP concentrations produced by CES-ASM1 and CES-ASM3 are higher from those predicted by the Jiang model. These differences are due to different default parameter combinations used in all three models.

SMP in all models increases with MLSS and decreases with SRT. The first relation is supported by the experimental results of Yigit et al. [267] who showed a linear upward relationship between the bulk liquid SMP concentration and MLSS. If we agree with the wide-spread and well supported hypothesis that SMP is one of the major foulants in MBR system then the second relationship is presumably correct as most of the authors claim that fouling propensity decreases with increasing SRT [44].

Jiang model tends to predict an increase in SMP concentration with temperature whereas in CES-ASM1 and CES-ASM3 this trend is slightly negative, i.e. a decrease in SMP with increasing temperature is observed. The relationship between SMP concentration and temperature in CES-ASM1 and CES-ASM3 is however weaker than in the Jiang's model. The observations presented in Drews et al. [47], Huang et al. [103] tend to at least qualitatively agree with the results obtained from CES-ASM1 and CES-ASM3.

Higher ambient temperatures lead to higher bacterial metabolism and thus higher SMP elimination rates. Temperature effects on SMP have been found to be higher during temperature transients than under steady-state conditions [47]. As already mentioned, the simulations described here were performed under steady state conditions, thus the relationship between SMP concentration and temperature is weak.

The models also differ in terms of predictions of SMP concentrations vs. DO. CES-ASM1 and CES-ASM3 show increased SMP production under higher DO concentrations whereas the Jiang model predicts a slight decrease. It was reported in some literature that higher DO concentrations lead to lower eliminations of SMP in MBR systems [47], but at the same time the results of other experimental studies show that mixed liquor SMP concentrations increase with DO, [100]. It is generally accepted that higher DO concentrations lead to reduced amounts of fouling but these effects can be attributed as well to better sludge filterability which depends not only on the SMP concentrations but can also be related to floc size distribution and floc shape.

CES-ASM1 and CES-ASM3 predict that EPS concentrations increase with MLSS, although the content of EPS in sludge decreases, just as observed in Yigit et al. [267]. EPS was also found to be in negative proportion to SRT and temperature. For intermediate sludge ages, EPS was found to be unrelated to SRT, [150], however the Author is of an opinion that EPS concentrations will decrease for systems with older sludges where endogenous respiration plays a bigger role in the system, [80, 150]. Relationship between EPS concentrations and temperature is controlled by the EPS hydrolysis temperature dependency coefficient which has been initially set equal to the temperature dependency coefficient for hydrolysis of X_S. Due to lack of good quality literature data which could determine the exact character of the relationship between EPS and temperature, these two coefficients have been set to an equal value of $\theta = 1.0408$. A slight increase in the concentration of EPS with DO can be observed in the model but this relationship is much weaker than for SMP.

Generally, SMP and EPS are produced in the system during metabolic activity of the microorganisms and in lysis while being taken up by heterotrophic microorganisms together with other organic substrates. Depending on the choice of kinetic and stoichiometric parameters for each of these processes the model will be able to show different trends in SMP and EPS versus MLSS, SRT, DO, and temperature. Additionally, the results will be different at steady state and under transient dynamic conditions. Comparisons of SMP and EPS concentrations vs. SRT may be ambiguous because SRT can be attained in the system either by changing the sludge inventory or influent load. In the first case, SRT correlates with the amount of solids in the tank. Thus, the total amount of organics in the system increases and so does the amount of EPS and usually SMP. In the second case, the amount of solids remains the same or decreasse slightly while the amount of organics coming with the influent decreases. Thus, the total amount of organic substrates in the system is reduced while the biomass growth-associated SMP and EPS decreases.

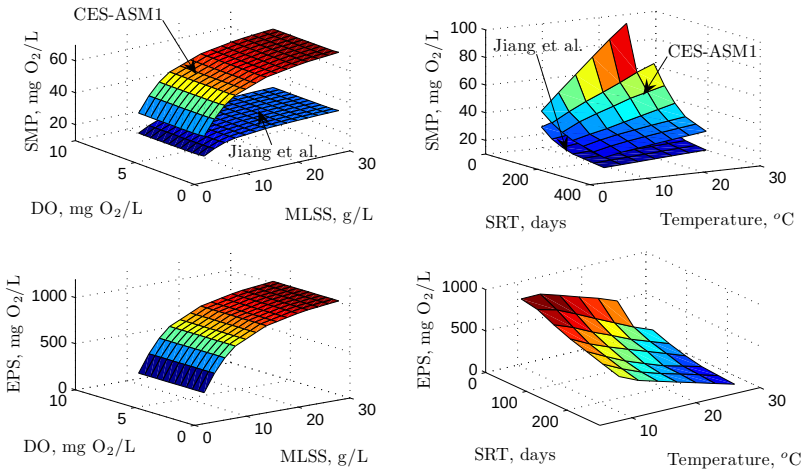

Figure 4.7: CES-ASM1 predictions of SMP and EPS at different DO, MLSS, SRT, and temperature setpoints.

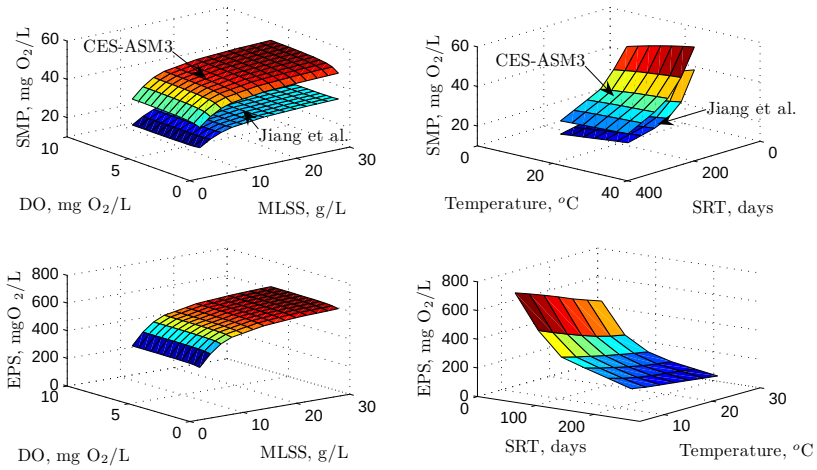

Figure 4.8: CES-ASM3 predictions of SMP and EPS at different DO, MLSS, SRT, and temperature setpoints.

4.6 Steady-state simulation results

The model layout previously used for comparison of all biopolymer ASM models as described in Section 3.7 of Chapter 3 is used to analyse the steady-state outputs ($\mathbf{x}$), their derivatives ($\dot{\mathbf{x}}$), and process rates ($\mathbf{r}$) of CES-ASM1 and CES-ASM3 at different operating points which are defined as combinations of MLSS, DO, temperature and HRT - see Section 3.7 for more details. The plant layout is shown in Figure 3.3 on page 73. Additionally, the eigenvalues of both models were calculated at selected operating points.

4.6.1 Eigenvalues

A wastewater treatment plant (WWTP) can be described with the following system of differential equations:

$$\dot{\mathbf{x}} = f\left(\mathbf{x}, \mathbf{u}, \mathbf{p}, t\right) \tag{4.10}$$

where $\mathbf{x}$ denotes the vector of state variables, $\mathbf{u}$ denotes the vector of inputs and $\mathbf{p}$ is the vector of model parameters. State variables in a single CSTR follow the following differential equation:

$$\dot{\mathbf{x}} = \frac{q}{V}\left(\mathbf{x}_{inf} - \mathbf{x}\right) + {\mathbf{A}_p}^T \mathbf{r} \tag{4.11}$$

where q denotes the influent rate, V is the reactor volume, $\mathbf{x}_{inf}$ denotes the vector of state variables in the influent stream, $\mathbf{r} = f\left(\mathbf{x}, \mathbf{p}\right)$ denotes the vector of reaction rates, where $\mathbf{r}$ is a vector of process rates, and $\mathbf{A}_p$ is a time-invariant Petersen matrix. The above equation can be expanded into the following form:

$$\dot{\mathbf{x}} = {\mathbf{A}_p}^T \mathbf{r} - \frac{q}{V}\,\mathbf{x} + \frac{q}{V}\,\mathbf{x}_{inf} \tag{4.12}$$

where $\dot{\mathbf{x}}$ is in a linear relationship with the inputs $\mathbf{x}_{inf}$ and in a non-linear function $f(\mathbf{x}, \mathbf{p}, t)$ with respect to $\mathbf{x}$ due to the nonlinearity of $\mathbf{r}$ with respect to $\mathbf{x}$. Once Equation 4.12 is analytically linearised it takes the following form:

$$\dot{\mathbf{x}} = \mathbf{A}\,\mathbf{x} + B\,\mathbf{x}_{inf} \tag{4.13}$$

where $B = \dfrac{q}{V}$. Matrix $\mathbf{A}$ is obtained through Taylor expansion around the equilibrium point $\mathbf{x}_{eq}$.

$$\mathbf{A} = {\mathbf{A}_p}^T \left.\frac{\partial \mathbf{r}}{\partial \mathbf{x}}\right|_{\mathbf{x}=\mathbf{x}_{eq}} - \frac{q}{V}\,\mathbf{I} \tag{4.14}$$

Matrix $\mathbf{A}$ is calculated for each operating point at an equilibrium point with Equation 4.14. The eigenvalues λ of each $\mathbf{A}$ matrix are then determined with the MATLAB function `eig` such that Equation 4.15 is satisfied.

$$\det\left(\lambda\,\mathbf{I} - \mathbf{A}\right) = 0 \tag{4.15}$$

Eigenvalues of CES-ASM1 and CES-ASM3 for the selected operating points are displayed respectively in Figure 4.9 and Figure 4.10.

All eigenvalues of the system are real and negative indicating stable equilibria at all operating points. The eigenvalues range between $\sim 10^{-4} - 10^{4}$ d^{-1} showing a large span of time constant between ($\sim 1\,\mathrm{min}$) – ($\sim 2.5\,\mathrm{years}$). Both models have zero eigenvalues (albeit not shown in Figure 4.9 and Figure 4.10) corresponding to a pure integration term in the transfer function and referring in this application to heterotrophic and autotrophic growth processes.

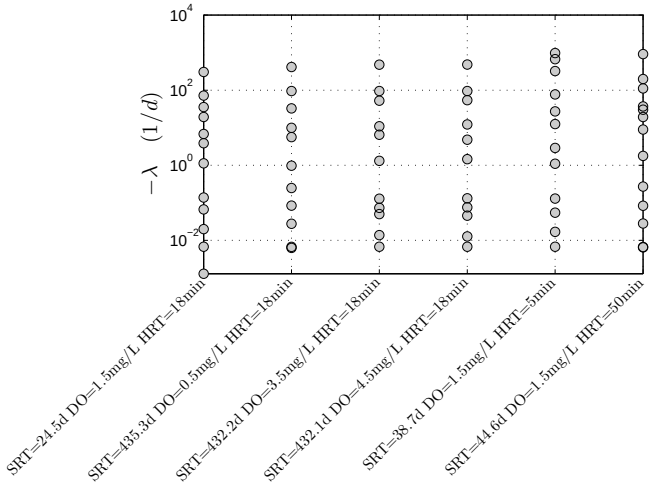

Figure 4.9: Eigenvalues of CES-ASM1 for six selected operating conditions.

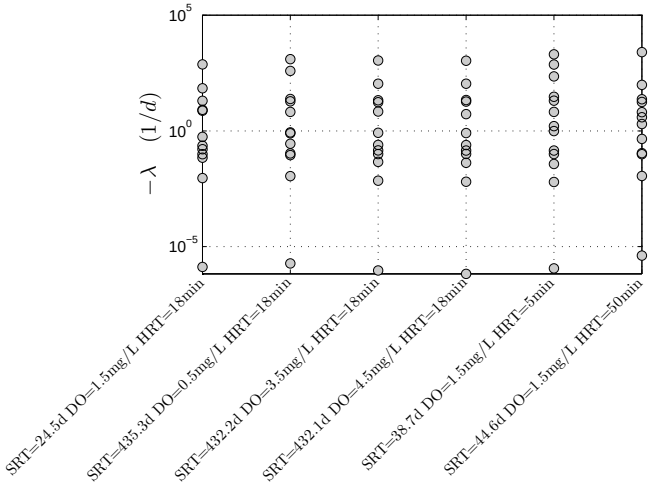

Figure 4.10: Eigenvalues of CES-ASM3 for six selected operating conditions.

4.6.2 Self organisizng map (SOM) projections

Sensitivity studies of ASM models which, as we know, contain large number of equations with many state variables and parameters, generate large amounts of multidimensional data which are hard to data-mine and visualise. In order to find correlations between either various process variables and model outputs or between outputs and model parameters we need to, first, develop an understanding of the data using various data-mining and visualisation methods, then extract the relevant information and, subsequently, present it in various formats of choice. Whilst the above steps can be realised using many different methods, the approach that the author adopted in this study is to use self organising maps (SOMs) [125]. Self organising maps are a type of artificial neural networks (ANNs) which are trained using unsupervised learning, i.e. they look for hidden structures present in the input data. The outcome of this learning process is a projection of a multidimensional input data onto a discretised, low-dimensional, usually two-dimensional (2D) space, called a *map*. This mapping of multidimensional space onto a lower dimensional space facilitates dimensionality reduction in a similar

fashion to singular value decomposition of a data matrix or an eigenvalue decomposition of a data covariance matrix as applied in principal component analysis (PCA) whilst preserving the topology, i.e. relative distances between the data points.

During the, so-called, *batch learning*, each of the M nodes (or neurons) in the map are initially assigned random weight vectors $\mathbf{w}_i$ where $i = 1 \dots M$. Each weight vector $\mathbf{w}_i = [w_{i,1}, w_{i,2}, \dots, w_{i,d}]^T$ is d-dimensional, where d is also the dimension of every input vector $\mathbf{x}$. In other words, the element with index i in the weight vector $\mathbf{w}$ corresponds to the element with the same index i in the input vector $\mathbf{x}$. The input data are first normalised to a zero mean value and a variance $\sigma^2 = 1$ thus allowing all considered inputs and outputs to fall within the same range of variability and therefore are implicitly assigned the same weights during the training process. The map in each time epoch is sequentially fed with N input vectors $\mathbf{x}_k$ where $k = 1 \dots N$. For each input vector $\mathbf{x}_k$, the learning algorithm calculates the, usually Euclidean, distance between the weight vector of each node and that input vector. The best matching unit (BMU) denoted as c is selected as the node which is closest to the input vector: $d(\mathbf{x}, \mathbf{w}_c) = \min_i \|\mathbf{x} - \mathbf{w}_i\|$. The algorithm then saves the position of the BMU in the map as well as the values of the so-called neighbourhood function values for all nodes in the map $h_{c(\mathbf{x}_k)i}$. This neighbourhood function determines how close the node is to BMU and therefore how much its weight vector will be adjusted during the learning process. The winning nodes are adjusted the most and the nodes next to this node are 'pulled' along while the nodes further away are affected to a smaller degree. Once all N input vectors have been fed into the map, all weight vector of all nodes are adjusted using the following formula:

$$\mathbf{w}_i = \frac{\sum_{k=1}^{N} \mathbf{x}_k h_{c(\mathbf{x}_k)i}}{\sum_{k=1}^{N} h_{c(\mathbf{x}_k)i}} \tag{4.16}$$

Then the process is iteratively repeated until a STOP criterion is reached. Although the learning algorithms may be assigned different STOP criteria and the neighbourhood function $h_{c(\mathbf{x}_k)i}$ may be calculated with different algorithms, the general method of *batch learning* of a SOM remains as explained above.

During this learning process, the nodes which best match certain input patterns are pulled towards these input data points whereas the nodes which match other input patterns are pulled towards those other inputs. After the learning has been completed, we are given a two-dimensional projection of a N dimensional data which is then easy to analyse for the presence of clusters and correlations.

Correlations between different elements of the input vectors, i.e. different input variables, are visualised using the, so called, component planes. These component planes represent the weights in all nodes associated with one given input variable. In other words, each component plane represents activation of all nodes in the map to one input variable. The correlations between different input variables are assessed by looking at activation of the same nodes across two (or more) component planes. High activation of

the same nodes in both component planes indicate positive correlation whereas if high activation of the nodes in one component plane is associated with low activation of the same nodes in the second component plane, this indicates a negative correlation. The degree of correlation can be judged by the similarity of the node patterns in different component planes, however a clearer visual understanding of the relationships between different variables can only be gained through analysis of the correlation plots.

SOM calculations presented in this study were carried out using the SOM Toolbox for Matlab 5 developed by Juha Vesanto, Johan Himberg, Esa Alhoniemi, and Juha Parhankangas. Introduction to this SOM toolbox can be found in Vesanto et al. [243].

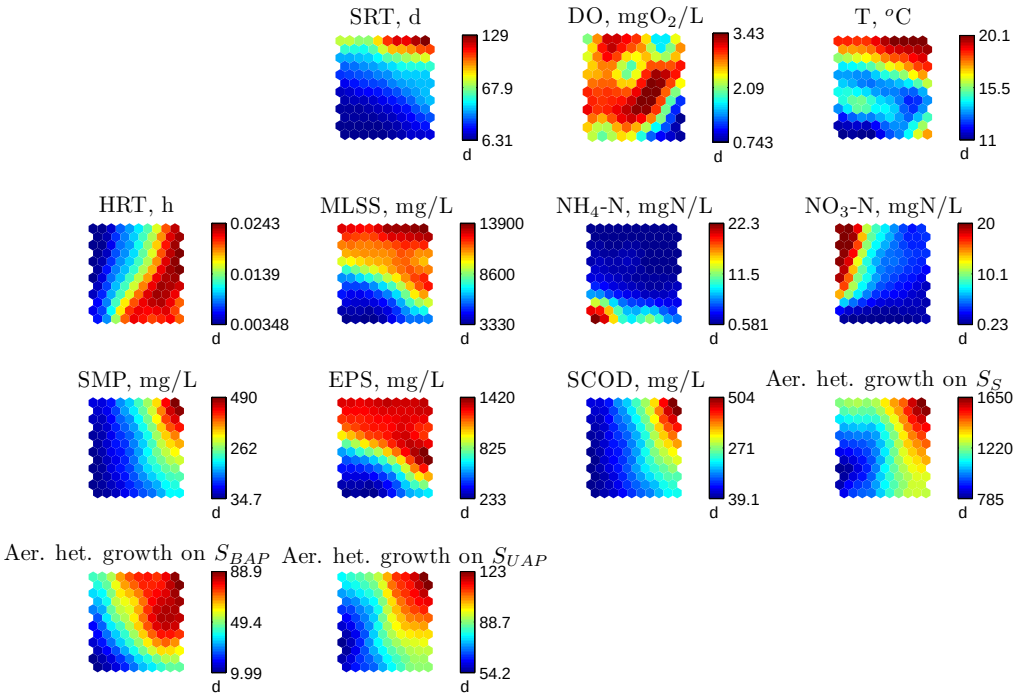

Figure 4.11: Component planes of the self organising map (SOM) trained on the inputs and outputs of the CES-ASM1 model - 1 out of 3.

Looking at the component planes of SOM trained on the outputs (state variables, derivatives of the state variables and process rates) of CES-ASM1, the following observations about SMP and EPS kinetics and the slow hydrolysis kinetics can be made:

1. SMP correlate with soluble chemical oxygen demand (SCOD), which means that the majority of SCOD in the system is composed of SMP,
2. EPS are associated with MLSS,
3. Highest rate of EPS production occurs under highest HRTs,
4. SMP coincide with aerobic heterotrophic growth rate on S_S, which means that SMP in the system is mostly related to biomass growth, not biomass decay,
5. Hydrolysis of X_{EPS}, X_I, and X_P depend more strongly on the SRT, and less strongly on MLSS, which suggests that the rates of these processes depend on the

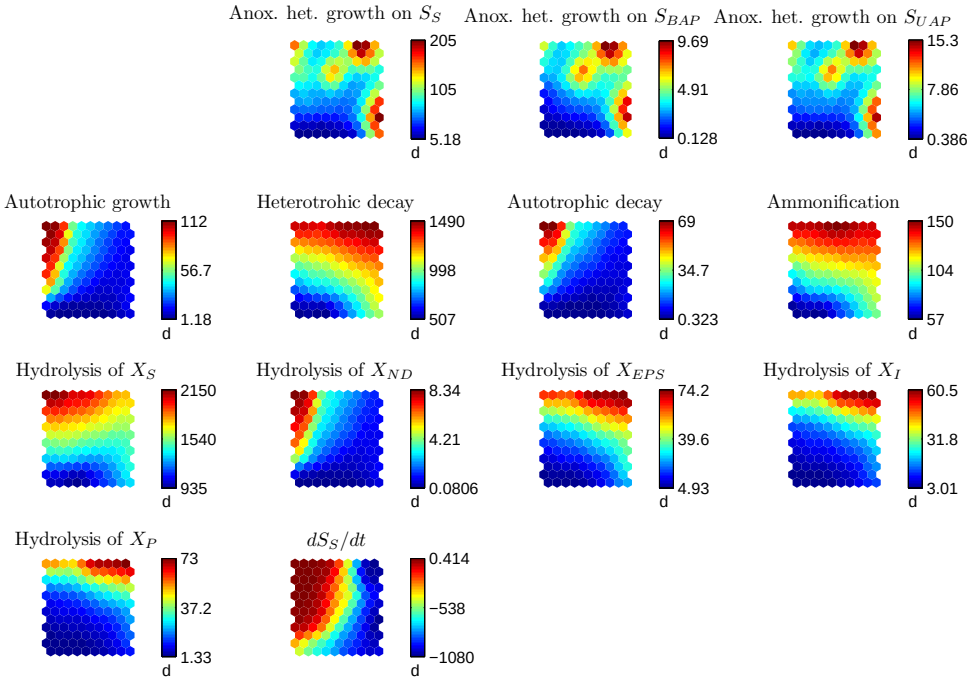

Figure 4.12: Component planes of the self organising map (SOM) trained on the inputs and outputs of the CES-ASM1 model - 2 out of 3.

age of the sludge, not on its mass. As the sludge gets older, hydrolysis of these substrates begins to dominate in the system,

6. Hydrolysis of EPS does not correlate well with the EPS concentration because EPS concentrations are governed by both EPS hydrolysis to BAP and biomass growth associated EPS release. None of these processes dominates over the other.

Similar findings are found by analysing the component planes of the SOM network trained on CES-ASM3 model outputs.

1. SMP correlate with SCOD,
2. EPS concentrations are proportional to MLSS,
3. $\frac{dX_{EPS}}{dt} \sim \frac{dX_H}{dt}$ which means that the majority of EPS production in the system is growth related,
4. SMP concentrations attain highest values at highest SRTs which coincide with the highest MLSS and temperature levels,
5. X_{EPS} and X_I hydrolysis coincide both with high MLSS levels as well as high SRTs.

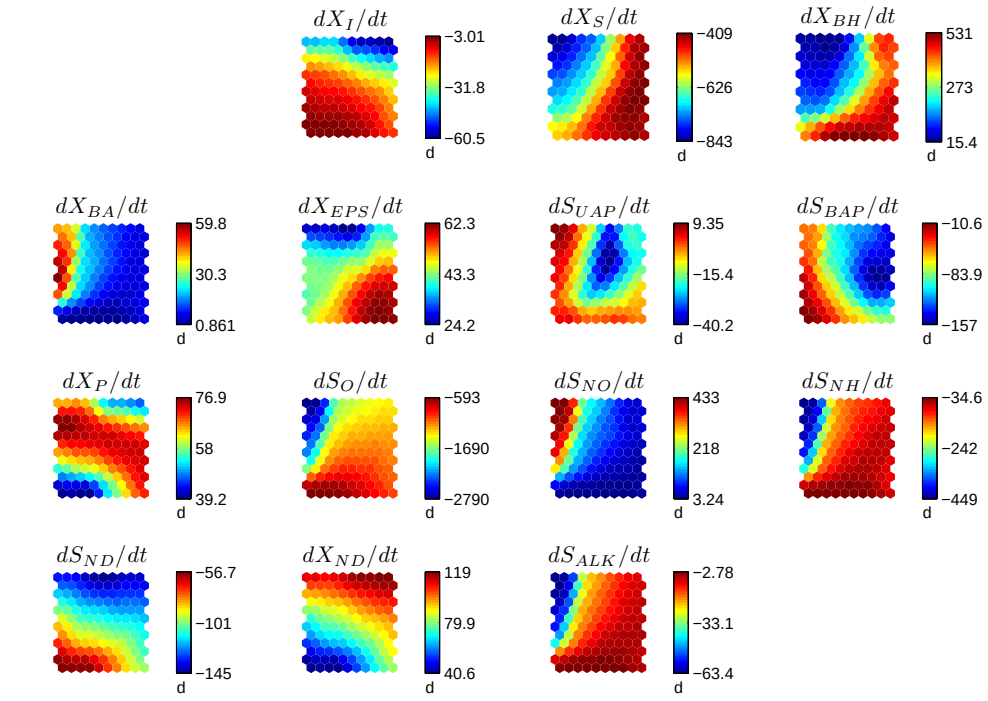

Figure 4.13: Component planes of the self organising map (SOM) trained on the inputs and outputs of the CES-ASM1 model - 3 out of 3.

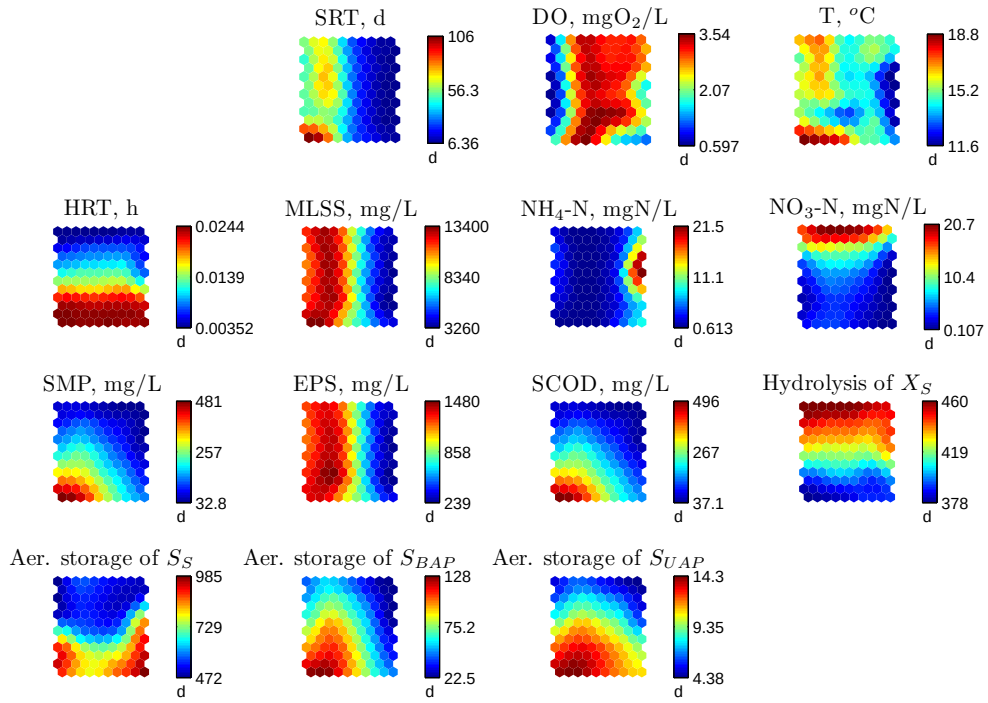

Figure 4.14: Component planes of the self organising map (SOM) trained on the inputs and outputs of the CES-ASM3 model - 1 out of 3.

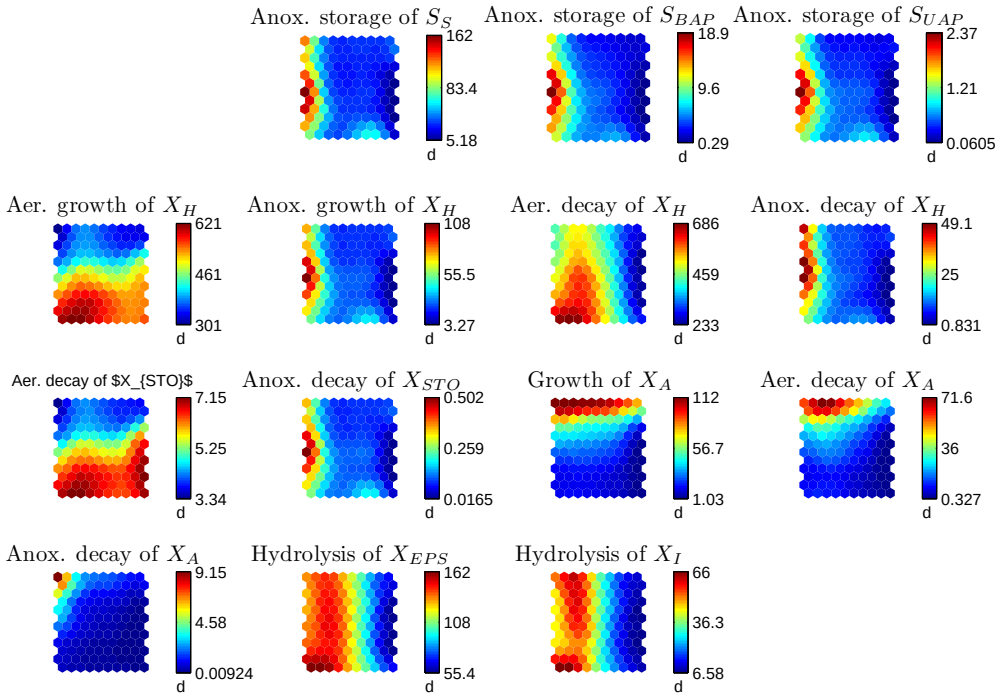

Figure 4.15: Component planes of the self organising map (SOM) trained on the inputs and outputs of the CES-ASM3 model - 2 out of 3.

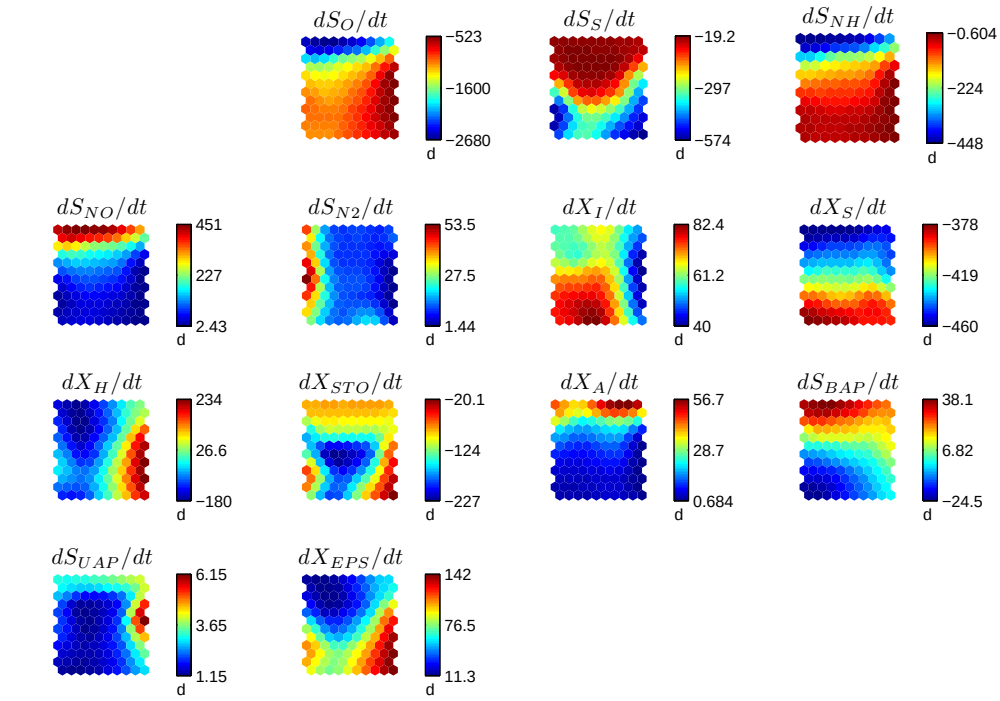

Figure 4.16: Component planes of the self organising map (SOM) trained on the inputs and outputs of the CES-ASM3 model - 3 out of 3.

4.7 Sensitivity analysis

Sensitivity analysis offers an additional source of information about the mathematical model through quantification of the dependence of model outputs $\mathbf{y}$ or model states $\mathbf{x}$ on model parameters $\mathbf{p}$. The study of sensitivity helps to identify those parameters which have the most influence on the model outputs and capture the essential characteristics of the system. Information about sensitivity coefficients δ, which are defined as partial derivatives of the model states with respect to model parameters $\delta_{i,j} = \frac{\partial x_i}{\partial p_j}$, where x_i denotes the i-th state and p_j denotes the j-th parameter, may be used for various purposes such as the ones defined below:

1. Selection of most sensitive parameters for model calibration,
2. Evaluation of model uncertainty in any variable according to the linear error propagation formula, [206],
3. Model discrimination and reduction,
4. Evaluation of model identifiability through analysis of the correlations between parameters,

In this study we are particularly interested in 1 and 4 although, as shall be shown later in this section, findings of this sensitivity study may also be used for further model analysis and perhaps even model reduction. As ASM models are generally over-parametrised, it is necessary to select just a few most-sensitive parameters for calibration whilst other, less-sensitive parameters are usually left at their default values. Establishing correlations between parameters is important for the assessment of the model's structural identifiability which manifests itself when each set of parameter values yields unique output trajectories. If two or more parameters in the model are correlated, the model will not be structurally identifiable as it will be possible to obtain multiple combinations of parameters which produce the same output trajectories. Although identifiability analysis is not performed in this study, results of the sensitivity analysis studies described in this Section form a preliminary step for such analysis and can identify possible identifiability issues in the model.

Sensitivity analysis presented in this section is linked and complement model calibration described earlier in Section 4.4. Although sensitivity of both models to model parameters is presented and analysed in this thesis after model calibration, these two studies were in fact carried out in parallel. First, behaviour of the model was analysed through observation of model outputs in response to manual changes in model parameters, i.e. manual sensitivity analysis. The model parameters identified as 'most sensitive' were then adjusted manually in order to obtain reasonable quality of fit between the measurements and the model outputs. Subsequently, dynamic sensitivity analysis was carried out in order to identify the most sensitive parameters and how their sensitivities change throughout the calibration experiment. Information gained from the dynamic sensitivity study was then used to identify the subset of parameters and create an appropriate objective function used in an automatic optimisation-based

model identification. The sensitivity study presented here was carried out after completion of the calibration study, i.e. on the model with identified parameters in order to provide the reader with more information on the sensitivity of model parameters. This information can be used to further assess the model structure, help with further calibrations and development of similar models.

Sensitivity analysis can be classified into two main categories: (1) *local sensitivity* which provides information on the effects of small changes in each parameter individually, and (2) *global sensitivity* which describe the effects of simultaneous 'arbitrary' variations of multiple parameters on the model outputs. Additionally, local sensitivity can be performed either under static or dynamic conditions. *Static sensitivity* analyses steady-state model response to the changes in model parameters. *Dynamic sensitivity* investigates variations in the model outputs to parameter changes under dynamic time-varying conditions such as response to step or impulse change in the input(s). In this Section we will investigate static as well as dynamic sensitivities.

Local sensitivity can be expressed in four different forms: (a) Absolute-absolute sensitivity function which quantifies absolute change in model output y per unit of change in the parameter p.

$$\delta_{a,a} = \frac{\partial y}{\partial p} \tag{4.17}$$

(b) Relative-absolute sensitivity function which quantifies the relative change in y per unit of change of p.

$$\delta_{r,a} = \frac{1}{y}\frac{\partial y}{\partial p} \tag{4.18}$$

(c) Absolute-relative sensitivity function quantifying the absolute change in y for a relative change in p

$$\delta_{a,r} = p\frac{\partial y}{\partial p} \tag{4.19}$$

(d) Relative-relative sensitivity function which computes the relative change in y for a relative change in p

$$\delta_{r,r} = \frac{p}{y}\frac{\partial y}{\partial p} \tag{4.20}$$

The derivatives used are usually calculated using first order finite difference scheme:

$$\frac{\partial y}{\partial p_i} \approx \frac{y\left(p_i + \Delta p_i\right) - y\left(p_i\right)}{\Delta p_i} \tag{4.21}$$

where Δp_i is chosen arbitrarily or calculated from a specific formula such as, e.g. Equation 4.24.

Whilst comparison of more than one of the above sensitivity functions, may help to extract more information about the nature of the model and its parameters, the relative-relative sensitivity function quantifies the 'significance' of each model parameter relative to its value hence identifies the most sensitive parameters whilst also providing the information about possible correlations between them. Dynamic relative-relative sensitivity functions for both models (CES-ASM1 and CES-ASM3 are calculated in

Section 4.7.1 below.

4.7.1 Dynamic sensitivity analysis

Dynamic relative-relative sensitivity functions presented here were calculated for CES-ASM1 and CES-ASM3 during final simulations of the batch and continuous flow experiments of Hsieh et al. [101] described in Section 4.4.1. Although, as already noted previously in Section 4.7 they have also been carried out at earlier stages of the calibration study in order to identify the most sensitive model parameters for calibration.

The sensitivity functions were calculated with function `SENS_SYS` written in MATLAB 5.3 by V.M. García Mollá and R. Gómez Padilla. `SENS_SYS` uses an iterative approximation method based on directional derivatives, similar to one described in Maly and Petzold [161]. In practical terms the function `SENS_SYS` is a wrapper function for MATLAB's stiff ordinary differential equation (ODE) solver ODE15s. The principle of the calculation method is outlined below:

For a system of ODE/DAE given in Equation 4.22

$$F(t, y, y', p) = 0 \tag{4.22}$$

sensitivity functions are obtained through differentiation of Equation 4.22 with respect to each parameter. Hence, a second system of ODE/DAE is produced. This new system representing sensitivity is then approximated through a directional derivative finite difference approximation, as described in more detail in Maly and Petzold [161].

$$\frac{F\left(t, y + dp_i\, s_i, y' + dp_i\, s_i', p + dp_i\, e_i\right) - F\left(t, y, y', p\right)}{dp_i} = 0, \quad i = 1, \ldots, n \tag{4.23}$$

where n denotes the number of parameters, dp_i denotes the increment of the i-th varied parameter (p_i), e_i is the i-th unit vector, and $s_i = \dfrac{dy}{dp_i}$ denotes the sensitivity of output y to the i-th parameter (p_i).

The calculated increment for the varied parameter p_i is based on the magnitude of the parameter and the accuracy of the ODE solver used (ε_i).

$$dp_i = \sqrt{\varepsilon_i}\left(|p_i| + 0.1\right) \tag{4.24}$$

The relative-relative sensitivity functions for most sensitive parameters in the batch experiment are shown for CES-ASM1 model in Figure 4.17.

Consumption of readily biodegradable substrates S_S is dominated by maximum heterotrophic growth rate μ_{H20} and, to a lesser degree, heterotrophic yield coefficient Y_H. The third most dominant parameter, which is almost as sensitive as Y_H, is the fraction of EPS produced during heterotrophic biomass growth (f_{epsh}). Since the yield coefficient for the heterotrophic biomass during heterotrophic growth is equal to $1-f_{epsh}$, increasing f_{epsh} leads to lower production of X_H at the cost of EPS which then undergo

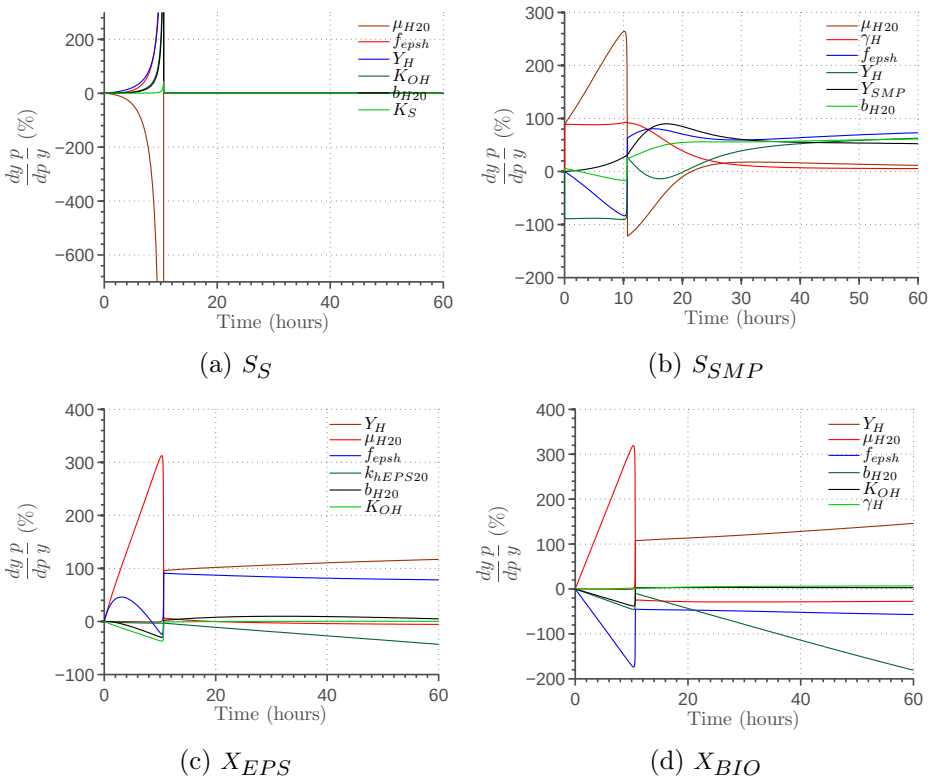

(a) S_S (b) S_{SMP}

(c) X_{EPS} (d) X_{BIO}

Figure 4.17: Dynamic relative-relative sensitivity functions for four model outputs: S_S, S_{SMP}, X_{EPS} and X_{BIO}, and six most sensitive model parameters in CES-ASM1 in the batch experiment of Hsieh et al. [101].

hydrolysis to S_{BAP} and S_S. Hence it is clear that EPS kinetics influence the fate of readily biodegradable organics in the system. After approximately 10 hours the concentration of S_S in the reactor is reduced to zero and thus all sensitivity functions are also zero or very close to zero.

In the course of calibration the half-saturation constant for readily biodegradable substrates (K_S) was reduced from a default value of 20mg COD/L to 5mg COD/L which resulted in a sharp break in the biomass profile in the batch experiment where the concentration of substrate reduces to near zero (see Figure 4.3). Although identification of K_S on this data set is not possible and hence a default value of K_S was used in the final parameter set for CES-ASM1 (see Table 4.7) lower value of K_S was still used in the final simulations and thus also in the dynamic sensitivity study. It seems that the discontinuity in the first derivative of the concentration profiles in Figure 4.3 generates perturbations in the used dynamic sensitivity algorithm. Thus the sensitivity outputs between the time of 10 hours and 25 hours need to be disregarded. This does not impair our analysis as we are still able to evaluate the sensitivities at two distinctly different conditions: under the surplus of organic substrates and in a so-called starvation period.

Under abundance of organic substrates, SMP production is mainly associated with biomass growth. Hence, the most sensitive parameters are on one hand μ_{H20} and on the other hand Y_H. With regards to biopolymer related parameters, sensitivity to γ_H remains approximately constant during an entire exponential growth phase while

sensitivity to $f_{EPS,h}$ increases as more EPS are produced in the system. In the starvation period production of SMP is dominated by three parameters: heterotrophic biomass decay rate (b_{H20}), yield coefficient for heterotrophic growth on SMP (Y_{SMP}) and fraction of EPS produced during cell growth ($f_{EPS,h}$). It is worth pointing out that despite of a complete depletion of readily biodegradable substrates biomass is still at 'some' growth in the starvation period due to biodegradability of SMP. This growth is significant enough that the parameter for decay-related SMP production such as f_{BAP} does not appear as a dominant parameter in the sensitivity plot. Biodegradability of various SMP compounds is not very well known and need to be investigated in the future.

Figure 4.17c shows that X_{EPS} concentration in the growth period is dominated by heterotrophic maximum growth rate (μ_{H20}) hence EPS production is proportional to biomass growth. As more EPS is produced during the growth phase EPS hydrolysis gains some importance although is insignificantly small compared to the heterotrophic growth process and its rate μ_{H20}. As the substrates deplete and biomass growth stops, EPS concentrations begin to depend more on the EPS hydrolysis rate constant $k_{h,EPS,20}$. Nevertheless, EPS are still highly dependent on growth associated parameters Y_H and f_{epsh} due to the death-regeneration concept adopted in the model in which the products of biomass decay or biomass associated products BAP form substrates for biomass growth, hence feeding back into the biomass growth cycle.

Biomass growth in the initial stage of the process under surplus of organic substrates - see Figure 4.17d is dominated by maximum heterotrophic growth rate (μ_{H20}) and fraction of EPS produced in heterotrophic growth ($f_{EPS,h}$). As the biomass grows part of organic substrates is used to produce EPS at the cost of biomass growth, hence the higher the value of $f_{EPS,h}$ the lower the biomass production and hence its concentration. As the substrate depletes and the biomass enters endogenous respiration, X_{BIO} becomes sensitive to $b_{H,20}$, i.e. heterotrophic biomass decay rate, although still remaining sensitive to heterotrophic yield coefficient (Y_H) due to the above mentioned death-regeneration model.

In the continuous flow bioreactor (see Figure 4.18) concentrations of readily biodegradable substrates (S_S) are almost null for low dilution rates and are rather insensitive to any of the model parameters except the maximum heterotrophic growth rate μ_{H20}. As dilution rates become higher and thus, contact time between the liquid phase and the solids phase becomes insufficient for all readily biodegradable substrates to be taken up by the biomass, effluent S_S concentrations increase and so do their sensitivity functions to kinetic and stoichiometric parameters. Similarly to the batch process S_S becomes sensitive under higher dilution rates to μ_{H20} and, albeit to a lesser degree, f_{epsh}.

SMP concentration is most sensitive to the fraction of S_{UAP} produced during heterotrophic growth (γ_H) and its sensitivity increases with dilution rate. However, at low dilution rates SMP is equally sensitive to $f_{EPS,h}$ and b_{H20}, i.e. fraction of EPS produced during biomass growth and heterotrophic decay rate, respectively. This sensitivity decreases significantly with dilution rate. Hence, at low dilution rates SMP is produced from hydrolysis of EPS and from biomass decay, i.e. as biomass associated

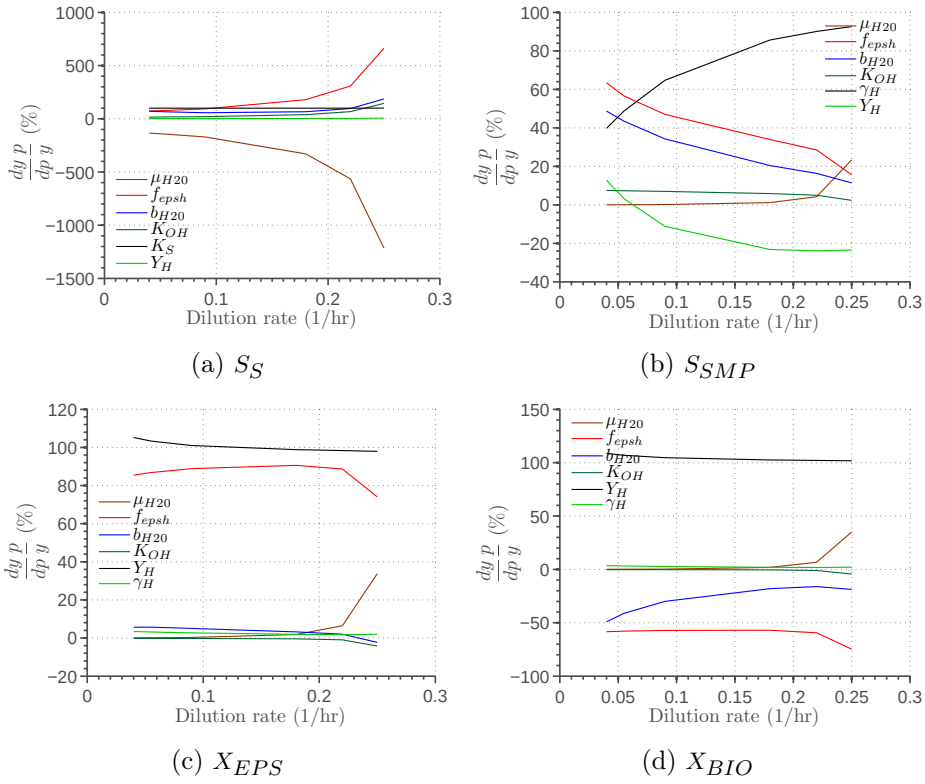

(a) S_S (b) S_{SMP}

(c) X_{EPS} (d) X_{BIO}

Figure 4.18: Dynamic relative-relative sensitivity functions for four model outputs: S_S, S_{SMP}, X_{EPS} and X_{BIO}, and six most sensitive model parameters in CES-ASM1 in the continuous flow experiment of Hsieh et al. [101].

products (BAP), at higher dilution rates SMP production is growth-associated not biomass associated.

X_{EPS} is almost equally sensitive to two parameters for all investigated dilution rates, namely: Y_H, $f_{EPS,h}$, which suggests that X_{EPS} originate from biomass growth, not from biomass maintenance and decay.

Biomass concentration (X_{BIO}) which is equal to X_H since the autotrophic biomass activity has been switched off, is positively related to the heterotrophic biomass yield coefficient (Y_H) across an entire operating region whilst being negatively related to $f_{EPS,h}$ and, to a lesser degree, b_{H20}. An increase in $f_{EPS,h}$ means that more organic substrates are used to generate EPS and less to form biomass, hence negative sensitivity of X_{BIO} to $f_{EPS,h}$. Whilst X_{BIO} is equally sensitive to b_{H20} as to $f_{EPS,h}$ at low dilution rates, this sensitivity decreases in magnitude as dilution rate is increased due to the fact that the reactor is more loaded with organic substrates and biomass decay processes are less prominent.

Dynamic sensitivity profiles for CES-ASM3 are shown in Figure 4.19 for the batch experiment and in Figure 4.20 for the continuous flow experiment.

Concentrations of S_S, S_{SMP}, X_{EPS}, and X_{BIO} in the batch experiment are all sensitive to the temperature dependence coefficient for growth and decay of heterotrophic organisms, storage of organic substrates, and hydrolysis (θ_2). From the model struc-

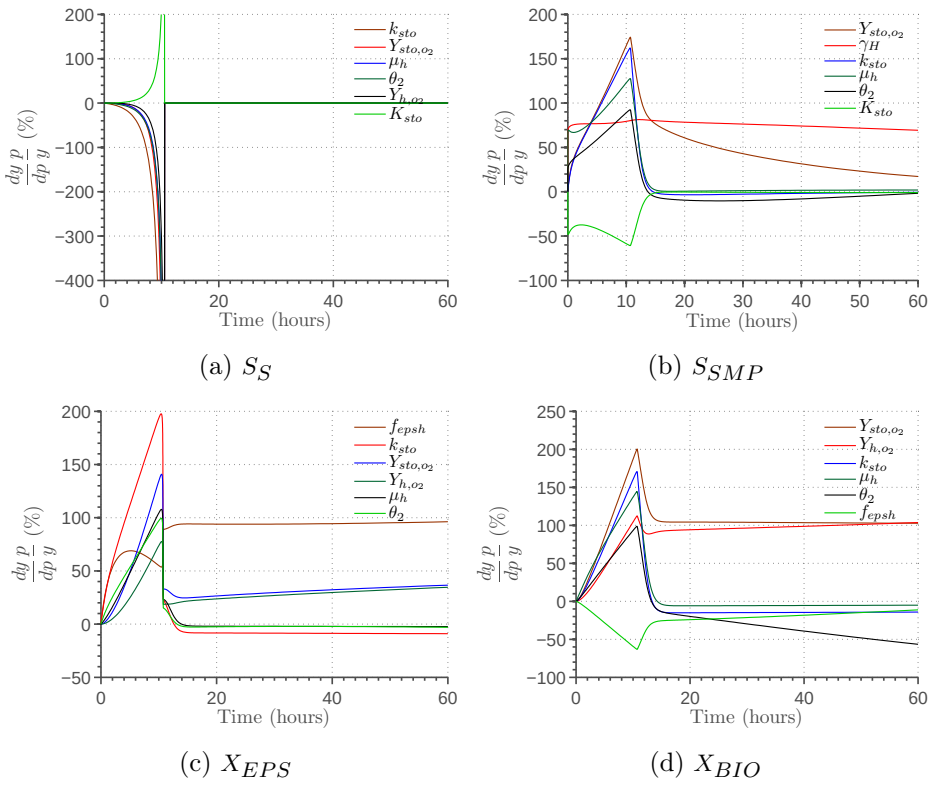

(a) S_S (b) S_{SMP}

(c) X_{EPS} (d) X_{BIO}

Figure 4.19: Dynamic relative-relative sensitivity functions for four model outputs: S_S, S_{SMP}, X_{EPS} and X_{BIO}, and six most sensitive model parameters in CES-ASM3 in the batch experiment of Hsieh et al. [101].

ture it can be inferred that this dependence will increase as the operating temperature diverges from the standard temperature of 20°C. In this experiment, the temperature was set at 25°C. It also becomes clear during a visual inspection of the plots that the ASM3-based model has more equally sensitive parameters and more correlated parameters than the ASM1-based model analysed previously. Moreover, the correlations exist between the base ASM3 model parameters not between the added biopolymer-related parameters, hence we may draw a preliminary conclusion that whilst ASM3 improves modelling of the flow of organic substrates through substitution of ASM1's death-regeneration concept with cell lysis and introduction of intermediate substrate storage, this comes at the cost of impaired parameters identifiability. Some authors postulate that bacteria simultaneously utilise and store organic substrates hence neither the ASM1's direct utilisation concept nor the ASM3 storage concept is entirely appropriate. Based on these findings modifications of ASM3 with simultaneous substrate utilisation and storage have been developed [217, 238]. It is however feared that introduction of two parallel substrate 'sink' processes will further impair the model's parameter identifiability. Although it is too early to give definite recommendations, it is felt that perhaps a ASM1-based biopolymer model is a better choice for initial studies on MBR system modelling and simulation due to less-complicated representation of the flow of organic substrates, hence better and simpler parameter identifiability.

In addition to θ_2, S_S in the batch experiment is almost equally sensitive, in the

initial growth period, to a large number of other parameters: Monod constant for storage of organic substrates (K_{STO}), storage rate constant (k_{STO}), heterotrophic maximum growth rate (μ_H), aerobic yield of heterotrophic biomass (Y_{H,O_2}), and aerobic yield of stored product per S_S (Y_{STO,O_2}).

SMP in the batch experiment is sensitive to a number of parameters out of which only one is specifically related to SMP production. In the biomass growth phase SMP is sensitive to Y_{STO,O_2} and k_{STO} which are additionally very highly correlated. SMP is also positively related to the heterotrophic maximum growth rate (μ_H) and the temperature dependency coefficient θ_2 whilst being in negative relationship with the Monod constant for storage of organic substrates (K_{STO}). Whilst sensitivity to all these parameters decrease over time and become almost zero after 20 hours except the sensitivity to Y_{STO,O_2} which decreases more slowly over time, the sensitivity to γ_H, i.e. fraction of UAP produced during heterotrophic cell growth, remains at a constant level of around 75% throughout the experiment in the exponential growth as well as in the cell lysis, decay and maintenance phase.

X_{EPS} sensitivity functions shown in Figure 4.19c indicate that EPS production in the growth phase is most sensitive to the rate of storage of organic substrates (k_{STO}), although several other growth-related parameters have a comparatively equal impact on EPS concentration at this stage of experiment: Y_{STO,O_2}, μ_H, θ_2, Y_{H,O_2}, and $f_{EPS,h}$. Some of these parameters seem to be highly correlated, e.g. k_{STO} and Y_{STO,O_2}, and μ_H with θ_2. In the second phase of the experiment production of EPS in the system is most sensitive to $f_{EPS,h}$, although Y_{STO,O_2} and μ_H still play some role in EPS dynamics.

Similarly to previous measured variables, biomass concentration in the system is initially sensitive to a large number of parameters, many of which seem to be highly correlated. All of these parameters but one ($f_{EPS,h}$) are the original parameters of the ASM3 model. This parameter however has a much lower impact on X_{BIO} than the most sensitive parameters such as Y_{STO,O_2} or k_{STO}, hence identification of EPS kinetics does not impair the model calibration with respect to biomass inventory. In the starvation period, X_{BIO} depends mainly on two stoichiometric parameters: Y_{STO,O_2} and Y_{H,O_2} which are approximately equally important.

Sensitivity functions for CES-ASM3 in the continuous flow system are presented in Figure 4.20. Similarly to previously investigated figures for the batch process, it is apparent that, compared to CES-ASM1 CES-ASM3 has more equally 'important' and correlated parameters, making selection of the most dominant parameters for calibration much harder. Although identifiability of both models has not been investigated here it becomes apparent that future research needs to focus on assessment of the local as well as global identifiability and related model investigation methods such as global sensitivity. Whilst local dynamic sensitivity served as an important tool for this study it is by no means exhaustive. It becomes especially visible that with such a high number of parameters local sensitivity does not provide a sufficient amount of information as different sensitivities will be obtained with different combinations of 'fixed' parameters. The above mentioned problems shall be addressed in future studies.

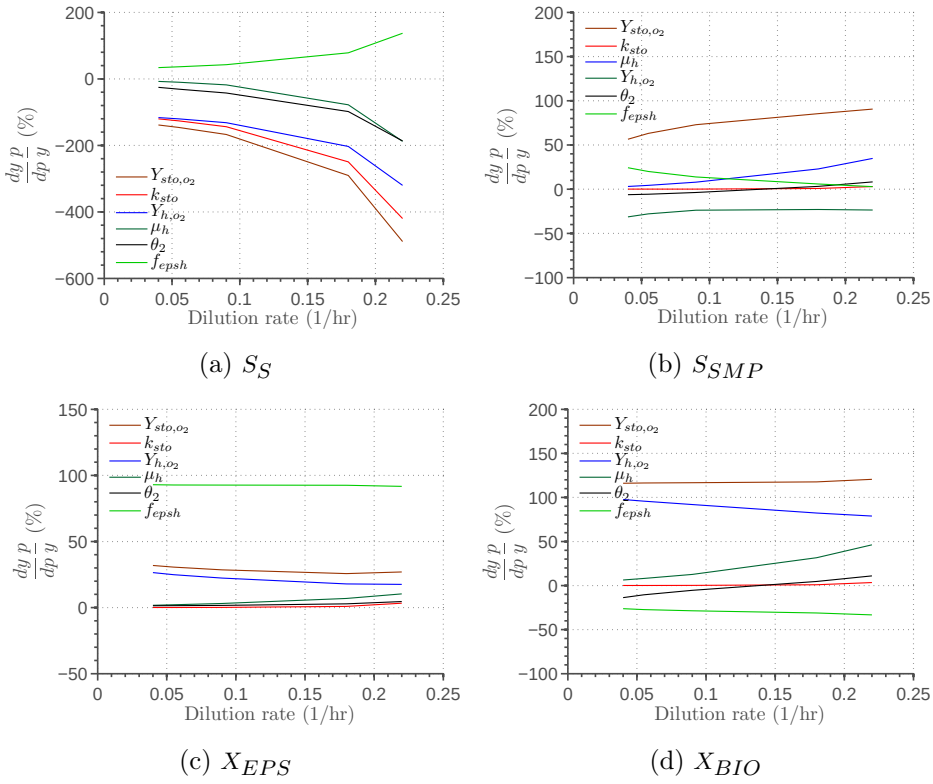

(a) S_S (b) S_{SMP}

(c) X_{EPS} (d) X_{BIO}

Figure 4.20: Dynamic relative-relative sensitivity functions for four model outputs: S_S, S_{SMP}, X_{EPS} and X_{BIO}, and six most sensitive model parameters in CES-ASM3 in the continuous flow experiment of Hsieh et al. [101].

The fate of readily biodegradable substrates (S_S) is dependent on a large number of parameters. Y_{H,O_2}, k_{STO}, Y_{STO,O_2} have a largest and negative effect on S_S. μ_H and θ_2 have approximately twice smaller and negative effect whilst $f_{EPS,h}$ have a positive effect on S_S concentration over an entire range of dilution rates. All of these parameters become more significant as dilution rate is increased.

SMP dynamics are dominated by storage yield coefficient Y_{STO,O_2}, hence by substrate storage and subsequent utilisation. Figure 4.20b shows a number of less significant parameters although none of them are specifically related to SMP dynamics. This does not mean that the SMP related kinetic and stoichiometric parameters do not play any role in the model, only that under the following set of default stoichiometric and kinetic parameters the parameters governing heterotrophic growth have a stronger influence on SMP dynamics than the SMP-related parameters embedded in the model. This observation emphasised the fact that it is important to look into global parameter sensitivity where several parameters are perturbed simultaneously rather than one parameter at a time and this study is recommended for further research on this topic.

X_{EPS} dynamics are dominated by just one parameter, namely $f_{EPS,H}$, what indicates that EPS are produced mainly during the biomass growth, not during the biomass decay and maintenance.

Biomass (X_{BIO}) dynamics are sensitive to a range of parameters which affect the biomass growth to similar degrees. These parameters are, respectively, $f_{EPS,H}$,

μ_H, Y_{H,O_2}, and Y_{STO,O_2}. Hence, similar biomass profiles can be obtained for various combinations of the three above mentioned parameters, hence the findings indicate issues with the model's parameter identifiability and signalise the need for a formal identifiability analysis and a subsequent model-based experiment design for parameter estimation.

4.7.2 Static steady-state sensitivity analysis

Static sensitivity profiles

Static sensitivity analysis was carried out on a single aerated CSTR plant layout which was previously used to perform final simulations with CES-ASM1 and CES-ASM3, as described in Section 4.5. The plant layout used for these final simulations as well as the static sensitivity study outlined here are shown in Figure 4.6 on page 105.

The Simulink model of the plant was simulated for a number of operating conditions defined as follows: MLSS = {5,000 ; 10,000 ; 15,000 ; 20,000} mg L^{-1}, DO = {0.5 ; 1.0 ; 2.0 ; 3.0} mgO_2 L^{-1}, Temperature (T) = {10 ; 15 ; 20 ; 25} °C, HRT = {4 ; 9 ; 14 ; 19} h, $f_{nr,SMP}$ = {0.25 ; 0.35 ; 0.45 ; 0.55}, where $f_{nr,SMP}$ denotes a non-dimensional SMP permeation factor and represents the fraction of SMP which is not retained by the membrane. For every combination of MLSS, DO, Temperature, HRT, and $f_{nr,SMP}$ the model was simulated with different values of stoichiometric and kinetic parameters for 2000 days, which was found sufficient to reach a steady-state condition in every simulation run. The model parameters are varied one at a time between -60% and +60% at 10% intervals.

Static sensitivity analysis was carried out to determine which of the new kinetic and stoichiometric parameters associated with biopolymer kinetics and slow hydrolysis have the largest effect on output SMP, EPS, SCOD, and soluble total nitrogen (STN) concentrations. Out of all tested combinations of operating parameters, exemplary sensitivity profiles are obtained for a single operational point defined by: HRT=14h, mixed liquor temperature T=16^{o}C, MLSS=15,000 mg L^{-1}, DO=3.0 mgO_2 L^{-1}, and $f_{nr,SMP}$=0.5. The SRT of the system with default parameter values was calculated as 52 days for CES-ASM1 and 40 days for CES-ASM3. The maximum observed deviation of SRT was −11% and +12% for a ± 60% deviation in the heterotrophic yield on SMP (Y_{SMP}) in CES-ASM1 model and −9% and +9% for maximum change in $Y_{STOSMP,aer}$ in CES-ASM3.

Figure 4.21 and Figure 4.22 show static sensitivity curves for the most sensitive biopolymer-associated parameters in respectively, CES-ASM1 and CES-ASM3. The most sensitive parameters are defined as the parameters which cause over 10% deviation in the selected output variable for ±60% change of the parameter value. The monitored output variables were respectively: SMP, EPS, SCOD, and STN.

Steady state SMP concentrations in CES-ASM1, as shown in Figure 4.21a, are influenced by six model parameters listed here in order of significance: $\mu_{UAP,20}$, $\mu_{BAP,20}$,

Y_{SMP}, $\gamma_{UAP,h}$, K_{UAP}, and K_{BAP}. This indicates that SMP kinetics under steady-state conditions are governed by growth of heterotrophs in the system and therefore, SMP are mostly utilisation-associated (UAP) rather than biomass-associated (BAP). EPS kinetics are governed by two main parameters: EPS hydrolysis rate ($k_{h,EPS,20}$) and the fraction of EPS released during heterotrophic biomass growth ($f_{EPS,h}$) which have opposing effects on the bulk liquid EPS concentrations. The decay associated EPS production coefficient $f_{EPS,dh}$ has a significantly lesser influence on EPS which indicates that the majority of EPS produced in the system is associated with biomass growth. SCOD (see Figure 4.21c) depends most strongly on the heterotrophic growth rate on UAP ($\mu_{UAP,20}$), heterotrophic yield coefficient on SMP (Y_{SMP}), and the heterotrophic growth rate on BAP ($\mu_{BAP,20}$). Since the sensitivities are quite significant and up to 30% for a 60% variation in the parameter, SCOD is expected to be mainly due to the presence of SMP. STN concentrations depend on six parameters, some of which are very highly correlated. However, the sensitivities of these parameters are very low and under 6% in all instances, which suggests that SMP and EPS related parameters do not significantly affect the concentrations of soluble inorganic nitrous compounds in the system, such as ammoniacal nitrogen (NH_4^+-N) and nitrate nitrogen (NO_3^--N).

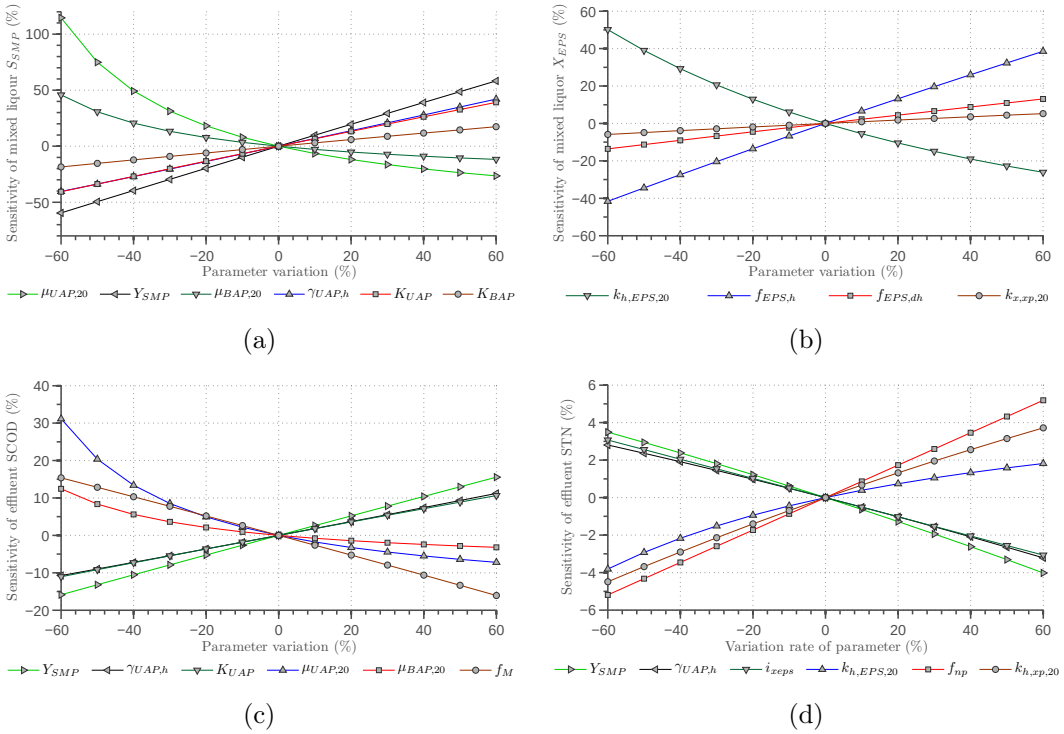

Figure 4.21: Variation of the mixed liquor S_{SMP}, X_{EPS}, $SCOD$, and STN concentrations in response to changes in most sensitive model parameters in CES-ASM1.

Sensitivity curves for CES-ASM3 are shown in Figure 4.22. SMP concentrations depend on a number of parameters, such as: $k_{sto,BAP}$, f_s, $f_{EPS,STO}$, and f_M. The make-up of the most sensitive parameters suggests that SMP in the system is composed more of BAP than UAP which contradicts to some degree the results obtained with CES-ASM1. Differences in the outputs from the two models are due to different choices

of default parameters in CES-ASM1 and CES-ASM3. Both models contain a significant amount of biopolymer-related stoichiometric and kinetic parameters allowing them to represent different biopolymer kinetics. SMP concentrations in CES-ASM3 were also found to depend on SMP retention coefficient on the membrane f_M. $f_M = 1 - f_{nr,SMP}$ where $f_{nr,SMP}$ denotes the fraction of SMP which permeate through the membrane. Appearance of f_M in the list of most sensitive parameters indicates that the membrane indeed has influence on the state of the bioreactor.

EPS concentrations are found to be dominated by EPS hydrolysis rate constant $k_{h,EPS}$. The other kinetic parameters affecting the amount of EPS in the system are: $f_{EPS,h}$, $f_{EPS,sto}$, and $f_{EPS,dh}$, which represent the fractions of EPS released due to, respectively, heterotrophic biomass growth, internal storage of organic substrates by heterotrophic organisms, and heterotrophic biomass decay. This means that EPS in the system is associated with both growth and decay of heterotrophic biomass.

SCOD in the bulk liquid is sensitive to a number of parameters, out of which the most significant are $k_{sto,BAP}$, $f_{EPS,sto}$, f_S, and $f_{EPS,h}$. Hence, SCOD dynamics depend not just on SMP utilisation and production kinetics but also on EPS kinetics, indicating that EPS and SMP related kinetic processes are highly inter-related in CES-ASM3.

STN concentrations are found to depend on a number of SMP and EPS-related stoichiometric and kinetic parameters. The sensitivity profiles of some indicate around ±20% change in STN concentration for ±60% change in the parameter. If we compare Figure 4.22d with Figure 4.21d, it becomes clear that nitrogen kinetics in CES-ASM3 are linked to biopolymer kinetics more than in CES-ASM1.

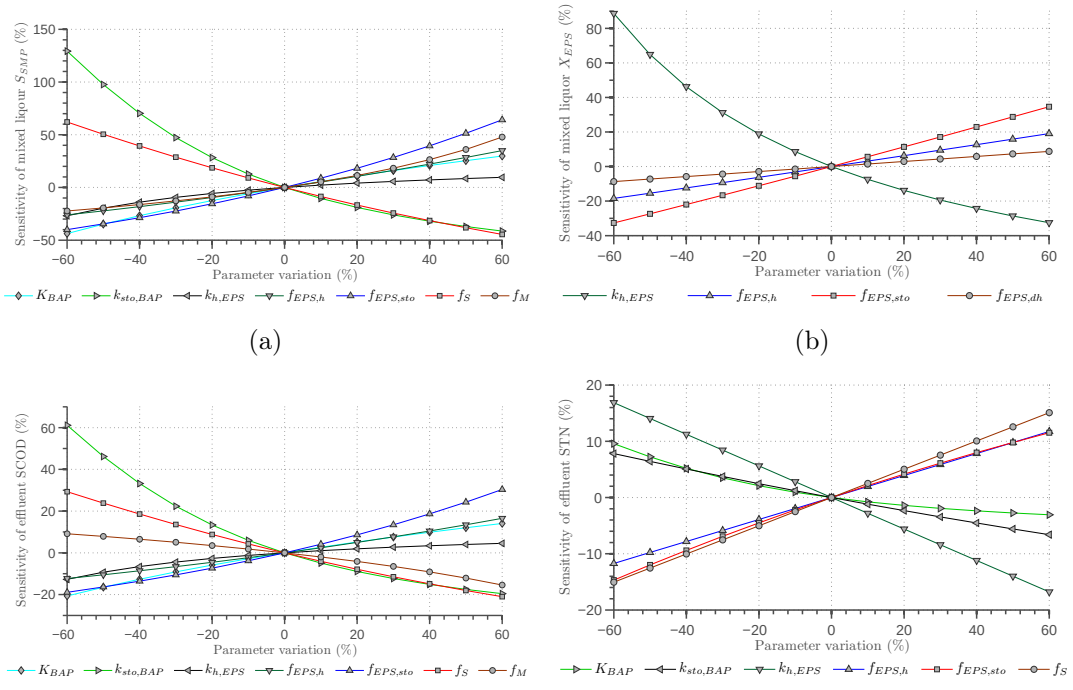

Figure 4.22: Variation of the mixed liquor S_{SMP}, X_{EPS}, $SCOD$, and STN concentrations in response to changes in most sensitive model parameters in CES-ASM3.

Most sensitive parameters

Static sensitivity profiles such as these shown in Figure 4.21 and Figure 4.22 were calculated for all operating points defined in Section 4.7.2 and for a number of model outputs defined in Table 4.9 and Table 4.9. These outputs are, respectively, bulk liquid S_{SMP}, bulk liquid X_{EPS}, O_2 demand, effluent S_{NH}, effluent soluble total Kjeldahl nitrogen (STKN), observed biomass yield Y_{obs}, and effluent SCOD. At each operating point the relative-relative static sensitivity of every output to each parameter was measured as the gradient of the line of best fit running through 5 points corresponding to -20%, -10%, 0%, +10%, and +20% variation in the parameter. The minimum, maximum and average values of these sensitivities were calculated for CES-ASM1 and CES-ASM3 and presented, respectively, in Table 4.9 and Table 4.10.

As both tables show, some parameters exhibit large variations of sensitivity while other parameters have fairly consistent values throughout all operating conditions. As was already explained in Section 4.7.1 during the analysis of the dynamic sensitivities, some parameters such as, e.g. $\mu_{UAP,20}$ in CES-ASM1 will have a strong effect on SMP production during intensive biomass growth periods but will have a lesser significance in starvation periods where BAP will be a dominant fraction of SMP.

In both models, SMP rejection factor f_M is found to be the most sensitive parameter for effluent SCOD and whilst SCOD is found to be composed mainly of SMP, f_M is the most sensitive parameter for effluent SMP as well. This finding indicates that effluent SMP concentrations and SCOD depend more on the properties of the membrane than on the biological processes themselves.

Parameter variability

Static sensitivity analysis results for CES-ASM1 and CES-ASM3 were used to train two separate self organising maps (SOMs) in the same way as described earlier in Section 4.6.2. Component planes of these two maps display the inputs and the selected, most variable, relative-relative sensitivities in CES-ASM1 and CES-ASM3 as shown, respectively, in Figure 4.23 and Figure 4.24.

Figure 4.23 shows that the highest absolute values of the sensitivity of X_{EPS} to $k_{h,EPS,20}$ coincide with the highest SRTs and MLSS concentrations, meaning that EPS production/loss under high SRTs is dominated by hydrolysis, not by substrate-associated production which occurs mainly under abundance of organic easily biodegradable substrates. Sensitivity of the unoxidised forms of nitrogen (S_{NH} and STKN) to various polymer-related model parameters is highest where SRT in the system is low but the bulk liquid temperature is sufficient enough to prevent the washout of nitrifying bacteria and therefore the loss of nitrification. Since nitrification under these conditions is at the brink of collapse, it is very sensitive to many parameters and a small change of one of these parameters can decide whether nitrification will continue or whether it will be lost.

Table 4.9: Variability of relative-relative static sensitivities of the selected outputs of CES-ASM1 to six most sensitive model parameters.

Output	Parameter 1			Parameter 2			Parameter 3			Parameter 4			Parameter 5			Parameter 6		
	Min	Ave	Max	Min	Ave	Max	Min	Ave	Max	Min	Ave	Max	Min	Ave	Max	Min	Ave	Max
S_{SMP}		$\mu_{UAP,20}$			Y_{SMP}			$\gamma_{UAP,h}$			K_{UAP}			$\mu_{BAP,20}$			f_M	
	-1.11	-0.883	-0.711	0.685	0.817	0.892	0.576	0.651	0.811	0.509	0.610	0.711	-0.398	-0.263	-0.094	0.024	0.100	0.398
X_{EPS}		$k_{h,EPS,20}$			$f_{eps,h}$			$f_{eps,dh}$			Y_{SMP}			$\gamma_{UAP,h}$			f_M	
	-0.945	-0.493	-0.109	0.583	0.607	0.660	0.158	0.206	0.237	-0.006	0.064	0.155	-0.005	0.052	0.117	-0.002	0.006	0.041
O_2 demand		Y_{SMP}			$\gamma_{UAP,h}$			$f_{eps,a}$			$f_{eps,h}$			f_M			$f_{eps,dh}$	
	-0.409	-0.079	-0.035	-0.390	-0.066	-0.025	-0.271	-0.003	0.000	-0.083	-0.022	-0.005	-0.076	0.013	0.059	-0.041	-0.011	-0.003
Effluent S_{NH}		Y_{SMP}			$\gamma_{UAP,h}$			i_{xeps}			$f_{eps,a}$			$f_{eps,a}$			f_M	
	-1.33	0.053	0.579	-1.19	0.046	0.546	-0.697	-0.013	0.000	0.000	0.092	0.483	-0.030	0.000	0.177	-0.075	0.007	0.171
Effluent STN		Y_{SMP}			$\gamma_{UAP,h}$			i_{xeps}			$f_{eps,a}$			f_M			f_{bap}	
	-1.09	-0.043	0.349	-0.989	-0.044	0.338	-0.585	-0.075	0.001	0.000	0.013	0.344	-0.183	-0.030	0.039	-0.006	0.046	0.157
Y_{obs}		Y_{SMP}			$\gamma_{UAP,h}$			$k_{h,EPS,20}$			$f_{eps,h}$			f_M			$f_{eps,dh}$	
	0.042	0.109	0.128	0.045	0.092	0.105	-0.063	-0.044	-0.005	0.007	0.034	0.049	0.003	0.011	0.038	0.006	0.019	0.024
Effluent SCOD		f_M			Y_{SMP}			$\mu_{UAP,20}$			$\gamma_{UAP,h}$			K_{UAP}			$\mu_{BAP,20}$	
	-1.47	-0.498	-0.157	0.094	0.267	0.448	-0.405	-0.239	-0.080	0.071	0.208	0.397	0.072	0.197	0.319	-0.155	-0.076	-0.018

Table 4.10: Variability of relative-relative static sensitivities of the selected outputs of CES-ASM3 to six most sensitive model parameters

Output	Parameter 1			Parameter 2			Parameter 3			Parameter 4			Parameter 5			Parameter 6		
	Min	Ave	Max	Min	Ave	Max	Min	Ave	Max	Min	Ave	Max	Min	Ave	Max	Min	Ave	Max
S_{SMP}		$k_{sto,bap}$			f_M			f_S			$f_{EPS,h2}$			K_{BAP}			$k_{h,EPS}$	
	-1.59	-0.760	-0.174	0.332	0.682	1.25	-1.14	-0.756	-0.513	0.347	0.537	0.761	0.144	0.385	0.563	0.103	0.282	0.540
X_{EPS}		$k_{h,EPS}$			$f_{EPS,h2}$			$f_{EPS,h}$			$f_{EPS,dh}$			$Y_{STOSMP,aer}$			f_M	
	-1.04	-0.772	-0.414	0.465	0.495	0.522	0.263	0.284	0.304	0.067	0.120	0.152	0.009	0.054	0.109	0.006	0.035	0.100
O_2 demand		$f_{EPS,a}$			$k_{h,EPS}$			$f_{EPS,h2}$			f_M			k_{h,X_I}			$f_{EPS,dh}$	
	-1.14	-0.014	0.000	0.012	0.038	0.374	-0.267	-0.063	-0.038	-0.133	0.026	0.063	0.012	0.062	0.126	-0.124	-0.025	-0.014
Effluent S_{NH}		$i_{N,XEPS}$			$f_{EPS,a}$			$k_{h,EPS}$			$f_{EPS,h2}$			f_M			f_{NI}	
	-1.02	-0.040	-0.012	0.000	0.228	0.968	-0.483	-0.055	0.073	-0.265	0.014	0.195	0.000	0.015	0.179	0.008	0.029	0.141
Effluent STN		$i_{N,XEPS}$			f_M			$f_{EPS,a}$			f_{NI}			k_{h,X_I}			$k_{sto,bap}$	
	-1.36	-0.345	-0.053	-0.971	-0.083	0.132	-0.001	0.023	0.844	0.010	0.185	0.839	-0.036	0.147	0.609	-0.546	-0.073	0.057
Y_{obs}		$Y_{STOSMP,aer}$			k_{h,X_I}			$k_{h,EPS}$			$f_{EPS,a}$			$f_{EPS,h2}$			f_M	
	-0.196	-0.061	-0.003	-0.165	-0.068	-0.006	-0.095	-0.079	-0.049	-0.016	0.000	0.059	0.009	0.028	0.049	0.005	0.019	0.043
Effluent SCOD		f_M			$k_{sto,bap}$			f_S			$f_{EPS,h2}$			K_{BAP}			$k_{h,EPS}$	
	-0.732	-0.307	-0.054	-0.357	-0.225	-0.061	-0.308	-0.233	-0.129	0.118	0.198	0.254	0.052	0.135	0.174	0.039	0.096	0.158

Similar conclusions can be drawn regarding the sensitivity of X_{EPS} to $k_{h,EPS,20}$ and the sensitivity of S_{NH} and STKN when we investigate the SOM component planes for CES-ASM3 presented in Figure 4.24. Additionally, Figure 4.24 shows that the sensitivity of O_2 demand to $f_{EPS,a}$ coincides with low SRT and low DO suggesting that at this point autotrophic organisms are again near the point of washout. By making a change to the fraction of EPS produced during autotrophic growth ($f_{EPS,a}$) we affect the autotrophic biomass yield and hence decide on the fate of autotrophs in the system. Nitrification is pretty much an on/off reaction under steady-state conditions, i.e. it will either occur or entirely disappear in the reactor. Since nitrification uses up large amounts of oxygen, presence of nitrification in the system will imply high O_2 demands, whilst lack of it will lead to significantly lower oxygen demands. Hence, we can observe a high sensitivity of O_2 demand to model parameters affecting nitrification at the points where nitrification is near the point of collapse.

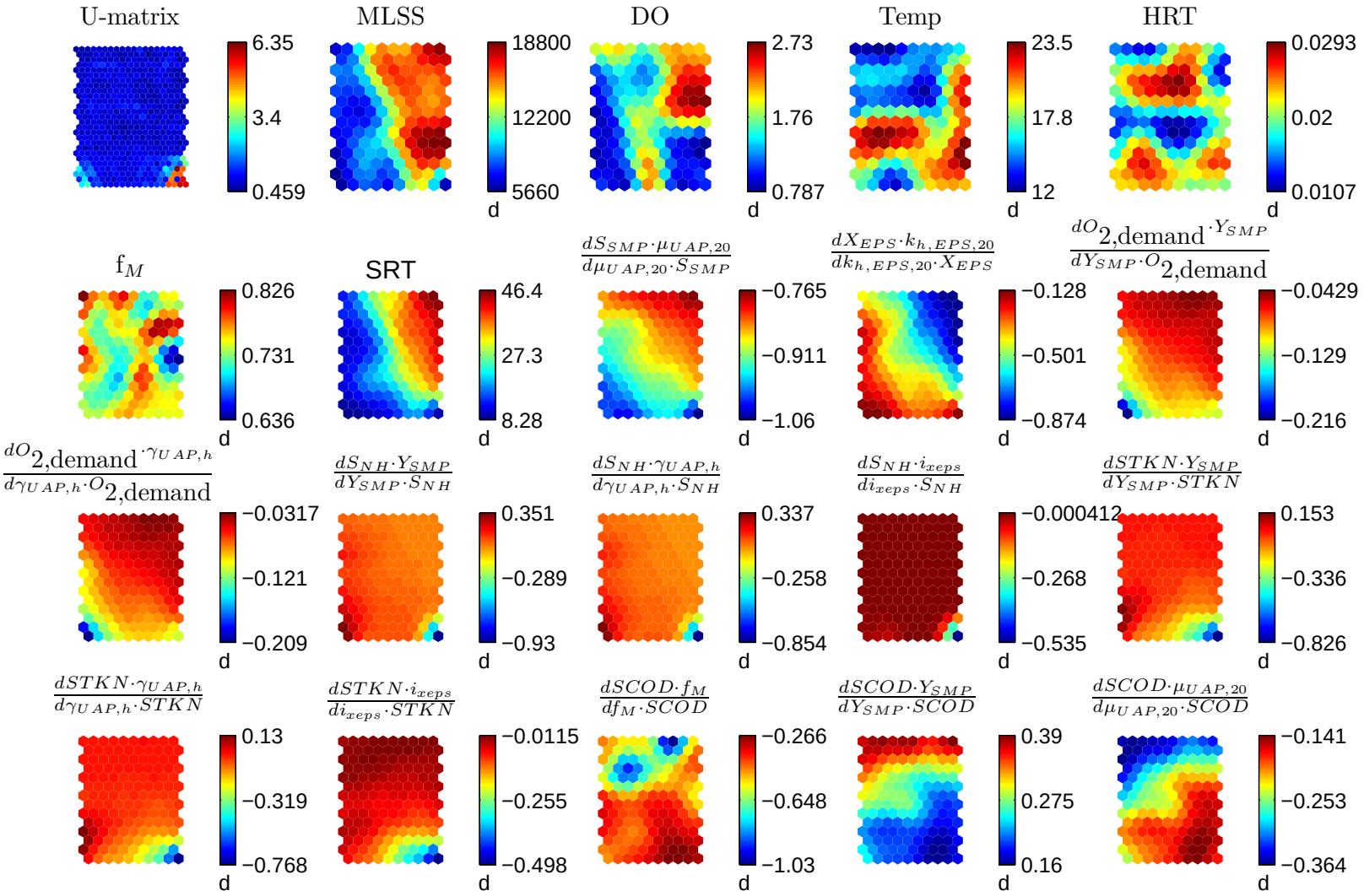

Figure 4.23: Component planes of SOM trained on the inputs and selected relative sensitivities of the CES-ASM1 model.

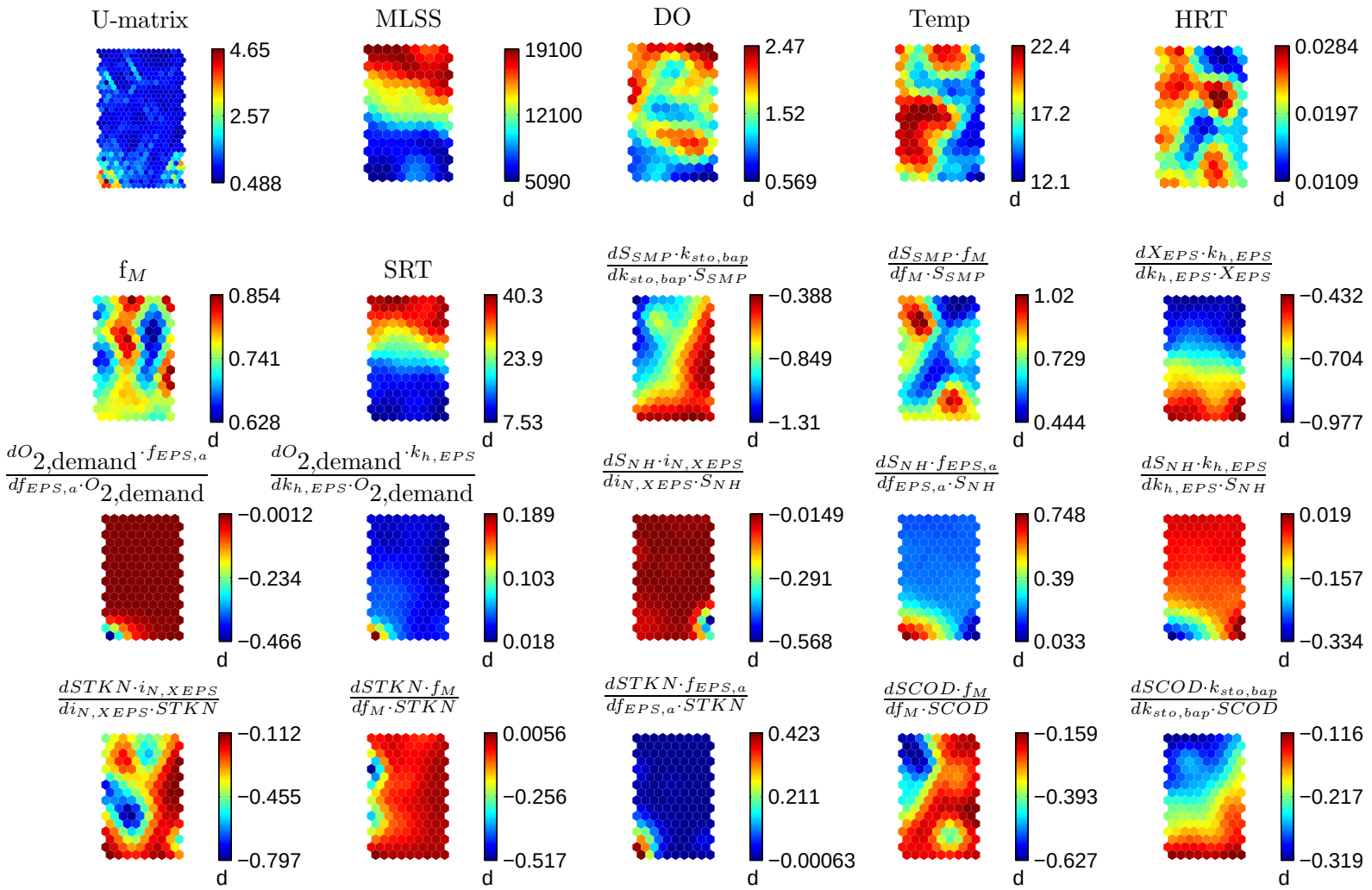

Figure 4.24: Component planes of SOM trained on the inputs and selected relative sensitivities of the CES-ASM3 model.

Part II

Modelling of Membrane Fouling

‘

Chapter 5

Mathematical modelling of membrane filtration and fouling

Contents

5.1 What is membrane fouling

Fouling is a process in which permeability of a membrane diminishes in time during filtration of solutes and suspensions. Membrane fouling in membrane bioreactors (MBRs)

is attributed to the physico-chemical interactions between the fluid and the membrane [23]. Fouling can be divided into various categories. From the point of view of its permanency, fouling is often subdivided into three subcategories: *reversible* fouling, *irreversible* fouling and *irrecoverable* fouling. *Reversible* fouling is caused by deposition of a mixture of suspended solids, gels, and colloids leading to formation of a cake layer on the membrane surface. Reversible fouling can be limited or even prevented if filtration flux is low and crossflow velocities CFVs and/or air sparging rates are high. The effects of reversible fouling are periodically removed by backwashing or relaxation. *Irreversible* fouling is caused by constriction and blocking of membrane pores by adsorption of dissolved matter and some colloidal matter. This type of fouling is not removed with mechanical means listed above but can be removed through chemical cleaning. *Irrecoverable* fouling is the type of fouling that can be removed neither by physical nor chemical methods and occurs over long periods. Whilst reversible fouling occurs at the rates of 0.1 to 1 mbar/min in a time-frame of about 10 minutes, the rates of irreversible fouling are within 10^{-3} to 10^{-1} mbar/min (6-12 month time frame), while the rates of irrecoverable fouling are between 10^{-4} to 10^{-3} mbar/min and hence irrecoverable fouling develops over years [45].

Fouling can also be subdivided from the point of view of the type of foulants into *biofouling*, *organic fouling*, and *inorganic fouling*. *Biofouling* refers to deposition, growth, and metabolism of bacterial cells or flocs on the membrane surface, [168]. Provided that the local environmental conditions are favourable, the deposited bacterial cells can form biofilms which are denser than cake and thus create more resistance, but can also promote further fouling by producing and releasing soluble microbial products (SMP) and extracellular polymeric substances (EPS). *Organic fouling* refers to deposition of soluble (SMP) and bound (EPS) biopolymers on the membrane surface and inside the membrane pores. *Inorganic fouling* refers to precipitation of inorganic compounds such as different metal salts, e.g. calcium carbonate $CaCO_3$ or struvite ($MgNH_4PO_4{\cdot}H_2O$). Precipitation of these and other inorganic compounds can occur either chemically when local ion concentrations begin to exceed their saturation concentrations, or can be promoted by the presence of bacterial cells and biopolymers, called biological precipitation. Fouling in MBRs is dominated by biofouling and organic fouling while inorganic fouling occurs under specific conditions such as high alkalinity or water hardness and on inorganic membranes.

Whilst foulants are brought into contact with the membrane mainly by convective transport and thus, are associated with the permeate flux, *conditioning fouling* is not associated with the permeate flux and is caused by passive adsorption of macromolecules, colloids and solutes before any flux-initiated deposition takes place. This initial passive adsorption was reported to account for 20-2000% of clean membrane resistance depending on the membrane pore size and to be almost independent of tangential shear, [189]. The importance of this phenomenon in the practical context is that the membranes lose often a significant portion of their "clean water" permeabilities right after their immersion inside the bulk liquid, which has to be accounted for by process engineers when

calculating the required membrane area for the MBR.

A comprehensive review of fouling in MBRs for wastewater treatment can be found in Le-Clech et al. [138]. Since the publication of their paper, Meng et al. [168] published a review of recent advances in MBRs focussing on membrane fouling and membrane materials, while Drews [45] reviewed membrane fouling in MBRs focussing on the contradictions in findings and possible cures for fouling. For further information on fouling, the reader is referred to the three above mentioned publications which provide thorough and comprehensive information on the subject.

Membrane permeability is also lost by *membrane clogging* aka. *sludging* which occurs when large pieces of solid material block membrane passages leading to local reduction of crossflow velocities and subsequent agglomeration of large solid deposits in the voids of the membrane modules. Although membrane clogging is detrimental to the performance of MBRs, it is not considered here due to limited amount of time and complexity of this process. Membrane clogging can be minimised by appropriate influent pretreatment using screens and sieves with perforations as low as 0.5 mm, [153].

5.1.1 Factors affecting membrane fouling

Membrane fouling in MBRs is caused by various types of foulants, which can be categorised based on their origin (i.e. organic molecules, inorganic molecules, living bacterial cells) or on their size or molecular weight (i.e. solutes, colloids, and suspended solids). As mentioned in the previous section, fouling is caused by many different mechanisms such as adsorption, scaling, cake formation, or biofilm growth over a wide range of temporal scales from minutes to months. Recent findings show that fouling in MBRs is influenced by the following factors: (a) *biomass characteristics*, e.g. floc size distribution (FSD) and floc structure, EPS content, chemical composition of EPS, and production and composition of SMP, [258]; (b) *physico-chemical properties of the influent*, e.g. temperature, viscosity, alkalinity, pH, salt concentrations, concentrations of transparent exopolymer particles (TEP), composition of organic substrates, deficiency of nutrients, etc.; (c) *operating conditions of the bioreactor and the membrane* such as bioreactor's hydraulic retention time (HRT) and sludge retention time (SRT), dissolved oxygen (DO) concentrations, value of permeate flux, sequence and duration of backwashing or relaxation, intensity of air sparging, and value of crossflow velocity (CFV), [167]; (d) membrane characteristics, e.g. pore size distribution (PSD), thickness, and membrane type and material which define its properties such as hydrophobicity, zeta potential, mechanical and chemical resistance, propensity of biofouling, etc. [30].

For a given membrane type and given operating conditions, fouling is found to depend mainly on SMP and EPS concentrations, chemical composition and molecular weight distribution (MWD) of SMP and EPS, floc size distribution (FSD) of the activated sludge, and electrostatic properties of activated sludge flocs. Despite of the vast amount of research carried out in the area, exact mechanisms and the impact of the above factors on fouling are often still unknown. It is generally accepted that SMP con-

tributes to irreversible fouling while suspended solids and bound EPS cause reversible fouling, although many findings are contradictory, as explained in the review paper of Drews [45]. For the purpose of modelling it was however assumed that SMP and EPS are the main causes of fouling. EPS is assumed to fill void spaces between flocs and lead to decrease cake permeability [186, 17]. SMP is assumed to adsorb on the membrane surface and inside the membrane pores leading to irreversible and irrecoverable fouling. The latest studies reveal that fouling depends on the chemical composition of SMP and EPS and their MWDs [78]. It was found that polysaccharides cause more fouling than proteins [143, 46] although it is uncertain whether different fouling propensities of polysaccharides and proteins are predominantly due to different chemical properties of these two groups of organic compounds or due to the difference in their MWDs. It was also found that EPS may cause some irreversible fouling by facilitating irreversible attachment of particles on the membrane surface while SMP attributes not only to irreversible but also to reversible fouling [98, 78]. Definitions of SMP and EPS are provided in Section 3.4 in Chapter 3.

5.1.2 Critical flux

The concept of critical flux was first introduced by Field et al. [62]. Field et al. [62] classified critical flux into two subcategories: the *strong form* and the *weak form*. In the *strong form*, critical flux is defined as the flux below which filtration of a colloidal suspension will yield the same flux as pure water for the same applied pressure [62, 259]. In the relaxed *weak form* the critical flux is defined as the flux below which a linear relationship exists between the applied pressure and the permeate flux. The slope of that linear relationship is allowed to differ from that of the pure water flux [62, 259]. In practical terms, in the context of MBR reactors, critical flux is defined as the permeate flux below which there is little of no fouling since the rate of back-transport is sufficient to eliminate particle deposition on the membrane [97]. MBRs are operated at filtration velocities below or slightly above the critical flux, since operation far above the critical flux results in a rapid trans-membrane pressure (TMP) rise during constant flux filtration and a rapid flux decline in a constant pressure filtration. Critical flux depends on the back-transport of particles from the membrane surface due to turbulence and crossflow and on the solute-membrane interactions which are affected by charge and hydrophobicity [138]. This means that the membrane can be operated with stable TMPs under higher fluxes if back-transport is increased by increasing i.e. CFV - although only to some extents. On the other hand, in MBRs for wastewater treatment, slow, irreversible fouling is found to occur under fluxes much smaller than the critical flux ultimately leading to a rapid TMP rise, also known as the TMP jump [27, 266]. The exact definition of *critical flux* has not been agreed to date and neither was a protocol for determination of the critical flux. A common method for critical flux determination is a flux-stepping method but this method was found to yield different results depending on the height and duration of the steps [137]. A hysteresis method was proposed by Espinasse et al. [53] in which critical flux is defined as the minimum

flux which creates an irreversible deposit on the membrane surface. The hysteresis method as well as the flux stepping method were criticized for not yielding predictive absolute permeability data for extended operation of complex fluids. For more reading on critical flux, the reader is referred to Le-Clech et al. [137; 138].

5.1.3 Sustainable flux and threshold flux

It was found by Field and Pearce [61] that although powerful, the concept of critical flux does not delineate all typical fouling circumstances found in membrane filtration. Two of such exceptions have been mentioned in the paper and are, respectively, biofouling and the slow flux decline that is observed in many industrial membrane applications also under low fluxes which might have been considered sub-critical. The authors therefore introduced the concept of 'threshold flux', which in general terms is the flux that divides a low fouling region from a high fouling region [61]. The threshold flux can be applied to cross-flow systems as well as dead-end systems for which the critical flux has a limited applicability as it may not exist due to the fact that end-end systems have no back-transport mechanisms. Threshold flux may be linked both to the critical flux concept and to the concept of a sustainable flux although all these three terms quantify different properties of the membrane filtration systems and carry different types of information. For complete information and description of these two flux concepts and how they are linked to critical flux, the reader is however advised to refer to the original paper of Field and Pearce [61].

The paper of Field and Pearce [61] mentions the following definition of sustainable flux which was proposed by an industrialist [237] in the informal communication with the authors: 'Sustainable flux is the net flux that can be maintained using mechanical and chemical enhancing means to meet an operation cost objective over the projected life of the membrane'. From this definition it is clear that the notion of sustainable flux is to define operating conditions which would give optimal balance between moderate operational expenditures (OPEX) and moderate capital expenditures (CAPEX) whilst maintaining the required productivity level. Hence, sustainable flux is a pragmatic concept for membrane design and operation and is only loosely related to the critical flux family which do not take into account the operating costs of the membrane, only the amount of fouling developing on the membrane for the given membrane and under given influent characteristics and operating conditions. As Field and Pearce [61] indicate sustainable flux is often higher than the critical as well as the threshold flux as it is economical to operate the plant with moderate albeit controlled fouling. The practical values of operating fluxes are based on the the expected productivity whilst taking into consideration the costs of energy, costs of chemicals, capital costs as well as other constraints such as safety factors, etc. whilst critical flux of various forms as well as the threshold flux rather refer to just the rate of fouling in the system.

In the presence of conditional fouling and biofouling critical flux may not be present. The same applies to dead-end filtration cells in which some level fouling is always present

regardless of the flux rate due to absence of back-transport. It is also possible that for certain systems under specific circumstances, the identified critical flux will have a very small value far below economically viable levels. Under such conditions the 'threshold flux' concept accordingly to Field and Pearce [61] gains merit. The authors developed a simple model which was used to identify critical flux values on the four sets of data from four different pilot plants treating different types of water. The identified threshold fluxes identified with the model were falling very close to the values identified through visual inspection of the plots.

5.1.4 Mitigation of fouling

Fouling can be mitigated, although not completely eliminated, with the following methods listed below:

1. Control of SMP production via adjustment of operating conditions in the bioreactors,
2. Control of SMP via addition of adsorbents/coagulants,
3. Control of hydrodynamic conditions, i.e. flux rates, CFV, air scouring rates,
4. Backwashing, relaxation, and chemical cleaning,
5. Control of bulking,
6. Modification of membrane surface properties,
7. Influent pretreatment,
8. Minimisation of transient conditions, e.g. through upstream load balancing,
9. Optimisation of the tank and membrane module geometries,
10. Addition of nanomaterials,
11. Inhibition of quorum sensing

As the properties of activated sludge depend on the operating conditions inside the bioreactor, control of the operating conditions in the bioreactor at near optimum levels allows to minimise organic and biomass-associated fouling. It is reported that increasing HRT leads to reduced fouling [167, 20] and increase of aeration intensity produces more permeable cakes [239]. Also, comparison of recent literature indicates an existence of an optimum SRT range which guarantees minimum fouling rates [168]. Existence of an optimum SRT was also showed by Jiang et al. [115], Tian et al. [238] in two simulation studies using the same SMP activated sludge model (ASM). These operating conditions are mainly linked to production of SMP and EPS and to sludge FSD and morphology.

Quoting after Meng et al. [168] addition of adsorbents and coagulants to sludge suspension can decrease the level of solutes and colloids or enhance the flocculation ability. Powdered activated carbon (PAC) will adsorb biopolymers in the sludge suspensions leading to lower soluble biopolymer concentrations. Additionally, activated sludge flocs with added powdered activated carbon (PAC) become heavier and thus accumulate less on the membrane surface. Coagulation can remove SMP by charge neutralisation and

bridging [260].

Increasing permeate flux leads to increased reversible fouling due to elevated cake accumulation promoted by higher convective velocities towards the membrane surface. High fluxes are also found to increase irreversible fouling caused by colloids and solutes as shown in Ye et al. [266] and corroborated in this study as shown in Figure 6.2 on page 190. Reversible fouling can be mitigated by provision of high CFVs and air scouring rates whilst irreversible fouling is found to be independent on the hydrodynamic conditions in the vicinity of the membrane.

Membrane surface is often modified in order to increase the membrane's hydrophilicity, produce narrower PSD, increase the membrane's porosity, and decrease surface roughness. Membrane surface modification is beyond the scope of work of this thesis. For more information about recent advances in surface modification and formation of the so called dynamic membrane, the reader is referred to the review paper of Meng et al. [168].

Influent pretreatment is generally limited to screening and sieving with fine screens and sieves with openings down to 0.5 mm in order to reduce the risk of clogging. In case of specific industrial influents, pH may be adjusted prior to biological treatment as pH was found to alter polymer aggregation, fouling and gelling propensities [45].

Dynamic changes in temperature, SRT setpoint, loading rate, and carbon source were observed to cause an increase in the amounts of loosely bound EPS in the system and resulted in worsened sludge volume index (SVI) and filterability [264]. Transients due to changes in influent composition can be minimised by upstream balancing while transients in SRT can be minimised by appropriate sludge wastage control strategies.

Optimisation of MBR's geometry involves positioning of the membrane modules, membrane module design, location of the coarse-bubble aeration grid, location of baffles, and overall tank geometry design. Optimisation of MBR geometry was approached by Prieske et al. [201], Böhm et al. [13] using Computational Fluid Dynamics (CFD) methods in order to reduce the propensity of the system to clogging and increase air-scouring efficiency in the system.

More information about mitigation of membrane fouling and amelioration of MBR performance can be found in Meng et al. [168], Drews [45].

5.1.5 Mathematical modelling of membrane filtration

A model of a membrane filtration unit can be subdivided into a number of smaller and distinct submodels.

1. membrane fouling
2. particle transport and hydrodynamics
3. membrane module clogging
4. internal membrane transport

5. back-flushing and relaxation
6. chemical cleaning
7. membrane ageing (degradation)

This subdivision and hierarchy is shown in Figure 5.1.

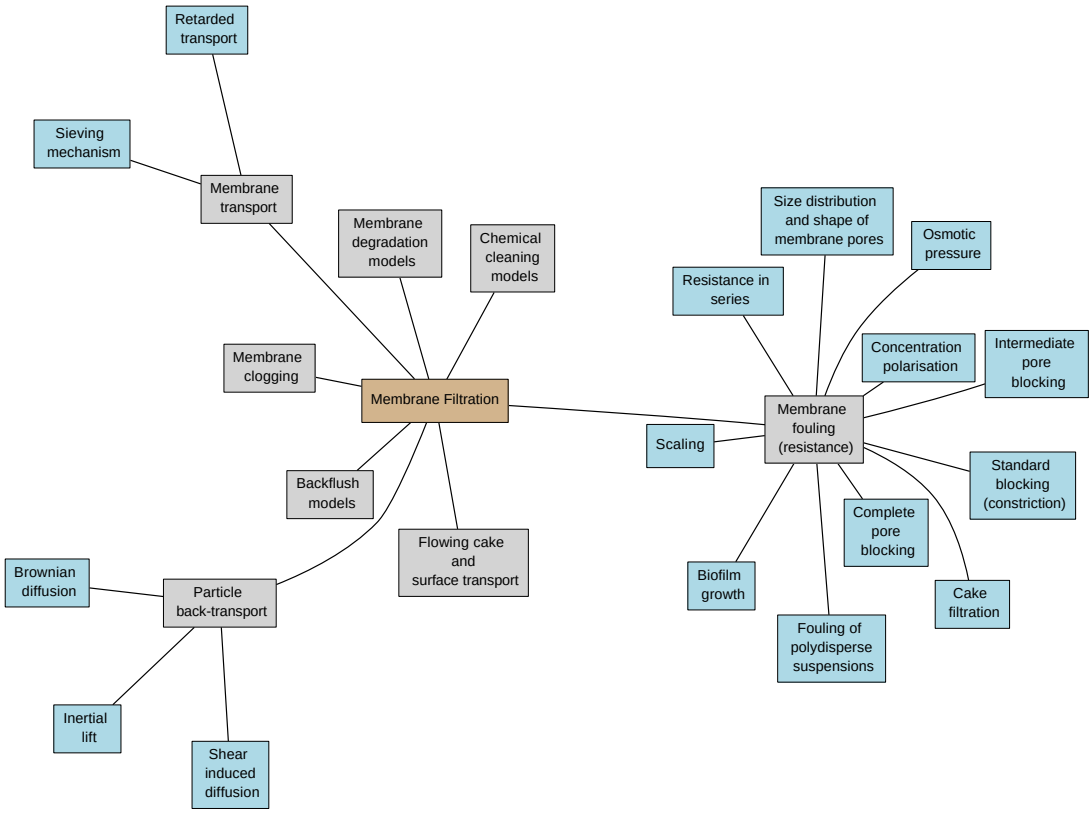

Figure 5.1: Subdivision and hierarchy of membrane filtration models.

Each of the individual membrane filtration submodels can be described using different modelling techniques, e.g. empirical, deterministic, stochastic, cellular automata, artificial intelligence (AI), etc. The number of scientific papers describing models of membrane fouling is so vast that it would be impossible and unreasonable to quote all of them in this place. Fouling models vary greatly depending on their intended application (i.e. design, optimisation, control, aid with understanding, etc.), the type of the system being modelled, the number and the types of fouling processes under consideration, the modelling approach, etc.

Often the fouling models are focused on individual aspects of filtration. For example, Hermanowicz [90], Chang et al. [24] developed, respectively, two-dimensional (2D) and three-dimensional (3D) biofilm models based on the concept of cellular automata. Kim and Liu [120] focused on determination of critical flux of hard sphere suspensions using a Monte Carlo method. Foley et al. [65] modelled the effects of particle polydispersity on specific cake resistance in cross-flow filtration. Zondervan et al. [272] developed a model able to predict the effects of irreversible fouling and chemical cleaning which can be used to optimise chemical cleaning cycle sequence in a MBR. Ye et al. [266]

attempted to develop a model which is able to predict the onset of a two-stage TMP profile in a subcritical filtration of model EPS suspensions.

Membrane hydrodynamics can be described on a micro-scale or macro-scale. On a micro-scale the model attempts to describe filtration on a particle level by considering interactions between individual particles. On a macro-scale the suspension is treated as a continuum where different phases are treated as inter-penetrating continua (fluids) using the concept of a phase volume fraction. Additionally, the flow domain around the membrane can either be considered as: (a) three-dimensional (3D) with the membrane modelled as a two-dimensional (2D) surface, (b) two-dimensional (2D) with the membrane modelled as a one-dimensional (1D) segment, or (c) one-dimensional (1D) with the membrane modelled as a single point. In addition to dimensionality of the flow domain around the membrane, the model can either take into consideration the thickness and the internal structure of the membrane or assume that the membrane has a zero thickness. If we decide to adopt one of the 'classical' methods of CFD with either finite difference (FD), finite volume (FV) or finite element (FE) differencing schemes, hydraulics of a MBR can be described with either Eulerian, Lagrangian or Eulerian-Lagrangian methods [242]

Although internal membrane transport is usually not considered and membranes are either treated as black-box models or as plates with ideal cylindrical pores, internal membrane structure might play a significant role in some modelling scenarios. For example, membranes with highly interconnected pores have a significantly higher capacity due to reduction in flux decline arising from the fluid flow under and around any surface blockage [275].

Although filtration, fouling, back-transport and various aspects of fluid flow within or around the membrane are most often described with mechanistic models, modelling of the lesser known phenomena associated with membrane filtration such as clogging, biofilm growth, chemical cleaning, ageing and back-flushing are generally described using much simpler empirical, behavioural, or data-driven models. Although mathematical description of simple filtration processes such as lab-scale dead-end filtration is possible with fully mechanistic approach, a thorough description of a full-scale membrane operation is always accomplished with grey-box models, i.e. with a combination of mechanistic (white-box) and black-box models.

5.1.6 Fouling models for MBR reactors

Ognier et al. [190] developed a model for sub-critical flux constant flux filtration. The model assumes that solutes in the bulk liquid deposit on the membrane leading to reduction of the number of open pores. Once local flux through open pores exceeds the critical flux, deposits begin to form on the membrane surface translating to very high hydraulic resistances causing the, so called, two-stage TMP profile.

Gehlert et al. [68] developed a resistance in series model using cake deposition as a main fouling mechanism. The model takes into account cake consolidation as

initially proposed by Nagaoka et al. [176], backwashing as well as cake back transport due to cross-flow. Cake is assumed to be compressible. The membrane is additionally discretised to gain more information on permeate flux, cake mass and transmembrane pressure distribution over an entire length of the module [68].

Liang et al. [149] proposed a resistance in series model in which fouling is described with two mechanisms: reversible fouling and irreversible fouling. The model was found to agree well with experimental data obtained from an immersed MBR system for wastewater treatment.

Broeckmann et al. [17] developed a resistance in series model for a hollow fibre (HF) immersed MBR system which considers the effects of pore blockage, cake formation and irreversible fouling. The model introduces two new phenomena: distribution of particle and membrane pore diameters and adhesion between particles and the membrane surface. Hydrodynamic conditions at the membrane are modelled as flow of uniform air bubbles through water channels [17].

Busch et al. [19] created a model for immersed HF/UF membranes for wastewater treatment. The model describes the system geometry, hydrodynamics of the feed and the permeate flow, and membrane fouling. Membrane fouling model takes into account membrane resistance, pore blocking, cake formation, polydispersity of particles, biofilm formation and concentration polarisation. The authors provided a highly detailed description of microfiltration (MF) and ultrafiltration (UF) processes and analyses the model's behaviour through numerous simulations and the parameter sensitivity study.

Li and Wang [147] published another model of an immersed MBR for wastewater treatment. The membrane is divided into N sections in order to account for uneven distribution of shear which results in uneven coverage of the membrane with cake. The model considers the following fouling mechanisms: pore constriction, cake growth and temporal sludge film coverage. Dynamics of biomass attachment and detachment from the membrane are related to filtration rate and air-scour aeration intensity.

Wu et al. [262] developed a model of membrane fouling in an immersed MBR which considers the effects of solid, colloidal and soluble components. Two fouling processes are considered: pore constriction and cake formation. Cake is assumed to consolidate as a result of entrapment of colloidal matter within the cake pores leading to a decrease in cake porosity and thus its specific resistance. Cake thickness and cake porosity are additionally related to, respectively, air scouring rate and floc size distribution (FSD).

5.2 Processes opposing membrane filtration

Hydraulic resistance experienced during filtration of solutes across the membrane is attributed to: (a) resistance of the clean membrane, (b) effects of reversible, irreversible and irrecoverable fouling, (c) accumulation of rejected solute (in UF membranes) near the membrane surface, called *concentration polarisation (CP)*, (d) precipitation of, normally macromolecular species at the membrane surface called *gel layer formation*, (e)

precipitation of inorganic molecules on the membrane surface, called *scaling*.

As mentioned in Section 5.1, fouling is defined as a combination of processes which all attribute to the loss of membrane's permeability causing deterioration in the performance of membrane filtration. During constant TMP filtration (ΔP = const), fouling causes flux to decline over time, whereas under constant flux filtration (J = const), as fouling progresses so does pressure loss around the membrane causing a TMP rise. In the classical approach fouling is assumed to be caused by just four mechanisms:

1. Pore constriction (standard pore blockage)
2. Complete pore blockage
3. Intermediate pore blockage
4. Cake formation

For constant pressure filtration, these mechanisms have been defined by Hermia [91] and expressed in a single equation (Equation 5.21) given on page 150.

The four above listed classical fouling mechanisms describe the accumulation of solutes, colloids and particles inside membrane pores and on the membrane surface leading to a reduction in the diameter of open pores (constriction), occlusion (i.e. blockage) of pores by particles larger than the pore size (standard and intermediate pore blockage) and deposition of layers of particles onto the blocked membrane surface (cake formation). These four fouling mechanisms are graphically represented in Figure 5.2 and are described in more detail below. Traditionally four classical fouling mechanisms were applied separately to model filtration of various solutions and suspensions. Depending on the composition of the liquid being filtered and the interactions between the membrane and the bulk liquid, one fouling process may dominate over the other three throughout the filtration process. In such situation, the mathematical model of the dominating process can be successfully applied to describe flux decline or TMP increase during filtration. As some researchers pointed out, e.g. Ho and Zydney [96], in many cases, a single classical fouling mechanism was not able to accurately describe the process over an entire course of filtration. Discrepancies between the measurements and the predictions obtained from classical fouling equations were attributed to simultaneous occurrence of several fouling processes and to sequential occurrence of fouling processes, i.e. different mechanisms will dominate at different stages of the filtration process. These findings formed the base for the development of the fouling models which consider simultaneous occurrence of three classical fouling mechanisms [50, 262] and the development of the new mechanistic fouling model explained in detail in Section 6.3 in which pore constriction and pore blockage are assumed to occur alongside one another while cake formation occurs in sequence after pore blockage.

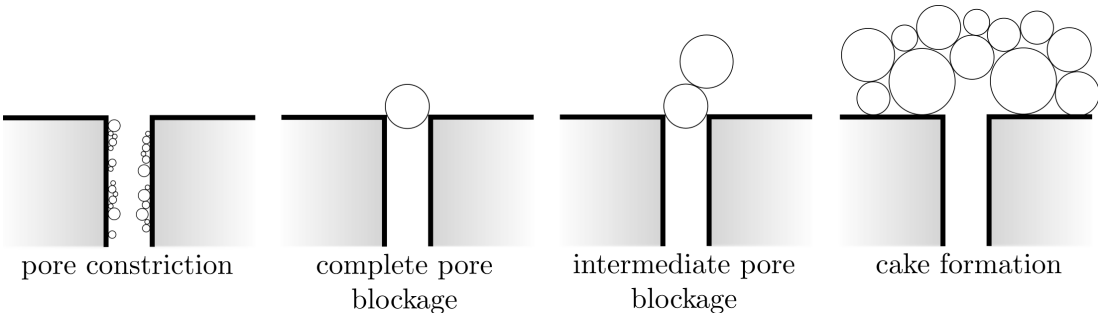

Figure 5.2: Visualisation of the classical fouling mechanisms as proposed by Hermia [91].

5.2.1 Classical fouling mechanisms

Pore constriction (standard pore blockage)

Pore constriction which is graphically represented in Figure 5.2 is modelled with a mass balance equation relating decrease of the total volume of membrane pores, V (m^3) to the mass flux of foulant brought to the membrane surface with the permeate flow, Q_u ($m^3\ s^{-1}$), where u stands for 'unblocked' flow as it is the flow of fluid passing through the unblocked part of the membrane. Total flow through the membrane, denoted Q, is equal to the sum of the 'unblocked' flow Q_u and the 'blocked' flow Q_b as shall be later explained in the latter sections of this chapter.

$$\frac{dV}{dt} = -\beta\, Q_u\, C_b = -\beta\, J_u\, A_u\, C_b \tag{5.1}$$

Equation 5.1 relates the rate of pore constriction to bulk liquid concentration C_b ($g\ m^{-3}$). However not all particles in the bulk liquid deposit inside the membrane pores or even reach the membrane surface as will be later explained and demonstrated through simulations in Section 5.4. Proportionality constant β ($m^3\ g^{-1}$) is an aggregate parameter describing combined effects of selective transport of particles from the bulk liquid into the membrane's boundary layer due to cross-flow - see Section 5.4, shape and size of particles, particle density, floc size distribution (FSD), etc. Hence, pore constriction is described macroscopically, neglecting the complex particle-particle and particle-membrane interactions occurring over various spacial scales including molecular. It is thus likely that β will vary with environmental conditions such as pH, salinity, turbulence, temperature and, in case of bioreactors for wastewater treatment, SRT, concentrations and chemical composition of SMP and EPS, FSD, floc morphology, etc. The permeate flow through unblocked area Q_u is equal to the 'unblocked' permeate flux J_u ($m^3\ m^{-2}\ s^{-1}$) multiplied by the 'unblocked' membrane surface area A_u (m^2) as shown in Equation 5.1. If we assume that the membrane is composed of equally distributed cylindrical pores of length L (m) and radius r (m), which are additionally exposed to the same rates of fouling, Equation 5.1 can be written as:

$$\frac{d(N\pi r^2 L)}{dt} = -\beta Q_u C_b = -\beta J_u A_u C_b \tag{5.2}$$

where N denotes the number of pores per area A. Equation 5.2 can be rearranged into the following expression describing reduction of pore radius r in time:

$$\frac{dr}{dt} = -\frac{\beta\, C_b\, J_u}{2\,\phi_p\,\pi\, L\, r} \tag{5.3}$$

where $\phi_p = \left(\frac{N}{A}\right)$ (m^{-2}) denotes the number of pores per unit area. ϕ_p remains constant in time when pore constriction occurs on its own but will decrease with time if pore constriction occurs in parallel with pore blockage. Membrane resistance R (m^{-1}) can be calculated from the pore radius r with the *Hagen-Poiseuille* equation:

$$R = \frac{8\, L\, A}{N\,\pi\, r^4} = \frac{8\, L}{\phi_p\,\pi\, r^4} = \frac{8\, L}{\varepsilon\, r^2} \tag{5.4}$$

where $\varepsilon = \frac{A_p}{A}$ denotes the membrane area porosity and A_p (m^2) denotes the total area of *open* pores. Provided that the nominal pore radius is known a priori, i.e. initial condition for Equation 5.2 $r(t = 0) = r_0$ is given and the membrane thickness L is provided, the last remaining unknown, the total number of membrane pores N can be calculated using Equation 5.5 shown below:

$$N = N_0 = \frac{8\mu L Q_0}{\pi {r_0}^4 \Delta P_0} = \frac{8\mu L J_0}{\pi {r_0}^4 A \Delta P_0} \tag{5.5}$$

where Q_0 ($\mathrm{m}^3\ \mathrm{s}^{-1}$), J_0 ($\mathrm{m\ s}^{-1}$), and ΔP_0 (Pa) denote the initial flow, flux and pressure difference at the beginning of the filtration experiment, respectively. Alternatively, if the intrinsic membrane resistance R_m (m^{-1}) is known beforehand, e.g. determined during clean water filtration experiment, total number of membrane pores N can be calculated with Equation 5.6.

$$N = N_0 = \frac{8LA}{\pi R_m r_0^4} \tag{5.6}$$

Under assumption that ΔP = const., i.e. for constant pressure filtration, integration of Equation 5.2 yields the following equation representing a decrease of the unblocked flux in time.

$$\frac{J_u}{J_0} = \frac{Q_u}{Q_0} = \left(1 + \frac{\beta\, C_b\, Q_0}{N\,\pi\, L\, {r_0}^2}\, t\right)^{-2} \tag{5.7}$$

According to Darcy law resistance $R \propto 1/Q$, thus:

$$\frac{R}{R_0} = \frac{Q_0}{Q} = \left(1 + \frac{\beta\, C_b\, Q_0}{N\,\pi\, L\, {r_0}^2}\, t\right)^{2} \tag{5.8}$$

where t (s) in the above two equations denotes the time elapsed from the beginning of the filtration process.

Complete pore blockage

Complete pore blockage is modelled as loss of unblocked area A_u (m^2) resulting from occlusion of open pores by single particles with diameters d_p (m) greater than the pore

diameter d (m). $A_u \propto N_u$, where N_u denotes the number of unblocked membrane pores. Graphical representation of complete pore blockage is shown in Figure 5.2. Complete pore blockage assumes that open membrane pores are 'plugged' by individual particles as they deposit on the pores dragged by the convective forces of permeate flow. The particles are assumed not to deposit on top of the earlier deposited particles as in case of *intermediate pore blockage* or deposit anywhere else on the membrane. The loss of unblocked membrane area A_u is proportional to the concentration of the foulant C_b (g m^{-3}) and the 'unblocked' flow $Q_u = J_u A_u$ (m^3 s^{-1}) times the proportionality constant α (m^2 g^{-1}) - see Equation 5.9. α, similarly to the parameter β in *pore constriction*, is an aggregate parameter taking into account combined effects of selective transport of particles from the bulk liquid to the membrane's boundary layer due to convective velocity field associated with permeate flow, cross-flow, effects of adhesion and desorption of particles from the membrane, shape and size of particles, floc size distribution (FSD), etc.

$$\frac{dA_u}{dt} = -\alpha\, C_b\, Q_u = -\alpha\, C_b\, J_u\, A_u \tag{5.9}$$

If we express A_u in terms of the 'unblocked' flux and the 'unblocked' flow rate: $A_u = \dfrac{Q_u}{J_u}$ and describe J_u with *Darcy's* equation: $J_u = \dfrac{\Delta P}{\mu R_m}$, Equation 5.9 can be rearranged to give Equation 5.10.

$$\frac{dQ_u}{dt} = -\alpha\, \frac{\Delta P}{\mu\, R_m}\, Q_u\, C_b \tag{5.10}$$

By integrating Equation 5.10 with initial condition $Q_u(t = 0) = Q_0$ and under assumption that $\Delta P = \text{const}$, we obtain two algebraic equations expressing reduction of permeate flow (Equation 5.11) and increase of total resistance (Equation 5.12) due to complete pore blockage in constant pressure filtration.

$$\frac{Q_u}{Q_0} = \exp\left(-\alpha\, \frac{\Delta P}{\mu\, R_m}\, C_b\, t\right) \tag{5.11}$$

$$\frac{R}{R_0} = \exp\left(\alpha\, \frac{\Delta P}{\mu\, R_m}\, C_b\, t\right) \tag{5.12}$$

Equation 5.12 is obtained by inverting Equation 5.11 due to the fact that $R \propto 1/Q$. Initial resistance $R(t = 0) = R_0 = R_m$. t in Equations 5.11 and 5.12 represents the time elapsed from the beginning of the filtration process.

Intermediate pore blockage

Whereas the rate of area loss in *complete pore blockage* is proportional to the bulk liquid foulant concentration C_b and the 'unblocked' flow rate Q_u, in case of *intermediate pore blockage* $\dfrac{dA_u}{dt}$ is additionally proportional to the unblocked area divided by the initial

unblocked area: $\frac{Au}{A_0}$ as expressed in Equation 5.13.

$$\frac{dA_u}{dt} = -\alpha' C_b Q_u \frac{A_u}{A_0} = -\alpha' C_b J_u \frac{{A_u}^2}{A_0} \tag{5.13}$$

In case of new or chemically cleaned membranes it is assumed that $A_0 = A$. The proportionality constant α' has the same physical meaning as α in the *complete pore blockage* mechanism although their values are likely to be different. As pore blocking progresses, $\frac{Au}{A_0}$ becomes smaller thus reducing the rate of blockage. Such behaviour results from an assumption that particles can deposit on top of already deposited particles as shown in Figure 5.2. Thus, a lesser fraction of suspended particles actually contributes to membrane pore plugging. Additionally, as the pores get plugged and the unblocked membrane area A_u reduces, the probability of a particle landing on the unblocked area becomes lower, hence the rate of unblocked membrane area decreases. The probability of a particle landing onto an unblocked fraction of a membrane is assumed to be proportional to the fraction of the unblocked area in the total membrane area, hence appearance of the $\frac{Au}{A_0}$ term in Equation 5.13. In the same fashion as described in Section 5.2.1, Equation 5.13 can be rearranged to give Equation 5.14.

$$\frac{dQ_u}{dt} = -\frac{\Delta P}{\mu R_m}\alpha' Q_u C_b \frac{Q_u}{Q_0} \tag{5.14}$$

where μ denotes the dynamic viscosity of the permeate (Pa $\cdot$ s), R_m is the clean membrane resistance (m^{-1}), ΔP is the pressure difference across the membrane (Pa), and Q_0 is the initial flow rate through the membrane ($m^3\ s^{-1}$). Integration of Equation 5.14 with an initial condition $Q_u(t = 0) = Q_0$ and where ΔP = const gives the following equations for, respectively, decrease of the 'unblocked' flow rate and increase of the total resistance in time for *intermediate pore blockage*.

$$\frac{Q}{Q_0} = \left(1 + \alpha' \frac{\Delta P}{\mu\, R_m} C_b\, t\right)^{-1} \tag{5.15}$$

$$\frac{R}{Q_0} = \left(1 + \alpha' \frac{\Delta P}{\mu\, R_m} C_b\, t\right) \tag{5.16}$$

where t represents the time elapsed from the beginning of the filtration process.

Cake formation

Cake formation is a process in which solid particles deposit on the membrane surface and on top of one another forming a continuous porous layer of a finite thickness. This layer of deposited particles adds additional resistance R_p (m^{-1}) which increases together with cake thickness and decreases with cake porosity. The rate of increase of cake resistance is proportional to the influx of solid particles $J_b\, C_b$ times specific cake resistance R'

(m kg^{-1}) and fraction of total solids which contribute to the growth of cake, f' (–).

$$\frac{dR_p}{dt} = f'\,R'\,J_b\,C_b \tag{5.17}$$

The permeate flux J_b (m s^{-1}) is termed 'blocked' flux because cake formation is assumed to occur only over the blocked membrane area. Equation 5.17 is integrated with initial condition $R_p(t = t_p) = R_m + R_{p0}$, where t_p (s) denotes the time moment in which the section of the membrane under consideration is blocked, R_m (m^{-1}) denotes the clean membrane resistance, and R_{p0} (m^{-1}) denotes the additional resistance caused by fouling at time t_p. The integrated equation describing the increase of R_p in time is shown below.

$$R_p = \sqrt{(R_m + R_{p0})^2 + 2f'R'\frac{\Delta P}{\mu}C_b\,(t - t_p)} - (R_m + R_{p0}) \tag{5.18}$$

After R_p is expressed as a function of flux J_b with the Darcy's law, Equation 5.17 takes the following form:

$$-\frac{\Delta P}{\mu J_b^2}\frac{dJ_b}{dt} = f'R'J_bC_b \tag{5.19}$$

Equation 5.19 is rearranged and integrated with initial condition $J(t = t_p) = J_0$ where $\Delta P = \text{const}$ to yield the following algebraic equation expressing the rate of decrease of permeate flux and flow in time due to cake buildup.

$$\frac{Q}{Q_0} = \frac{J}{J_0} = \left(1 + f'R'\,\frac{2\,\Delta P}{\mu\,{R_m}^2}\,C_b\,(t - t_p)\right)^{-\frac{1}{2}} \tag{5.20}$$

Although R' is assumed here to remain constant, its value is likely to be changing in time during filtration in full-scale systems such as MBRs due to variations in hydrodynamic conditions affecting selective particle deposition, compressibility effects, changes in the particle shape and the particle size distribution, etc.

Hermia's equation

All four classical fouling laws for dead-end constant TMP filtration can be represented with a single second order differential equation first introduced by Hermia [91].

$$\frac{d^2t}{dV^2} = k\left(\frac{dt}{dV}\right)^n \tag{5.21}$$

where the value of n determines the fouling mechanism: $n = 2$ for complete pore blocking, $n = 1.5$ for standard pore blocking (aka pore constriction), $n = 1$ for intermediate pore blocking and $n = 0$ for cake filtration.

The first derivative $\dfrac{dt}{dV}$ is a reciprocal of $\dfrac{dV}{dt}$ which represents the volumetric flow rate $Q = J\,A$. Thus

$$\frac{dt}{dV} = \frac{1}{J\,A} \tag{5.22}$$

The second derivative $\frac{d^2t}{dV^2} = \frac{d}{dV}\left(\frac{dt}{dV}\right)$ can be written as $\frac{d}{dV}\left(\frac{1}{JA}\right)$ which after differentiation gives: $-\frac{1}{J^2\,A}\frac{dJ}{dV}$. Given that $dV = Q\,dt = J\,A\,dt$ the second derivative $\frac{d^2t}{dV^2}$ can be written as:

$$\frac{d^2t}{dV^2} = -\frac{1}{J^3\,A}\frac{dJ}{dt} \tag{5.23}$$

Once Equation 5.22 and Equation 5.23 are substituted into Equation 5.21 and after appropriate rearrangements, Equation 5.21 becomes:

$$\frac{dJ}{dt} = -k\,J^{3-n}\,A^{2-n} \tag{5.24}$$

Equation 5.24 describes how permeate flux decreases in time according to each classical fouling mechanism. Since Equation 5.21 as well as Equation 5.24 describe dead-end constant pressure filtration with no back-transport, the equation of Hermia was extended by Field et al. [62] to include the effects of crossflow. Equations 5.21-5.24 as well as the modified constant-pressure blocking equations incorporating cross-flow removal mechanisms can be found in the Appendix of the original research paper of Field et al. [62]. Hlavacek and Bouchet [95] reformulated Hermia equations for dead-end unstirred constant flux filtration. In the general form, constant flux unstirred filtration is expressed as:

$$\frac{d^2t}{d(\Delta P)^2} = k\left(\frac{dt}{d(\Delta P)}\right)^n \tag{5.25}$$

5.2.2 Concentration polarisation and gel layer formation

During filtration, a convective transport of solids, colloids and solutes from the bulk liquid towards the membrane surface is balanced by the rate of permeation of these solids, colloids and solutes into the effluent stream and the rate of back-transport from the membrane surface to the bulk liquid. The resulting mass balance can be expressed by the following equation:

$$J\,C = \dot{M}_b + J\,C_p \tag{5.26}$$

where $J\,C$ is the influx of solids, colloids and solutes towards the membrane surface, $J\,C_p$ is the rate of loss of solutes, colloids and solids due to permeation and $\dot{M}_b$ stands for the rate of back-transport. J denotes the permeate, C_p denotes the permeate stream concentration and C is the sought concentration vs. distance from the membrane surface.

When convective transport of solutes, colloids and solids exceeds the combined effect of back-transport and permeation though the membrane, these substances accumulate at the membrane-solution interface within a concentration boundary layer. As the accumulation progresses, a high concentration gradient developing near the membrane surface promotes back-transport of the accumulating material back to the bulk liquid finally leading to attainment of a steady-state concentration profile in which convective

transport is balanced with back-transport and permeation. Back-transport is usually proportional to the concentration gradient $M_b = D\frac{dC}{dz}$ where the proportionality constant D is a measure of diffusivity which in absence of turbulence is due to Brownian motion of particles and is magnified by shear in the presence of velocity gradients.

Development of concentration gradients near the membrane is known as *concentration polarisation* and is graphically described in Figure 5.3. *Concentration polarisation* has a negative effect on permeability because it increases the osmotic pressure π (see Section 5.2.3) and enhances fouling and scaling. Scaling develops when concentrations of low solubility salts near the membrane wall exceed their saturation concentrations leading to scale deposition on the membrane surface. Fouling is caused by elevated concentrations of biopolymers such as SMP and EPS which enhance such processes as cake formation and pore constriction. Furthermore, CP may trigger precipitation of organic solutes in the boundary layer leading to formation of a *gel layer* (see Figure 5.3), which may have greater selectivity and lower permeability than the membrane itself. Another detrimental effect of CP is increased permeation of the rejected materials due to locally increased trans-membrane concentration gradient and thus increased osmotic pressure. As described later in Section 5.4, the rate of back-transport of suspended matter and

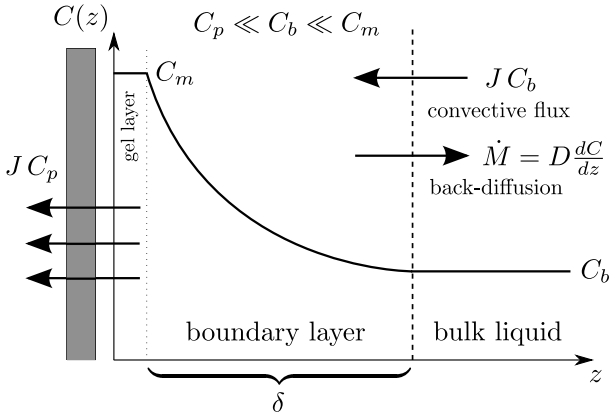

Figure 5.3: Concentration polarisation in the vicinity of the membrane.

colloids from the membrane back to the bulk liquid is proportional to particle diameter raised to the fourth power, $\dot{M}_b \propto {d_p}^4$. As a result, majority of solids is kept away from the membrane surface and thus *concentration polarisation* applies only to solutes and very small particles in the colloidal and macromolecular range. In microfiltration (MF) and ultrafiltration (UF) membranes with pore sizes in the range of 0.1 – 10 μ m and 0.01 – 0.1 μm respectively most of the constituents which may build up on the membrane surface due to *concentration polarisation* pass through the membrane thus decreasing or completely eliminating the concentration polarisation effect which may only occur due to existence of phase slip between the solvent and the solute in the membrane. *Concentration polarisation* may however become more prominent on heavily fouled membranes with clogged and constricted pores. Nevertheless, concentration polarisation becomes significant only in nanofiltration (NF) and reverse osmosis (RO) systems due to small pore sizes and hence, high rejection of macromolecular and solute materials.

5.2.3 Osmotic pressure

Osmotic pressure is the pressure which needs to be applied to a solution to prevent the inward flow of solvent across a semipermeable membrane [245]. Osmotic pressure arises from the tendency of a pure solvent to move through a semi-permeable membrane into solution containing a solute to which the membrane is impermeable. The flow of pure solvent is driven by osmotic pressure difference between the side where the solute concentration is low (i.e. osmotic pressure is high) and the side with higher solute concentration associated with lower osmotic pressure. Effects of osmotic pressure can be accounted for in the Darcy's equation expressed below:

$$J = \frac{\Delta P - \sigma_0 \, \Delta \pi}{\mu \, R_{tot}} \tag{5.27}$$

where J (m s^{-1}) denotes the permeate flux, μ (Pa s) denotes the dynamic permeate (solution) viscosity, ΔP (Pa) denotes the applied transmembrane pressure, R_{tot} (m^{-1}) is the total membrane resistance, and σ_0 and $\Delta\pi$ are the osmotic reflection coefficient and the osmotic pressure difference across the membrane, respectively. The osmotic reflection coefficient is a measure of the permselectivity of the membrane to the foulant and varies from one for a fully retentive membrane to zero for a non-retentive membrane. The osmotic pressure term is most often neglected in the classical fouling model, because it was found to be relatively small compared to the pressure loss caused by hydraulic membrane resistance and fouling. However, osmotic pressure may become important for ultrafiltration membranes or for heavily fouled microfiltration membranes where retention of smaller colloidal solutes becomes significant [97].

5.2.4 Biofilm growth

Biofilms are structured habitats of microorganisms within a polymer-EPS-matrix, which is produced by the microorganisms themselves [38]. Biofilms initially form on clean surfaces submerged in aqueous environments due to deposition and attachment of individual microorganisms, which is then followed by growth and EPS production. Biofilm growth occurs in all aqueous environments, especially those such as activated sludge systems within MBRs where bulk liquid concentrations of bacterial biomass and EPS are very high. In MBR systems biofilm growth is especially undesired as it forms on the surface of semipermeable membranes leading to partly reversible, partly irreversible fouling. It would therefore seem vital that biofilm growth is included as one of the fouling mechanisms in the membrane filtration model. Unfortunately, biofilm models are very complex and contain many unidentifiable parameters. Microbial growth kinetics and EPS production in biofilms are very hard to measure and mechanisms of EPS formation are still not well understood. Biofilm detachment rates, biofilm densities and degree of cross-linking are even harder to predict as the mechanisms are hardly understood today and little experimental data is available. Therefore, quantitative prediction of resistance caused by biofilm formation is very difficult and additionally, may

be computationally intensive. For these reasons, the biofilm model is not included in the model of membrane filtration and instead, the effects of biofilm formation are taken into account partly through mechanisms of pore constriction/irreversible fouling and cake formation/reversible fouling.

5.2.5 Scaling

Scaling can be neglected in microfiltration (MF) and also in ultrafiltration (UF) processes of majority of municipal wastewater (WW) in which concentrations of inorganic substances close to their maximum solubility levels are rare [19]. The situation may be different at some industrial wastewater treatment plants (WWTPs), especially those employing the UF process where concentration polarisation effects can lead to local existence of such high concentrations of inorganic substances in the vicinity of the membrane which will exceed their maximum solubility and thus will trigger the process of scaling. Since the MBR model developed here is for municipal wastewater only, scaling will not be modelled.

5.2.6 Resistance in series

Total pressure drop ΔP_t across a fouled membrane is usually subdivided for the purpose of modelling and analysis into several smaller pressure losses, each one corresponding to a different fouling mechanism. Hence, $\Delta P_t = \sum_i \Delta P_i$. As $\Delta P \propto R$ where R denotes resistance (m^{-1}), total membrane resistance R_t can be represented as the sum of resistances caused by individual fouling mechanisms, concentration polarisation (CP), biofilm growth, etc., as if the resistances were connected in series.

$$R_t = \sum_i R_i \tag{5.28}$$

Depending on the type of fouling mechanisms taking place on the membrane, R_i (m^{-1}) may be equal to: R_m for clean membrane resistance, R_c for cake resistance, R_i for resistance caused by pore constriction, R_b for resistance caused by pore blockage, R_{cp} for resistance caused by concentration polarisation, R_g for resistance caused by gel layer formation, and R_{bf} for resistance caused by biofilm growth. In the most complete model R_t then becomes:

$$R_t = R_m + R_c + R_i + R_b + R_{cp} + R_g + R_{bf} \tag{5.29}$$

5.3 Solute transport through a membrane

MF and UF membranes retain not just particulate materials but also some solutes and colloids such as SMP. SMP concentrations in the retentate stream have been found to be significantly lower from the concentrations in the bulk liquid. Drews et al. [47] reported

20-70% rejection for proteins (PP) and 75-100% rejection for polysaccharides (PS). However these values are likely to vary with the molecular weight distribution (MWD) of SMP, type of the membrane and the operating conditions. Retentive properties of the membrane may be represented by a dimensionless parameter $f_M = \frac{C_e}{C_b}$, where C_e and C_b denote the SMP concentrations (in g m^{-3}), respectively in the effluent (permeate) and in the bulk liquid. $f_M = R_F - 1$, where R_F denotes the membrane's rejection factor as later described in Section 7.2. Due to retentive properties of MF and UF membranes, SMP accumulates inside the bioreactor.

As explained in Chapter 3, SMP together with EPS have an influence on the physical properties of activated sludge such as FSD, non-settleable solids (NSS) fraction, SVI, zone settling velocity (ZSV), capillary suction time (CST), specific cake resistance (SCR) and viscosity. They also influence the activated sludge process kinetics [31] and, most importantly, they are found to be very strong membrane foulants. The above mentioned parameters additionally have an impact on performance of the downstream processes, especially sludge thickening and dewatering, by affecting the required energy inputs, coagulant and flocculant doses and dry solids content in the thickened and dewatered sludge.

Ability to predict SMP and EPS concentrations in the bioreactor is therefore of great significance as it allows us to quantify the bulk liquid's filterability, settling, thickening and dewatering properties. Modelling of SMP and EPS kinetics has been explained in Chapter 3 and Chapter 4. As shown in Tables 4.9 and 4.10 in Section 4.7.2, predictions of the effluent soluble chemical oxygen demand (SCOD) are more sensitive to f_M than to any of the kinetic or stoichiometric parameters in the biokinetic activated sludge model, while f_M can additionally substantially affect the bulk liquid SMP concentrations. A correct representation of SMP rejection on MF and UF membranes is therefore very important for three reasons: (a) it is mandatory to correctly predict the fouling propensity of bulk liquid, (b) it is required for estimation of kinetic and stoichiometric parameters of SMP and EPS kinetics in the activated sludge model, (c) it is required correctly predict the effluent SCOD in MBR effluents.

Some researchers postulate that rejection of SMP by MF and UF membranes occurs primarily through sieving, i.e. exclusion of SMP molecules with diameters larger than the diameters of the membrane pores, [26, 104, 222]. Although influents to WWTPs contain soluble organic matter (SOM) of, generally, very low molecular weight (MW) fractions below 0.5 kDa [8] which will pass entirely through a MF membrane (see Figure 2.2 on page 34), biological effluents and bulk liquids in activated sludge bioreactors contain organic compounds with a broad MW spectra from <0.5 kDa to >50kDa which tend to contain larger MW material under higher SRTs. Shin and Kang [222] observed that 20% of SOM in the supernatant from three MBRs operating at SRTs between 40 and 130 days had MWs of over 100 kDa. These organic molecules are larger than the molecular weight cut-off (MWCO) of a MF membrane and would therefore be entirely captured on ground of size exclusion (sieving). However, often higher SMP rejection

rates than MWD of SMP would suggest, are observed in MBR reactors. It is postulated that these additional rejection effects may be attributed to additional sieving by thin, low-porosity fouling layers forming on the membrane surface and by agglomeration and precipitation of SMP molecules in the concentration polarisation region. Song et al. [226] proposed another theory postulating that SMP rejection on MF membranes might also happen due to lower mobility of SMP inside the membrane in comparison to the solvent [210, 40]. As SMP has higher affinity to membrane material than water, convection velocity of SMP (v_s) is slower from water velocity (v_w), resulting in the so-called 'phase-slip'. This effect is described in Equation 5.30

$$v_s = \alpha_R \, v_w \tag{5.30}$$

where α_R (–) denotes the so-called SMP retardation coefficient. Song et al. [226] described the transport of SMP through a porous membrane with a stationary advection/dispersion equation where dispersion coefficient D (m^2 s^{-1}) is related to the flow velocity v_w through a proportionality constant β_L (m) denoting the longitudinal dispersion length.

$$D = \beta_L \, v_w \tag{5.31}$$

Solute transport in porous media is governed by advection/dispersion equation, [188, 60] where advection is caused by forward, convective transport of solutes with fluid flow, whilst dispersion is due to existence of different flow paths in the porous medium. Transport of SMP through a MF membrane can be modelled in the same fashion with a one-dimensional parabolic advection-dispersion equation first introduced by Lapidus and Amundson [134]. The equation is expanded with source and sink terms to represent loss and production of SMP as a result of sorption/desorption processes. Advection-dispersion partial differential equation (PDE) was used by Song et al. [226] to describe solute transport through a MF membrane. Wrong interpretation of the equation led to the conclusion that dispersion leads to reduction of SMP concentration, i.e. is a mass sink. This is naturally not true as dispersion does not affect mass balance, only the temporal and spatial distribution of solute concentration in the membrane and time response characteristics, as shown in Figure 5.4.

$$\frac{\partial C}{\partial t} = \beta_L \, v_w \, \frac{\partial^2 C}{\partial x^2} - \alpha_R \, v_w \, \frac{\partial C}{\partial x} + \sum \text{sources} - \sum \text{sinks} \tag{5.32}$$

Since SMP is not produced anywhere inside the membrane $\sum \text{sources} = 0$. SMP mass sinks $\left(\sum \text{sinks}\right)$ are caused by deposition of SMP inside the membrane pores, i.e. by pore constriction. This process is is assumed to be described with reversible non-linear sorption kinetics [188].

$$\frac{\partial S}{\partial t} = k_s \, C^{N_s} - k_r \, S \tag{5.33}$$

$$\frac{\partial C}{\partial t} = -\frac{\partial S}{\partial t} \tag{5.34}$$

where S (g m^{-3}) denotes the amount of SMP sorbed onto the pore surface, and k_s

(g^{1-N} m^{3N_s-3} s^{-1}) and k_r (s^{-1}) are the rates of, respectively, sorption and desorption, and N_s is a non-dimensional sorption non-linearity constant. Whilst, for the purpose of this study, it is appropriate to assume that parameters k_s, k_r and N_s are constant for a given membrane configuration, Ye et al. [266] found that the rate of protein deposition/sorption inside or on the membrane surface is in the positive relationship with permeate flux. Ye et al. [266] found this relationship to be exponential and described it with the film model. Exponential relationship between the rate of irreversible fouling and permeate flux was also experimentally found in Chapter 6, as shown in Figure 6.2 on page 190. The film model assumes that diffusion through a laminar boundary layer is a limiting process in sorption, which leads to quite a different equation for the rate of sorption than Equation 5.33. As the main aim of this study is to determine whether SMP sorption inside the membrane might have any effect on permeate SMP concentrations, accurate formulation of SMP sorption vs. flux is not crucial. Hence, it was decided that the process is modelled with the earlier chosen Equations 5.33 and 5.34 in which the parameters k_s, k_r and N_s are assumed to remain constant regardless of flux.

Solution of Equation 5.33 under equilibrium produces the Freundlich isotherm. Obtaining information about sorbed concentration S is not as important as information about the pore diameter, which is gradually reduced as SMP is being sorbed inside the membrane pores. The rate of pore constriction, i.e. reduction of pore diameter can be related to the rate of sorption as shown in Equation 5.35

$$\frac{\partial d_p}{\partial t} = \frac{\partial S}{\partial t}\frac{d_p}{2\,\rho_s} \tag{5.35}$$

where ρ_s (kg m^{-3}) denotes the SMP density. ρ_s is assumed to be equal to protein density, whose well established value is 1.35 kg m^{-3}.

Equations 5.33-5.35 are collated by the author and supplemented with the following initial and boundary conditions to create a well-formed initial boundary value problem (IBVP):

$$\begin{aligned}
\frac{\partial C}{\partial t} &= \beta_L\, v_w \frac{\partial^2 C}{\partial x^2} - \alpha_R\, v_w \frac{\partial C}{\partial x} + k_s\, C^{N_s} - k_r\, S \\
\frac{\partial d_p}{\partial t} &= \frac{\partial S}{\partial t}\frac{d_p}{2\,\rho_s} \\
\mathbf{S}(t=0) &= 0 \\
\mathbf{C}(t=0) &= 0 \\
\mathbf{d}_p(t=0) &= d_{p0} \\
C(x=0) &= f\,\frac{v_s}{v_w} C_b \\
\left.\frac{\partial C}{\partial x}\right|_{x=L} &= 0
\end{aligned} \tag{5.36}$$

Here, d_{p0} (m) denotes the initial pore diameter, C_b (kg m^{-3}) denotes the SMP concentration in the bulk liquid, v_s and v_w are the advection velocities of, respectively, SMP and water (m s^{-1}) and f is a non-dimensional parameter describing the fraction

of SMP which infiltrates into the membrane. The above IBVP problem is formulated using an explicit time-marching finite difference scheme. Equation 5.32 is discretised using a *leapfrog scheme* for the time derivative and a 1st order backward difference for the advection term.

$$\frac{C_i^{j+1} - C_i^{j-1}}{2\,\Delta t} = \beta_L\, v_w\, \frac{C_{i-1}^{j-1} - 2\,C_i^{j-1} + C_{i+1}^{j-1}}{\Delta x^2} + \alpha_R\, v_w\, \frac{C_i^j - C_{i-1}^j}{\Delta x} + k_s\, {C_i^j}^{N_s} - k_r\, S_i^j \tag{5.37}$$

The equations were discretised in space with a uniform grid where each point has an associated index $i = 1 : M$ where $M = \dfrac{L}{\Delta x} + 1$. The time domain was divided into N points with indices $j = 1 : N$ where $N = \dfrac{t_{end} - t_0}{\Delta t}$. With membrane thickness L arbitrarily discretised into 500 points ($M = 500$) in the longitudinal direction, the time step Δt was calculated from Δx and advection velocity v_s using a maximum Courant number criterion $\Delta t \leqslant Co\,\dfrac{\Delta x}{v_s}$, where $Co = 0.4$. Diffusion term in the equation is evaluated in the previous time step $j - 1$ instead of $j = 1$ to eliminate numerical instability. The system of discretised equations is formulated as follows:

$$\forall\, i \in \langle 2, M\rangle \quad C_i^{j=1} = 0 \tag{5.38}$$

$$\forall\, i \in \langle 1, M\rangle \quad S_i^{j=1} = 0 \tag{5.39}$$

$$\forall\, i \in \langle 1, M\rangle \quad d_{p,i}^{j=1} = d_{p0} \tag{5.40}$$

$$\forall\, j \in \langle 1, N\rangle \quad C_{i=1}^j = f\,\frac{v_s}{v_w}\,C_b \tag{5.41}$$

$$\forall\, i \in \langle 2, M-1\rangle, j \in \langle 2, N-1\rangle \quad C_i^{j+1} = C_i^{j-1} + \Big(\beta_L\, v_w \frac{C_{i-1}^{j-1} - 2\,C_i^{j-1} + C_{i+1}^{j-1}}{\Delta x^2} + \alpha_R\, v_w \frac{C_i^j - C_{i-1}^j}{\Delta x} + k_s\, {C_i^j}^{N_s} - k_r\, S_i^j\Big)\,\Delta t \tag{5.42}$$

$$\forall\, j \in \langle 2, N-1\rangle \quad C_M^{j+1} = C_M^{j-1} + \Big(\beta_L\, v_w \frac{C_{M-1}^{j-1} - C_M^{j-1}}{\Delta x^2} + \alpha_R\, v_w \frac{C_M^j - C_{M-1}^j}{\Delta x} + k_s\, {C_M^j}^{N_s} - k_r\, S_M^j\Big)\,\Delta t \tag{5.43}$$

$$\forall\, i \in \langle 1, M\rangle, j \in \langle 2, N-1\rangle \quad d_{p,i}^{j+1} = d_{p,i}^{j-1} - \Big(k_s\, {C_i^j}^{N_s} - k_r\, S_i^j\Big)\,\frac{d_{p,i}^j\,\Delta t}{\rho_p} \tag{5.44}$$

Equations 5.38 - 5.44 are solved with two different sets of parameters resulting in two simulation scenarios (**Simu 1** & **Simu 2**). The parameters used in both simulation scenarios are presented in Table 5.1. The first simulation run (**Simu 1**) was carried out for two permeate fluxes: $J = 20$ L m^{-2} h^{-1} and $J = 40$ L m^{-2} h^{-1} with SMP retardation coefficient $\alpha_R = 0.5$. The results of **Simu 1** for four different time snapshots: $t = 2$, 8, 15 and 1800 seconds are presented in Figure 5.5 which shows the movement of the SMP concentration front across the membrane as a result of step change in the bulk SMP concentration C_b. The SMP concentration inside the membrane $C(x, t)$ can reach a maximum value of $f\,\alpha_R\,C_b$ which for $f = 1$ and $\alpha_R = 0.5$ is equal to 50% of C_b.

Translation velocity of the moving front is proportional to the solute velocity v_s minus diffusion-like effects represented here by SMP dispersion factor β_L. These diffusion-like effects have no relation to Brownian diffusion but result from solute particles taking different routes (channels) as they pass through porous membrane material. Contrary to the earlier mentioned results of Song et al. [226], reduction of SMP across the membrane is only due to sieving and retardation effects, not to dispersion which only changes the shape of the concentration front, not its magnitude.

Effluent SMP concentrations C_e resulting from a step change in bulk SMP concentration C_b are calculated for three different dispersion factors β_L in the 2$^{\text{nd}}$ simulation run (**Simu 2**) as shown in Figure 5.4. Although dispersion affects the membrane's time response characteristics, the measured time-constants are found to be very low, usually less than a minute. As can be seen in Figure 5.4, for the largest of the three dispersion factors $\beta_L = 9$ and for a relatively low permeate flux of 20 L m^{-2} h^{-1} time constant is less than 20 seconds. The membrane's dynamics are therefore much faster then the bioreactor's dynamics and hence it is justifiable to neglect the membrane's dynamic effects in modelling of MBR reactors. SMP sorption inside the membrane pores was

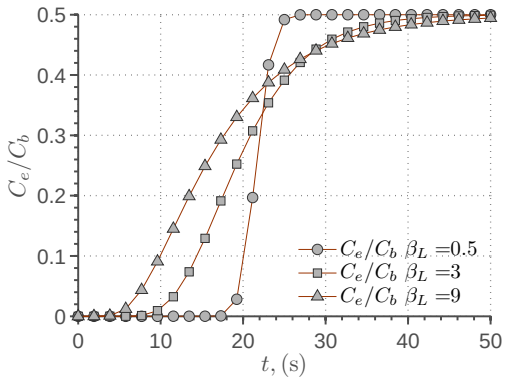

Figure 5.4: SMP concentration on the permeate side vs. time after step change in the bulk liquid concentration for different proportionality constants β_L of the dispersion coefficient D.

found to have no effect on effluent SMP concentrations C_e. As can be seen in Figure 5.5 after sufficient amount of time, given that C_b remains constant, the effluent SMP concentration C_e is stabilised at the value equal to the SMP concentration at the front end of the membrane. Hence, no SMP gradient across the membrane is observed. Although with the chosen kinetics, sorption had no effect on effluent SMP concentrations, it led to a significant reduction in membrane permeability. The results of the 1$^{\text{st}}$ simulation run (**Simu 1**) show a 12% reduction in the mean pore diameter within just 30 minutes (1800 seconds) from the beginning of the filtration experiment, which is a very large loss of permeability given such a short time-scale. To summarise, it was shown that sorption of solutes inside the membrane has no effect on effluent SMP concentrations and that despite of dispersion effects due to differences in pore channel lengths and connectivity between the pores, the membrane exhibited very fast dynamics in range of seconds compared to the dynamics of the bioreactor (minutes-hours). Membrane

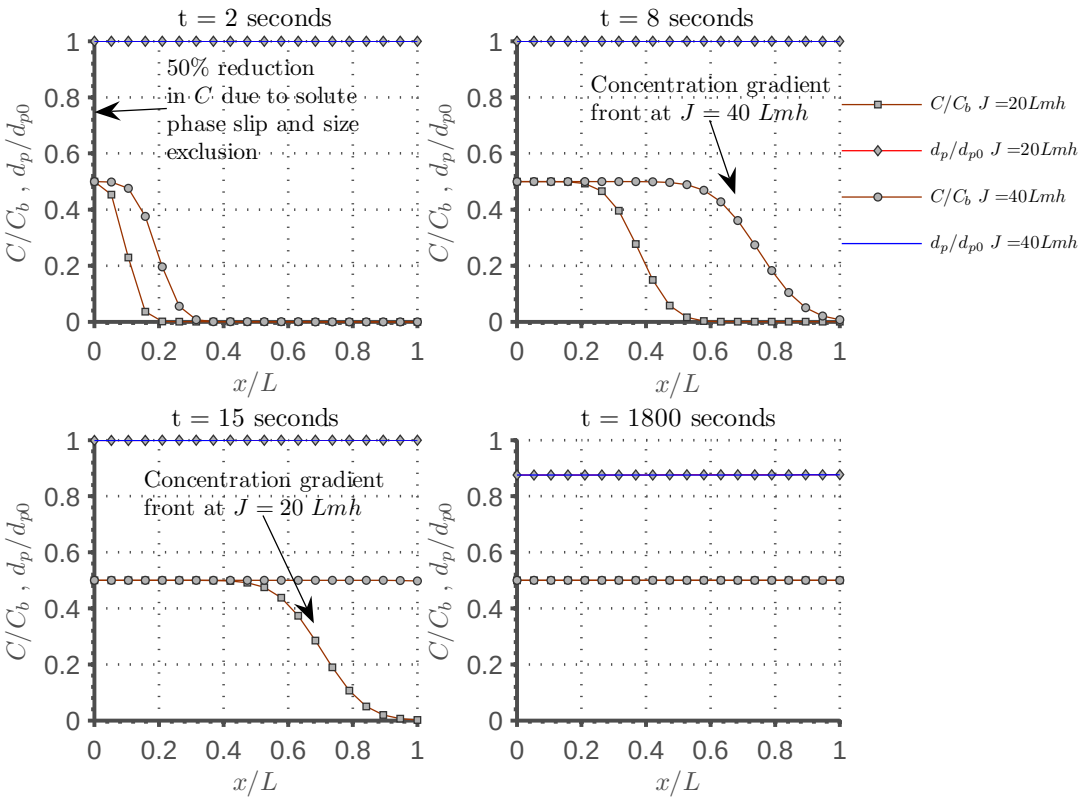

Figure 5.5: Solute concentration profiles C/C_b along the membrane thickness and membrane pore diameters d_p obtained at four selected time moments during the simulation of unsteady convective-dispersive transport with adsorption of solutes.

dynamics can therefore be neglected in MBR models without sacrificing the model's accuracy. The membrane's selectivity and retentive properties to SMP are on the other hand of great importance as they influence the effluent SMP and SCOD concentrations - see Table 4.9 and Table 4.10. To what degree the retentive properties of MF and UF membranes depend on just sieving and to which on transport retardation effects is however unknown.

Table 5.1: Model parameters used in the simulation of SMP transport through a membrane with an unsteady convective-dispersive transport model with adsorption of solutes.

Parameter	Description	Unit	Value	
			Simu 1	Simu 2
Membrane thickness	L	μm	100	
Fraction of SMP in permeate	f	–	1	
SMP retardation coefficient	α_R	–	0.5	
SMP dispersion factor	β_L	–	1	$[0.5, 3, 9]$
Permeate flux	J	L m^{-2} h^{-1}	$[20, 40]$	20
Initial SMP concentration in the membrane	C_0	kg m^{-3}	0	
Bulk SMP concentration	C_b	kg m^{-3}	200	
Membrane porosity	ε	–	0.6	
Mean pore diameter	d_p	μm	0.1	
Density of proteins	ρ_p	kg m^{-3}	1.35	
Sorption rate	k_s	s^{-1}	$2 \cdot 10^{-6}$	
Desorption rate	k_r	s^{-1}	$1 \cdot 10^{-6}$	
Non-linearity coefficient in the sorption model	N_s	–	1	

5.4 Balance of forces on a particle during filtration

Classical macroscopic fouling equations described in Sections 5.2.1-5.2.1 proved successful at predicting filtration characteristics of different kinds of monodisperse as well as polydisperse suspensions through various types of membranes [96, 50, 261]. The model equation parameters do, however, need to be calibrated on a case by case basis. Although the classical fouling equations assume these parameters are invariant in time, they, as shall be shown later, depend on a number of often time-varying external factors such as operating conditions of the membrane filtration unit and the bioreactor, biochemical and physical characteristics of the liquid being filtered and the physico-chemical properties of the membrane. In particular, the rates of pore blockage and cake formation and specific cake resistance depend on the suspension's floc size distribution (FSD), pore size distribution (PSD) of the membrane and hydrodynamic conditions in the vicinity of the membrane. In order to describe these effects, we need to look at filtration from the microscopic rather than macroscopic point of view by analysing the behaviour and fate of individual particles in the suspension while it is being filtered through the membrane.

The fate of a particle which came to find itself in the proximity of the membrane depends on the balance of forces acting upon it. The particle will deposit on the membrane causing pore blockage or cake growth or inside the membrane causing pore constriction if the drag force associated with permeate flux and the adhesive forces between the particle and the membrane prevail over the turbulence induced forces of back-diffusion and inertial lift. In case back-diffusion and inertial lift prevail over the adhesive and drag forces, the particle will be kept away from the membrane and carried back into the bulk liquid. The forces responsible for carrying the particle towards the membrane and the forces acting on the particle in the reverse direction to the direction of flow happen to be proportional to particle diameter d_p raised to different exponents.

These differences in functional relationships between different forces acting on a particle and particle sizes explains the phenomenon of selective deposition, where particles with diameter larger than the so-called *cut-off diameter* are kept away from the membrane whilst smaller particles deposit on the membrane or cake, within the cake, inside the membrane pores or pass through the membrane into permeate. Although calculation of forces acting on single individual particles may be very challenging or even impossible due to lack of reliable measurement probes and thus difficulties in identification of model parameters, simplified theoretical analysis is still possible and may help us broaden our understanding of fouling processes. In particular, the observed effects of air scouring rates, CFVs and permeate fluxes on rates of pore constriction, pore blockage, cake formation and specific cake resistance can be better understood and explained on a theoretical basis.

In this section equations published by different researchers in various scientific publications are combined by the author in order to formulate a complete model of selective deposition of particles in an air-sparged immersed system. This model is then simulated for a wide range of particle diameters in order to calculate cut-off diameters corresponding to different permeate fluxes and air scouring rates. It is necessary to point out that the selective deposition model which shall be described in more detail in the next section is purely theoretical and has not been validated in any manner in this study. The model is therefore not used to provide exact numerical values of i.e. cut-off diameters but to theoretically examine the fate of particles in the suspension under filtration conditions and to derive approximate functional characteristics between cut-off diameters, permeate fluxes and air scouring rates.

Dominant forces acting on a single particle in the vicinity of the membrane and after the particle has deposited on the membrane surface are presented in Figure 5.6. The directions and magnitudes of forces acting on a particle will depend not only on the operating conditions of the filtration unit but also on positioning and configuration of the membrane. The two main types of filtration are, as explained in Chapter 2, Moderate cross-flow filtration implemented in immersed flat sheet (FS) and HF MBRs and high cross-flow filtration implemented in sidestream MBR configurations. The type of filtration considered in this study is, as mentioned already in the previous paragraph, an air-sparged immersed system which will be considered in Chapter 7 during the development of an integrated MBR model.

Selective deposition of particles in immersed systems was recently covered by Hwang and Chen [106], whereas in cross-flow systems this subject was thoroughly covered by a greater number of scientists such as Wang et al. [250], Altmann and Rippergen [5], Vyas et al. [246] and Knutsen and Davis [124].

5.4.1 Force balance analysis in an immersed MBR configuration

The balance of forces acting on a single particle can be calculated for a particle which finds itself in the vicinity of the membrane but is not attached to it and for a particle that

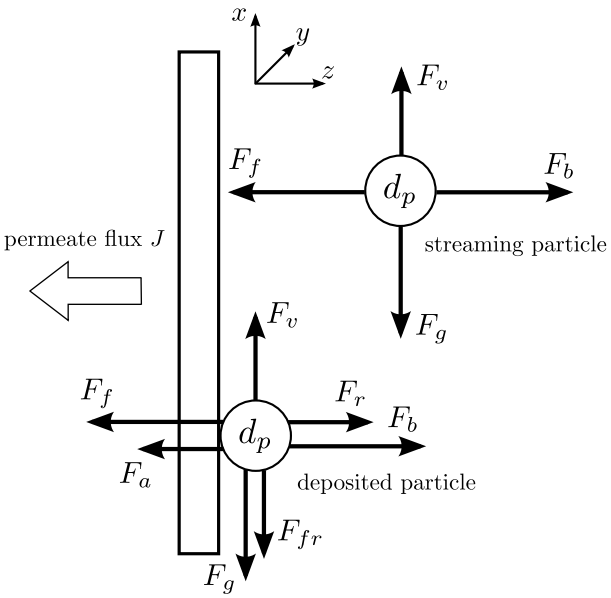

Figure 5.6: Balance of forces acting on a single particle deposited on the membrane surface and in the vicinity of the membrane during filtration.

F_v - drag force due to tangential flow [a], F_f - drag force due to permeate flow, F_g - net force due to gravity and buoyancy, F_a - adhesive force, F_{fr} - friction force, F_b - forces of back-transport, F_r - repelling force.

[a] Depending on the configuration of the filtration unit, tangential flow effects are caused by either the velocity of liquid passing around the membrane, the movement of rising air bubbles, slugs or caps, or a combination of the two.

is already deposited on the membrane surface. These two scenarios are distinct as these two particles will be subjected to different types of forces. Whilst the streaming particle is subjected only to hydrodynamic forces of the fluid flow, the particle deposited on the membrane is additionally subjected to interparticle forces and surface wall friction.

A single spherical particle in the feed experiences drag by the velocity field pointing towards the membrane and associated with the permeate flow J. The resulting force F_f is calculated from the Stokes law under a valid assumption that the flow is laminar (i.e. low velocities or particle diameters) and a not-so valid assumption that the particle is isolated in a continuous viscous fluid (no interactions between the particles). The equation is multiplied by an empirical correction factor C_1 which increases the magnitude of the force from Stokes' law to take into account the the effects of the proximity of porous wall, i.e. membrane. The equation then becomes:

$$F_f = 3\,C_1\,\pi\,\eta_b\,d_p\,J \tag{5.45}$$

where η_b denotes the feed viscosity (Pa s), d_p denotes the particle diameter (m) and J is the permeate flux (m s^{-1})

The correction factor C_1 may be calculated using several different equations developed by various researchers such as Equation 5.46 by Goren [75], Equation 5.47 by Sherwood [220] or Equation 5.48 by Chang and Acrivos [22]. In this study the model of Chang and Acrivos [22] is used as the first two models tend to favour larger particles

too much leading to the behaviour where larger particles are subjected to stronger longitudinal forces than smaller particles and, in consequence, the particle cut-off effect is not predicted.

Having said this, the model of Chang and Acrivos [22] needs to be treated with some reservation. Although for high porosities the qualitative behaviour of the model is correct as the drag correction coefficient rightfully tends to 1 meaning that the wall effects reduce to zero as the additional resistance of the wall disappears, the model behaviour at the lower end of porosities is, at best, questionable. For porosities tending to 0 the correction factor tends to infinity, which is obviously incorrect. From the shape of the curve, it looks like the lower end of membrane porosities to which the equation is likely to be correct is 0.2, for which the predicted correction coefficient is equal to 1000. For lower porosities below 0.2 the outputs of the equation rapidly rise to very high, physically incorrect values. It is possible that the equation was fitted to limited number of data points covering a limited range of porosities beyond which the model loses its application. Although this operating region is not known to the author, this study is based under an assumption that $\phi = 0.25$ which is very close to the porosity value of 0.3 applied by Wang et al. [250] in their study of particle deposition in crossflow filtration employing the same equation of Chang and Acrivos [22]. Hence, it is very likely that we are within the intended operating reqion of the equation and out study is valid (under an additional assumption that the equation of Chang and Acrivos [22] is universal and applies to our system).

$$C_1 = 0.36 \left(\frac{R_t \, {d_p}^2}{4 \, L} \right)^{0.4} \tag{5.46}$$

where R_t denotes the total membrane resistance (m^{-1}) and L denotes the membrane thickness (m).

$$C_1 = \sqrt{\frac{R_t \, d_p}{3} + (1.072)^2} \tag{5.47}$$

where R_t denotes the total membrane resistance (m^{-1}).

$$C_1 = 10 \, \frac{1 - \phi}{\phi^3} \tag{5.48}$$

where ϕ denotes the membrane porosity (–) and the value of $\phi = 0.25$ has been used in this study.

The particle is also subjected to a tangential drag force F_v resulting from mechanical agitation and bubble flow. F_v is calculated again with a modified Stokes equation with a correction factor C_2 describing the proximity effects of the membrane and cake.

$$F_v = 3 \, C_2 \, \pi \, \eta \, d_p \, u_0 \tag{5.49}$$

where u_0 (m s^{-1}) denotes the fluid velocity around the deposited particle caused by turbulence, i.e. eddy velocity.

The non-dimensional correction factor C_2 is equal to 1.70 according to O'Neill [194] whereas Rubin [215] found this coefficient to be slightly larger and equal to 2.11. In this study the former coefficient of O'Neill [194] has been chosen; however the final results, i.e. calculated cut-off particle diameters were found to be insensitive to the choice of C_2.

Although Equation 5.49 is valid only for very low particle concentrations where particle interactions are minimal, the effects of higher particle concentrations will not be considered in this study due to lack of available information for identification of model parameters and for simplicity. For more information about correction factors accounting for the presence of particles at higher concentrations, the reader is referred to Brinkmann [16] and Tam [235].

Fluid velocity around the particle u_0 (m s^{-1}) is calculated from the apparent shear intensity of fluid turbulence G (s^{-1}) and Kolmogorov eddy size λ_k (m).

$$u_0 = \lambda_k \, G \tag{5.50}$$

The apparent shear intensity G is obtained from Equation 5.51 ofy Logan [155] as proposed in Li and Wang [147] and Wu et al. [262].

$$G = \left(\frac{\rho_b \, g \, v_{csg}}{\eta_b} \right)^{0.5} \tag{5.51}$$

where ρ_b (kg m^{-3}) and η_b (Pa $\cdot$ s) denote, respectively, the bulk liquid density and dynamic viscosity, and v_{csg} (m s^{-1}) denotes the superficial air velocity which is obtained by dividing total air flow Q_a (m^3 s^{-1}) by net cross-sectional area of the membrane A (m^2): $v_{csg} = \dfrac{Q_a}{A}$. $A = A_t - A_m$ where A_t is the total cross-sectional area of the membrane tank and A_m is the cross-sectional area occupied by the membrane.

Whilst it is assumed that bulk liquid density is equal to water density, i.e. $\rho_b = \rho_w$, dynamic bulk liquid viscosity η_b is calculated as a function of mixed liquor suspended solids (MLSS) with equations introduced in Section 5.6.1 on page 176.

The value of λ_k (m) is obtained from Equation 5.52 [155].

$$\lambda_k = \left(\frac{\eta_b}{\rho_b \, G} \right)^{0.5} \tag{5.52}$$

The force of back-transport (F_b) which keeps the particles away from the membrane surface can be attributed to three mechanisms: *inertial lift*, *shear-induced diffusion* and *Brownian diffusion*. The theory of inertial lift was introduced by Green and Belfort [77], Altena and Belfort [4] and Weigand et al. [254] and states that the net particle transport towards the membrane is reduced by the lift force directed away from the membrane surface and resulting from the interactions between the flow field and the membrane wall. The shear-induced diffusion on the other hand arises from particle-particle, not particle-wall interactions in a shear field which results in lateral migrations of particles from their instantaneous trajectories. Brownian diffusion is a lateral migration of particles from

their main trajectories (e.g. set by liquid flow) due to random drifting.

The force of back-diffusion is calculated, similarly as in the case of F_v and F_f, with the Stokes' law where back-transport velocity term v_b (m s^{-1}) is calculated either from the theory of back-diffusion, inertial lift or Brownian diffusion:

$$F_b = 3\,\pi\,\eta\,d_p\,v_b \tag{5.53}$$

where v_b (m s^{-1}) is the back diffusion velocity.

The Brownian diffusion coefficient, and ultimately the the Brownian diffusion velocity v_b is estimated from the Stokes-Einstein equation: $D_b = \dfrac{kT}{3\,\pi\,\eta\,d_p}$ where k is the Boltzmann's constant (1.38×10^{-6} g cm^2 s^{-2} K^{-1}) and T (K) is the absolute temperature. Since Brownian diffusion is inversely proportional to particle diameter d_p, it only affects the motion of the particles of submicron dimensions such as macromolecules. Its effects are negligible for larger particles of colloidal dimensions and above and thus Brownian diffusion shall not be considered in this model. Transport models based only on Brownian diffusion as back-transport mechanism, such as *gel polarisation model* or *film theory* are found to grossly underpredict the fluxes for e.g. colloidal suspensions due to low diffusivity of colloids and particles. This discrepancy was discovered by Green and Belfort [77] and termed *"flux paradox"*.

As, by definition, shear induced diffusion is a product of particle-particle interactions, the magnitude of back-diffusion from the membrane surface to the bulk liquid depends on particle concentration. Eckstein et al. [51] proposed the following empirical equation for the diffusivity of rigid spherical particles due to particle collisions:

$$D(\phi) = \begin{cases} 0.1\,\dot{\gamma}\,\dfrac{d_p^2}{4}\,\phi & \text{if } 0.0 < \phi < 0.2 \\ 0.025\,\dot{\gamma}\,\dfrac{d_p^2}{4} & \text{if } 0.2 < \phi < 0.5 \end{cases} \tag{5.54}$$

where $\dot{\gamma}$ denotes the shear rate (s^{-1}) and ϕ is the particle volume fraction.

Leighton and Acrivos [141; 142] found a different correlation based on their own results arguing that the results by Eckstein et al. [51] were biased by wall effects which led to underestimation of the diffusion coefficient.

$$D_s = \frac{\dot{\gamma}\,d_p^2\,\hat{D}_s(\phi)}{4} \tag{5.55}$$

where $\hat{D}_s(\phi)$ is a dimensionless function of the local particle volume fraction ϕ:

$$\hat{D}_s(\phi) = 0.33\,\phi^2\left(1 + 0.5\,\mathrm{e}^{8.8\phi}\right) \tag{5.56}$$

and is reported to be valid for particle volume fractions up to $\phi = 0.5$.

So far, no expression for the force of back-transport due to shear induced diffu-

sion has been proposed and then validated, according to the author's current state of knowledge, for an immersed MBR. Whilst a number of alternative expressions for shear-induced back diffusion exist it is hard to say which ones may be applicable to immersed membrane systems for wastewater treatment without prior study and validation. Since no data for validation are available in this study and straight off-the-shelf adoption of one of the published shear induced diffusion models for cross-flow filtration units may be too risky, shear induced diffusion has not been adopted in this particle deposition model.

In inertial lift, which is selected in this study as the only particle back transport mechanism, the back diffusion velocity v_b is substituted with inertial lift velocity v_l which is calculated from Equation 5.57 [246].

$$v_l = \frac{b\,\rho_b\,{\gamma_w}^2\left(\frac{d_p}{2}\right)^3}{16\,\eta_b} \tag{5.57}$$

where ρ_b (kg m^{-3}) denotes the bulk liquid density, γ_w (s^{-1}) is the shear rate at the wall, η_b (Pa $\cdot$ s) denotes the dynamic viscosity of the feed, and b is a dimensionless parameter which is a function of a dimensionless distance from the membrane wall. Vyas et al. [246] found this parameter to be equal $b = 0.577$. The same equation for calculating inertial lift velocity was used by Vasseur and Cox [241] although in their paper they used the value of $b = 1.694$ which is about three time that of Vyas et al. [246]. In this study, the value of $b = 2.885$ which is five times that of Vyas et al. [246] had to be adopted in order to obtain qualitatively plausible values of particle cut-off diameters.

The shear stress at the membrane wall τ_w is calculated from fluid velocity around the particle u_0 using Equation 5.50.

$$\tau_w = \frac{2\,\eta_b\,u_0}{d_p} \tag{5.58}$$

The shear rate at the wall γ_w is then calculated from τ_w

$$\gamma_w = \frac{\tau_w}{\eta_b} \tag{5.59}$$

where dynamic bulk liquid viscosity η_b is calculated from dynamic water viscosity η_w and bulk solids concentration X_{MLSS} using Equation 5.77 shown on page 176.

After substituting the back-diffusion velocity v_b with the inertial lift velocity v_l, Equation 5.53 becomes:

$$F_b = 3\,\pi\,\eta\,d_p\,v_l = 3\,\pi\,\eta\,d_p\,\frac{b\,\rho_b\,{\gamma_w}^2\left(\frac{d_p}{2}\right)^3}{16\,\eta_b} \tag{5.60}$$

Adhesive forces acting on the deposited particle result from a combination of several intermolecular forces: Van der Waals forces, electrostatic forces and capillary forces.

The capillary forces can be neglected in aqueous solutions [17]. The electrostatic forces can be divided into attractive and repelling parts. As in MBRs these forces are mainly repelling, the attractive part can also be neglected [118]. The repelling electrostatic force can be calculated e.g. using the sphere-plane electrical double-layer force expression by Hogg et al. [99].

$$F_e = 2\pi\, a\, \epsilon\, \epsilon_0\, \kappa\, \left(\zeta_m^2 + \zeta_p^2\right) \left(\frac{2\,\zeta_m \zeta_p}{\zeta_m^2 + \zeta_p^2} - e^{-\kappa\delta}\right) \left(\frac{e^{-\kappa\delta}}{1 - e^{-2\kappa\delta}}\right) \tag{5.61}$$

where ϵ and ϵ_0 are the relative permittivities of respectively water and vacuum, δ (m) is the separation between particle and nominal membrane surface, κ is the inverse Debye length ($\kappa = 3.28 \times 10^3\, I^{1/2}\ \mu\mathrm{m}^{-1}$, where I is the ionic strength in mol L^{-1}), and ζ_m and ζ_p are membrane's and particle's zeta potentials, respectively. As electrostatic forces are only expected to be significant where the particle is in contact with small asperities, i.e. where δ is very small, these forces will not be considered in this study. Therefore, the adhesive forces are assumed to be entirely the product of the attractive *van der Waals* interactions occurring between two spherical particles. The particles are assumed to deform under strain [244].

$$F_a = F_{vdW} = \frac{\hbar\varpi\, d_p}{32\,\pi\, a^2} + \frac{\hbar\varpi\, {r_c}^2}{8\,\pi\, a^3} \tag{5.62}$$

where $\hbar\varpi$ is the Lifschitz-van der Waals constant (10^{-20} J), a denotes the adhesive distance between two spheres and $a = 0.4 \times 10^{-9}$ m [5], whereas r_c (m) denotes the radius of the contact area.

Radius of the contact area depends on the forces acting on the particle and the particle's elasticity and is calculated from the following theoretical equation [246]:

$$r_c = \left[\frac{3}{8}\, d_p\, F \left(\frac{1 - {\sigma_1}^2}{E_1} + \frac{1 - {\sigma_2}^2}{E_2}\right)\right]^{\frac{1}{3}} \tag{5.63}$$

where σ_1 and σ_2 are the Poisson's ratios of materials, E_1 and E_2 (Pa) denote the elastic deformation moduli of materials, and F (N) is the force causing deformation. $r_c = \left(0.5625\, d_p\, \frac{F_f}{E}\right)$ [246] where $E = E_1 = E_2$ and $\sigma = \sigma_1 = \sigma_2$ (two particles of the same material). The Young modulus of a particle is generally not known unless we deal with model suspensions of a known composition. Vyas et al. [246] proposed that $E = (1 \times 10^5) \div (1 \times 10^8)$ Pa which is a range of moduli for soft to semi-hard materials.

Friction force between the deposited particle and the membrane surface is given by:

$$F_{fr} = \max\left(\mu\left(F_f + F_a - F_b - F_r\right), 0\right) \tag{5.64}$$

where μ (–) is the friction coefficient combining the gliding and rolling movement of the particle along the membrane surface. Halow [82] showed that μ ranges between 0.06 and 1.0, however his investigations were carried out for rather large particles of 20-5000 μm dia. and the value of μ will additionally depend on the shape, size and properties

of the particle and the properties of the membrane. Jeon and Jung [113] produced a validated model for dust filtration cakes with μ between 0.1 and 0.3. Broeckmann et al. [17] quoted Czichos [39], Stiess [229] that friction in solid systems is an order of magnitude higher than in liquid systems and thus adopted the value of $\mu = 0.03$.

The net force due to gravity and buoyancy is calculated as:

$$F_g = \frac{1}{6}\,\pi\,{d_p}^3\,(\rho_p - \rho_l)\;g \tag{5.65}$$

where ρ_p and ρ_l denote respectively the particle and the liquid density (kg m^{-3}) and g is the gravitational acceleration (9.81 m s^{-2}).

5.4.2 Criterion for particle deposition

The fate of a particle dragged in a permeate flow stream towards the membrane, i.e. whether it will deposit and adhere to the membrane, deposit and roll on the membrane surface or be carried away from the membrane, can be predicted through analysis of the equilibrium of forces and torques [124]. Such analysis requires however a detailed information about the membrane asperity and friction coefficients. Instead of this approach, deposition of a particle was analysed by looking at the angle of repose θ which is calculated from the balance of forces as described in Vyas et al. [246]

$$\theta = \arctan\left(\frac{F_v - F_{fr} - F_g}{F_f + F_a - F_b}\right) \tag{5.66}$$

If the angle of repose θ is less than the critical angle of repose θ_{crit} the particle will adhere to the membrane, whereas if $\theta \geqslant \theta_{crit}$ the particle will either not reach the membrane or will bounce off after coming in contact with the membrane.

5.4.3 Cut-off diameter and cake properties

Whilst increase of the aeration rate (in immersed MBRs) or CFV (in sidestream MBRs) leads to a decrease in the cake layer thickness, it also reduces the cut-off diameter leading to denser cakes of higher packing density and thus higher specific resistance. These effects depend on the PSD of polydisperse suspensions and may lead, under specific circumstances, to the situation where increasing the air scouring rate or CFV leads to unexpectedly higher, rather than lower filtration resistances, i.e. increase of resistance due to an increased specific cake resistance caused by formation of denser cake exceeds the decrease of resistance due caused by reduction of the cake layer thickness. Such observations have been made, e.g. by Wakeman and Tarleton [247] and Mackley and Sherman [159] for classical MF/UF systems.

5.4.4 Simulation results

Particle deposition in an immersed MBR was modelled with a set of equations introduced in Section 5.4.1. Drag force due to permeate flow F_f was calculated using Equation 5.45 with coefficient C_1 found from Equation 5.48 accordingly to the model of Wang et al. [250]. Drag force due to tangential flow F_v was calculated with Equation 5.49 where coefficient $C_2 = 1.70$. Back-transport was modelled with inertial lift accordingly to Equation 5.60. Adhesive force F_a was calculated with Equation 5.62. Repelling force F_r was neglected. Friction force F_{fr} was calculated with Equation 5.64, whereas gravitational force F_g was found from Equation 5.65. All the above forces were then used to calculate the angle of repose with Equation 5.66. Critical angle of repose θ_{crit} and parameter b in Equation 5.60 had to be adjusted in the process to obtain the desired output characteristics. Other parameters used in the model were either assumed or taken from literature as listed in Table 5.2.

The model was simulated for a range of particle diameters, permeate fluxes and aeration rates. The ranges of variability for these three variables are as follows: particle diameter $d_p = \{0.001 : 0.05 : 1000\}$ μm, permeate flux $J = \{30 : 5 : 120\}$ L m^{-2} h^{-1}, air flow rate per tank cross sectional area $q_a = \{10 : 50 : 300\}$ L m^{-2} s^{-1}.

Table 5.2: Model parameters used in the simulation of particle deposition with the force balance analysis model.

Parameter	Name	Value	Unit	Reference
X_{MLSS}	MLSS concentration	20,000	mg/L	assumed
T	Absolute temperature	293	K	assumed
ρ_w	Water density	1000	kg m^{-3}	
ρ_p	Particle density	1060	kg m^{-3}	
η_w	Dynamic water viscosity	1.002×10^{-3}	Pa s	
$\hbar\varpi$	Lifschitz-van der Waals constant	10^{-20}	J	[5]
a	Adhesive distance between two spheres	0.4×10^{-9}	m	[5]
E	Young modulus of the particle	10^{6}	–	[246]
R_t	Total membrane resistance	10^{13}	m^{-1}	assumed
L	Membrane thickness	100×10^{-6}	m	assumed
A	Membrane tank cross sectional area	20	m^2	assumed
b	Parameter in the lift velocity equation	2.885	–	adjusted
μ	Friction coefficient	0.03	–	[17]
θ_{crit}	Critical angle of repose	50	^{o}	adjusted
ϕ	Membrane wall porosity	0.25	–	assumed

The calculated angles of repose for different diameters, airflow rates and fluxes are shown in two sub-figures in Figure 5.7. Figure 5.7a shows the angle of repose θ as a function of d_p and q_a for two extreme values of permeate flux: $J_1 = 30$ Lmh and $J_1 = 120$ Lmh, while Figure 5.7b represents θ as a function of d_p and J for two extreme values of unit aeration rates: $q_{a,1} = 10$ L m^{-2} s^{-1} and $q_{a,2} = 300$ L m^{-2} s^{-1}. Both sub-figures indicate that θ remains approximately constant over a wide range of particle diameters and increases rapidly around the range of diameters for which the forces of back-diffusion and forces due to tangential flow begin to dominate over the forces of adhesion and drag forces due to permeate flow.

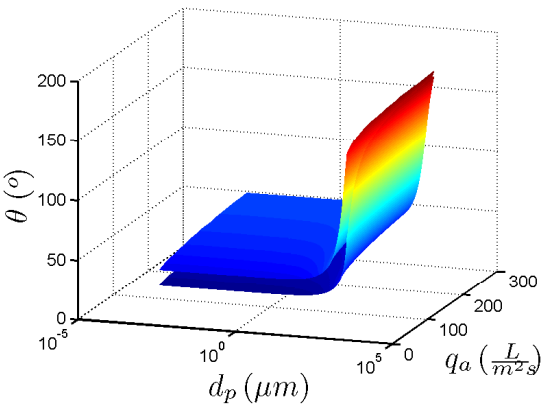

(a) Angle of repose θ for different particle diameters d_p and unit aeration rates q_a.

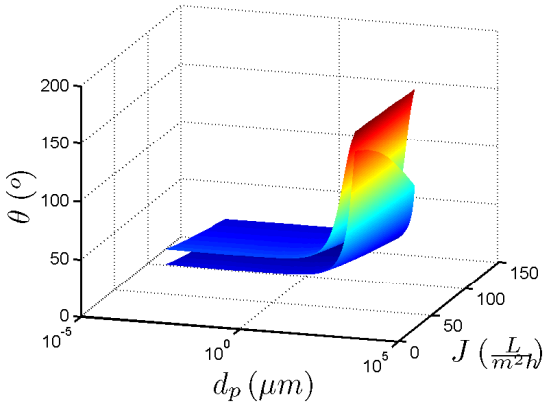

(b) Angle of repose θ for different particle diameters d_p and permeate fluxes J.

Figure 5.7: Angles of repose θ for different particle diameters d_p, unit aeration rates q_a and permeate fluxes J obtained from simulation.

The cut-off diameter $d_{p,cutoff}$ was calculated as the minimum particle diameter for which $\theta \geqslant \theta_{crit}$. Cut-off diameters for different permeate fluxes and unit airflow rates displayed in Figure 5.8 which shows that an average cut-off diameter in the system is approximately 100μm. $d_{p,cutoff}$ decreases as q_a is increased while smaller particles are kept away from the membrane. This relationship between q_a and $d_{p,cutoff}$ is steeper for lower permeate fluxes. For a given amount of airflow the cut-off diameter increases with permeate flux as more particles are kept on the membrane by the drag force associated with permeate flow.

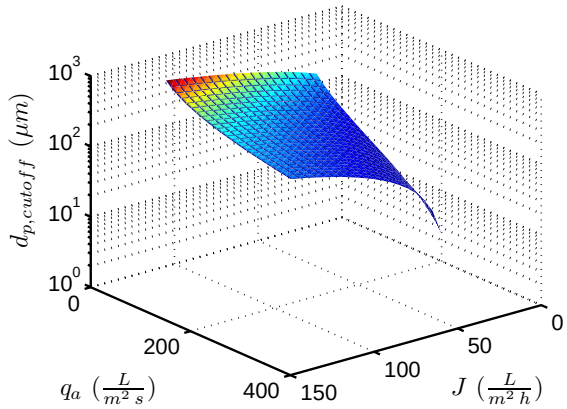

Figure 5.8: Particle cut-off diameter $d_{p,cutoff}$ vs. permeate flux J and unit aeration rate q_a obtained from simulation.

All forces acting on a single particle for the selected operating point defined by permeate flux $J = 35$ Lmh and unit air-scouring rate $q_a = 60$ L m^{-2} s^{-1} are shown in Figure 5.9. F_f, F_v and F_a increase linearly with d_p, whilst F_a ad F_v additionally happen to have very similar values and F_f is approximately one third of F_v and F_a. The force of friction F_{fr} is found to be very low for lower particle diameters and becomes zero as the forces of inertial lift begin to exceed the sum of adhesive forces and the drag force

due to permeate flow. The net force due to gravity and buoyancy increases with the cube of d_p whilst the force of inertial lift increases with d_p raised to the power of four and is found to be the dominant force acting on the particle.

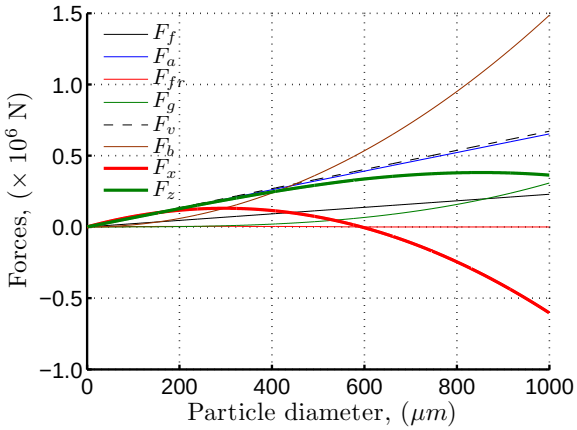

Figure 5.9: Forces acting on a single particle of diameter d_p deposited on the membrane surface obtained from simulation.

Particle cut-off has an impact on the of the cake's particle size distribution, which is different from the particle distribution in the bulk liquid as shown in Figure 5.10. In general terms, the cake is made up of smaller particles and is therefore denser than the particle size distribution of activated sludge would have suggested.

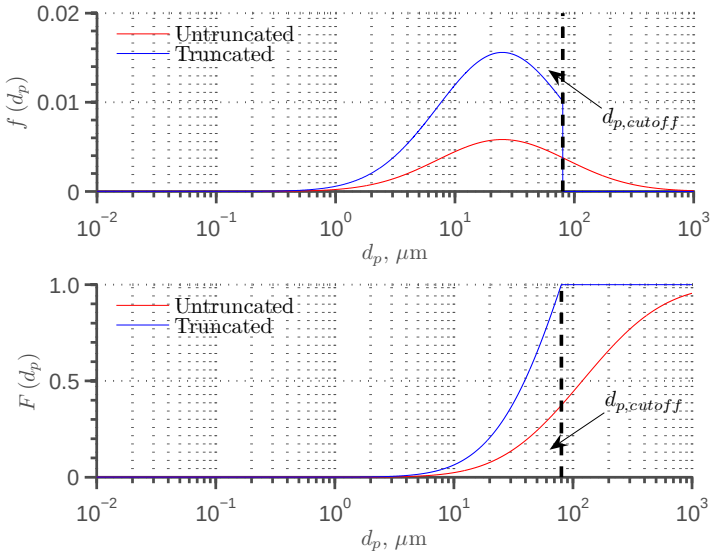

Figure 5.10: Theoretical probability density function (PDF) and cumulative density function (CDF) for activated sludge particles filtered through semipermeable membrane in a immersed membrane bioreactor (iMBR).

If we assume that the floc size distribution (FSD) of the activated sludge is described with a log-normal probability density function (PDF) represented by Equation 5.67 and the corresponding cumulative density function (CDF) is given in Equation 5.68, PSD of the particles forming the cake will be described with a truncated

log-normal PDF and CDF described by Equation 5.69 and Equation 5.70 respectively.

$$f\left(x \,|\, \mu, \sigma\right) = \frac{1}{x\,\sigma\,\sqrt{2\,\pi}}\,\exp\left(-\frac{\left(\ln\,x-\mu\right)^2}{2\,\sigma^2}\right) \tag{5.67}$$

$$F\left(x \,|\, \mu, \sigma\right) = \frac{1}{\sigma\,\sqrt{2\,\pi}}\int\limits_{-\infty}^{x}\exp\left(-\frac{\left(\ln\,x-\mu\right)^2}{2\,\sigma^2}\right)\mathrm{d}x \tag{5.68}$$

$$f_T\left(x \,|\, \mu, \sigma, d_{p,cutoff}\right) = \begin{cases} K\,f\left(x \,|\, \mu, \sigma\right) & \text{for} \quad x < d_{p,cutoff} \\ 0 & \text{for} \quad x \geqslant d_{p,cutoff} \end{cases} \tag{5.69}$$

$$F_T\left(x \,|\, \mu, \sigma, d_{p,cutoff}\right) = \begin{cases} K\,F\left(x \,|\, \mu, \sigma\right) & \text{for} \quad x < d_{p,cutoff} \\ 1 & \text{for} \quad x \geqslant d_{p,cutoff} \end{cases} \tag{5.70}$$

where x denotes the particle diameter, σ denotes the standard deviation of the associated normal PDF, μ denotes the equivalent mean in the normal PDF, and $K = \frac{1}{F\left(d_{p,cutoff} \,|\, \mu, \sigma\right)}$.

5.5 Cake back-transport

Whilst the force balance analysis carried out in Section 5.4 allows, in principle, to predict formation of cake and specific cake resistance during filtration of polydisperse suspensions, such a model contains many parameters and requires a significant amount of data for calibration and validation. On a macroscopic level where suspensions are considered as continua and described with a single parameter denoting particle concentration, back-transport needs to be described with a purely empirical model, or a partly empirical partly mechanistic macroscopic model with empirically determined coefficients. Two of such back-transport models are described in Section 5.5.1 and Section 5.5.2 below. These mathematical expressions will be later used for the formulation of fouling models described in Chapter 6.

5.5.1 Shear induction - Nagaoka et al. [176]

Nagaoka et al. [176] presented a mathematical relationship between cake detachment rate k_r (s^{-1}) and shear stresses τ_m (Pa) acting on the cake as a result of crossflow velocity (CFV) and/or air bubble flow. The cake detachment force resulting from shear stresses is diminished by a pressure dependent static friction term $\lambda_m\,\Delta P$ which represents combined effects of cake consistency and cake attachment to the membrane surface. The expression for $k_{r,N}$ (s^{-1}) which denotes the cake detachment rate k_r according to Nagaoka is presented in Equation 5.71.

$$k_{r,N} = \gamma_m\,\left(\tau_m - \lambda_m\,\Delta P\right) \tag{5.71}$$

where γ_m (Pa^{-1} s^{-1}) is an empirically determined proportionality constant and λ_m is a non-dimensional static friction coefficient. Equation 5.71 can be incorporated into the cake mass balance equation which describes the rate of cake mass growth $\frac{dm_r}{dt}$ (kg m^{-2} s^{-1}) due to flux of solids towards the membrane $J\,X_{MLSS}$ where J denotes the permeate flux and X_{MLSS} is the MLSS concentration, minus back-transport of cake ($k_{r,N}\,m_r$).

$$\frac{dm_r}{dt} = J\,X_{MLSS} - k_{r,N}\,m_r \tag{5.72}$$

The shear stress τ_m can be either empirically correlated with CFV and/or aeration intensity or calculated with the equations of fluid mechanics. The latter approach was chosen to formulate the relationship between shear stresses on hollow fibre (HF) membrane fibres and coarse bubble air flow and is described in Section 7.5 in Chapter 7. Through empirical or theoretical approaches, detachment rate parameter k_r can be directly linked to the operational conditions in a MBR system.

5.5.2 Back transport phenomenon - Ho and Zydney [97]

Ho and Zydney [97] introduced a back transport equation which determines the rate of cake removal due to inertial lift and shear induced diffusion mechanisms. The calculated back transport rate, is equivalent to the term $k_{r,N}\,m_r$ in Equation 5.72. The cake back transport model of Ho and Zydney [97] is described with Equation 5.73.

$$\dot{m}_{r,back} = \frac{dm_{r,back}}{dt} = k\,\gamma^n\,X_{MLSS} \tag{5.73}$$

where $\dot{m}_{r,back}$ (kg m^{-2} s^{-1}) denotes the cake back transport rate per unit area, k (m s^{n-1}) is the proportionality constant, X_{MLSS} (kg m^{-3}) denotes the mixed liquor suspended solids (MLSS) concentration, and γ (s^{-1}) is the shear rate created by CFV or coarse bubble airflow. Exponent n next to γ depends on the type of back-transport forces acting on the cake and is equal $n = 1$ for shear induced diffusion and $n = 2$ for inertial lift.

The complete term $k\,\gamma^n$ refers to the steady state back-flux of solids from the membrane surface to the bulk liquid which increases with increasing particle radius, r. This term is found to be proportional to r^3 for inertial lift and $r^{1.33}$ for shear induced diffusion. Thus, large cells and flocculated material tend to be kept away from the membrane surface with the steady state flux dominated by smaller colloidal matter [97].

A number of researchers have developed different empirical macroscopic correlations for the steady state back flux of cake in relation to wastewater properties and operating conditions [128, 221]. However the functional form and parameters are likely to be unique to the membrane, module design, wastewater, and biological condition of the activated sludge, what limits their applicability on a wider scale.

5.6 Back-flushing

Back flushing, i.e. periodic removal of particles deposited on the membrane in the form of cake is carried out by reversing the direction of flow through the membrane. The rate of cake and biofilm removal during back-flushing depends on the reverse flow rate (q_{bf}), compactness of the cake and the adhesive forces between the deposited particles and the membrane. The efficiency, i.e. the fractional amount of biofilm and cake removed through back-flushing is additionally dependent on back-flush duration time (t_{bf}). The properties of the cake and the biofilm change as the filtration progresses due to continuous cake growth and detachment, deposition of macromolecules within the void spaces in the cake, growth of biofilm, and variations of the operating conditions such as CFV and TMP. Cake properties will therefore depend on the history of filtration and this means that there is a direct link between forward filtration and the energy input required for back-flushing.

The processes taking place during back-flushing are very complicated and are yet not well understood. In order to develop a mechanistic model for back-flushing one has to fully understand how the properties of the cake evolve with filtration and how these properties later affect cake detachment during back-flushing. One also needs to understand the intricacies of fluid flow characteristics during back-flush, the velocity and pressure fields, shear stresses, and shear rates exerted on the cake in this very complex unsteady multiphase flow. The author has not yet come across a deterministic back-flush model and even if such a model has recently been published and was overlooked, it would most likely require a large number of either yet unidentified or generally unidentifiable parameters which would limit its practical use in a wider range of applications. Therefore back-flushing at present will need to be modelled in a rather simplistic fashion.

In the simplest possible approach, removal of cake during back-flushing can be considered as an instantaneous process in which the unit mass of cake per membrane area (kg m^{-2}) at the beginning of the $(j+1)^{\text{th}}$ filtration cycle (${m_c}^{j+1}(\tau = 0)$) is related to the unit mass of cake at the end of the previous j^{th} filtration cycle (${m_c}^{j}(\tau = t_f)$).

$$\forall j \in \mathbb{N} \; : \; m_c^{j+1}(\tau = 0) = \eta \, m_c^{j}(\tau = t_f) \tag{5.74}$$

where t_f (s) denotes filtration cycle duration time, ${m_c}^{j}(\tau)$ (kg m^{-2}) denotes the unit mass of cake per membrane area in the j^{th} filtration cycle at filtration time (τ) and η is a dimensionless parameter representing the fraction of cake (or cake resistance) which cannot be removed through back-flushing. Filtration time in the j^{th} filtration cycle τ^j can be calculated from the total filtration time t if we assume that filtration times t_f (s) and back-flush times t_{bf} (s) are constant throughout the filtration process.

$$\forall j \in \mathbb{N} \; : \; \tau^j = t - (j-1) \, (t_f + t_{bf}) \tag{5.75}$$

5.6.1 Viscosity as a function of temperature and MLSS

Dynamic water viscosity η_w (Pa · s) is temperature dependent and this dependence is usually modelled with an exponential curve of the following form [143]:

$$\eta_w\,(T) = \eta_{w,20}\; e^{-0.0239\,(T-20)} \tag{5.76}$$

where $\eta_{w,20} = 1.002 \times 10^{-3}$ Pa·s denotes the dynamic water viscosity at 20 ^{o}C and T (^{o}C) denotes water temperature.

Viscosity of a suspension is usually higher than that of pure solvent due to additional friction forces created between suspended particles in motion. Activated sludge suspensions considered here additionally exhibit non-Newtonian properties, meaning that their viscosity changes under applied shear. Activated sludge suspensions, especially at higher concentrations, usually behave like Herschel-Bulkley fluids [92] which exhibit shear-thinning properties (i.e. viscosity decreases with shear) and which are capable of bearing some stress called yield stress before they begin to flow. However, as explained in the review paper of Ratkovich et al. [205], many other viscosity models have been successfully applied to describe the rheology of activated sludge suspensions, such as, e.g. simpler two-parameter Bingham plastic model or a more complex Casson plastic model.

Whilst suspended solids at the levels observed in activated sludge suspensions within MBRs tend to substantially affect the liquid's viscosity and other rheological properties such as presence of yield stress, non-Newtonian flow characteristics and thixotrophic behaviour, the latter are often neglected. Activated sludge is thus treated as a Newtonian fluid but with viscosity larger than that of pure water. Several relationships between viscosity and MLSS of activated sludge can be found in literature and most of them are of an exponential form. Krauth and Staab [128] proposed the following relationship:

$$\eta_b\,(MLSS) = 1.05\,\eta_w\,e^{\,0.08\,X_{MLSS}} \tag{5.77}$$

where η_w (Pa · s) denotes the dynamic viscosity of water and X_{MLSS} (kg m^{-3}) is the concentration of mixed liquor suspended solids.

Meng and Yang [167] found a very similar relationship to Krauth and Staab [128], but with different coefficients resulting in slightly smaller viscosities but a similar sensitivity to MLSS:

$$\eta_b\,(MLSS) = 0.909\,\eta_w\,e^{\,0.0861\,X_{MLSS}} \tag{5.78}$$

The exponential curve of Ng and Kim [179] derived from their experimental data produces $\sim 60\%$ larger viscosities than the previous functions and a lower sensitivity to MLSS:

$$\eta_b\,(MLSS) = 1.61\,\eta_w\,e^{\,0.07\,X_{MLSS}} \tag{5.79}$$

Equation 5.76 was combined with Equation 5.77 to give the following relationship

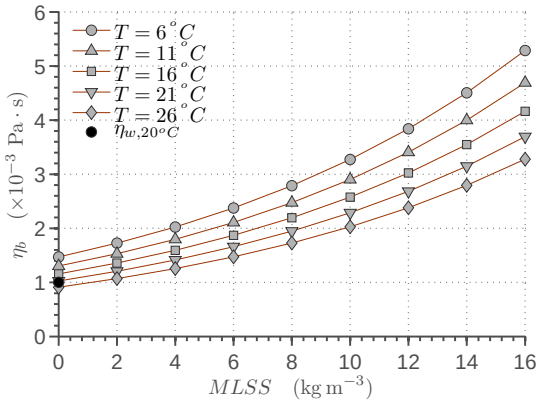

Figure 5.11: Bulk liquid dynamic viscosity η_b as a function of temperature T and MLSS obtained from Equation 5.80.

representing the viscosity of activated sludge suspension in a function of temperature and MLSS:

$$\eta_b\,(T, MLSS) = 1.05\,\eta_{w,20}\; e^{-1.912\times10^{-3}\,(T-20)\,X_{MLSS}} \tag{5.80}$$

Dynamic viscosities of bulk liquid calculated with Equation 5.80 for different MLSS concentrations and temperatures are shown in Figure 5.11.

Nevertheless, it has to be noted that the above correlations are purely empirical and hence do not capture the underlying mechanisms of fluid flow. They are only used to demonstrate that energy requirements for mixing and sludge recirculation in MBR systems are likely to be substantially higher compared to conventional activated sludge processes (ASPs) where solids concentrations are lower. As indicated in Ratkovich et al. [205] accurate modelling of activated sludge rheology is very difficult due to a very complex nature of activated sludge suspensions. Moreover, the rheological models published in literature are created based on the data obtained from different rheometers using different measuremement protocols and settings. Since it has been found that different types of rheometers or the same rheometers with different settings and measurement protocols will give different viscosity readings on the same sample it is difficult to compare viscosity readings from different sources and hence the viscosity models developed on the base of those readings. Additionally Ratkovich et al. [205] found that good modelling practices were not always followed during the development of various activated sludge viscosity models, hence they are not very trustworthy and need to be applied with caution.

Chapter 6

Development of new fouling models

Contents

6.1 Introduction

This chapter describes the formulation, calibration and validation of the following two fouling models:

1. Behavioural fouling model of reversible and irreversible fouling
2. Three mechanism fouling model based on classical fouling equations

The first model is based on the development of Liang et al. [149] in which fouling is divided into short-term reversible fouling tantamount with cake deposition and long-term irreversible fouling representing combined effects of irreversible particle deposition on the membrane surface and inside membrane pores. Both fouling processes are modelled with first order ordinary differential equations (ODEs). The model additionally accounts for cake compressibility, cake detachment due to presence of airflow/crossflow, back-flushing, and flux-dependent soluble microbial products (SMP) deposition. It can be configured to predict flux decline in constant trans-membrane pressure filtration as well as trans-membrane pressure (TMP) increase in constant flux filtration. The model was calibrated on the data obtained in a short-term flux stepping experiment and in a long-term operation of a pilot-scale membrane bioreactor (MBR).

The second model is based on the publication of Duclos-Orsello et al. [50] which describes fouling as a combination of three classical fouling mechanisms. It is assumed that *pore constriction* and *pore blockage* occur simultaneously whereas *cake buildup* occurs only on the blocked part of the membrane. Whilst the model of Duclos-Orsello et al. [50] is presented in the form of a single integral what restricts its use to constant pressure filtration with time-invariant parameters and properties of the filtered suspension, the model presented here is described with a set of ODEs. Thus, it can be used to simulate membrane filtration under time-varying conditions and with time-varying parameters. Each of the three classical fouling mechanisms is described with an ODE presented earlier in Chapter 5. Two additional ODEs are provided by the Author in order to model sequential occurrence of pore blockage and cake formation. Similarly to the previous model, this one is also formulated in two ways which allows it to describe constant TMP filtration as well as constant flux filtration. The model was calibrated on the same constant-pressure filtration data as used in Duclos-Orsello et al. [50] as well as on the constant-flux filtration data published by Ye et al. [266].

6.2 Development of a behavioural fouling model

The model is intended to provide a reasonable level of prediction accuracy at low computational cost and with minimum amount of effort required for calibration. The model is intended specifically for filtration of activated sludge suspensions on microfiltration (MF) and ultrafiltration (UF) membranes operating either as a cross-flow or dead-end process. Unlike classical fouling equations that divide fouling into three mechanisms: *pore constriction*, *pore blockage*, and *cake formation* - see Section 5.2.1 in Chapter 5, this model divides fouling into just two processes: *reversible fouling* and *irreversible fouling*. Both processes are modelled with first order ODEs which describe an increase of membrane resistance R in time. Although the shape of these equations, as will be shown later, is different from the shapes of the classical fouling equations, this model is nevertheless capable of representing fouling on MF and UF membranes in short as well as long time-scales under certain operating conditions.

This model can be successfully applied to describe membrane fouling provided that the operating conditions, such as filtration fluxes, mixed liquor suspended solids (MLSS) and TMPs fall within technical norms, i.e. the membrane is not subjected to conditions which will result in very fast and heavy fouling. Therefore, the purpose of this model is solely for optimisation of pilot-scale and full-scale systems, control applications such as e.g. model predictive control (MPC) and linking with ASM models. As the full-scale systems are operated such that the amount of fouling is reduced to economically viable levels, the model will not be operating outside its intended operating range. This model fails to describe some phenomena of membrane fouling such as the two-stage TMP jump described in Ognier et al. [190] and Ye et al. [266]. The results of constant-flux simulations with the behavioural fouling model are provided later in Section 6.2.4.

The model is termed 'behavioural' as it neither falls into the mechanistic nor em-

pirical model category. It has been created to represent the behaviour of MF and UF membranes without providing any detailed, mechanistic description of the underlying processes of fouling, hydrodynamic conditions, and fouling control mechanisms. Due to non-mechanistic approach, the range of application of the model is limited to low fluxes below or slightly above the threshold flux and intermediate filtration times or fluxes significantly above the threshold flux and short filtration times in which the membranes do not have the chance to foul substantially. By the term 'threshold flux' the Author means in this particular modelling context an approximate and visually defined flux value which divides a region of fluxes for which no perceptual increase in TMP due to either reversible or irreversible fouling can be observed within the observation time-scales and the region in which TMP gradients due to ongoing fouling are observed.The first scenario applies to membrane operation in the, so called, sustainable flux region in which the membranes are operated within economically viable levels of fouling which balance the operating costs with capital costs and the membrane productivity. In the second scenario, the membranes exhibit significant levels of fouling due to operation under fluxes surpassing the threshold flux as well as sustainable flux defined by the operators.

A short explanation of the notion of 'sustainable flux' and the definition of 'threshold flux' as introduced by Field and Pearce [61] can be found in Section 5.1.3 on page 139.

Development of this mathematical model is based on an earlier published model of Liang et al. [149] which however did not represent backwashing, cake compressibility, and particle back-transport due to crossflow velocity (CFV) or air-scouring. These mechanisms were added in order to allow the model to be used in various simulation studies including integration with ASM models for complete simulation of MBR reactors. The model was also upgraded to allow irreversible fouling to depend on the permeate flux. Flux-dependent SMP deposition was identified on the data obtained in the short-term flux-stepping experiment performed on a pilot scale membrane filtration unit equipped with horizontal hollow fibres with a mean pore diameter of 0.1μm. The information gathered in this experiment was also used to identify other model parameters describing reversible fouling, irreversible fouling and solids back-transport as will be later described in Section 6.2.3. The second calibration was performed on long-term filtration data from a MBR pilot plant equipped with vertical hollow fibres of a similar pore size. As will be shown later, the model proved to be in good agreement with the measurements in both cases.

Since the purpose of this fouling model is to be used in conjunction with the biological ASM model for MBR plant design, optimisation, and model-based operation and control, the model needs to possess a set of certain characteristics. It needs to be simple, fast to compute, adaptable to various MBR configurations and have a small number of adjustable parameters. These parameters additionally need to be able to be identified from plant design and operational characteristics, directly measured, or computed in model calibration studies based on the measurements taken at the plant (usually inputs and outputs, and sometimes intermediate process measurements). On

the other hand, the model needs to provide a desired level of accuracy for a range of operating conditions encountered in real life. In particular, the model needs to be applicable to simulation of three main MBR configurations:

1. Immersed hollow fibre (HF) MBRs which are back-flushed and are equipped with coarse bubble air scouring systems,
2. Immersed flat sheet (FS) MBRs which are usually 'non-backflushable' and are also equipped with coarse bubble air scouring systems,
3. Side stream crossflow (CF) MBRs which are operated under high tangential shear rate and usualy are not air-sparged.

6.2.1 Model formulation

Governing equations

This model is based on the classic resistance in series concept described earlier in Section 5.2.6 of Chapter 5. Total membrane resistance R_t (m^{-1}) is divided into three parts:

$$R_t(t) = R_m + R_r(t) + R_i(t) \tag{6.1}$$

where R_m (m^{-1}) denotes the clean (unfouled) membrane resistance, R_r (m^{-1}) denotes the resistance due to reversible fouling (mainly cake formation) and R_i (m^{-1}) denotes the resistance caused by irreversible fouling (modelled here as SMP deposition).

Depending on the intended application, the model can either receive permeate flux J as an input and calculate pressure loss on the membrane ΔP or, conversely, receive ΔP as an input and calculate the resulting permeate flux J. In both instances, the relationship between flux and pressure loss is modelled with a well known Darcy's equation, neglecting any dynamic effects of flow through the membrane. The equations take the following forms respectively:

$$\Delta P = J\,\mu \sum R_i = J\,\mu\,R_t \tag{6.2}$$

and

$$J = \frac{\Delta P}{\mu \sum R_i} = \frac{\Delta P}{\mu\,R_t} \tag{6.3}$$

where J ($m\ s^{-1}$) denotes the permeate flux, ΔP (Pa) denotes the pressure difference across the membrane, μ ($Pa \cdot s$) denotes the permeate's dynamic viscosity and R_t (m^{-1}) is the total membrane resistance.

The resistances calculated in the model: resistance due to cake build-up (reversible fouling) R_r and resistance due to SMP deposition (irreversible fouling) R_i are proportional to the unit masses per membrane area of, respectively, cake: m_r ($kg\ m^{-2}$) and SMP: m_i ($kg\ m^{-2}$) deposited on and within the membrane:

$$R_r = \alpha_c \cdot m_r \tag{6.4}$$

$$R_i = k_i \cdot m_i \tag{6.5}$$

where α_c (m kg^{-1}) denotes the specific cake resistance and k_i (m kg^{-1}) is the irreversible fouling strength factor.

Accumulation of m_r and m_i on the membrane is modelled with two ordinary differential equations (ODEs).

$$\frac{dm_r}{dt} = f_r \, J \, X_{TSS} - \dot{m}_{r,back} \tag{6.6}$$

$$\frac{dm_i}{dt} = f_i \, J \, S_{SMP} \tag{6.7}$$

where X_{TSS} (kg m^{-3}) denotes the feed total suspended solids (TSS) concentration, $\dot{m}_{r,back}$ (kg m^{-2} s^{-1}) denotes the unit mass flux of solids detaching from the cake and the membrane and S_{SMP} (kg m^{-3}) is the feed SMP concentration. f_r (–) and f_i (–) denote the fractions of respectively solids and SMP contributing to reversible and irreversible fouling. Whilst it is assumed that $f_r = 1$, f_i is rather low and depends on the amount of flux - See Section 6.2.3 for more details.

Cake thickness δ (m) can be calculated from the amount of cake deposited on the membrane m_r using Equation 6.8.

$$\delta = \frac{m_r}{\rho_c \, (1 - \varepsilon_c)} \tag{6.8}$$

where ρ_c (kg m^{-3}) denotes the wet cake density and ε_c (–) denotes the cake porosity. ε_c was found by Wu et al. [262] to fall between 0.59 and 0.66. Wu et al. [262] also postulate that cake porosity varies in time due to consolidation and entrapment of colloidal components within the cake matrix. The wet cake density ρ_c was identified by Wu et al. [262] through calibration as $\sim 1.24 \times 10^3$ kg m^{-3} whereas Li and Yuan [148] found $\rho_c = 1.06 \times 10^3$ kg m^{-3}.

As activated sludge cakes are usually compressible, wet cake density (ρ_c) depend on the trans-membrane pressure (TMP). However, as the sole purpose of cake thickness calculations in this model is for indication only, selection of a single value for cake density is considered a good enough approximation.

The original model of Liang et al. [149] assumes that all SMP in the feed contributes to irreversible fouling ($f_i = 1$). However, as was shown in Section 5.3 only a fraction of SMP actually enters the membrane pores due to sieving and retarded transport effects and from all the SMP that finds its way into the membrane pores only a tiny fraction of SMP actually deposits inside the membrane. Parameters governing irreversible fouling in the model were identified on the experimental data form the short-term flux-stepping experiment as described in Section 6.2.3. Additionally f_i was found to be in an exponential relationship with the permeate flux.

Sludge cake deposits on the membrane surface by the work of advection (i.e. mass flow of water through the membrane) but, at the same time, is also being detached

by shear stresses caused by air bubble-flow and/or cross-flow velocity. The rate of cake back-transport ($\dot{m}_{r,back}$) can be described by different empirical and mechanistic models. Back-transport models employed in this model are described in Chapter 5 in Sections 5.5.1 and 5.5.2.

Backwashing

HF membranes in a typical submerged MBR plant are 'backwashable'. Therefore back-washing needs to be represented in the model. The backwash (or backflush) sequence is modelled with Equation 6.9 earlier introduced in Chapter 5. The equation is presented again for completeness.

$$\forall j \in \mathbb{N} \; : \; m_r^{j+1}(\tau = 0) = \eta \, m_r^j \, (\tau = t_f) \tag{6.9}$$

Equation 6.9 is implemented in the model by resetting the initial condition of Equation 6.6 in each time-step during the backwash cycle. After the backwash cycle is completed, the unit mass of cake m_r (kg m^{-2}) remaining on the membrane is equal to the fraction of the amount of cake present at the beginning of the backwash cycle. The amount of cake that is left after the backwash is governed by adjustable non-dimensional parameter η. Forward filtration and backwash cycles are controlled in the model by a binary backwash logic signal where 0 stands for forward filtration and 1 for a backwash cycle. It is assumed that back-washing does not remove any irreversible fouling, in other terms, backwashing does not diminish the mass of SMP (m_i) deposited on and inside the membrane.

Due to lack of knowledge and reliable data for validation of backwash models it is assumed that cake removal during backwash periods occurs instantaneously. The effects of backwash water and air flow rates and backwash duration times on the efficiency of cake removal are therefore not represented. In real world applications it was found that although cake layer was instantaneously lifted off after permeate flux had been reversed, in order to remove the cake completely from the membrane module, the backflush flow rate needed to be at least three times larger than the forward filtration flow rate [218]. Also air was found to improve the backwash efficiency.

Cake compressibility

Biological slurries produced in biological treatment are found to be very compressible [202]. Compressibility of biological slurries is usually described with Equation 6.10 [197] or Equation 6.11 [63, 139]. According to the latter authors, Equation 6.11 had been proven more accurate than Equation 6.10 for modelling cake compression. Both equations relate the specific cake resistance α_c (m kg^{-1}) to the pressure (ΔP) exerted on the cake.

$$\alpha_c = \alpha_{c,0} \; (\Delta P)^n \tag{6.10}$$

$$\alpha_c = \alpha_{c,0} \left(\frac{\Delta P}{\Delta P_{crit}} \right)^n \tag{6.11}$$

where $\alpha_{c,0}$ (m kg^{-1}) denotes the specific cake resistance at atmospheric pressure, n denotes a dimensionless cake compressibility factor and ΔP_{crit} (Pa) is the threshold pressure below which no cake compression occurs.

Both equations have been successfully used to predict cake compressibility in activated sludge systems. In Equation 6.11 the threshold pressure ΔP_{crit} for activated sludge was found to be around 30 kPa whilst cake compressibility n was found to take values between 0.7 and 1.5 [202]. The n coefficient in Equation 6.10 was found to vary within a similar range. Kim et al. [122] measured n in a laboratory study and obtained values between 0.79 and 1.4.

The model assumes that the cake is compressible and α_c changes with pressure accordingly to Equation 6.11 where parameters ΔP_{crit} and n are chosen to equal 30 kPa and 1 respectively [202]. With $n = 1$ the exponential relationship between α_c and ΔP in Equation 6.11 reduces to a linear relationship with gradient $\frac{\alpha_{c,0}}{\Delta P_{crit}}$.

It is also assumed that although cake compressibility is significant enough to affect the TMPs across the membrane, SMP deposits are incompressible. This is justified as SMP deposits do not form a thick layer on top of the membrane alike solids, but create dense thin layers of molecules inside the membrane pores, where, a) pressures are lower than on the bulk liquid side and b) macromolecules bound with one another by van der Waals and electrostatic forces are harder to shuffle than larger solid particles forming porous layers.

Deposition of SMP on and inside the membrane

Ye et al. [266] found through experimental analysis that the fraction of alginate proteins depositing inside membrane pores is in an exponential relationship with permeate flux. The authors explained this behaviour with a film model theory which describes sorption as a diffusion limited process through a laminar layer forming on the interface (here, the interface between the liquid and the membrane surface). Thickness of the laminar layer under laminar flow conditions that are experienced in membrane filtration is, accordingly to the Blasius equation, inversely proportional to the square root of the freestream velocity. Therefore, an increase in the membrane flux and thus the flow velocity through the membrane pores leads to the reduction of the film thickness, which in turn increases diffusion and ultimately sorption of solutes inside the membrane pores.

The assumption made by Liang et al. [149] that deposition of SMP does not depend on permeate flux is thus invalidated by the findings of Ye et al. [266] and are confirmed by the observations made in this study. As shown in Figure 6.2a, the rate of pressure gradient due to SMP deposition was observed to increase as the flux was being stepped up in the flux stepping experiment. Analysis of the data obtained in the flux stepping experiment confirmed the existence of an exponential relationship between the fraction

of SMP contributing to irreversible fouling f_i (–) and the permeate flux J (m s^{-1}) as was initially proposed by Ye et al. [266] - see Section 6.2.3 for more details. This relationship is shown in Equation 6.12.

$$f_i = a\, e^{b\, J} \tag{6.12}$$

where a (–) and b (s m^{-1}) are the proportionality coefficients which shall be identified on a case by case basis.

Deposition of solids (cake formation)

As shown in Figure 5.8 on page 171 only the solid particles with diameters smaller than the cut-off diameter $d_{p,cutoff}$ will deposit on the membrane whilst larger particles will either not reach the membrane surface at all or will be removed from the membrane due to combined effects of shear-induced diffusion, inertial lift and cross-flow. These effects can either be modelled with Computational Fluid Dynamics (CFD) or, as in our case, can be described with single mass transport equations such as Equation 5.72 and Equation 5.73 introduced in Chapter 5.

Cake back-transport is described by term $\dot{m}_{r,back}$. This term can be expressed as a product of $k_r\, m_r$ where the cake detachment constant k_r is either measured, inferred during model calibration, or calculated from CFV or air bubble flow rate Q_{air} using e.g the model of Nagaoka et al. [176] - see Equation 5.71 on page 173. Alternatively, the term $\dot{m}_{r,back}$ can be expressed with the model of Ho and Zydney [97] as shown in Equation 5.73 on page 174. The model of Ho and Zydney relates the mass flux of cake back to the bulk liquid to shear rates caused by inertial-lift and back-diffusion mechanisms.

6.2.2 Experimental methods

The model was formulated in Simulink® under MATLAB® 2006a. Then, it was calibrated on two sets of data. The first one was obtained from a short-term flux stepping experiment performed on the ITT Sanitaire® pilot membrane filtration unit. The second set of data covers 640 hours of operation of a submerged pilot MBR plant.

The first unit was a simple filtration cell receiving a sequencing batch reactor (SBR) effluent characterised by low bulk liquid total suspended solids (TSS) concentration and low chemical oxygen demand (COD). Additionally most of the organic substrates in the effluent were found to be composed of SMP. The pilot plant was installed at the Cardiff wastewater treatment plant (WWTP) and was under operation in 2007. Low TSS levels mean that multiple flux steps could be carried out in the unit on a single day. This speeded up the experimental procedure and prevented repeated clogging or even permanent membrane damage. Although TSS concentration in the liquid was only around 25 mg L^{-1}, the concentration was still large enough to lead to a significant cake buildup on the membrane surface under all fluxes as demonstrated in Figure 6.1.

Temperature throughout the test remained at 17°C and the rate of airflow for cake removal was kept at 13 Nm^3/hr. Cake growth was required in the experimental setup for identification of the model parameters responsible for cake formation.

In this flux stepping experiment the membrane was subjected to a range of fluxes ranging from 30 L m^{-2} h^{-1} to 55 L m^{-2} h^{-1} stepped up and down in 5 L m^{-2} h^{-1} increments. Each flux was run through 3 filtration/backwash cycles as shown in Figure 6.1. The selected flux range and step size allowed for testing the irreversible and reversible fouling under various conditions both below and above the critical flux [1]. The unit's main operational data is listed in Table 6.1.

The model parameters were first adjusted manually in an iterative fashion until a reasonable fit between the model outputs and the experimental data was obtained. It was made sure that the chosen parameters are within the range of values reported in literature to ascertain a realistic initial starting point for the automatic calibration procedure to follow. The final 'optimal' set of parameters that leads to a minimum value of the sum of absolute deviations between the measurements and the model outputs as shown in Equation 6.13 was obtained by running a nonlinear simplex optimisation algorithm of Nelder and Mead [178].

$$\min \sum_{i=1}^{n} |y_i - f(x_i)| \tag{6.13}$$

where y_i denotes the i-th measurement and x_i denotes the i-th model output.

The algorithm is implemented in the MATLAB® function `fminsearch`.

Table 6.1: Operational data for the pilot membrane filtration unit used in the flux-stepping experiment (ITT Sanitaire, Dr. Alan Merry, personal communication)

Membrane filtration unit fed with SBR effluent	
Membrane type and area	Horizontal 'Kolon' fibres; PVDF 0.1μm pore size; 20 m^2
Feed flow; permeate flow; backwash	1-2.4 m^3/h; 0.6-1 m^3/h; 1.2-1.8 m^3/h
Backwash interval and duration	Every 4 min with 30 s ON
TMP	300-500 mbar
Aeration rate	13 Nm^3/h from coarse bubble tube diffuser
Cleaning regime	Hypochlorite dosed 4 times daily into permeate tank
Biological feed data	COD∼50 mgO_2/L; TSS∼25 mg/L
SMP feed data	Glucose∼5 mg/L; proteins∼100 mg/L

The second experiment was carried out on an immersed MBR pilot plant equipped with vertical hollow fibre polyethersulfone (PES) membranes and fed with brewery wastewater. The pilot plant was installed by ITT Sanitaire® at the Coors Shobnall Maltings site in the Midlands and was operational between August 2004 and February 2005. Wastewater was fed with an inlet pump to the anoxic tank, then entered the aerobic reactor and finally flew over a weir into the membrane tank. The permeate was withdrawn from the membrane tank with a permeate suction pump. The plant

[1] Critical flux has been defined and explained in Section 5.1.2 on page 138

was equipped with a recirculation pump which reversed the mixed liquor from the membrane tank back to the anoxic zone thus allowing nitrates to be removed through denitrification in the anoxic tank. The variable speed permeate suction pump operated in an automatic fashion and was controlled by a central pilot plant programmable logic controller (PLC) which turned the pump on and off, adjusted the pump speed and direction of flow. The permeate pump periodically operated in reverse mode to perform membrane backwash or an occasional periodic chemical clean with sodium hypochlorite. The plant was also equipped with a small chemical dosing tank which could be used to dose various chemicals such as coagulants, powdered activated carbon (PAC), or various external carbon sources into the anoxic tank. The aerobic tank was aerated with a tubular diffuser aeration system linked to a small compressor.

The plant was operating at a the MLSS concentration of $\sim 10,000$ mg L^{-1}, hence it was possible to calibrate the model under suspended solids concentrations characteristic of a full scale MBR. For this calibration exercise, filtration period of 640 hour was used. The relevant operational data for the plant is listed in Table 6.2.

Table 6.2: Operational data for the MBR pilot plant (ITT Sanitaire, Dr. Alan Merry, personal communication)

MBR pilot plant	
Membrane type and area	Vertical 'Puron' fibres; PES 0.04 μm pore size; 20 m^2
Permeate flow; backwash flow	0.6 m^3/h; 1.1 m^3/h
Permeate recirculation flow	0.27 m^3/h
Backwash interval and duration	Every 6 min with 45 s ON
TMP	300-500 mbar
dissolved oxygen (DO) operating range	2-4 mg O_2/L
Full air scour flow	27 Nm^3/h for 15 s every 60 s
Low air scour flow	~2 Nm^3/h for 45 s every 60 s
MLSS concentration	~7,500 mg/L
Bioreactor tank	Volume 1 m^3; operating level of weir 1.9-2.0 m

6.2.3 Model calibration

Short-term flux stepping experiment

Flux and TMP measurements in the flux-stepping experiment are shown in Figure 6.1. As the flux is increased in a step-wise fashion the TMP gradients between each backwash become larger due to increasing levels of fouling. These upward TMP gradients between consecutive backwashes are attributed to the combined effects of reversible and irreversible fouling where reversible fouling (i.e. cake buildup) is a dominant process. Figure 6.1 also shows that TMP right after backwash at the beginning of the next cycle is always higher from the TMP at the beginning of the previous cycle. This TMP difference is attributed to fouling which cannot be removed with backwashing and hence represents the irreversible fouling.

Therefore, flux and TMP data gathered in the flux stepping experiment offers two types of information: (a) the rate of pressure increase associated mainly, although not entirely, with reversible fouling at different permeate fluxes and (b) the rate of pressure increase associated with irreversible fouling at different fluxes. This piece of information is extracted from the flux stepping experiment and used for the identification of model parameters as described in Section 6.2.3.

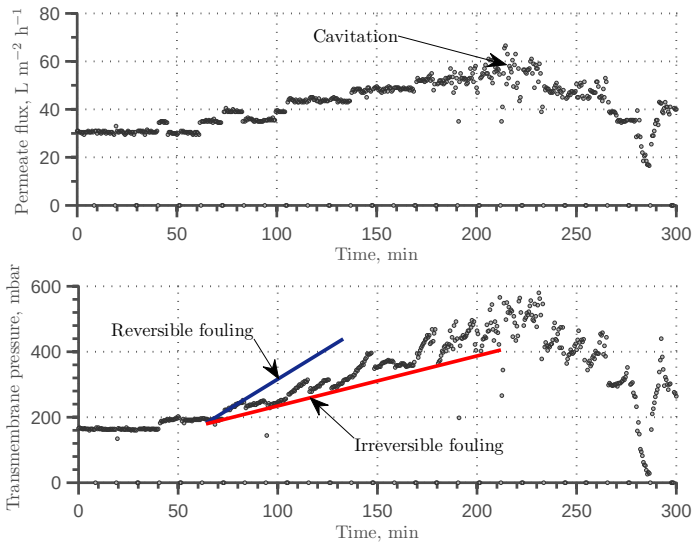

Figure 6.1: TMP and permeate flux measurements in a filtration unit during the flux stepping experiment with indicated TMP gradients due to irreversible and reversible fouling - measurements collected by Dr. Alan Merry, ITT Sanitaire.

Identification of model parameters on the data obtained from the flux stepping experiment

The rate of pressure buildup during filtration $\left(\frac{d(\Delta P)}{dt}\right)$ which, as mentioned earlier, is caused by combined effects of reversible and irreversible fouling, was measured by calculating the gradient of the line of best fit for all TMP data points in each filtration cycle. Similar procedure was carried out to find the rates of pressure increase caused by irreversible fouling by calculating the differences in TMP at the ends of two consecutive backwashes for each filtration cycle. Since for each value of flux, the filtration cycle was repeated three times, the pressure gradient under each flux was calculated as an average of the three values.

The calculated averaged pressure gradients associated with irreversible fouling at different flux rates are plotted in Figure 6.2a. These data points are then approximated with a curve of a general form: $y = m\,x^2\,e^{n\,x}$ where parameters a and b are identified with nonlinear regression using the MATLAB's® Curve Fitting Toolbox™. The form of the curve is derived from the model equations 6.3, 6.5, and 6.7 which, when rearranged,

yield the following equation for the TMP gradient due to irreversible fouling.

$$\begin{aligned} \frac{d(\Delta P)}{dt} &= \mu\, k_i\, S_{SMP}\, f_i\, J^2 \\ &= \mu\, k_i\, S_{SMP}\, a\, e^{b\,J}\, J^2 \end{aligned} \tag{6.14}$$

where μ (Pa·s) denotes the permeate's dynamic viscosity, k_i (m kg^{-1}) denotes the irreversible fouling strength factor, f_i (–) denotes the fraction of SMP contributing to irreversible membrane fouling, and S_{SMP} (g m^{-3}) denotes the SMP concentration. Parameter m obtained from curve fitting is equal to $a\,\mu\,k_i\,S_{SMP}$ in Equation 6.14 and, whilst μ and S_{SMP} are both given, identification of m allows us to find the value of $a\,k_i$, but not a and k_i individually.

Additionally, the pressure gradient points were approximated with a simpler curve of a form: $y = m\,x^2$ which corresponds to the scenario where SMP deposition remains constant during the flux stepping experiment. Hence, parameter m is equal to $k_i\,S_{SMP}\,f_i$. The curve fit is shown in Figure 6.2a in blue colour. It is apparent that the simpler model fits the data significantly worse with the sum of squared residuals of 8.516×10^{-4} on 6 degrees of freedom, compared to 2.017×10^{-4} on 5 degrees of freedom for the more complex model. The analysis of variance performed on both models produced an $\mathcal{F}$-value of 16.1. The reported p-value, 0.010, is far below the standard cutoff of 0.05, hence we reject the null hypothesis that the simpler model is statistically better and we adopt the more complex model, i.e. the model which assumes that the amount of SMP contributing to irreversible fouling depends exponentially on flux.

Since the pressure gradient in each filtration cycle is due not only to reversible fouling but also due to the effects of irreversible fouling, the values of $\frac{d(\Delta P)}{dt}$ obtained from regression as explained in the beginning of this section for each filtration cycle need to be reduced by the values of $\frac{d(\Delta P)}{dt}$ due to irreversible fouling in order to represent the true sole effects of cake buildup. To serve the purpose, TMP gradients calculated from Equation 6.14 were subtracted from the pressure gradients calculated in individual filtration cycles. The resulting data points are then approximated with a quadratic polynomial of the form $y = a\,x^2 + b\,x + c$ as shown in Figure 6.2b.

As in the previous example, MATLAB's® Curve Fitting Toolbox™ was used for identification of the unknown coefficients a and b, while the third coefficient c is set to zero. The fitted curve has the same shape as the expression for TMP increase in time due to reversible fouling presented in Equation 6.15. Thus, $a = \mu\,\alpha_c\,f_r\,X_{TSS}$ and $b = -\mu\,\alpha_c\,\dot{m}_{r,back}$, where μ (Pa·s) is the dynamic permeate viscosity, α_c (m kg^{-1}) denotes the specific cake resistance, f_r (–) denotes the fraction of suspended solids contributing to cake buildup, X_{TSS} (g m^{-3}) is the TSS concentration in the membrane feed, and $\dot{m}_{r,back}$ (kg m^{-2} s^{-1}) denotes the rate of cake back-transport.

Since μ and X_{TSS} are given and, for the sake of simplicity, we can assume that $f_r = 1$, α_c and $\dot{m}_{r,back}$ can be explicitly calculated from the identified parameters a and

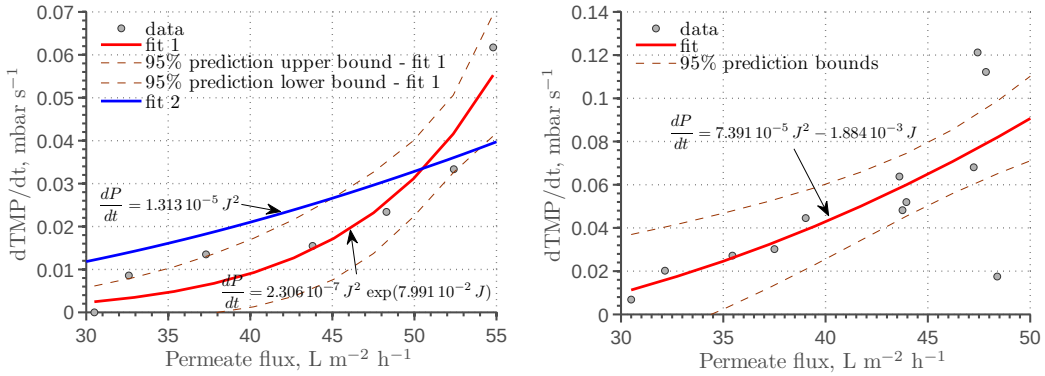

(a) (b)

Figure 6.2: Relationship between the rate of TMP increase in time due to (a) irreversible and (b) reversible fouling, and flux rate.

b.

$$\begin{aligned} \frac{d(\Delta P)}{dt} &= \mu\, J\, \alpha_c\, (f_r\, J\, X_{TSS} - \dot{m}_{r,back}) \\ &= \mu\, \alpha_c\, f_r\, X_{TSS}\, J^2 - \mu\, \alpha_c\, \dot{m}_{r,back}\, J \end{aligned} \tag{6.15}$$

Equation 6.15 is obtained by rearranging and combining Equations 6.3, 6.4, and 6.26 and by substituting the total resistance R_t in Equation 6.3 with the resistance caused by cake buildup R_r.

The identified model parameters are presented in Table 6.3. While fitting the quadratic curve from Equation 6.15 to the second set of data, it has been assumed that the amount of cake back-transport $\dot{m}_{r,back}$ remains constant throughout the flux stepping experiment. Although this might theoretically be true under high CFVs, usually $\dot{m}_{r,back}$ will depend on the amount of cake on the membrane in addition to CFV, thus it is seldom constant. If we look again at the quality of the curve fits in Figure 6.2, we can see that whilst the curve in Figure 6.2a fits the data well, the points in Figure 6.2b appear to be more scattered and further away from the curve for higher fluxes where TMP measurements become more erratic possibly due to pump cavitation. Nevertheless, when we compare the parameter values obtained from curve fitting shown in Table 6.3 with the values obtained from the optimisation-based parameter calibration shown in Table 6.4, we can see that it was sufficient to adjust only the value of $\dot{m}_{r,back}$ in the non-linear model calibration whilst $a\,k_i$ and α_c determined from the curve fits have been successfully used in final simulations. Hence, it seems that the model can be successfully identified with a 'pen and ruler' technique based on the flux and pressure data obtained from flux-stepping experiments without the need for complicated parameter estimation procedures.

The non-linear parameter calibration is explained below. The model was calibrated in four different model configurations:

[1] calculated under assumption that $f_r = 1$

Table 6.3: Parameters identified from the $\frac{d\,\mathrm{TMP}}{d\,t}$ vs. J data generated from the flux-stepping experiment.

Identified lumped and single parameters	Unit	Value
$a\,\mu\,k_i\,S_{SMP}$	mbar s^{-1} $(Lmh)^{-2}$	2.306×10^{-7}
b	$(Lmh)^{-1}$	7.991×10^{-2}
$\mu\,\alpha_c\,f_r\,X_{TSS}$	mbar s^{-1} $(Lmh)^{-2}$	7.391×10^{-5}
$\mu\,\alpha_c\,\dot{m}_{r,back}$	mbar s^{-1} $(Lmh)^{-1}$	1.884×10^{-3}
Recalculated parameters	**Unit**	**Value**
$a\,k_i$	m kg^{-1}	2.397×10^{12}
α_c [1]	m kg^{-1}	5.061×10^{15}
$\dot{m}_{r,back}$	kg m^{-2} d^{-1}	1.040×10^{-2}

Option 1 Constant SMP deposition rate; Cake detachment rate k_r expressed as a single constant value.

Option 2 Flux dependent SMP deposition rate; Cake detachment rate k_r expressed as a single constant value.

Option 3 Flux dependent SMP deposition rate; Cake detachment rate k_r calculated with the shear induction model of Nagaoka et al. [176].

Option 4 Flux dependent SMP deposition rate; Cake detachment $\dot{m}_r$ modelled with the back transport model of Ho and Zydney [97].

In Option 1 the model takes the form of the original model of Liang et al. [149]. Option 2 introduces flux-dependent SMP deposition fraction but keeps the original description of cake back transport. Option 3 and Option 4 additionally introduce the cake back transport models of Nagaoka et al. [176] and Ho and Zydney [97], respectively. Each option assumes that cake is compressible accordingly to Equation 6.11 and introduces back-flushing (Equation 6.9).

Optimum parameter values for the cake detachment models were calculated with MATLAB's `fminsearch` function employing a multidimensional unconstrained nonlinear derivative-free minimization algorithm of Nelder-Mead [133]. The objective function Θ to be minimised is shown below.

$$\Theta = \frac{\sum_{i=1}^{i=N} \left(\Delta P^i_{meas} - \Delta P^i_{simu}\right)^2}{N} \tag{6.16}$$

where N denotes the number of TMP measurements and ΔP^i_{meas} and ΔP^i_{simu} (mbar) denote, respectively, the measured and the predicted TMPs in the i-th time step.

Figure 6.3a shows good quality of fit between the original model in Option 1 and the measurements. However, one can observe some discrepancies between the predicted and the measured TMPs under lower permeate fluxes in the first 40 minutes of the experiment. Whilst the model predicts cake formation (reversible fouling) under sub-

critical fluxes, the experimental data shows no accumulation of cake in this region. To remind the reader, reversible fouling manifests itself on the graphs with TMP gradients in filtration periods. This model behaviour results from the chosen representation of $\dot{m}_{r,back}$ which is modelled as $k_r\, m_r$ and which thus tends to zero for very low m_r values. Small back-transport $\dot{m}_{r,back}$ in turn creates an opportunity for thin layers of cake to build up on the membrane surface. Although the predicted cake thicknesses are small, high α_c values lead to noticeable additional resistances causing the visible predicted pressure gradients in Figure 6.3a.

Figure 6.3a also shows that the predicted long-term TMP gradient due to irreversible fouling under low permeate fluxes is higher than what is manifested by the experimental data. The data shows that the long-term TMP gradient in the first 40 minutes of operation where flux was kept at a constant value of ~ 30 L m^{-2} h^{-1} was not noticeable. This observation leads to the conclusion that SMP deposition at low sub-critical fluxes in this experiment either does not occur or, what is more probable, occurs at very slow rates. The pressure gradient caused by irreversible fouling is found to increase with the applied permeate flux, which indicates that SMP deposition rates are dependent on the value of permeate flux. As the model in Option 1 uses a single SMP deposition constant f_i for an entire range of fluxes, the model over-predicts SMP deposition under lower flux rates in order to remain in agreement with the measurements under higher fluxes where the rates of SMP deposition and hence irreversible fouling are larger.

Figure 6.3b shows the measurements and the model outputs in Option 2. The model introduces flux dependent SMP deposition constant f_i which increases exponentially with flux in accordance with Equation 6.12. Cake detachment model is the same as in Option 1. As can be seen in Figure 6.3b the long-term gradient under low fluxes is slightly reduced but the model still over-predicts the amount of cake buildup under low fluxes.

The models in Option 3 and Option 4 incorporate flux dependent SMP deposition and additionally introduce cake detachment models of, respectively, Nagaoka et al. [176] and Ho and Zydney [97]. Results obtained from these two fouling models are shown in Figures 6.4a and 6.4b. Whilst Figure 6.4a is almost identical to Figure 6.3a, Figure 6.4b shows the best quality of fit between the model and the data out of all four figures. The pressure gradients due to cake growth under sub-critical fluxes are lower than in the previous simulations and additionally the amount of irreversible fouling under low fluxes is reduced. The most accurate predictions are thus offered with the model incorporating flux dependent SMP deposition and cake back-transport model of Ho and Zydney [97].

All calibrated parameters for Option 1 - Option 4 are presented in Table 6.4.

Long-term filtration under sub-critical flux

Reversible and irreversible fouling occur at different temporal scales. Under 'favourable' conditions for the occurrence of fouling, such as low CFV or air scouring rate, reversible

Table 6.4: Values of behavioural model parameters identified on the flux-stepping experiment measurements collected by Dr. Alan Merry, ITT Sanitaire.

Description	Parameter	Unit	Option				Source
			1	2	3	4	
Bulk liquid temperature	T	^{o}C	15	15	15	15	Measured
Clean membrane resistance	R_m	m^{-1}	1.68×10^{12}	1.68×10^{12}	1.68×10^{12}	1.68×10^{12}	Calibrated
TMP below which compression does not occur	ΔP_{crit}	Pa	$30,000$	$30,000$	$30,000$	$30,000$	[202]
Exponent in cake compressibility equation	n_{α_c}	–	1.0	1.0	1.0	1.0	[202]
SMP deposition fraction times its fouling strength	$f_i\, k_i$	m kg^{-1}	2.40×10^{12}	x	x	x	Calibrated
Specific cake resistance	α_c	m kg^{-1}	5.06×10^{15}	5.06×10^{15}	5.06×10^{15}	5.06×10^{15}	Calibrated
SMP fouling strength	k_i	m kg^{-1}	x	2.40×10^{12}	2.40×10^{12}	2.40×10^{12}	Calibrated
Exponent in SMP deposition formula	b	–	x	6.80×10^{-2}	6.80×10^{-2}	6.80×10^{-2}	Calibrated
Cake detachment rate	k_r	d^{-1}	200	200	x	x	Calibrated
Static friction coefficient	λ_m	–	x	x	1.00×10^{-3}	x	[176]
Proportionality coefficient	γ_m	d^{-1} Pa^{-1}	x	x	1.00×10^{-1}	x	[176]
Shear stress at the membrane wall	τ_m	Pa	x	x	1.00×10^{2}	x	Calibrated
Shear rate at the membrane wall	γ	d^{-1}	x	x	x	155	Calibrated
Exponent in the back-transport model	n	–	x	x	x	1.5	[97]
Proportionality coefficient in the back transport model	k	m s^{n-1}	x	x	x	0.07	[97]

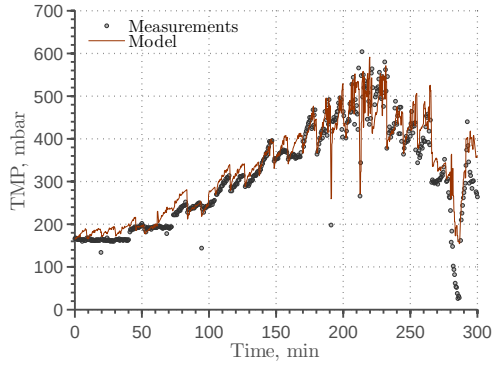

(a) Option 1

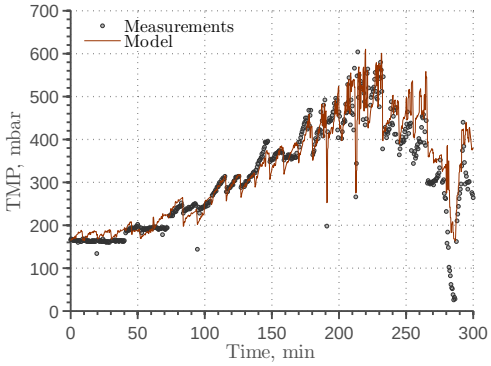

(b) Option 2

Figure 6.3: Results of calibration of the behavioural model on Cardiff flux stepping data - Option 1 and Option 2

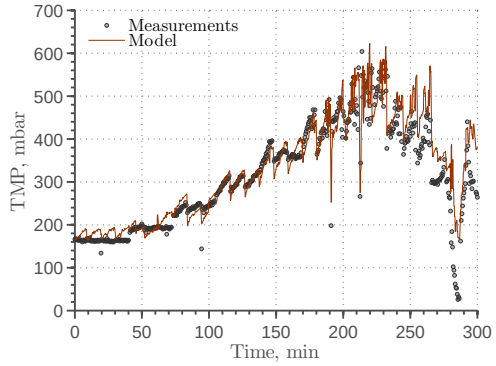

(a) Option 3

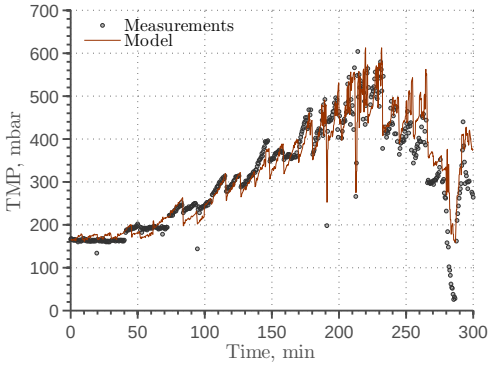

(b) Option 4

Figure 6.4: Results of calibration of the behavioural model on Cardiff flux stepping data - Option 3 and Option 4

fouling happens very quickly in the range of seconds to minutes. Irreversible fouling in turn is a long-term process attributing to a slow but constant increase of membrane resistance. Since it takes many days for irreversible fouling to develop under sub-critical fluxes while flux-stepping experiment took only 5 hours, irreversible fouling equation could not be properly tested in the previous calibration exercise. Hence, the model was additionally calibrated on 640 hours (i.e. $\sim$ 27 days) of filtration data obtained from an immersed MBR pilot plant equipped with vertical hollow fibre PES membranes and fed with brewery wastewater. As mentioned in the beginning of this chapter, the pilot plant was installed by ITT Sanitaire® at the Coors Shobnall Maltings site in the Midlands, UK. On-line data recorded at 2s intervals was supplied by ITT Sanitaire® and is composed of permeate fluxes and TMPs. Off-line information included average MLSS concentrations, membrane area and bulk liquid temperature. Model parameters that remained constant during calibration are listed in Table 6.5.

The model adopted for calibration is the basic unmodified model of Liang (Option 1). Due to very high cross-flow velocities and thus almost complete absence of cake buildup in the pilot plant, except for Calibration 4 where cake formation did occur, it

Table 6.5: Model parameters set to remain constant during the long-term calibration experiment.

Parameter	Value	Unit	Description	Source
T	15	^{o}C	Bulk liquid temperature	Provided
X_{TSS}	$10,000$	g m^{-3}	Total suspended solids concentration	Provided
R_m	1.68×10^{12}	m^{-1}	Clean membrane resistance	Initial condition
A_m	34	m^2	Membrane area	Provided
k_i	1.1×10^{16}	m kg^{-1}	SMP fouling strength	[265]
α_c	4.0×10^{13}	m kg^{-1}	Specific cake resistance	Assumed
n_{α_c}	1.0	–	Exponent in cake compressibility equation	[202]
ΔP_{crit}	$30,000$	Pa	TMP below which compression does not occur	[202]

was sufficient to describe cake detachment with a simple $k_r\, m_r$ term as in the original model of Liang et al. [149]. Modelling of the flux dependency of irreversible fouling was also not required as the pilot plant was operating at a constant flux of $\sim$ 19.2 Lmh except for the initial 48 hours where flux was kept at $\sim$ 17.7 Lmh - see Figure 6.6a and Figure 6.5.

In order to calibrate the model, the measurements had to be split into 5 separate data sets (see Figure 6.5). The model was then calibrated individually for each set of measurements using the same nonlinear simplex optimisation algorithm of Nelder and Mead [178] as used in the previous study. Two parameters were selected for calibration: the cake detachment rate (k_r) and SMP deposition fraction times SMP concentration ($f_i\, S_{SMP}$). The SMP deposition fraction f_i could not be identified individually due to lack of information about SMP concentrations in the system. The fouling strength k_i was neither known nor could be identified due to lack of appropriate measurements, hence the value of 1.1×10^{16} m kg^{-1} was adopted after Ye et al. [265] as shown in Table 6.5. Clean membrane resistance (R_m) was identified from initial TMP at the beginning of the filtration period and was found to be equal to 1.68×10^{11} m^{-1}.

Values of the calibrated parameters for each calibration period are shown in Table 6.6. The table is additionally supplemented with the values of specific cake resistance α_c which is kept at a constant value of 4.0×10^{13} m kg^{-1} except for Calibration 4 where α_c had to be increased to 5.0×10^{13} m kg^{-1} in order to match the data.

Table 6.6: List of model parameters identified in the long-term calibration experiment.

	k_r (d^{-1})	$f_i \times S_{SMP}$ (g m^{-3})	α_c (m kg^{-1})
Calibration 1	7.5×10^3	0.040	4.0×10^{13}
Calibration 2	3.5×10^3	0.225	4.0×10^{13}
Calibration 3	8.5×10^3	0.000	4.0×10^{13}
Calibration 4	0	1.250	5.0×10^{13}
Calibration 5	8.5×10^3	0.000	4.0×10^{13}

For the purpose of visualisation the measurements and model outputs were filtered

to remove the data points associated with backwash periods. Thus, the data points corresponding to filtration were isolated from an entire set of data including forward filtration and backwash. Next, the data which, as mentioned before, were collected every 2 seconds, were averaged over 2-hour time windows. The averaged flux and TMP data and model outputs are shown in Figure 6.5. As Figure 6.5 indicates, the model performed very well at predicting pressure losses across the membrane for each calibration period.

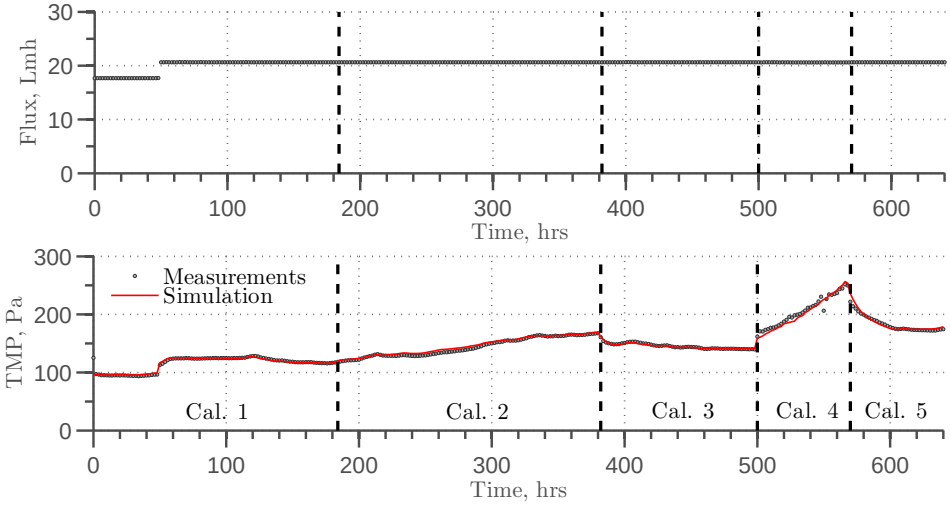

Figure 6.5: Combined results of calibration of the behavioural model on all experimental data from the Coors plant.

Calibration results for each individual calibration period are shown in Figures 6.6, 6.7, and 6.8. In Calibration 3 and Calibration 5 TMP was found to decrease in time while flux remained constant, what indicates an increase in the membrane permeability. The reason for this permeability recovery effect was unknown and because very little information about operational conditions in the pilot-plant was available, it could only be assumed that this permeability recovery might have been caused by gradual redissolution of irreversible foulants due to e.g. change of pH in the influent wastewater. The observed permeability recovery was modelled with 1st order exponential decay of the mass of irreversible foulant (m_i) as shown in Figure 6.8b. The measured flux and the measured and simulated TMPs in the Calibration period 3 and Calibration period 5 are shown in Figure 6.7a and Figure 6.8a respectively.

Although not shown here, the simulated and measured TMPs were found to diverge slightly in backwash cycles. This discrepancy may be due to several reasons. Firstly, the backwash model is very crude and predicts instantaneous removal of the entire cake mass, which does not happen in reality. Additionally, since the backwash flow is almost double the forward flow but only lasts for a short period of time, the pressure transients developing during instantaneous changes in the direction of flow could have been causing pressure and flow fluctuations which are not represented in the Darcy's equation used in the model.

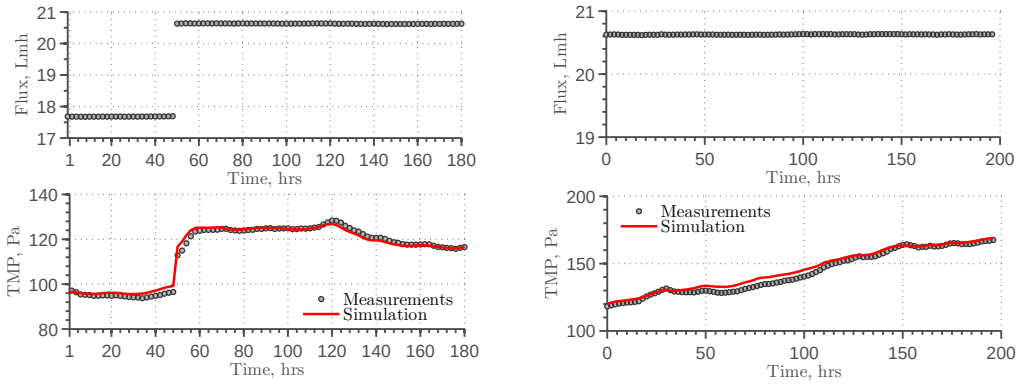

(a) Calibration 1 (b) Calibration 2

Figure 6.6: TMP predictions of the calibrated behavioural model vs. measurements for time periods 1 and 2.

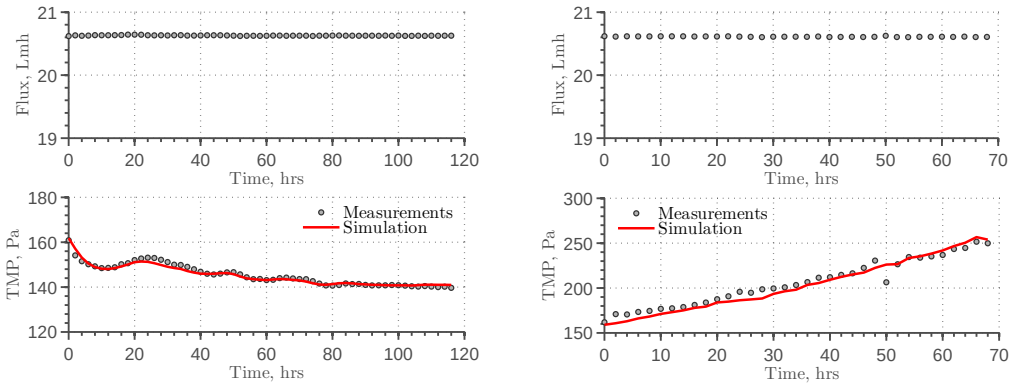

(a) Calibration 3 (b) Calibration 4

Figure 6.7: TMP predictions of the calibrated behavioural model vs. measurements for time periods 3 and 4.

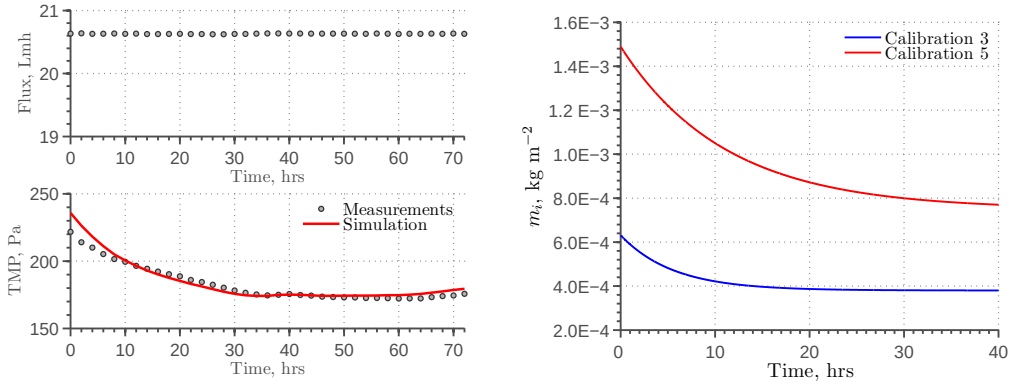

(a) Calibration 5 (b) Recovery of irreversible fouling

Figure 6.8: TMP predictions of the calibrated behavioural model vs. measurements for time period 5 (a) and decrease in m_i over time for calibration periods 3 and 5 (b).

6.2.4 Two-stage TMP profiles

The model was additionally simulated under sub-critical fluxes of 2, 4, 6, and 7 Lmh. Backwashing was switched off whilst cake removal constant k_r was kept at 0.75×10^4 d^{-1}. Irreversible fouling was modelled with two different equations. Whilst in the first option the original Equation 6.7 for irreversible fouling is used, the second option incorporates Hagen-Poiseuille equation which calculates the pressure loss across the membrane under assumption that a) flow is laminar b) membrane is a sheet of constant thickness with uniformly spaced cylindrical pores of equal diameters. Whilst in Equation 6.7 resistance is proportional to the amount of irreversible foulant m_i, membrane resistance in Hagen-Poiseuille equation is inversely proportional to the square of pore diameter d_p (m) and directly proportional to the membrane thickness L (m).

$$R_i = \frac{128\, L\, A}{N\, \pi\, {d_p}^2} \tag{6.17}$$

In Equation 6.17, R_i (m^{-1}) denotes the resistance due to irreversible fouling, A (m^2) denotes the total membrane area, and N (–) denotes the total number of (open) pores in the membrane.

The internal pore diameter decreases in size starting from an initial pore diameter d_{p0} due to deposition of SMP inside the pores. It is assumed that SMP deposits uniformly along the length of the pore and leads to a decrease in pore diameter according to Equation 6.18.

$$\frac{d\, d_p}{d\, t} = -2\, k_a\, e^{b\, J}\, \frac{S_{SMP}\, J\, A}{\rho_{SMP}\, L\, \pi\, d_p\, N} \tag{6.18}$$

where $\rho_{SMP} = 1,060 \times 3.45$ kg m^{-3} denotes SMP density and $k_a = 10^{-19}$ and $b = 0.01$ are flux dependent SMP deposition parameters.

Due to gradual decrease in the size of pore diameters, the total area of pores A_{open} (m^2) and, as a result, the membrane porosity ε_p (%) decrease accordingly.

$$A_{open} = 0.25\, N\, \pi\, {d_p}^2 \tag{6.19}$$

$$\varepsilon_p = \frac{A_{open}}{A}\, 100\% \tag{6.20}$$

Pressure loss across the membrane is then calculated in both options using the Darcy's law.

$$\Delta P = \mu\, J\, (R_m + R_i + R_r) \tag{6.21}$$

Results of the simulations carried out with both model options are presented in Figure 6.9. Figure 6.9 shows that whilst Hagen Poiseuille equation predicts high rate of pressure rise after a specific amount of time in which pore constriction becomes advanced enough to create an almost infinite amount of resistance, the response of Equation 6.7 is very different and it is clear that Equation 6.7 is unable to represent the so-called two-stage TMP profile which will be explained in more detail in Section 6.3. It will be

later demonstrated that a two-stage TMP profile can be modelled with a combination of three classical filtration laws: pore constriction, complete pore blockage and cake formation. The model described here is unable to predict this behaviour, however it is able to represent certain behaviour of MF membranes as outlined in the previous sections.

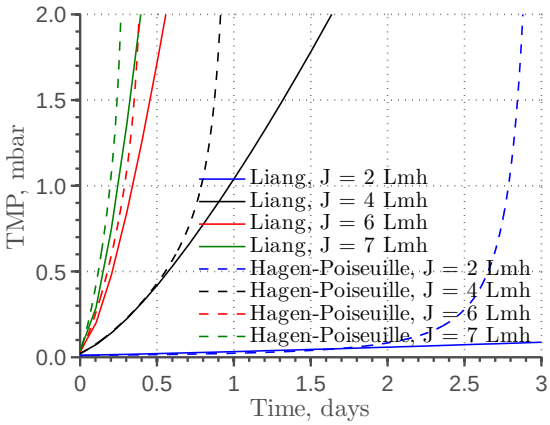

Figure 6.9: Comparison of models with (a) irreversible fouling described accordingly to Liang et al. [149] and (b) with Hagen-Poiseuille equation for pore constriction, under constant sub-critical flux operation.

6.3 Development of the mechanistic fouling model

6.3.1 Model formulation

As described in Hwang et al. [107] and Hwang and Chen [105] microfiltration of liquids containing dissolved organic matter (DOM) and suspended solids (SS) often cannot be described by only one mechanistic fouling model such as *pore constriction*, *intermediate pore blockage*, *complete pore blockage* and *cake formation*. Each of the above mentioned fundamental fouling processes can be described by Equation 6.22 introduced by Hermia [91] where $n = 2$ for complete pore blockage, $n = 1$ for intermediate pore blockage, $n = 3/2$ for pore constriction and $n = 0$ for cake filtration. As demonstrated by Hwang and Chen [105] the value of n is usually not constant throughout the entire course of filtration but varies in time as a consequence of simultaneous occurrence and mutual interactions between pore constriction, blockage and cake filtration. In order to simulate membrane filtration in situations where pore constriction, pore blockage and cake buildup contribute to membrane fouling at comparative levels and none of these processes dominate over the rest, it is necessary to use a mathematical model taking into consideration all three of these processes.

$$\frac{d^2t}{dV^2} = k\left(\frac{dt}{dV}\right)^n \tag{6.22}$$

The fouling model presented here is based on the idea described in Duclos-Orsello et al. [50] where three fundamental fouling processes: pore constriction, complete pore blockage and cake formation are incorporated within a single mathematical model. The authors of the above mentioned paper analytically integrated each one of the three classical fouling equations and provided a closed solution in the form of a single expression describing the reduction of total flow through a membrane in constant pressure filtration. Their final solution is presented, for the convenience of the reader, in Equation 6.23.

$$\begin{aligned}\frac{Q}{Q_0} &= \frac{1}{\left(1+\tilde{\beta}Q_0C_bt\right)^2}\,\exp\left(-\frac{\alpha C_bJ_0t}{1+\tilde{\beta}Q_0C_bt}\right)\\ &+\int_0^t \frac{\dfrac{\alpha C_bJ_0}{\left(1+\tilde{\beta}Q_0C_bt_p\right)^2}\,\exp\left(-\dfrac{\alpha C_bJ_0t_p}{1+\tilde{\beta}Q_0C_bt_p}\right)}{\sqrt{\left(\dfrac{R_{p0}}{R_m}+\left(1+\tilde{\beta}Q_0C_bt_p\right)^2\right)^2+2\,\dfrac{f'R'\Delta PC_b}{\mu {R_m}^2}\,(t-t_p)}}\,\mathrm{d}t \end{aligned} \quad (6.23)$$

The first two factors before the integral describe the effects of pore constriction and pore blockage. The extent of pore blockage is reduced by simultaneously occurring pore constriction. The third term under the integral describes reduction of flow due to cake formation on the membrane surface. Q_0 and J_0 denote the initial flow and initial flux, C_b is the bulk concentration of the foulant and R_m is the clean membrane resistance. Parameters $\tilde{\beta}$ and α govern the rates of, respectively, pore constriction and pore blockage. $\tilde{\beta}$ is an auxiliary variable and is equal to $\dfrac{\beta}{N_0\pi r_0^2 L}$ where β is a pore constriction parameter in Equation 6.24. f' and R' govern the process of cake formation. f' is the fraction of the foulant which contributes to cake formation and R' is the specific resistance of the fouling layer. R_{p0} denotes the resistance of a single layer of foulant causing pore blockage. Succession of pore blockage and cake formation processes is ascertained by solving the cake growth Equation 6.26 over the time interval t_p to t where t_p denotes the time moment at which the considered region of the membrane was first blocked. It is however difficult to understand from the original paper how the value of t_p is determined or calculated. The Author understands that in order to simulate constant pressure dead-end filtration with Equation 6.23 one has to discretise the membrane area and solve this equation for each discrete element with t_p individually calculated as the time at which this elemental area is entirely blocked which in turn can be obtained from the pore blocking equation described in Duclos-Orsello et al. [50]. Whilst discretisation of the membrane area might offer benefits in providing insight into development of spatial inhomogeneities in the membrane with regards to the levels of fouling caused by individual fouling processes, solution of such a model might be very computationally intensive. Additionally the use of an analytically integrated equation only allows modelling of filtration under constant TMP. For this reason an alternative solution to the three-mechanism fouling model of Duclos-Orsello et al. [50] was sought and is described in the latter parts of this section.

Three classical fouling models used in this work are shown in Equations 6.24-6.26.

$$\frac{d(N_u\,\pi\,{r_p}^2\,L)}{dt} = -f\,\beta\,J_u\,A_u\,S_{SMP} \tag{6.24}$$

$$\frac{dA_u}{dt} = -\alpha\,X_{TSS}\,J_u\,A_u \tag{6.25}$$

$$\frac{dR_p}{dt} = f'\,R'\,J_b\,X_{TSS} - k_r\,R_p \tag{6.26}$$

where N_u (–) denotes the number of open membrane pores, r_p (m) denotes the average pore diameter, L (m) denotes the membrane thickness, f (–) is the fraction of foulant contributing to pore constriction, β ($m^3\ kg^{-1}$) is the pore constriction parameter, J_u ($m^3\ m^{-2}\ s^{-1}$) denotes the permeate flux through unblocked area, A_u (m^2) denotes the unblocked membrane surface, S_{SMP} ($g\ m^{-1}$) denotes the SMP concentration in the membrane feed, α ($m^2\ kg^{-1}$) is the pore blocking parameter, X_{TSS} ($g\ m^{-3}$) is the concentration of TSS in the membrane feed, R_p (m^{-1}) is the resistance of cake deposit, f' (–) is the fraction of foulant contributing to cake growth, k_r ($m\ kg^{-1}\ s^{-1}$) is the cake detachment coefficient, R' ($m\ kg^{-1}$) is the specific resistance of the fouling layer and J_b ($m^3\ m^{-2}\ s^{-1}$) denotes the permeate flux through the blocked area.

Pore constriction is modelled with Equation 6.24 which describes reduction of pore volume due to deposition of the foulant. Reduction of pore volume is proportional to the fraction of S_{SMP}, described with parameter f, absorbed on the internal pore surface. This equation assumes uniform spatial distribution of pores, uniform pore diameter (r_p) and uniform length (L). It is solved with an initial condition $r_p(0) = r_{p,0}$ where $r_{p,0}$ denotes the initial membrane pore diameter and is calculated from Equation 6.30 in which R_{inb} has been substituted with clean membrane resistance R_m.

Complete pore blockage is described with Equation 6.25 whereas cake formation is governed by Equation 6.26. The second part of Equation 6.26 represented by term $k_r\,R_p$ models the effects of turbulence-induced shear on accumulation of cake mass on the membrane area. In this equation, the rate of change of cake resistance R_p is in direct proportion to the flux of suspended solids ($J_b\,X_{MLSS}$), where J_b ($m^3\ m^{-2}\ s^{-1}$) denotes the permeate flux through blocked area and X_{TSS} ($g\ m^{-3}$) is the TSS concentration. The back-flux of solids due to cake detachment is proportional to the cake detachment coefficient k_r times the unit mass of cake accumulated on the membrane m_c ($kg\ m^{-2}$). m_c can be calculated as a ratio between the current cake resistance R_p and the specific cake resistance R' ($R_p = R'\,m_c$). Equations 6.25 and 6.26 are solved with initial conditions $A_u(0) = A$ and $R_p(0) = R_{p,0}$, where often $R_{p,0} = n0$, i.e. initial cake resistance is assumed to be zero.

Equation 6.24 can be rearranged to yield an expression for the rate of change of the membrane pore diameter in time as shown in Equation 6.27.

$$\frac{dr_p}{dt} = -\frac{f\,\beta\,J_u\,S_{SMP}}{2\,\pi\,\rho_p\,L\,r_p} \tag{6.27}$$

where the newly introduced parameter $\rho_p = \frac{N}{A} = \frac{N_u}{A_u}$ denotes the membrane pore density. It is assumed that the pore density in a membrane is constant in every part of the membrane.

As shown in Figure 6.10 flux through the membrane is divided into two parts, the so called *unblocked flux* J_u which denotes the flux passing through an unblocked portion of the membrane with area A_u (calculated from Equation 6.25) and *blocked flux* J_b which denotes the flux through the blocked area A_b.

Although Equations 6.24-6.26 can be solved via analytic integration as described in Duclos-Orsello et al. [50] and outlined above, this approach suffers from three major drawbacks. First, it requires the membrane area to be discretised thus leading to simultaneous solution of multiple instances of Equation 6.23, each for one elemental area. Second, it only allows to simulate filtration under constant TMP with model parameters kept constant throughout duration of the filtration process. Third, it only allows calculation of the flux decline under a given pressure difference ΔP. Hence, calculations of TMP increase under a given permeate flux would not be possible.

The alternative is to solve Equations 6.24-6.26 numerically treating the membrane as a single point in space with properties r_p, A and L. In order to do so, we need to calculate the resistance under the blocked area A_b (R_{ib}) which is required by Equation 6.37 to compute the blocked flux J_b. J_b is also used in Equation 6.26 to calculate the flux of solids per unit area leading to cake formation ($f' J_b X_{TSS}$). Thanks to the introduction of R_{ib}, discretisation of the membrane area and explicit calculation of t_p as required in Equation 6.23 are avoided. Pore blockage and the principle of calculating the blocked membrane resistance R_{ib} are graphically described in Figure 6.10. As the

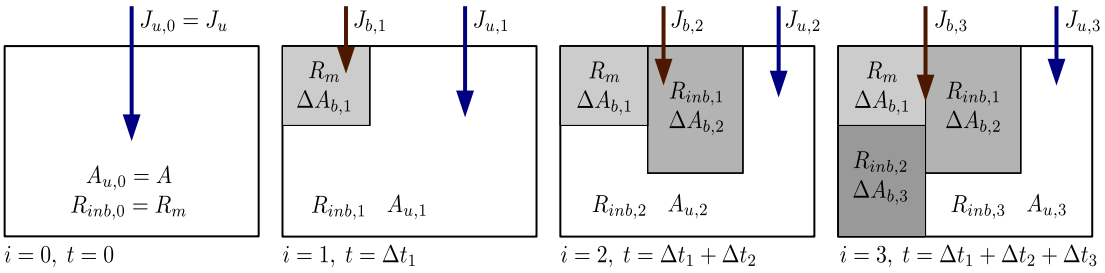

Figure 6.10: Graphical representation of the evolution of blocked area A_b and resistance under blocked area R_{ib} at elementary time steps Δt_i during filtration of solutes and suspensions.

time goes by during filtration, open pores in an unblocked part of the membrane are gradually covered with blocking layer having an initial resistance $R_{b,0}$. The number of blocked pores N_b are proportional to the blocked area (A_b) accordingly to relation $N_u = \rho_p A_u$ and hence $N_b = \rho_p A_b$, where ρ_p (m^{-2}) denotes the density of homogeneously distributed pores in the membrane. In each time increment i, the resistance of the additional blocked area $\Delta A_{b,i}$ is equal to the resistance of the unblocked area from the previous time step ($R_{inb,i-1}$) plus $R_{b,0}$. The resistance of an entire blocked area minus R_p at the time step i is calculated from the resistances of the elemental

blocked surfaces $\Delta A_{b,j}$ calculated in all previous time steps ($j = 2 : i$) such that the flow through the entire blocked area (A_b) is equal to the sum of elemental flows through all elemental areas. This relationship is based on the Darcy's law and is represented in Equation 6.28.

$$\sum_{j=2}^{i} \frac{\Delta P}{\mu \left(R_{inb,j-1} + R_{b,0}\right)} \Delta A_{b,j} = \frac{\Delta P}{\mu \, R_{ib,i}} A_{b,i} \tag{6.28}$$

where R_{inb} (m^{-1}) denotes the membrane resistance under the unblocked area, whereas R_{ib} (m^{-1}) denotes the membrane resistance under the blocked area.

After appropriate mathematical rearrangements it is possible to derive a difference Equation 6.29 which calculates R_{ib} in each time step during filtration. The parameter $R_{b,0}$ denotes the resistance of a single blocking layer.

$$R_{ib,i} = R_{ib,i-1} + \frac{\Delta A_{b,i} \left(\sum_{j=1}^{i-1} \frac{\Delta A_{b,j}}{R_{inb,j-1} + R_{b,0}} - \frac{A_{b,i-1}}{R_{inb,i-1} + R_{b,0}} \right)}{\sum_{j=1}^{i-1} \frac{\Delta A_{b,j}}{R_{inb,j-1} + R_{b,0}} \sum_{j=1}^{i} \frac{\Delta A_{b,j}}{R_{inb,j-1} + R_{b,0}}} \tag{6.29}$$

Resistance of the unblocked area R_{inb} is obtained from Hagen-Poiseuille equation in which the value of r_p is obtained from Equation 6.27. ρ_p is calculated from as a ratio of total number of pores in the membrane and total membrane surface: $\rho_p = \frac{N}{A}$.

$$R_{inb} = \frac{8L}{\pi \, \rho_p \, r_p^4} \tag{6.30}$$

It is possible to convert Equation 6.29 into two ordinary first order differential equations. Let's introduce a new variable K which represents the product of average blocked membrane conductivity and the blocked area (A_b). The value of K in time step $i-1$, $K_{i-1} = \sum_{j=1}^{i-1} \frac{\Delta A_{b,j}}{R_{inb,j-1} + R_{b,0}}$ while K in time step i can be represented as: $K_i = \sum_{j=1}^{i} \frac{\Delta A_{b,j}}{R_{inb,j-1} + R_{b,0}}$. K_i can be written as a function of K_{i-1}: $K_i = K_{i-1} + \frac{\Delta A_{b,i}}{R_{inb,i-1} + R_{b,0}}$, which can be rearranged to form the following difference equation: $\frac{K_i - K_{i-1}}{\Delta t} = \frac{\Delta A_{b,i}}{\Delta t} \frac{1}{R_{inb,i-1} + R_{b,0}}$. This difference equation represents the Euler difference scheme for the following differential equation:

$$\frac{dK}{dt} = \frac{dA_b}{dt} \frac{1}{R^*_{inb} + R_{b,0}} \tag{6.31}$$

where the subscript* denotes the numerical value from the previous time step. As $dt \to \infty$, $K^* \to K$, hence Equation 6.31 becomes:

$$\frac{dK}{dt} = \frac{dA_b}{dt} \frac{1}{R_{inb} + R_{b,0}} \tag{6.32}$$

After K_{i-1} and K_i have been substituted into Equation 6.29, Equation 6.29 takes the following form: $R_{ib,i} = R_{ib,i-1} + \dfrac{\Delta A_{b,i}\left(K_{i-1} - \dfrac{A_{b,i-1}}{R_{inb,i-1}+R_{b,0}}\right)}{K_{i-1}\,K_i}$. This equation is then rearranged into: $\dfrac{R_{ib,i}-R_{ib,i-1}}{\Delta t} = \dfrac{\Delta A_{b,i}}{\Delta t}\dfrac{\left(K_{i-1} - \dfrac{A_{b,i-1}}{R_{inb,i-1}+R_{b,0}}\right)}{K_{i-1}K_i}$ which represents the Euler difference scheme for the following differential equation:

$$\frac{dR_{ib}}{dt} = \frac{dA_b}{dt}\frac{K^* - \dfrac{A_b^*}{R_{inb}^*}}{K^* K} \tag{6.33}$$

As $dt \to \infty$, then $K^* \to K$, $A_b^* \to A_b$, and $R_{inb}^* \to R_{inb}$. Hence, Equation 6.33 becomes:

$$\frac{R_{ib}}{dt} = \frac{dA_b}{dt}\left(\frac{1}{K} - \frac{A_b}{K^2\,R_{inb}}\right) \tag{6.34}$$

The value of A_b in Equation 6.34 is calculated from A_u which, in turn, is obtained from Equation 6.25. The rate of pore blocking $\dfrac{dA_b}{dt}$ equals $-\dfrac{dA_u}{dt}$, although A_b is simply computed with Equation 6.25.

$$A_b = A - A_u \tag{6.35}$$

Permeate fluxes through unblocked and blocked areas J_u and J_b are calculated with Equation 6.36 and Equation 6.37.

$$J_u = \frac{\Delta P}{\mu\,R_{inb}} \tag{6.36}$$

$$J_b = \frac{\Delta P}{\mu\,(R_{ib}+R_p)} \tag{6.37}$$

Table 6.7: Equations used for the formulation of the mechanistic fouling model in the differential-difference form.

Equation	Reference
Eq. 3	Equation 6.24
Eq. 4	Equation 6.25
Eq. 5	Equation 6.26
Eq. 6	Equation 6.28
Eq. 7	Equation 6.29
Eq. 8	Equation 6.30
Eq. 9	Equation 6.35
Eq. 10	Equation 6.36
Eq. 11	Equation 6.37
Eq. 12	Equation 6.38
Eq. 13	Equation 6.39
Eq. 14	Equation 6.40

The model can be used to simulate flux decline under a given TMP or TMP

increase under a given amount of flux. In both cases the model inputs, i.e. ΔP and J respectively can vary in time. Equations used in both model configurations are collated in Table 6.7. The difference Equation 6.29 in Table 6.7 can be substituted with two differential equations - Equation 6.32 and Equation 6.34. Thus, the mixed difference-differential set of equations is converted into a system of ordinary differential equations.

Model for the predictions of flux decline under a given TMP is composed of four main differential and difference equations: 6.24, 6.25, 6.26, and 6.29 and four algebraic equations: 6.30, 6.35, 6.36, and 6.37. Solution flow diagram and the connections between all constituting equations shown as blocks are presented in Figure 6.11. Total flow and total flux at a given time moment are equal to: $Q = J_u\,A_u + J_b\,A_b$ and $J = {}^{Q}/_{A}$, respectively.

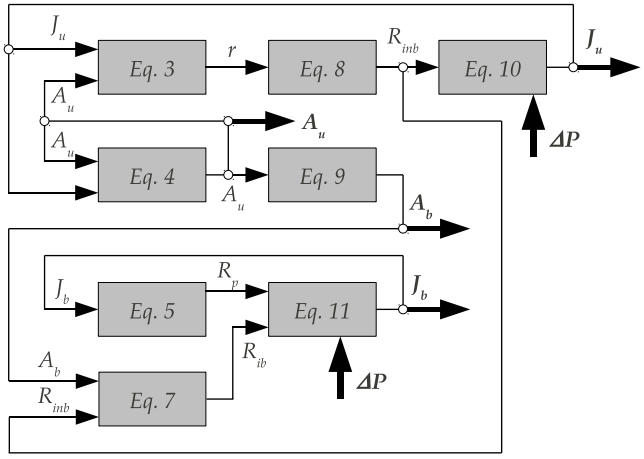

Figure 6.11: Flow diagram of the three mechanism fouling model configured to simulate pressure driven filtration.

Where it is required to predict the TMP in filtration of a liquid under known flux, solution sequence of the constituting equations needs to be reordered. The known permeate flow is split into the unblocked flow (Q_u) and the blocked flow (Q_b) where $Q_u = J_u A_u$ and $Q_b = J_b A_b$. Under a given total flow Q, the split into Q_u and Q_b can be calculated from Equation 6.36 and Equation 6.37 and the continuity equation: $Q = Q_u + Q_b$. The unblocked and blocked fluxes resulting from this derivation are given in Equations 6.38 and 6.39. Either unblocked or blocked flux can be then used to calculate the pressure drop across the membrane with Equation 6.40.

$$J_u = \frac{JA\,(R_{ib} + R_p)}{R_{inb}\,A_b + A_u\,(R_{ib} + R_p)} \tag{6.38}$$

$$J_b = \frac{JAR_{inb}}{R_{inb}\,A_b + A_u\,(R_{ib} + R_p)} \tag{6.39}$$

$$\Delta P = J_u\,\mu\,R_{inb} = J_b\,\mu\,(R_{ib} + R_p) \tag{6.40}$$

The flow diagram of the model for calculation of TMP under known flux is shown in Figure 6.12.

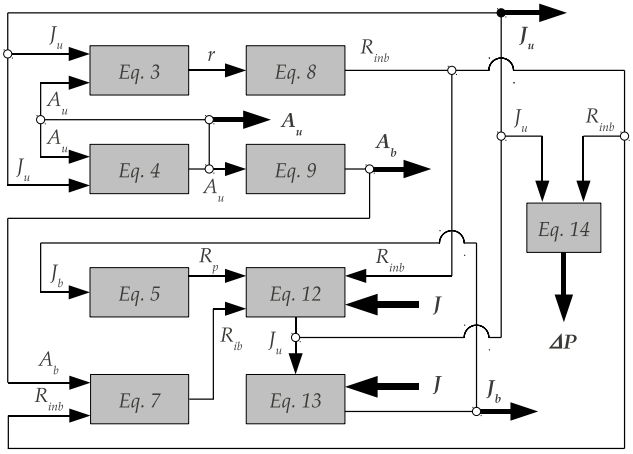

Figure 6.12: Flow diagram of the three mechanism fouling model configured to simulate flux driven filtration.

6.3.2 Model calibration

The model was calibrated on two sets of experimental data obtained from two different sources.

The first set of data was obtained by Duclos-Orsello et al. [50] from a 25mm diameter Amicon stirred ultrafiltration cell. The stirring was switched off and the cell operated under constant TMP of 14 kPa. Four filtration experiments were carried out for different solutions and on different membranes as shall be explained in the next section. Each experiment was performed at various solution concentrations which resulted in a family of flux and resistance curves for model calibration.

The second calibration exercise was carried out on the data obtained by Ye et al. [266] from a crossflow filtration cell receiving a 100 mg L^{-1} sodium alginate solution at different sub-critical flux rates. For each preset flux rate the cell was operating for a period of time between 10 hours and 250 hours which, depending on the flux rate, was sufficient to observe a two-stage TMP profile with slow gradual pressure rise over a relatively long period of time followed by a rapid TMP rise.

Experimental methods

Detailed description of the experimental methods is provided in the original papers of Duclos-Orsello et al. [50] and Ye et al. [266]. Nevertheless the experimental methods are briefly outlined here for the benefit of the reader.

The four filtration experiments described in Duclos-Orsello et al. [50] were performed in a 25mm dia. stirred ultrafiltration cell Model 8010 by Amicon, Co. Filtration was performed without stirring at a constant TMP of 14kPa. All experiments were performed at a constant temperature of 20°C. The permeate flow rate was measured by timed collection using a digital balance (PB3002-S, DeltaRange, Mettler Toledo) [50]. Filtration was carried out on three different membranes (0.2 μm polycarbonate track

etched, 0.22 μm hydrophobic Durapore® membrane (GVHP), and 0.22 μm hydrophilic Durapore® membrane (GVWP)), with three different solutions (polystyrene microsphere solution, bovine serum albumen (BSA) solution, and BSA solution prefiltered through 0.1μm hydrophilic Durapore® membrane).

Data for the second calibration study was obtained form a crossflow filtration cell equipped with a 0.22μm hydrophilic polyvinylidene fluoride (PVDF) membrane from Millipore, Australia. TMP was measured with a pressure transducer connected to both the feed and the permeate sides of the membrane. CFV and permeate flux were controlled with a flow sensor and the balance. CFV was maintained at 0.33 m/s which equals for this particular system to Reynolds number Re=660. 100 mg L^{-1} sodium alginate was used as a model extracellular polymeric substances (EPS) solution. 0.02% NaN_3 was additionally added to the solution to prevent bacterial growth. The average size of the alginate was measured by ZetaPals particle size analyser (Brookhaven Instruments Corp.) and was found to equal 0.2μm. The critical flux for this alginate solution was found in a flux stepping experiment to be 66 L m^{-2} h^{-1}. The pH value and the solution viscosity were found to remain constant indicating no alginate degradation during the filtration procedure citepYe2006. The experiment was run for up to 250 hours under constant five different flux rates of, respectively, 40, 45, 50, 55, and 60 L m^{-2} h^{-1}. Each of the five experiments were carried out on a virgin membrane.

Calibration on constant TMP filtration data

Parameters in each model were identified with a Nelder-Mead nonlinear simplex algorithm [178] with bound constraints by transformation of variables which allowed to convert a bound constrained problem into an unconstrained problem. The constrained optimisation procedure was implemented in function `fminsearchbnd` written by John D'Errico in Matlab®.

In the first calibration study, four model parameters were calibrated in four separate calibrations corresponding to different data sets: pore constriction parameter β, pore blockage parameter α, specific cake resistance times fraction of foulant contributing to deposit growth $f'\,R'$, and initial resistance of cake deposit $R_{p,0}$. `fminsearchbnd` was used to minimise the sum of squared errors between the calculated and the predicted $\left(\frac{Q}{Q_0}\right)$ fractions and the predicted and calculated total resistances R_{tot}. Experimental data and model outputs were normalised to 0-1 range to ascertain that the errors in flows and resistances are assigned equal weights. The objective function Ω for minimisation is shown in Equation 6.41

$$\Omega = \frac{\sum_{j=1}^{N} \frac{\sum_{i=1}^{n_j} \left(\frac{\hat{Q}}{Q_0}^{j}_{norm,i} - \frac{Q}{Q_0}^{j}_{norm,i} \right)^2}{n_j} + \sum_{j=1}^{N} \frac{\sum_{i=1}^{n_j} \left(\hat{R}^{j}_{norm,i} - R^{j}_{norm,i} \right)^2}{n_j}}{N} \tag{6.41}$$

where N (–) denotes the number of data series (curves), n_j (–) is the number of data

points in the j-th series, $\frac{Q}{Q_0}$ (–) denotes the amount of flow per initial flow and $R = R_{tot}$ (m^{-1}) denotes the total membrane resistance.

Final (calibrated) parameter values are given in Table 6.8.

Table 6.8: Values of model parameters identified on dead-end constant pressure filtration data borrowed from Duclos-Orsello et al. [50].

Experiment	β (m^3 kg^{-1})	α (m^2 kg^{-1})	$f'R'$ (m kg^{-1})	$R_{p,0}$ (m kg^{-1})
Polystyrene beads	0	5.370×10^{4}	2.253×10^{14}	2.95×10^{-1}
BSA-GVHP	1.971×10^{-7}	5.260×10^{-2}	2.021×10^{10}	3.88×10^{-3}
Prefiltered BSA-GVHP	1.606×10^{-7}	5.235×10^{-5}	1.671×10^{10}	7.93×10^{-3}
BSA-GVWP	7.689×10^{-8}	1.117	1.243×10^{10}	1.62×10^{-1}

Figures 6.13-6.16 show very good agreement between the model outputs and the measurements. Polystyrene beads in the first simulation are larger from the pore diameters and thus are completely rejected by the membrane. Pore constriction is therefore completely eliminated and fouling is composed of just pore blocking and cake formation. Lack of pore constriction is visible in Figure 6.13b where resistance curves are all concave (concave downwards). The initial loss of filtrate flow is highest for the highest concentration of beads $C_b = 0.004\%$ where pore blocking and subsequent cake formation mechanisms have the highest rates. At lower concentrations of polystyrene beads the loss of permeate flow is more gradual suggesting that a longer amount of time required to achieve a complete coverage of the membrane.

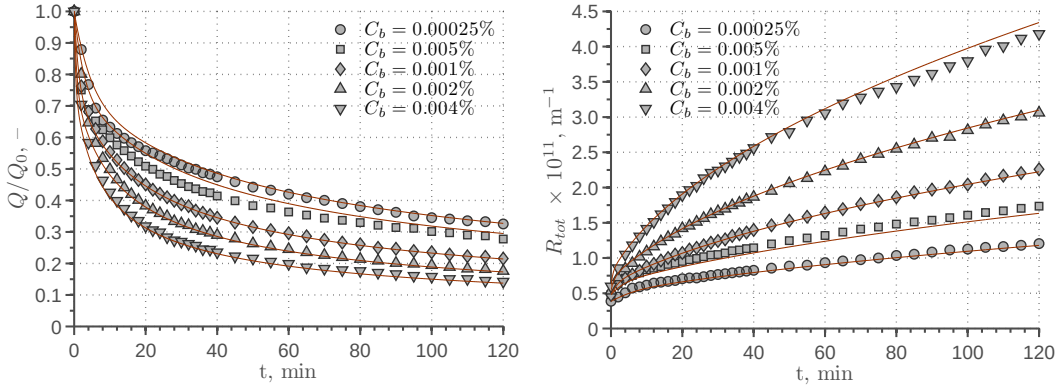

(a) (b)

Figure 6.13: Flow decline and resistance increase during filtration of 0.25μm polystyrene microsphere solutions through 0.2μm polycarbonate track etched membranes (data obtained from the paper of Duclos-Orsello et al. [50] through digitisation).

Figure 6.14 shows the flux decline and total membrane resistance vs. time during filtration of a standard BSA solution through a hydrophobic Durapore membrane. Resistance curves in Figure 6.14b are now, contrary to the previous simulation, convex (concave upwards) indicating pore constriction. The initial flux decline is slower than in Figure 6.13a suggesting that pore blockage and cake formation is slower whilst, initially, flux decrease is mainly due to pore constriction.

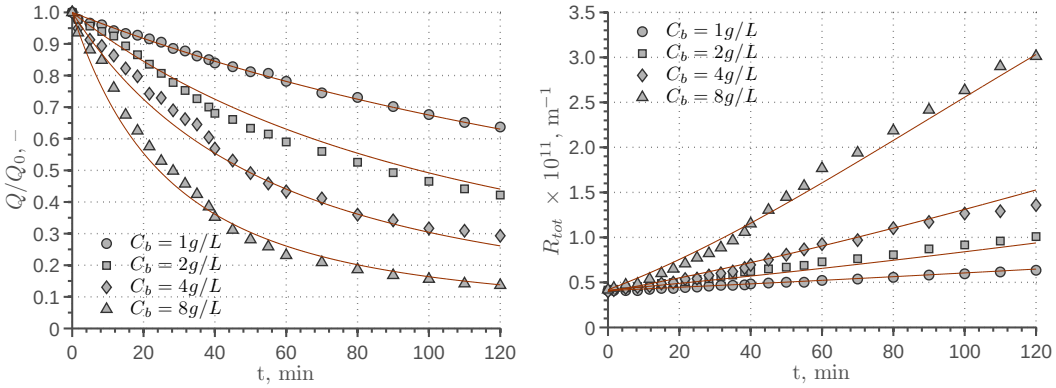

(a) (b)

Figure 6.14: Flow decline and resistance increase during filtration of standard BSA solutions through 0.22μm hydrophobic Durapore membranes (GVHP) (data obtained from the paper of Duclos-Orsello et al. [50] through digitisation).

In experiment 3, BSA has been initially prefiltered through a 0.1μm hydrophilic membrane prior to filtration on a 0.22μm hydrophobic Durapore membrane. Since larger particles have been removed from the solution prior to the experiment, the rate of pore blocking is significantly decreased whilst pore constriction happens to occur at a similar rate. Therefore contribution of pore constriction in the overall fouling process is larger, which manifests itself in the resistance curves which are convex (concave upwards) throughout the filtration process.

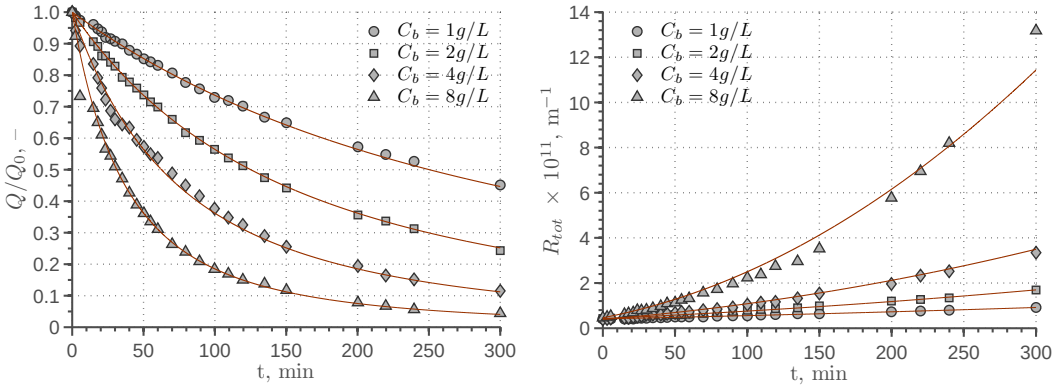

(a) (b)

Figure 6.15: Flow decline and resistance increase during filtration of 0.1μm prefiltered BSA solutions through 0.22μm hydrophobic Durapore membranes (GVHP) (data obtained from the paper of Duclos-Orsello et al. [50] through digitisation).

Figure 6.16 shows the flux decline and total resistance vs. time during filtration of BSA through 0.22μm hydrophilic Durapore membrane. The flux decline in Figure 6.16a is slower from flux decline in Figure 6.14a due to slower pore constriction. Figure 6.14b indicates that fouling occurs mainly due to cake formation as all resistance curves are concave (concave downwards). All of the observations are reflected in the model parameters values presented in Table 6.8.

Similarly to Duclos-Orsello et al. [50] the values of $\frac{d^2t}{dV^2}$ expressed in Equation 5.21

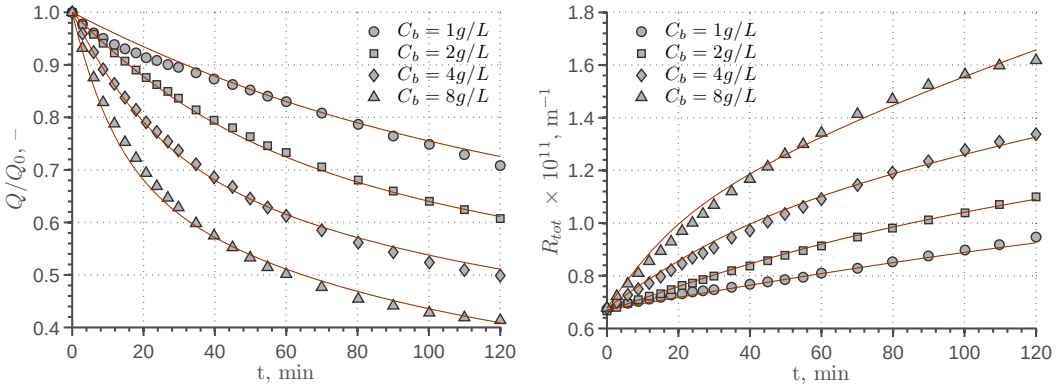

(a) (b)

Figure 6.16: Flow decline and resistance increase during filtration of standard BSA solutions through 0.22μm hydrophilic Durapore membranes (GVWP) (data obtained from the paper of Duclos-Orsello et al. [50] through digitisation).

are plotted against $\frac{dt}{dV}$ which have been calculated with Equation 5.22 on a double logarithmic scale for each filtration experiment. The slope of the curve in each graph represents the value of the n coefficient in the Hermia equation according to Equation 6.42.

$$n = \frac{d\left[\log\left(\frac{d^2t}{dV^2}\right)\right]}{d\left[\log\left(\frac{dt}{dV}\right)\right]} \tag{6.42}$$

The value of n determines the fouling mechanism: $n = 2$ denotes complete pore blocking, $n = 1.5$ denotes standard pore blocking (pore constriction), $n = 1$ denotes intermediate pore blocking and $n = 0$ denotes cake filtration.

Figure 6.17a shows that although the n values are initially negative due to interaction of pore blocking and cake formation mechanisms, the plots quickly become flat indicating complete blockage of an entire membrane area followed by cake formation. n in Figure 6.17b remains at a constant value of ~ 1.4. Since n is very close to 1.5 the plots indicate the dominance of pore constriction over other fouling processes. The slope is reduced by slow cake formation which becomes most prominent for $C_b = 8$ g/L where the onset of cake formation is indicated as a curvature at the end of the corresponding data series. Figure 6.18a indicates that $n = 1.5$ what is understandable and correct since pore blockage and cake formation processes are eliminated by prefiltering BSA on a membrane with an average pore size over twice smaller from the main filtration membrane. n values in Figure 6.18b are similar to Figure 6.17a although filtration times are not sufficiently large to allow cake filtration to dominate in the filtration process, except for $C_b = 8$ g/L where n becomes null at the end of filtration.

Calibration on constant flux filtration data

The 'inverted' model shown in Figure 6.12 was calibrated on the long term constant flux filtration data of Ye et al. [266] as earlier outlined in the beginning of Section 6.3.2. The model parameters were identified individually for each permeate flux.

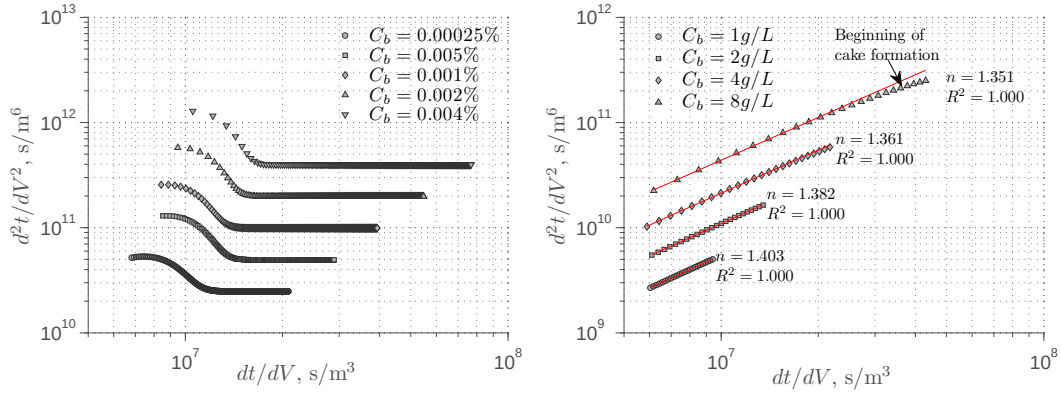

(a) (b)

Figure 6.17: Hernia plots for (a) filtration of 0.25μm polystyrene microsphere solutions through 0.2μm polycarbonate track etched membranes and (b) filtration of standard BSA solutions through 0.22μm hydrophobic Durapore membranes (GVHP).

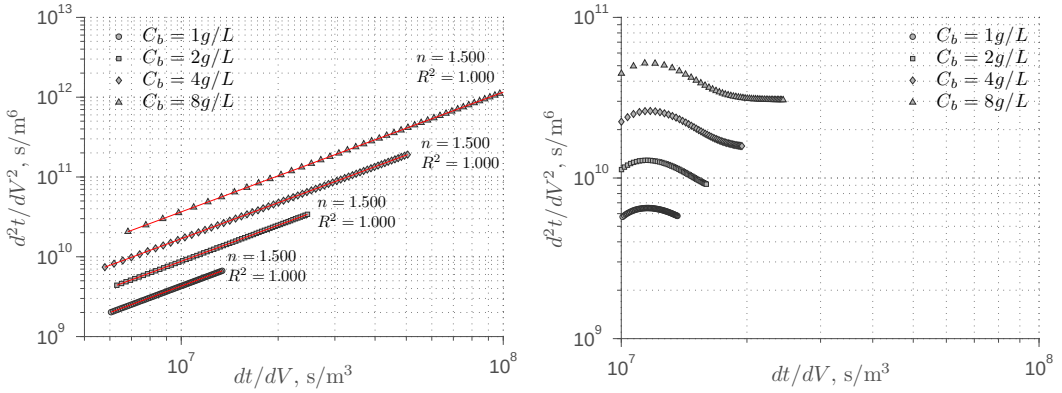

(a) (b)

Figure 6.18: Hernia plots for (a) filtration of 0.1μm prefiltered BSA solutions through 0.22μm hydrophobic Durapore membranes (GVHP) and (b) filtration of standard BSA solutions through 0.22μm hydrophilic Durapore membranes (GVWP).

Specific cake resistance R' was calculated from the slope of the linear portion of the ΔP vs. t curve at end of the two-stage TMP profile as indicated in Figure 6.19. Values of R' for each value of the permeate flux are shown in Table 6.9. The other two unknown model parameters, i.e. pore blockage parameter (α) and pore constriction parameter (β) were identified using the same function `fminsearchbnd` as used in the previous calibration study. The algorithm was set to minimise the sum of squared errors between the measured and the predicted TMPs. The values of the calibrated parameters α and β are shown alongside the R' values in Table 6.9.

α, β and R' as a function of flux J are plotted in Figure 6.20a, Figure 6.20b, and Figure 6.21 respectively. The data points in the individual figures were approximated with an exponential curve $y = a\,\exp(b\,J)$ using non-linear regression. Whilst the regression for α and R' has a relatively high measure of goodness of fit with R^2 equal of, respectively, 0.90 and 0.88, pore blocking parameter β does not seem to form any clear functional relationship with the flux.

Nevertheless, the model was simulated with the parameters identified from the

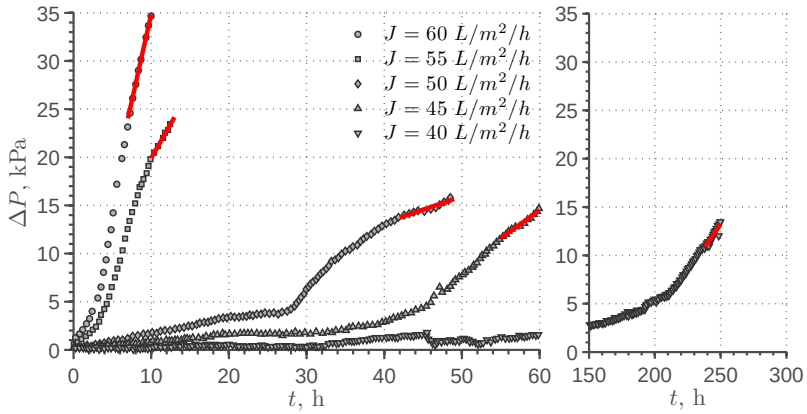

Figure 6.19: Determination of specific cake resistance R' in long-term constant flux filtration experiment (data obtained from the paper of Ye et al. [266] through digitisation).

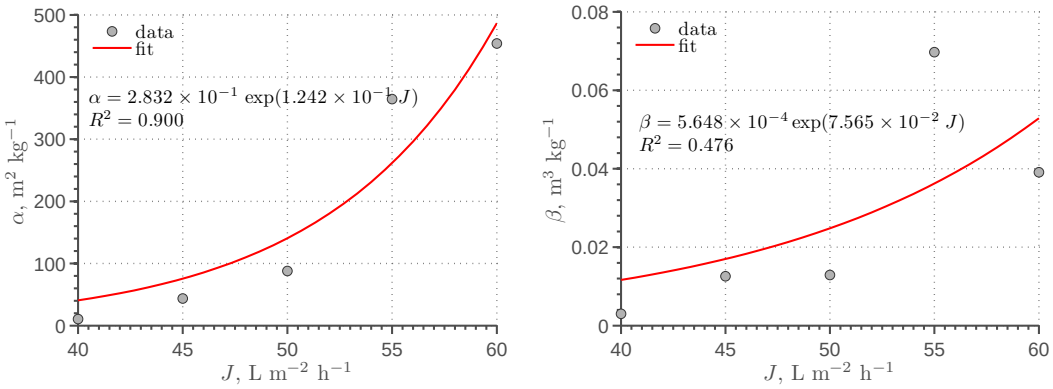

(a) (b)

Figure 6.20: Dependence of (a) pore blocking parameter α and (b) pore constriction parameter β on permeate flux J - data obtained from individual model calibrations supplemented with results of non-linear regression with a general exponential curve of the form $y = a \exp(b\,J)$.

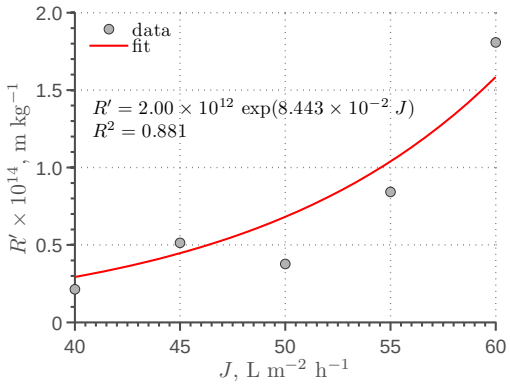

Figure 6.21: Dependence of specific cake resistance R' on permeate flux J - data obtained from individual model calibrations supplemented with results of non-linear regression with a general exponential curve of the form $y = a \exp(b\,J)$.

Table 6.9: Values of model paramters identified on long-term constant flux filtration data of Ye et al. [266].

Fluxes, Lmh		60	55	50	45	40
Parameter	Unit					
$R' \times 10^{14}$	m kg^{-1}	3.62	1.68	0.754	1.03	0.427
α	m^2 kg^{-1}	454	365	88.0	43.6	10.6
$\beta \times 10^2$	m^3 kg^{-1}	3.91	6.97	1.29	1.26	0.303

measurements and additionally with the parameters obtained from the fitted curves. Results of the simulation are presented in Figure 6.22. Figure 6.22 shows that the three-mechanism mechanistic fouling model based on classical fouling equations is able to reproduce a TMP jump during constant flux filtration. Hence, it seems that the TMP jump is not necessarily caused by such mechanisms as cake consolidation or local development of fluxes exceeding the critical flux as postulated by some researchers. TMP jump can also be explained by sequential occurrence of different fouling mechanisms where pore constriction and pore blockage occur in parallel while cake formation occurs only on the previously blocked parts of the membrane, i.e. after pore blockage has taken place. Although the values of pore constriction parameter, pore blockage parameter and specific cake resistance seem to depend on the value of flux, accurate relationships between these parameters could not be established. As a result, model outputs where the parameters were obtained from the curve fits are far away from the measurements. Hence, although two stage TMP profiles could be represented by the model, accurate prediction of the time in which TMP jump would occur is not possible with this model.

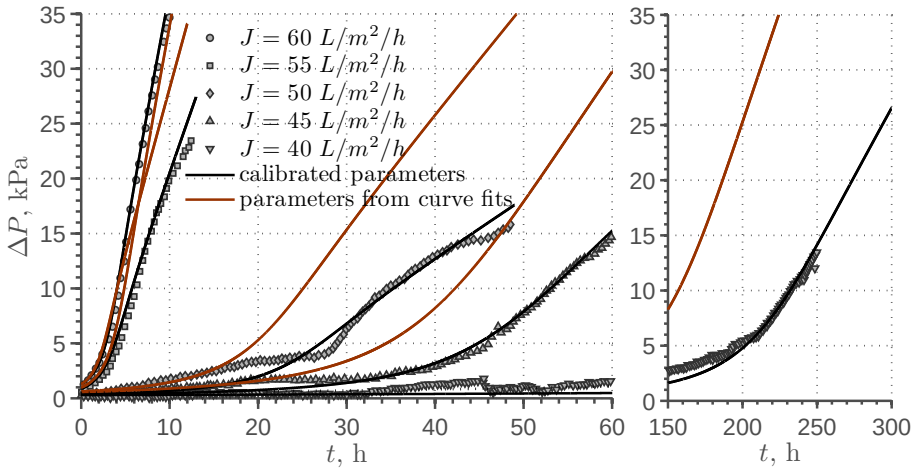

Figure 6.22: Calibration results of the mechanistic model with parameters identified in individual calibrations and obtained from curve fits on constant flux filtration data in a crossflow microfiltration cell (data obtained from the paper of Ye et al. [266] through digitisation).

Part III

Membrane Bioreactor Model

Chapter 7

Development of an immersed MBR model

Contents

7.1 Introduction

In this chapter the CES-ASM1 model described in Chapter 4 is combined with the behavioural fouling model developed in Chapter 6 to formulate a complete model of an immersed membrane bioreactor (MBR). The MBR model layout is based on the MBR benchmark simulation model (BSM-MBR) published by Maere et al. [160] whereas the model inputs, operational parameters and simulation scenarios are taken directly from the original COST Benchmark Model [37, 36].

Selection of an activated sludge model was not easy, because both of the newly developed bespoke ASM models (CES-ASM1 and CES-ASM3) possess different strengths and weaknesses with regards to this simulation study. Whilst the original COST Benchmark Model as well as the MBR benchmark simulation model (BSM-MBR) are both based on the Activated Sludge Model No. 1 (ASM1) and thus it would be logical and convenient to use the ASM1-based model, the death-regeneration concept used in ASM1 to describe the cycle of organic substrates in the system had been found to lose its validity under high sludge retention times (SRTs) and thus, ASM1-based approach may not be appropriate for MBR systems. On the other hand combined extracellular polymeric substances (EPS) and soluble microbial products (SMP) production ASM3-based model (CES-ASM3) is based on the Activated Sludge Model No. 3 (ASM3) which contains different processes and state variables to ASM1. Hence, creation of input files and comparison of model results between BSM-MBR and the new MBR benchmark model can be difficult if CES-ASM3 becomes the biokinetic model of choice. For this reason combined EPS and SMP production ASM1-based model (CES-ASM1) has been selected despite known weaknesses of its base kinetic model (ASM1) such as e.g. over-prediction of denitrification rates due to overestimation of organic cycle in the system. Its limitations will however be taken into account whilst analysing and interpreting the final simulation results.

The membrane is described with the behavioural fouling model which has been chosen over the three mechanism model for its overall simplicity, speed of execution, ease of calibration and easy implementation of various fouling control mechanisms such as backwashing and cake removal due to crossflow velocity (CFV) and air scouring. Although, as already stated in Chapter 6, the behavioural fouling model is unable to predict the so called trans-membrane pressure (TMP) jump during long-term constant flux filtration and TMP gradients during long-term filtration at supra-critical flux conditions, these limitations are not detrimental for the integrated MBR model which is intended to simulate membrane operation under economically viable, usually sub-critical flux conditions.

The two above-mentioned models are then combined to form an integrated model of an immersed MBR. In order to provide bi-lateral links between the biological submodel and the membrane filtration submodel, the following processes are additionally described and included in the model.

1. Impact of coarse-bubble aeration on cake detachment.
2. SMP rejection by the membrane.
3. Impact of SMP concentration on irreversible fouling.
4. Impact of permeate flux on the rate of SMP adsorption on and inside the membrane.
5. Impact of EPS content in activated sludge on specific cake resistance α_c.

Additionally, the model takes into account the negative impact of mixed liquor suspended solids (MLSS) on oxygen transfer coefficient α. The structure of the integrated

model including the above listed links between both parts of the system are described in the subsequent sections of this chapter.

7.2 Conceptual model of a MBR

Model of a generic wastewater treatment process such as an MBR process can be described with a set of ordinary differential equations.

$$\dot{\mathbf{x}} = f\left(\mathbf{x}(t), \mathbf{u}(t), \mathbf{z}(t), \mathbf{w}(t), \mathbf{m}(t)\right) \tag{7.1}$$

where $\mathbf{x}(t)$ denotes the vector of system states, $\mathbf{u}(t)$ is the vector of inputs from other subsystems, $\mathbf{z}(t)$ are the inputs associated with wastewater inflow, $\mathbf{w}(t)$ is the vector of external inputs and disturbances, and $\mathbf{m}(t)$ is the vector of manipulated (control) variables.

The model outputs $\mathbf{y}(t)$ are in a functional relationship with the model states.

$$\mathbf{y}(t) = g\left(\mathbf{x}(t)\right) \tag{7.2}$$

A block diagram of such a typical wastewater treatment process is shown in Figure 7.1.

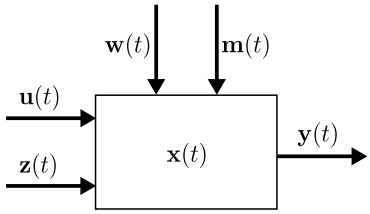

Figure 7.1: Representation of a typical wastewater treatment process model.

Membrane bioreactor (MBR) is a combination of two distinctly different processes inside one process unit: an activated sludge process (ASP) where biochemical treatment occurs and a microfiltration (MF) or ultrafiltration (UF) microporous membrane which acts as a barrier for suspended matter, bacteria and viruses. These membranes can either be immersed in the bioreactor or placed outside the reactor in a so-called sidestream configuration. In both cases these two processes are interdependent meaning that one or more states, outputs, or properties of one process have direct and indirect impacts on the states and outputs of the other process. Outputs of the bioreactor form direct inputs to the membrane whilst the parameters and state of the membrane have a direct effect on the states of the bioreactor.

These complex relationships between the bioreactor and the membrane are presented in a graphical manner in Figure 7.2 in which the bioreactor and the membrane are divided into different subcategories. The bioreactor is divided into four subcategories: *liquid phase*, *solid phase*, *bulk liquid* and *operating conditions*. The membrane

is divided into *membrane properties*, *module properties* and *operating conditions*. These subcategories are later divided into the properties which directly or indirectly influence other properties and processes. Directions of these causal relationships are marked with an arrow. A positive relation is shown with a blue line, negative relation is presented with a red line and where the character of the relation is either not known, or can be either positive or negative depending on e.g. process conditions, the line is drawn in grey colour. Some of the rectangles in Figure 7.2 have been drawn with dotted lines. These rectangles indicate the quantities which are not included of the mathematical equations in the developed integrated MBR model.

A conceptual block diagram of a generic integrated MBR model is shown in Figure 7.3. The MBR plant is divided into three distinctive parts: the *bioreactor*, the *membrane* and the *interface*. The membrane receives the bioreactor outputs ($\mathbf{y_1}(t)$) and the outputs from the interface ($\mathbf{u_3}(t)$). The bioreactor receives the membrane's outputs ($\mathbf{y_{2,2}}(t)$) which are fed back with the recirculation stream. $\mathbf{y_{2,3}}(t)$ represents the vector of outputs from the membrane associated with the waste activated sludge (WAS) (also known as surplus activated sludge (SAS)) stream. The links between the bioreactor and the membrane described in the Interface and presented in Figure 7.2 are further explained in Sections 7.5, 7.6 and 7.7.

The vector of wastewater flow associated inputs $\mathbf{z}_1$ is made up of wastewater quality parameters $\mathbf{S}_{inf}$ and $\mathbf{X}_{inf}$ and wastewater flow rate q_{inf}. Vector $\mathbf{S}_{inf}$ represents the concentrations of all soluble state variables in the influent, whereas $\mathbf{X}_{inf}$ is a vector of all particulate state variables in the influent. The make-up and the size of $\mathbf{S}_{inf}$ and $\mathbf{X}_{inf}$ depend on the choice of the biological activated sludge model. Compositions of $\mathbf{S}_{inf}$ and $\mathbf{X}_{inf}$ in ASM1 and CES-ASM1 are later explained in Section 7.3.

$$\mathbf{z}_1 = \left(\mathbf{S}_{inf}\ \mathbf{X}_{inf}\ q_{inf}\right)^T \tag{7.3}$$

The bioreactor has only one external input - the bulk liquid temperature (T) . Temperature variations create an external disturbance by affecting the biochemical reaction rates, oxygen solubility and can promote higher production of SMP and EPS. Thus $\mathbf{w}_1 = \left(T\right)$.

The vector of manipulated (control) variables for the bioreactor $\mathbf{m}_1 = \mathbf{m}_1(t)$ has four elements: fine-bubble air flow rate $q_{a,bio}$, sludge wastage rate q_w, external (sludge) recirculation rate q_{rec}, and internal recirculation rate, q_{ir}.

$$\mathbf{m}_1 = \left(q_{a,bio}\ q_w\ q_{rec}\ q_{ir}\right)^T \tag{7.4}$$

Biological and chemical composition of the bulk liquid, i.e. bioreactor states depend on the retentive properties of the membrane. This unidirectional link between the membrane and the bioreactor is modelled by a feedback loop $\mathbf{y}_{2,2} = \mathbf{u}_1$ which returns

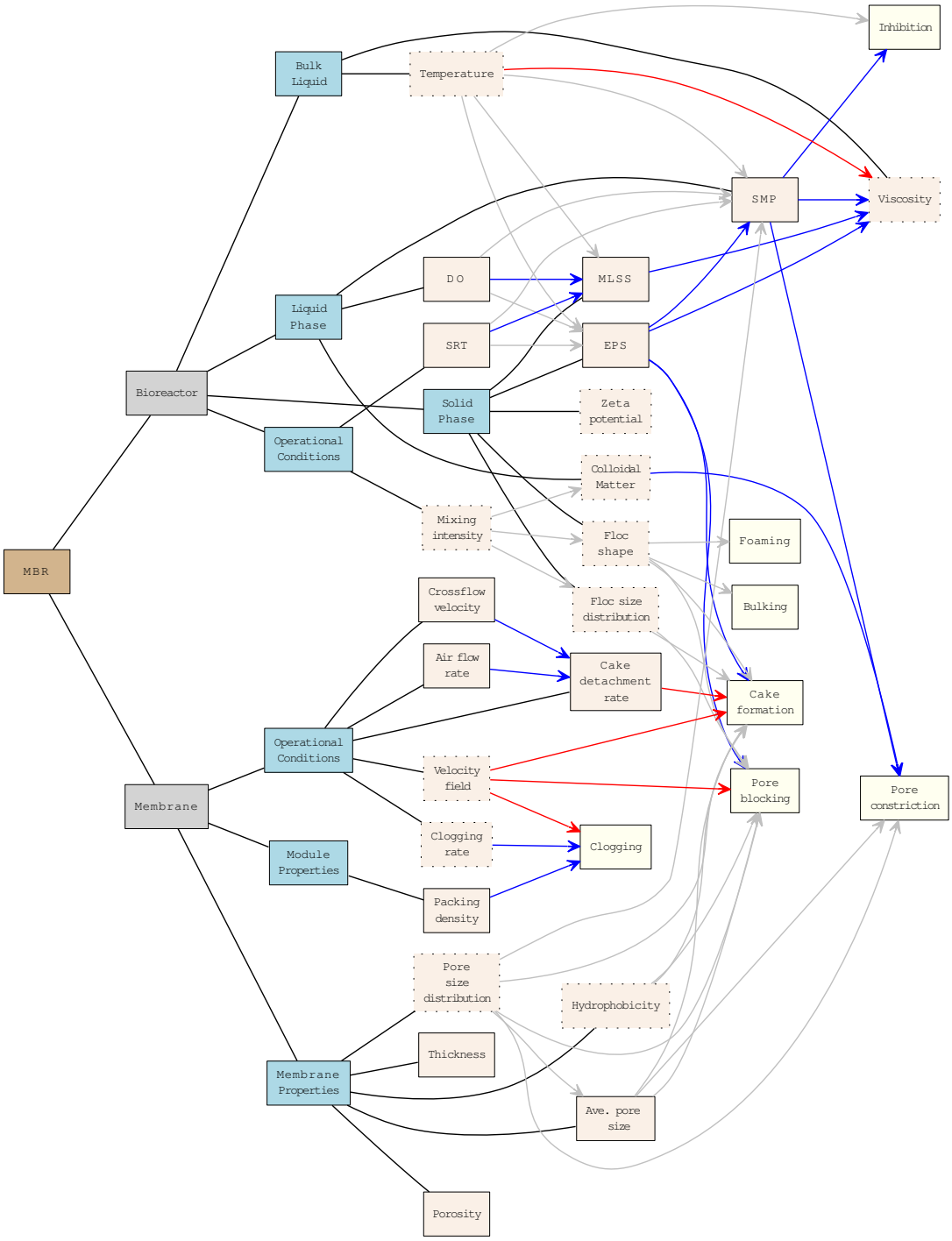

Figure 7.2: LGraphical representation of links and relations between different parts of a MBR reactor.

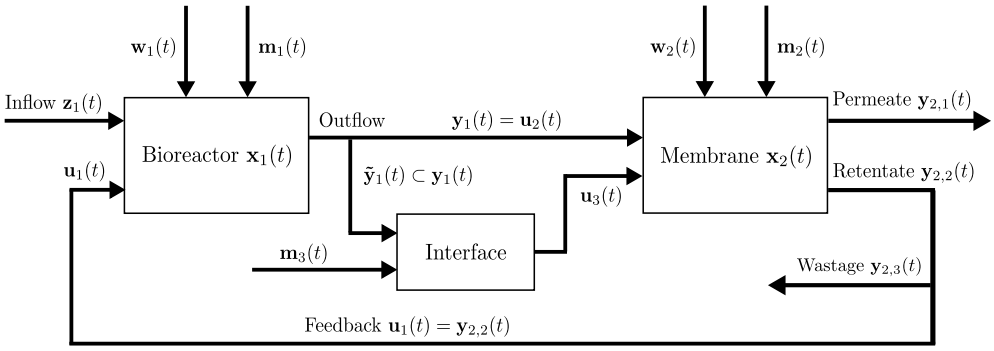

Figure 7.3: Block structure of the MBR plant model implemented in this study.

the components retained on the membrane back to the bulk liquid.

$$\mathbf{u}_1 = \mathbf{y}_{2,2} = \left(\mathbf{S}_{ret}\ \mathbf{X}_{ret}\ q_{ret}\right)^T \tag{7.5}$$

where $\mathbf{S}_{ret}$ denotes the vector of concentrations of all soluble wastewater constituents, $\mathbf{X}_{ret}$ is the vector of all particulate wastewater constituents, and q_{ret} denotes the recirculation flow rate.

Concentrations of all wastewater constituents both soluble and particulate in the retentate stream are calculated from the mass balance equation around the membrane shown in Equation 7.6.

$$q_{feed}\, c_{feed} = q_{perm}\, c_{perm} + q_{ret}\, c_{ret} \tag{7.6}$$

where q_{feed} and c_{feed} denote, respectively, the feed flow and the feed concentration, q_{perm} and c_{perm} are, respectively, the permeate flow and the substance concentration in the permeate stream and q_{ret} and c_{ret} denote the flow rate and the concentration of that substance in the retentate stream.

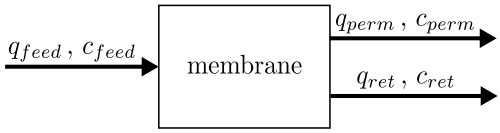

Figure 7.4: Block diagram representing the mass balance across the membrane.

Equation 7.6 can be rearranged to solve for c_{ret}:

$$c_{ret} = c_{feed}\,\frac{q_{feed}}{q_{ret}} - c_{perm}\,\frac{q_{perm}}{q_{ret}} \tag{7.7}$$

Concentration of a particular substance (component) in the permeate stream c_{perm} can be expressed as a function of the so called **retention factor** (r_F) defined as one minus the ratio of the permeate concentration (c_{perm}) to the retentate concentration (c_{ret}) of this component ($r_F = 1 - \frac{c_{perm}}{c_{ret}}$) [126]. Alternatively, c_{perm} can be calculated from the concentration of this substance in the feed stream c_{feed} based on the value of the **rejection factor** R_F defined as one minus the ratio of the concentrations of this

component in, respectively, downstream and upstream sides of the membrane [126]. For extractive membranes $R_F = 1 - \frac{c_{perm}}{c_{feed}}$. r_F and R_F characterise the properties of a membrane and substance being filtered, and depend on the size distribution and shape of the membrane pores, size distribution and shape of the particles, electric charge of the substance and the membrane, hydrophobicity, properties of the dynamic layer forming on the membrane and others. Substances being completely retained by the membrane are associated with retention factor r_F and rejection factor R_F of 1 whereas substances which end up entirely in the permeate stream are characterised with retention factor and rejection factor of zero. Any substance which is not fully retained nor fully permeates through the membrane will have r_F and R_F between 0 and 1. If we introduce the notion of **recovery parameter** defined in Judd [116] as the ratio of permeate to feed flow ($\eta = \frac{q_{perm}}{q_{feed}}$), Equation 7.7 can be presented as:

$$c_{ret} = \frac{c_{feed}}{1 - \eta\, r_F} \tag{7.8}$$

or

$$c_{ret} = c_{feed} \left(1 + R_F\, \frac{\eta}{1 - \eta}\right) \tag{7.9}$$

Input vector to the membrane ($\mathbf{u}_2$) is equal to the output vector of the bioreactor ($\mathbf{y}_1$), which is made up of the bioreactor state variables $\mathbf{x}_1$ and the membrane influent flow rate $q_{perm} + q_{ret}$. The bioreactor state vector $\mathbf{x}_1 = \left(\mathbf{S}_{bio}\ \mathbf{X}_{bio}\right)^T$ is composed of the vector of soluble state variables ($\mathbf{S}_{bio}$) and particulate state variables ($\mathbf{X}_{bio}$).

$$\mathbf{u}_2 = \mathbf{y}_1 = \left(\mathbf{S}_{bio}\ \mathbf{X}_{bio}\ q_{perm} + q_{ret}\right)^T \tag{7.10}$$

The vector of external inputs and disturbances to the membrane is, alike in case of the bioreactor, composed of a single element: $\mathbf{w}_2 = T$, which affects liquid viscosity and thus the pressure drop across the membrane.

An immersed hollow fibre (HF) membrane modelled here has three manipulated variables: q_{perm}, t_{filt}, and t_{flush}, where q_{perm} denotes the permeation rate, t_{filt} denotes the filtration time, and t_{flush} is the backflush time. If the membrane undergoes periodic relaxation instead of backflushing, t_{flush} will be replaced with membrane relaxation time t_{rel}. Since in an immersed configuration the membrane is fully submerged in the bioreactor and the solids mass transfer between the bulk liquid and the membrane surface is mainly facilitated by the velocity flow field inside the bioreactor, provision of external recirculation is not required.

$$\mathbf{m}_2 = \left(q_{perm}\, t_{filt}\, t_{flush}\right)^T \tag{7.11}$$

Another control variable in HF membranes is the backflush flow rate but since the effects of backflush intensity on cake detachment are not modelled in this study this variable is not included in $\mathbf{m}_2$.

The membrane has two output streams- one on the retentate side of the membrane ($\mathbf{y}_{2,2}$) - see Equation 7.5 and the second one ($\mathbf{y}_{2,1}$) on the permeate side. $\mathbf{y}_{2,1}$ is composed of four elements: the vector of soluble wastewater constituents $\mathbf{S}_{perm}$, the vector of particulate wastewater constituents $\mathbf{X}_{perm}$ usually assumed to be equal to zero, permeate flow rate q_{perm} and total membrane resistance R_{tot}.

$$\mathbf{y}_{2,1} = \begin{pmatrix} \mathbf{S}_{perm} & \mathbf{X}_{perm} & q_{perm} & R_{tot} \end{pmatrix}^T \tag{7.12}$$

The vector of membrane state variables $\mathbf{z}_2$ depends on the choice of the fouling model. If the behavioural fouling model described in Section 6.2 is applied in the MBR model, the vector of states will be given as

$$\mathbf{x}_2 = \mathbf{x}_{2,a} = \begin{pmatrix} R_r & R_i \end{pmatrix}^T \tag{7.13}$$

where R_r denotes the resistance due to reversible fouling and R_i denotes the resistance caused by irreversible fouling.

If the mechanistic three mechanism fouling model described in Section 6.3 is implemented in the MBR model the vector of states will be composed of four variables: the blocked membrane surface area A_b, the resistance due to irreversible fouling under the blocked surface R_{ib}, the resistance due to irreversible fouling under the unblocked surface R_{inb}, and cake resistance R_c.

$$\mathbf{x}_2 = \mathbf{x}_{2,b} = \begin{pmatrix} A_b & R_{ib} & R_{inb} & R_c \end{pmatrix}^T \tag{7.14}$$

The interface has only one manipulated variable $\mathbf{m}_3 = q_{a,mem}$, where $q_{a,mem}$ denotes the air-scouring flow rate. If the MBR is equipped with side-stream non-aerated membranes then $\mathbf{m}_3 = v_{cf}$, where v_{cf} denotes the cross-flow velocity.

The input vector $\tilde{\mathbf{y}}_1 = \begin{pmatrix} X_{EPS} & X_{MLVSS} \end{pmatrix}^T$ contains two elements, mixed liquor EPS and mixed liquor volatile suspended solids (MLVSS) concentrations, respectively. The interface then calculates the cake back-transport rate $\dot{m}_r$ as a function of air-scouring rate $q_{a,mem}$ and specific cake resistance α_c as a function of the EPS/MLVSS ratio. The two above values form the vector of interface outputs.

$$\mathbf{u}_3 = \begin{pmatrix} \dot{m}_r & \alpha_c \end{pmatrix}^T \tag{7.15}$$

7.3 MBR benchmark model layout

The MBR benchmark model described in Chapter 8 is based on the plant layout proposed by Maere et al. [160] where the bioreactor is divided into five completely stirred tank reactors (CSTRs). However, whilst in the BSM-MBR model of Maere et al. [160] each reactor is given an active volume of 1,500 m^3, in the integrated bioreactor and membrane fouling MBR model (IBMF-MBR) anoxic volume has been increased at the

cost of the aerobic volume. In IBMF-MBR, each anoxic tank $V_{ax,1}$ and $V_{ax,2}$ has been given an active volume of 1,800 m^3 wheareas each aerobic tank $V_{ox,1}$, $V_{ox,2}$, and V_{mem} has been assigned an active volume of 1,300 m^3. Thus, the anoxic fraction is increased from 40% to 51.4% which is closer to the value recommended by MUNLV [172] for pre-denitrification MBR plants. It has also been found that denitrification kinetics predicted in CES-ASM1 are somehow slower from those in ASM1 due to an altered flow of organic substrates caused by introduction of SMP and EPS kinetics. Therefore, the anoxic volume needed to be increased in the model for the outputs to be comparable with the outputs of the MBR benchmark simulation model (BSM-MBR) of Maere et al. [160]. As a word of notice, denitrification kinetics in pre-denitrificaiton MBR plants are much slower from conventional activated sludge plants due to high operational SRT and high oxygen carry-over from the membrane tank to the anoxic tank.

The plant has two recirculation streams: q_{ir} which recycles nitrate rich mixed liquor from the second aerobic tank to the first anoxic tank, and q_{rec} recycling high MLSS mixed liquor from the membrane tank back to the first aerobic tank. The benchmark plant layout is shown in Figure 7.5.

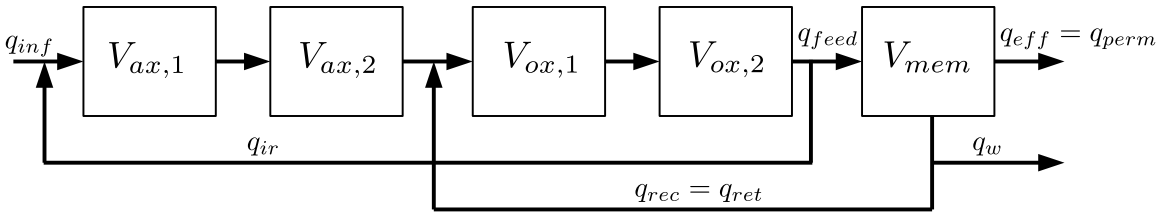

Figure 7.5: MBR benchmark layout and flow scheme.

Composition of the vector of state variables for each reactor denoted by j where $j = 1 : 5$ depends on the choice of the activated sludge model. For ASM1 $\mathbf{x}_1^j$ is equal to:

$$\mathbf{x}_1^j = \left(S_I^j\, S_S^j\, X_I^j\, X_S^j\, X_{BH}^j\, X_{BA}^j\, X_P^j\, S_O^j\, S_{NO}^j\, S_{NH}^j\, S_{ND}^j\, X_{ND}^j\, S_{ALK}^j\right)^T \tag{7.16}$$

In CES-ASM1 $\mathbf{x}_1^j$ contains additional three state variables - concentration of biomass associated products S_{BAP}, concentration of utilisation associated products S_{UAP} and concentration of extracellular polymeric substances X_{EPS}, hence:

$$\mathbf{x}_1^j = \left(S_O^j\, S_S^j\, S_{NH}^j\, S_{NO}^j\, S_{N_2}^j\, S_{ALK}^j\, S_I^j\, X_I^j\, X_S^j\, X_{BH}^j\, X_{STO}^j\, X_{BA}^j\, X_{TSS}^j\, S_{BAP}^j\, S_{UAP}^j\, X_{EPS}^j\right)^T \tag{7.17}$$

7.4 Aeration and oxygen transfer

7.4.1 Oxygen transfer

Oxygen mass balance for a single variable volume CSTR (and thus for a constant volume CSTR in which $q_{eff} = q_{inf}$) takes the following form:

$$V\frac{dS_O}{dt} = \underbrace{q_{inf}\,S_{O,inf} - q_{eff}\,S_O}_{t_1} + \underbrace{k_La\,(S_O^* - S_O)\,V}_{t_2} + \underbrace{r_M\,V}_{t_3} \tag{7.18}$$

Here, r_M ($gO_2\ m^{-3}\ d^{-1}$) denotes the oxygen uptake rate (OUR) resulting from respiration of microorganisms in the activated sludge, S_O^* ($gO_2\ m^{-3}$) denotes the oxygen saturation concentration under field conditions, and k_La (d^{-1}) denotes the oxygen mass transfer coefficient. S_O ($gO_2\ m^{-3}$) denotes the O_2 concentration and V (m^3) denotes the reactor volume.

Term t_2 describes transfer of oxygen from air to the liquid according to the the two film theory of transfer of sparingly soluble gases [145]. Under static conditions, i.e. when $\frac{dS_O}{dt} = 0$, the mass transfer of oxygen from gas into liquid needs to counterbalance oxygen uptake caused by respiration of microorganisms in the activated sludge (t_3) and the usually negative oxygen balance due to loss of oxygen with the outflow (t_1).

Oxygen mass transfer coefficient k_La in term t_2 describes the rate of mass flow of oxygen into the bioreactor. Depending on the type of aeration device used, it is associated either with the rotational speed of a surface aerator, volumetric flow of liquid in jet aeration systems or the flow of air, q_{air} in diffused air aeration systems. As this modelling study considers *fine bubble diffused air aeration* for the main two bioreactors and *coarse bubble diffused air aeration* for the membrane tank, we will restrict our thinking to just these two aeration systems.

The actual oxygen transfer rate (AOTR) described in term t_2 is proportional to airflow rate q_{air}, specific oxygen transfer efficiency (SOTE), difference between oxygen saturation concentration S_O^* and mixed liquor oxygen concentration S_O, diffuser submersion depth (h_{sub}), type of wastewater, and various local and operating conditions. AOTR as a function of SOTE is described in Equation 7.19.

$$AOTR = \gamma\ q_{air}\ \rho_a\ O_{a,m}\ SOTE\ h_{sub} \tag{7.19}$$

where h_{sub} (m) denotes the diffuser submersion depth, ρ_a ($kg\ m^{-3}$) denotes the air density under standard temperature and pressure, and $O_{a.m}$ ($-$) is the mass fraction of oxygen in air. In this study it is assumed that diffuser submersion depth is equal to tank depth, i.e. $h_{sub} = h$.

Non-dimensional coefficient γ describes the effects of local conditions and wastewater characteristics on oxygen solubility described with oxygen saturation concentration (S_O^*) and is used to relate specific oxygen transfer efficiency (SOTE) in wastewater un-

der field conditions to the, so called, 'standard conditions' - tap water, 20^{o}C at mean sea level. The γ coefficient is used to recalculate actual oxygen transfer rates (AOTRs) and actual oxygen transfer efficienciess (AOTEs), i.e. oxygen transfer under local conditions from, respectively, SOTR and SOTE usually provided by vendors and measured in clean water under laboratory controlled conditions.

$$\gamma = \alpha\, F \left(\frac{\beta\, S^{*,ave}_{O,T} - S_O}{S^{*}_{O,20^o\mathrm{C}}} \right) \theta^{T-20} \tag{7.20}$$

where F (–) is the non-dimensional diffuser fouling factor, θ is the non-dimensional temperature dependency coefficient, T (^{o}C) denotes the air temperature, β denotes the O_2 solubility reduction due to the presence of salts, $S^{*,ave}_{O,T}$ (mgO_2 L^{-1}) denotes the average O_2 saturation concentration in clean water in the aeration tank at temperature T and atmospheric pressure at the sea level, and $S_{O,20^o\mathrm{C}}$ (mgO_2 L^{-1}) denotes the O_2 saturation concentration in water at 20°C.

Parameter α in Equation 7.20 describes reduction of oxygen mass transfer coefficient in wastewater in relation to tap water: $\alpha = \frac{k_La \text{ wastewater}}{k_La \text{ tap water}}$. α depends on the multitude of factors such as the type of aeration device, tank geometry, level of turbulence in the tank, concentration of solids and wastewater characteristics. A rough estimate of α can often be provided by the aeration equipment vendor given some influent wastewater characteristics or, to ensure more accuracy, α can be determined experimentally either on a full-scale plant, pilot-plant or in a laboratory scale reactor.

Although α is dependent on wastewater characteristics, solids concentrations, and hydrodynamic conditions inside the bioreactor, which all vary throughout the operation of the treatment plant, α is usually assumed to remain constant during the simulation. Whilst for the purpose of modelling conventional activated sludge processs (CASPs) this assumption is generally acceptable, elevated MLSS concentrations in MBRs hinder the oxygen transfer to such extent that introduction of a dependency function $\alpha = f(\text{MLSS})$ is necessary for accurate predictions of the system's air demand. Whilst MLSS concentrations in CASP systems are usually between $2,000$ and $5,000$ mg/L and α values range between $0.45 - 0.75$ [236], in immersed MBRs with MLSS up to $20,000$ mg/L, α can attain values as small as 0.2. Reduction of α with MLSS is usually modelled with an exponential function given in Equation 7.21 where ω varies on a case-by-case basis. ω depends stronly on air bubble size and is assumed to be equal to 0.05 for coarse bubble aeration and 0.083 for fine bubble aeration as originally proposed by Maere et al. [160]. Oxygen transfer variability with MLSS concentration is explained in more detail in Section 7.4.2.

$$\alpha = e^{-\omega\, X_{TSS}} \tag{7.21}$$

Parameter β in Equation 7.20 is a reduction factor describing lower O_2 solubility in wastewater compared to clean water due to presence of salts, particulates and surfactants: $\beta = \frac{S^*_O \text{ wastewater}}{S^*_O \text{ tap water}}$. The value of β for typical domestic wastewaters ranges between $0.70 - 0.98$ [236] and, in the absence of measurements, is often assumed to be

equal to 0.95 - see Table 7.1.

Parameter F is termed the diffuser fouling factor and describes the loss of diffuser membrane porosity due to bacterial growth (biofouling) and deposition of calcium carbonate (scaling) on the surface of the porous membrane. F is typically between 0.65 and 0.90.

The effects that temperature has on AOTR and AOTE are modelled with a non-dimensional Arrhenius coefficient θ which, for aeration systems, is equal to 1.024.

So far the aeration model equations listed above have followed the modelling approach adopted in the MBR benchmark simulation model of Maere et al. [160]. The model which was used in BSM-MBR was however found to slow down the execution times due to its iterative nature where $S_{O,T}^{*,ave}$ used in calculation of $AOTE$ was dependent on $AOTE$ itself. Solution of that model thus necessitates using an iterative solution algorithm for systems of non-linear algebraic equations such as MATLAB's `fsolve`. In order to avoid the need for solving a system of non-linear algebraic equations at each integration step a simpler modelling approach used in GPS-X v.4.5 WWTP simulation package by Hydromantis® [109] was adopted as explained below.

The average dissolved oxygen saturation concentration in clean water in the aeration tank, at temperature T, and the atmospheric pressure at the sea level $S_{O,T}^{*,ave}$ is calculated with Equation 7.22.

$$S_{O,T}^{*,ave} = \frac{1777.8\,\beta\,\rho_w\,P_{O_2}}{k_H} \tag{7.22}$$

where 1777.8 is a unit conversion coefficient from $\mathrm{molO_2/molH_2O}$ to $\mathrm{gO_2/m^3H_2O}$, P_{O_2} (atm) is the corrected partial pressure of oxygen and k_H (atm/mol fraction) denotes the Henry's law constant for dissolved oxygen (DO) which is calculated using a linear regression equation shown below.

$$k_H = 708\,T + 25700 \tag{7.23}$$

The partial pressure of oxygen P_{O_2} depends on the fraction of oxygen in the gas phase $O_{A,v}$, which for air is equal to 21%, and the average pressure of the gas phase as shown in Equation 7.24.

$$P_{O_2} = O_{A,v}\left(P_{atm} + \frac{\rho_s\,g\,h}{2\,P_{atm,std}}\right) \tag{7.24}$$

$P_{atm,std}$ is equal to 101325 Pa and denotes the standard atmospheric pressure at the sea level, P_{atm} (atm) denotes the local atmospheric pressure at the site, and h (m) is the tank depth. Whilst the mixed liquor density ρ_s (kg $\mathrm{m^{-3}}$) depends on the temperature, pressure, salinity, MLSS and DO concentration, MLSS concentration is the dominant factor in ρ_s which is found to be in an exponential relationship with MLSS as shown in Equation 7.25.

$$\rho_s = 0.99959\,\rho_w\,\exp\left(4.397\times10^{-4}\,X_{TSS}\right) \tag{7.25}$$

where ρ_w (kg $\mathrm{m^{-3}}$) denotes the water density and X_{TSS} (kg $\mathrm{m^{-3}}$) denotes the local

concentration of suspended solids.

Water density ρ_w is assumed to vary with temperature T (^{o}C) accordingly to Equation 7.26 [164].

$$\rho_w(T) = 1000 \left(1 - \frac{\left(T + 2.889414 \times 10^2\right) \left(T - 3.9863\right)^2}{\left(5.089292 \times 10^5\right) \left(T + 68.12963\right)} \right) \tag{7.26}$$

Whilst the atmospheric pressure under standard conditions ($P_{atm,std}$) is considered constant and equal to 1013.25 hPa - see Table 7.1 for reference, the actual atmospheric pressure under field conditions (P_{atm}) is assumed to depend on local elevation above the mean sea level h_{elev} (m) according to Equation 7.27 [109].

$$p_{atm} = p_{atm,std}\, e^{-\frac{h_{elev}}{7992}} \tag{7.27}$$

$S^*_{O,20^oC}$ in Equation 7.20 is calculated with a third order polynomial in T given in Equation 7.28 [109] where $T = 20^o$C.

$$S^*_{O,T} = -6.588 \times 10^{-5}\, T^{\,3} + 7.311 \times 10^{-3}\, T^{\,2} - 3.825 \times 10^{-1}\, T + 13.89 \tag{7.28}$$

Air density ρ_a (kg m^{-3}) depends on the local atmospheric pressure P_{atm} and air temperature T_{air} ($^\circ$C) and is obtained from the following correlation published in Hyd [109].

$$\rho_a = 293.16 \frac{P_{atm}}{\left(T_{air} + 273.16\right) P_{atm,std}} \tag{7.29}$$

SOTE (% m^{-1}) which is used to determine AOTE and AOTR characterises the type of air diffusers and depends on wastewater composition, airflow per diffuser and diffuser location and density. Dependency of SOTE on the airflow per diffuser and airflow density is shown in Figure 7.6.

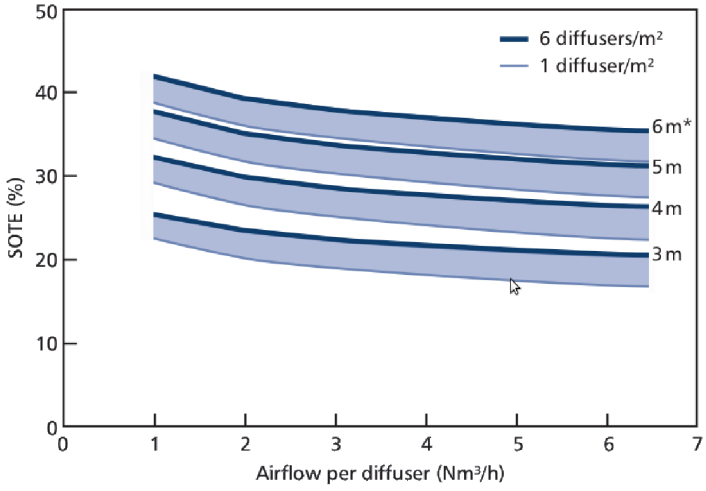

Figure 7.6: SOTE vs. air flow per diffuser and diffuser density - Sanitaire Silver Series II (`http://www.sanitaire.com`).

Table 7.1: Oxygen transfer model parameters applied to the MBR simulation model - Maere et al. [160].

Parameter	Unit	Values
β	–	0.95
F	–	0.9* – 0.7**
g	m s^{-2}	9.81
$O_{A,v}$	%	21
$P_{atm,0}$	Pa	101325
ρ_a	g m^{-3}	1200
ρ_{sludge}	g m^{-3}	10000
$SOTE$	% m^{-1}	2* – 6**
T	^{o}C	15
h	m	3.5* – 5**
θ	–	1.024
ω	–	0.05* – 0.083**
c_{SI}	–	29.7
e	–	0.5
n	–	0.283
R	J mol^{-1} K^{-1}	8.314
T_{air}	^{o}C	20

* - coarse bubble aeration (membrane air scouring), ** - fine bubble aeration (process aeration)

The observed values of SOTE are typically between 5% m^{-1} and 8% m^{-1} for fine bubble aeration and 1% m^{-1} and 3% m^{-1} for coarse bubble aeration. Respectively, specific oxygen transfer rate (SOTR) is usually found to fall between 10 g O_2 m^{-3} m^{-1} and 15 g O_2 m^{-3} m^{-1} in fine bubble aeration systems and between 5 g O_2 m^{-3} m^{-1} and 7 g O_2 m^{-3} m^{-1} for coarse bubble aeration.

The list of all variables introduced in the aeration model used in the author's implementation of BSM-MBR and the own model IBMF-MBR is provided in Table 7.1.

7.4.2 Oxygen transfer coefficient as a function of MLSS

In membrane bioreactors (MBRs) where, due to large SRTs, MLSS concentrations are $\sim (3-5)$ times higher than in conventional activated sludge systems, effects of solids on oxygen transfer coefficient α become significant. As mentioned in the previous section, studies on the dependence of α on MLSS in activated sludge systems show an exponential relationship between these two parameters. Günder [81], Krampe and Krauth [127] and Rosenberger [213] proposed a simple exponential relationship where the value of the exponent is proportional to MLSS:

$$\alpha = e^{-\omega\, MLSS} \tag{7.30}$$

where the proportionality constant ω is equal to 0.083, 0.0879 and 0.049 respectively.

Whereas Günder [81] and Krampe and Krauth [127] observed virtually the same functional relationship between α and MLSS, the α values observed by Rosenberger

[213] are generally higher and less sensitive to MLSS. A similar exponential trend to Rosenberger's was found by Müller et al. [171] who, through regression, derived the following equation: $\alpha = 1.05074\, e^{-0.0446\, MLSS}$. The most recent observations of Germain et al. [69] led to another correlation described with equation: $\alpha = 6.77\, e^{-0.26\, MLSS}$ in which MLSS has the largest effect on α out of all the studies mentioned above.

All of the above functions are plotted in Figure 7.7 which shows two distinctive trend patterns - one of Günder [81] and Krampe and Krauth [127] and the other of Rosenberger [213] and Müller et al. [171], whereas the function proposed by Germain et al. [69] describes the most dramatic decrease of α with MLSS and is not similar to any other functions.

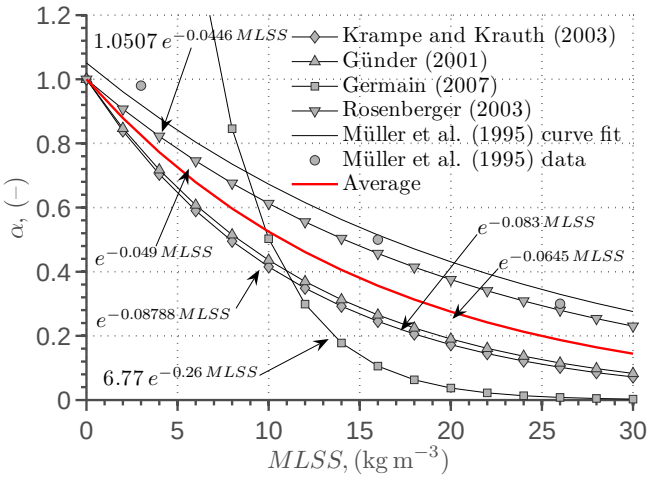

Figure 7.7: Oxygen transfer coefficient α as a function of MLSS - findings of different researchers supplemented with an averaged model.

As these two observed trend characteristics are equally plausible, the approach taken in this study was to average the exponent coefficients of Günder [81] and Rosenberger [213] and use this coefficient ω in the MBR model. Hence, the following expression for α vs. MLSS was proposed.

$$\alpha = e^{-0.0645\, MLSS} \tag{7.31}$$

The curve in Equation 7.31 is later used used in the MBR benchmark model simulations described in Chapter 8. For more information on inhibition of oxygen transfer by suspended solids the reader is referred to Germain et al. [69] who described in detail the effects of various physical and biochemical mixed liquor characteristics on oxygen transfer in MBR systems.

As mentioned in the review paper on rheological models for activated sludge suspensions by Ratkovich et al. [205], reduction of α with MLSS concentration was attributed by Fabiyi and Novak [54] to higher viscosity of activated sludge suspensions at increased solids concentrations. Whist at low fluid viscosities in air sparged systems bubbles leaving the sparger were small and the bubble plume was similar to the diameter of the sparger, at higher fluid viscosities bubble diameter increased while the size

of the plume decreased. Ratkovich et al. [205] then, rightfully postulated, that plumes of larger bubble diameters are characterised with lower area per volume and will hence produce lower O_2 transfer rates, while reduction of the plume diameter means that less liquid in the tank is exposed to air bubbles, hence the contact time between both phases is reduced. Ratkovich et al. [205] suggested that bubble coalescence occurs due to the effect of the viscosity of the liquid continuous phase on the critical detachment bubble diameter. It is however not clear when reading the review paper whether higher fluid viscosities in the experiment of Fabiyi and Novak [54] were attributed to higher solids concentrations, i.e. the dispersed phase or higher continuous phase viscosities, i.e. the dispersant. While in the body of the text the former was stated, the figure demonstrating the differences in bubble diameter, shape and the size of the plume indicates that higher viscosity in the investigated system was, either fully or partly, achieved by using a more viscous continuous phase, specifically carboxymethyl cellulose, CMC. It is quite possible that the mechanisms of bubble formation and rheology of the system would be quite different in these two systems. It may be hypothesised that coalescence may be promoted by the presence of solids not only at the surface of the sparger but also during the upwards flow of the bubbles due to collisions with the suspended matter. It is also possible that the smallest bubbles might attach to bigger flocs and coalesce on their surface. In order to quantify these effects more research is needed on activated sludge rheology and the effects of the dispersed phase on the motion of air bubbles as opposed to just the viscosity of the liquid phase.

7.4.3 Power requirements for compressed air provision

Power demand which is later used to calculate energy consumption for aeration is calculated with an adiabatic compression equation published in Tchobanoglous et al. [236] and shown below.

$$P_w = \frac{w\,R\,(273 + T_{air})}{c_{SI}\,n\,e}\left[\left(\frac{p_2}{p_1} - 1\right)^{0.283}\right] \tag{7.32}$$

where P_w (kW) denotes the power requirement of the air blowers, w (kg s^{-1}) denotes the mass flow of air, $R = 8.314$ (kJ kmol^{-1} K^{-1}) is the engineering gas constant for air, T_{air} (°C) is the absolute inlet temperature, p_{in} and p_{out} (atm) are the absolute inlet and outlet pressures respectively, $n = (k-1)/k = 0.283$ is the theoretical coefficient for air where $k = 1.395$, $c_{SI} = 29.7$ is the constant for SI unit conversion, and e (-) denotes the blower efficiency and is usually equal between 0.70 and 0.90.

7.5 Modelling air scour with the slug-flow model

7.5.1 Introduction

Prevention of cake buildup in immersed MBRs is accomplished mainly through coarse bubble aeration, i.e. injection of air bubbles of $\sim 6 - 13$ mm dia. at the bottom of the

membrane modules. These air bubbles rise and coalesce to form larger bubbles, usually occupying most of the free space and which, whilst flowing upwards in the vicinity of the membrane and cake, create shear stresses leading to cake detachment.

Coarse-bubble aeration leads to a two-phase air-water flow which may exhibit different patterns depending on the relative concentration of the two phases and the flow rate [152]. In case of immersed MBRs liquid phase flow is dependent on the gas flow velocity which induces circulating flow through and around the membrane modules. The functional relationship between gas and liquid flow rates depends on the tank and membrane module geometry and the type and location of the aeration grid. Two-phase gas-liquid flow patterns in a vertical upward flow have been investigated by various researchers. One of the most well-known studies is a study of Hewitt and Roberts [93] who developed a flow regime map shown in Figure 7.8 for and upward two-phase flow. The map is based on a fairly wide range of experimental data.

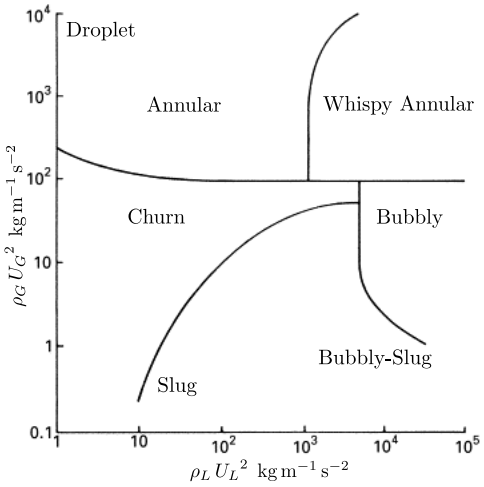

Figure 7.8: Flow regime map for a vertical upward two-phase flow [93].

Horizontal and vertical coordinates of the map denote the superficial momenta of liquid $\left(\rho_L U_L{}^2\right)$ and gas $\left(\rho_G U_G{}^2\right)$ phases and explicitly identify the type of the flow regime present in the system. Whilst all of these flow regimes are outlined below, the favourable type of flow in immersed MBRs is slug flow as it is found to create high levels of shear and turbulence per amount of air provided to the system. The fluctuating movement of liquid slugs and air pockets induces shear stresses on the boundaries of the flow domain and create wakes which produce additional turbulence-induced shear. These turbulence and shear stresses promote back-transport of cake from the membrane to the bulk liquid.

- *Bubbly flow.* Defined as flow of gas bubbles dispersed in a continuous liquid phase. The bubbles' sizes and shapes may vary widely but they are typically spherical and small compared to the cross-sectional dimension of the flow domain.
- *Slug flow.* Higher gas flow rates lead to larger gas void fractions inside the flow domain to the point where proximity of the bubbles is sufficiently small for them to start coalescing and forming larger bubbles. These bubbles are characterised

with a similar cross-sectional dimension as the length-scale of the flow domain (e.g. tube diameter), have a characteristic bullet-like shape with a hemispherical nose and a blunt tail-end, and are commonly referred to as *Taylor bubbles (TBs)*. Taylor bubbles are separated from one another by sections of liquid called slugs which themselves, depending on the ratio between gas and liquid mass flow rates (see Figure 7.8) may contain more or less gas bubbles. Taylor bubbles are surrounded by a thin liquid film forming between them and the tube wall, which may flow downwards due to the force of gravity, even though the net flow of fluid is upwards. The slug flow problem is schematically presented in Figure 7.10 and is further explained and modelled in Section 7.5.2.

- *Churn flow.* As the gas flow rate grows further, the structure of the flow becomes unstable with the liquid phase experiencing an oscillatory intermittent upward and downward motion but with a net upward flow. This instability is the result of the relative parity of the gravity and shear forces acting in opposing directions on the thin film of liquid around Taylor bubbles. The resulting oscillatory pattern is termed churn flow and constitutes an intermediate regime between slug flow and annular flow.
- *Annular flow.* Once the interfacial shear caused by high velocity gas flow on the liquid film begins to dominate over gravity, the liquid phase is expelled form the centre of the flow domain (e.g. vertical tube) and flows as a thin film on the wall forming an annual ring of liquid while the gas phase flows as a continuous phase up the centre of the tube. The interface is disturbed by high frequency waves and ripples. It is also possible that some of the liquid may be entrained as small droplets in the gas core, or that some bubbles may be entrained in the liquid film.
- *Wispy annular flow.* This type of flow falls between annular and misty flow and exists where gas flow velocity is further increased (in annular flow) causing the droplets entrained in the central core gas phase to form coherent and transient structures resembling clouds or whisps.

Studies on the characteristics of two-phase vertical flows, such as the one published by Hewitt and Roberts [93], do not explicitly mention any intermediate flow patterns which occur during transition between the, so called, independent flow regimes. One such flow regime, which is of particular interest in this study, is cap bubbly flow briefly described below.

- *Cap bubbly flow* occurs during transition between bubbly and slug flow [232] and leads to formation of the, so called, cap bubbles which are substantially different in shape and their motion and produce different drag and shear forces to small bubbles in bubbly flow and bullet-like Taylor bubbles in slug flow. Cap bubbly flow may occur in immersed MBRs when the air-flow in a given flow domain is less than required for the development of full slug-flow. Cap bubbly flow was observed to develop in MBRs where spaces between membrane bundles are greater than 15 cm. Drews et al. [48] also showed through experiments and simulation that the bubbles of larger diameters undergo larger deformations during the upward flow

due to drag forces and, as a consequence, develop cap-like rather than spherical shapes. Fabre and Liné [55] observed caps forming in spacings as little as 8cm.

Results of the simulations carried out in this study (see Section 7.5.7 for details) support the findings of Drews et al. [48]. Under specific aeration demands per membrane area SAD_m of 0.2–1.2 $Nm^3m^{-2}h^{-1}$ normally applied in immersed membrane bioreactors (iMBRs), the fraction of gas phase in a membrane module is characteristic of bubbly and cap-bubbly flow rather than slug-flow. The predicted Taylor bubble lengths are very short in comparison to the lengths of liquid slugs, which indicates formation of cap-like short air-bubbles.

7.5.2 Modelling of slug-flow

Two-phase flows are very difficult to model due to their inherent temporal and spatial variability. In bubbly-slug, slug, or cap-bubbly flow as well as other two-phase flows the interfacial topology constantly changes as both phases, here air and water, interact by exchanging energy, momentum and mass. Any point along the flow domain will experience alternating high and low gas fractions. We may therefore confidently state that there is no such thing as a *steady-state slug flow*, but we will use this term to describe constant average mass flows and slug and bubble lengths under time-varying flow conditions.

All macroscopic two-phase models begin with the formulation of mass, momentum and energy conservation equations for each phase. In order to obtain closure, these equations are then supplemented with the, so called, constitutive equations which describe the interactions between the phases and between each phase and the medium in which the flow occurs [152]. In case of coarse-bubble aeration these constitutive relations describe the interfacial exchange of mass between phases by the mechanism of phase change, interfacial exchange of momentum resulting from the slip velocity between the phases, and the interactions between the phases and the containing medium, e.g. wall shear due to friction.

The most accurate, yet very computationally intensive approach to modelling slug-flow would be to apply general methods of Computational Fluid Dynamics (CFD) to solve a set of discretised partial differential equations (PDEs) for mass, momentum and energy conservation together with the appropriate constitutive equations on a two-dimensional (2D) or three-dimensional (3D) spacial grid covering an entire domain of flow. Such a model allows to capture both the spacial as well as temporal dynamics of the flow. Complexity of such a model would however exceed the complexity of the biological and fouling models combined. With slug-flow description being only a mere addition to ASM and fouling models which form the core of the integrated MBR model, the approach adopted in this study is to formulate a much simpler, time and spatially averaged one-dimensional (1D) steady-state description of the two-phase slug flow.

It is assumed that slug flow is fully developed, axially symmetric, isothermal,

steady-state, and under low pressure conditions. Both phases are at an equilibrium, i.e. no one-directional mass transfer occurs between the phases whilst coalescence and breakage happen at equal rates. As mentioned earlier, in reality, this type of flow is highly fluctuating and displays a spatial and temporal distribution of both phases within the flow domain, but for the purpose of modelling the flow is idealised and the model can be considered to give temporally and spatially averaged values for the parameters involved. It is also assumed that the flow geometry does not change with time, i.e. hollow-fibre membrane bundles in the iMBR do not sway due to velocity and pressure gradients developing in the bulk liquid. Although hollow-fibre bundles are known to move in the tank, it would have been very hard, if not impossible, to include these effects in the *steady-state* model considered in this study.

As already mentioned, the flow pattern inside an air-sparged iMBR is likely to resemble more of a cap-bubbly flow than a slug-flow. However, since reliable models of cap-bubbly flow have not yet been developed and transition conditions between slug and cap-bubbly flow are difficult to establish, it is assumed that the flow pattern developing in the system under consideration falls into the slug-flow category. This is quite a significant assumption and shall be taken into consideration when interpreting the simulation results.

7.5.3 Investigated slug-flow models

Two mathematical models of slug flow have been investigated:

1. Plug flow model of Busch et al. [19]
2. Slug flow model of Zaisha and Dukler [268]

The model of Busch et al. [19] simplifies a slug-flow problem to the, so called, plug-flow where liquid slugs are assumed to be devoid of any gas bubbles. The model also assumes no mass and momentum transfer between the gas and the liquid phase. Gas and liquid velocities are calculated with mass balance equations under an assumption that the gas phase is incompressible. The film thickness around Taylor bubbles and their mean rise velocity due to buoyancy are calculated with correlation equations proposed by Wallis [248]. The superficial liquid velocity is obtained from Bernoulli equation for an upward non-ideal liquid flow across the membrane module in which the resistance coefficient λ is calculated according to Blasius' equation for smooth tubes.

The model of Zaisha and Dukler [268] is an extension and improvement of the 'model of two-phase slug flow in vertical tubes' published by Fernandes et al. [59]. The model of Zaisha and Dukler [268] extends the original model with improved formulation of gas entrainment by falling liquid film leading to improved predictions of void fraction in the liquid slugs. The new model also describes the development of liquid film around Taylor bubbles and is valid also for short, not just long Taylor bubbles. The model uses 12 original equations of Fernandes et al. [59] and adds 10 new equations leading to 22 equations and 22 variables overall. The superficial liquid velocity has to be specified by

the user or calculated either with the same set of Bernoulli equations for smooth tubes as in the model of Busch et al. [19] or with a different hydraulic model of the system.

Both models were initially solved for a different number of air flow rates and starting conditions using MATLAB's Optimization Toolbox function `lsqnonlin` which solves nonlinear least-squares problems of the form:

$$\min_{\mathbf{x}} \left\| \mathbf{f}(\mathbf{x}) \right\|_2^2 = \min_{\mathbf{x}} \left(f_1(\mathbf{x})^2 + f_2(\mathbf{x})^2 + \ldots + f_n(\mathbf{x})^2 \right) \tag{7.33}$$

where $\mathbf{f}(\mathbf{x})$ denotes the vector of n known equations and $\mathbf{x}$ denotes the vector of unknowns. Here, residuals of the individual equations were minimised to find the solution of the system of equations defining the slug flow model.

The default 'trust-region-reflective' algorithm was used for its ability, contrary to the alternative 'Levenberg-Marquardt' algorithm, to handle bound constraints.

Both of the above models were found to converge to different solutions depending on the choice of a starting point. For example, different combinations of the gas fraction in Taylor bubbles α_{TB} and the TB-to-liquid slug ratio β in the plug flow model of Busch et al. [19] produce the same air flow rates and thus superficial gas velocities v_{sg} but different superficial liquid velocities v_{sl}. It is therefore possible, for the same airflow rate, to obtain short Taylor bubbles with high α_{TB} and long slugs leading to lower superficial liquid velocity v_{sl} and therefore high gas fraction ε or long Taylor bubbles with low α_{TB} and short liquid slugs leading to higher superficial liquid velocity v_{sl} and thus low gas fraction. Although, no formal mathematical analysis of both models was performed, it seems possible that a unique solution may exist provided that the computational domain of the model is limited by setting appropriate lower and upper bounds on calculated variables or by additional equations. These additional pieces of information may be obtained from own experimental studies or from published studies on the same subject.

The model of Busch et al. [19] appears to exhibit poorer convergence than the more complex model of Zaisha and Dukler [268], possibly due to its simpler, less physical treatment of mass and momentum exchange between gas bubbles and liquid slugs. Whilst the model of Zaisha and Dukler [268] provides an in depth description of gas exchange and entrainment between the gas and the liquid phase, the model of Busch et al. [19] assumes that liquid slugs do not contain any gaseous phase, despite the reports that the gas fraction in liquid slugs may be as high as 20%. It is possible that the model of Busch et al. [19] is too much of an oversimplification of the slug flow problem considered here and therefore physically significant results may be difficult to obtain. Hence, further investigations of slug flow in the immersed hollow fibre outside-in membrane module will be carried out with a modified version of the model of Zaisha and Dukler [268]. This model together with additional supporting equations found in literature is presented below.

It was later discovered that convergence and uniqueness of solutions are negatively affected by the Bernoulli model linking the superficial liquid velocity to the superficial

gas velocity inside the membrane module. Although no formal and rigorous mathematical analysis of the model was performed in this study, nevertheless the Bernoulli equation was eliminated from the model and instead, Equation 7.42 introduced in Böhm et al. [13] was adopted.

7.5.4 Geometric model of a hollow fibre module

Geometric model of a hollow fibre module is adopted from Busch et al. [19] where it is assumed that all fibres are staggered, such that three neighbouring fibres form an equilateral triangle. An entire module area can then be represented with the structure shown in Figure 7.9, where each hexagon represents the catchment area A_{hex} (m^2) of a single fibre [19].

$$A_{hex} = \frac{\sqrt{3}\, {l_f}^2}{2} - \frac{\pi}{4}\, {d_{f,o}}^2 \tag{7.34}$$

where l_f (m) denotes the distance between two fibres and $d_{f,o}$ (m) denotes the outer fibre diameter. Total free area A_{mod} (m^2) of the module is then given by

$$A_{mod} = n_f\, A_{hex} \tag{7.35}$$

where n_f (–) denotes the number of fibres in the module.

As stated in the original paper of Busch et al. [19], rising Taylor bubbles are assumed to occupy the maximum available space with cross-sectional area A_{slug} (m^2) and diameter d_{slug} (m) - see Figure 7.9. A_{slug} and d_{slug} are calculated as follows.

$$d_{slug} = \frac{2\, l_f}{\sqrt{3}} - d_{f,o} \tag{7.36}$$

$$A_{slug} = \pi \frac{d_{slug}^2}{4} \tag{7.37}$$

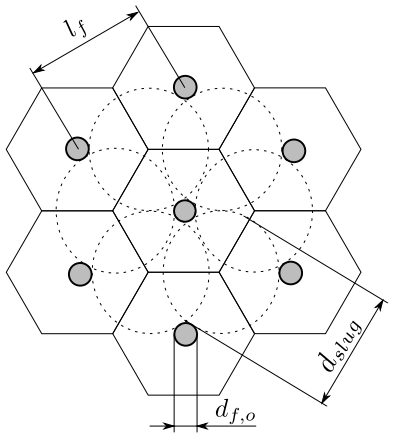

Figure 7.9: Hollow fibre module geometry in a horizontal cross-section adopted from Busch et al. [19]

7.5.5 Bulk phase density and viscosity

Dynamic viscosities of water and bulk liquid (η_w and η_l respectively) as well as bulk liquid density (ρ_l) are calculated with correlations of Ohle [191] as proposed in Busch et al. [19]. Dynamic water viscosity η_w (Pa·s) is a function of the bulk liquid temperature T_l (^{o}C).

$$\eta_w = 1.78 \times 10^{-3} \ \exp\left(-0.041\, T_l^{0.875}\right) \tag{7.38}$$

Bulk liquid viscosity η_l (Pa s) and density ρ_l (kg m^{-3}) depend on, respectively, the viscosity η_w and density ρ_w of water and the suspended solids concentration in the bulk liquid X_{TSS} (kg m^{-3})

$$\eta_l = \eta_w \left(0.0254 \ (X_{TSS})^2 - 0.1674\, X_{TSS} + 1.5918\right) \tag{7.39}$$

$$\rho_l = 0.99959\, \rho_w \ \exp\left(4.397 \times 10^{-4} \ X_{TSS}\right) \tag{7.40}$$

The bulk liquid viscosity calculated in Equation 7.39 is only indicative and likely to differ substantially from the actual viscosity value in a real system. As briefly explained in Section 5.6.1 activated sludge suspensions behave like non-Newtonian fluids and their viscosities will depend on the amount of shear they are exposed to. However, as the purpose of this study is to demonstrate the nature of slug flow within the HF membrane modules in a qualitative, rather than quantitative manner, accurate rheological model of an activated sludge suspension is not needed here.

7.5.6 Equations of slug flow

This section lists all equations used in the slug-flow simulations of coarse-bubble aeration on the HF outside-in iMBR geometry. Most of the governing and constitutive equations are borrowed from the model of Zaisha and Dukler [268] except the geometric model of the membrane module which has been obtained from the paper of Busch et al. [19], the model of superficial functional relationship between liquid velocity and superficial gas velocity which has been borrowed form Böhm et al. [13] and the model of average shear stresses on fibre surface which has also been adopted from Busch et al. [19].

Superficial velocities of gas and water

The superficial air velocity v_{sg} (m s^{-1}) is calculated by dividing the volumetric air flow rate Q_{air} (Nm^3 s^{-1}) by the cross-sectional free area of the module A_{mod}.

$$v_{sg} = \frac{Q_{air}}{A_{mod}} \tag{7.41}$$

The flow of liquid is directly related to the amount of air injected into the membrane module. Injection of air bubbles at the bottom of the membrane creates the velocity field and a density current leading to a circulating motion of fluid with upwards movement

inside the membrane modules and downwards movement outside the modules. This superficial liquid velocity v_{sl} (m s^{-1}) can be calculated using Bernoulli's energy mass balance equation across the membrane module as proposed by Busch et al. [19] but this approach was found to lead to poor convergence of the slug-flow model and hence has not been used in this study. Instead, the model implements a modified Chisti equation as proposed by Böhm et al. [13], where v_{sl} is in a quadratic relationship with v_{sl}.

$$v_{sl} = 47.119\, v_{sg}^2 - 6.624\, v_{sg} - 9.835 \times 10^{-2} \tag{7.42}$$

The mean superficial rising velocity of Taylor bubbles and liquid slugs $v_{s,tot}$ (m s^{-1}) is then given by

$$v_{s,tot} = v_{sg} + v_{sl} \tag{7.43}$$

A vertical slug flow can be represented, as briefly described in Section 7.5.2, with a number of mass and momentum conservation equations supplemented with a number of, so called, constitutive equations describing the interactions between the two phases and between the phases and the boundaries of the flow domain. The first of the conservation equations is the mass balance in **A-A** section of the flow geometry (see Figure 7.10).

$$Q_l^{LS} + Q_g^{LS} + Q_l^{TB} = Q_g^{TB} \tag{7.44}$$

where Q_l^{LS}, Q_l^{TB}, Q_g^{LS} and Q_g^{TB} (m^3 s^{-1}) are the volumetric flow rates of, respectively, liquid phase in liquid slugs, liquid phase in Taylor bubbles, gas phase in liquid slugs, and gas phase in Taylor bubbles. The above equation can be reformulated by dividing both parts by the free cross-sectional module area A_{mod}.

$$v_l^{LS}\,(1-\alpha_{LS}) + v_g^{LS}\,\alpha_{LS} + v_l^{TB}\,(1-\alpha_{TB}) = v_g^{TB}\,\alpha_{TB} \tag{7.45}$$

where v_l^{LS}, v_l^{TB}, v_g^{LS} and v_g^{TB} (m s^{-1}) are the velocities of, respectively, liquid phase in liquid slugs, liquid phase in Taylor bubbles, gas phase in liquid slugs, and gas phase in Taylor bubbles, and α_{LS} and α_{TB} (–) denote void fraction in liquid slugs and Taylor bubbles, respectively. The balance of liquid and gas flow for an entire volume of the slug unit are given in Equations 7.46 and 7.47 [59].

$$v_{sl} = (1-\beta)\left[(1-\alpha_{LS})\,(1-\gamma)\,v_l^{LS} + (1-\alpha_H)\,\gamma\,v_H^{LS}\right] - \beta\,(1-\alpha_{TB})\,v_l^{TB} \tag{7.46}$$

$$v_{sg} = \beta\,\alpha_{TB}\,v_g^{TB} + (1-\beta)\,\alpha_{LS}\,v_g^{LS} \tag{7.47}$$

where α_H (–) and v_H^{LS} denote, respectively the void fraction and the liquid velocity in the high voidage circulation zone of a liquid slug and

$$\gamma = \frac{L_{HLS}}{L_{LS}} \tag{7.48}$$

is the length ratio of the circulation zone L_{HLS} (m) to the length of the liquid slug L_{LS}

(m). β denotes the length ratio of TB to the whole slug unit.

$$\beta = \frac{L_{TB}}{L_{slug}} = \frac{L_{TB}}{L_{TB} + L_{LS}} \tag{7.49}$$

where L_{TB}, L_{LS}, and L_{slug} are, respectively, the lengths of the Taylor bubble, the liquid slug and the entire slug unit. Void fraction in the circulation zone α_H (–) is calculated as

$$\alpha_H = \frac{{Q_C}'}{{Q_C}' + Q_l^{TB\prime}} \tag{7.50}$$

where $Q_l^{TB\prime}$ (m^3 s^{-1}) denotes the flow of liquid film relative to the liquid slug.

$$Q_l^{TB\prime} = \frac{\pi}{4} d_{slug}^2 \left(1 - \alpha_{TB}\right) \left(v_N + v_l^{TB}\right) \tag{7.51}$$

Liquid velocity in the circulation zone v_H^{LS} is given by

$$v_H^{LS} = v_N - \frac{4 Q_l^{TB\prime}}{\pi d_{slug}^2} \tag{7.52}$$

The two other mass balances, for the gaseous and liquid phases respectively, as published in Fernandes et al. [59], are calculated relative to the nose of the Taylor bubble.

$$\left(v_N - v_g^{LS}\right) \alpha_{LS} = \left(v_N - v_g^{TB}\right) \alpha_{TB} \tag{7.53}$$

$$\left(v_N - v_l^{LS}\right) \left(1 - \alpha_{LS}\right) = \left(v_N - v_l^{TB}\right) \left(1 - \alpha_{TB}\right) \tag{7.54}$$

where v_N (m s^{-1}) denotes the TB rise velocity.

The rising velocity of Taylor bubbles is given as

$$v_N = C\ v_{s,tot} + v_0 = C\ \left(v_{sg} + v_{sl}\right) + 0.351 \sqrt{g\, d_{slug}} \tag{7.55}$$

where v_0 (m s^{-1}) denotes the bubble rise velocity in stagnant liquid [184] and C is a dimensionless coefficient that depends on the velocity profile ahead of the bubble, and can be seen as the ratio of the maximum to the mean velocity in the profile [233]. The values of C under fully developed turbulent and laminar conditions were determined in the early work on slug flow by Nicklin et al. [184] and later confirmed in the work of various other researchers [76, 12, 34, 200].

$$C \cong \begin{cases} 2.0 & \text{if } Re_{cs} \leqslant 8000 \\ 1.2 & \text{if } Re_{cs} > 8000 \end{cases} \tag{7.56}$$

where Re_{cs} denotes the Reynolds number based on the mean slug flow velocity

$$Re_{cs} = \frac{v_{cs,tot}\ d_{slug}\ \rho_l}{\eta_l} \tag{7.57}$$

However, in order to avoid poor convergence issues, the model of Zaisha and Dukler [268] used in this study adopts just a single value of $C = 1.29$ regardless of the Reynolds

number.

Taylor bubbles exchange gas with liquid slugs at the top (nose), the bottom, and at the periphery of the bubble. As Taylor bubbles move faster from the liquid slugs, they coalesce and entrain little gas bubbles present in the liquid slugs. At the same time, little gas bubbles detach from TBs under shear forces developing around the bubble and get entrained in the liquid slugs. Under a pseudo-steady state condition, gas flow into TB and out from TB into the liquid slugs is at an equilibrium, which can be expressed as

$$Q_A{}' + Q_B{}' = Q_C{}' \tag{7.58}$$

where $Q_A{}'$, $Q_B{}'$, and $Q_C{}'$ ($\mathrm{m^3\ s^{-1}}$) denote, respectively, gas flow into Taylor bubbles at the top and at the bottom, and gas entrainment from Taylor bubbles into liquid slugs, all relative to TB nose.

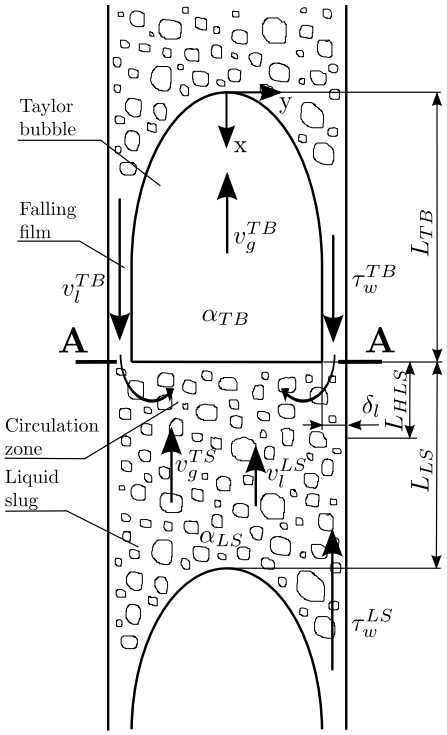

Figure 7.10: Graphical representation of a slug flow problem - adopted from Zaisha and Dukler [268].

The gas exchange flow rates $Q_A{}'$, $Q_B{}'$, and $Q_C{}'$ in Equation 7.58 are obtained from the following three constitutive equations [59, 268].

$$Q_A{}' = \frac{\pi}{4}\, d_{slug}^2\, \alpha_{LS}\, \left(v_N - v_g^{LS}\right) \tag{7.59}$$

$$Q_B{}' = \frac{\pi}{4}\, \left(d_{slug} - 2\,(\delta_l + \delta_g)\right)^2\ \alpha_H\, \left(0.25\, \left(1.15\, v_l^{TB} + v_N\right)\right) \tag{7.60}$$

$$Q_C{}' = \frac{1}{3}\sqrt{\frac{2\,\eta_g}{\rho_l\, g}}\, \left(v_l^{TB} + v_N\right)^{1.5}\, L\, f \tag{7.61}$$

where η_g (Pa·s) denotes the dynamic gas viscosity and is calculated with the Suther-

land's formula, $f = 40.85$ is a correction coefficient for enhancement of entrainment due to waviness of the liquid film and L (m) is the TB periphery at its bottom and is equal to $L = \pi\,(d_{slug} - \delta_g)$ where δ_g is calculated from Equation 7.67. The rising velocity of gas bubbles in the liquid slugs v_g^{LS} in Equation 7.59 is calculated from Equation 7.62 below [84, 273].

$$v_g^{LS} = v_l^{LS} + 1.53 \left(\frac{\sigma_{l,g}\, g\, (\rho_l - \rho_g)}{\rho_l^2} \right)^{\frac{1}{4}} \sqrt{1 - \alpha_{LS}} \tag{7.62}$$

where $\sigma_{l,g}$ (N m^{-1}) denotes the surface tension between the gaseous and the liquid phase. Terminal velocity of falling liquid film v_l^{TB} in Equations 7.60 and 7.61 is calculated as

$$v_l^{TB} = \left(v_l^{TB,0} + v_N \right) \left[1 - b\, \exp(-c\, Y) \right] - v_N \tag{7.63}$$

where $v_l^{TB,0}$ is an equilibrium terminal velocity of falling liquid film and is given by

$$v_l^{TB,0} = 9.916 \sqrt{g\, d_{slug}\, (1 - \sqrt{\alpha_{TB}})} \tag{7.64}$$

and Y denotes a transformed axial distance from the TB nose

$$Y = 2 \left(\frac{x}{d_{slug}} \right) \left(\frac{\eta_l}{\eta_w} \right)^{\frac{2}{3}} \tag{7.65}$$

where η_l and η_w (Pa·s) denote, respectively, the dynamic viscosities of bulk liquid and water. Thickness of a falling liquid film δ_l around the cylindrical part of a TB is derived from the void fraction in the Taylor bubble α_{TB}

$$\delta_l = \frac{d_{slug}}{2} \left(1 - \sqrt{1 - \alpha_{TB}} \right) \tag{7.66}$$

whereas the entrained gaseous film thickness δ_g is given by [268]

$$\delta_g = \frac{2 Q_C{}'}{\pi\, (d_{slug} - 2\, \delta_l)\, \left(v_l^{TB} + v_N \right)} \tag{7.67}$$

Length of the circulation zone and the liquid slug

The model does not calculate the lengths of the circulation zone L_{HLS} and the liquid slug L_{LS} and thus, these quantities have to either be measured, assumed or calculated with additional equations provided. The original paper of Zaisha and Dukler [268] assumes that

$$L_{HLS} = 5\, d_{slug} \tag{7.68}$$

as originally reported by Shermer and Barnea [219] and

$$L_{LS} = 20\, d_{slug} \tag{7.69}$$

Although the model of Zaisha and Dukler [268] used in this study adopts the two above simple relationships which assume that L_{HLS} and the liquid slug L_{LS} remain constant regardless of the hydrodynamic conditions present, many researchers reported that these two lengths vary with flow conditions. Fernandes et al. [59] reported $L_{LS} = 16-22\,d_{slug}$ whilst Zhang et al. [270] found L_{LS} to be in a function of Reynolds number based on the relative velocity at the bottom of the Taylor bubble, Re_n (–).

$$L_{LS} = \left(4.0 + 0.0526\sqrt{Re_n}\right) d_{slug} \tag{7.70}$$

$$Re_n = \frac{\rho_L \left(v_g^{TB} - v_l^{TB}\right) d_{slug}}{\eta_l} \tag{7.71}$$

Shear stress on the fibre surface

Under the assumption that slug flow through a HF membrane module can be modelled in the same manner as slug flow in a vertical tube, shear stress caused on the surface of a fibre in the slug unit can be divided into two parts [271]

1. Positive shear stress τ_w^{TB} due to the falling liquid film.
2. Negative shear stress τ_w^{LS} due to the rising liquid slug.

Average shear stress on the fibre surface τ_w is then calculated as a weighed sum of τ_w^{TB} and τ_w^{LS}

$$\tau_w = \beta \left|\tau_w^{TB}\right| + (1-\beta) \left|\tau_w^{LS}\right| \tag{7.72}$$

where β (–) denotes the TB to liquid slug ratio.

Although absolute values of individual shear stresses caused by the motion of falling liquid film and rising liquid slugs, rather than average shear stress, will govern the system behaviour, i.e. detachment of cake from the membrane surface, in order to describe cake detachment as a function of these shear stresses one has to be in possession of a dynamic cake detachment model. Whilst shear stresses due to the falling liquid film τ_w^{TB} are found to be much higher than the shear stresses caused by rising liquid slugs τ_w^{LS}, the membrane in this study is exposed to them for only a very short amount of time as the air bubbles are very short compared to liquid slugs. Hence, although shear stresses τ_w^{TB} are high, the membrane exposure time to these shear stresses may not be sufficient for the cake to detach from the membrane surface. Due to the lack of available information on the dynamics of cake detachment the two shear stress components are temporarily averaged according to Equation 7.72 and this averaged shear stress value is used as the input to the cake detachment model given in Equation 5.71. The produced shear stress value τ_w represents a time-averaged shear stress on the membrane surface.

Shear force in the liquid slug (τ_w^{LS}) is calculated from the Blasius' equation for smooth tubes [19]

$$\tau_w^{LS} = \frac{\rho_l \lambda_{slug} \left(v_l^{LS}\right)^2}{8} \tag{7.73}$$

where λ_{slug} is calculated as

$$\lambda_{slug} = 0.316\ {Re_{cs}}^{-0.25} \tag{7.74}$$

Shear forces caused by a falling liquid film around Taylor bubbles are calculated with Equation 7.75 under the assumption that shear forces between liquid, gas and film curvature can be neglected [19].

$$\tau_w^{TB} = (\rho_l - \rho_g)\ g\ \delta_l \tag{7.75}$$

7.5.7 Model simulation and results

The slug-flow model described above was simulated for a range of superficial gas velocities between 1 and 5 m s^{-1} which satisfy the aeration demands per membrane area (SADm) of 0.20 - 1.00 m^3 m^{-2} h^{-1}. All relevant inputs and parameters of the slug model are presented in Table 7.2.

Table 7.2: Values of the slug-flow model parameters adopted in the simulations.

Parameter	Description	Unit	Value
l_f	Distance between neighbouring fibres	m	0.01
$d_{f,o}$	Fibre's outer diameter	m	0.0025
h	Membrane module's (fibre's) height	m	1.8
A_{mod}	Module cross-section area	m^2	402.8
ρ_w	Density of water	kg m^{-3}	998.2
ρ_g	Density of air	kg m^{-3}	1.15
$\eta_{g,0}$	Dynamic gas viscosity under normal conditions	Pa · s	1.827×10^{-5}
$\sigma_{l,g}$	Surface tension between water and air	N m^{-1}	0.0729
v_{sg}	Superficial gas velocity	cm s^{-1}	$\{1 : 0.25 : 5\}$
X_{TSS}	Total Suspended Solids	kg m^{-3}	$\{6, 13, 20\}$
T_l	Bulk liquid temperature	^{o}C	$\{8, 14, 20\}$
b	Coefficient in Equation 7.63	–	0.807
c	Coefficient in Equation 7.63	–	0.0671
f	Correction coefficient in Equation 7.61	–	40.85

The average shear stresses τ_w on the fibre surface were calculated for all given superficial gas velocities v_{sg}, bulk liquid temperatures T_l and suspended solids concentrations x_{TSS}. The results are shown in Figure 7.11. Each continuous sequence of points in Figure 7.11 represents the relationship between τ_w and v_{sg} for a chosen combination of x_{TSS} and T_l maintained at a constant level throughout the simulation. τ_w, as logic indicates, increases with the aeration rate and so does the superficial gas velocity v_{sg}. Gradient of the $\tau_w = f(v_{sg})$ curve however gets smaller as v_{sg} is increased. The amount of shear created by aeration is found to increase with x_{TSS} and decrease with T_l, although the influence of x_{TSS} is stronger than of the liquid temperature T_l.

Each of the nine sets of points shown in Figure 7.11 were approximated with a third-order polynomial of the following form:

$$\tau_w(v_{sg}) = p_1\,(v_{sg})^3 + p_2\,(v_{sg})^2 + p_3\,(v_{sg}) + p_4 \tag{7.76}$$

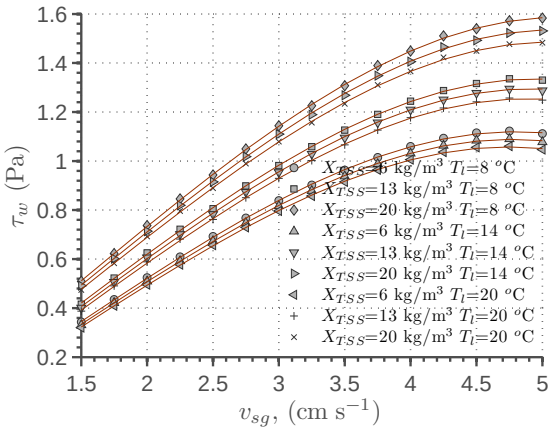

Figure 7.11: Average shear stresses on the fibre surface τ_w under different superficial gas velocities v_{sg}, suspended solids concentrations x_{TSS} and bulk liquid temperatures T_l.

The approximations were carried out with MATLAB's Curve Fitting Toolbox `cftool`, results of which are listed in Table 7.3.

Table 7.3: Coefficients of interpolating polynomials for τ_w vs v_{sg} data for each combination of x_{TSS} and T_l.

Simulation	x_{TSS}	T_l	p_1	p_2	p_3	p_4
	kg m^{-3}	^{o}C	Pa s^3 m^{-3}	Pa s^2 m^{-2}	Pa s m^{-1}	Pa
1	6	8	-0.01039	0.04406	0.2949	-0.1607
2	13	8	-0.01101	0.04783	0.3328	-0.1489
3	20	8	-0.01137	0.05117	0.3695	-0.1193
4	6	14	-0.01034	0.04374	0.2888	-0.1629
5	13	14	-0.01093	0.04731	0.3255	-0.1519
6	20	14	-0.01136	0.05123	0.3586	-0.1214
7	6	20	-0.01030	0.04345	0.2833	-0.1649
8	13	20	-0.01086	0.04683	0.3190	-0.1547
9	20	20	-0.01134	0.05129	0.3488	-0.1234

It is assumed that each of the four sets of polynomials shown in columns in Table 7.3 form a continuous function with x_{TSS} and T_l:

$$\forall_{i=1:4} \quad p_i = f_i(x_{TSS}, T_l) \tag{7.77}$$

It was found that the polynomial given in Equation 7.78 is able to give the highest quality of fit out of all tested polynomials with $R^2 > 0.995$ in all instances.

$$p_i = a_1 + a_2\, x_{TSS} + a_3\, T_l + a_4\, (x_{TSS})^2 + a_5\, (x_{TSS}\, T_l) \tag{7.78}$$

The approximations were carried out, similarly to the previous task, with MATLAB's Toolbox `cftool`. All four polynomial coefficients in Table 7.3 can be expressed in the

following form:

$$p_1 = -9.884 \times 10^{-3} - 1.106 \times 10^{-4} \, (x_{TSS}) + 1.256 \times 10^{-5} \, (T_l) + 1.669 \times 10^{-6} \, (x_{TSS})^2 - 3.722 \times 10^{-7} \, (x_{TSS} \, T_l) \quad (7.79)$$

$$p_2 = 4.231 \times 10^{-2} + 3.862 \times 10^{-4} \, (x_{TSS}) - 9.708 \times 10^{-5} \, (T_l) + 3.378 \times 10^{-6} \, (x_{TSS})^2 + 4.288 \times 10^{-6} \, (x_{TSS} \, T_l) \quad (7.80)$$

$$p_3 = 0.2627 + 6.695 \times 10^{-3} \, (x_{TSS}) - 5.703 \times 10^{-4} \, (T_l) - 3.598 \times 10^{-5} \, (x_{TSS})^2 - 5.445 \times 10^{-5} \, (x_{TSS} \, T_l) \quad (7.81)$$

$$p_4 = -0.151 - 2.212 \times 10^{-3} \, (x_{TSS}) - 4.014 \times 10^{-4} \, (T_l) + 1.985 \times 10^{-4} \, (x_{TSS})^2 + 8.685 \times 10^{-7} \, (x_{TSS} \, T_l) \quad (7.82)$$

Equation 7.76 was then solved with p_1, p_2, p_3 and p_4 obtained from Equations 7.79-7.82 for all values of v_{sg}, x_{TSS}, and T_l used in the simulation. The resulting curves were plotted along the simulation results in Figure 7.11 and exhibit a perfect visual fit. We therefore come to the conclusion that for this particular HF iMBR system under consideration, the polynomial presented in Equation 7.76 with coefficients calculated from Equations 7.79-7.82 is able to produce the same values of wall shear stress on the fibre surface as the slug-flow model of Zaisha and Dukler [268].

Figure 7.12 shows the two components of τ_w: shear stress caused by the motion of liquid slugs τ_w^{LS} and Taylor bubbles τ_w^{TB} at different operating points defined in the simulation. Figure 7.12 shows that whilst τ_w^{LS} depends on x_{TSS} and T_l and is in a positive almost linear relationship with v_{sg}, τ_w^{TB} is independent of x_{TSS} and T_l, is $\sim 6 \times \tau_w^{LS}$ and decreases rapidly with v_{sg}. Decrease in τ_w^{TB} under higher gas velocities is caused by decreasing thickness of liquid film around the Taylor Bubble δ_l and is responsible for the curvature of $\tau_w = f(v_{sg})$ shown in Figure 7.11.

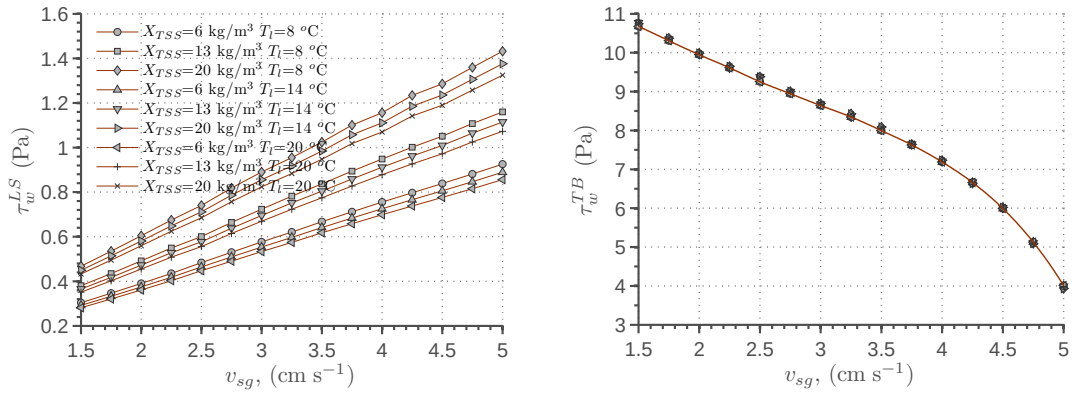

Figure 7.12: Shear stresses caused by the motion of liquid slugs τ_w^{LS} and Taylor bubbles τ_w^{TB} at different superficial gas velocities v_{sg}, suspended solids concentrations x_{TSS} and bulk liquid temperatures T_l.

The model predicts, for a given set of inputs and parameters, rather low values of gas fraction ε between 7-14% and similarly low TB to slug unit ratios β, which are

found to increase with v_{sg} and range approximately between 0.004 and 0.06. On one hand the model tends to support the findings of other researchers, e.g. [48] that under specific aeration rates $\mathrm{SAD_m}$ applied to iMBRs, the air-liquid flow pattern resembles more of a cap-bubbly flow with cap-like small air bubbles rather than a fully developed slug-flow. On the other hand, the results presented here are obtained with a number of risky assumptions. The adopted functional relationship between v_{sg} and v_{sl} is likely not to represent the specific system under study, the HF module geometry is simplified with a geometric model in Figure 7.9, it is assumed that the flow domain does not vary in time, i.e. the fibres remain rigid and do not sway, the highly time-varying shear stresses are calculated as a weighed sum of τ_w^{TB} and τ_w^{LS} according to Equation 7.72. Last but not least, the slug-flow model itself constitutes a significant simplification of slug-flow because, as already explained in Section 7.5.2 and mentioned indirectly above, it leads to spatial and temporal averaging of a highly variable and chaotic process. This means that the model might be flawed in its basic assumptions as it may not be possible to approximate a highly variable process of this kind with a spatially and temporally averaged approximation.

Thus, the results provided above are very unlikely to be quantitatively accurate. However, bearing in mind the lack of empirical data, they do introduce some insight into the nature of the system and can serve as a theoretical basis for further investigations. The results are complemented with gas fractions ε and length ratios of TB to the whole slug unit β at different superficial gas velocities v_{sg}, suspended solids concentrations x_{TSS} and bulk liquid temperatures T_l shown in Figure 7.13 and Figure **??**. x_{TSS} and T_l do not have any influence on the predicted values of ε and β, hence both figures show single curves instead of families of curves.

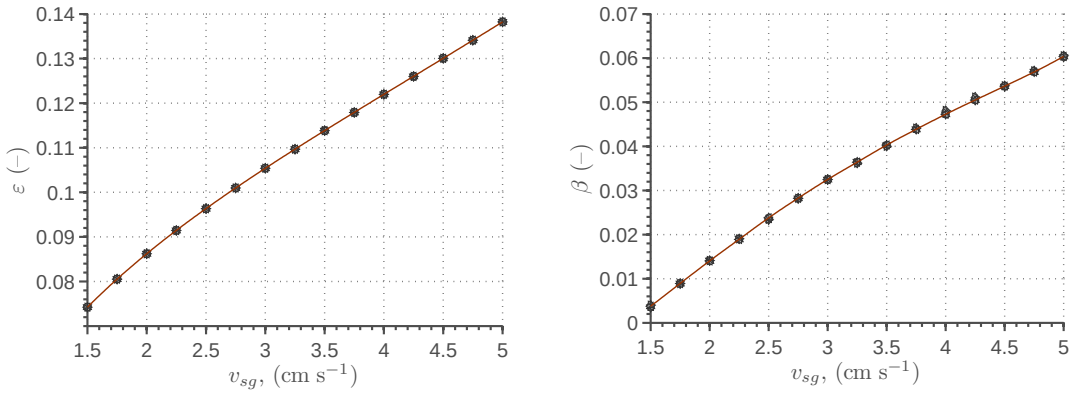

Figure 7.13: Gas fractions ε and length ratios of TB to the whole slug unit β at different superficial gas velocities v_{sg}, suspended solids concentrations x_{TSS} and bulk liquid temperatures T_l.

Back transport of cake $\dfrac{dm_c}{dt}$ (kg m^{-2} s^{-1}) has also been empirically linked to the superficial air velocity v_{sg} (m/s) with the following power relationship [72].

$$\frac{dm_c}{dt} = -\alpha_v \, (v_{sg})^{\beta_v} \tag{7.83}$$

where α_v (–) is a dimensionless air scouring coefficient, v_{sg} (m/s) denotes the superficial air velocity, and β_v denotes the dimensionless air scouring exponent.

7.6 EPS and SMP effects on fouling

Dependence of specific cake resistance α_c on EPS

Results of various research studies on dependence of specific cake resistance α_c on EPS content in activated sludge are so far not conclusive, however it is understood that specific cake resistance does depend on EPS.

Nuengjamnong et al. [187] measured the specific cake resistance α_c of washed and unwashed sludge of three laboratory-scale iMBRs operating at a constant subcritical permeate flux of 12.5 Lmh, equipped with a flat-sheet microfiltration membrane with a 0.25 μm pore size at three different SRTs of 8, 20 and 80 days. The reactors were fed with synthetic wastewater based on glucose as a carbon source. EPS were extracted using a cation- exchange resin (CER, Dowex 50x80, 20-50 mesh, sodium form, Aldrich 42878-7) method. The obtained results shown in Figure 7.14 indicate that α_c increases with the EPS content, although the type of this relationship is difficult to identify due to limited number of data points and large errors associated with the measurements. Nevertheless the data points for the washed and unwashed sludge were fitted with two separate linear regression models with a reasonable quality of fit characterised by R^2 of respectively 0.724 and 0.672.

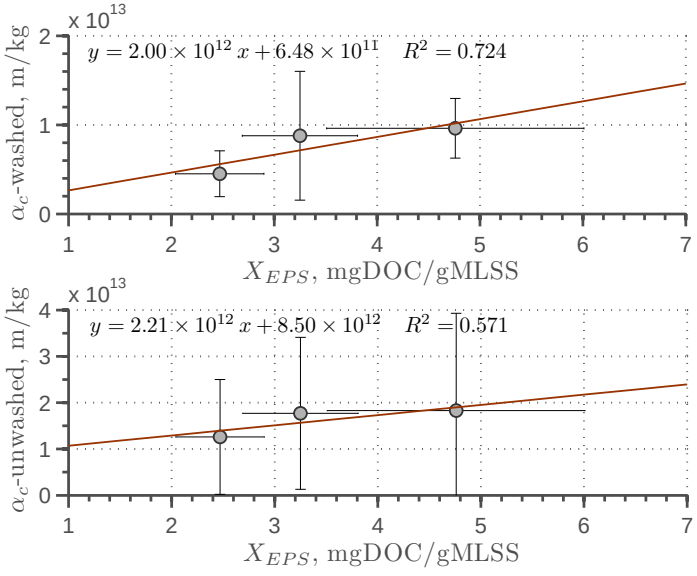

Figure 7.14: Specific cake resistance α_c as a function of EPS content in the cake - Nuengjamnong et al. [187].

Cho et al. [29] measured the specific cake resistance of activated sludge samples characterised with different MLSS concentrations and EPS/MLVSS ratios. Specific cake resistance was measured at different pressures in dead-end filtration experiments performed using an unstirred batch cell equipment, called Amicon Cell (AmiconTM, USA)

equipped with a 0.2μm, polyethersulfone, hydrophilic membrane. EPS was extracted using cation exchange resin (DOWEX 508, 20-50 mesh in the sodium form, Aldrich 42878-7) accordingly to Frølund et al. [66].

Cho et al. [29] found that

$$\mu^2\, TMP^{-1}\, \alpha_c = f(EPS/MLVSS) \tag{7.84}$$

where $f(EPS/MLVSS) = A + B\,(1 - \exp(-C\,x))^D$ and A, B, C, D are adjustable parameters.

Equation 7.84 was fitted to the measurements, however the curve published in Cho et al. [29] doesn't seem to reproduce the data. Therefore the curve in Equation 7.84 was fitted by the author of this thesis producing the following relationship between α_c, ΔP, μ and $\dfrac{EPS}{MLVSS}$ and shown in Figure 7.15b.

$$\alpha_c = \frac{\Delta P}{\mu^2}\left(1057 + 17707\left(1 - \exp\left(-118.6\,\frac{EPS}{MLVSS}\right)\right)^{40.33}\right) \tag{7.85}$$

When we substitute μ with the value for dynamic viscosity of water at 20°C , i.e. $\mu = \mu_{w,20^oC} = 1.002 \times 10^{-3}$ Pa·s, Equation 7.85 becomes:

$$\alpha_c = \Delta P\left(1.053 \times 10^9 + 1.764 \times 10^{10}\left(1 - \exp\left(-118.6\,\frac{EPS}{MLVSS}\right)\right)^{40.33}\right) \tag{7.86}$$

which shows that α_c is found to depend on pressure according to the relationship $\alpha_c = \alpha_0\, TMP^n$ where $n = 1$. The relationship between α_c and TMP is shown in Figure 7.15a.

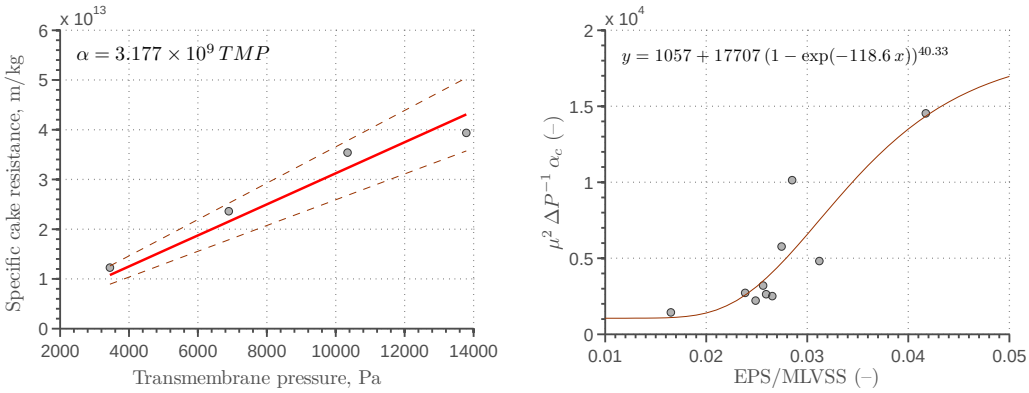

(a) (b)

Figure 7.15: (a) Dependence of cake resistance on trans-membrane pressure (TMP) and (b) relationship between EPS/MLVSS, dynamic viscosity μ, specific cake resistance α_c and TMP.

The effect of TMP on the relationship for α_c vs EPS/MLVSS described in Equation 7.85 is shown in Figure 7.16 and indicates that the relationship becomes more linear for lower TMP.

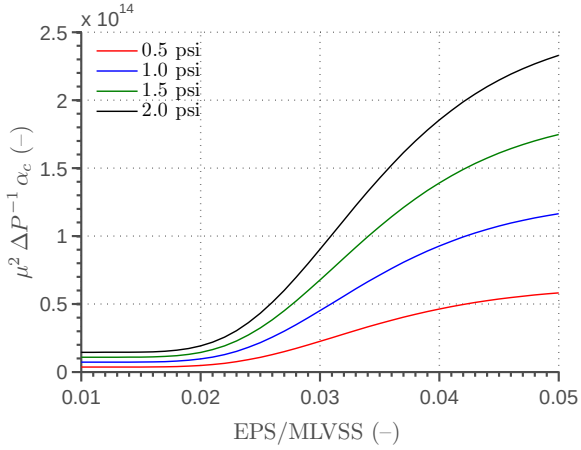

Figure 7.16: Specific cake resistance α_c as a function of EPS content in the cake at different TMPs.

Ahmed et al. [1] investigated the the effects of SRT on membrane fouling in a MBR equipped with the sequential anoxic/anaerobic reactor. At each studied SRT, they measured specific cake resistance α_c, TMP, MLVSS and MLSS and EPS. The measurements of Ahmed et al. [1] were used to create the α_c vs EPS/MLVSS plot shown in Figure 7.17.

Although Figure 7.17 suggests a nonlinear relationship between α_c and EPS/MLVSS, small number of data points with significant measurements errors prevent to infer an accurate form of this relationship. Hence a simple straight line equation was fitted to the data as shown in the figure.

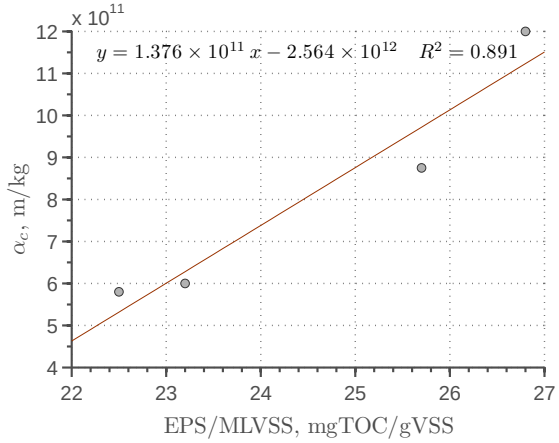

Figure 7.17: Specific cake resistance α_c as a function of EPS content in the cake - Ahmed et al. [1].

7.7 SMP rejection by the membrane

Song et al. [226] identified the following relationship between effluent SMP concentration $S_{SMP,e}$ and bulk liquid SMP concentration $S_{SMP,bio}$ as a function of the plant's SRT

(θ).

$$S_{SMP,e} = S_{SMP,bio}\,(0.425 - 0.005\,\theta) \tag{7.87}$$

Here, $S_{SMP,e}$ was found to decrease with SRT possibly due to the changes in sludge floc size distribution (FSD) and retentive properties of the dynamic layer.

However, the above relationship is only valid for one particular system whereas SMP rejection will normally depend on the number of factors such as FSD of the bulk liquid, particle size distribution of the cake, composition of the dynamic layer, degree of fouling on the membrane, properties of the membrane, etc. Hence, it was decided to refrain from any attempts of modelling SMP rejection and hence the membrane's retentive properties are instead described with a single parameter f_{nr} which denotes the fraction of non-retained SMP, i.e. the fraction of SMP which ends up in the permeate.

7.8 Output and process evaluation criteria

Outputs of the integrated MBR model (IBMF-MBR) developed in this thesis are assessed in the same way as the outputs of the COST/IWA benchmark simulation model no.1 (BSM1) [36, 37] and of the MBR benchmark simulation model (BSM-MBR) [160]. As shall later be described in Chapter 8 all three models are simulated with different scenarios under constant and time-varying inputs called respectively, *steady-state* and *dynamic* simulations.

The recorded results of steady state simulations include the flow averaged state variable concentrations in the influent, effluent and underflow streams and time-averaged process variables: SRT, hydraulic retention time (HRT), aeration energy, pumping energy, mixing energy, sludge production, and observed sludge yield. Outputs of the dynamic simulations include flow averaged influent and effluent loads and concentrations of state and composite variables. The recorded process variables are respectively: average SRT, HRT and sludge yield. The effluent and operational cost performance criteria are respectively: influent quality index (IQI), effluent quality index (EQI), 95%-ile concentrations of the effluent ammoniacal nitrogen (NH_4^+-N), total nitrogen (TN), total suspended solids (TSS), chemical oxygen demand (COD) and biological oxygen demand in five days (BOD_5), number of effluent consent violations and percent of time under violation of these state and composite variables, as well as average sludge production, energy demand for aeration, pumping and mixing, and operational cost index (OCI).

The calculation procedure for composite variables in IBMF-MBR was adopted from BSM1 and takes into account three new state variables: S_{UAP}, S_{BAP} and X_{EPS} present

in CES-ASM1.

$$TSS = 0.75\,(X_S + X_H + X_A + X_P + X_I + X_{EPS}) \tag{7.88}$$

$$COD = S_S + S_I + X_S + X_H + X_A + X_P + X_I + X_{EPS} + S_{UAP} + S_{BAP} \tag{7.89}$$

$$BOD_5 = f_{BOD}\,(S_S + X_S + (1 - f_P)(X_H + X_A) + X_{EPS} + S_{UAP} + S_{BAP}) \tag{7.90}$$

$$TKN = S_{NH} + S_{ND} + X_{ND} + i_{XB}\,(X_H + X_A) + i_{XP}\,(X_P + X_I) + i_{XBAP}\,S_{BAP} + i_{XEPS}\,X_{EPS} \tag{7.91}$$

$$TN = TKN + S_{NO} \tag{7.92}$$

where $f_{BOD} = 0.25$ in the effluent stream and $f_{BOD} = 0.65$ in the influent stream. It is assumed that X_{EPS} contribute to the amount of solids in the system and that X_{EPS}, S_{UAP}, and S_{BAP} are biodegradable, hence contribute to both COD and BOD_5. Whilst S_{BAP} contains nitrogen (N), S_{UAP} is devoid of any nitrogen and hence does not appear in the equation for total Kjeldahl nitrogen (TKN).

The effluent quality, i.e. pollution emitted to the receiving body is characterised with a combination of flow-proportionally averaged state and composite effluent parameters, 95%-ile concentrations of the selected effluent parameters, number of consent violations, % of time in violation of the effluent consent limits and the effluent quality index (EQI). All of the above quantities are calculated from raw simulation results recorded at a 15-min sampling interval.

The number of consent violations and % of time in violation in IBMF-MBR are calculated with reference to the same effluent consent limits as applied in BSM1 and BSM-MBR, i.e. $S_{NH,eff}^{max} = 4$ gN m^{-3}, $N_{tot,eff}^{max} = 18$ gN m^{-3}, $BOD_{eff}^{max} = 10$ gO_2 m^{-3}, $COD_{eff}^{max} = 100$ gO_2 m^{-3}, $TSS_{eff}^{max} = 30$ gSS m^{-3}.

IBMF-MBR model is simulated under the same scenarios and with the same protocol as introduced in [37, 160]. The model is first brought to the steady-state, then simulated for 14 days under dry-weather inputs followed by a 14 day simulation under either dry-weather, rain-event or storm-event conditions. The model's performance is evaluated for the last 7 days of operation, i.e. between day 22 and day 28, hence the simulation time used for the eavaluation of effluent quality and process performance $t_{sim} = 7$ d.

EQI is calculated with Equation 7.93 published in COST624 [37].

$$EQI = \frac{1}{1000\;t_{sim}} \int_{t_0}^{t_0+t_{sim}} \Big[\; \beta_{TSS}\,TSS_{eff}(t) + \beta_{COD}\,COD_{eff}(t) + \beta_{BOD}\,BOD_{eff}(t) + \beta_{TKN}\,TKN_{eff}(t) + \beta_{NO}\,NO_{eff}(t) \Big]\, q_{eff}(t)\; dt \tag{7.93}$$

where $\beta_{TSS} = 2$, $\beta_{COD} = 1$, $\beta_{BOD} = 2$, $\beta_{TKN} = 20$, and $\beta_{NO} = 20$. TSS_{eff}, COD_{eff}, BOD_{eff}, TKN_{eff}, and NO_{eff} denote, respectively, the effluent concentrations of TSS, COD, biological oxygen demand (BOD), TKN, and nitrates+nitrites.

IQI is calculated with the same equation as EQI after the substitution of the effluent flow and concentrations with the influent-related flow and concentrations.

Production of sludge for disposal $P_{sludge,disp}$ is calculated with Equation 7.94 [37]

$$P_{sludge,disp} = \frac{\Delta M_{TSS,bio} + M_{TSS,was}}{t_{sim}} \tag{7.94}$$

where the amount of sludge for disposal generated within the simulation time t_{sim} is computed as the sum of the mass of sludge wasted $M_{TSS,was}$ (in the WAS stream and at volume flow rate q_w) and the mass of biomass grown in the bioreactor $\Delta M_{TSS,bio}$. $\Delta M_{TSS,bio} = M_{TSS,bio}^{\text{end of day 28}} - M_{TSS,bio}^{\text{end of day 21}}$. The total mass of biosolids $M_{TSS,bio}$ is equal to the sum of masses of solids in each of the five bioreactors.

$$M_{TSS,bio} = \sum_{i=1}^{5} X_{TSS}^{i} V_i \tag{7.95}$$

where V_i and X_{TSS}^{i} denotes the volume and TSS concentration in the i$^{\text{th}}$ bioreactor, respectively. The mass of solids disposed of in the WAS stream is calculated with Equation 7.96

$$M_{TSS,was} = 0.75 \int_{0}^{t_{sim}} \left[X_{S,w} + X_{H,w} + X_{A,w} + X_{I,w} + X_{P,w} + X_{EPS,w}\right] q_w(t)\, dt \tag{7.96}$$

The mass of solids lost in the effluent stream is calculated with Equation 7.97

$$M_{TSS,e} = 0.75 \int_{0}^{t_{sim}} \left[X_{S,e} + X_{H,e} + X_{A,e} + X_{I,e} + X_{P,e} + X_{EPS,e}\right] q_e(t)\, dt \tag{7.97}$$

Then the total sludge production in the system $P_{sludge,tot}$ (kg d^{-1}) is calculated as

$$P_{sludge,tot} = P_{sludge,disp} + \frac{M_{TSS,e}}{t_{sim}} \tag{7.98}$$

Pumping energy PE (kWh d^{-1}) is calculated in BSM1 and BSM-MBR by multiplication of the flow rate by the pumping economy coefficient PF (kWh m^{-3}).

$$PE = \frac{1}{t_{simu}} \sum_{i=1}^{i=N} PF_i \int_{t_0}^{t_0+t_{simu}} q_i(t)\, dt \tag{7.99}$$

where $N = 3$ in BSM1 and $N = 4$ BSM-MBR. $q_1(t) = q_w(t)$, $q_2(t) = q_{int}(t)$, $q_3(t) = q_r(t)$, $q_4(t) = q_e(t)$

Equation 7.99 is replaced in IBMF-MBR with pump Equation 7.100 which calculates the amount energy required to lift a given volume of water up to a specified

Table 7.4: Values of the parameters used in pumping equations 7.99 and 7.100

Model	Parameter	Symbol	Unit	Flow				
				q_w	q_{int}	q_r	q_e	q_b
BSM1	Pumping economy	PF	kWh m^{-3}	0.04	0.04	0.04	–	–
BSM-MBR	Pumping economy	PF	kWh m^{-3}	0.05	0.0075	0.0075	0.075	–
	Geometric height	h_g	m	7.0	0.50	0.50	calc	calc
IBMF-MBR	Sum of losses	h_l	m	2.17	1.42	1.42	0.5	0.5
	Efficiency	η	–	0.5	0.7	0.7	0.7	0.7

height.

$$PE = \frac{60\,\rho_w\,g}{1000\,t_{simu}} \sum_{i=1}^{i=5} \frac{h_g^i + h_l^i}{\eta_i} \int_{t_0}^{t_0+t_{simu}} q_i(t)\,dt \tag{7.100}$$

where ρ_w (kg m^{-3}) denotes the water density, h_g (m) denotes the geometric height, h_l (m) denotes the sum of hydraulic losses, η (–) denotes the pump efficiency, and $q_5 = q_e$ (m^3 d^{-1}) denotes the permeate (effluent) flow rate.

The parameter values used in Equation 7.99 and Equation 7.100 are listed in Table 7.4. Geometric height for permeate pumping and during backflush periods is calculated in IBMF-MBR from the fouling model. Backwash flow is assumed to be twice that of the average permeate flow and corresponds to a backwash flux of ∼40 L m^{-2} h^{-1}. Membrane resistance during backwash periods is assumed to be equal to the resistance of the clean membrane R_m plus additional resistance caused by irreversible fouling R_i. Resistance due to cake formation R_r is assumed zero, i.e. removal of cake is assumed to occur instantaneously.

Whilst energy demand for aeration AE (kWh d^{-1}) in BSM1 is calculated with Equation 7.101 shown below which relates AE to the oxygen mass transfer coefficient k_La in each bioreactor, aeration energy in BSM-MBR and IBMF-MBR is calculated with Equation 7.32 presented on page 230 which describes the energy input required for adiabatic compression of an ideal gas.

$$AE = \frac{24}{t_{sim}} \int_{t_0}^{t_0+t_{sim}} \sum_{i=1}^{i=5} \left[0.4032\,k_La_i(t)^2 + 7.8408\,k_La_i(t)\right]\,dt \tag{7.101}$$

Parameters used in the adiabatic compression equation are given in Table 7.1 on page 228.

Power requirements and energy demand for mixing ME (kWh d^{-1}) is calculated in the same manner as described in Copp [36] and Maere et al. [160], i.e. using Equation 7.102 in the BSM1 model and Equation 7.103 in BSM-MBR and IBMF-MBR.

$$ME = \begin{cases} 0 & \text{if } k_La \geqslant k_La_{min} \\ 24\,k_{mix}\,V & \text{if } k_La < k_La_{min} \end{cases} \tag{7.102}$$

$$ME = \begin{cases} 0 & \text{if } q_a \geqslant q_{a,min} \\ 24\, k_{mix}\, V & \text{if } q_a < q_{a,min} \end{cases} \tag{7.103}$$

where k_{mix} (kW m^{-3}) denotes the unit power requirement for mixing of one cubic metre of activated sludge and V (m^3) is the bioreactor volume. In BSM1 $k_{mix} = 0.005$ kW m^{-3} whereas in BSM-MBR and IBMF-MBR k_{mix} is higher and equal to 0.008 kW m^{-3} due to higher solids contents in the bioreactors and thus, higher propensity of the bulk liquid to settling. In BSM1 $k_L a_{min} = 20$ d^{-1} whilst $q_{a,min}$ in BSM-MBR and IBMF-MBR is equal to 660 Nm^3 h^{-1} for the anoxic and aerobic tanks and 480 Nm^3 h^{-1} for the membrane tank based on the minimum specific aeration rate per square metre of ground surface area of 2.2 m^3 h^{-1} m^{-2} [160].

Chapter 8

Benchmark model setup and simulation results

Contents

8.1 Introduction

8.1.1 Overview of the published integrated MBR models

Despite of the recent developments in modelling SMP and EPS production in activated sludge systems, e.g. Lu et al. [157], Jiang et al. [115], Janus and Ulanicki [111], Chen et al. [25] and the abundance of scientific literature examining various membrane fouling models, the scientific community has so far seen only a handful of journal publications in the area of integrated modelling of membrane bioreactors (MBRs). The gap between state of the art in modelling individual components of MBR reactors and complete, integrated MBR models stems from the fact that the interactions existing between biological and physical (membrane filtration) parts of the MBR are very complex and

hence difficult to describe. Research in this area seems however to have been gaining momentum in the last couple of years which manifested itself in recent publications of several integrated MBR models. The most well known of these models are briefly introduced and outlined below.

Integration of activated sludge models with membrane fouling was first attempted over a decade ago. However, MBR models developed back then were quite simple and did not account for many bi-lateral interactions between the bioreactor and the membrane. Lee et al. [140] modelled an immersed membrane bioreactor (iMBR) for wastewater treatment with the ASM1-based model of Lu et al. [157] and a simple membrane filtration model where fouling was described only with a cake formation mechanism. The authors did not describe any links between concentrations of soluble microbial products (SMP) in the bulk liquid and the rates of fouling, nor was the model validated, hence its practical applicability is unknown [179]. Wintgens et al. [257] developed a model of a hollow fibre (HF) iMBR for wastewater treatment. The bioreactor was modelled with the IAWQ Activated Sludge Model No. 3 (ASM3), hence production of the main membrane foulants - SMP and extracellular polymeric substances (EPS), was not described. Membrane filtration was modelled with a very simple filtration model based on Darcy's equation in which total membrane resistance was expressed as the sum of clean membrane resistance, cake layer resistance, and the resistance due to concentration polarisation. Although the model was able to reproduce long-term changes in membrane permeability in a full scale MBR wastewater treatment plant (WWTP) it did not describe the complexities of membrane fouling and the links existing between membrane fouling and biological processes in the membrane bioreactor.

A short review of modelling studies on membrane bioreactors (MBRs) was published in 2007 by Ng and Kim [179]. A year later two significantly more complex integrated MBR models were published by Zarragoitia-González et al. [269] and Bella et al. [11]. Zarragoitia-González et al. [269] linked the activated sludge model of Lu et al. [157] described in Chapter 3 on page 65 with a comprehensive membrane fouling model of Li and Wang [147] where fouling is assumed to be the product of pore constriction, sludge cake accumulation, and dynamic film layer formation. Specific cake resistance was linked to the concentration of soluble EPS in the bulk liquid while cake detachment from the membrane surface was related to coarse bubble aeration rate. The model was simulated under intermittent filtration and coarse bubble aeration and was found to be in a reasonable agreement with the experimental results obtained from a lab-scale MBR reactor. Bella et al. [11] linked a ASM1-based activated sludge model with SMP kinetics closely resembling the model of Lu et al. [157] with a comprehensive membrane filtration and fouling model heavily based on the model of Lee et al. [140]. The authors were mainly focussed on prediction of chemical oxygen demand (COD) in the permeate whilst, unfortunately, the links between SMP concentration and irreversible fouling have not been modelled. COD was assumed to decrease across the membrane due selective characteristics of the membrane and pre-sieving on the cake layer which were described with deep-bed theory. The model was calibrated with very good results on

the measurements obtained from a iMBR pilot plant. The obtained parameter values of the biological model might not however be representative of the physical system due to the fact that the Petersen matrix of the biological model used in the study does not pass a mass-balance check, similarly to the model of Lu et al. [157].

Mannina et al. [163] improved the model of Bella et al. [11] by swapping the non-mass and charge conserving model of Lu et al. [157] with a modified Activated Sludge Model No. 1 (ASM1) implementing the SMP kinetics first introduced in Jiang et al. [115]. The filtration model was modified to include more fouling mechanisms whilst keeping the sectional model approach of Lee et al. [140] and the deep bed filtration equations introduced originally in Bella et al. [11]. Calibration was carried out with the procedure for calibration of activated sludge models introduced by Mannina et al. [162] which is based on a comprehensive sensitivity analysis and a novel step-wise Monte Carlo-based calibration of the subset of most influential parameters. Although the model was found to be in a good agreement with the measurements obtained from a MBR pilot plant, it suffers from the same weakness as the model of Bella et al. [11], i.e. irreversible fouling has not been related to the SMP concentration in the bulk liquid. SMP was assumed to influence the specific cake resistance according to the model of Cho et al. [29]. However the adopted equation was originally derived as a correlation between specific cake resistance and EPS not SMP, hence the assumption of Mannina et al. [163] is questionable.

Most recently Suh et al. [231] developed an integrated MBR model based on the benchmark simulation layout of Maere et al. [160]. The authors selected the combined EPS and SMP production ASM3-based model (CES-ASM3) described in Chapter 4 and developed by the author of this thesis as their activated sludge model (ASM) of choice. The membrane fouling model was borrowed from Li and Wang [147] similarly to the integrated MBR models outlined previously. The model was used to evaluate different membrane fouling control strategies, such as coarse bubble aeration intensity during membrane filtration and idle-cleaning. Energy consumption was evaluated with the same equations as used in Copp [36], Maere et al. [160]. Coarse bubble aeration and idle cleaning time were identified as the main parameters influencing membrane fouling. The model suffers from the same limitation as the previously outlined integrated models due to the fact that no links have been provided between the irreversible fouling and the bulk liquid SMP concentration.

As demonstrated above, research in the area of integrated MBR modelling is beginning to pick up speed and more original research papers in the topic are being published in the top peer-reviewed journals. At the same time we have recently seen quite a few review papers in the subject. Fenu et al. [57] wrote a comprehensive review of ASM based modelling of MBR reactors focussed on MBR-specific modelling issues whilst the review papers of Zuthi et al. [274], Naessens et al. [173; 174] were concentrated on integration of biological and filtration models.

Although this is not strictly an example of an integrated MBR model, Maere et al. [160] developed a MBR benchmark simulation model (BSM-MBR) for an immersed

membrane bioreactor (iMBR) in which the activated sludge process is described with ASM1. Pressure drop across the membrane was not modelled at all whilst retentive properties of the membrane were represented with a single-point ideal clarifier which assumes 100% retention of particulate components, no retention of soluble components and no temporal or spatial dynamics. According to Maere et al. [160] BSM-MBR is intended to serve as a tool for the evaluation of operational and control strategies in MBR-based plants in terms of effluent quality and operational costs [160]. It was developed on the basis of COST/IWA benchmark simulation model no.1 (BSM1) [36] and hence uses the same inputs and the same ASM1 biological model. Although the idea of developing a simulation model for benchmarking control and operational strategies at MBR-based WWTPs is very good, BSM-MBR lacks some of the crucial components required for an adequate representation of a MBR plant. These are: a biological model capable of predicting the concentrations of the main membrane foulants, a membrane fouling model, and an interface model linking the biological and the physical parts of the system. Author of this thesis postulates that only an integrated MBR model can guarantee that the effects of the changes in the operational and control strategies on the effluent quality and the operational costs are realistically evaluated, although it is understood that the task of developing such a model is not trivial. Nevertheless, development of such an integrated model was attempted in this thesis and is described in the following sections of this chapter.

8.1.2 Overview of the the developed IBMF-MBR model

As already mentioned in Section 7.3 of Chapter 7 the integrated bioreactor and membrane fouling MBR model (IBMF-MBR) developed here is based on the same plant layout as implemented in the BSM-MBR model of Maere et al. [160] - see Figure 7.5 on page 223. Whilst the plant layout in Figure 7.5 shows the configuration of tanks and flow streams, it does not explain any functional relationships that exist between the bioreactor and the membrane. These relationships are therefore presented separately in Figure 8.1 and are explained below.

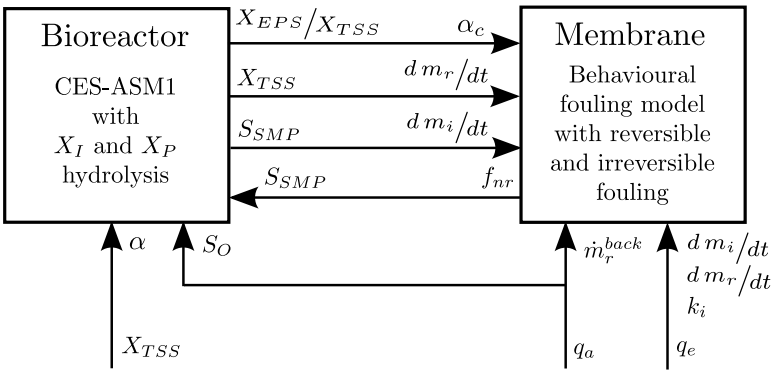

Figure 8.1: Graphical representation of the links existing between the biological and the filtration part of the IBMF-MBR model.

The bioreactor is modelled with the combined EPS and SMP production ASM1-based model (CES-ASM1) developed in Section 4.3.1 of Chapter 4 while the membrane is described with the behavioural fouling model developed in Section 6.2 of Chapter 6. The rationale behind selecting CES-ASM1 over CES-ASM3 is explained in Section 7.1 of Chapter 7. The choice was made on the grounds of similarity of CES-ASM1 model structure to ASM1 used in the BSM1 and BSM-MBR simulation benchmarks, hence easier comparison to BSM1 and BSM-MBR results and easier adaptation of the BSM1 input signals (influent wastewater concentrations) in the new model. The behavioural fouling model was chosen over the more complicated three-mechanism fouling model for its simplicity and its ease of calibration.

CES-ASM1 was initially extended with slow X_I and X_P hydrolysis mechanisms described in Section 4.2 in an attempt to eliminate overestimation of sludge yields characteristic of ASM1 when applied to modelling high sludge retention time (SRT) systems [227]. However, introduction of SMP and EPS kinetics changed the flow of organic substances and altered the death-regeneration mechanism in the base ASM1 model resulting in lower predicted sludge yields compared to the original ASM1 model. Although the added biopolymer kinetics were found to have little effect on predictions of sludge production at intermediate sludge ages, as discussed in Chapter 3, sludge yields predicted by CES-ASM1 in the benchmark MBR model are found to be about 0.13 kgSS $kg^{-1}BOD_5$ lower from the ones predicted by ASM1. Whist BSM-MBR calculates an observed steady-state sludge yield of ~ 0.70 kgSS $kg^{-1}BOD_5$ under dry-weather conditions, the sludge yield predicted by CES-ASM1 is ~ 0.57 kgSS $kg^{-1}BOD_5$. Since the predicted sludge production in IBMF-MBR is already lower compared to the previous benchmark model, kinetics of X_I and X_P hydrolysis have been set to zero.

EPS fraction in activated sludge $\left(\frac{X_{EPS}}{X_{TSS}}\right)$ determines the value of the specific cake resistance α_c according to the model of Ahmed et al. [1] presented in Figure 7.17 on page 249. Total solids concentration X_{TSS} affects the amount of reversible fouling $\frac{dm_r}{dt}$ whilst SMP in the bulk liquid affects the rate of irreversible fouling $\frac{dm_i}{dt}$. SMP concentration in the bioreactor (S_{SMP}) depends not only on the biopolymer kinetics in the activated sludge but also on the retentive properties of the membrane. SMP retention on the membrane is modelled with parameter f_{nr} which denotes the fraction of non-retained SMP, i.e. the fraction of SMP which ends up in the permeate. The lower the value of this parameter the higher the amount of SMP retained by the membrane and hence, bulk liquid SMP concentration.

The rate of cake back-transport from the membrane is in a functional relationship with coarse-bubble aeration rate q_a. Air bubbles create shear stresses τ_w on the membrane surface causing detachment and removal of solid particles deposited on the membrane. The relationship between q_a and τ_w is described with Equation 7.76 shown on page 243. The shear stresses are linked to the cake detachment constant $k_r = k_{r,N}$ in accordance to the model of Nagaoka et al. [176] described with Equation 5.71 presented on page 173. The cake detachment constant then appears in the model of cake mass balance on the membrane surface described with Equation 5.72. Moreover, coarse

bubble aeration leads to an increase in oxygen concentration (S_O) in the membrane tank as a result of the mass transfer of oxygen from the air bubbles to the bulk liquid. The oxygen mass transfer coefficient α is hindered by the presence of suspended solids X_{TSS} accordingly to Equation 7.31 shown on page 229. The rates of reversible $\frac{dm_r}{dt}$ and irreversible $\frac{dm_i}{dt}$ fouling are linked to the permeate flux as shown in Equations 6.6 and 6.7 respectively. Whilst $\frac{dm_r}{dt} \propto q_e$, $\frac{dm_i}{dt}$ is in a non-linear relationship with q_e due to the fact that the proportionality constant k_i in Equation 6.7 is itself dependent on permeate flux J and hence the permeate flow rate (q_e).

The membrane is assumed to be 'backflushable' hence operation of the membrane is assumed to be composed of filtration and backflush cycles, whilst idle/relaxation cycles are not modelled.

8.2 Piping and instrumentation diagram

The piping and instrumentation diagram (P&ID) of the IBMF-MBR simulation benchmark scheme is shown in Figure 8.2. Air supply to the first aerobic tank $V_{ox,1}$, second

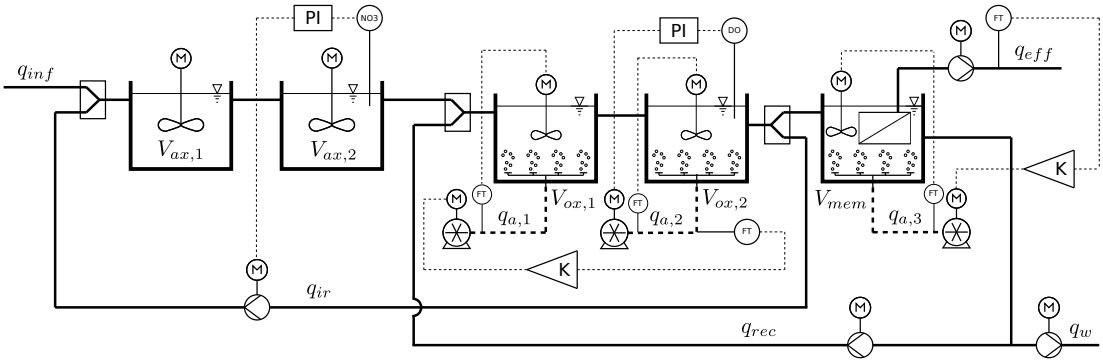

Figure 8.2: Process and instrumentation diagram of the IBMF-MBR simulation benchmark scheme.

aerobic tank $V_{ox,2}$ and membrane tank V_{mem} is facilitated by three separate air blowers. Whilst the anoxic tanks ($V_{ax,1}$ and $V_{ax,2}$) are constantly mixed with energy inputs of 0.008 kW m^{-3} both aerobic tanks and the membrane tank are only mixed if aeration rate to the tank corresponds to less than 2.2 Nm^3 h^{-1} per m^2 of ground surface area.

IBMF-MBR is simulated in the same fashion as BSM-MBR, i.e. first under constant flow-averaged inputs for a period of 300 days in order to reach a steady-state condition, then under time-varying inputs and three 14-day long weather scenarios: dry weather, rain event, and storm event. Each simulation sequence, i.e. steady-state→dry weather→dry weather, steady-state→dry weather→rain event, and steady-state→dry weather→storm event is performed under 4 levels of process control: (a) open-loop, (b) closed-loop with dissolved oxygen (DO) control, (c) closed-loop with DO and nitrate nitrogen (NO_3^--N) control, and (d) closed-loop with DO, NO_3^--N and specific aeration demand per membrane area (SAD_m) control.

Under all of the process control variants listed above the return activated sludge

flow q_{rec} is assigned a constant value of 55,338 m^3 d^{-1} which is equal to 3 times the rate of dry weather flow (DWF). Sludge wastage rate q_w is assigned a constant value of 160 m^3 d^{-1} which guarantees a steady-state mixed liquor suspended solids (MLSS) concentration in the membrane tank of $\sim$ 10 kg m^{-3}. The sludge wastage rate q_w in IBMF-MBR is lower from the 200 m^3 d^{-1} setpoint assigned in BSM-MBR due to alteration of the flow of organic substrates in CES-ASM1 compared to ASM1 caused by introduction of biopolymer kinetics. This resulted in $\sim$ 18.5% lower predicted sludge yields in CES-ASM1 compared to ASM1.

In open-loop simulations, internal recirculation q_{ir} is kept at a constant rate of 55,338 m^3 d^{-1}, i.e. at the same value as the sludge recirculation rate q_{rec}. Fine-bubble aeration flow rates $q_{a,1}$ and $q_{a,2}$ are maintained at 3,440 Nm^3 d^{-1} and 3360 Nm^3 d^{-1} respectively. Total fine bubble aeration flow rate is thus equal to 6,800 Nm^3 d^{-1}, which is 300 Nm^3 d^{-1} higher than in the BSM-MBR benchmark model. Although the difference in total airflow is minimal the flow split between both aeration tanks is quite different. Whilst the airflow in BSM-MBR was split between $V_{ox,1}$ and $V_{ox,2}$ at the ratio of 1.89 : 1, the flow split in CES-ASM1 is near 1 : 1 in the open-loop simulations and has been assigned a more uniform value of 1.3 : 1 in closed-loop simulations with DO control. Coarse-bubble aeration flow rate $q_{a,3}$ is kept at 20,025 Nm^3 d^{-1} which corresponds to SAD_m of 0.3 Nm^3 h^{-1} m^{-2} on total membrane area A_{mem} of 66,750 m^2. The membrane area is slightly lower from 71,500 m^2 adopted in Maere et al. [160] due to reduction of the membrane tank volume from 1,500 m^3 to 1,300 m^3.

In the closed-loop simulation scenario with DO control, oxygen concentration S_O in the second aerobic tank is maintained at 1.5 mgO_2 L^{-1} via a PI controller set to adjust the air flow rate to the second aerobic tank ($q_{a,2}$) based on the signal received from the DO probe. The air flow rate to the first aerobic tank $q_{a,1}$ is adjusted proportionally to $q_{a,2}$ at 1.3 : 1 ratio. The proportional integral (PI) controller is assigned a proportional gain K_p = 500 Nm^3 h^{-1} per mgO_2 L^{-1} and integral time t_I = 0.002 d, i.e. the same values as in the BSM-MBR benchmark model of Maere et al. [160].

In the closed-loop simulation scenario with DO and nitrate control, in addition to aeration control, denitrification is controlled via a PI controller which receives the NO_3^--N concentration signal from the nitrate probe located in the second anoxic tank and manipulates the internal recirculation rate q_{ir} in order to maintain the concentration of nitrates in the second anoxic tank at 1.0 $mgNO_3^-$ L^{-1}. The PI controller is assigned a proportional gain of $K_p = 15,000$ m^3 d^{-1} per $mgNO_3^-$ L^{-1} and an integral time of t_I = 0.05 d. The internal recirculation rate q_{ir} is capped at 92,230 m^3 d^{-1}, i.e. 5×DWF.

In the closed-loop simulation scenario with DO, nitrate, and SAD_m control, coarse-bubble aeration in the membrane tank is additionally controlled in proportion to the permeate flux J in the same fashion as originally introduced in Maere et al. [160]. A proportional (P) controller receives the permeate flow (q_e) signal from the flow transmitter positioned on the discharge side of the permeate suction pump, calculates the value of the permeate flux J and adjusts the SAD_m setpoint in proportion to J. The controller is assigned a proportional gain K_p of 0.015 Nm^3 h^{-1} m^{-2} per Lmh.

SAD_m is capped from the top and the bottom at $SAD_m^{min} = 0.15$ Nm^3 h^{-1} m^{-2} and $SAD_m^{max} = 0.30$ Nm^3 h^{-1} m^{-2} which correspond to permeate fluxes of 10 Lmh and 20 Lmh, respectively.

All the above control strategies, i.e. DO and SAD_m control strategies of Maere et al. [160] and the NO_3^--N control strategy adopted from COST624 [37] are not indicated to be the most adequate strategies for this particular system, but serve the purpose of demonstrating how different control strategies can be compared using benchmark models such as BSM-MBR or IBMF-MBR. The IBMF-MBR benchmark model developed here adopts the same control strategies as BSM-MBR in order to demonstrate the similarities and the differences between both models under different operating conditions.

All control loops assume that the actuators and the sensors are ideal, i.e. without any noise and delay. As a word of notice, the purpose of the P&ID diagram presented in Figure 8.2 is solely for visualisation of control loops implemented in the simulations. Hence, no effort was made to produce realistic piping and instrumentation, especially with regards to placement of isolation valves and penstocks. In particular, flow routing and flow control on the permeate side of the membrane required for implementation of backwash cycles and periodic cleaning in place (CiP) procedures has not been shown.

8.3 Model inputs

The input files used in BSM1 and BSM-MBR simulation benchmarks had to be modified to take into account three new variables introduced in CES-ASM1, i.e. X_{EPS}, S_{UAP}, and S_{BAP}. It is assumed that influent wastewater does not contain any utilisation associated products (UAP), hence $S_{UAP} = 0$, whilst concentration of biomass associated products (BAP) is assumed to be equal to 70% of the influent soluble inert substrates S_I in BSM1 and BSM-MBR. X_{EPS} is assumed to constitute 5% of the biomass, i.e. the sum of X_H and X_A, in the original BSM1 input files. EPS and BAP are assumed to contain 6% of nitrogen (N) whilst UAP is assumed to be composed only of organic matter. Calculation of new state variables and recalculation of old state variables, i.e. X_H, X_A, S_I and X_{ND} in order to maintain the same carbon (C) and N loads to the plant were carried out using Equations 8.1-8.7 listed below.

$$X_{EPS}^{CES-ASM1} = f_{EPS}\,(X_H + X_A) \tag{8.1}$$

$$S_{BAP}^{CES-ASM1} = f_{SMP}\,S_I \tag{8.2}$$

$$S_{UAP}^{CES-ASM1} = 0 \tag{8.3}$$

$$X_H^{CES-ASM1} = (1 - f_{EPS})\;X_H \tag{8.4}$$

$$X_A^{CES-ASM1} = (1 - f_{EPS})\;X_A \tag{8.5}$$

$$S_I^{CES-ASM1} = (1 - f_{SMP})\;S_I \tag{8.6}$$

$$X_{ND}^{CES-ASM1} = X_{ND} + f_{EPS}\;(X_H + X_A)\,(i_{XB} + i_{XEPS}) - i_{XBAP}\,f_{SMP}\,S_I \tag{8.7}$$

In the equations above, f_{EPS} denotes the fraction of biomass which becomes EPS in the BSM-MBR model. f_{SMP} denotes the fraction of S_I in BSM1 model which becomes S_{BAP} in the BSM-MBR model. i_{XB} denotes the N content of the biomass whereas i_{XEPS} and i_{XBAP} represent the N content in EPS and BAP respectively. All of the above influent stoichiometric parameters are assigned the following values: $f_{EPS} = 0.05$, $f_{SMP} = 0.7$, $i_{XB} = 0.086$, $i_{XEPS} = 0.06$, $i_{XBAP} = 0.06$.

8.3.1 Flow averaged influent concentrations

The flow proportionally averaged influent concentrations for the ASM1-based benchmark simulation models are shown in Table 8.1 whilst the modified flow proportionally averaged influent composition in IBMF-MBR taking into account the bound and soluble polymer concentrations is presented in Table 8.2. Both tables cover all three weather scenarios and additionally include the average, minimum, and maximum flow rates measured during each weather scenario.

Table 8.1: Flow proportionally averaged influent composition for the ASM1-based benchmark simulation models, BSM1 and BSM-MBR.

Compound	Unit	Dry weather	Rain weather	Storm weather
S_I	gCOD m^{-3}	30.00	25.96	28.03
S_S	gCOD m^{-3}	69.50	60.13	64.93
X_I	gCOD m^{-3}	51.20	44.30	51.92
X_S	gCOD m^{-3}	202.32	175.05	193.32
X_H	gCOD m^{-3}	28.17	24.37	27.25
X_A	gCOD m^{-3}	0.00	0.00	0.00
X_P	gCOD m^{-3}	0.00	0.00	0.00
S_O	gO_2 m^{-3}	0.00	0.00	0.00
S_{NO}	gN m^{-3}	0.00	0.00	0.00
S_{NH}	gN m^{-3}	31.56	27.30	29.48
S_{ND}	gN m^{-3}	6.95	6.01	6.49
X_{ND}	gN m^{-3}	10.59	9.16	10.24
S_{ALK}	molHCO_3^- m^{-3}	7.00	7.00	7.00
q_{ave}	m^3 d^{-1}	18446.33	21319.75	19744.72
q_{min}	m^3 d^{-1}	10000.00	10000.00	10000.00
q_{max}	m^3 d^{-1}	32180.00	52126.00	60000.00

8.3.2 Influent composite variables under time-varying conditions

Influent flows, CODs, and total Kjeldahl nitrogen (TKN), and total suspended solids (TSS) concentrations in dry-, rain- and storm-weather are plotted in Figure 8.3 and Figure 8.4. Both figures show that the main composite variables in the IBMF-MBR model exactly match the influent composite variables in BSM1 and BSM-MBR, hence all three models have the same organic, nitrogen and suspended solids loadings and thus, their outputs can be quantitatively compared.

All three weather scenarios exhibit a diurnal flow and load pattern relating to changes in human activity over the course of the day. In the dry-weather scenario hydraulic organic and solids loading to the plant are lower on Saturday and Sunday

Table 8.2: Flow proportionally averaged influent composition for the IBMF-MBR benchmark simulation model.

Compound	Unit	Dry weather	Rain weather	Storm weather
S_I	gCOD m^{-3}	9.00	7.78	8.41
S_S	gCOD m^{-3}	69.50	60.13	64.93
X_I	gCOD m^{-3}	51.20	44.30	51.92
X_S	gCOD m^{-3}	202.32	175.05	193.32
X_H	gCOD m^{-3}	26.76	23.15	25.89
X_A	gCOD m^{-3}	0.00	0.00	0.00
X_{EPS}	gCOD m^{-3}	1.41	1.22	1.36
S_{UAP}	gCOD m^{-3}	0.00	0.00	0.00
S_{BAP}	gCOD m^{-3}	21.00	18.17	19.62
X_P	gCOD m^{-3}	0.00	0.00	0.00
S_O	gO_2 m^{-3}	0.00	0.00	0.00
S_{NO}	gN m^{-3}	0.00	0.00	0.00
S_{NH}	gN m^{-3}	31.56	27.30	29.48
S_{ND}	gN m^{-3}	6.95	6.01	6.49
X_{ND}	gN m^{-3}	9.37	8.10	9.10
S_{ALK}	molHCO_3^- m^{-3}	7.00	7.00	7.00
q_{ave}	m^3 d^{-1}	18446.33	21319.75	19744.72
q_{min}	m^3 d^{-1}	10000.00	10000.00	10000.00
q_{max}	m^3 d^{-1}	32180.00	52126.00	60000.00

compared to the rest of the week whilst TKN loading remains constant over the whole week.

In the rain weather scenario the instantaneous influent flow rate increases around 2.2 times compared to dry weather flow (DWF) for a period of about 1.5 days then decreases over the course of the next day returning back to the dry weather diurnal flow pattern until the end of day 14. Although this is not an entirely valid assumption, it is postulated that rainwater does not contain any contamination and has a diluting effect on all influent concentrations, leading to a decrease in COD, TKN and TSS loading rates.

The storm weather scenario features two large storms - the first short-duration storm which occurs on the 8^{th} day and the second, longer-duration one, occurring 2 days after the end of the first storm. It is assumed that the first storm causes resuspension of solid deposits in the sewer network leading to an increase in the influent suspended solids concentrations and particulate COD. Once the sewer system has been flushed by the first storm and the sewer deposits have been removed, the second storm has a similar effect to rain, i.e. leads to dilution of TKN and TSS concentrations and COD levels.

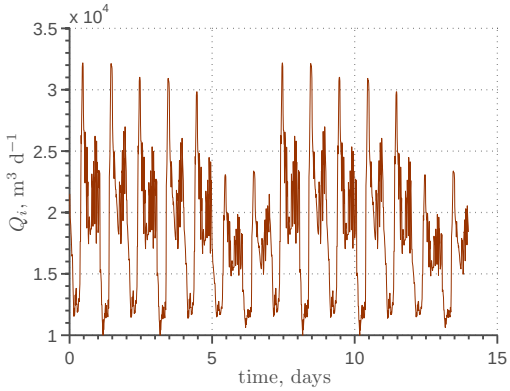

(a) Influent flow rate in dry weather.

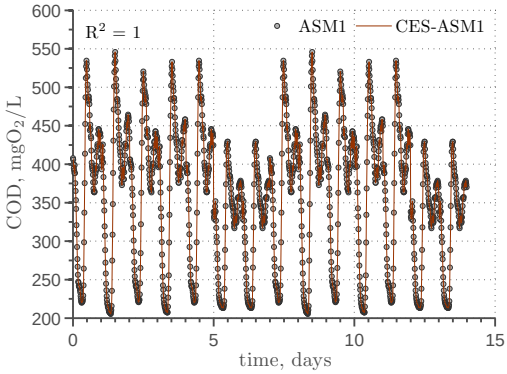

(b) Influent COD in dry weather.

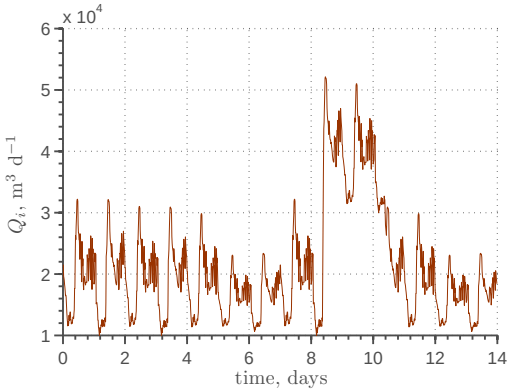

(c) Influent flow rate during rain event.

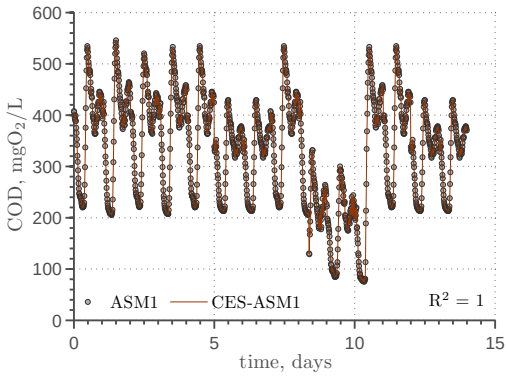

(d) Influent COD during rain event.

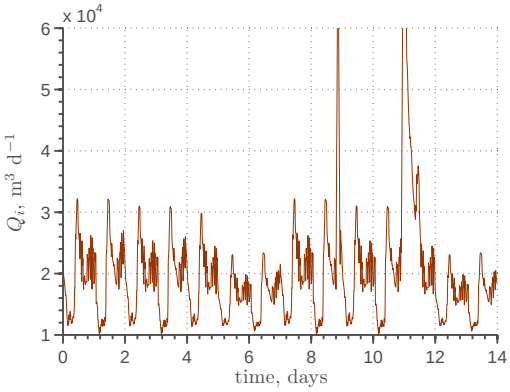

(e) Influent flow rate during storm event.

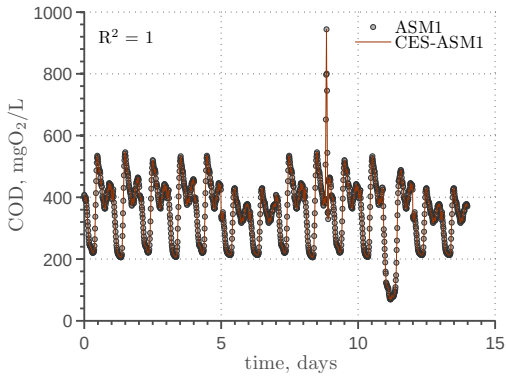

(f) Influent COD during storm event.

Figure 8.3: Influent flow rates (a),(c),(e) and COD levels (b),(d),(f) under dry weather, rain, and storm events.

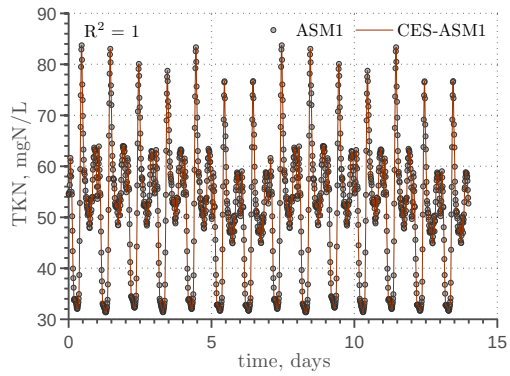

(a) Influent TKN in dry weather.

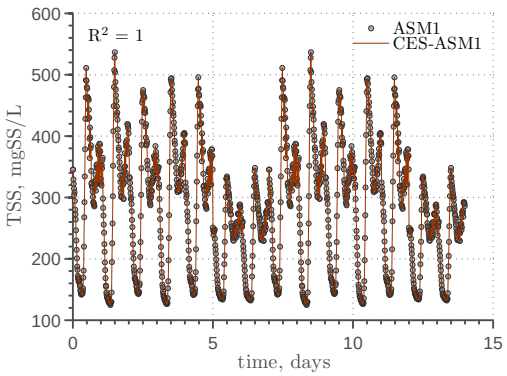

(b) Influent TSS in dry weather.

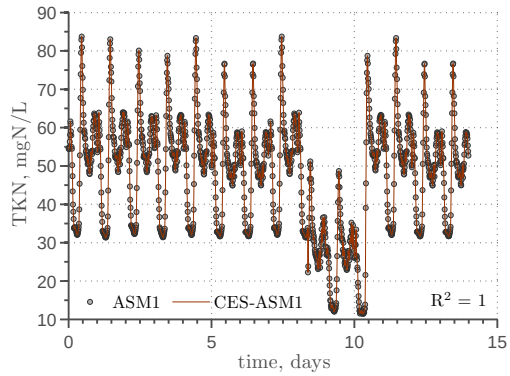

(c) Influent TKN during rain event.

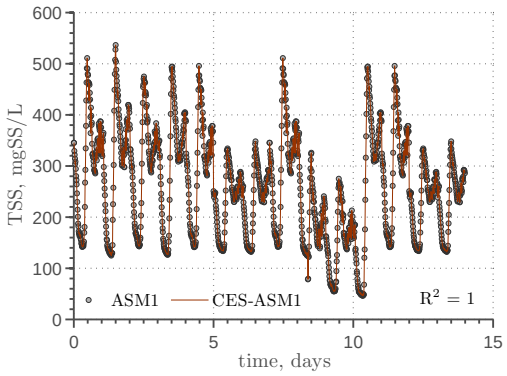

(d) Influent TSS during rain event.

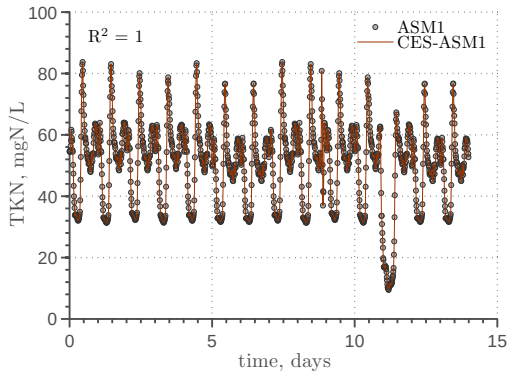

(e) Influent TKN during storm event.

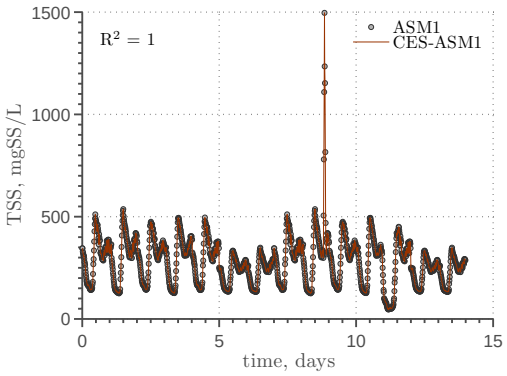

(f) Influent TSS during storm event.

Figure 8.4: Influent TKN (a),(c),(e) and TSS (b),(d),(f) concentrations under dry weather, rain, and storm events.

8.4 Model parameters

Parameters of the aeration model were listed in Table 7.1 on page 228. Recirculation, sludge wastage and airflow rates in open-loop simulations and controller setpoints and gains in closed-loop scenarios are listed in Section 8.2. Individual reactor volumes are given in Section 7.3 on page 222. Parameters of the pumping cost equations are given in Table 7.4. Default parameter values of the CES-ASM1 biological model listed in Table 4.7 on page 103 were adopted in this study except 3 biopolymer kinetic and stoichiometric parameters listed below.

The fraction of X_{EPS} produced from heterotrophic growth ($f_{EPS,h}$) and decay ($f_{EPS,dh}$) were decreased, respectively from 0.18 to 0.1 gX_{EPS} g^{-1} X_H and 0.045 to 0.025 gX_{EPS} g^{-1} X_H to reduce the production of EPS in the model in order to bring the bulk liquid EPS concentrations closer to the values reported in Ahmed et al. [1]. The maximum specific heterotrophic growth rate on S_{BAP} (μ_{BAP}) was increased from 0.05 d^{-1} to 0.15 d^{-1} to reduce the dominance of BAP production over UAP production in the bioreator.

Simulations with IBMF-MBR are performed at the same temperatures as used in BSM-MBR, i.e. at wastewater temperature T of 15°C and air temperature T_{air} of 20°C.

The membrane module in the membrane tank is modelled with a hollow fibre module geometry of Busch et al. [19] described in Section 7.5.4. The geometric parameters of the module are listed in Table 7.2 on page 243. Outer diameter of the HF fibre $d_{f,o}$ is equal to 2.5 mm, distance between neighbouring fibres l_f equals 1 cm and membrane module height is equal $h = 1.8$ m. The module is assumed to cover 100% of the tank's floor plan area. The resulting membrane packing density is equal to 49.4 m^2 m^{-3} which is slightly higher from the packing density of 46.2 m^2 m^{-3} used in Maere et al. [160].

The membrane is operated in the cycle of 10 minute-long filtration followed by 1 minute-long backwash. The module is aerated during filtration whilst aeration is switched off during the backwash periods. Other membrane and fouling-specific parameters of the membrane filtration model used in the simulations are listed in Table 8.3.

Table 8.3: Parameters of the membrane filtration and fouling model applied in the IBMF-MBR model.

Symbol	Value	Unit	Description	Equation
R_m	3.0×10^{12}	m^{-1}	Clean membrane resistance	
ΔP_{crit}	30	kPa	Threshold pressure below which no cake compression occurs	6.11
n_α	0.25	–	Dimensionless cake compressibility factor	6.11
b	6.8×10^{-2}	–	Dimensionless proportionality coefficient	6.12
k_i	1.0×10^{11}	m kg^{-1}	Irreversible fouling strength factor	6.5
γ_m	1500	d^{-1} Pa^{-1}	Proportionality constant	5.72
λ_m	2.0×10^{-6}	–	Static friction coefficient	5.72

8.5 Steady-state simulation results

Results of the simulations at the steady state conditions with open-loop configuration and closed-loop configuration with DO, NO_3^--N and SAD_m control are listed in Table 8.4 and Table 8.5 respectively.

Table 8.4: Steady state open-loop IBMF-MBR results for all reactor zones and the membrane permeate and retentate stream.

	Inf	R.1	R.2	R.3	R.4	R.5	Perm	Ret
S_I	9.00	9.00	9.00	9.00	9.00	9.00	9.00	9.00
S_S	69.50	4.53	4.24	2.91	2.51	1.90	1.90	1.90
X_I	51.20	3342.24	3342.24	4439.27	4439.27	5901.99	0.00	5901.99
X_S	202.32	64.46	60.04	34.81	27.33	24.32	0.00	24.32
X_H	26.76	1298.25	1292.43	1716.50	1716.94	2277.89	0.00	2277.89
X_A	0.00	119.73	119.29	159.87	160.18	212.86	0.00	212.86
X_{EPS}	1.41	550.59	550.32	732.31	732.56	974.03	0.00	974.03
S_{UAP}	0.00	10.31	11.10	11.65	11.59	11.97	5.99	11.97
S_{BAP}	21.00	25.81	26.54	27.64	27.29	29.92	14.96	29.92
X_P	0.00	2161.24	2162.84	2878.66	2879.53	3831.03	0.00	3831.03
S_O	0.00	0.01	0.00	1.34	1.81	7.08	7.08	7.08
S_{NO}	0.00	3.44	0.60	8.37	10.487	12.43	12.43	12.43
S_{NH}	31.56	9.50	10.23	3.18	1.248	0.23	0.23	0.23
S_{ND}	6.95	1.15	0.77	0.98	0.990	0.88	0.88	0.88
X_{ND}	9.37	4.04	4.13	2.63	2.157	2.05	0.00	2.05
S_{ALK}	7.00	5.18	5.43	4.38	4.086	3.87	3.87	3.87
TSS	211.27	5652.38	5645.37	7471.06	7466.85	9916.58	0.000	9916.58
Q	18446.33	73784.33	73784.33	129122.33	129122.33	129122.33	18286.33	55498.00

The values listed in individual columns in Tables 8.4 and 8.5 denote, respectively, the final concentrations of state variables and TSS, and flow rate in the influent stream (Inf), each of the five reactor zones (R1, R2, R3, R4, and R5), permeate stream (Perm) and retentante stream (Ret). Reactors R1 and R2 refer to the first two anoxic zones, R3 and R4 refer to aerobic zones, and R5 denotes the (aerobic) membrane tank.

Under both modes of operation the plant achieves similar effluent quality but, as will be show in the next sections, at different costs. SMP concentration in the membrane tank is found to be around 42 mgCOD L^{-1} while the EPS/MLSS ratio is equal to ∼98.2mgCOD g^{-1} TSS. The plant produces a relatively low steady state nitrate concentration S_{NO} of about 12 mgN L^{-1} and a very low ammoniacal N concentration of ∼0.25 mgN L^{-1}.

It is important to emphasise that the biomass is not uniformly distributed in the bioreactor but exhibits an upward gradient with lower MLSS concentrations of around 6 kgSS m^{-3} in the anoxic tanks and higher MLSS concentrations in the aerobic tanks and the membrane tank of, respectively 7.5 kgSS m^{-3} and 10 kgSS m^{-3}. As a result, despite of the volumetric anoxic fraction being very large compared to the anoxic fractions characteristic of conventional activated sludge processs (CASPs) and equal to $V_{ax}/V_{tot} = 0.50$, the anoxic mass fraction is significantly lower and equals $M_{ax}/M_{tot} = 0.124$. Hence, it seems, that although replacement of a final settlement tank (FST) with the membrane allows to reduce the aerobic reactor volume, the ben-

efits of membrane technology with regards to denitrification and, similarly, biological phosphorus removal in pre-denitrification systems are less clear.

Table 8.5: Steady state closed-loop IBMF-MBR results with DO, SAD_m and NO_3^--N control for all reactor zones and the membrane permeate and retentate stream.

	Inf	R.1	R.2	R.3	R.4	R.5	Perm	Ret
S_I	9.00	9.00	9.00	9.00	9.00	9.00	9.00	9.00
S_S	69.50	4.35	3.34	2.90	2.55	1.94	1.94	1.9
X_I	51.20	3466.97	3466.97	4439.76	4439.76	5902.64	0.00	5902.64
X_S	202.32	61.27	58.01	35.09	28.01	24.78	0.00	24.78
X_{BH}	26.76	1329.57	1324.45	1696.30	1696.77	2251.41	0.00	2251.41
X_{BA}	0.00	122.84	122.44	158.02	158.30	210.37	0.00	210.37
X_{EPS}	1.41	565.27	565.04	724.74	724.98	963.97	0.00	963.97
S_{UAP}	0.00	10.22	10.71	11.35	11.35	11.83	5.91	11.83
S_{BAP}	21.00	25.61	26.08	27.11	26.82	29.46	14.73	29.46
X_P	0.00	2248.04	2249.49	2885.59	2886.39	3840.12	0.000	3840.12
S_O	0.00	0.01	0.00	1.69	1.50	4.49	4.49	4.49
S_{NO}	0.00	3.661	1.000	7.900	9.77	11.670	11.670	11.67
S_{NH}	31.56	8.616	9.258	3.018	1.29	0.240	0.240	0.24
S_{ND}	6.95	1.129	0.762	0.985	1.00	0.889	0.889	0.89
X_{ND}	9.37	3.886	4.008	2.648	2.20	2.081	0.000	2.08
S_{ALK}	7.00	5.100	5.336	4.397	4.14	3.930	3.930	3.93
TSS	211.27	5845.47	5839.80	7454.62	7450.66	9894.97	0.00	9894.97
Q	18446.33	83217.50	83217.50	138555.50	138555.50	129122.33	18286.33	55498.00

Table 8.6: Comparison of effluent concentrations from steady state simulations with IBMF-MBR and BSM-MBR.

Output	Unit	BSM-MBR		IBMF-MBR	
		Open-loop	Closed-loop*)	Open-loop	Closed-loop*)
S_I	gCOD m^{-3}	30.00	30.00	9.00	9.00
S_S	gCOD m^{-3}	0.68	0.69	1.90	1.94
X_I	gCOD m^{-3}	0.00	0.00	0.00	0.00
X_S	gCOD m^{-3}	0.00	0.00	0.00	0.00
X_H	gCOD m^{-3}	0.00	0.00	0.00	0.00
X_A	gCOD m^{-3}	0.00	0.00	0.00	0.00
X_{EPS}	gCOD m^{-3}	–	–	0.00	0.00
S_{UAP}	gCOD m^{-3}	–	–	5.99	5.91
S_{BAP}	gCOD m^{-3}	–	–	14.96	14.73
X_P	gCOD m^{-3}	0.00	0.00	0.00	0.00
S_O	gO_2 m^{-3}	7.69	5.19	7.08	4.49
S_{NO}	gN m^{-3}	12.03	11.71	12.43	11.67
S_{NH}	gN m^{-3}	0.076	0.080	0.23	0.24
S_{ND}	gN m^{-3}	0.59	0.59	0.88	0.89
X_{ND}	gN m^{-3}	0.00	0.00	0.00	0.00
S_{ALK}	molHCO_3^- m^{-3}	3.89	3.92	3.87	3.93

*) DO, NO_3^--N, and SAD_m control

Effluent concentrations produced from IBMF-MBR are compared in Table 8.6 with the outputs of the BSM-MBR simulation benchmark of Maere et al. [160]. The results show that the outputs of both models are very similar with minor differences in S_S, S_{NO} and S_{NH} concentrations.

8.6 Dynamic simulation results

Dynamic simulations were performed with BSM-MBR and IBMF-MBR models in dry-, rain- and storm-weather under four levels of process control: open-loop (a), closed-loop with DO control (b), closed-loop with DO and NO_3^--N control (c), and closed-loop with DO, NO_3^--N and SAD_m control (d).The results obtained in each of the 9 resulting simulation scenarios were assessed with regards to effluent quality, cost performance and process variables. Each weather scenario is defined by a 14-day long sequence of influent flow and state variables, although the first 7 days of data is common in all three scenarios whilst the last 7 days define the dry-weather diurnal pattern, the rain event and the storm event. Hence, the results are evaluated in each scenario for the last 7 days of the simulation.

8.6.1 Effluent concentrations

The flow-proportionally averaged effluent results of the open-loop and closed loop simulations under all three weather scenarios are listed, respectively in Table 8.7 and Table 8.8. As in case of steady-state simulation results, closed loop dynamic simulation refers to the simulation variant with the maximum level of process control, i.e. DO, SAD_m and NO_3^--N control.

Table 8.7: Flow proportionally averaged effluent results from dynamic open-loop simulations with BSM-MBR and IBMF-MBR in dry-, rain- and storm-weather.

Variable	Unit	BSM-MBR			IBMF-MBR		
		Dry	Rain	Storm	Dry	Rain	Storm
Effluent state variables							
S_I	gCOD m^{-3}	30.00	22.86	26.30	9.00	6.86	7.89
S_S	gCOD m^{-3}	0.73	0.75	0.76	1.96	1.97	2.02
X_I	gCOD m^{-3}	0.00	0.00	0.00	0.00	0.00	0.00
X_S	gCOD m^{-3}	0.00	0.00	0.00	0.00	0.00	0.00
X_H	gCOD m^{-3}	0.00	0.00	0.00	0.00	0.00	0.00
X_A	gCOD m^{-3}	0.00	0.00	0.00	0.00	0.00	0.00
X_{EPS}	gCOD m^{-3}	–	–	–	0.00	0.00	0.00
S_{UAP}	gCOD m^{-3}	–	–	–	6.20	6.05	6.30
S_{BAP}	gCOD m^{-3}	–	–	–	15.26	13.68	14.63
X_P	gCOD m^{-3}	0.00	0.00	0.00	0.00	0.00	0.00
S_O	gO_2 m^{-3}	6.97	6.32	6.27	5.96	5.35	5.23
S_{NO}	gN m^{-3}	12.21	10.76	11.26	12.74	11.14	11.63
S_{NH}	gN m^{-3}	0.15	0.15	0.17	0.45	0.44	0.54
S_{ND}	gN m^{-3}	0.61	0.62	0.64	0.89	0.89	0.90
X_{ND}	gN m^{-3}	0.00	0.00	0.00	0.00	0.00	0.00
S_{ALK}	molHCO_3^- m^{-3}	3.88	4.52	4.23	3.87	4.52	4.23
Effluent composite variables							
TSS	g m^{-3}	0.00	0.00	0.00	0.00	0.00	0.00
TKN	gN m^{-3}	0.76	0.78	0.81	2.25	2.15	2.31
TN	gN m^{-3}	12.98	11.54	12.07	14.99	13.29	13.94
COD	gO_2 m^{-3}	30.73	23.61	27.06	32.43	28.55	30.84
BOD_5	gO_2 m^{-3}	0.18	0.19	0.19	0.49	0.49	0.50

Results presented in Table 8.7 and Table 8.8 show that IBMF-MBR produces, on

Table 8.8: Flow proportionally averaged effluent results from dynamic closed-loop simulations (DO. NO_3^--N and SAD_m control) with BSM-MBR and IBMF-MBR in dry-, rain- and storm-weather.

Variable	Unit	BSM-MBR			IBMF-MBR		
		Dry	Rain	Storm	Dry	Rain	Storm
Effluent state variables							
S_I	gCOD m^{-3}	30.00	22.86	26.30	9.00	6.86	7.89
S_S	gCOD m^{-3}	0.70	0.72	0.73	2.01	2.03	2.07
X_I	gCOD m^{-3}	0.00	0.00	0.00	0.00	0.00	0.00
X_S	gCOD m^{-3}	0.00	0.00	0.00	0.00	0.00	0.00
X_H	gCOD m^{-3}	0.00	0.00	0.00	0.00	0.00	0.00
X_A	gCOD m^{-3}	0.00	0.00	0.00	0.00	0.00	0.00
X_{EPS}	gCOD m^{-3}	–	–	–	0.00	0.00	0.00
S_{UAP}	gCOD m^{-3}	–	–	–	6.07	5.95	6.09
S_{BAP}	gCOD m^{-3}	–	–	–	14.93	13.48	14.14
X_P	gCOD m^{-3}	0.00	0.00	0.00	0.0	0.00	0.00
S_O	gO_2 m^{-3}	5.33	5.65	5.20	3.90	4.29	3.75
S_{NO}	gN m^{-3}	12.19	10.35	11.15	11.89	10.27	10.86
S_{NH}	gN m^{-3}	0.10	0.10	0.10	0.39	0.37	0.40
S_{ND}	gN m^{-3}	0.60	0.61	0.62	0.91	0.91	0.92
X_{ND}	gN m^{-3}	0.00	0.00	0.00	0.00	0.00	0.00
S_{ALK}	molHCO_3^- m^{-3}	3.88	4.24	4.23	3.93	4.58	4.28
Effluent composite variables							
TSS	g m^{-3}	0.00	0.00	0.00	0.00	0.00	0.00
TKN	gN m^{-3}	0.70	0.71	0.72	2.19	2.09	2.17
TN	gN m^{-3}	12.89	11.06	11.87	14.08	12.36	13.03
COD	gO_2 m^{-3}	30.70	23.58	27.03	32.00	28.32	30.20
BOD_5	gO_2 m^{-3}	0.18	0.18	0.18	0.50	0.51	0.52

average, 1 mgN/L higher effluent total nitrogen (TN) concentrations than the ASM1-based BSM-MBR as a result of slightly higher produced effluent nitrate (S_{NO}) and ammoniacal nitrogen (NH_4^+-N) (S_{NH}) levels. Effluent TKN concentrations produced by IBMF-MBR model are again about 1.5 mgN/L higher than those in the BSM-MBR benchmark model as a result of higher NH_4^+-N (S_{NH}) and soluble organic nitrogen (S_{ND}) concentrations. The rest of effluent state and composite variables in both models have similar values except soluble inert organics S_I which are lower in IBMF-MBR due to lower influent S_I concentrations which had been reduced in order to accommodate three new biopolymer state variables.

Due to variations in the influent flow rate as demonstrated in Figures 8.3a, 8.3c and 8.3e, MLSS concentration in the individual sections (tanks) of the bioreactor exhibit often very large fluctuations as the biomass is shifted towards the downstream end of the bioreactor. This behaviour is observed during the periods when the flow of wastewater is large enough that the flux of suspended solids through the bioreactor exceeds the sludge return rate. At these elevated flow periods the sludge is shifted towards the membrane tank as indicated in Figure 8.5. Unfortunately, this increased sludge loading coincides with higher required permeate flow rates causing increased reversible fouling as well as simultaneous irreversible fouling promoted which is promoted by high permeate fluxes.

Dissolved oxygen (DO) concentrations in both aerobic tanks exhibit very high

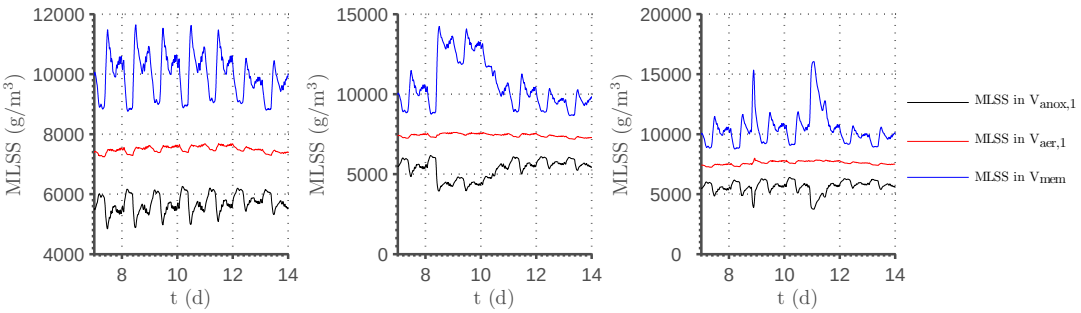

Figure 8.5: MLSS concentrations during (from left to right) dry-, rain- and storm-weather conditions.

fluctuations in open-loop simulations where airflow rates are constant. Once DO control is put into action, DO concentration in the second aerobic tank is kept at an almost steady value of 1.5 mgO_2 L^{-1} while O_2 concentration in the first aerobic tank varies between 1.4 mgO_2 L^{-1} and 2.1 mgO_2 L^{-1}. Introduction of DO control leads to reduction of effluent NH_4^+-N concentrations, although already at a very low levels, but cause an increase in effluent TN, as can be seen when we compare the plant's performance under both simulation variants- see Table 8.9 and Table 8.10. As the system is characterised with large aerobic SRT the rate of nitrification is very high whilst nitrogen removal is limited by denitrification. Under open-loop operation, fluctuations of DO in both aerobic tank were leading to temporary, cyclic development of anoxic conditions inside both aerobic tanks thus increasing the denitrification capacity in the system. Once DO control is turned on both aerobic tank become fully aerobic at all times, hence reducing the denitrification potential of the plant. Although DO control does not offer many advantages in this particular case, the positive effects may be seen in the long run when wastewater temperatures are lower during colder seasons.

DO concentration in the membrane tank fluctuates significantly between nearly 0 mgO_2 L^{-1} to almost its saturation concentration of around 9 mgO_2 L^{-1}. At such high oxygen concentrations, significant amounts of oxygen are being introduced into the anoxic zone with the return stream, what in turn impairs denitrification. Hence, once SAD_m control is introduced and oxygen concentrations in the membrane tank become lower, the effluent TN concentrations and the amount of time at violation decrease compared to the simulation scenario with just DO control as has been demonstrated in Table 8.11.

As already mentioned, effluent NH_4^+-N concentrations are very low at all times during all weather conditions and under all operating scenarios due to high nitrification capacity of the system. At no point in time effluent NH_4^+-N exceeded the effluent NH_4^+-N concentration constraint $S_{NH,max}$ = 4 mgN L^{-1} whilst S_{NH} was below 1 mgN L^{-1} at around $\sim$ 90% of the time.

On the other hand, effluent total nitrogen (TN) concentration is predicted to exceed the effluent TN constraint of 18 mgN L^{-1} at some point of time in each weather scenario and under each level of process control as shown in Figure 8.8 and in the process

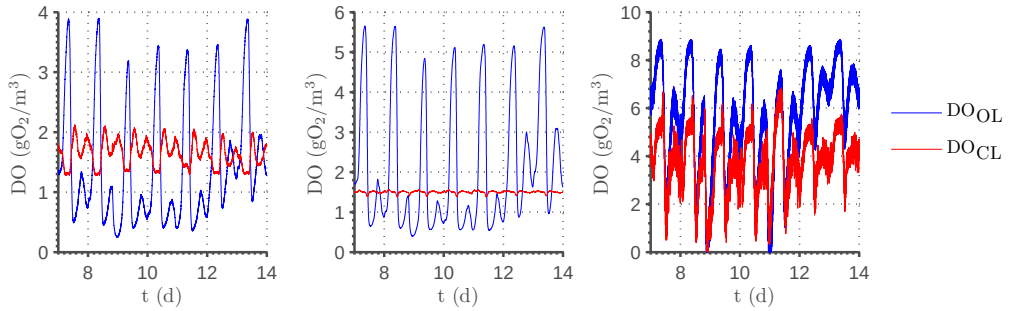

Figure 8.6: DO concentrations during in the (from left to righ) first aerobic tank, second aerobic tank, and membrane tank in dry-weather conditions.

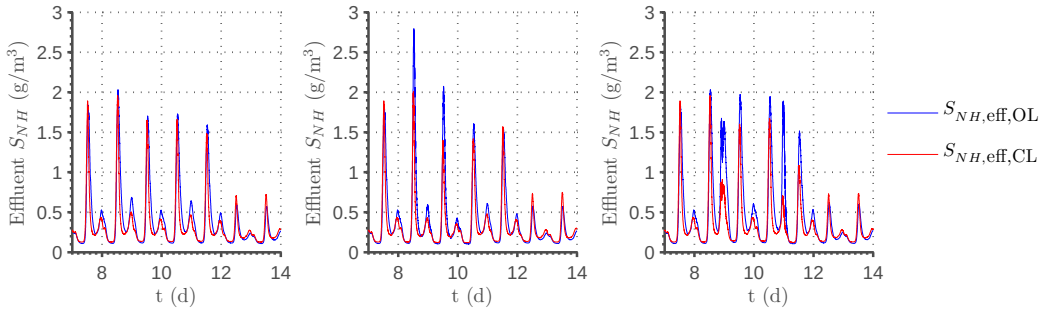

Figure 8.7: Effluent NH_4^+-N concentrations during (from left to right) dry-, rain- and storm-weather conditions.

performance comparison Tables 8.9-8.12.

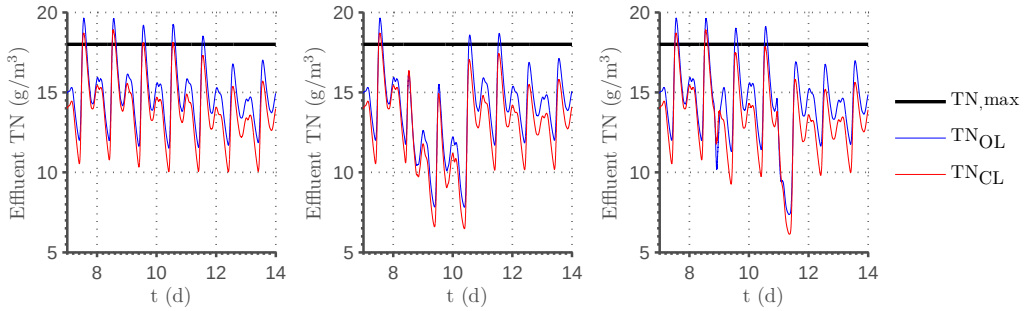

Figure 8.8: Effluent TN concentrations during (from left to right) dry-, rain- and storm-weather conditions.

8.6.2 Effluent quality measures, cost performance and process variables

Performance of the BSM-MBR benchmark simulation model and the IBMF-MBR model in each weather scenario and under each level of process control is summarised in Table 8.9, Table 8.10, Table 8.11 and Table 8.12. These tables correspond to, respectively, open-loop, closed-loop with DO control, closed-loop with DO and SAD_m control, and closed-loop with DO, SAD_m and NO_3^--N control.

Table 8.9: Comparison of dynamic open-loop effluent quality and operating cost performance criteria between BSM-MBR and IBMF-MBR models.

Criterion	Unit	BSM-MBR			IBMF-MBR		
		Dry	Rain	Storm	Dry	Rain	Storm
I.Q.	kgPU d^{-1}	52115.2	52115.2	54074.5	52052.1	52050.2	54029.5
E.Q.	kgPU d^{-1}	3216.9	3423.6	3423.6	4177.5	4935.9	4544.6
$S_{NH,95}$	gN m^{-3}	0.475	0.473	0.491	1.42	1.40	1.59
TN_{95}	gN m^{-3}	16.49	15.42	16.32	18.64	17.73	18.55
TSS_{95}	g m^{-3}	0	0	0	0	0	0
COD_{95}	gO_2 m^{-3}	30.90	30.80	30.86	34.78	34.31	35.16
$BOD_{5,95}$	gO_2 m^{-3}	0.225	0.232	0.237	0.605	0.610	0.638
$S_{NH,violations}$	–	0	0	0	0	0	0
(4 gN m^{-3})	% of time	0	0	0	0	0	0
$TN_{violations}$	–	0	0	0	5	3	4
(18 gN m^{-3})	% of time	0	0	0	8.16	4.31	6.87
$BOD_{5,violations}$	–	0	0	0	0	0	0
(10 gO_2 m^{-3})	% of time	0	0	0	0	0	0
$COD_{violations}$	–	0	0	0	0	0	0
(100 gO_2 m^{-3})	% of time	0	0	0	0	0	0
$TSS_{violations}$	–	0	0	0	0	0	0
(30 g m^{-3})	% of time	0	0	0	0	0	0
SP_{tot}	kgTSS d^{-1}	1971.2	1982.9	2198.5	1590.1	1587.6	1772.0
SP_{disp}	kgTSS d^{-1}	1971.2	1982.9	2198.5	1590.1	1587.6	1772.0
$AE_{bioreactor}$	kWh d^{-1}	3878.6	3878.6	3878.6	4075.6	4075.6	4075.6
$AE_{membrane}$	kWh d^{-1}	9680.7	9680.7	9680.7	9018.1	9018.1	9018.1
AE_{total}	kWh d^{-1}	13559.3	13559.3	13559.3	13093.7	13093.7	13093.7
PE_{total}	kWh d^{-1}	2209.2	2639.6	2403.2	1023.6	1128.3	1078.2
PE_{sludge}	kWh d^{-1}	840.1	840.1	840.1	835.2	835.2	835.2
$PE_{permeate}$	kWh d^{-1}	1369.2	1800.0	1563.2	188.33	293.03	243.00
PE_{q_w}	kWh d^{-1}	Not recorded	Not recorded	Not recorded	8.00	8.00	8.00
$PE_{q_{int}}$	kWh d^{-1}				413.61	413.61	413.61
PE_{q_r}	kWh d^{-1}				413.61	413.61	413.61
PE_{q_e}	kWh d^{-1}				145.94	250.53	200.55
$PE_{q_{back}}$	kWh d^{-1}				42.39	42.50	42.25
ME	kWh d^{-1}	576	576	576	714.38	714.38	714.38
OCI	–	26200.4	26690.0	27531.2	22763.9	22856.1	23728.2
Total SRT	d	27.51	25.90	26.83	33.38	31.24	32.47
Aerobic SRT	d	18.85	18.17	18.56	20.41	19.67	20.09
Y_{obs}	–	0.700	0.743	0.732	0.565	0.603	0.591

The first section in all tables lists the influent quality (IQ) index and the effluent quality (EQ) index. The second section lists 95%-iles of the effluent NH_4^+-N, TN and TSS concentrations, as well as effluent COD and biological oxygen demand in five days (BOD_5). The third section shows the number of violations and % of time under violation during last 7 days of dynamic simulation for, respectively, NH_4^+-N, TN, BOD_5, COD and TSS. The fourth section lists total sludge production (SP_{tot}) and the amount of sludge for disposal (SP_{disp}) which, for MBR systems are equal, since no solids are lost in the effluent due to complete rejection of solids by the membrane. The fifth section lists the aeration energy used for fine-bubble aeration ($AE_{bioreactor}$), coarse-bubble aeration ($AE_{membrane}$), as well as the total energy demand for aeration (AE_{total}).

Section number six deals with energy consumption due to pumping and mixing. PE_{total} denotes the total energy demand for pumping, PE_{sludge} denotes the amount of energy spent on pumping of mixed liquor, whilst $PE_{permeate}$ is the energy demand for producing sufficient amounts of suction pressure to transport the permeate across the membrane. The columns dedicated to the IBMF-MBR simulation model additionally list pumping energy demands for individual pumped flows, i.e. waste activated sludge (WAS) flow (PE_{q_w}), internal recirculation ($PE_{q_{int}}$), sludge recirculation (PE_{q_r}), permeate pumping (PE_{q_e}), and backwashing ($PE_{q_{back}}$). ME denotes the amount of energy required to mix the anoxic tanks and the aerobic tanks if the amount of air provided is not sufficient for a thorough mixing of the tank contents. The last section lists the operational cost index (OCI), total and aerobic SRT and the observed sludge yield Y_{obs}.

Table 8.10: Comparison of dynamic closed-loop effluent quality and operating cost performance criteria between BSM-MBR and IBMF-MBR models with DO control.

Criterion	Unit	BSM-MBR			IBMF-MBR		
		Dry	Rain	Storm	Dry	Rain	Storm
I.Q.	kgPU d^{-1}	52115.4	52115.4	54074.5	52052.1	52050.2	54029.5
E.Q.	kgPU d^{-1}	3222.5	3714.4	3456.8	4145.9	4894.3	4504.4
$S_{NH,95}$	gN m^{-3}	0.169	0.175	0.176	0.784	0.783	0.747
TN_{95}	gN m^{-3}	17.43	16.18	17.23	19.62	18.52	19.54
TSS_{95}	g m^{-3}	0	0	0	0	0	0
COD_{95}	gO_2 m^{-3}	30.82	30.75	30.78	34.13	33.60	34.49
$BOD_{5,95}$	gO_2 m^{-3}	0.205	0.210	0.215	0.584	0.591	0.612
$S_{NH,violations}$	–	0	0	0	0	0	0
(4 gN m^{-3})	% of time	0	0	0	0	0	0
$TN_{violations}$	–	4	1	4	5	3	5
(18 gN m^{-3})	% of time	2.38	0.743	2.53	11.06	6.11	10.00
$BOD_{5,violations}$	–	0	0	0	0	0	0
(10 gO_2 m^{-3})	% of time	0	0	0	0	0	0
$COD_{violations}$	–	0	0	0	0	0	0
(100 gO_2 m^{-3})	% of time	0	0	0	0	0	0
$TSS_{violations}$	–	0	0	0	0	0	0
(30 g m^{-3})	% of time	0	0	0	0	0	0
SP_{tot}	kgTSS d^{-1}	1978.2	1990.6	2182.1	1588.4	1584.7	1764.3
SP_{disp}	kgTSS d^{-1}	1978.2	1990.6	2182.1	1588.4	1584.7	1764.3
$AE_{bioreactor}$	kWh d^{-1}	3834.3	3791.5	3945.3	4070.6	3981.4	4169.5
$AE_{membrane}$	kWh d^{-1}	9680.7	9680.7	9680.7	9018.1	9018.1	9018.1
AE_{total}	kWh d^{-1}	13515.0	13472.2	13626.0	13088.7	12999.5	13187.6
PE_{total}	kWh d^{-1}	2209.2	2639.6	2403.2	1023.5	1128.2	1078.2
PE_{sludge}	kWh d^{-1}	840.1	840.1	840.1	835.22	835.22	835.22
$PE_{permeate}$	kWh d^{-1}	1369.2	1799.5	1563.2	188.32	293.01	242.98
PE_{q_w}	kWh d^{-1}	Not recorded	Not recorded	Not recorded	8.00	8.00	8.00
$PE_{q_{int}}$	kWh d^{-1}				413.61	413.61	413.61
PE_{q_r}	kWh d^{-1}				413.61	413.61	413.61
PE_{q_e}	kWh d^{-1}				145.93	250.52	200.54
$PE_{q_{back}}$	kWh d^{-1}				42.39	42.49	42.44
ME	kWh d^{-1}	576	576	576	714.38	714.38	714.38
OCI	–	26191.3	26640.8	27505.8	23954.9	22765.5	25123.1
Total SRT	d	27.51	25.89	26.83	33.38	31.24	32.48
Aerobic SRT	d	18.85	18.17	18.56	20.41	19.67	20.10
Y_{obs}	–	0.702	0.744	0.732	0.565	0.603	0.591

IBMF-MBR produces higher TN concentrations to the BSM-MBR benchmark model as indicated by the value of TN_{95}, number of TN consent limit violations and % of time under violation. While in BSM-MBR no TN violations are reported under open-loop operation and closed-loop operation with DO, SAD_m and NO_3^--N control, IBMF-MBR is found to exceed the maximum allowed TN concentration under all weather conditions and all levels of process control despite higher anoxic volume fraction. The difference in the effluent TN_{95} concentration produced by BSM-MBR and IBMF-MBR is on average about 2 mgN L^{-1} in favour of BSM-MBR.

Table 8.11: Comparison of dynamic closed-loop effluent quality and operating cost performance criteria between BSM-MBR and IBMF-MBR models with DO and SAD_m control.

Criterion	Unit	BSM-MBR			IBMF-MBR		
		Dry	Rain	Storm	Dry	Rain	Storm
I.Q.	kgPU d^{-1}	52115.4	52115.4	54074.6	52052.1	52050.2	54029.5
E.Q.	kgPU d^{-1}	3197.2	3696.0	3432.0	4112.4	4871.0	4470.9
$S_{NH,95}$	gN m^{-3}	0.174	0.179	0.178	0.882	0.842	0.815
TN_{95}	gN m^{-3}	17.32	16.08	17.12	19.31	18.26	19.22
TSS_{95}	g m^{-3}	0	0	0	0	0	0
COD_{95}	gO_2 m^{-3}	30.82	30.75	30.79	34.28	33.76	34.62
$BOD_{5,95}$	gO_2 m^{-3}	0.205	0.211	0.216	0.586	0.592	0.614
$S_{NH,violations}$	–	0	0	0	0	0	0
(4 gN m^{-3})	% of time	0	0	0	0	0	0
$TN_{violations}$	–	3	1	3	5	3	5
(18 gN m^{-3})	% of time	1.63	0.594	1.63	10.16	5.56	8.81
$BOD_{5,violations}$	–	0	0	0	0	0	0
(10 gO_2 m^{-3})	% of time	0	0	0	0	0	0
$COD_{violations}$	–	0	0	0	0	0	0
(100 gO_2 m^{-3})	% of time	0	0	0	0	0	0
$TSS_{violations}$	–	0	0	0	0	0	0
(30 g m^{-3})	% of time	0	0	0	0	0	0
SP_{tot}	kgTSS d^{-1}	1977.1	1991.0	2181.2	1587.7	1584.7	1763.4
SP_{disp}	kgTSS d^{-1}	1977.1	1991.0	2181.2	1587.7	1584.7	1763.4
$AE_{bioreactor}$	kWh d^{-1}	3911.8	3848.2	4007.9	4152.4	4039.7	4246.2
$AE_{membrane}$	kWh d^{-1}	5597.0	6647.8	5970.9	5469.5	6409.9	5809.3
AE_{total}	kWh d^{-1}	9508.9	10486.0	9988.8	9621.9	10449.6	10055.7
PE_{total}	kWh d^{-1}	2209.2	2639.6	2403.2	1025.5	1129.7	1080.0
PE_{sludge}	kWh d^{-1}	840.07	840.07	840.07	835.22	835.22	835.22
$PE_{permeate}$	kWh d^{-1}	1396.2	1799.5	1563.2	190.29	294.43	244.8
PE_{q_w}	kWh d^{-1}	Not recorded	Not recorded	Not recorded	8.00	8.00	8.00
$PE_{q_{int}}$	kWh d^{-1}				413.61	413.61	413.61
PE_{q_r}	kWh d^{-1}				413.61	413.61	413.61
PE_{q_e}	kWh d^{-1}				147.90	251.93	202.36
$PE_{q_{back}}$	kWh d^{-1}				42.39	42.49	42.44
ME	kWh d^{-1}	576	576	576	714.38	714.38	714.38
OCI	–	22179.6	23666.5	23864.1	19301.0	20217.2	20667.1
Total SRT	d	27.51	25.89	26.83	33.38	31.24	32.48
Aerobic SRT	d	18.85	18.17	18.56	20.41	19.67	20.10
Y_{obs}	–	0.701	0.744	0.732	0.565	0.603	0.591

IBMF-MBR also produces less surplus activated sludge (SAS) leading to ~ 20% lower observed sludge yields (Y_{obs}) and proportionally higher total and aerobic SRTs.

Whilst energy demand for fine bubble aeration is slightly higher in IBMF-MBR, energy demand for air scouring is less due to lower installed membrane area. In consequence, similar energy requirements for aeration are predicted in both models.

Mixing energy requirement is $\sim$ 24% higher in IBMF-MBR due to larger total anoxic tank volume, whilst energy consumption for pumping is significantly lower due to lower energy requirements for permeate pumping. Energy requirements for permeate pumping are found to be significantly exaggerated in the BSM-MBR benchmark. The trans-membrane pressure (TMP) calculations in the IBMF-MBR model indicate an eight fold decrease in permeate pumping requirements despite of rather average for an ultrafiltration (UF) module permeabilities of about 80–100 Lmh bar^{-1}.

Table 8.12: Comparison of dynamic closed-loop effluent quality and operating cost performance criteria between BSM-MBR and IBMF-MBR models with DO, SAD_m and NO_3^--N control.

Criterion	Unit	BSM-MBR			IBMF-MBR		
		Dry	Rain	Storm	Dry	Rain	Storm
I.Q.	kgPU d^{-1}	52115.4	52115.4	54074.5	52052.1	52050.2	54029.5
E.Q.	kgPU d^{-1}	3174.8	3569.5	3345.7	3980.8	4679.1	4280.6
$S_{NH,95}$	gN m^{-3}	0.191	0.207	0.201	1.16	1.07	1.05
TN_{95}	gN m^{-3}	16.72	15.22	16.48	17.82	16.64	17.45
TSS_{95}	g m^{-3}	0	0	0	0	0	0
COD_{95}	gO_2 m^{-3}	30.80	30.75	30.79	34.10	33.61	34.50
$BOD_{5,95}$	gO_2 m^{-3}	0.200	0.206	0.211	0.609	0.624	0.641
$S_{NH,violations}$	–	0	0	0	0	0	0
(4 gN m^{-3})	% of time	0	0	0	0	0	0
$TN_{violations}$	–	0	0	0	4	1	2
(18 gN m^{-3})	% of time	0	0	0	3.90	1.38	2.89
$BOD_{5,violations}$	–	0	0	0	0	0	0
(10 gO_2 m^{-3})	% of time	0	0	0	0	0	0
$COD_{violations}$	–	0	0	0	0	0	0
(100 gO_2 m^{-3})	% of time	0	0	0	0	0	0
$TSS_{violations}$	–	0	0	0	0	0	0
(30 g m^{-3})	% of time	0	0	0	0	0	0
SP_{tot}	kgTSS d^{-1}	1978.2	1992.2	2180.5	1584.5	1577.0	1757.1
SP_{disp}	kgTSS d^{-1}	1978.2	1992.2	2180.5	1584.5	1577.0	1757.1
$AE_{bioreactor}$	kWh d^{-1}	3897.8	3806.9	3974.1	4096.4	3951.3	4159.2
$AE_{membrane}$	kWh d^{-1}	5596.9	6647.6	5970.4	5469.4	6410.0	5809.2
AE_{total}	kWh d^{-1}	9494.7	10454.5	9944.5	9565.8	10361.3	9968.4
PE_{total}	kWh d^{-1}	2198.4	2682.0	2428.2	1092.3	1238.8	1188.0
PE_{sludge}	kWh d^{-1}	829.18	882.42	864.98	902.14	945.00	943.63
$PE_{permeate}$	kWh d^{-1}	1369.2	1799.5	1563.2	190.16	293.80	244.35
PE_{q_w}	kWh d^{-1}	Not recorded	Not recorded	Not recorded	8.00	8.00	8.00
$PE_{q_{int}}$	kWh d^{-1}				480.53	523.39	522.02
PE_{q_r}	kWh d^{-1}				413.61	413.61	413.61
PE_{q_e}	kWh d^{-1}				147.77	251.31	201.91
$PE_{q_{back}}$	kWh d^{-1}				42.39	42.49	42.44
ME	kWh d^{-1}	576	576	576	714.38	714.38	714.38
OCI	–	22160.0	23673.3	23851.3	20479.6	20199.6	20656.3
Total SRT	d	27.44	26.04	26.91	33.80	31.90	33.11
Aerobic SRT	d	18.85	18.17	18.56	20.41	19.67	20.10
Y_{obs}	–	0.706	0.743	0.732	0.566	0.599	0.587

8.6.3 Membrane fouling and biopolymer production

Bulk liquid SMP concentrations in the membrane tank under all three weather scenarios are plotted in Figure 8.9. Figure 8.9 shows rather moderate variations in the concentrations of S_{UAP} and S_{BAP} which are mainly due to diurnal influent flow pattern and dilution effects during rain and storm events. This behaviour stems from the fact that CES-ASM1, similarly to other published biopolymer ASM models, has not been designed to predict the changes in biopolymer production in a response to large variations in the influent quantity and quality and operating conditions, such as large variations in DO concentration, salinity, pH, changes in the type of organic substrates, toxic effects, shear stresses, etc. The model was calibrated on the data obtained during cultivation of bacterial cultures under rather slowly changing environmental conditions and under constant influent flow rates, hence the sort of dynamics present at full-scale WWTPs have not been captured. Therefore, whilst the system might experience additional SMP dynamics under time varying conditions in response to environmental stress, these effects have not modelled and will need to be studied in more detail in order to formulate an appropriate model which is going to take these effects into account.

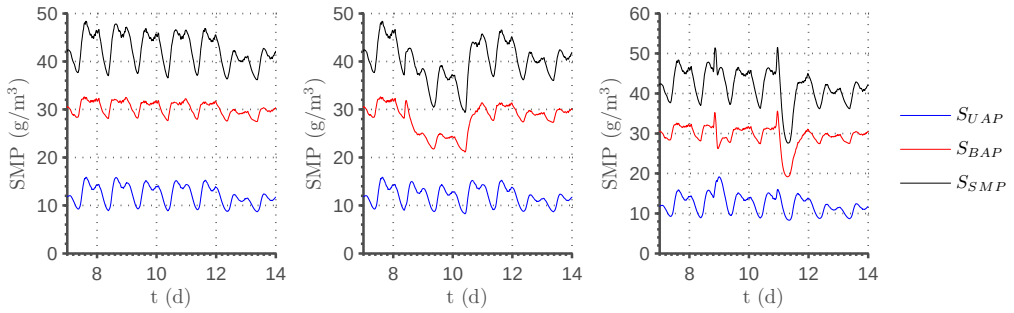

Figure 8.9: SMP concentrations in the membrane bioreactor during (from left to right) dry-, rain- and storm-weather conditions.

Figure 8.10 shows irreversible fouling resistance R_i and the SMP/MLSS ratio in the membrane tank under all three weather scenarios. The figure shows that whilst under dry-weather flow resistance R_i increases slowly and steadily at a rate of about 1.10×10^{-2} m kg^{-1} h^{-1}, under the elevated flow conditions in wet periods the rate of R_i increase is up to four fold higher and about 4.58×10^{-2} m kg^{-1} h^{-1} during the rain event and up to ~ 0.21 m kg^{-1} h^{-1} during the storm event. These elevated irreversible fouling rates coincide with the decrease of SMP concentration and SMP/MLSS ratio, indicating that the rate of irreversible fouling is dominated by flux rate, not but SMP concentrations in the bulk liquid.

The membrane flux rates for all three weather scenarios are plotted in Figure 8.11 which shows that the membrane is operating under rather small fluxes between 8 and 20 Lmh in dry-weather periods and up to 32 Lmh and 38 Lmh during rain and storm events, respectively. Hence, the plant requires very small energy input for permeate pumping.

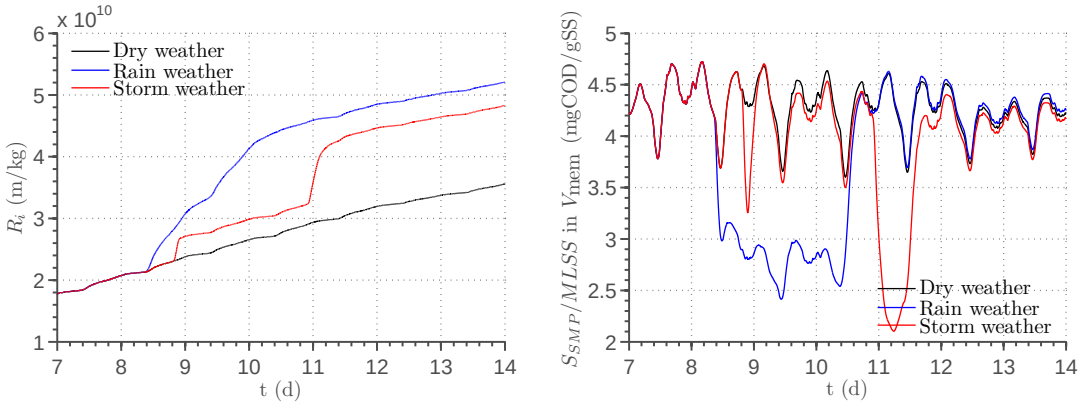

Figure 8.10: (a) Resistance due to irreversible fouling R_i and (b) SMP fraction in MLSS vs. time during open-loop simulation in dry-, wet-, and storm-weather conditions.

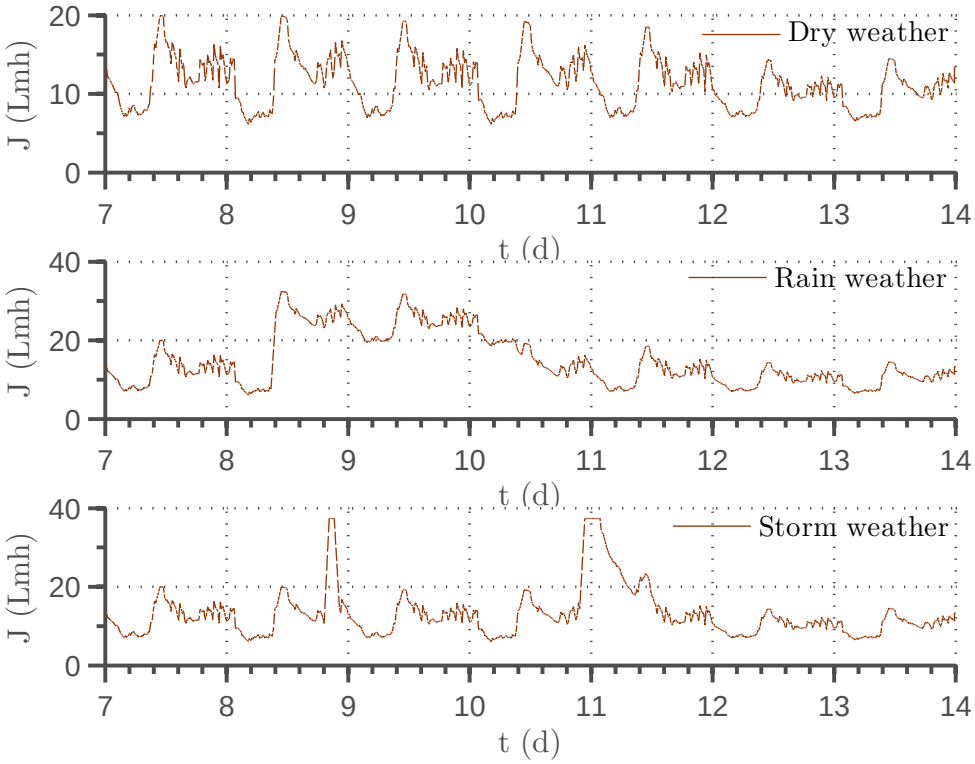

Figure 8.11: Permeate flux rates during dry-, rain- and storm-weather conditions.

As previously stated in Section 8.1.2 of this Chapter, specific cake resistance α_c is calculated in the IBMF-MBR model according to the α_c vs. MLSS relationship proposed by Ahmed et al. [1] and shown in Figure 7.17. The specific cake resistance figures obtained from the model were then increased ten fold to produce 'observable' reversible fouling which was otherwise so small that short-term TMP increse during filtration periods could not be observed. Although introduction of such a 'fudge' factor may sound as a dubious decision, in the absence of validation data the model presented here is only intended to give indicative figures and to illustrate the proof of concept, hence no rigorous checking of model parameters is required at this stage.

Figure 8.12 shows, as one would expect, that specific cake resistance changes in proportion to EPS content in the activated sludge. However, as EPS do not vary much over the course of simulation, α_c remains at a relatively constant value of $\sim 1.12 - 1.16$ m kg^{-1}.

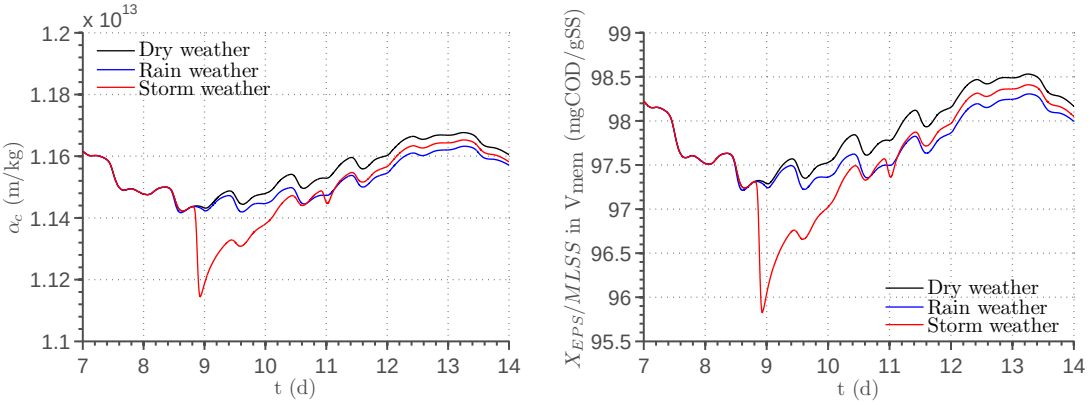

Figure 8.12: Specific cake resistance α_c and EPS fraction in MLSS vs. time during the open-loop simulation in dry-, wet-, and storm-weather conditions.

Transmembrane pressure (TMP) during rain- and storm-weather and under open-loop as well as closed-loop scenario with SAD_m control is plotted in Figure 8.13 and Figure 8.14, respectively. Both figures indicate increased reversible fouling in wet weather conditions due to a combined effect of higher permeate flux and higher MLSS concentration in the membrane tank. Although the effects of cake deposition on the membrane are visible at higher fluxes under both, open-loop and closed-loop operation, cake buildup at lower fluxes is almost non-existing when constant air-scouring rate is applied throughout the simulation period. This indicates the possibility for energy saving through reduction of coarse-bubble airflow rate when permeate fluxes are low. When SAD_m control is applied, energy demand for coarse aeration is reduced by about a third whilst reversible fouling under low flux rates increased only slightly and is still insignificantly small compared to the overall membrane resistance.

8.6.4 Energy consumption

Energy consumption per m^3 of treated wastewater in IBMF-MBR is compared against the results obtained with the BSM-MBR benchmark model and the measurements performed on three full-scale MBR plants. The results are collated in Table **??** which extends the table originally published in Maere et al. [160].

The energy demand predicted from IBMF-MBR in open-loop operation is similar to the energy consumption estimated with BSM-MBR except earlier mentioned energy for permeate pumping which is the lowest among all effluent pumping figures in the table. The reasons for that are two-fold. First, the permeate fluxes in the model under dry-weather conditions are at the lower end of sustainable long-term fluxes used on this sort of membranes at full-scale municipal MBR plants. Second, the effects of irreversible fouling on the overall operational costs including permeate pumping cannot be evaluated

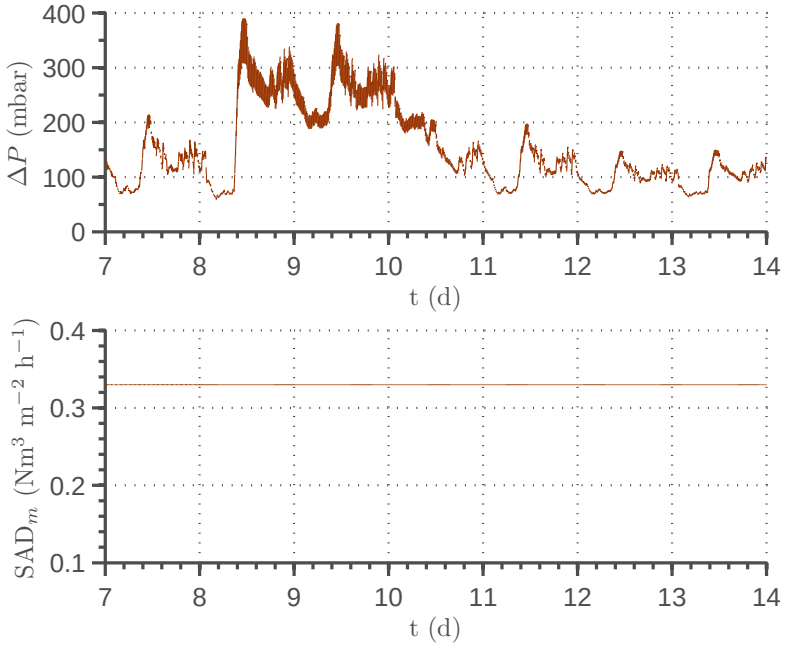

(a) Operation under constant SAD_m.

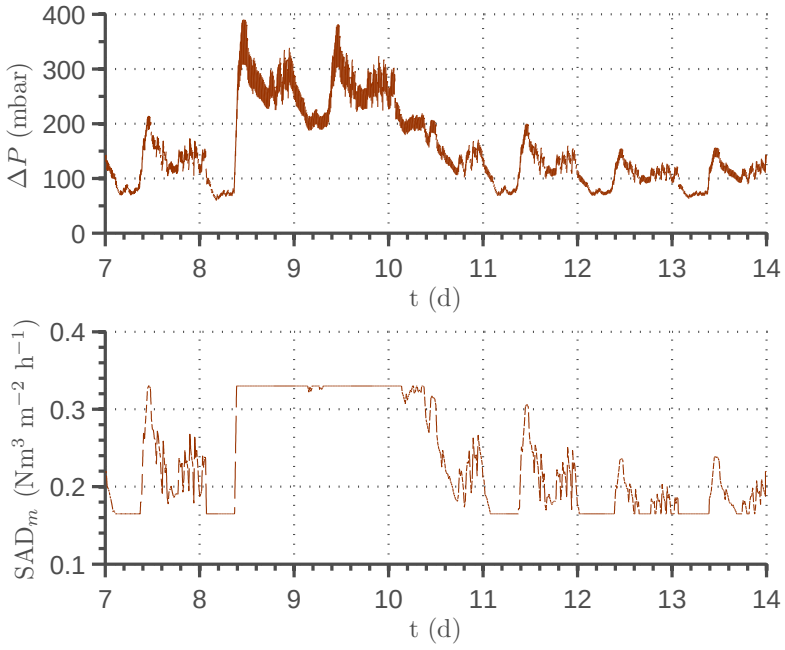

(b) Operation with SAD_m proportional to permeate flux.

Figure 8.13: Transmembrane pressure (TMP) and specific aeration demand (SAD_m) with and without SAD_m control during rain-weather conditions.

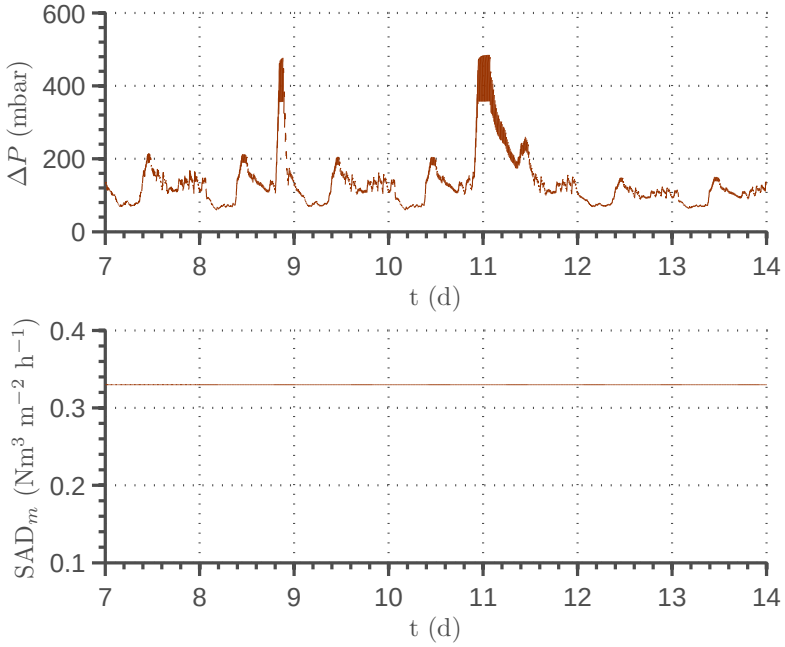

(a) Operation under constant SAD_m.

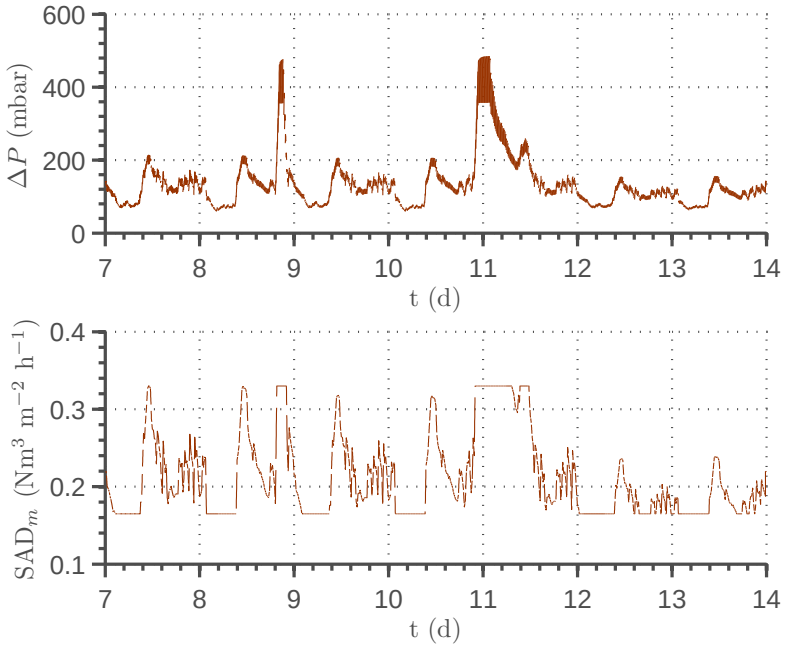

(b) Operation with SAD_m proportional to permeate flux.

Figure 8.14: Transmembrane pressure (TMP) and specific aeration demand (SAD_m) with and without SAD_m control during storm-weather conditions

in such a short time scale as 14 days. Hence, permeate pumping costs calculated here will be typical for initial periods of operation where the membranes do not yet show any effects of irreversible fouling and hence the permeabilities are high. In order to quantify the overall permeate pumping costs, the model first and foremost needs to be calibrated and validated and secondly, the simulation horizon needs to be extended to at least a few months such that the effects of long-term irreversible fouling can be accounted for in the estimation of energy demand. Extended simulation periods will also allow to quantify chemical cleaning costs if the model is extended with a chemical cleaning processes and cost model.

The percent share of various energy consuming processes in the simulated benchmark plant under dry-weather and rain-weather are shown respectively in Figure 8.15 and Figure 8.16. Both figures show that energy demand distribution does not differ between dry-weather and rain-weather conditions although changes significantly between open-loop and closed-loop operation with DO, SAD_m and NO_3^--N control. Whilst in open-loop scenario 61% of all energy is used for coarse-bubble aeration and 27% for fine bubble aeration, the amount of energy required for air-scouring is reduced to 48% under closed-loop operation while, due to overall reduction of total energy demand at the plant, the share of energy being used for fine-bubble aeration increased to 26% in dry-weather and 33% in rain-weather. Fine-bubble and coarse-bubble aeration are hence the most energy demanding processes at the plant. Rest of the energy is utilised for internal and sludge recirculation (3-4% each) and anoxic mixing (5-6%). Permeate pumping accounts for just 1-2% while energy costs for backwashing and WAS pumping are insignificant and account for less than 1% of the overall energy costs.

Table 8.13: Comparison of energy costs between IBMF-MBR, BSM-MBR and three full-scale municipal MBR WWTPs - modified from Maere et al. [160].

Energy cost ($kWh\ m^{-3}$)	Schilde [1)]	Varsseveld [2)]	Nordkanal [3)]	BSM-MBR	IBMF-MBR	
					Open-loop*)	Closed-loop*)
ME	0.05	0.04	0.11	0.03	0.039	0.039
PE_{sludge}	0.10	0.11	0.01	0.05	0.046	0.049
$PE_{effluent}$	0.07	0.12	0.02	0.07	0.008	0.008
$AE_{bioreactor}$	0.07	0.24	0.11	0.21	0.22	0.22
$AE_{membrane}$	0.23	0.34	0.45	0.53	0.49	0.30
Total	0.52	0.85	0.71	0.90	0.81	0.62

*) dry-weather conditions with average permeate flow rate $q_{perm,ave}$ = 18286.3 $m^3\ d^{-1}$

1) Fenu et al. [58]

2) Wever et al. [255]

3) Brepols et al. [15]

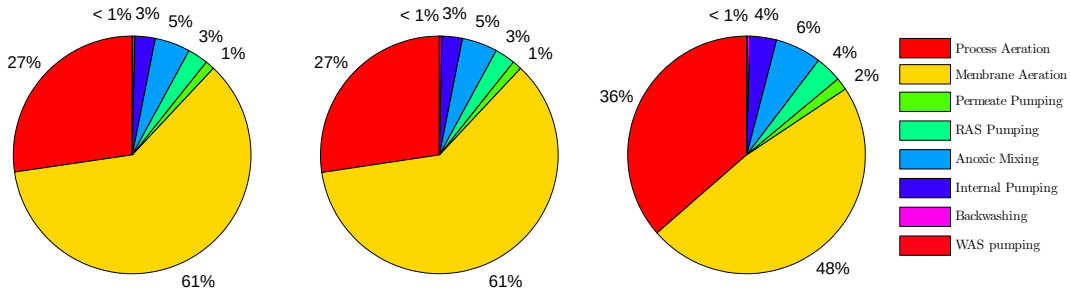

Figure 8.15: Energy consumption during dry-weather conditions in (from left to right) open-loop simulation, closed-loop simulation with DO control, closed-loop simulation with DO,NO_3^--N and SAD_m control.

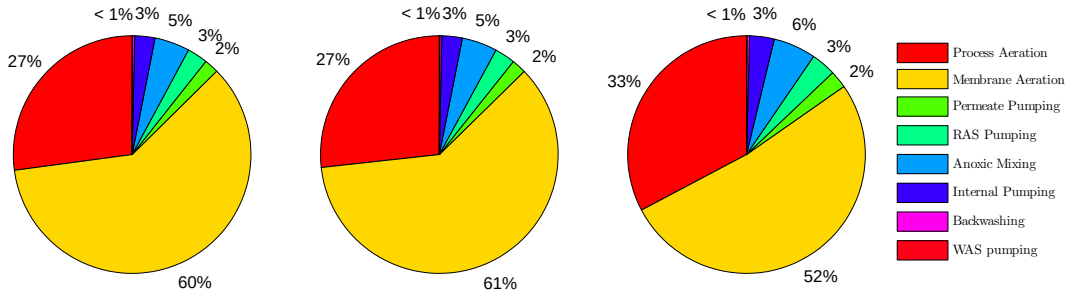

Figure 8.16: Energy consumption during rain event in (from left to right) open-loop simulation, closed-loop simulation with DO control, closed-loop simulation with DO,NO_3^--N and SAD_m control.

Chapter 9

General Conclusions

9.1 Overall summary

This thesis is divided into three distinct parts, each focusing on different aspects of modelling membrane bioreactors (MBRs) for wastewater treatment.

The first part describes the development of two activated sludge models (ASMs) extended with kinetics of extracellular polymeric substances (EPS) and soluble microbial products (SMP). The first model is based on the Activated Sludge Model No. 1 (ASM1) whilst the second model is based on a more recently developed Activated Sludge Model No. 3 (ASM3). Both models are calibrated and assigned default parameter sets, and produce similar outputs with regards to original state variables present in their base models as well as the added state variables: concentrations of utilisation associated products (UAP), biomass associated products (BAP) and extracellular polymeric substances (EPS).

The second part describes the formulation of two membrane fouling models. The first model is an extension of a rather uncomplicated model of Liang et al. [149] which is based on two ordinary differential equations (ODEs) describing an increase of membrane resistance due to reversible and irreversible fouling, respectively. The model of Liang et al. [149] is extended to allow simulation of the effects of membrane backwashing, prediction of cake removal rates according to the models of Nagaoka et al. [176] and Ho and Zydney [97], and prediction of irreversible fouling rates as a function of permeate flux. The second fouling model is based on the concept of Duclos-Orsello et al. [50] where three classical fouling equations: pore constriction, complete pore blockage and cake formation, are solved simultaneously to predict the loss of membrane permeability during filtration. Whilst the original model has been presented in an integral form and is limited to description of permeate flux reduction flux during constant trans-membrane pressure (TMP) filtration, the extended model is presented with differential equations allowing simulations under time-varying inputs. In order to describe the sequential occurrence of pore blockage and cake filtration the model is extended with two ODEs which calculate the resistance under the blocked area. Both models can be used for

predicting flux decrease under a given pressure or for calculating TMP increase under a given flux.

The third part describes integration of the combined EPS and SMP production ASM1-based model (CES-ASM1) developed in Part I with the modified Liang model developed in Part II. Irreversible fouling is linked to SMP concentrations whilst specific cake resistance used in the reversible fouling equation is made dependent on EPS concentrations, which, together with SMP are predicted by the CES-ASM1 model. Cake detachment rate is linked to coarse bubble aeration rate through modelling of shear stresses on the membrane surface as a function of the superficial air velocity with a two-phase slug-flow model of Zaisha and Dukler [268]. The integrated model is applied on the plant layout defined in the MBR benchmark simulation model (BSM-MBR) of Maere et al. [160].

9.2 Summary of achievements

The work presented in this thesis can be divided into following four categories:

1. Collection and presentation of recent research related to different aspects of modelling MBR systems.
2. Analysis, comparison and evaluation of various mathematical models published in the scientific literature.
3. Development of new models, modification of the existing models and adaptation of the existing models to new fields of science.
4. Integration of models and formulation of the integrated bioreactor and membrane fouling MBR model (IBMF-MBR).

With regards to point 1 this thesis provides a comprehensive overview of different aspects of modelling MBR systems as well as activated sludge systems in general. According to the author's knowledge this is the first published PhD thesis of this kind and it may serve as a comprehensive literature review and as a roadmap for PhD students and researchers working in this area.

With regards to point 2 this thesis analyses several published ASM models, theoretical equations of forces acting on a single particle in the vicinity of the membrane surface and the model of slug-flow by Zaisha and Dukler [268]. The models were evaluated in terms of produced outputs, sensitivity to parameters and, although not with rigorous mathematical methods, existence of unique solutions and parameter identifiability.

With regards to point 3 this thesis provides two new ASM models with SMP and EPS kinetics and two membrane fouling models. All of the above were calibrated on various sets of experimental data obtained from project partners and from literature.

CES-ASM1 and the modified fouling model of Liang et al. [149] were integrated using a number of interface relationships: (1) shear stresses on the membrane surface due to forces caused by lateral movement of air bubbles are calculated for a given

membrane module geometry with a two-phase slug flow model of Zaisha and Dukler [268], (2) EPS fraction in activated sludge is correlated with specific cake resistance, (3) irreversible fouling rate is in a functional relationship with SMP concentration and permeate flux. Through establishment of links between the membrane model and the bioreactor model we are allowed to describe a MBR as a whole and evaluate the effects of various operational strategies on both parts of the MBR, not just one.

9.3 Summary of main findings

Whilst the models presented in this thesis were not validated and hence drawing definite conclusions regarding the behaviour of the physical systems from the model outputs would be inadequate, the author made several observations with regards to the quality of the published models, behaviour of the newly developed models, the models' limitations as well as their advantages. The main findings are listed below.

1. The published biopolymer ASM models of Lu et al. [157] and Oliveira-Esquerre et al. [192] are found to be structurally incorrect as the first model does not conserve mass and the second model is unable to predict correct SMP concentrations without sacrificing the predictability of other state variables such as ammoniacal nitrogen (NH_4^+-N) or nitrate nitrogen (NO_3^--N).
2. The way that combined biopolymer ASM models are formulated, addition of biopolymer kinetics affect the process rates of the original state variables in the base ASM models. These links can be seen in the Petersen matrix in which bioppolymer-related stoichiometric parameters appear in the stoichiometric coefficients of the non-biopolymer related reactions. For example, production of EPS by the biomass comes at the cost of biomass growth, hence the stoichiometric parameter for biomass in the biomass growth process is equal to $1 - f_{eps}$ instead of 1 where f_{eps} denotes the fraction of EPS produced during biomass growth. As the biopolymer kinetics are being adjusted, kinetics of other state variables are affected as well which poses additional difficulties during model calibration. Moreover, Petersen matrices in the new biopolymer models are different from those of the standard International Association on Water Quality (IAWQ) ASM models, hence it is advisable that the new models are thoroughly calibrated in the same fashion as had been done with the standard ASM models.
3. Based on own observations, the author hypothesizes that different relationships between biopolymer concentrations and environmental conditions such as e.g. dissolved oxygen (DO) or sludge retention time (SRT) observed by various authors are due to relative parity between the rates of different biopolymer kinetics, such as, e.g. biomass associated production and utilisation associated production. In order to verify (or disprove) this hypothesis the models need to be simulated for a number of different combinations of different biopolymer-associated kinetic and stoichiometric parameters with e.g. Monte-Carlo methods.

4. Whilst different researchers suggested different mechanisms as the cause of occurrence of the so called 'two-stage' TMP profiles during constant flux filtration, such as e.g. cake layer collapse or local transgression of the critical flux, simulations with the three-mechanism fouling model indicate that two-stage TMP profiles can be explained by modelling cake deposition in sequence with combined effects of pore constriction and pore blockage.
5. Irreversible fouling has been found to occur at significantly faster rates during rain events where SMP concentrations were significantly lower due to dilution effects but flux began to exceed critical flux. This observation suggests that irreversible fouling depends more on flux than on SMP concentrations in the bulk liquid.
6. Although irreversible fouling entails higher operational expenditures (OPEX) associated with pumping costs and chemical cleaning, as well as capital expenditures (CAPEX) associated with membrane replacements, reversible fouling puts far more significant demands on energy and is the main culprit causing high operating costs of MBR plants. Another significant detrimental process in MBR plants is membrane clogging, i.e. blockage of passages inside membrane modules, although it receives less attention in the scientific community than membrane fouling.
7. Irreversible fouling is a very slow process whose process time constant exceeds the simulation horizon of the benchmark simulation model. Hence its effects on the MBR's operating costs cannot be properly evaluated. For appropriate evaluation of the MBR's operating costs, the plant may need to be simulated over much longer times, e.g. 609 days as implemented in the long term benchmark simulation model no.1 (BSM1_LT) of Rosen et al. [212]. Such a long simulation horizon may allow to properly evaluate the effects of irreversible fouling on the membrane permeability and hence the energy requirements for permeate pumping as well as other OPEX and CAPEX associated with control and amelioration of fouling. We may then capture these costs directly in the simulation model and formulate a cost measure of fouling which could be used for comparison of control strategies from the point of view of fouling. Such a proposed measure of fouling termed FCI (CU d^{-1} m^{-3}) for 'Fouling Cost Index' may be expressed in the following manner.

$$FCI = \frac{\int_{t_{start}}^{t_{end}} \left(\sum_{i=1}^{i=6} c_i \right) dt}{(t_{end} - t_{start})\,(V_{perm} - N\,V_{backwash})} \tag{9.1}$$

where c_1, c_2, c_3, c_4, and c_5 (CU) denote the costs associated, respectively, with air scouring, backwashing, permeate pumping, chemical cleaning, additives (chemicals) and, finally, membrane replacement, where CU (-) is a unified cost unit. t_{start} (d) and t_{end} (d) are, respectively, the beginning and the end of the process evaluation period, and $V_{perm} - N\,V_{backwash}$ (m^3) is the total (net) volume of the permeate produced in the plant, where N (-) denotes the number of backwashes

in the evaluation period and $V_{backwash}$ (m^3) denotes the volume of each backwash under an assumption that each backwash uses the same volume of water (permeate). Introduction of such a cost measure of fouling will however necessitate prior quantification of the unit costs of chemical membrane cleaning, backwashing and membrane replacement. These costs may be either calculated from the mathematical models developed bespoke for this purpose or inferred from the OPEX and CAPEX costs observed on full scale municipal MBR-based wastewater treatment plants (WWTPs).

8. Looking at the simulation results from the IBMF-MBR model it becomes apparent that the plant suffers from three problems, which shall be listed below. We might therefore ask ourselves a question whether it would be possible to obtain better effluent quality and/or process efficiency within the same volumes if the process was reconfigured, i.e. the order and volumes of individual reactors were changed, reactors were added/removed, and the flow streams between the reactors were altered. The benchmark model at current configuration is characterised with low anoxic mass fraction despite of 50% volumetric anoxic fraction due to uneven distribution of sludge between individual reactors. Additionally the first anoxic tank is subjected to ingress of large amounts of oxygen coming with the recirculation stream from the membrane tank what additionally impairs denitrification. The third problem experienced in this model configuration is the shift of solids downstream to the membrane tank under elevated flow rates. This phenomenon causes simultaneous occurrence of irreversible and reversible fouling on the membrane which has a negative effect on membrane performance. It seems therefore like a very attractive idea to come up with a better process configuration or, perhaps, to create a framework for comparison of different MBR configurations together with operational and control strategies. This task would however necessitate formulation of an objective function which would take into account not only the process performance and OPEX criteria but also CAPEX and yet unknown measures of process reliability and complexity. Such an optimisation problem would fall into the mixed integer non-linear programming (MINLP) category and is something to look forward to developing in future research studies.

9.4 Recommendations for future work

Despite of being on the market for almost two decades, MBRs are still in a heavy research and development stage with hundreds of scientific papers published each month on different aspects of MBR design, manufacturing, operation and control. Whilst membrane filtration is used in many branches of industry, the fundamental processes occurring on the membrane are still not entirely understood. The same applies to activated sludge systems which, although invented in the beginning of the last century, are still not well understood with regards to production of biopolymers, flocculation and deflocculation, bulking and foaming or responses to shock loads and toxicity.

There is still an active debate in the scientific community about what actually causes fouling and reports of different researchers are often conflicting. With regards to biopolymer production in activated sludge systems, first and foremost the biopolymer production models have not been extensively validated against the data from real wastewater treatment plants and secondly, mechanisms of SMP and EPS production are still unknown. Whilst models such as the model of Jiang et al. [115] or the author's own models: CES-ASM1 and CES-ASM3 differentiate between utilisation associated and biomass associated biopolymer production, additional production of biopolymers in a response to changing environmental conditions or environmental stress such as substrate and nutrient deficiency, toxicity, shear, or shock loads is not accounted for.

On the membrane filtration side, the role of SMP and EPS in fouling is not well understood and whilst it has been found that polysascharide fraction of SMP might cause more fouling than the protein fraction, it is not known whether the difference in fouling strengths of these two groups of substances are due to differences in their chemical composition or molecular weight distributions (MWDs). Moreover, the effects of membrane porosity, pore shape and pore size distribution (PSD) as well as particle size distribution and particle shapes on membrane fouling are very difficult to measure and even harder to describe in mathematical terms. The same applies to modelling gel-layer formation, biofilm growth and passive adsorption which are usually disregarded in the published fouling models. Links between cake detachment and air scouring rates are currently being intensively investigated using experimental methods as well as Computational Fluid Dynamics (CFD). At present, cake detachment is predicted with simple empirical equations as the 'quasi-static' mechanistic two-phase slug-flow models contain far too many risky assumptions. Improvement of predictions of cake detachment will require better understanding of flow dynamics inside the membrane modules and will allow to improve our understanding of membrane clogging and will enable us to further reduce the energy consumption for coarse bubble aeration.

With regards to the links between biopolymer production and membrane fouling it is just a mere hypothesis that SMP causes irreversible fouling whilst EPS is responsible for reversible fouling. In fact these two hypotheses may be entirely wrong as the relationships between SMP, EPS and different fouling mechanisms are likely to be more complicated and thus need to be further investigated. Moreover, although the benchmark model presented here assumes that SMP rejection by the membrane is constant, SMP rejection and permeation through the membrane is likely to vary in time due to changing MWD of the SMP and changing rejection properties of the membrane, dynamic layer and cake. Although Song et al. [226] derived a relationship between SMP rejection and SRT, their model is purely empirical and the underlying mechanisms causing such effects need to be better understood. Rejective properties of the membrane are of utmost importance as they are found to have a dominant effect on the effluent chemical oxygen demands (CODs) and SMP concentrations in the bulk liquid, hence the bulk liquid's fouling propensity.

The list of unknowns when it comes to modelling MBRs is vast and hence much

more fundamental research, modelling and especially validation are required to ensure that the models reflect reality. All of the research presented in this thesis is preliminary and will require far more efforts in order to provide definite answers in relation to derivation of optimum operating strategies and design of more energy-efficient reactors, i.e. the aims set out in the beginning of this thesis. However, it creates a reference framework for other researchers to continue the work on modelling and simulation of MBR reactors.

The most urging research questions and tasks are presented in a list below.

1. SMP and EPS mechanisms need to be better understood especially with regards to their production in response to dynamic changes in influent composition and operating conditions.
2. The biopolymer kinetics need to be identified on the data obtained from MBR processes operating on real sewage using full ASM models.
3. Calibration protocols for the developed biopolymer ASM models need to be developed to assist the modellers with design of experiments and subsequent model identification.
4. Fouling strengths of different groups of SMP need to be measured under various operating conditions and process configurations to identify whether different observed strengths of SMP are due to differences in their chemical compositions or different MWDs.
5. As SMP retention on the membrane is found to have a dominant effect on effluent CODs and bulk liquid SMP concentrations in the bioreactor, it is vital that retentive properties of the membrane are investigated and the findings are encapsulated within a mathematical model in order to improve the accuracy of integrated MBR models in terms of irreversible fouling and effluent COD levels. It is hypothesized that SMP retention on the membrane is in a function of its MWD and molecular weight (MW) cutoff of the membrane, dynamic layer and the cake.
6. From the point of view of modelling pore constriction, pore blockage and cake formation mechanisms it is important to answer the question whether pore constriction stops after the pores have been blocked or whether it still occurs in the pores, although at lower rates due to pre-filtering effects of the cake and the pore blocking layer.
7. Hydraulic models of air-water flow in membrane modules need to be created and validated to allow better predictions of membrane clogging and cake detachment.
8. Modelling and identification of passive adsorption, gel layer formation and biofilm growth mechanisms in MBRs need to be carried out such that these processes can be included in the fouling models and their effects can be quantitatively compared against the effects of the so-called classical fouling mechanisms: pore constriction, pore blockage and cake formation.
9. Integrated MBR models need to be calibrated and validated on the measurements obtained from full scale WWTPs treating real sewage.

10. After calibration and validation the benchmark model needs to be extended with irreversible fouling control mechanisms such as cleaning in place (CiP) and simulated over longer time horizons such as in the BSM1_LT model of Rosen et al. [212] in order to properly quantify the effects of irreversible fouling on the overall operational expenditures (OPEX).

Bibliography

[1] Zubair Ahmed, Jinwoo Cho, Byung-Ran Lim, Kyung-Guen Song, and Kyu-Hong Ahn. Effects of sludge retention time on membrane fouling and microbial community structure in a membrane bioreactor. *Journal of Membrane Science*, 287: 211–218, 2007.

[2] Y. T. Ahn, Y. K. Choi, H. S. Jeong, S. R. Chae, and H. S. Shin. Modeling of extracellular polymeric substances and soluble microbial products production in a submerged membrane bioreactor at various SRTs. *Water Science and Technology*, 53(7):209–216, 2006.

[3] J. Alex, G. Kolisch, and K. Krause. Model structure identification for wastewater simulation based on computational fluid dynamics. *Water Science and Technology*, 45(4-5):325–334, 2002.

[4] F.W. Altena and G. Belfort. Lateral migration of spherical particles in porous flow channels: Application to membrane filtration. *Chemical Engineering Science*, 39:343–355, 1984.

[5] Justus Altmann and Siegfried Rippergen. Particle deposition and layer formation at the crossflow microfiltration. *Journal of Membrane Science*, 124:119–128, 1997.

[6] S. Aquino and D. Stuckey. Production of soluble microbial products (SMP) in anaerobic chemostats under nutrient deficiency. *Journal of Environmental Engineering*, 129(11):1007–1014, 2003.

[7] Sergio F. Aquino and David C. Stuckey. Integrated model of the production of soluble microbial products (SMP) and extracellular polymeric substances (EPS) in anaerobic chemostats during transient conditions. *Biochemical Engineering Journal*, 38:138–146, 2008.

[8] Duncan J. Barker and David C. Stuckey. A review of soluble microbial products (SMP) in wastewater treatment systems. *Water Research*, 33(14):3063–3082, 1999. ISSN 0043-1354.

[9] P.S. Barker and P.L. Dold. General model for biological nutrient removal activated sludge systems: Model presentation. *Water Environment Research*, 69:969–984, 1997.

[10] P.S. Barker and P.L. Dold. General model for biological nutrient removal activated sludge systems: Model application. *Water Environment Research*, 69:985–991, 1997.

[11] Gaetano Di Bella, Georgio Mannina, and Gaspare Viviani. An integrated model for physical-biological wastewater organic removal in a submerged membrane bioreactor: Model development and parameter estimation. *Journal of Membrane Science*, 322:1–12, 2008.

[12] K.H. Bendiksen. On the motion of long bubbles in vertical tubes. *International Journal of Multiphase Flow*, 11:797–812, 1985.

[13] Lutz Böhm, Anja Drews, Helmut Prieske, Pierre R. Bérubé, and Matthias Kraume. The importance of fluid dynamics for MBR fouling mitigation. *Bioresource Technology*, 122(0):50 – 61, 2012. ISSN 0960-8524.

[14] A.J. Bosma and B.A. Reitsma. Hydraulic design of activated sludge tanks with CFD. In *Proceedings of the COMSOL Users Conference 2007 Grenoble*, 2007.

[15] C. Brepols, H. Schafer, and N. Engelhardt. Considerations on the design and financial feasibility of full-scale membrane bioreactors for municipal applications. *Water Science and Technology*, 61(10):2461–2468, 2010.

[16] H.C. Brinkmann. A calculation of the viscous force exerted by a flowing fluid on a dense swarm of particles. *Applied Science Research*, A1:27–35, 1947.

[17] A. Broeckmann, J. Busch, T. Wintgens, and W. Marquardt. Modeling of pore blocking and cake layer formation in membrane filtration for wastewater treatment. *Desalination*, 189(1-3):97–109, 2006. ISSN 0011-9164. Selected paper from the 10th Aachen Membrane Colloquium.

[18] R. Brun, M. Kuehni, H. Siegrist, W. Gujer, and P. Reichert. Practical identifiability of ASM2d parameters - systematic selection and tuning of parameter subsets. *Water Research*, 36(16):4113–4127, 2002.

[19] Jan Busch, Andreas Cruse, and Wolfgang Marquardt. Modeling submerged hollow-fiber membrane filtration for wastewater treatment. *Journal of Membrane Science*, 288(1-2):94 – 111, 2007. ISSN 0376-7388.

[20] S. Chae, Y. Ahn, S. Kang, and H. Shin. Mitigated membrane fouling in a vertical submerged membrane bioreactor (VSMBR). *Journal of Membrane Science*, 280 (1-2):572–581, 2006.

[21] S.R. Chae and H.S. Shin. Kinetic estimation of low excess sludge and extracellular polymeric substance accumulation in a vertical submerged membrane bioreactor (VSMBR). *Water Practice and Technology*, 1(3):18–36, 2006.

[22] E.Y. Chang and A. Acrivos. The effective permeability of a random dispersion of spheres. *Physico Chemical Hydrodynamics*, 10:579, 1988.

[23] In-Soung Chang, Pierre Le Clech, Bruce Jefferson, and Simon Judd. Membrane fouling in membrane bioreactors for wastewater treatment. *Journal of Environmental Engineering*, 128(11):1018–1029, 2002.

[24] Ivan Chang, Eric S. Gilbert, Natalya Eliashberg, and Jay D. Keasling. A three-dimensional, stochastic simulation of biofilm growth and transport-related factors that affect structure. *Microbiology*, 149:2859–2871, 2003.

[25] Lin Chen, Yu Tian, Chuqing Cao, Sai Zhang, and Shuai Zhang. Sensitivity and uncertainty analyses of an extended ASM3-SMP model describing membrane bioreactor operation. *Journal of Membrane Science*, 389:99–109, 2012.

[26] C. Chiemchaisri, Y.K. Wong, T. Urase, and K. Yamamoto. Organic stabilisation and nitrogen removal in a membrane separation bioreactor for domestic wastewater treatment. *Filtration & Separation*, 30(3):247–240, 1993. ISSN 0015-1882.

[27] B.D. Cho and A.G. Fane. Fouling transients in nominally sub-critical flux operation of a membrane bioreactor. *Journal of Membrane Science*, 209(2):391–403, 2002.

[28] Jin Woo Cho, Kyu Hong Ahn, Youngwoo Seo, and Y. Lee. Modification of ASM No.1 for a submerged membrane bioreactor system: Including the effects of soluble microbial products (SMP) on membrane fouling. *Water Science and Technology*, 47(12):177–181, 2001.

[29] Jinwoo Cho, Kyung-Guen Song, and Kyu-Hong Ahn. The activated sludge and microbial substances influences on membrane fouling in submerged membrane bioreactor: unstirred batch cell test. *Desalination*, 183:425–429, 2005.

[30] Hyeok Choi, Kai Zhang, Dionysios D. Dionysiou, Daniel B. Oerther, and George A. Sorial. Effect of permeate flux and tangential flow on membrane fouling for wastewater treatment. *Separation and Purification Technology*, 45(1):68–78, 2005. ISSN 1383-5866.

[31] Jan Chudoba. Inhibitory effect of refractory organic compounds produced by activated sludge micro-organisms on microbial activity and flocculation. *Water Research*, 19(2):197–200, 1985. ISSN 0043-1354.

[32] Jan Chudoba. Quantitative estimation in COD units of refractory organic compounds produced by activated sludge microorganisms. *Water Research*, 19(1): 37–43, 1985.

[33] K. Cierkens, I. Nopens, W. De Keyser, S. Van Hulle, S. Plano, E. Torfs, Y. Amerlinck, L. Benedetti, A. van Nieuwenhuijzen, S. Weijers, and J. De Jonge. Integrated model-based optimisation at the WWTP of Eindhoven. *Water Practice & Technology*, 7(2), 2012.

[34] R. Collins, F.F. De Moraes, J.F. Davidson, and D. Harrison. The motion of a large gas bubble rising through liquid flowing in a tube. *Journal of Fluid Mechanics*, 89:497–514, 1978.

[35] Sophie Comte, Gilles Guibaud, and Michel Baudu. Biosorption properties of extracellular polymeric substances (EPS) resulting from activated sludge according to their type: Soluble or bound. *Process Biochemistry*, 41(4):815–823, 2006. ISSN 1359-5113.

[36] J. B. Copp. *The COST simulation benchmark - description and simulator manual.* Luxembourg: Office for Official Publicatios of the European Communities, 2002. ISBN: 92-894-1658-0.

[37] COST624. Cost action 624 website, http://www.ensic.inpl-nancy.fr/costwwtp, 2002.

[38] J. W. Costerton. Microbial biofilms. *Cambridge University Press*, pages 282–300, 1995.

[39] H. Czichos. *Die Grundlagen der Ingenieursissenschaften.* Springer, Berlin, Heidelberg, New York, 1996.

[40] M. W. Deen. Hindered transport of large molecules in liquid-filled pores. *AIChE Journal*, 33(9):1409–1425, 1987.

[41] F. Delrue, JM. Choubert, AE. Stricker, M. Sperandino, M. Miletton-Peuchot, and Y. Racault. Modelling a full scale membrane bioreactor using Activated Sludge Model No.1: challenges and solutions. *Water Science and Technology*, 62(10): 2205–2217, 2010.

[42] Z. Do-Quang, A. Cockx, A. Liné, and M. Roustan. Computational fluid dynamics applied to water and wastewater treatment facility modeling. *Environmental Engineering and Policy*, 1(3):137–147, July 1999.

[43] P.L. Dold, P.M. Fairlamb, R. Jones, I. Takács, and S. Murthy. Sidestream modelling incorporated into whole plant simulation. In *Clonic Workshop, Barcelona, Spain*, 2007.

[44] A. Drews, M. Vocks, U. Bracklow, V. Iversen, and M. Kraume. Does fouling in MBRs depend on SMP? *Desalination*, 231(1-3):141–149, 2008. ISSN 0011-9164. Selected Papers Presented at the 4th International IWA Conference on Membranes for Water and Wastewater Treatment, 15-17 May 2007, Harrogate, UK. Guest Edited by Simon Judd; and Papers Presented at the International Workshop on Membranes and Solid-Liquid Separation Processes, 11 July 2007, INSA, Toulouse, France. Guest edited by Saravanamuthu Vigneswaran and Jaya Kandasamy.

[45] Anja Drews. Membrane fouling in membrane bioreactors - characterisation, contradictions, cause and cures. *Journal of Membrane Science*, 361:1–28, 2010.

[46] Anja Drews, Chung-Hak Lee, and Matthias Kraume. Membrane fouling - a review on the role of EPS. *Desalination*, 200(1-3):186–188, 2006. ISSN 0011-9164. Euromembrane 2006.

[47] Anja Drews, Jan Mante, Vera Iversen, Martin Vocks, Boris Lesjean, and Matthias Kraume. Impact of ambient conditions on SMP elimination and rejection in MBRs. *Water Research*, 41(17):3850–3858, 2007.

[48] Anja Drews, Helmut Prieske, Eva-Lena Meyer, Gerrit Senger, and Matthias Kraume. Advantageous and detrimental effects of air sparging in membrane filtration: Bubble movement, exerted shear and particle classification. *Desalination*, 250:1083–1086, 2010.

[49] M. Dubois, KA Giles, PA Rebers, and F Smith. Colorimetric method for determination of sugar and related substances. *Analytical Chemistry*, 28:350–356, 1956.

[50] Chase Duclos-Orsello, Weiyi Li, and Chia-Chi Ho. A three mechanism model to describe fouling of microfiltration membranes. *Journal of Membrane Science*, 280 (1-2):856–866, 2006. ISSN 0376-7388.

[51] E.C. Eckstein, D.G. Bailey, and A.H. Shapiro. Self diffusion of particles in shear flow of a suspension. *Journal of Fluid Mechanics*, 79:191–208, 1977.

[52] Envirosim. Company website, 2012. URL `http://www.envirosim.com`.

[53] B. Espinasse, P. Bacchin, and P. Aimar. On an experimental method to measaure critical flux in ultrafiltration. *Desalination*, 146:91–96, 2002.

[54] M.E. Fabiyi and R. Novak. Evaluation of the factors that impact successful membrane biological reactor ooperation at high solids concentration. *Proceedings of the Water Environment Federation*, 1:503–512, 2008.

[55] J. Fabre and A. Liné. Modeling of two-phase slug flow. *Annual Review of Fluid Mechanics*, 24:21–46, 1992.

[56] C. Fall, MA. Espinosa-Rodriguez, N. Flores-Alamo, MC. van Loosdrecht, and CM Hooijmans. Stepwise calibration of the Activated Sludge Model No. 1 at a partially denitrifying large wastewater treatment plant. *Water Environment Research*, 83(11):2036–2048, 2011.

[57] A. Fenu, G. Guglielmi, J. Jimenez, M. Spèrandio, D. Saroj, B. Lesjean, C. Brepols, C. Thoeye, and I. Nopens. Activated sludge model (ASM) based modelling of membrane bioreactor (MBR) processes: A critical review with special regard to MBR specificities. *Water Research*, 44(15):4272–4294, 2010. ISSN 0043-1354.

[58] A. Fenu, J. Roels, T. Wambecq, K. De Gussem, C. Thoeye, G. De Gueldre, and B. Van De Steene. Energy audit of a full-scale MBR system. *Desalination*, 1-3: 121–128, 2010.

[59] R.C. Fernandes, R. Semiat, and A.E. Dukler. Hydrodynamic model for gas liquid slug flow in vertical tubes. *AIChE Journal*, 29:981–989, 1983.

[60] Claudia Fesch, Werner Simon, Stefan B. Haderlein, Peter Reichert, and Rene P. Schwarzenbach. Nonlinear sorption and nonequilibrium solute transport in aggregated porous meia: Experiments, process indenfitication and modeling. *Journal of Contaminant Hydrology*, 31:373–407, 1998.

[61] Robert W. Field and Graeme K. Pearce. Critical, sustainable and threshold fluxes for membrane filtration with water industry applications. *Advances in Colloid and Interface Science*, 164(1–2):38 – 44, 2011. ISSN 0001-8686.

[62] R.W. Field, D. Wu, J.A. Howell, and B.B. Gupta. Critical flux concept for microfiltration fouling. *Journal of Membrane Science*, 100:259–272, 1995.

[63] Hans-Kurt Flemming and Swami Amano. *Biofouling bei Membranprozessen*. Springer, Berlin, 1995.

[64] M.C. Flickinger and S.W. Drew. *Encyclopedia of bioprocess technology: fermentation, biocatalysis, and bioseparation*. Number 4 in Wiley biotechnology encyclopedias. John Wiley, 1999. ISBN 9780471138228.

[65] Greg Foley, Dermot M. Malone, and Frank MacLoughlin. Modelling the effects of particle polydispersity in crossflow filtration. *Journal of Membrane Science*, 99 (1):77–88, 1995. ISSN 0376-7388.

[66] B. Frølund, R. Palmgren, K. Keiding, and P.H. Nielsen. Extraction of extracellular polymers from activated sludge using cation exchange resin. *Water Research*, 30 (8):1749–1758, 1996.

[67] Noah I. Galil and Lila Jacob. Comparative characterization of biosolids from a membrane bioreactor and from a sequencing batch reactor. *Environmental Engineering Science*, 26(5), 2009.

[68] Gunther Gehlert, Mariati Abdulkadir, Jan Fuhrmann, and Jobst Hapke. Dynamic modeling of an ultrafiltration module for use in a membrane bioreactor. *Journal of Membrane Science*, 248(1-2):63–71, 2005. ISSN 0376-7388.

[69] E. Germain, F. Nelles, A. Drews, P. Pearce, M. Kraume, E. Reid, S.J. Judd, and T. Stephenson. Biomass effects on oxygen transfer in membrane bioreactors. *Water Research*, 41(5):1038–1044, 2007.

[70] Krist V Gernaey, Mark C.M van Loosdrecht, Mogens Henze, Morten Lind, and Sten B Jørgensen. Activated sludge wastewater treatment plant modelling and simulation: state of the art. *Environmental Modelling & Software*, 19(9):763–783, 2004. ISSN 1364-8152. Environmental Sciences and Artificial Intelligence.

[71] Ali Hadi Ghawi and Jozef Kriš. A Computational Fluid Dynamics Model of Flow and Settling in Sedimentation Tanks. In Prof. Hyoung Woo Oh, editor, *Applied Computational Fluid Dynamics*. 2012.

[72] Eugenio Giraldo and Mark LeChevalier. Dynamic mathematical modeling of membrane fouling in submerged membrane bioreactors. In *WEFTEC*, 2006.

[73] Global Industry Analysts. Global MBR market forecast to reach 888 million US Dollars by 2017. *Membrane Technology*, 2012(1):8, 2012.

[74] Rajeev Goel, Jacek Mąkinia, Oliver Schraa, Spencer Snowling, and Hank Andres. Modeling pH Dynamics in the Nutrient Removal Activated Sludge Process. In *Proceedings of the Water Environment Federation, WEFTEC 2010: Session 11 through Session 20*, number 9, pages 733–741, 2010.

[75] Simon L Goren. The hydrodynamic force resisting the approach of a sphere to a plane permeable wall. *Journal of Colloid and Interface Science*, 69(1):78 – 85, 1979. ISSN 0021-9797.

[76] J.R. Grace and R. Clift. Dependence of slug rise velocity on tube Reynolds number in vertical gas-liquid flow.matsuo. *Chemical Engineering Science*, 34:1348–1350, 1979.

[77] G. Green and G. Belfort. Fouling of ultrafiltration membranes: Lateral migration and the particle trajectory model. *Desalination*, 35:129–147, 1980.

[78] Patricia Grelier, Sandra Rosenberger, and Annie Tazi-Pain. Influence of sludge retention time on membrane bioreactor hydraulic performance. *Desalination*, 192 (1-3):10–17, 2006. ISSN 0011-9164. International Congress on Membranes and Membrane Processes.

[79] Willi Gujer, Mogens Henze, Takahashi Mino, and Mark van Loosdrecht. Activated Sludge Model No. 3. *Water Science and Technology*, 39(1):183–193, 1999. ISSN 0273-1223.

[80] V. Gulas, M. Bond, and L. Benefield. Use of extracellular polymers for thickening and dewatering activated sludge. *Journal of Water Pollution Control Federation*, 51(4):798–807, 1979.

[81] Berthold Günder. *The membrane-coupled activated sludge process in municipal wastewater treatment.* Technomic Publishing Company, 2001. ISBN 9781566769594.

[82] J.S. Halow. Incipient rolling, sliding and suspension of particles in horizontal and inclined turbulent flow. *Chemical Engineering Science*, 28:1–12, 1973.

[83] Xiaodi Hao, Qilin Wang, Yali Cao, and Mark C.M. van Loosdrecht. Evaluating sludge minimization caused by predation and viral infection based on the extended Activated Sludge Model No. 2d. *Water Research*, 45(16):5130–5140, 2011. ISSN 0043-1354.

[84] T. Z. Harmathy. Velocity of large drops and bubbles in media of infinite or restricted extent. *AIChE Journal*, 6:281–288, 1960.

[85] Mogens Henze, C. Grady, Willi Gujer, G. Marais, and Tomonori Matsuo. A general model for single-sludge wastewater treatment systems. *Water Resources*, 21(5):505–515, 1987.

[86] Mogens Henze, C. Grady, Willi Gujer, G. Marais, and Tomonori Matsuo. Activated Sludge Model No. 1. Technical Report No. 1, IAWQ Scientific and Technical Report, London, 1987.

[87] Mogens Henze, Willi Gujer Takahashi Mino, Mark C. Wentzel, Tomonori Matsuo, and G Marais. Activated Sludge Model No. 2. Technical Report No. 3, IAWQ Scientific and Technical Report, London, 1995.

[88] Mogens Henze, Willi Gujer, Takahashi Mino, Tomonori Matsuo, Mark C. Wentzel, Gerrit v.R. Marais, and Mark C.M van Loosdrecht. Activated Sludge Model No. 2d, ASM2d. *Water Science and Technology*, 39(1):165–182, 1999.

[89] Mogens Henze, Willi Gujer, Takashi Mino, and Mark van Loosdrecht. *Activated sludge models ASM1, ASM2, ASM2d and ASM3.* IWA Publishing, 2000.

[90] Slawomir W. Hermanowicz. A simple 2D biofilm model yields a variety of morphological features. *Mathematical Biosciences*, 169:1–14, 2001.

[91] J. Hermia. Consant pressure blocking filtration laws - application to power-law non-newtonian fluids. *Transactions of the Institution of Chemical Engineers*, 60 (3):183–187, 1982.

[92] Winslow Herschel and Ronal Bulkley. Konsistenzmessungen von gummibenzollösungen. *Colloid and Polymer Science*, 39:291–300, 1926. ISSN 0303-402X.

[93] G.F. Hewitt and D.N. Roberts. Studies of two phase flow patterns by simultaneous X-ray and flash photography. Technical report, UKAEA Report No. AERE-M2159., 1969.

[94] Zakir M. Hirani, James F. DeCarolis, Samer S. Adham, and Joseph G. Jacangelo. Peak flux performance and microbial removal by selected membrane bioreactor systems. *Water Research*, 44(8):2431 – 2440, 2010. ISSN 0043-1354.

[95] M. Hlavacek and F. Bouchet. Constant flowrate blocking laws and an example of their application to dead-end microfiltration of protein solutions. *Journal of Membrane Science*, 82(3):285–295, 1993.

[96] Ho and Zydney. A combined pore blockage and cake filtration model for protein fouling during microfiltration. *Journal of Colloid Interface Science*, 232(2):389–399, Dec 2000.

[97] Chia-Chi Ho and Andrew L. Zydney. Overview of fouling phenomena and modeling approaches for membrane bioreactors. *Separation Science and Technology*, 41:1231–1251, June 2006.

[98] PT Hoa, L Nair, and C Visvanathan. The effect of nutrients on extracellular polymeric substance production and its influence on sludge properties. *Water SA*, 29(Part 4):437–442, 2003.

[99] R.I. Hogg, T.W. Healy, and D.W. Fuerstenau. Mutual coagulation of colloidal dispersions. *Transactions of the Faraday Society*, 62:1638, 1966.

[100] Ladan Holakoo, George Nakhla, Amarjeet S. Bassi, and Ernest K. Yanful. Long term performance of MBR for biological nitrogen removal from synthetic municipal wastewater. *Chemosphere*, 66(5):849–857, 2007. ISSN 0045-6535.

[101] K. M. Hsieh, G. A. Murgel, L. W. Lion, and M. L. Shuler. Interactions of microbial biofilms with toxic trace metals: 2. prediction and verification of an integrated computer model of lead (II) distribution in the presence of microbial activity. *Biotechnology & Bioengineering*, 44(2):232–239, Jun 1994.

[102] K. M. Hsieh, G. A. Murgel, L. W. Lion, and M. L. Shulera. Interactions of microbial biofilms with toxic trace metals: 1. observation and modeling of cell growth, attachment, and production of extracellular polymer. *Biotechnology & Bioengineering*, 44(2):219–231, Jun 1994.

[103] Guangtuan Huang, Gang Jin, Jinghui Wu, and Yongdi Liu. Effects of glucose and phenol on soluble microbial products (SMP) in sequencing batch reactor systems. *International Biodeterioration & Biodegradation*, 62(2):104–108, 2008. ISSN 0964-8305.

[104] Xia Huang, Rui Liu, and Yi Qian. Behaviour of soluble microbial products in a membrane bioreactor. *Process Biochemistry*, 36(5):401–406, 2000. ISSN 1359-5113.

[105] Kuo-Jen Hwang and Fung-Fu Chen. Interpretation of particle fouling in submerged membrane filtration by blocking models. *Tamkang Journal of Science and Engineering*, 12(1):9–16, 2009.

[106] Kuo-Jen Hwang and Hsieng-Chia Chen. Selective deposition of fine particles in constant-flux submerged membrane filtration. *Chemical Engineering Journal*, 157 (2–3):323–330, 2010. ISSN 1385-8947.

[107] Kuo-Jen Hwang, Chien-Yao Liao, and Kuo-Lun Tung. Analysis of particle fouling during microfiltration by use of blocking models. *Journal of Membrane Science*, 287:287–293, 2007.

[108] Hydromantis. Company website, 2012. URL `http://www.hydromantis.com/GPS-X.html`.

[109] *GPS-X 4.1 Technical Reference*. Hydromantis Inc., June 2003.

[110] Ilenia Iacopozzi, Valentina Innocenti, Stefano Marsili-Libelli, and Elisabetta Giusti. A modified Activated Sludge Model No. 3 (ASM3) with two-step

nitrification–denitrification. *Environmental Modelling & Software*, 22(6):847–861, 2007. ISSN 1364-8152.

[111] Tomasz Janus and Bogumil Ulanicki. Modelling SMP and EPS formation and degradation kinetics with an extended ASM3 model. *Desalination*, 261(1-2):117–125, 2010.

[112] Tomasz Janus, David Burt, Anna Taylor, and Vincent Glancy. Application of CFD and dynamic process simulation for retroffitting of a 800,000 PE trickling filter WWTP. In *1st European Water and Wastewater Management Conference, Aquaenviro, Newcastle*, 2007.

[113] K.J. Jeon and Y.W. Jung. A simulation study on the compression behaviour of dust cakes. *Powder Technology*, 141:1–11, 2004.

[114] T. Jiang, X. Liu, MD. Kennedy, JC. Schippers, and PA. Vanrolleghem. Calibrating a side-stream membrane bioreactor using Activated Sludge Model No. 1. *Water Science and Technology*, 52(10-11):359–367, 2005.

[115] Tao Jiang, Silvie Myngheer, Dirk J.W. De Pauw, Henri Spanjers, Ingmar Nopens, Maria D. Kennedy, Gary Amy, and Peter A. Vanrolleghem. Modelling the production and degradation of soluble microbial products (SMP) in membrane bioreactors (MBR). *Water Research*, 42(20):4955–4964, 2008. ISSN 0043-1354.

[116] Simon Judd. *The MBR Book - Principles and Applications of Membrane Bioreactors for Water and Wastewater Treatment*. Number 978-0-08-096682-3. Butterworth-Heinemann, 2nd edition, 2011.

[117] David Kaelin, Reto Manser, Leiv Rieger, Jack Eugster, Karin Rottermann, and Hansruedi Siegrist. Extension of ASM3 for two-step nitrification and denitrification and its calibration and validation with batch tests and pilot scale data. *Water Research*, 43(6):1680–1692, 2009. ISSN 0043-1354.

[118] J. Kaulitzky. *Untersuchungen zur Regeneration herkömmlicher und neuartiger Filtermaterialen zur Tiefenfiltration trübstoffhaltiger Wässer*. PhD thesis, Energie-, Machinen- und Fertigungstechnik, Gerhard-Mercator-Universität, Duisburg, 1999.

[119] Jens Peter Kerrn-Jespersen and Mogens Henze. Biological phosphorus uptake under anoxic and aerobic conditions. *Water Research*, 27(4):617–624, 1993. ISSN 0043-1354.

[120] Albert S. Kim and Yuewei Liu. Critical flux of hard sphere suspensions in crossflow filtration: Hydrodynamic force bias Monte Carlo simulations. *Journal of Membrane Science*, 323(1):67–76, 2008. ISSN 0376-7388.

[121] Jae-Seok Kim, Chung-Hak Lee, and In-Soung Chang. Effect of pump shear on the performance of a crossflow membrane bioreactor. *Water Research*, 35(9): 2137–2144, 2001. ISSN 0043-1354.

[122] J.S. Kim, W.Y. Ahn, and C.H. Lee. Comparison of ultrafiltration characteristics between attached and suspended growth microorganisms in submerged membrane bioreactor. *Water Research*, 35(10):2435, 1998.

[123] Rober Kjellstrand. Hydraulic behaviour in an activated sludge tank - from tracer test through hydraulic modelling to full-scale implementation. Thesis for the degree of licenciate in engineering, Department of Chemical Reaction Engineering, Chalmers University of Technology, Göteborg, Sweden, 2006.

[124] Jeffrey S. Knutsen and Robert H. Davis. Deposition of foulant particles during tangential flow filtration. *Journal of Membrane Science*, 271(1–2):101–113, 2006. ISSN 0376-7388.

[125] Teuvo Kohonen. *Self-Organizing Maps*. Springer Series in Information Sciences. Springer-Verlag GmbH, 2001.

[126] W.J. Koros, Y.H. Ma, and T. Shimidzu. Terminology for membranes and membrane processes. *International Union of Pure and Applied Chemistry*, 68:1479–1489, 1996.

[127] J. Krampe and K. Krauth. Oxygen transfer into activated sludge with high MLSS concentrations. *Water Science and Technology*, 47:297–303, 2003.

[128] K. Krauth and K.F. Staab. Pressurized bioreactor with membrane filtration for wastewater treatment. *Water Resources*, 27:405–411, 1993.

[129] W. C. Kuo. *Production of soluble microbial chelators and their impact on anaerobic treatment*. PhD thesis, University of Iowa, Iowa City, 1993.

[130] G.J. Kynch. A theory of sedimentation. *Transactions of the Faraday Society*, 48: 166–176, 1952.

[131] G Ladiges and NP Bertram. Optimisation of Hamburg's wastewater treatment plants - three years of experience with the new concept. *Water Science and Technology*, 50(7):45–48, 2004.

[132] G Ladiges and C Günner. Theoretical and prectical results of the optimisation of hamburg's WWTPs with dynamic simulation. *Water Science and Technology*, 47 (12):27–33, 2003.

[133] J.C. Lagarias, J. A. Reeds, M. H. Wright, and P. E. Wright. Convergence Properties of the Nelder-Mead Simplex Method in Low Dimensions. *SIAM Journal of Optimization*, 9:112–147, 1998.

[134] L. Lapidus and N.R. Amundson. Mathematics of adsorption beds: VI. the effect of longitudinal diffusion in ion exchange and chromatographic columns. *Journal of Physical Chemistry*, 56:984–988, 1952.

[135] Chrysi S. Laspidou and Bruce E. Rittmann. A unified theory for extracellular polymeric substances, soluble microbial products, and active and inert biomass. *Water Research*, 36(11):2711–2720, 2002. ISSN 0043-1354.

[136] Chrysi S. Laspidou and Bruce E. Rittmann. Non-steady state modeling of extracellular polymeric substances, soluble microbial products, and active and inert biomass. *Water Research*, 36(8):1983–1992, 2002. ISSN 0043-1354.

[137] Pierre Le-Clech, Bruce Jefferson, In Soung Chang, and Simon J. Judd. Critical flux determination by the flux-step method in a submerged membrane bioreactor. *Journal of Membrane Science*, 227:81–93, 2003.

[138] Pierre Le-Clech, Vicki Chen, and Tony A.G. Fane. Fouling in membrane bioreactors used in wastewater treatment. *Journal of Membrane Science*, 284(1-2):17–53, 2006. ISSN 0376-7388.

[139] D. J. Lee and C. H. Wang. Theories of cake filtration and consolidation and implications to sludge dewatering. *Water Research*, 34(1):1–20, 2000. ISSN 0043-1354.

[140] Yonghun Lee, Jinwoo Cho, Youngwoo Seo, Jae Woo Lee, and Kyu-Hong Ahn. Modeling of submerged membrane bioreactor process for wastewater treatment. *Desalination*, 146(1-3):451–457, 2002. ISSN 0011-9164.

[141] D. Leighton and A. Acrivos. Measurement of shear-induced self-diffusion in concentrated suspensions of spheres. *Journal of Fluid Mechanics*, 177:109–131, 1987.

[142] D. Leighton and A. Acrivos. The shear-induced migration of particles in concentrated suspensions. *Journal of Fluid Mechanics*, 181:415–430, 1987.

[143] B. Lesjean, S. Rosenberger, C. Laabs, M. Jekel, R. Gnirss, and G. Amy. Correlation between membrane fouling and soluble/colloidal organic substances in membrane bioreactors for municipal wastewater treatment. *Water Science and Technology*, 51:1–8, 2005.

[144] R. Leudeking and EL. Piret. A kinetic study of lactic acid fermentation. *Journal of Biochemical and Microbiological Technology and Engineering*, 1:393–412, 1959.

[145] W.K. Lewis and W.G. Whitman. Principles of gas absorption. *Industrial and Engineering Chemistry*, 16:1215–1220, 1924.

[146] Jianfeng Li, Fenglin Yang, Yaozhong Li, Fook-Sin Wong, and Hwee Chuan Chua. Impact of biological constituents and properties of activated sludge on membrane fouling in a novel submerged membrane bioreactor. *Desalination*, 225:356–365, 2008.

[147] Xiao-Yan Li and Xiao-Mao Wang. Modelling of membrane fouling in a submerged membrane bioreactor. *Journal of Membrane Science*, 278:151–161, 2006.

[148] Xiao-Yan Li and Yuan Yuan. Collision frequencies of microbial aggregates with small particles by differential sedimentation. *Environmental Science & Technology*, 36(3):387–393, Feb 2002.

[149] Shuang Liang, Lianfa Song, Guihe Tao, Kiran Arun Kekre, and Harry Seah. A modeling study of fouling development in membrane bioreactors for wastewater treatment. *Water Environment Research*, 78(8):857–863, Aug 2006.

[150] B. Q. Liao, D. G. Allen, I. G. Droppo, G. G. Leppard, and S. N. Liss. Surface properties of sludge and their role in bioflocculation and settleability. *Water Research*, 35(2):339–350, 2001. ISSN 0043-1354.

[151] B. Q. Liao, D. G. Allen, G. G. Leppard, I. G. Droppo, and S. N. Liss. Interparticle interactions affecting the stability of sludge flocs. *Journal of Colloid and Interface Science*, 249(2):372–380, 2002. ISSN 0021-9797.

[152] Dennis R. Liles. Two-phase flow (in reactors). Technical report, Los Alamos Technical Reports DVD 1, http://www.fas.org/sgp/othergov/doe/lanl/index1b.html, 1977.

[153] C. Linden, F.B. Frechen, and W. Schier. Pre-treatment of municipal MBR applications. *Desalination*, 231:108–114, 2008.

[154] Y. Liu and H.H.P. Fang. Influence of extracellular polymeric substances (EPS) on flocculation, settling, and dewatering of activated sludge. *Critical Reviews in Environmental Science and Technology*, 33:237–273, 2003.

[155] B.E. Logan. *Environmental Transport Processes*. Wiley, New York, 1999.

[156] O.H. Lowry, N.J. Rosenbrough, A.L. Farr, and R.J. Randall. Protein measurement with the folin phenol reagent. *Journal of Biology and Chemistry*, 193:265–275, 1951.

[157] S. G. Lu, T. Imai, M. Ukita, M. Sekine, T. Higuchi, and M. Fukagawa. A model for membrane bioreactor process based on the concept of formation and degradation of soluble microbial products. *Water Research*, 35(8):2038–2048, 2001. ISSN 0043-1354.

[158] C. Lubello, S. Caffaz, R. Gori, and G. Munz. A modified activated sludge model to estimate solids production at low and high solids retention time. *Water Research*, 43(18):4539–4548, 2009. ISSN 0043-1354.

[159] M.R. Mackley and N.E. Sherman. Crossflow filtration mechanisms and kinetics. *Chemical Engineering Science*, 47:2085–3067, 1992.

[160] Thomas Maere, Bart Verrecht, Stefanie Moerenhout, Simon Judd, and Ingmar Nopens. BSM-MBR: A benchmark simulation model to compare control and operational strategies for membrane bioreactors. *Water Research*, 45(6):2181–2190, 2011. ISSN 0043-1354.

[161] T. Maly and L.R. Petzold. Numerical methods and software for sensitivity analysis of differential-algebraic systems. *Applied Numerical Mathematics*, 20:57–79, 1996.

[162] Giorgio Mannina, Alida Cosenza, Peter A. Vanrolleghem, and Gaspare Viviani. A practical protocol for calibration of nutrient removal wastewater treatment models. *Journal of Hydroinformatics*, 13.4:575–595, 2011.

[163] Giorgio Mannina, Gaetano di Bella, and Gaspare Viviani. An integrated model for biological and physical process simulation in membrane bioreactors (MBRs). *Journal of Membrane Science*, 376:56–69, 2011.

[164] S.C. McCutcheon, J.L Martin, and T.O. Jr. Barnwell. *David R. Maidment - Handbook of Hydrology*, chapter Water Quality. McGraw-Hill, New York, 1993.

[165] Jens Meinhold, Carlos D.M. Filipe, Glen T. Daigger, and Steven Isaacs. Characterization of the denitrifying fraction of phosphate accumulating organisms in biological phosphate removal. *Water Science and Technology*, 39(1):31–42, 1999.

[166] Henryk Melcer, Peter L. Dold, Richard M. Jones, Christopher M. Bye, Imre Takacs, H. David Stensel, A. Warren Wilson, Paul Sun, and Scott Bury. Methods for wastewater characterization in activated sludge modeling. Technical Report Report 99-WWF-3, WERF, 2004.

[167] Fangang Meng and Fenglin Yang. Fouling mechanisms of deflocculated sludge, normal sludge, and bulking sludge in membrane bioreactor. *Journal of Membrane Science*, 305(1-2):48–56, 2007. ISSN 0376-7388.

[168] Fengang Meng, So-Ryong Chae, Anja Drews, Matthias Kraume, Hang-Sik Shin, and Fenglin Yang. Recent advances in membrane bioreactors (MBRs): Membrane fouling and membrane material. *Water Research*, 43:1489–1512, 2009.

[169] Adrienne Menniti and Eberhard Morgenroth. Mechanisms of SMP production in membrane bioreactors: Choosing an appropriate mathematical model structure. *Water Research*, 44:5240–5251, 2010.

[170] Takashi Mino, Wen-Tso Liu, Futoshi Kurisu, and Tomonori Matsuo. Modelling glycogen storage and denitrification capability of microorganisms in enhanced biological phosphate removal processes. *Water Science and Technology*, 31(2): 25–34, 1995.

[171] E.B. Müller, A.H. Stouthammer, H.W. Vanverseveld, and D.H. Eikelboom. Aerobic domestic waste-water treatment in a pilot-plant with complete sludge retention by cross-flow filtration. *Water Research*, 29:1179–1189, 1995.

[172] MUNLV. Waste Water Treatment with Membrane Technology (Abwasserreinigung mit Membrantechnik). *Ministerium für Umwelt und Naturschutz, Landwirtschaft und Verbraucherschutz des Landes Nordrhein-Westfalen (Hrsg.)*, 2003.

[173] N. Naessens, T. Maere, and I. Nopens. Critical review of membrane bioraector models - part 1: Biokinetic and filtration models. *Bioresource Technology*, 122: 95–106, 2012.

[174] N. Naessens, T. Maere, N. Ratkovich, S. Vedantam, and I. Nopens. Critical review of membrane bioreactor models - part 2: Hydrodynamic and integrated models. *Bioresource Technology*, 122:107–118, 2012.

[175] H. Nagaoka, S. Ueda, and A. Miya. Influence of bacterial extracellular polymers on the membrane separation activated sludge process. *Water Science and Technology*, 34(9):165–172, 1996. ISSN 0273-1223.

[176] H. Nagaoka, S. Yamanishi, and A. Miya. Modeling of biofouling by extracellular polymers in a membrane separation activated sludge system. *Water Science and Technology*, 38(4-5):497–504, 1998. ISSN 0273-1223.

[177] Anna Narębska. *Membrany i membranowe techniki rozdzialu (Polish).* Nicolaus Copernicus University in Toruń, 1997.

[178] J.A. Nelder and R.A. Mead. Simplex method for function minimization. *Computer Journal*, 7:308–313, 1965.

[179] Aileen N.L. Ng and Albert S. Kim. A mini-review of modeling studies on membrane bioreactor (MBR) treatment for municipal wastewaters. *Desalination*, 212 (1-3):261–281, 2007. ISSN 0011-9164.

[180] Bing-Jie Ni and Han-Qing Yu. An approach for modeling two-step denitrification in activated sludge systems. *Chemical Engineering Science*, 63(6):1449–1459, 2008. ISSN 0009-2509.

[181] Bing-Jie Ni, Fang Fang, and Bruce E. Rittmann. Modeling microbial products in activated sludge under feast-famine conditions. *Environmental Science Technology*, 43:2489–2497, 2009.

[182] Bing-Jie Ni, Bruce E. Rittmann, Fang Fang, and Juan Xu. Long-term formation of microbial products in a sequencing batch reactor. *Water Research*, 44:3787–3796, 2010.

[183] Bing-Jie Ni, Guo-Ping Sheng, and Han-Qing Yu. Model-based characterization of endogenous maintenance, cell death and predation processes of activated sludge in sequencing batch reactors. *Chemical Engineering Science*, 66(4):747–754, 2011. ISSN 0009-2509.

[184] D.J. Nicklin, J.O. Wilkes, and J.F. Davidson. Two-phase flow in vertical tubes. *Transactions of the Institution of Chemical Engineers*, 40(1):61–68, 1962.

[185] DR Noguera, N Araki, and BE Rittmann. Soluble microbial products (SMP) in anaerobic chemostats. *Biotechnology & Bioengineering*, 44(9):1040–7, 1994. ISSN 0006-3592.

[186] Chackrit Nuengjamnong. The investigation of soluble microbial products in membrane fouling. *Thai Journal of Veterinary Medicine*, 36:31–38, 2006.

[187] Chackrit Nuengjamnong, Ji Hyang Kweon, Jinwoo Cho, Chongrak Polprasert, and Kyu-Hong Ahn. Membrane fouling caused by extracellular polymeric substances during microfiltration processes. *Desalination*, 179(1-3):117–124, 2005. ISSN 0011-9164. Membranes in Drinking and Industrial Water Production.

[188] Nuclear Energy Agency OECD. *Modelling in Aquatic Chemistry*. OECD Publishing, illustrated edition, 1997.

[189] S. Ognier, C. Wisniewski, and A. Grasmick. Membrane fouling during constant flux filtration in membrane bioreactors. *Membrane Technology*, 2002:6–10, 2002.

[190] S. Ognier, C. Wisniewski, and A. Grasmick. Membrane bioreactor fouling in subcritical filtration conditions: a local critical flux concept. *Journal of Membrane Science*, 229(1-2):171–177, 2004. ISSN 0376-7388.

[191] P. Ohle. *Bemessung von Membranbioreaktoren für die kommunale Abwasserreinigung*. PhD thesis, Institut für Siedlungswasserwirtschaft, RWTH Aachen University, 1999.

[192] K. P. Oliveira-Esquerre, H. Narita, N. Yamato, N. Funamizu, and Y. Watanabe. Incorporation of the concept of microbial product formation into ASM3 and the modelling of a membrane bioreactor for wastewater treatment. *Brazilian Journal of Chemical Engineering*, 23(04):461–471, 2006.

[193] Gustaf Olsson and Bob Newell. *Wastewater Treatment Systems*. IWA, June 1999.

[194] M.E. O'Neill. A sphere in contact with a plane wall in a slow linear shear flow. *Chemical Engineering Science*, 23(11):1293–1298, 1968. ISSN 0009-2509.

[195] W. F. Owen, D.C. Stuckey, J.B. Healy Jr., L. Y. Young, and P. L. McCarthy. Bioassays for monitoring biochemical methane potential and anaerobic toxicity. *Water Research*, 13:485–492, 1979.

[196] T.Y. Pai, H.Y. Chang, T.J. Wan, S.H. Chuang, and Y.P. Tsai. Using an extended activated sludge model to simulate nitrite and nitrate variations in TNCU2 process. *Applied Mathematical Modelling*, 33(11):4259–4268, 2009. ISSN 0307-904X.

[197] K. Parameshwaran, A. G. Fane, B. D. Cho, and K. J. Kim. Analysis of microfiltration performance with constant flux processing of secondary effluent. *Water Research*, 35(18):4349–4358, 2001. ISSN 0043-1354.

[198] J.P. Pereira, A. Karpinska, P.J. Gomes, A.A. Martins, M.M. Dias, J.C.B. Lopes, and R.J. Santos. *Single and Two-Phase Flows on Chemical and Biomedical Engineering*, volume 1, chapter Activated Sludge Models Coupled to CFD Simulations, pages 153–173. Bentham Science, 2012.

[199] R.M. Platt, G.G. Geesey, J.D. Davis, and D.C. White. Isolation and partial chemical analysis of firmly bound exopolysaccharide from adherent cells of a freshwater bacterium. *Canadian Journal of Microbiology*, 31:657–680, 1985.

[200] S. Polonsky, L. Shermer, and D. Barnea. The relation between the Taylor bubble motion and the velocity field ahead of it. *International Journal of Multiphase Flow*, 25:957–975, 1999.

[201] H. Prieske, L. Böhm, A. Drews, and M. Kraume. Optimised hydrodynamics for membrane bioreactors with immersed flat sheet membrane modules. *Desalination and Water Treatment*, 18:270–276, 2010.

[202] C. Psoch and S. Schiewer. Anti-fouling application of air sparging and backflushing for MBR. *Journal of Membrane Science*, 283(1-2):273–280, 2006. ISSN 0376-7388.

[203] Jelena Radjenović, Marin Matošić, Ivan Mijatović, Mira Petrović, and Damià Barceló. *Emerging contaminants from industrial and municipal waste: Removal technologies*, chapter S2 (Membrane Bioreactor (MBR) as an Advanced Wastewater Treatment Technology), pages 37–101. Springer-Verlag Berlin / Heidelberg, 2007.

[204] S. M. Rappaport, M. G. Richard, M. C. Hollstein, and R. E. Talcott. Mutagenic activity in organic wastewater concentration. *Environmental Science Technology*, 13:957–961, 1979.

[205] N. Ratkovich, W. Horn, F.P. Helmus, S. Rosenberger, W. Naessens, I. Nopens, and T.R. Bentzen. Activated sludge rheology: A critical review on data collection and modelling. *Water Research*, 47(2):463 – 482, 2013. ISSN 0043-1354.

[206] Peter Reichert. *AQUASIM 2.0 - User Manual, Computer Program for the Identification and Simulation of Aquatic Systems.* Swiss Federal Institute of Environmental Science and Technology (EAWAG), CH-8600 Dübendorf, Switzerland, September 1998.

[207] E. Reid, Xingrong Liu, and Simon Judd. Sludge characteristics and membrane fouling in full-scale submerged membrane bioreactors. *Desalination*, 219:240–249, 2008.

[208] L. Rieger, G. Koch, M. Kühni, W. Gujer, and H. Siegrist. The EAWAG Bio-P module for Activated Sludge Model No. 3. *Water Research*, 35(16):3887–3903, 2001. ISSN 0043-1354.

[209] BE Rittmann and PL McCarty. *Environmental biotechnology: principles and applications.* Mc-Graw Hill, 2001.

[210] P. V. Roberts, M. N. Goltz, and D. M. Mackay. A natural gradient experiment on solute transport in a sand aquifer, 3: Retardation estimates and mass balances for organic solutes. *Water Resources Research*, 22(13):2047–2058, 1986.

[211] L. Rodriguez-Roda, M. Sànchez-Marrè, J. Comas, J. Baeza, J. Colprim, J. Lafuente, U. Cortés, and M. Poch. A hybrid supervisory system to support WWTP operation: implementation and validation. *Water Science and Technology*, 45(4): 289–297, 2002.

[212] C. Rosen, U. Jeppsson, and P.A. Vanrolleghem. Towards a common benchmark for long-term process control and monitoring performance evaluation. *Water Science and Technology*, 50(11):41–49, 2004.

[213] S. Rosenberger. *Charakterisierung von belebtem Schlamm in Membranbelebungsreaktoren zur Abwasserreinigung*. PhD thesis, TU Berlin, Fortschr.-Ber.VDI Reihe 3 Nr. 769, VDI-Verlag, Düsseldorf, 2003.

[214] Sandra Rosenberger and Matthias Kraume. Filterability of activated sludge in membrane bioreactors. *Desalination*, 146(1-3):373–379, 2002. ISSN 0011-9164.

[215] G. Rubin. *Widerstands- und Auftriebsbeiwerte von ruhenden kugelförmigen Partikeln in stationären, wandnahen laminaren Grenzschichten*. PhD thesis, TH Karlsruhe, 1977.

[216] Alberto Saa and Omar Teschke. Extracellular polymeric bacterial coverages as minimal area surfaces. *Journal of Colloid and Interface Science*, 304(2):554–557, 2006. ISSN 0021-9797.

[217] Davendra P. Saroj, Giuseppe Guglielmi, Daniele Chiarani, and Gianni Andretolla. Modeling and simulation of membrane bioreactors by incorporating simultaneous storage and growth concept: an especial attention to fouling while modeling the biological process. *Desalination*, 221:475–482, 2008.

[218] Christophe Serra, Laurence Durand-Bourlierb, Michael J. Cliftona, Philippe Moulina, Jean-Christophe Roucha, and Philippe Aptel. Use of air sparging to improve backwash effciency in hollow-fiber modules. *Journal of Membrane Science*, 161:95–113, 1999.

[219] L. Shermer and D. Barnea. *Physico Chemical Hydrodynamics*, 8:243, 1987.

[220] J. D. Sherwood. The force on a sphere pulled away from a permeable half-space. *Journal of Physicochemical Hydrodynamics*, 10:3–12, 1988.

[221] Kazuhiro Shimizu, Satoshi Takada, Takanori Takahashi, and Yoshinori Kawase. Phenomenological simulation model for gas hold-ups and volumetric mass transfer coefficients in external-loop airlift reactors. *Chemical Engineering Journal*, 84(3): 599–603, 2001. ISSN 1385-8947.

[222] HS Shin and ST Kang. Characteristics and fates of soluble microbial products in ceramic membrane bioreactor at various sludge retention times. *Water Research*, 37(1):121–127, 2003.

[223] Fredrick J. Simmons, David H.-W. Kuo, and Irene Xagoraraki. Removal of human enteric viruses by a full-scale membrane bioreactor during municipal wastewater processing. *Water Research*, 45(9):2739 – 2750, 2011. ISSN 0043-1354.

[224] G. Sin, A. Guisasola, D.J.W. De Pauw, J.A. Baeza, J. Carrera, and P.A. Vanrolleghem. A new approach for modeling simultaneous storage and growth processes for activated sludge system under aerobic conditions. *Biotechnology and Bioengineering*, 92(5):600–613, 2005.

[225] Ilse Y. Smets, Jeroen V. Haegebaert, Ronald Carrette, and Jan F. Van Impe. Linearization of the activated sludge model ASM1 for fast and reliable predictions. *Water Research*, 37(8):1831–1851, 2003. ISSN 0043-1354.

[226] Lianfa Song, Shuang Liang, and Liangyong Yuan. Retarded transport and accumulation of soluble microbial products in a membrane bioreactor. *Journal of Environmental Engineering*, 133(No. 1):36–43, 2007.

[227] M. Spérandio and M.C. Espinoza. Modelling an aerobic submerged membrane bioreactor with ASM models on a large range of sludge retention time. *Desalination*, 231:82–90, 2008.

[228] M. Spérandio, M. Massé, M.C. Espinoza-Bouchot, and C. Cabassud. Characterization of sludge structure and activity in submerged membrane bioreactor. *Water Science and Technology*, 52(10-11):401–408, 2005.

[229] M Stiess. *Mechanische Verfahrenstechnik 1.* Springer, Berlin, Heidelberg, New York, 2004.

[230] A.-E. Stricker and Y. Racault. Application of Activated Sludge Model No. 1 to biological treatment of pure winery effluents: case studies. *Water Science and Technology*, 51(1):121–127, 2005.

[231] Changwon Suh, Seokheon Lee, and Jinwoo Cho. Investigation of the effects of membrane foulig control strategies with the integrated membrane bioreactor model. *Journal of Membrane Science*, 429:268–281, 2013.

[232] X. Sun, S. Kuran, and M. Ishii. Cap bubbly-to-slug flow regime transition in a vertical annulus. *Experiments in Fluids*, 37:458–464, 2004.

[233] Taha Taha and Z.F. Cui. CFD modelling of slug flow in vertical tubes. *Chemical Engineering Science*, 61(2):676 – 687, 2006. ISSN 0009-2509.

[234] Imre Takacs. *Experiments in activated sludge modelling.* PhD thesis, Ghent University, Belgium, 2008.

[235] C. Tam. The drag on a cloud of spherical particles in low Reynolds number flow. *Journal of Fluid Mechanics*, 38(3):537–546, 1969.

[236] George Tchobanoglous, Franklin L. Burton, H. David Stensel, and Metcalf&Eddy. *Wastewater Engineering: treatment and reuse*. McGraw-Hill series in civil and environmental engineering. Mc-Graw Hill, 4 edition, 2003. ISBN 9780070418783.

[237] Pierre Cote (then of Zenon). Personal communication prior to Critical Flux Workshop, Oxford, September 14-16th 2003.

[238] Yu Tian, Lin Chen, and Tianling Jiang. Characterization and modeling of the soluble microbial products in membrane bioreactor. *Separation and Purification Technology*, 76:316–324, 2011.

[239] R. Shane Trussell, Rion P. Merlo, Slawomir W. Hermanowicz, and David Jenkins. Influence of mixed liquor properties and aeration intensity on membrane fouling in a submerged membrane bioreactor at high mixed liquor suspended solids concentrations. *Water Research*, 41(5):947–958, 2007.

[240] Satoshi Tsuneda, Jaekook Jung, Hiroshi Hayashi, Hirotoshi Aikawa, Akira Hirata, and Hiroshi Sasaki. Influence of extracellular polymers on electrokinetic properties of heterotrophic bacterial cells examined by soft particle electrophoresis theory. *Colloids and Surfaces B: Biointerfaces*, 29(2-3):181–188, 2003. ISSN 0927-7765.

[241] P. Vasseur and R. G. Cox. The lateral migration of a spherical particle in two-dimensional shear flows. *Journal of Fluid Mechanics*, 78:385–413, 1976.

[242] H.H.K. Versteeg and W. Malalasekera. *An Introduction to Computational Fluid Dynamics: The Finite Volume Method*. Pearson/Prentice Hall, 2007. ISBN 9780131274983.

[243] Juha Vesanto, Johan Himberg, Esa Alhoniemi, and Juha Parhankangas. Self-organizing map in Matlab: the SOM Toolbox. In *Proceedings of the Matlab DSP Conference, Espo, Finland*, volume 16-17, pages 35–40, November 1999.

[244] J. Visser. Colloid and other forces in particle adhesion and particle removal. In *Proceedings of the Symposium on Deposition and Filtration of Particles from Gases and Liquids*, pages 121–141. Loughborough University, UK Society of Chemical Industry, 1978.

[245] Donald Voet, Judith G. Voet, and Charlotte W. Pratt. *Fundamentals of Biochemistry (Rev. ed.)*. Number 978-0-471-41759-0. New York: Wiley, 2001.

[246] Harit K Vyas, R.J Bennett, and A.D Marshall. Cake resistance and force balance mechanism in the crossflow microfiltration of lactalbumin particles. *Journal of Membrane Science*, 192(1–2):165–176, 2001. ISSN 0376-7388.

[247] R.J. Wakeman and E.S. Tarleton. Colloidal fouling of microfiltration membranes during the treatment of aqueous feed streams. *Desalination*, 83(1-3):35–52, 1991.

[248] G.B. Wallis. *One-dimensional two-phase flow*. McGraw-Hill, 1969.

[249] Chuang Wang, Yingzhi Zeng, Jing Lou, and Ping Wu. Dynamic simulation of a WWTP operated at low dissolved oxygen condition by integrating activated sludge model and a floc model. *Biochemical Engineering Journal*, 33(3):217–227, 2007. ISSN 1369-703X.

[250] Wen Wang, Xiaodong Jia, and Graham A. Davies. A theoretical study of transient cross-flow filtration using force balance analysis. *The Chemical Engineering Journal and the Biochemical Engineering Journal*, 60(1–3):55–62, 1995. ISSN 0923-0467.

[251] Xiao-Mao Wang and T. David Waite. Impact of gel layer formation on colloid retention in membrane filtration processes. *Journal of Membrane Science*, 325(1): 486 – 494, 2008. ISSN 0376-7388.

[252] Xiao-Mao Wang and T. David Waite. Gel layer formation and hollow fiber membrane filterability of polysaccharide dispersions. *Journal of Membrane Science*, 322(1):204 – 213, 2008. ISSN 0376-7388.

[253] Zhiwei Wang, Zhichao Wu, and Shujuan Tang. Extracellular polymeric substances (EPS) properties and their effects on membrane fouling in a submerged membrane bioreactor. *Water Research*, 43(9):2504–2512, 2009. ISSN 0043-1354.

[254] R.J Weigand, F.W. Altena, and G. Belfort. Lateral migration of spherical particles in laminar porous tube flows: Application to membrane filtration. *Physicochemical Hydrodynamics*, 6:393–413, 1985.

[255] H. De Wever, C. Brepols, and B. Lesjean. Decision tree for full-scale submerged MBR configurations. *Final MBR-Network Workshop, 31 March - 1 April, Berlin Germany*, 2009.

[256] Jost Wingender, Thomas R. Neu, and Hans-Curt Flemming. *Microbial Extracellular Polymeric Substances: Characterization, Structures and Function*. Springer-Verlag, Berlin, Heidelberg, 1999.

[257] T. Wintgens, J. Rosen, T. Melin, C. Brepols, K. Drensla, and N. Engelhardt. Modelling of a membrane bioreactor system for municipal wastewater treatment. *Journal of Membrane Science*, 216:55–65, 2003.

[258] C. Wisniewski and A. Grasmick. Floc size distribution in a membrane bioreactor and consequences for membrane fouling. *Colloids and Surfaces A: Physicochemical and Engineering Aspects*, 138(2-3):403–411, 1998. ISSN 0927-7757.

[259] D. Wu, J.A. Howell, and R.W. Field. Critical flux measurement for model colloids. *Journal of Membrane Science*, 152:89–98, 1999.

[260] Jinling Wu, Futai Chen, Xia Huang, Wenyan Geng, and Xianghua Wen. Using inorganic coagulants to control membrane fouling in a submerged membrane bioreactor. *Desalination*, 197(1-3):124–136, 2006.

[261] Jun Wu, Chengda He, Xinyue Jiang, and Miao Zhang. Modeling of the submerged membrane bioreactor fouling by the combined pore constriction, pore blockage and cake formation mechanisms. *Desalination*, 279:127–134, 2011.

[262] Jun Wu, Chengda He, and Yaping Zhang. Modelling of membrane fouling in a submerged membrane bioreactor by considering the role of solid, colloidal and soluble components. *Journal of Membrane Science*, 397-398:102–111, 2012.

[263] I. Yamanoi and K. Kageyama. Evaluation of bubble flow properties between flat sheet membranes in membrane bioreactor. *Journal of Membrane Science*, 360 (1-2):102–108, 2010.

[264] S.F. Yang and X.Y. Li. Influences of extracellular polymeric substances (EPS) on the characteristics of activated sludge under non-steady-state conditions. *Process Biochemistry*, 44:91–96, 2009.

[265] Y. Ye, P. Le-Clech, and A.G. Fane. Evolution of fouling during crossflow filtration of model EPS solutions. *Journal of Membrane Science*, 264(1-2):190–199, 2005.

[266] Y. Ye, V. Chen, and A.G. Fane. Modeling long-term subcritical filtration of model EPS solutions. *Desalination*, 191(1-3):318–327, 2006. ISSN 0011-9164. International Congress on Membranes and Membrane Processes.

[267] N.O. Yigit, I. Harman, G. Civelekoglu, H. Koseoglu, N. Cicek, and M. Kitis. Membrane fouling in a pilot-scale submerged membrane bioreactor operated under various conditions. *Desalination*, 231(1-3):124–132, 2008. ISSN 0011-9164. Selected Papers Presented at the 4th International IWA Conference on Membranes for Water and Wastewater Treatment, 15-17 May 2007, Harrogate, UK. Guest Edited by Simon Judd.

[268] Mao Zaisha and A. E. Dukler. Improved hydrodynamic model of two-phase slug flow in vertical tubes. *Chinese Journal of Chemical Engineering*, 1(1):18–29, 1993.

[269] Alain Zarragoitia-González, Sylvie Schetrite, Marion Alliet, and Ulises Jáuregui-Haza ad Claire Albasi. Modelling of submerged membrane bioreactor: Conceptual study about link between activated sludge biokinetics, aeration and fouling process. *Journal of Membrane Science*, 325:612–624, 2008.

[270] H. Q. Zhang, M. Lu, C. G. Lian, and S. L. Zhu. The hydrodynamic model for gas liquid slug flow in vertical tube. *Journal of Chemical Engineering of Chinese Universities*, 5:102–111, 1991.

[271] Donghong Zheng, Defu Che, and Yinhe Liu. Experimental investigation on gas-liquid two-phase slug flow enhanced carbon dioxide corrosion in vertical upward pipeline. *Corrosion Science*, 50:3005–3020, 2008.

[272] Edwin Zondervan, Ben H.L. Betlem, Bastiaan Blankert, and Brian Roffel. Modeling and optimization of a sequence of chemical cleaning factors in dead-end ultrafiltration. *Journal of Membrane Science*, 2007.

[273] N. Zuber and J. Hench. Steady state and transient void fraction of bubbling systems and their operating limit. Part 1. Steady state operation. Technical Report 62GL100, General Electric Report, 1962.

[274] M.F.R. Zuthi, H.H. Ngo, and W.S.Guo. Modelling bioprocesses and membrane foulig in membrane bioreactor (MBR): A review towards finding an integrated model framework. *Bioresource Technology*, 122:119–129, 2012.

[275] Andrew L. Zydney and Chia-Chi Ho. Effect of membrane morphology on system capacity during normal flow filtraiton. *Biotechnology and Bioengineering*, 83(5): 537–543, 2003.

Acronyms

1D one-dimensional . . . 233

2D two-dimensional . . . 233

3D three-dimensional . . . 233

ABR anaerobic baffled reactor . . . 60

AE algebraic equation . . . 5

AI artificial intelligence . . . 142

ANN artificial neural network . . . 109

AOTE actual oxygen transfer efficiencies . . . 225

AOTR actual oxygen transfer rate . . . 224

ARD average relative deviation . . . 79

AS activated sludge . . . 39

ASDM activated sludge and digestion model . . . 57

ASM activated sludge model . . . 285

ASM1 Activated Sludge Model No. 1 . . . 285

ASM2 Activated Sludge Model No. 2 . . . 51

ASM2d Activated Sludge Model No. 2d . . . 51

ASM3 Activated Sludge Model No. 3 . . . 285

ASP activated sludge process . . . 217

CP concentration polarisation 144

CST capillary suction time 155

CSTR completely stirred tank reactor 222

DAE differential algebraic equation

DO dissolved oxygen 287

DOM dissolved organic matter 199

DPAO denitrifying phosphorus accumulating organisms 54

DSS decision support system 5

DWF dry weather flow 261

DTI Department of Trade and Industry 7

EAP environment associated products 63

EBPR excess biological phosphorus removal 83

EPS extracellular polymeric substances 285

EQ effluent quality 274

EQI effluent quality index 250

FCI fouling cost index

FD finite difference 143

FE finite element 143

F:M food to mass ratio 105

FV finite volume 143

FS flat sheet 181

FSD floc size distribution 250

FST final settlement tank 268

HF hollow fibre . . . 256

HRT hydraulic retention time . . . 250

iMBR immersed membrane bioreactor . . . 256

IAWQ International Association on Water Quality . . . 287

IBMF-MBR integrated bioreactor and membrane fouling MBR model . . . 286

IBVP initial boundary value problem . . . 157

iMBR immersed membrane bioreactor . . . 256

IQ influent quality . . . 274

IQI influent quality index . . . 250

ISS inert suspended solids . . . 90

IUPAC International Union of Pure and Applied Chemistry . . . 27

IWA International Water Association . . . 326

MAPE mean absolute percentage error . . . 97

MBR membrane bioreactor . . . 285

MF microfiltration . . . 217

MINLP mixed integer non-linear programming . . . 289

MLSS mixed liquor suspended solids . . . 261

MLVSS mixed liquor volatile suspended solids . . . 222

MP microbial products . . . 66

MPC model predictive control . . . 179

MT multi-tube . . . 31

MW molecular weight . . . 291

MWCO molecular weight cut-off . . . 155

MWD molecular weight distribution . . . 290

N nitrogen 328

NF nanofiltration 152

NH_4^+-N ammoniacal nitrogen 287

NO_3^--N nitrate nitrogen 287

NSS non-settleable solids 155

OCI operational cost index 275

ODE ordinary differential equation 285

OPEX operational expenditures 288

OUR oxygen uptake rate 224

P phosphorus 48

PAC powdered activated carbon 187

PAO phosphorus accumulating organisms 53

PCA principal component analysis 110

PDE partial differential equation 233

PDF probability density function xvii

PES polyethersulfone 186

PF plate and frame

PHA polyhydroxyalkanoates 53

PI proportional integral 261

PLC programmable logic controller 187

P&ID piping and instrumentation diagram 260

PP proteins 155

PS polysaccharides 155

PSD pore size distribution 290

PVDF polyvinylidene fluoride 207

RAS recirculated activated sludge 34

RMSPE root mean square percentage error 97

RO reverse osmosis 152

RTD residence time distribution 43

SAD_m specific aeration demand per membrane area 260

SAS surplus activated sludge 276

$SBOD_5$ soluble biological oxygen demand in five days

$SBOD_\infty$ soluble ultimate biological oxygen demand

SBR sequencing batch reactor 185

SCADA supervisory control and data acquisition 5

SCOD soluble chemical oxygen demand 155

SCR specific cake resistance 155

SMP soluble microbial products 285

SND simultaneous nitrification and denitrification 57

SOM soluble organic matter 155

SOM self organising map 109

SOTE specific oxygen transfer efficiency 224

SOTR specific oxygen transfer rate 228

SRT sludge retention time 287

SS suspended solids 199

STKN soluble total Kjeldahl nitrogen 127

STN soluble total nitrogen 124

SVI sludge volume index . . . 141

SSVI stirred sludge volume index . . . 58

T tubular

TB Taylor bubble . . . 232

TEP transparent exopolymer particles . . . 137

ThCOD theoretical chemical oxygen demand . . . 96

TKN total Kjeldahl nitrogen . . . 263

TMP trans-membrane pressure . . . 285

TN total nitrogen . . . 271

TSS total suspended solids . . . 263

UAP utilisation associated products . . . 285

UF ultrafiltration . . . 277

UFV upflow velocity . . . 34

VSS volatile suspended solids . . . 90

WAS waste activated sludge . . . 275

VFA volatile fatty acids . . . 59

WW wastewater . . . 154

WWTP wastewater treatment plant . . . 289

XBOD$_5$ particulate biological oxygen demand in five days

XBOD$_\infty$ particulate ultimate biological oxygen demand

XCOD particulate chemical oxygen demand . . . 90

XTKN particulate total Kjeldahl nitrogen

ZSV zone settling velocity . . . 155

Part IV

Appendix

Combined EPS and SMP Activated Sludge Model CES-ASM1

Table 9.1: CES-ASM1 state variables.

Name	Description	Unit
S_I	Soluble inert organic matter	gCOD m^{-3}
S_S	Readily biodegradable substrate	gCOD m^{-3}
X_I	Particulate inert organic matter	gCOD m^{-3}
X_S	Slowly biodegradable substrate	gCOD m^{-3}
X_H	Heterotrophic biomass	gCOD m^{-3}
X_{EPS}	Extracellular polymeric substances	gCOD m^{-3}
S_{UAP}	Utilisation associated products	gCOD m^{-3}
S_{BAP}	Biomass associated products	gCOD m^{-3}
X_A	Autotrophic biomass	gCOD m^{-3}
X_P	Particulate products arising from biomass decay	gCOD m^{-3}
S_O	Dissolved oxygen	gO_2 m^{-3}
S_{NO}	Nitrate and Nitrite nitrogen	gN m^{-3}
S_{N_2}	Dinitrogen	gN m^{-3}
S_{NH}	NH_4^+ and NH_3 nitrogen	gN m^{-3}
S_{ND}	Soluble biodegradable organic nitrogen	gN m^{-3}
X_{ND}	Particulate biodegradable organic nitrogen	gN m^{-3}
S_{ALK}	Alkalinity	moleHCO_3^- m^{-3}

Table 9.2: Stoichiometric and composition matrix for CES-ASM1, j: process, i: component.

	Model components i	1	2	3	4	5	6	7	8	9	10	11	12	13	14	15	16	17
j	Processes	S_I	S_S	X_I	X_S	X_H	X_{EPS}	S_{UAP}	S_{BAP}	X_A	X_P	S_O	S_{NO}	S_{N_2}	S_{NH}	S_{ND}	X_{ND}	S_{ALK}
	Heterotrophic organisms																	
p_1	Ammonification														1	−1		$\frac{1}{14}$
p_{2a}	Aer. growth on S_S		$-\frac{1}{Y_H}$			$1-\frac{}{f_{EPS,h}}$	$f_{EPS,h}$	$\frac{\gamma_H}{Y_H}$				x_{2a}			y_{2a}			$-\frac{i_{XB}}{14}$
p_{2b}	Aer. growth on S_{BAP}					$1-\frac{}{f_{EPS,h}}$	$f_{EPS,h}$		$-\frac{1}{Y_{SMP}}$			x_{2b}			y_{2b}			$-\frac{i_{XB}}{14}$
p_{2c}	Aer. growth on S_{UAP}					$1-\frac{}{f_{EPS,h}}$	$f_{EPS,h}$	$-\frac{1}{Y_{SMP}}$				x_{2c}			y_{2c}			$-\frac{i_{XB}}{14}$
p_{3a}	Anox. growth on S_S		$-\frac{1}{Y_H}$			$1-\frac{}{f_{EPS,h}}$	$f_{EPS,h}$	$\frac{\gamma_H}{Y_H}$					x_{3a}	$-x_{3a}$	y_{3a}			$\frac{1-Y_H}{40\,Y_H}-\frac{i_{XB}}{14}$
p_{3b}	Anox. growth on S_{BAP}					$1-\frac{}{f_{EPS,h}}$	$f_{EPS,h}$		$-\frac{1}{Y_{SMP}}$				x_{3b}	$-x_{3b}$	y_{3b}			$\frac{1-Y_H}{40\,Y_H}-\frac{i_{XB}}{14}$
p_{3c}	Anox. growth on S_{UAP}					$1-\frac{}{f_{EPS,h}}$	$f_{EPS,h}$	$-\frac{1}{Y_{SMP}}$					x_{3c}	$-x_{3c}$	y_{3c}			$\frac{1-Y_H}{40\,Y_H}-\frac{i_{XB}}{14}$
p_4	Decay of heterotrophs				$1-f_P-f_{EPS,dh}-f_{BAP}$	−1	$f_{EPS.dh}$		f_{BAP}		f_P						$i_{XP}-f_P\,i_{XP}$	
p_5	Hydrolysis of org. compounds		1		−1													
p_6	Hydrolysis of org. N															1	−1	
p_7	Hydrolysis of X_{EPS}		f_S				−1	$1-f_S$								$i_{XEPS}-i_{XBAP}\,(1-f_S)$		
p_8	Hydrolysis of X_I	$f_{I,I}$	$1-f_{I,I}$	−1											$f_{N,I}$			
p_9	Hydrolysis of X_P	$f_{I,P}$	$1-f_{I,P}$								−1				$f_{N,P}$			
	Autotrophic organisms																	
p_{10}	Aerobic growth of autotrophs						$f_{EPS,a}$	$\frac{\gamma_A}{Y_A}$		$1-f_{EPS,a}$		$-\frac{64/14-Y_A}{Y_A}$	$\frac{1}{Y_A}$		$-i_{XB}-\frac{1}{Y_A}$			$-\frac{i_{XB}}{14}-\frac{1}{7\,Y_A}$
p_{11}	Decay of autotrophs				$1-f_P-f_{EPS,da}-f_{BAP}$		$f_{EPS,da}$		f_{BAP}	−1	f_P						$i_{XP}-f_P\,i_{XP}$	
	Composition matrix																	
1	ThOD (g ThOD)	1	1	1	1	1	1	1	1	1	1	-1	$-\frac{64}{14}$	$-\frac{24}{14}$				
2	Nitrogen (g N)					i_{XB}	i_{XEPS}		i_{XBAP}	i_{XB}	i_{XP}		1	1	1	1	1	
3	Ionic charge (Mole$^+$)												$-\frac{1}{14}$		$\frac{1}{14}$			-1

This model assumes that ThOD is identical to the measured COD. 1 gS_O = -1 gThOD, 1 gS_{NH} = 0 gThOD, 1gS_{NO} = -64/14 gThOD, 1 gS_{N_2} = -24/14 gThOD.

Table 9.3: Process rate equations of the CES-ASM1 moedel.

Process	Process rate
p_1	$k_{a,20}\, e^{-0.069\,(20-T)}\; S_{ND}\; X_H$
p_{2a}	$\mu_{H,20}\, e^{-0.069\,(20-T)}\; \frac{S_S}{K_S+S_S}\, \frac{S_O}{K_{OH}+S_O}\, \frac{S_{ALK}}{K_{ALKH}+S_{ALK}}\; X_H$
p_{2b}	$\mu_{BAP,20}\, e^{-0.069\,(20-T)}\; \frac{S_{BAP}}{K_{BAP}+S_{BAP}}\, \frac{S_O}{K_{OH}+S_O}\, \frac{S_{ALK}}{K_{ALKH}+S_{ALK}}\; X_H$
p_{2c}	$\mu_{UAP,20}\, e^{-0.069\,(20-T)}\; \frac{S_{UAP}}{K_{UAP}+S_{UAP}}\, \frac{S_O}{K_{OH}+S_O}\, \frac{S_{ALK}}{K_{ALKH}+S_{ALK}}\; X_H$
p_{3a}	$\mu_{H,20}\, e^{-0.069\,(20-T)}\; \eta_g\, \frac{S_S}{K_S+S_S}\, \frac{K_{OH}}{K_{OH}+S_O}\, \frac{S_{NO}}{K_{NO}+S_{NO}}\, \frac{S_{ALK}}{K_{ALKH}+S_{ALK}}\; X_H$
p_{3b}	$\mu_{BAP,20}\, e^{-0.069\,(20-T)}\; \eta_g\, \frac{S_{BAP}}{K_{BAP}+S_{BAP}}\, \frac{K_{OH}}{K_{OH}+S_O}\, \frac{S_{NO}}{K_{NO}+S_{NO}}\, \frac{S_{ALK}}{K_{ALKH}+S_{ALK}}\; X_H$
p_{3c}	$\mu_{UAP,20}\, e^{-0.069\,(20-T)}\; \eta_g\, \frac{S_{UAP}}{K_{UAP}+S_{UAP}}\, \frac{K_{OH}}{K_{OH}+S_O}\, \frac{S_{NO}}{K_{NO}+S_{NO}}\, \frac{S_{ALK}}{K_{ALKH}+S_{ALK}}\; X_H$
p_4	$b_{H,20}\, e^{-0.11\,(20-T)}\; X_H$
p_5	$k_{h,20}\, e^{-0.11\,(20-T)}\; \frac{\frac{X_S}{X_H}}{K_{X20}\, e^{-0.11\,(20-T)}+\frac{X_S}{X_H}} \left(\frac{S_O}{K_{OH}+S_O} + \eta_h\, \frac{K_{OH}}{K_{OH}+S_O}\, \frac{S_{NO}}{K_{NO}+S_{NO}} + \eta_{h,A}\; \frac{K_{Oan}}{K_{Oan}+S_O+S_{NO}} \right) X_H$
p_6	$p_5\; \frac{X_{ND}}{X_S}$
p_7	$k_{h,EPS,20}\, e^{-0.11\,(20-T)}\; X_{EPS}$
p_8	$k_{h,X_I,20}\, e^{-0.11\,(20-T)}\; X_I$
p_9	$k_{h,X_P,20}\, e^{-0.11\,(20-T)}\; X_P$
p_{10}	$\mu_{A,20}\, e^{-0.098\,(20-T)}\; \frac{S_{NH}}{K_{NH}+S_{NH}}\, \frac{S_O}{K_{OA}+S_O}\, \frac{S_{ALK}}{K_{ALKA}+S_{ALK}}\; X_A$
p_{11}	$b_{A,20}\, e^{-0.098\,(20-T)}\; X_A$

* T denotes the temperature of the bulk liquid

** In the original version of the ASM1 model published by International Water Association (IWA) in 1987, the Monod constant K_{X20} in equation p_5 was not dependent on temperature T. Moreover, hydrolysis of organic substrates was assumed not to occur under anaerobic conditions. Here, equation p_5 was amended to include dependency of K_{X20} on temperature and allow hydrolysis to occur under anaerobic conditions with a reduced rate determined by parameter $\eta_{h,A}$

*** All above equations are temperature dependent. These temperature dependency functions are also an addition to ASM1 in its original shape and form.

**** This model assumes that process rates p_{2a}, p_{2b}, p_{3a}, p_{3b}, and p_7 depend on alkalinity S_{ALK}. Original formulation of ASM1 neglected any impacts alkalinity would have on process kinetics. This model also assumes that heterotrophic bacteria can assimilate nitrogen not only from $NH_4 - N$ (S_{NH}) as initially postulated in ASM1 (p_{2a} and p_{3a}) but during its absence also from nitrites and nitrates S_{NO} (p_{2b} and p_{3b}).

Table 9.4: Stoichiometric parameters in the Petersen matrix of the CES-ASM1 model.

Parameter	Expression
x_{2a}	$-\frac{1-Y_H-\gamma_H}{Y_H}$
x_{2b}	$-\frac{1-Y_{SMP}}{Y_{SMP}}$
x_{2c}	$-\frac{1-Y_{SMP}}{Y_{SMP}}$
x_{3a}	$\frac{x_{2a}}{40/14}$
x_{3b}	$\frac{x_{2b}}{40/14}$
x_{3c}	$\frac{x_{2c}}{40/14}$
y_{2a}	$-(1-f_{EPS,h})\,i_{XB}-f_{EPS,h}\,i_{XEPS}$
y_{2b}	$-(1-f_{EPS,h})\,i_{XB}+\frac{1}{Y_{SMP}}\,i_{XBAP}-f_{EPS,h}\,i_{XEPS}$
y_{2c}	$-(1-f_{EPS,h})\,i_{XB}-f_{EPS,h}\,i_{XEPS}$
y_{3a}	y_{2a}
y_{3b}	y_{2b}
y_{3c}	y_{2c}

Table 9.5: Default stoichiometric and kinetic parameters in CES-ASM1

	Default value	Description	Unit
ASM1 kinetic parameters			
$\mu_{H,20}$	6.0	Maximum specific growth rate of heterotrophic biomass	d^{-1}
$\mu_{A,20}$	0.8	Maximum specific growth rate of autotrophic biomass	d^{-1}
$b_{H,20}$	0.62	Decay rate for heterotrophic biomass	d^{-1}
$b_{A,20}$	0.15	Decay rate for autotrophic biomass	d^{-1}
$k_{h,20}$	3	Maximum specific hydrolysis rate	d^{-1}
$k_{a,20}$	0.08	Maximum specific ammonification rate	m^3 $gCOD^{-1}$ d^{-1}
ASM1 stoichiometric parameters			
Y_H	0.67	Yield coefficient for heterotrophic biomass	gCOD $gCOD^{-1}$
Y_A	0.24	Yield coefficient for autotrophic biomass	gCOD $gCOD^{-1}$
i_{XB}	0.086	N content of biomass, X_H, X_A	gN $gCOD^{-1}$
i_{XP}	0.06	N content of products of biomass decay, X_P	gN $gCOD^{-1}$
f_P	0.08	Fraction of biomass leading to particulate products	gCOD $gCOD^{-1}$
K_S	20	Half saturation coefficient for substrate in heterotrophic growth	gCOD m^{-3}
K_{OH}	0.2	Half saturation coefficient for oxygen in heterotrophic growth	gO_2 m^{-3}
K_{NO}	0.5	Half saturation coefficient for NO_3^- in heterotrophic growth	gN m^{-3}
η_g	0.8	Correction factor for μ_H under anoxic conditions	–
η_h	0.4	Correction factor for hydrolysis under anoxic conditions	–
$\eta_{h,A}$	0.65	Correction factor for hydrolysis under anaerobic conditions	–
$K_{X,20}$	0.03	Half saturation coefficient for hydrolysis of organic compounds	–
K_{NH}	1	Half saturation coefficient for ammoniacal N in autotrophic growth	gN m^{-3}
K_{OA}	0.4	Half saturation coefficient for oxygen in autotrophic growth	gO_2 m^{-3}
K_{ALKH}	0.1	Half saturation coefficient for alkalinity (HCO_3^-) in heterotrophic growth	mole HCO_3^- m^{-3}
K_{ALKA}	0.25	Half saturation coefficient for alkalinity (HCO_3^-) in autotrophic growth	mole HCO_3^- m^{-3}
K_{Oan}	0.2	Inhibition coefficient for S_O and S_{NO} in hydrolysis of organics under anaerobic conditions	gO_2 m^{-3}
K_{NHNO}	0.1	Half saturation coefficient for S_{NH} in heterotrophic growth	gN m^{-3}
CES-ASM1 kinetic parameters			
$\mu_{UAP,20}$	0.35	Maximum specific growth rate of heterotrophs on S_{UAP}	d^{-1}
$\mu_{BAP,20}$	0.25	Maximum specific growth rate of heterotrophs on S_{BAP}	d^{-1}
$k_{h,EPS,20}$	0.3	Maximum X_{EPS} hydrolysis rate	d^{-1}
$k_{h,X_I,20}$	0.013	Maximum X_I hydrolysis rate	d^{-1}
$k_{h,X_P,20}$	0.013	Maximum X_P hydrolysis rate	d^{-1}
CES-ASM1 stoichiometric parameters			
Y_{SMP}	0.5	Yield coefficient for heterotrophic growth on SMP	gCOD $gCOD^{-1}$
γ_H	0.0335	Fraction of S_{UAP} produced during heterotrophic growth	gCOD $gCOD^{-1}$
γ_A	0.012	Fraction of S_{UAP} produced during autotrophic growth	gCOD $gCOD^{-1}$
i_{XBAP}	0.06	N content of S_{BAP}	gN $gCOD^{-1}$
i_{XEPS}	0.06	N content of X_{EPS}	gN $gCOD^{-1}$
K_{UAP}	100	Half saturation constant for S_{UAP}	gCOD m^{-3}
f_S	0.4	Fraction of S_S produced from X_{EPS} hydrolysis	gCOD $gCOD^{-1}$
$f_{EPS,dh}$	0.05	Fraction of X_{EPS} produced from heterotrophic biomass decay	gCOD $gCOD^{-1}$
$f_{EPS,da}$	0.05	Fraction of X_{EPS} produced from autotrophic biomass decay	gCOD $gCOD^{-1}$
$f_{EPS,h}$	0.35	Fraction of X_{EPS} produced from heterotrophic biomass activity	gCOD $gCOD^{-1}$
$f_{EPS,a}$	0.2	Fraction of X_{EPS} produced during autotrophic growth	gCOD $gCOD^{-1}$
K_{BAP}	85	Half saturation constant for S_{BAP}	gCOD m^{-3}
f_{BAP}	0.0215	Fraction of S_{BAP} produced from biomass decay	gCOD $gCOD^{-1}$
$f_{N,I}$	0.02	Fraction of nitrogen (N) released during X_I hydrolysis	gN $gCOD^{-1}$
$f_{N,P}$	0.086	Fraction of N released during X_P hydrolysis	gN $gCOD^{-1}$
$f_{I,I}$	0	Fraction of S_I generated during X_I hydrolysis	gCOD $gCOD^{-1}$
$f_{I,P}$	0	Fraction of S_I generated during X_P hydrolysis	gCOD $gCOD^{-1}$

Combined EPS and SMP Activated Sludge Model CES-ASM3

Table 9.6: CES-ASM3 state variables.

Name	Description	Unit
S_O	Dissolved oxygen	$gO_2\ m^{-3}$
S_S	Readily biodegradable substrate	$gCOD\ m^{-3}$
S_{NH}	NH_4^+ and NH_3 nitrogen	$gN\ m^{-3}$
S_{NO}	Nitrate and Nitrite nitrogen	$gN\ m^{-3}$
S_{N_2}	Dinitrogen	$gN\ m^{-3}$
S_{ALK}	Alkalinity	$moleHCO_3^-\ m^{-3}$
S_I	Soluble inert organic matter	$gCOD\ m^{-3}$
X_I	Particulate inert organic matter	$gCOD\ m^{-3}$
X_S	Slowly biodegradable substrate	$gCOD\ m^{-3}$
X_H	Heterotrophic biomass	$gCOD\ m^{-3}$
X_{STO}	Organic storage products	$gCOD\ m^{-3}$
X_A	Autotrophic biomass	$gCOD\ m^{-3}$
X_{TSS}	Particulate material	$gTSS\ m^{-3}$
S_{BAP}	Biomass Associated Products (BAP)	$gCOD\ m^{-3}$
S_{UAP}	Utilisation Associated Products (UAP)	$gCOD\ m^{-3}$
X_{EPS}	Extracellular Polymeric Substances (EPS)	$gCOD\ m^{-3}$

Table 9.7: Stoichiometric and composition matrix for CES-ASM3, j: process, i: component.

	Model components i	1	2	3	4	5	6	7	8	9	10	11	12	13	14	15	16
j	Processes	S_O	S_I	S_S	S_{NH}	S_{N2}	S_{NO}	S_{HCO}	S_{BAP}	S_{UAP}	X_I	X_S	X_H	X_{STO}	X_A	X_{EPS}	X_{TSS}
	Heterotrophic organisms																
p_1	Hydrolysis		f_{S_I}	$1-f_{S_I}$	y_1			z_1				-1					t_1
$p_{2,a}$	Aerobic storage of S_S	x_{2a}		-1	y_{2a}			z_{2a}						$Y_{STO,O_2}-f_{EPS,STO}$		$f_{EPS,STO}$	t_{2a}
$p_{2,b}$	Aerobic storage of S_{BAP}	x_{2b}			y_{2b}			z_{2b}	-1					$Y_{STO,SMP,O_2}-f_{EPS,STO}$		$f_{EPS,STO}$	t_{2b}
$p_{2,c}$	Aerobic storage of S_{UAP}	x_{2c}			y_{2c}			z_{2c}		-1			$Y_{STO,SMP,O_2}-f_{EPS,STO}$			$f_{EPS,STO}$	t_{2c}
$p_{3,a}$	Anoxic storage of S_S			-1	y_{3a}	$-x_{3a}$	x_{3a}	z_{3a}						$Y_{STO,NO}-f_{EPS,STO}$		$f_{EPS,STO}$	t_{3a}
$p_{3,b}$	Anoxic storage of S_{BAP}				y_{3b}	$-x_{3b}$	x_{3b}	z_{3b}	-1					$Y_{STO,SMP,NO}-f_{EPS,STO}$		$f_{EPS,STO}$	t_{3b}
$p_{3,b}$	Anoxic storage of S_{UAP}				y_{3c}	$-x_{3c}$	x_{3c}	z_{3c}		-1			$Y_{STO,SMP,NO}-f_{EPS,STO}$			$f_{EPS,STO}$	t_{3c}
p_4	Aerobic growth	x_4			y_4			z_4		$\gamma_H/Y_{H,O_2}$			$1-f_{EPS,h}$	$-1/Y_{H,O_2}$		$f_{EPS,h}$	t_4
p_5	Anoxic growth				y_5	$-x_5$	x_5	z_5		$\gamma_H/Y_{H,NO}$			$1-f_{EPS,h}$	$-1/Y_{H,NO}$		$f_{EPS,h}$	t_5
p_6	Aerobic endogenous respiration	x_6			y_6			z_6	f_{BAP}		f_{X_I}		-1			$f_{EPS,dh}$	t_6
p_7	Anoxic endogenous respiration				y_7	$-x_7$	x_7	z_7	f_{BAP}		f_{X_I}		-1			$f_{EPS,dh}$	t_7
p_8	Aerobic respiration of X_{STO}	x_8												-1			t_8
p_9	Anoxic respiration of X_{STO}					$-x_9$	x_9	z_9						-1			t_9
	Autotrophic organisms																
p_{10}	Nitrification	x_{10}			y_{10}		$1/Y_A$	z_{10}		γ_A/Y_A					$1-f_{EPS,a}$	$f_{EPS,a}$	t_{10}
p_{11}	Aerobic endogenous respiration	x_{11}			y_{11}			z_{11}	f_{BAP}		f_{X_I}				-1	$f_{EPS,da}$	t_{11}
p_{12}	Anoxic endogenous respiration				y_{12}	$-x_{12}$	x_{12}	z_{12}	f_{BAP}		f_{X_I}				-1	$f_{EPS,da}$	t_{12}
	EPS and X_I hydrolysis																
p_{13}	Hydrolysis of X_{EPS}			f_S					$1-f_S$							-1	t_{13}
p_{14}	Hydrolysis of X_I		$f_{I,I}$	$1-f_{I,I}$	$f_{N,I}$						-1						t_{14}
1	ThOD (g ThOD)	-1	1	1		$-24/14$	$-64/14$		1	1	1	1	1	1	1	1	
2	Nitrogen (g N)		i_{N,S_I}	i_{N,S_S}	1	1	1		$i_{N,S_{BAP}}$		i_{NX_I}	i_{NX_S}	$i_{N,BM}$		$i_{N,BM}$	$i_{N,EPS}$	
3	Ionic charge (Mole$^+$)				1/14		$-1/14$	-1									
4	TSS (g TSS)										i_{TSS,X_I}	i_{TSS,X_S}	$i_{TSS,BM}$	$i_{TSS,STO}$	$i_{TSS,BM}$	$i_{TSS,EPS}$	1

This model assumes that ThOD is identical to the measured COD. 1 gS_O = -1 gThOD, 1 gS_{NH} = 0 gThOD, 1gS_{NO} = -64/14 gThOD, 1 gS_{N_2} = -24/14 gThOD.

Stoichiometric parameters x_i y_i z_i and t_i were calculated from mass and electric charge conservation equations and are given in Table 9.9.

Table 9.8: Process rate equations of the CES-ASM3 model.

	Process rate
p_1	$e^{-0.04\,(20-T)} \cdot k_{h,20} \cdot \frac{\frac{X_S}{X_H}}{K_X+\frac{X_S}{X_H}} \cdot X_H$
$p_{2,a}$	$e^{-0.07\,(20-T)} \cdot k_{sto,20} \cdot \frac{S_O}{K_{H,O_2}+S_O} \cdot \frac{S_S}{K_{H,S_S}+S_S} \cdot X_H$
$p_{2,b}$	$e^{-0.07\,(20-T)} \cdot k_{sto,BAP,20} \cdot \frac{S_O}{K_{H,O_2}+S_O} \cdot \frac{S_{BAP}}{K_{BAP}+S_{BAP}} \cdot X_H$
$p_{2,c}$	$e^{-0.07\,(20-T)} \cdot k_{sto,UAP,20} \cdot \frac{S_O}{K_{H,O_2}+S_O} \cdot \frac{S_{UAP}}{K_{UAP}+S_{UAP}} \cdot X_H$
$p_{3,a}$	$e^{-0.07\,(20-T)} \cdot k_{sto,20} \cdot \eta_{H,NO} \cdot \frac{K_{H,O_2}}{K_{H,O_2}+S_O} \cdot \frac{S_S}{K_{H,SS}+S_S} \cdot \frac{S_{NO}}{K_{H,NO}+S_{NO}} \cdot X_H$
$p_{3,b}$	$e^{-0.07\,(20-T)} \cdot k_{sto,BAP,20} \cdot \eta_{H,NO} \cdot \frac{K_{H,O_2}}{K_{H,O_2}+S_O} \cdot \frac{S_{BAP}}{K_{BAP}+S_{BAP}} \cdot \frac{S_{NO}}{K_{H,NO}+S_{NO}} \cdot X_H$
$p_{3,c}$	$e^{-0.07\,(20-T)} \cdot k_{sto,UAP,20} \cdot \eta_{H,NO} \cdot \frac{K_{H,O_2}}{K_{H,O_2}+S_O} \cdot \frac{S_{UAP}}{K_{UAP}+S_{UAP}} \cdot \frac{S_{NO}}{K_{H,NO}+S_{NO}} \cdot X_H$
p_4	$e^{-0.07\,(20-T)} \cdot \mu_{H,20} \cdot \frac{S_O}{K_{H,O_2}+S_O} \cdot \frac{S_{NH}}{K_{H,NH_4}+S_{NH}} \cdot \frac{S_{ALK}}{K_{H,ALK}+S_{ALK}} \cdot \frac{\frac{X_{STO}}{X_H}}{K_{H,STO}+\frac{X_{STO}}{X_H}} \cdot X_H$
p_5	$e^{-0.07\,(20-T)} \cdot \mu_{H,20} \cdot \eta_{H,NO} \cdot \frac{K_{H,O_2}}{K_{H,O_2}+S_O} \cdot \frac{S_{NH}}{K_{H,NH_4}+S_{NH}} \cdot \frac{S_{ALK}}{K_{H,ALK}+S_{ALK}} \cdot \frac{\frac{X_{STO}}{X_H}}{K_{H,STO}+\frac{X_{STO}}{X_H}} \cdot \frac{S_{NO}}{K_{H,NO}+S_{NO}} \cdot X_H$
p_6	$e^{-0.07\,(20-T)} \cdot b_{H,20} \cdot \frac{S_O}{K_{H,O_2}+S_O} \cdot X_H$
p_7	$e^{-0.07\,(20-T)} \cdot b_{H,20} \cdot \eta_{H,end} \cdot \frac{K_{H,O_2}}{K_{H,O_2}+S_O} \cdot \frac{S_{NO}}{K_{H,NO}+S_{NO}} \cdot X_H$
p_8	$e^{-0.07\,(20-T)} \cdot b_{H,20} \cdot \frac{S_O}{K_{H,O_2}+S_O} \cdot X_{STO}$
p_9	$e^{-0.07\,(20-T)} \cdot b_{H,20} \cdot \eta_{H,end} \cdot \frac{K_{H,O_2}}{K_{H,O_2}+S_O} \cdot \frac{S_{NO}}{K_{H,NO}+S_{NO}} \cdot X_{STO}$
p_{10}	$e^{-0.105\,(20-T)} \cdot \mu_{AUT,20} \cdot \frac{S_O}{K_{N,O_2}+S_O} \cdot \frac{S_{NH}}{K_{N,NH_4}+S_{NH}} \cdot \frac{S_{ALK}}{K_{N,ALK}+S_{ALK}} \cdot X_A$
p_{11}	$e^{-0.105\,(20-T)} \cdot b_{AUT,20} \cdot \frac{S_O}{K_{H,O_2}+S_O} \cdot X_A$
p_{12}	$e^{-0.105\,(20-T)} \cdot b_{AUT,20} \cdot \eta_{N,end} \cdot \frac{S_{NO}}{K_{H,NO}+S_{NO}} \cdot \frac{K_{H,O_2}}{K_{H,O_2}+S_O} \cdot X_A$
p_{13}	$e^{-0.04\,(20-T)} \cdot k_{h.EPS,20} \cdot X_{EPS}$
p_{14}	$e^{-0.04\,(20-T)} \cdot k_{h,X_I,20} \cdot X_I$

where T denotes the temperature of the bulk liquid

Table 9.9: Stoichiometric parameters in the Petersen matrix of the CES-ASM3 model.

Parameter	Expression
x_{2a}	$Y_{STO,O_2} - 1$
x_{2b}	$Y_{STO,SMP,O_2} - 1$
x_{2c}	$Y_{STO,SMP,O_2} - 1$
x_{3a}	$\frac{Y_{STO,NO} - 1}{40/14}$
x_{3b}	$\frac{Y_{STO,SMP,NO} - 1}{40/14}$
x_{3c}	$\frac{Y_{STO,SMP,NO} - 1}{40/14}$
x_4	$1 - \frac{1-\gamma_H}{Y_{H,O_2}}$

Table 9.9: Stoichiometric parameters in the Petersen matrix of the CES-ASM3 model.

Parameter	Expression
x_5	$\frac{1-(1-\gamma_H)/(Y_{H,NO})}{40/14}$
x_6	$-(1-f_{X_I}-f_{BAP}-f_{EPSdh})$
x_7	$\frac{f_{X_I}+f_{BAP}+f_{EPS,dh}-1}{40/14}$
x_8	-1
x_9	$-14/40$
x_{10}	$1+\frac{-64/14-\gamma_A}{Y_A}$
x_{12}	$\frac{f_{X_I}+f_{BAP}+f_{EPS,da}-1}{40/14}$
y_1	$i_{N,X_S}-i_{N,S_I}\,f_{S_I}-(1-f_{S_I})\,i_{N,S_S}$
y_{2a}	$i_{N,S_S}-f_{EPS,STO}\,i_{N,EPS}$
y_{2b}	$i_{N,S_{BAP}}-f_{EPS,STO}\,i_{N,EPS}$
y_{2c}	$-f_{EPS,STO}\,i_{N,EPS}$
y_{3a}	$i_{N,S_S}-f_{EPS,STO}\,i_{N,EPS}$
y_{3b}	$i_{N,S_{BAP}}-f_{EPS,STO}\,i_{N,EPS}$
y_{3c}	$-f_{EPS,STO}\,i_{N,EPS}$
y_4	$-(1-f_{EPS,h})\,i_{N,BM}-f_{EPS,h}\,i_{N,EPS}$
y_5	$-(1-f_{EPS,h})\,i_{N,BM}-f_{EPS,h}\,i_{N,EPS}$
y_6	$-f_{X_I}\,i_{N,X_I}+i_{N,BM}-f_{BAP}\,i_{N,S_{BAP}}-f_{EPS,dh}\,i_{N,EPS}$
y_7	$-f_{X_I}\,i_{N,X_I}+i_{N,BM}-f_{BAP}\,i_{N,S_{BAP}}-f_{EPS,dh}\,i_{N,EPS}$
y_{10}	$-1/Y_A-(1-f_{EPS,a})\,i_{N,BM}-f_{EPS,a}\,i_{N,EPS}$
y_{11}	$-f_{X_I}\,i_{N,X_I}+i_{N,BM}-f_{BAP}\,i_{N,S_{BAP}}-f_{EPS,da}\,i_{N,EPS}$
y_{12}	$-f_{X_I}\,i_{N,X_I}+i_{N,BM}-f_{BAP}\,i_{N,S_{BAP}}-f_{EPS,da}\,i_{N,EPS}$
z_1	$y_1/14$
z_{2a}	$y_{2a}/14$
z_{2b}	$y_{2b}/14$
z_{2c}	$y_{2c}/14$
z_{3a}	$\frac{y_{3a}-x_{3a}}{14}$
z_{3b}	$\frac{y_{3b}}{14}-\frac{Y_{STO,SMP,NO}-1}{40}$
z_{3c}	$\frac{y_{3c}}{14}-\frac{Y_{STO,SMP,NO}-1}{40}$
z_4	$y_4/14$
z_5	$\frac{y_5-x_5}{14}$
z_6	$y_6/14$
z_7	$\frac{y_7-x_7}{14}$

Table 9.9: Stoichiometric parameters in the Petersen matrix of the CES-ASM3 model.

Parameter	Expression
z_9	$1/40$
z_{10}	$\frac{y_{10} - x_{10}}{14}$
z_{11}	$y_{11}/14$
z_{12}	$\frac{y_{12} - x_{12}}{14}$
t_1	$-i_{TSS,X_S}$
t_{2a}	$(Y_{STO,O_2} - f_{EPS,STO})\, i_{TSS,STO} + f_{EPS,STO}\, i_{TSS,EPS}$
t_{2b}	$(Y_{STO,O_2} - f_{EPS,STO})\, i_{TSS,STO} + f_{EPS,STO}\, i_{TSS,EPS}$
t_{2c}	$(Y_{STO,O_2} - f_{EPS,STO})\, i_{TSS,STO} + f_{EPS,STO}\, i_{TSS,EPS}$
t_{3a}	$(Y_{STO,NO} - f_{EPS,STO})\, i_{TSS,STO} + f_{EPS,STO}\, i_{TSS,EPS}$
t_{3b}	$(Y_{STO,NO} - f_{EPS,STO})\, i_{TSS,STO} + f_{EPS,STO}\, i_{TSS,EPS}$
t_{3c}	$(Y_{STO,NO} - f_{EPS,STO})\, i_{TSS,STO} + f_{EPS,STO}\, i_{TSS,EPS}$
t_4	$(-1/Y_{H,O_2})\, i_{TSS,STO} + (1 - f_{EPS,h})\, i_{TSS,BM} + f_{EPS,h}\, i_{TSS,EPS}$
t_5	$(-1/Y_{H,NO})\, i_{TSS,STO} + (1 - f_{EPS,h})\, i_{TSS,BM} + f_{EPS,h}\, i_{TSS,EPS}$
t_6	$-i_{TSS,BM} + f_{X_I}\, i_{TSS,X_I} + f_{EPSdh}\, i_{TSS,EPS}$
t_7	$-i_{TSS,BM} + f_{X_I}\, i_{TSS,X_I} + f_{EPSdh}\, i_{TSS,EPS}$
t_8	$-i_{TSS,STO}$
t_9	$-i_{TSS,STO}$
t_{10}	$i_{TSS,BM}\,(1 - f_{EPS,a}) + f_{EPS,a}\, i_{TSS,EPS}$
t_{11}	$-i_{TSS,BM} + f_{X_I}\, i_{TSS,X_I} + f_{EPS,da}\, i_{TSS,EPS}$
t_{12}	$-i_{TSS,BM} + f_{X_I}\, i_{TSS,X_I} + f_{EPS,da}\, i_{TSS,EPS}$
t_{13}	$-i_{TSS,EPS}$
t_{14}	$-i_{TSS,X_I}$

Table 9.10: Default stoichiometric and kinetic parameters in the CES-ASM3 model.

Parameter	Default value	Description	Unit
ASM3 kinetic parameters			
$k_{h,20}$	9	Hydrolysis rate constant	d^{-1}
$k_{sto,20}$	12.5	Maximum storage rate	d^{-1}
$\mu_{H,20}$	3.0	Maximum growth rate on substrate	d^{-1}
$b_{H,20}$	0.3	Rate constant for lysis and decay	d^{-1}
$\mu_{A,20}$	1	Maximum growth rate of X_A	d^{-1}

Table 9.10: Default stoichiometric and kinetic parameters in the CES-ASM3 model.

Parameter	Default value	Description	Unit
$b_{A,20}$	0.2	Decay rate of X_A	d^{-1}
ASM3 stoichiometric parameters			
i_{N,S_I}	0.01	N content of inert soluble COD S_I	gN $gCOD^{-1}$
i_{N,S_S}	0.03	N content of readily biodegradable substrate S_S	gN $gCOD^{-1}$
i_{N,X_I}	0.03	N content of inert particulate COD X_I	gN $gCOD^{-1}$
i_{N,X_S}	0.035	N content of slowly biodegradable substrate X_S	gN $gCOD^{-1}$
$i_{N,BM}$	0.07	N content of biomass, X_H, X_A	gN $gCOD^{-1}$
i_{TSS,X_I}	0.75	TSS to COD ratio for X_I	gTSS $gCOD^{-1}$
i_{TSS,X_S}	0.75	TSS to COD ratio for X_S	gTSS $gCOD^{-1}$
$i_{TSS,STO}$	0.6	TSS to COD ratio for X_{STO}	gTSS $gCOD^{-1}$
$i_{TSS,BM}$	0.9	TSS to COD ratio for biomass X_H, X_A	gTSS $gCOD^{-1}$
f_{S_I}	0.00	Production of S_I in hydrolysis	gCOD $gCOD^{-1}$
Y_{H,O_2}	0.80	Yield coefficient for heterotrophs in aerobic growth	gCOD $gCOD^{-1}$
$Y_{H,NO}$	0.65	Yield coefficient for heterotrophs in anoxic growth	gCOD $gCOD^{-1}$
Y_{STO,O_2}	0.80	Yield coefficient for X_{STO} in aerobic growth	gCOD $gCOD^{-1}$
$Y_{STO,NO}$	0.70	Yield coefficient for X_{STO} in anoxic growth	gCOD $gCOD^{-1}$
f_{X_I}	0.20	Fraction of X_I generated in biomass lysis	gCOD $gCOD^{-1}$
Y_A	0.24	Yield coefficient for autotrophs	gCOD $gCOD^{-1}$
K_X	1.0	Saturation/inhibition coefficient for X_S	gCOD $gCOD^{-1}$
$\eta_{H,NO}$	0.8	Reduction factor for denitrification	–
$\eta_{H,end}$	0.33	Reduction factor for b_H under anoxic conditions	–
$\eta_{N,end}$	0.5	Reduction factor for b_{AUT} under anoxic conditions	–
K_{H,O_2}	0.2	Saturation/inhibition coefficient for O_2, heter. growth	gO_2 m^{-3}
K_{H,S_S}	10	Saturation/inhibition coefficient for S_S, heter. growth	gCOD m^{-3}
$K_{H,NO}$	0.5	Saturation/inhibition coefficient for NO_3^-	gN m^{-3}
K_{H,NH_4}	0.01	Saturation/inhibition coefficient for NH_4^+	gN m^{-3}
$K_{H,ALK}$	0.1	Saturation coefficient for alkalinity (HCO_3^-)	$moleHCO_3^-$ m^{-3}
$K_{H,STO}$	0.1	Saturation coefficient for storage products	gCOD m^{-3}
K_{NO_2}	0.5	Saturation coefficient for oxygen in autotrophic growth	gO_2 m^{-3}
K_{N,NH_4}	1	Saturation coefficient for ammonium in autotrophic growth	gN m^{-3}
$K_{N,ALK}$	0.5	Saturation coefficient for alkalinity in autotrophic growth	$moleHCO_3^-$ m^{-3}
CES-ASM3 kinetic parameters			
$k_{STO,UAP,20}$	0.1	Maximum S_{UAP} storage rate	d^{-1}
$k_{STO,BAP,20}$	0.1	Maximum S_{BAP} storage rate	d^{-1}
$k_{h,EPS,20}$	0.17	Maximum X_{EPS} hydrolysis rate	d^{-1}
$k_{h,X_I,20}$	0.013	Maximum X_I hydrolysis rate	d^{-1}
CES-ASM3 stoichiometric parameters			
γ_H	0.0193	Fraction of S_{UAP} produced during cell growth of X_H	gCOD $gCOD^{-1}$
γ_A	0*	Fraction of S_{UAP} produced during cell growth of X_A	gCOD $gCOD^{-1}$
K_{UAP}	100	Saturation constant for S_{UAP}	gCOD m^{-3}
K_{BAP}	85	Saturation constant for S_{BAP}	gCOD m^{-3}

Table 9.10: Default stoichiometric and kinetic parameters in the CES-ASM3 model.

Parameter	Default value	Description	Unit
Y_{STO,SMP,O_2}	0.80	Aerobic yield of stored product per S_{BAP} and S_{UAP} (SMP)	gCOD gCOD^{-1}
$Y_{STO,SMP,NO}$	0.70	Anoxic yield of stored product per S_{BAP} and S_{UAP} (SMP)	gCOD gCOD^{-1}
f_{BAP}	0.0215	Fraction of S_{BAP} produced during cell lysis	gCOD gCOD^{-1}
$f_{EPS,h}$	0.12	Fraction of X_{EPS} produced during cell growth of X_H	gCOD gCOD^{-1}
$f_{EPS,a}$	0*	Fraction of X_{EPS} produced during cell growth of X_A	gCOD gCOD^{-1}
$f_{EPS,STO}$	0.12	Fraction of X_{EPS} produced during storage of internal substrates	gCOD gCOD^{-1}
$f_{EPS,dh}$	0.05	Fraction of X_{EPS} produced during cell decay of X_H	gCOD gCOD^{-1}
$f_{EPS,da}$	0*	Fraction of X_{EPS} produced during cell decay of X_A	gCOD gCOD^{-1}
f_S	0.4	Fraction of S_S produced during hydrolysis of X_{EPS}	gCOD gCOD^{-1}
$i_{N,S_{BAP}}$	0.07	N content of S_{BAP}	gN gCOD^{-1}
$i_{N,EPS}$	0.07	N content of X_{EPS}	gN gCOD^{-1}
$i_{TSS,EPS}$	0.9	TSS to COD ratio for X_{EPS}	gTSS gCOD^{-1}
$f_{N,I}$	0.02	Fraction of N released during X_I hydrolysis	gN gCOD^{-1}
$f_{I,I}$	0	Fraction of S_I generated during X_I hydrolysis	gCOD gCOD^{-1}

* EPS and SMP formation kinetic parameters for autotrophic biomass are set to zero as they have been found not to affect SMP and EPS concentrations. Parameter fitting was performed manually (parameters adjusted by hand) during the two described calibration exercises. Some of the parameters have been calculated as a function of other parameters which had been fitted, assumed or taken from the literature.
** Value of the parameter differs from the default value in the ASM3 model.